Modeling the Effect of Vapor Wall Deposition on the Formation of Secondary Organic Aerosol in Chamber Studies

Thesis by

Renee Catherine McVay

In Partial Fulfillment of the Requirements

for the Degree of

Doctor of Philosophy

California Institute of Technology

Pasadena, California

2016

(Defended 8 June 2016)

והארץ חנפה תחת ישביה

ישעיהו 24:5

Acknowledgements

I first wish to thank John Seinfeld, my graduate advisor at Caltech, for guidance and mentorship over the past five years. Your supportive yet hands-off advising style allowed me to develop the independence and maturity to become an independent researcher. I am grateful for the freedom you gave me to pursue many of my own projects and for your encouragement to travel to France for a five-month research collaboration. Your textbook introduced me to the field of atmospheric science, a field I have become passionate about. I am excited to continue in this field and look forward to collaborating with you in the future.

I thank Paul Wennberg for teaching me so much about atmospheric chemistry, both inside and outside the classroom. You were an invaluable resource as I waded through the α-pinene and isoprene mechanisms. Thank you as well for being willing to serve on my committee.

I thank Rick Flagan for teaching me about aerosol dynamics, which has been crucial for my research, and for serving on my committee. I also thank Mitchio Okumura for serving on my committee.

Je remercie Bernard Aumont pour m'accueillir à son laboratoire en France et pour m'enseigner à utiliser le modèle GECKO-A. C'était une très bonne expérience et j'ai beaucoup appris. Vous étiez toujours disponible à m'aider ou m'enseigner. Je remercie aussi Stéphanie La, Richard Valorso, et Marie Camredon pour m'aider à apprendre utiliser GECKO-A et pour m'aider à pratiquer mon français. Je vous remercie pour être de bons amis.

I thank all of my group members at Caltech, current and past. I thank Joey Ensberg for being an excellent mentor my first few years in the group. You introduced me to modeling and taught me much of what I know about Fortran and Linux. You were an excellent role model and provided a

good example of what it means to be a modeler. I thank Xuan Zhang for all our many collaborations. It was a great experience working closely with you and learning so much about how experiments are run. Your insight and suggestions made me a better modeler. I thank Becky Schwantes for numerous discussions about chamber experiments and for her patience and willingness to answer all of my questions. I've had a lot of fun traveling to conferences with you. I thank Jill Craven for being a fantastic mentor, both in research and in life. Your energy and excitement made our group fun. I loved being part of the Faith and Climate Change discussion group with you and discussing ways to reduce our environmental footprint. And I had a great time meeting up with you in Zurich, despite our near-death experience sledding down a mountain! I thank Kate Schilling for being a fun and supportive office-mate and for going on daily coffee breaks with me. I also thank other past and present group members: Matt Coggon, Natasha Hodas, Kelvin Bates, Tran Nguyen, Manabu Shiraiwa, Andi Zuend, Jean Chen, Christine Loza, Lindsay Yee, Stephanie Kong, Chris Kenseth, Bill Napier, Wilton Mui, Mandy Grantz, Yuanlong Huang, Hanna Lignell, Ran Zhao, and Johannes Leppa.

I thank my incoming Chemical Engineering class for helping me make it through the gauntlet that was first year and qualifying exams. Spending every Saturday and all of winter break holed up in the library studying or working on problem sets was more enjoyable than it should have been because we were together: Carolyn Richmonds, Mike Webb, Peter Rapp, Joel Schmidt, Mark Deimund, Josh Pacheco, Mu Wang, Cristofer Flowers, and Ryan Frederick.

As Francis Bacon said, "It is a mere and miserable solitude to want true friends; without which the world is but a wilderness." I could not have made it through my time at Caltech without the support of my wonderful friends, both near and far. I thank my lunch group for fun, energetic, meaningful, informative, and occassionally awkward conversations every day: Erik Verlage, Samantha Johnson, Kevin Fiedler, Fadl Saadi, John Lloyd, Mark Harfouche, Sunita Darbe, and Ivan Papusha. Our lunch group was frequently the highlight of my day. I thank Samantha Johnson for introducing me to the lunch group, for swapping recipes with me, and for being a very supportive friend. I thank Erik Verlage for being my music buddy, for advice and encouragement, and for introducing me to

Avalon! I thank those friends who indulged my wish to form a book club and tolerated my barrage of reminder emails about books and meetings: Erik Verlage, Samantha Johnson, Kevin Fiedler, Fadl Saadi, Mark Harfouche, Melissa Yeung, Andrew Hoff, Loren Vitello, and Max Jones. I thank my friends from Mosaic for their friendship and support, and for the chance to get out of the scientific bubble of Caltech: Stormie Dorrell, Katie Horning, Edrina Calderon, and Kris and Meghan YDeen. I thank the early-morning crowd in the women's locker room at the Caltech gym: Jan Burden, Michelle Effros, Ada Sann, Anne Marie Richardson-Gibbs, Olivia Dawson, Solange Ramirez, Nayiri Partamian, Liz O'Brien, and Mary Uchiyama. Seeing you all every morning motivated me to get up at 5:30 am even on days when I would have much rather kept sleeping! I thank my good friends from Texas: Tessia Lamison, Laura Acuff Tolentino, and Kathryn Nevels Baker for phone/skype chats and for visits back and forth. You have seen me through the worst and best times of my life. I thank David Corrigan for being so supportive and dependable, and for all the fun times dancing, sailing, hiking, and skiing. You made my last year here pretty terrific!

I thank Rebecca Rose, Cheryl Craig, Karen David, and Adriana Diaz for invaluable support, guidance, and counsel during several very difficult years.

I thank the Pasadena Public Library for enabling my reading obsession, which provided much-needed distraction and kept me sane.

Lastly, I thank my family. I thank my parents, Tillie and Duane McVay for their continued love and support. Because you are both engineering Ph.D.s, I grew up thinking that was the normal course of action. I realize now that it is not, but I am grateful for the example you provided. And though as a child, I rolled my eyes when Dad described the geological layers of the Grand Canyon while backpacking or Mom made us read every sign in the Glen Canyon Dam exhibit, you instilled in me a deep desire to learn that continues to motivate me. I thank my brother Paul McVay for being both a fun, teasing younger brother and an "older" brother whom I could go to for advice. And I'm sure you'll be horrified, but I wrote this entire thesis in Vim! I thank my sister Karen McVay for our long Skype calls and for being a good listener. I am so grateful to consider you one of my closest friends in addition to my sister.

Abstract

Laboratory chamber experiments are used to investigate formation of secondary organic aerosol (SOA) from biogenic and anthropogenic precursors under a variety of environmental conditions. Simulations of these experiments test our understanding of the prevailing chemistry of SOA formation as well as the dynamic processes occurring in the chamber itself. One dynamic process occurring in the chamber that was only recently recognized is the deposition of vapor species to the Teflon walls of the chamber. Low-volatility products formed from the oxidation of volatile organic compounds (VOCs) deposit on the walls rather than forming SOA, decreasing the amount of SOA formed (quantified as the SOA yield: mass of SOA formed per mass of VOC reacted). In this work, several modeling studies are presented that address the effect of vapor wall deposition on SOA formation in chambers.

A coupled vapor–particle dynamics model is used to examine the competition among the rates of gas-phase oxidation to low volatility products, wall deposition of these products, and mass transfer to the particle phase. The relative time scales of these rates control the amount of SOA formed by affecting the influence of vapor wall deposition. Simulations show that an effect on SOA yield of changing the vapor–particle mass transfer rate is only observed when SOA formation is kinetically limited. For systems with kinetically limited SOA formation, increasing the rate of vapor–particle mass transfer by increasing the concentration of seed particles is an effective way to minimize the effect of vapor wall deposition.

This coupled vapor–particle dynamics model is then applied to α-pinene ozonolysis SOA experiments. Experiments show that the SOA yield is affected when changing the oxidation rate but not when changing the rate of gas–particle mass transfer by changing the concentration of seed particles.

Model simulations show that the absence of an effect of changing the seed particle concentration is consistent with SOA formation being governed by quasi-equilibrium growth, in which gas–particle equilibrium is established much faster than the rate of change of the gas-phase concentration. The observed effect of oxidation rate on SOA yield arises due to the presence of vapor wall deposition: gas-phase oxidation products are produced more quickly and condense preferentially onto seed particles before being lost to the walls. Therefore, for α-pinene ozonolysis, increasing the oxidation rate is the most effective way to mitigate the influence of vapor wall deposition.

Finally, the detailed model GECKO-A (Generator for Explicit Chemistry and Kinetics of Organics in the Atmosphere) is used to simulate α-pinene photooxidation SOA experiments. Unexpectedly, α-pinene OH oxidation experiments show no effect when changing either the oxidation rate or the vapor–particle mass transfer rate, whereas GECKO-A predicts that changing the oxidation rate should drastically affect the SOA yield. Sensitivity studies show that the assumed magnitude of the vapor wall deposition rate can greatly affect conclusions drawn from comparisons between simulations and experiments. If vapor wall loss in the Caltech chamber is of order 10^{-5} s^{-1}, GECKO-A greatly overpredicts SOA during high UV experiments, likely due to an overprediction of second-generation products. However, if instead vapor wall loss in the Caltech chamber is of order 10^{-3} s^{-1}, GECKO-A greatly underpredicts SOA during low UV experiments, possibly due to missing autoxidation pathways in the α-pinene mechanism.

Published Content and Contributions

McVay, R. C., Cappa, C. D., and Seinfeld, J. H.: Vapor-Wall Deposition in Chambers: Theoretical Considerations, *Environmental Science and Technology*, 48, 10251–10258, doi:10.1021/es502170j, 2014.

R.C.M. participated in the design of the project, performed and analyzed simulations, and wrote the paper.

Nah, T., McVay, R. C., Zhang, X., Boyd, C. M., Seinfeld, J. H., and Ng, N. L.: Influence of Seed Aerosol Surface Area and Oxidation Rate on Vapor-Wall Deposition and SOA Mass Yields: A case study with α-pinene Ozonolysis, *Atmospheric Chemistry and Physics Discussion*, doi:10.5194/acp-2016-269, in review, 2016.

R.C.M. performed and analyzed simulations, and participated in the writing of the paper.

McVay, R. C., Zhang, X., Aumont, B., Valorso, R., Camredon, M., La, Y. S., Wennberg, P. O., and Seinfeld, J. H.: SOA formation from the photooxidation of α-pinene: systematic exploration of the simulation of chamber data, *Atmospheric Chemistry and Physics*, 16, 2785–2802, doi:10.5194/acp-16-2785-2016, 2016.

R.C.M. designed the project, performed and analyzed simulations, and wrote the paper.

Zhang, X., Cappa, C. D., Jathar, S. H., McVay, R. C., Ensberg, J. J., Kleeman, M. J., and Seinfeld, J. H.: Influence of vapor wall loss in laboratory chambers on yields of secondary organic aerosol, *Proceedings of the National Academy of Sciences of the United States of America*, 111, 5802–5807, doi:10.1073/pnas.1404727111, 2014.

R.C.M. analyzed data.

Zhang, X., Schwantes, R. H., McVay, R. C., Lignell, H., Coggon, M. M., Flagan, R. C., and Seinfeld, J. H.: Vapor wall deposition in Teflon chambers, *Atmospheric Chemistry and Physics*, 15, 4197–4214, doi:10.5194/acp-15-4197-2015, 2015.

R.C.M. analyzed data.

Zhang, X., McVay, R. C., Huang, D. D., Dalleska, N. F., Aumont, B., Flagan, R. C., and Seinfeld J. H.: Formation and evolution of molecular products in α-pinene secondary organic aerosol, *Proceedings of the National Academy of Sciences of the United States of America*, 112, 14168–14173, doi:10.1073/pnas.1517742112, 2015.

R.C.M. analyzed data and performed model simulations.

Contents

List of Tables

List of Figures

Chapter 1

Introduction

Atmospheric aerosols, defined as solid or liquid particles suspended in a gas with typical diameters of a few nanometers to tens of micrometers, have significant impacts on climate and human health (*Seinfeld and Pandis*, 2006). Aerosols affect climate directly by absorbing or scattering solar and infrared radiation, altering the radiative balance of the earth (*Forster et al.*, 2007). Aerosols also affect climate indirectly by acting as cloud condensation nuclei, thereby altering the cloud albedo or lifetime (*Forster et al.*, 2007). However, aerosols currently have the largest uncertainty of all radiative forcing due to uncertainties in emissions, optical properties, mixing, and vertical structure (*Forster et al.*, 2007). Furthermore, long-term exposure to fine particulate air pollution (particles less than 2.5 μm in diameter) has been shown to increase risk for cardiopulmonary and lung cancer mortality (*Pope et al.*, 2002). However, the overall premature mortality due to exposure to fine particulate air pollution is very uncertain, in part due to the difficulty of quantifying particulate exposure (*Ford and Heald*, 2016). Enhanced knowledge of aerosol concentrations and properties worldwide is necessary to more accurately predict their climate and health effects.

Atmospheric particles can be emitted directly (primary aerosols) or formed in the atmosphere by gas-to-particle conversion (secondary aerosol) (*Seinfeld and Pandis*, 2006). A significant fraction of atmospheric particulate mass (20-90%) is organic aerosol (*Kanakidou et al.*, 2005), in large part secondary organic aerosol (SOA) (*Jimenez et al.*, 2009). SOA is composed of a complex mixture of thousands of organic molecules, a substantial fraction of which have not been directly measured or identified (*Goldstein and Galbally*, 2007). SOA forms in the atmosphere through a series of steps (*Seinfeld and Pandis*, 2006):

1. Emission of volatile organic compounds (VOCs) from anthropogenic (vehicular, power plant, etc.) and biogenic (vegetation, volcanic, etc.) sources.

2. Gas-phase reaction of VOCs to produce oxidation products capable of forming SOA. These consist of reaction with OH radicals during daylight, reaction with nitrate radicals during nighttime, reaction with ozone during day and night, and photolysis (*Atkinson*, 2000). These reactions can be composed of single or multiple reaction steps and lead to products with a wide range of volatility.

3. Mass transfer of low-volatility oxidation products from the gas to the particle phase and/or heterogeneous and aqueous reactions of gas-phase products to form SOA (*Ervens et al.*, 2011; *Surratt et al.*, 2010).

4. Further transformation of SOA compounds within the particulate phase.

Environmental chambers are used worldwide to study gas-phase atmospheric chemistry and SOA formation. In batch environmental chambers, gases (and frequently particles) are introduced into a Teflon or glass chamber and allowed to mix. Gas-phase reactions are then initiated by the introduction of oxidants or use of radiation. Concentrations of gases and particles are monitored with a suite of instruments. The amount of SOA formed from the oxidation of different precursors is measured, and the SOA yield is calculated as the mass of SOA formed divided by the mass of precursor reacted. Detailed chemical and physical mechanisms are developed on the basis of chamber data in order to describe the gas-phase chemistry and SOA formation occurring in the chamber. Parameterizations and simplified models are developed from SOA yield data for use in regional and global chemical transport models (CTMs) (*Odum et al.*, 1996; *Carlton et al.*, 2010; *Pye et al.*, 2010).

Historically, models developed from chamber SOA data substantially underpredicted ambient SOA concentrations (*Heald et al.*, 2005; *Volkamer et al.*, 2006; *Ensberg et al.*, 2014). One reason for this underprediction has been shown to be vapor wall deposition (*Matsunaga and Ziemann*, 2010; *Kokkola et al.*, 2014; *Zhang et al.*, 2014; *Yeh and Ziemann*, 2014, 2015; *Bian et al.*, 2015; *La et al.*, 2016). Low-volatility products formed from the oxidation of VOCs deposit on the walls of the chamber rather than forming SOA, lowering the observed SOA yield. Because vapor wall deposition will not occur during atmospheric SOA formation, chamber-derived yields will then underpredict ambient SOA formation rates. Understanding and correcting for the influence of vapor wall deposition is crucial to accurately predicting ambient SOA levels worldwide.

Box models describing gas-phase chemistry, SOA formation, and aerosol dynamics are used to simulate chamber experiments to test our level of understanding of the chemical and physical processes occurring within the chamber. Comparison of simulation results with experimental observations can elucidate missing processes within the model or can illustrate the role of vapor wall

deposition in influencing observed SOA yields. Here, a number of studies are presented simulating a variety of chamber experiments using box models of varying complexity.

Chapter 2 describes the development of a coupled vapor–particle dynamics model, in which particle growth, wall deposition, and coagulation are simulated, along with simplified gas-phase chemistry and vapor wall deposition. Three different time scales govern the behavior of gas-phase species in a chamber (for an experiment without aqueous or heterogeneous reactions):

1. The oxidation rate: the rate at which gas-phase products form and then react to produce further products.

2. The rate of mass transfer to the particle: this rate is dependent on the particle surface area available for condensation, the compound-specific gas-phase diffusion coefficient, and the gas–particle accommodation coefficient α_p, the fraction of collisions that lead to incorporation of a vapor species into the particle (*Seinfeld and Pandis*, 2006).

3. The rate of vapor wall deposition: this rate is less well-understood but is thought to depend on the compound-specific gas-phase diffusion coefficient, the eddy diffusivity of the chamber, the surface-to-volume ratio of the chamber, and the gas–wall accommodation coefficient α_w (*McMurry and Grosjean*, 1985).

The model is used to illustrate how the relative time scales of these three rates affect the SOA yield. Furthermore, the role of vapor wall deposition in depressing the observed SOA yield changes as the relative time scales of these processes change.

Chapter 3 describes the application of this model to the α-pinene ozonolysis system. Simulations are compared to experiments in which both the oxidation rate and the vapor–particle mass transfer rate are varied separately and simultaneously. An effect on the SOA yield is observed when changing the oxidation rate but not when changing the vapor–particle mass transfer rate. These observations constrain the value of α_p and the rate of vapor wall deposition. It is concluded that for the α-pinene ozonolysis system, the most effective method to mitigate the effect of vapor wall deposition is to increase the oxidation rate.

Chapter 4 describes the simulation of α-pinene photooxidation SOA experiments using the detailed model GECKO-A (Generator for Explicit Chemistry and Kinetics of Organics in the Atmosphere). GECKO-A generates a near-explicit gas-phase oxidation mechanism for a selected VOC using reactions and rate constants based on experimental data and structure-activity relationships (*Aumont et al.*, 2005). α-pinene OH oxidation experiments were conducted in the Caltech chamber again varying both the oxidation rate and the vapor–particle mass transfer rate. Unexpectedly, experiments show no effect when changing either the oxidation rate or the vapor–particle mass transfer rate, whereas GECKO-A predicts that changing the oxidation rate should drastically affect the SOA yield. Various chemical and physical processes are explored to rationalize this discrepancy, and the still uncertain nature of vapor wall deposition is highlighted.

Finally, Chapter 5 summarizes the conclusions of these chapters and suggests future work.

Bibliography

Atkinson, R.: Atmospheric chemistry of VOCs and NOx, *Atmos. Environ.*, 34, 2063–2101, 2000.

Aumont, B., Szopa, S., and Madronich, S.: Modelling the evolution of organic carbon during its gas-phase tropospheric oxidation: development of an explicit model based on a self generating approach, *Atmos. Chem. Phys.*, 5, 2497–2517, doi:10.5194/acp-5-2497-2005, 2005.

Bian, Q., May, A. A., Kreidenweis, S. M., and Pierce, J. R.: Investigation of particle and vapor wall-loss effects on controlled wood-smoke smog-chamber experiments, *Atmos. Chem. Phys.*, 15, 11027–11045, doi:10.5194/acp-15-11027-2015, 2015.

Carlton, A. G., Bhave, P. V., Napelenok, S. L., Edney, E. O., Sarwar, G., Pinder, R. W., Pouliot, G. A., and Houyoux, M.: Model representation of secondary organic aerosol in CMAQv4.7, *Environ. Sci. Technol.*, 44, 8553-8560, 2010.

Ensberg, J. J., Hayes, P. L., Jimenez, J. L., Gilman, J. B., Kuster, W. C., de Gouw, J. A., Holloway, J. S., Gordon, T. D., Jathar, S., Robinson, A. L., and Seinfeld, J. H.: Emission factor ratios, SOA mass yields, and the impact of vehicular emissions on SOA formation, *Atmos. Chem. Phys.*, 14, 2383–2397, 2014.

Ervens, B., Turpin, B. J., and Weber, R. J.: Secondary organic aerosol formation in cloud droplets and aqueous particles (aqSOA): a review of laboratory, field and model studies, *Atmos. Chem. Phys.*, 11, 11069–11102, 2011.

Ford, B. and Heald, C. L.: Exploring the uncertainty associated with satellite-based estimates of premature mortality due to exposure to fine particulate matter, *Atmos. Chem. Phys.*, 16, 3499–3523, 2016.

Forster, P., Ramaswamy, V., Artaxo, P., Berntsen, T., Betts, R., Fahey, D. W., Haywood, J., Lean, J., Lowe, D. C., Myhre, G., Nganga, J., Prinn, R., Raga, G., Schulz, M., and Van Dorland, R.: Changes in atmospheric constituents and radiative forcing, In: Climate Change 2007: The Physical

Science Basis. Contribution of Working Group I to the Fourth Assessment Report of the Intergovernmental Panel on Climate Change [Solomon, S., D. Qin, M. Manning, Z. Chen, M. Marquis, K.B. Averyt, M.Tignor and H.L. Miller (eds.)]. Cambridge University Press, Cambridge, United Kingdom and New York, NY, USA, 2007.

Goldstein, A. H. and Galbally, I. E.: Known and unexplored organic constituents in the earth's atmosphere, *Environ. Sci. Technol.*, 41, 1514–1521, 2007.

Heald, C. L., Jacob, D. J., Park, R. J., Russell, L. M., Huebert, B. J., Seinfeld, J. H., Liao, H., and Weber, R. J.: A large organic aerosol source in the free troposphere missing from current models, *Geophys. Res. Lett.*, 32, L18809, doi:10.1029/2005GL023831, 2005.

Jimenez, J. L., Canagaratna, M. R., Donahue, N. M., Prévôt, A. S., Zhang, Q., Kroll, J. H., DeCarlo, P. F., Allan, J. D., Coe, H., Ng, N. L., Aiken, A. C., Docherty, K. S., Ulbrich, I. M., Grieshop, A. P., Robinson, A. L., Duplissy, J., Smith, J. D., Wilson, K. R., Lanz, V. A., Hueglin, C., Sun, Y. L., Tian, J., Laaksonen, A., Raatikainen, T., Rautiainen, J., Vaattovaara, P., Ehn, M., Kulmala, M., Tomlinson, J. M., Collins, D. R., Cubison, M. J., Dunlea, E. J., Huffman, J. A., Onasch, T. B., Alfarra, M. R., Williams, P. I., Bower, K., Kondo, Y., Schneider, J., Drewnick, F., Borrmann, S., Weimer, S., Demerjian, K., Salcedo, D., Cottrell, L., Griffin, R., Takami, A., Miyoshi, T., Hatakeyama, S., Shimono, A., Sun, J. Y., Zhang, Y. M., Dzepina, K., Kimmel, J. R., Sueper, D., Jayne, J. T., Herndon, S. C., Trimborn, A. M., Williams, L. R., Wood, E. C., Middlebrook, A. M., Kolb, C. E., Baltensperger, U., and Worsnop, D. R.: Evolution of organic aerosols in the atmosphere, *Science*, 326, 1525–1529, 2009.

Kanakidou, M., Seinfeld, J. H., Pandis, S. N., Barnes, I., Dentener, F. J., Facchini, M. C., Van Dingenen, R., Ervens, B., Nenes, A., Nielsen, C. J., Swietlicki, E., Putaud, J. P., Balkanski, Y., Fuzzi, S., Horth, J., Moortgat, G. K., Winterhalter, R., Myhre, C. E. L., Tsigaridis, K., Vignati, E., Stephanou, E. G., and Wilson, J.: Organic aerosol and global climate modelling: a review, *Atmos. Chem. Phys.*, 5, 1053–1123, 2005.

Kokkola, H., Yli-Pirilä, P., Vesterinen, M., Korhonen, H., Keskinen, H., Romakkaniemi, S., Hao,

L., Kortelainen, A., Joutsensaari, J., Worsnop, D. R., Virtanen, A., and Lehtinen, K. E. J.: The role of low volatile organics on secondary organic aerosol formation, *Atmos. Chem. Phys.*, 14, 1689–1700, doi:10.5194/acp-14-1689-2014, 2014.

La, Y. S., Camredon, M., Ziemann, P. J., Valorso, R., Matsunaga, A., Lannuque, V., Lee-Taylor, J., Hodzic, A., Madronich, S., and Aumont, B.: Impact of chamber wall loss of gaseous organic compounds on secondary organic aerosol formation: explicit modeling of SOA formation from alkane and alkene oxidation, *Atmos. Chem. Phys.*, 16, 1417–1431, doi:10.5194/acp-16-1417-2016, 2016.

Matsunaga, A. and Ziemann, P. J.: Gas-wall partitioning of organic compounds in a teflon film chamber and potential effects on reaction product and aerosol yield measurements, *Aerosol Sci. Tech.*, 44, 881–892, 2010.

McMurry, P. H. and Grosjean, D.: Gas and aerosol wall losses in teflon film smog chambers, *Environ. Sci. Technol.*, 19, 1176–1182, 1985.

Odum, J. R., Hoffmann, T., Bowman, F., Collins, D., Flagan, R. C., and Seinfeld, J. H.: Gas/particle partitioning and secondary organic aerosol yields, *Environ. Sci. Technol.*, 30, 2580-2585, 1996.

Pope, C. A., Burnett, R. T., Thun, M. J., Calle, E. E., Krewski, D., Kazuhiko, I., and Thurston, G. D.: Lung cancer, cardiopulmonary mortality, and long-term exposure to fine particulate air pollution, *J. Amer. Med. Assoc.*, 287, 1132–1141, 2002.

Pye, H. O. T., Chan, A. W. H., Barkley, M. P., and Seinfeld, J. H.: Global modeling of organic aerosol: the importance of reactive nitrogen (NOx and NO3), *Atmos. Chem. Phys.*, 10, 11261–11276, 2010.

Seinfeld, J. H. and Pandis, S. N.: Atmospheric Chemistry and Physics: From Air Pollution to Climate Change, 2nd Edn. Wiley, Hoboken, N. J., 2006.

Surratt, J. D., Chan, A. W. H., Eddingsaas, N. C., Chan, M., Loza, C. L., Kwan, A. J., Hersey, S. P.,

Flagan, R. C., and Seinfeld, J. H.: Reactive intermediates revealed in secondary organic aerosol formation from isoprene, *P. Natl. Acad. Sci. USA*, 107, 6640–6645, 2010.

Volkamer, R., Jimenez, J. L., San Martini, F., Dzepina, K., Zhang, Q., Salcedo, D., Molina, L. T., Worsnop, D. R., and Molina, M. J.: Secondary organic aerosol formation from anthropogenic air pollution: Rapid and higher than expected, *Geophys. Res. Lett.*, 33, L17811, doi:10.1029/2006GL026899, 2006.

Yeh, G. K. and Ziemann, P. J.: Alkyl nitrate formation from the reactions of C_8-C_{14} *n*-alkanes with OH radicals in the presence of NO_x: measured yields with essential corrections for gas-wall partitioning, *J. Phys. Chem. A.*, 118, 8147–8157, 2014.

Yeh, G. K. and Ziemann, P. J.: Gas-wall partitioning of oxygenated organic compounds: measurements, structure-activity relationships, and correlation with gas chromatographic retention factor, *Aerosol. Sci. Tech.*, 49, 727–738, 2015.

Zhang, X., Cappa, C. D., Jathar, S. H., McVay, R. C., Ensberg, J. J., Kleeman, M. J., and Seinfeld, J. H.: Influence of vapor wall-loss in laboratory chambers on yields of secondary organic aerosol, *P. Natl. Acad. Sci. USA*, 111, 5802–5807, doi:10.1073/pnas.1404727111, 2014.

Chapter 2

Vapor-Wall Deposition in Chambers: Theoretical Considerations *

*Reproduced with permission from "Vapor-Wall Deposition in Chambers: Theoretical Considerations" by McVay, R. C., Cappa, C. D., and Seinfeld, J. H., *Environmental Science and Technology*, 48, 10251–10258, doi:10.1021/es502170j, 2014.

2.1 Abstract

In order to constrain the effects of vapor–wall deposition on measured secondary organic aerosol (SOA) yields in laboratory chambers, researchers recently varied the seed aerosol surface area in toluene oxidation and observed a clear increase in the SOA yield with increasing seed surface area (*Zhang et al.*, 2014). Using a coupled vapor–particle dynamics model, we examine the extent to which this increase is the result of vapor–wall deposition versus kinetic limitations arising from imperfect accommodation of organic species into the particle phase. We show that a seed surface area dependence of the SOA yield is present only when condensation of vapors onto particles is kinetically limited. The existence of kinetic limitation can be predicted by comparing the characteristic time scales of gas-phase reaction, vapor–wall deposition, and gas–particle equilibration. The gas–particle equilibration time scale depends on the gas–particle accommodation coefficient α_p. Regardless of the extent of kinetic limitation, vapor–wall deposition depresses the SOA yield from that in its absence since vapor molecules that might otherwise condense on particles deposit on the walls. To accurately extrapolate chamber-derived yields to atmospheric conditions, both vapor–wall deposition and kinetic limitations must be taken into account.

2.2 Introduction

The formation of secondary organic aerosol (SOA) is represented in atmospheric models by SOA yields (mass of SOA formed per mass of parent volatile organic compound (VOC) reacted), which are determined in laboratory chambers. It has been established that current atmospheric models using chamber-derived yields significantly underpredict ambient SOA levels (*Ensberg et al.*, 2014; *de Gouw et al.*, 2005; *Volkamer et al.*, 2006; *Johnson et al.*, 2006; *de Gouw et al.*, 2008; *Kleinman et al.*, 2008; *Matsui et al.*, 2009). Recent work has suggested that experimentally determined SOA yields could be systematically biased low due to wall deposition of organic vapors that would otherwise contribute to SOA growth (*Loza et al.*, 2010; *Matsunaga and Ziemann*, 2010; *Pathak et al.*, 2008).

Zhang et al. (2014) reported the results of chamber studies aimed to constrain experimentally the effect of vapor–wall deposition on SOA yields. In these experiments, involving toluene as the parent VOC, the level of seed aerosol was systematically varied in order to modulate the competition between growing particles and the chamber walls for condensable vapors. The statistical oxidation model (SOM) of Cappa et al. (*Cappa et al.*, 2012, 2013), updated to account for dynamic partitioning between vapors and particles and vapors and the chamber walls, was fit to the data. The results demonstrate clear experimental evidence of the role of vapor–wall deposition on measured SOA yield. The present work analyzes theoretically the observed dependence of SOA yields on seed surface area by simulating the key elements of VOC oxidation and aerosol chamber dynamics. The representation of gas-phase VOC oxidation chemistry in such an analysis need not be complex, as the essential factors are the rate of progressive oxidation and the volatilities of the oxidation products. The present study is intended to provide a theoretical structure for assessing the effects of key processes on vapor–wall deposition in laboratory chamber studies of SOA formation.

2.3 Methods

2.3.1 Gas-Phase VOC Oxidation

To evaluate theoretically the effect of vapor–wall deposition in a typical chamber experiment, the gas-phase chemistry need only represent the progressive oxidation of a parent VOC. We consider oxidation of a parent VOC, species A, occurring sequentially according to A→B→C→D. Species A represents the completely volatile parent VOC, and species B–D are oxidation products, with mass saturation concentrations decreasing by 1 order of magnitude per generation of reaction. Each oxidation step can be considered to represent reaction with OH, although the chemical details are not required. With no loss of generality, each species in this idealized mechanism is assigned the same molecular weight (200 g mol^{-1}); in so doing, the maximum SOA yield possible is 1.0. Since oxidation leads to progressively lower volatility species, the maximum yield will always be reached at sufficiently long time if there are no additional vapor loss mechanisms, such as wall deposition.

2.3.2 Aerosol Dynamic Model

We have developed a coupled vapor–particle dynamics model following the framework of the aerosol parameter estimation (APE) model of *Pierce et al.* (2008). The model simulates coagulation, condensation/evaporation, and particle–wall and vapor–wall deposition in a well-mixed laboratory chamber in which a VOC is being oxidized to SOA. The SOA yield is determined as the ratio of the total mass of organic oxidation products condensed on both suspended and wall-deposited particles to the total mass of VOC reacted (both expressed in units of μg m^{-3}).

The aerosol size distribution is represented using fixed size bins, with specified mean diameters, so that the evolution of the chamber aerosol is reflected by the time variation of the particle number concentration in each bin. The aerosol general dynamic equation is expressed in terms of the particle size distribution function $n(D_p, t)$ as

$$\left(\frac{\partial n(D_p,t)}{\partial t}\right) = \left(\frac{\partial n(D_p,t)}{\partial t}\right)_{coag} + \left(\frac{\partial n(D_p,t)}{\partial t}\right)_{cond/evap} + \left(\frac{\partial n(D_p,t)}{\partial t}\right)_{wall\ loss} \tag{2.1}$$

where D_p is the particle diameter.

The equation governing the change in the number distribution due to coagulation is (*Seinfeld and Pandis*, 2006; *Pierce et al.*, 2008)

$$\left(\frac{\partial n(D_p,t)}{\partial t}\right)_{coag} = \frac{1}{2}\int_0^{D_p} K((D_p^3 - q^3)^{1/3}, q)n((D_p^3)^{1/3}, t)n(q,t)dq - n(D_p,t)\int_0^{\infty} K(q, D_p)n(q,t)dq \tag{2.2}$$

where $K(D_{p1}, D_{p2})$ is the coagulation kernel (*Seinfeld and Pandis*, 2006) between particles of diameters D_{p1} and D_{p2}.

The change in aerosol number distribution due to particle wall deposition is expressed as

$$\left(\frac{\partial n(D_p,t)}{\partial t}\right)_{wall\ loss} = -\beta(D_p)n(D_p,t) \tag{2.3}$$

where $\beta(D_p)$ is the size-dependent first-order loss rate coefficient. The $\beta(D_p)$ values used in the

present simulations are those determined experimentally for the Caltech chamber (*Loza et al.*, 2012). Particles that deposit on the wall during the course of an experiment are treated theoretically in one of two ways for computing the SOA yield (*Loza et al.*, 2012). In the so-called lower limit, once particles are lost to the walls, they are assumed to cease participation in condensation/evaporation or coagulation. The mass of condensed oxidation products on each particle at the time of its deposition is added to that of suspended particles in computing the SOA yield. The lower limit will be used in the simulations presented here. Historically, yields have also been reported using the so-called upper limit, in which particles lost to the wall are assumed to continue to participate in condensation/evaporation as if they had remained suspended. This approach includes some transfer of organic vapors to chamber walls but does not account for differences in wall versus particle transport time scales (*Zhang et al.*, 2014).

The rate of vapor condensation onto a spherical aerosol particle can be expressed as (*Seinfeld and Pandis*, 2006):

$$J_i = 2\pi D_i D_p (G_i - G_i^{eq}) F_{FS} \tag{2.4}$$

where G_i represents the gas-phase concentration of species i, and G_i^{eq} is the equilibrium gas-phase concentration, both expressed in μg m^{-3}. D_i is the molecular diffusivity of species i in air. The Fuchs-Sutugin correction for non-continuum gas-phase diffusion is (*Seinfeld and Pandis*, 2006)

$$F_{FS} = \frac{0.75\alpha_p(1+\mathrm{Kn})}{\mathrm{Kn}^2 + \mathrm{Kn} + 0.283\mathrm{Kn}\alpha_p + 0.75\alpha_p} \tag{2.5}$$

where α_p is the accommodation coefficient of the vapor species on the particle. Kn is the Knudsen number, defined as $\mathrm{Kn} = 2\lambda_{AB}/D_p$. λ_{AB} is the mean free path of the diffusing molecule in air, given by $\lambda_{AB} = 3D_i/\bar{c_A}$, and $\bar{c_A}$ is the mean speed of the diffusing molecule, $\bar{c_A} = (8RT/\pi M_A)^{1/2}$, where R is the ideal gas constant, T is the temperature, and M_A is the molecular weight of the diffusing molecule. Numerical values for all parameters that are used in the simulations are given in Table 2.1. Equations 2.4 and 2.5 are applied in each size bin to calculate the condensation or evaporation flux of each vapor species to or from a single particle and then scaled by the number

concentration of particles in that size bin. The flux summed over all size bins produces the rate of change of each vapor species due to evaporation or condensation.

The vapor–particle accommodation coefficient α_p encompasses all resistances to vapor–particle mass transfer, including surface accommodation and diffusion limitations in the particle phase (*Vaden et al.*, 2011; *Saleh et al.*, 2013). Vapor-particle accommodation coefficients are difficult to predict from molecular properties alone, but have been measured experimentally in both thermodenuders and evaporation chamber studies (*Stanier et al.*, 2007; *Saleh et al.*, 2013; *Grieshop et al.*, 2007; *Pierce et al.*, 2011; *Vaden et al.*, 2011). A range of values have been determined, even for the same systems. For example, *Stanier et al.* (2007) measured evaporation rates of α-pinene SOA using tandem differential mobility analysis and found accommodation coefficients <0.1. *Saleh et al.* (2013) measured gas–particle equilibrium time scales of α-pinene SOA in a thermodenuder and concluded the accommodation coefficient was of order 0.1. However, *Lee et al.* (2011) measured the volatility of monoterpene SOA (including that from α-pinene), and found that depending on the heat of vaporization assumed, accommodation coefficients needed to fit evaporation rates in a thermodenuder ranged from 0.002 to 0.05. *Grieshop et al.* (2007) used isothermal dilution to measure evaporation of α-pinene SOA, and deduced accommodation coefficients of order 0.001–0.01. It should be noted that the accommodation coefficients determined from these evaporation studies are not independent of the assumed volatility distribution for the SOA compounds, and may underestimate the influence of condensed phase reactions (*Trump et al.*, 2014). For toluene SOA, *Zhang et al.* (2014) measured SOA yields at different initial seed particle surface areas and found $\alpha_p = 0.001$ based on the observed aerosol growth; $\alpha_p = 0.001$ is used as the base value in the current simulations.

Calculation of G_i^{eq} is based on the saturation mass concentrations and the organic aerosol concentrations in the particle phase (*Pankow*, 1994; *Bowman et al.*, 1997):

$$G_i^{eq} = \frac{A_i\, C_i^*}{\sum_k A_k + M_{init}} \tag{2.6}$$

In this equation, A_i is the concentration of species i in the particle phase, C_i^* is the saturation concentration of species i, $\sum_k A_k$ is the sum of all species in the condensed phase, of which i is a

subset, and M_{init} is the mass concentration of any initially present absorbing organic concentration, all expressed in terms of μg m^{-3} of air. In general, G_i^{eq} varies for each size bin, based on the mass concentration of species i and the total organic concentration in that size bin. For computational convenience, owing to the presence of coagulation, the concentration of each organic species i in each size bin is not tracked dynamically; only the total condensed mass of each species over the entire size distribution is determined. The total mass in each size bin is also tracked, but this mass is not resolved into organic and inorganic masses because the number of particles in each size bin changes with time. Consequently, G_i^{eq} is calculated globally over the entire size distribution, based on the total mass of condensed species i and the total mass of condensed organics. (The total amount of species i in the condensed phase includes, as noted, the mass condensed onto particles that subsequently deposited on the wall.) We validated that this simplification of the actual size-dependent concentration dynamics captures the basic dependence of SOA yield on aerosol surface area by creating an equivalent moving bin model without coagulation, in which the total number of particles in each bin is conserved. The concentrations of each species i in each bin are then used to calculate G_i^{eq} for each bin. SOA yields predicted in this manner are virtually identical to those of the fixed bin model. A nominal (0.01 μg m^{-3}) nonvolatile initial organic seed aerosol concentration, M_{init}, is assumed to be present in the chamber regardless of initial inorganic seed number concentration merely to avoid numerical errors in Equation 2.6 at the first time step. Results are insensitive to this value up to 1 μg m^{-3}. Simulations (not shown) demonstrate that including the Kelvin effect in the calculation of the equilibrium vapor pressure has a negligible influence on the computed SOA yields for size distributions typical of seeded SOA chamber experiments.

Vapor–wall deposition is assumed to occur for species B–D and is characterized by a first-order deposition coefficient, $k_{wall,on}$ (*McMurry and Grosjean*, 1985):

$$k_{wall,on} = \left(\frac{A}{V}\right) \frac{\frac{\alpha_{wall}\bar{c}}{4}}{1.0 + \frac{\pi}{2}\left[\frac{\alpha_{wall}\bar{c}}{4(k_e D_i)^{0.5}}\right]} \tag{2.7}$$

where A/V is the surface area-to-volume ratio of the chamber, α_{wall} is the accommodation coefficient for vapor species on the wall layer, and k_e is the coefficient of eddy diffusion that characterizes the

degree of mixing in the chamber. For convenience, a single value of α_{wall} is assumed to apply for each of species B–D. The nominal value of α_{wall} is set to 1x10^{-5} (estimated experimentally in *Matsunaga and Ziemann* (2010)), and $k_e = 0.015$ s^{-1} (estimated for the Caltech chamber in *Zhang et al.* (2014) *SI*). These values yield $k_{wall,on} = 1.7\text{x}10^{-4}\text{s}^{-1}$, in good agreement with the optimal $k_{wall,on}$ obtained by fitting toluene SOA data in *Zhang et al.* (2014) ($k_{wall,on} = 2.5\text{x}10^{-4}\text{s}^{-1}$). The value of $k_{wall,on}$ is not sensitive to $\alpha_{wall} > 10^{-5}$ (see Fig. S4 of *Zhang et al.* (2014)).

Matsunaga and Ziemann (2010) showed that vapor species can dissolve and equilibrate in the Teflon walls of conventional laboratory chambers and introduced the parameter C_w to represent the capacity of Teflon to take up organics. While C_w has units of concentration, it does not necessarily represent a physical layer of organic material on the wall. In the present model, vapor interaction with the wall is similarly assumed to be reversible, with a rate of desorption of $k_{wall,off}$ (*Matsunaga and Ziemann*, 2010):

$$k_{wall,off} = \frac{k_{wall,on}}{K_w C_w} = k_{wall,on}\left(\frac{C_i^* M_w \gamma_w}{C_w M_p \gamma_p}\right) \tag{2.8}$$

where K_w is the vapor-wall partitioning coefficient, M_w is the effective molecular weight of the wall material, γ_w is the activity coefficient of the species in the wall layer, M_p is the average molecular weight of the organic species in the particle, and γ_p is the activity coefficient of the species in the particle. This equation is derived using the definition $K_w = RT/M_w\gamma_w P_i^o$ and the relationship $C_i^* = M_p\gamma_p P_i^o/RT$ to convert vapor pressure P_i^o into saturation concentration (*Matsunaga and Ziemann*, 2010). For convenience, we assume that $M_w = M_p$ and $\gamma_p = \gamma_w$ (*Zhang et al.*, 2014). As noted, the saturation concentration C_i^* is taken to decrease progressively by one order of magnitude for species B–D. The nominal value for C_w is set at 10 mg m^{-3}, based on observations of *Matsunaga and Ziemann* (2010) that C_w varies between 2 and 24 mg m^{-3} for different compounds.

2.3.3 Numerical Experiments

The coupled vapor-aerosol dynamics-wall model is used to explore the sensitivity of SOA yield to vapor–wall deposition. The assumed seed aerosol size distribution is based on typical distributions in

the Caltech laboratory chamber, encompassing 53 size bins, spanning the diameter range from 15 to 800 nm and log-normal with a standard deviation of 1.5. The initial particle number concentration is varied for different simulations in order to vary the total initial seed surface area. For each combination of parameters, seven different initial particle number concentrations, given in Table 2.2, are used in order to generate seven initial seed surface areas. The ratio of the initial seed surface area to the surface area of the chamber walls, based on the Caltech laboratory chambers, is also given in Table 2.2 for each case. The estimated surface area of the Caltech chamber is 41 m^2 assuming a rectangular shape with sides of 2.74 m, 2.43 m, and 2.69 m. Each simulation is run for 20 h of oxidation, and the SOA yield is calculated at the end of each simulation.

The parameters used in each simulation are given in Table 2.1. For $k[\mathrm{OH}]_{A\rightarrow B}$, the base value is assigned as 10^{-5} s^{-1} to represent the product of the toluene–OH rate constant of $5.6\text{x}10^{-12}$ cm^3 $molec^{-1}$ s^{-1} and an OH concentration of $\sim 2\text{x}10^6$ molec cm^{-3}, the approximate value observed during the toluene SOA experiments in *Zhang et al.* (2014). The k[OH] for each successive reaction, B→C, etc., is assumed to be five times the previous k[OH] in order to approximate the increase in reaction rate as species become more oxidized. Results are insensitive to this reaction rate scaling factor for values between 1 and 5. α_p is varied from 0.001, the best fit value determined by *Zhang et al.* (2014), to 1, the ideal accommodation. The saturation concentrations for species B–D are set as $[10^1\ 10^0\ 10^{-1}]$ μg m^{-3}.

2.4 Results and Discussion

2.4.1 Increased Partitioning versus Wall Deposition Effect

The clear increase in SOA yield observed by *Zhang et al.* (2014) with increased seed particle surface area can arise from two separate effects: (1) increased organic aerosol concentration C_{OA} via gas–particle partitioning if condensation is kinetically limited; and (2) reduction in the deposition of vapor organics to the wall. To evaluate these separate, but potentially overlapping, effects, numerical experiments were performed with different α_p values and in the presence or absence of vapor–wall

deposition at varying initial seed surface areas. Figure 2.1 shows C_{OA} at the end of 20 h numerical experiments starting with a parent VOC mixing ratio of 40 ppb (concentration G_A^0=327 μg m^{-3}). Pie charts are shown giving the distribution of products in the organic aerosol phase at the end of the simulations for the highest initial seed surface area. For $\alpha_p = 0.001$, C_{OA} increases as surface area increases both in the presence and absence of vapor–wall deposition. The surface area dependence of C_{OA} even in the absence of vapor–wall deposition indicates that the observation of surface area-dependent yields is not sufficient to prove the existence of vapor–wall deposition.

The increase in C_{OA} in both the presence and absence of wall deposition is attributable to the kinetic limitations on organic vapor condensation on particles imposed by a low value of α_p. This limitation is illustrated by comparing the characteristic time scale for gas–particle equilibration with the time scales for reaction and wall deposition (Figure 2.2). The characteristic time scale for gas–particle equilibration $\tau_{g,p}$ (i.e., the e-folding time for an aerosol to reestablish vapor–particle equilibrium after a slight perturbation) is (*Seinfeld and Pandis*, 2006)

$$\tau_{g,p} = \frac{1}{2\pi D_i(\sum_{bins} n(D_p) D_p F_{FS})} \tag{2.9}$$

This time scale is not necessarily that for vapor and particle phases to establish equilibrium in an SOA formation experiment, which depends on other factors such as the rate of reaction and the volatilities of the products (*Riipinen et al.*, 2010). In Figure 2.2, $\tau_{g,p}$ is calculated based on the initial size distribution, but its value will change with time as $n(D_p)$ in each size bin evolves (as discussed below). Quasi-equilibrium growth occurs when the net production rate of condensable vapors is slow compared to the time to establish gas–particle equilibrium; in this limit, the vapor and particle phases maintain equilibrium (*Shiraiwa et al.*, 2012; *Zhang et al.*, 2012). The magnitude of $\tau_{g,p}$ relative to time scales for other processes in the system governs the transition between kinetically limited and quasi-equilibrium growth (*Shiraiwa et al.*, 2012). Gas–particle equilibrium is governed by the total organic mass in the system and is not dependent on the surface area of the inorganic seed. In contrast, kinetically limited condensation, when $\tau_{g,p}$ is competitive with the time scale for production of condensable vapors, depends on the aerosol surface area. The

reaction time scale τ_{rxn} controls the production rate of condensable vapors. In Figure 2.2, τ_{rxn} is calculated based on $k[\mathrm{OH}]_{C\rightarrow D}$ because this reaction controls the production rate for the least volatile species. For $\alpha_p = 0.001$, $\tau_{g,p}$ exceeds τ_{rxn} at the lowest seed surface areas, indicating that condensation is kinetically limited, and C_{OA} for $\alpha_p = 0.001$ in the absence of wall deposition in Figure 2.1 consequently increases sharply with seed surface area. As the seed surface area increases at $\alpha_p = 0.001$, $\tau_{g,p}$ becomes an order of magnitude smaller than τ_{rxn}, and C_{OA} achieves a plateau at the highest seed surface areas. As α_p increases, $\tau_{g,p}$ decreases with respect to τ_{rxn} and condensation shifts towards quasi-equilibrium growth. This shift is evident in Figure 2.1, as C_{OA} in the absence of wall deposition becomes less dependent on seed surface area as α_p increases.

The presence of vapor–wall deposition introduces an additional time scale into the system, $\tau_{g,w} = 1/k_{wall,on}$, the characteristic time scale of vapor–wall deposition. $\tau_{g,p}$ must be less than τ_{rxn} and $\tau_{g,w}$ for quasi-equilibrium growth. When $\tau_{rxn} \approx \tau_{g,w}$, C_{OA} in the presence of vapor–wall deposition becomes less dependent on seed surface area as α_p increases. *Ehn et al.* (2014) observed SOA yields from the ozonolysis of α-pinene to increase with increasing particle surface area but required $\alpha_p = 1.0$ to fit the observed growth data. The observed vapor–wall deposition rate was much greater in their continuously stirred reactor than that in the Caltech chamber (0.011 s^{-1} versus 2.5x10^{-4} s^{-1}). In their reactor, $\tau_{g,p} \approx \tau_{g,w}$ even at $\alpha_p = 1.0$, and condensation is kinetically limited. The presence of vapor–wall deposition depresses the SOA yield from that calculated in the absence of wall deposition regardless of the value of α_p, as seen in Figure 2.1.

Condensation that is kinetically limited produces a narrowing of the particle size distribution, while condensation dominated by quasi-equilibrium growth produces a broadening of the size distribution (*Zhang et al.*, 2012; *Shiraiwa et al.*, 2012). If condensation shifts towards quasi-equilibrium growth as seed surface area is increased, the evolution of the particle size distribution should theoretically reflect this shift. However, as seed surface area is increased, coagulation will become more important and may mask any broadening of the size distribution, as smaller particles are scavenged by larger particles.

Particle distributions shown in the pie charts to the right of Figure 2.1 demonstrate another effect

of changing the gas–particle equilibration time: decreasing $\tau_{g,p}$ by increasing α_p shifts the product distribution towards earlier generation products. As $\tau_{g,p}$ decreases, partitioning of species B to the particle increases preferentially relative to conversion to C and (in the presence of wall deposition) deposition to the walls.

Yields as a function of C_{OA} at a constant temperature have historically been parameterized for use in air quality models (AQMs) such as CMAQ (*Carlton et al.*, 2010) with models such as the two-product model and the volatility basis set (VBS) (*Presto et al.*, 2006), each of which assumes instantaneous gas–particle equilibrium. As shown in Figure 2.1, for $\alpha_p = 0.001$ in this system, condensation is kinetically limited. Consequently, yields simulated starting with varying G_A^0 and at varying seed surface areas cannot be described by a single two-product or VBS fit (Figure 2.3). The points in Figure 2.3 were generated by varying both G_A^0 and seed surface area with (circles) and without (diamonds) vapor–wall deposition. The size of the markers increases as G_A^0 increases, and colors correspond to different values of the initial seed surface area. For simplicity, the lines were generated by fitting a two-product model to the datapoints. (This fit merely illustrates the discrepancy between the simulation results and common partitioning model predictions.) For a fixed G_A^0 (indicated in Figure 2.3 by markers of the same size), the SOA yield increases as both C_{OA} and seed surface area increase. At a fixed seed surface area, the yield increases as G_A^0 and C_{OA} increase. For a fixed final C_{OA} (visualized by drawing vertical lines in Figure 2.3), the yield increases as seed surface area increases and G_A^0 *decreases*. As a result of the kinetic limitation imposed by the low α_p, the yields depend on G_A^0 in addition to the seed surface area because the time required to reach a fixed C_{OA} depends on both parameters. As surface area increases, the same final C_{OA} is achieved with decreasing G_A^0, and the lower ΔVOC results in a higher yield.

By contrast, Figure A.1 shows simulations with $\alpha_p = 0.01$, i.e. 10 times larger. In the absence of vapor–wall deposition, condensation shifts towards quasi-equilibrium growth with the higher α_p, and the yields approach a single curve with little seed area dependence. Yields calculated in the presence of vapor–wall deposition for $\alpha_p = 0.01$ maintain a seed surface area dependence at low seed surface areas but lose this dependence at the highest surface areas. If a similar plot is generated

for $\alpha_p = 1.0$ (not shown), yields in the presence and absence of wall deposition collapse onto single (but separate) curves. This further illustrates that yields increase as seed surface area increases only when condensation is kinetically limited.

2.4.2 Influence of Volatility Distributions

The simulations are based on saturation concentrations that decrease by an order of magnitude per each generation of reaction. Different combinations of saturation concentrations were also used with $\alpha_p = 0.001$: $C_B^* = 10^2$ μg m^{-3} with subsequent saturation concentrations decreasing by an order of magnitude per generation, $C_B^* = 10^2$ or 10^3 μg m^{-3} with subsequent saturation concentrations decreasing by 2 orders of magnitude per generation, and all saturation concentrations set to zero. Each combination produces similar dependence of yield on seed surface area and a depression of the yield due to vapor–wall deposition (not shown). Saturation concentrations were also varied to determine if the observed behavior of *Zhang et al.* (2014) could be qualitatively reproduced using the present model. Figures A.2-A.5 show that the behavior can be reproduced, supporting the simplifications employed in the model. More discussion is given in Appendix A.

2.4.3 Influence of Reaction Time Scale

It has been observed experimentally that SOA yields are higher at faster oxidation rates, as the impact of vapor–wall deposition is lessened (*Ng et al.*, 2007). In Figure 2.4, $k[\mathrm{OH}]_{A\rightarrow B}$ is increased by an order of magnitude (with $k[\mathrm{OH}]_{B\rightarrow C}$ and $k[\mathrm{OH}]_{C\rightarrow D}$ again five times the previous $k[\mathrm{OH}]$), and yields are shown after 20 h of simulation (ΔVOC will necessarily vary with $k[\mathrm{OH}]_{A\rightarrow B}$ because the simulations are run for the equivalent amount of time rather than equivalent amount of OH exposure). For $k[\mathrm{OH}]_{A\rightarrow B} = 10^{-4}$ s^{-1} in the absence of vapor–wall deposition, the yield is approximately 1.0 regardless of seed surface area. The lack of dependence of yield on surface area seems to contradict the earlier discussion of kinetically limited versus quasi-equilibrium condensational growth: because increasing $k[\mathrm{OH}]_{A\rightarrow B}$ decreases τ_{rxn} with respect to $\tau_{g,p}$, the system should become more kinetically limited and show a stronger dependence on seed surface area. However,

this effect is observed only if yields are considered at equivalent OH exposure times (see Figure A.6). For $k[\mathrm{OH}]_{A\rightarrow B} = 10^{-4}$ s^{-1} in a 20 h simulation, species A is virtually depleted after 15 h. In the absence of vapor–wall deposition, the total concentration of condensable vapors (species B–D) is no longer changing except via condensation. Condensation will therefore be governed by quasi-equilibrium growth and is independent of seed surface area. In the presence of vapor–wall deposition, SOA yields maintain the surface area dependence for $k[\mathrm{OH}]_{A\rightarrow B} = 10^{-4}$ s^{-1} because vapor–wall deposition causes condensation to remain kinetically limited throughout the experiment.

This analysis reveals the subtleties in comparing yields measured under different experimental conditions such as different OH levels, because the effects of both kinetic condensation limitations and vapor–wall deposition will change with both the rate of oxidation and the duration of an experiment.

2.4.4 Evolution of $\tau_{g,p}$

The preceding analysis has been based on an assumed initial seed aerosol size distribution: yields are determined as a function of the initial seed surface area, and $\tau_{g,p}$ (Figure 2.2) is calculated based on the initial size distribution. The aerosol size distribution changes continuously as particles grow by condensation and are lost by coagulation or wall deposition. To examine the extent to which the initial size distribution is a robust metric for comparing different experimental conditions, we consider the time evolution of $\tau_{g,p}$ for $\alpha_p = 0.001$ with vapor–wall deposition at each initial seed surface area (Figure A.7). $\tau_{g,p}$ increases by approximately half an order of magnitude for all seed surface areas considered but remains within roughly one order of magnitude of $\tau_{g,w}$, for which vapor–wall deposition and vapor condensation remain competitive. Furthermore, differences in the values of $\tau_{g,p}$ between different intial seed surface areas remain similar throughout the simulation. These results indicate that although vapor condensation may become more kinetically limited as the oxidation progresses, the initial seed aerosol size distribution is a robust metric for comparing oxidation trajectories.

2.4.5 Vapor–Wall Deposition Bias in SOA Yield

Figures 2.1-2.4 indicate that the mere increase of SOA yield as seed surface area increases does not, in itself, prove that vapor–wall deposition is occurring. Furthermore, separating the impacts of condensational kinetic limitations and vapor–wall deposition is not straightforward. *Zhang et al.* (2014) introduced the concept of a wall deposition bias R_{wall},

$$R_{wall} = \frac{Y^0}{Y} \tag{2.10}$$

the ratio of the SOA yield in the absence of wall deposition, Y^0, to that obtained in an equivalent experiment with wall deposition, Y. R_{wall} is shown as a function of the seed surface area in Figure 2.5 for $\alpha_p = 0.001, 0.01, \text{and } 1$. For $\alpha_p = 0.001$ (and, to a lesser extent, $\alpha_p = 0.01$), R_{wall} decreases as the seed surface area increases and then reaches a plateau, as observed experimentally in *Zhang et al.* (2014). The analysis presented here suggests that the behavior of R_{wall} at low surface areas is influenced by the kinetic limitations that are a consequence of a small α_p. Furthermore, R_{wall} changes with $k[\text{OH}]_{A\rightarrow B}$ and G_{AO} because these parameters affect yields calculated both in the presence and absence of vapor–wall deposition.

The multi-faceted dependencies of SOA yield and R_{wall} complicate the extrapolation of chamber-derived yields to atmospheric models. If condensation in the atmosphere is dominated by quasi-equilibrium growth, chamber experiments should be carried out, if possible, at high seed surface areas, with high G_{AO} and under rapid oxidation conditions, to minimize the effects of both kinetic limitations and vapor–wall deposition. If, however, condensation in the atmosphere is also kinetically limited, chamber experiments can be conducted at seed concentrations typical of those in the atmosphere and a vapor–particle dynamics model, similar to those presented here and in *Zhang et al.* (2014), can be used in order to correct for vapor–wall deposition. Thus, challenges will need to be met in designing experiments that simultaneously minimize the magnitude of vapor deposition to the chamber walls yet ensure conditions similar to those encountered in the ambient atmosphere. The strong sensitivity of R_{wall} to the value of the vapor–particle accommodation coefficient α_p points to

a need for constraining the value of this parameter, establishing the extent to which it varies among different chemical systems and under differing reaction conditions, and ultimately determining a value most relevant for the atmosphere.

2.4.6 Effect of Semi-solid SOA

The present simulations do not explicitly address the microphysical nature of the particles. Recent evidence suggests that SOA often exists in a semi-solid state (e.g. *Virtanen et al.* (2010); *Saukko et al.* (2012)). In such a case, $\tau_{g,p}$ increases relative to $\tau_{g,w}$ and τ_{rxn} (*Shiraiwa et al.*, 2012). Retarded gas–particle partitioning resulting from condensed phase diffusion limitations will drive the system towards kinetically limited SOA growth, and is essentially captured by α_p values < 1. Overall particle growth is dictated by accommodation into the particle bulk and is thus sensitive to limitations imposed by particle phase morphology. The results here demonstrate that the dependence of both the SOA yield and R_{wall} on seed surface area is important only when SOA growth is kinetically limited. This suggests that SOA systems in which the SOA exists in a semi-solid state may exhibit a stronger seed surface area dependence and may exhibit larger wall biases than those for which the SOA is more liquid-like (i.e., in which bulk accommodation is not a retarding factor).

Figures A.1-A.7 are provided in Appendix A.

Acknowledgements

We thank Jeffrey Pierce for providing the APE model, which served as a framework for the present model, and Sally Ng and Joseph Ensberg for useful input. R.C.M. acknowledges support by a National Science Foundation Graduate Research Fellowship under Grant No. DGE-1144469. This work was supported by the Office of Science (BER), U.S. Department of Energy grant DE-SC0006626, NOAA Climate Program Office's AC4 program, award #NA13OAR4310058, and the State of California Air Resources Board Contract 12-312.

Bibliography

Bowman, F. M., Odum, J. R., Seinfeld, J. H., and Pandis, S. N.: Mathematical model for gas-particle partitioning of secondary organic aerosols, *Atmos. Environ.*, 31, 3921–3931, 1997.

Cappa, C. D. and Wilson, K. R.: Multi-generation gas-phase oxidation, equilibrium partitioning, and the formation and evolution of secondary organic aerosol, *Atmos. Chem. Phys.*, 12, 9505–9528, 2012.

Cappa, C. D., Zhang, X., Loza, C. L., Craven, J. S., Yee, L. D., and Seinfeld, J. H.: Application of the Statistical Oxidation Model (SOM) to secondary organic aerosol formation from photooxidation of C12 Alkanes, *Atmos. Chem. Phys.*, 13, 1591–1606, 2013.

Carlton, A. G., Bhave, P. V., Napelenok, S. L., Edney, E. D., Sarwar, G., Pinder, R. W., Pouliot, G. A., and Houyoux, M.: Model Representation of Secondary Organic Aerosol in CMAQv4.7, *Environ. Sci. Technol.* 44, 8553-8560, doi:10.1021/es100636q, 2010.

de Gouw, J. A., Middlebrook, A. M., Warneke, C., Goldan, P. D., Kuster, W. C., Roberts, J. M., Fehsenfeld, F. C., Worsnop, D. R., Canagaratna, M. R., Pszenny, A. A. P., Keene, W. C., Marchewka, M., Bertman, S. B., and Bates, T. S.: Budget of organic carbon in a polluted atmosphere: Results from the New England Air Quality Study in 2002, *J. Geophys. Res.-Atmos.*, 110, 27781–27794, 2005.

de Gouw, J. A., Brock, C. A., Atlas, E. L., Bates, T. S., Fehsenfeld, F. C., Goldan, P. D., Holloway, J. S., Kuster, W. C., Lerner, B. M., Matther, B. M., Middlebrook, A. M., Onasch, T. B., Peltier, R. E., Quinn, P. K., Senff, C. J., Stohl, A., Sullivan, A. P., Trainer, M., Warneke, C., Weber, R. J., and Williams, E. J.: Sources of particulate matter in the northeastern United States: 1. Direct emissions and secondary formation of organic matter in urban plumes, *J. Geophys. Res.-Atmos.*, 113, 27781, 2008.

Ehn, M., Thornton, J. A., Kleist, E., Sipilä, M., Junninen, H., Pullinen, I., Springer, M., Rubach, F., Tillmann, R., Lee, B., Lopez-Hilfiker, F., Andres, S., Acir, I.-H., Rissanen, M., Jokinen, T.,

Schobesberger, S., Kangasluoma, J., Kontkanen, J., Nieminen, T., Kurtén, T., Nielsen, L. B., Jørgensen, S., Kjaergaard, H. G., Canagaratna, M., Maso, M. D., Berndt, T., Petäjä, T., Wahner, A., Kerminen, V.-M. Kulmala, M., Worsnop, D. R., Wildt, J., and Mentel, T. F.: A large source of low-volatility secondary organic aerosol, *Nature*, 506, 476–479, doi:10.1038/nature13032, 2014.

Ensberg, J. J., Hayes, P. L., Jimenez, J. L., Gilman, J. B., Kuster, W. C., de Gouw, J. A., Holloway, J. S., Gordon, T. D., Jathar, S., Robinson, A. L., and Seinfeld, J. H.: Emission factor ratios, SOA mass yields, and the impact of vehicular emissions on SOA formation, *Atmos. Chem. Phys.*, 14, 2383–2397, doi:10.5194/acpd-14-2383-2014, 2014.

Grieshop, A. P., Donahue, N. M., and Robinson, A. L.: Is the gas-particle partitioning in alpha-pinene secondary organic aerosol reversible? *Geophys. Res. Lett*, 34, L14810, 2007.

Johnson, D., Utembe, S. R., Jenkin, M. E., Derwent, R. G., Hayman, G. D., Alfarra, M. R., Coe, H., and McFiggans, G.: Simulating regional scale secondary organic aerosol formation during the TORCH 2003 campaign in the southern UK, *Atmos. Chem. Phys.*, 6, 403-418, 2006.

Kleinman, L. I., Springston, S. R., Daum, P. H., Lee, Y.-N., Nunnermacker, L. J., Senum, G. I., Wang, J., Weinstein-Lloyd, J., Alexander, M. L., Hubbe, J., Ortega, J., Canagaratna, M. R., and Jayne, J.: The time evolution of aerosol composition over the Mexico City plateau, *Atmos. Chem. Phys.*, 8, 1559–1575, 2008.

Lee, B., Pierce, J. R., Engelhart, G. J., and Pandis, S. N.: Volatility of secondary organic aerosol from the ozonolysis of monoterpenes, *Atmos. Environ.*, 45, 2443–2452, 2011.

Loza, C. L., Chan, A. W., Galloway, M. M., Keutsch, F. N., Flagan, R. C., and Seinfeld, J. H.: Characterization of vapor wall loss in laboratory chambers, *Environ. Sci. Technol.*, 44, 5074–5078, 2010.

Loza, C. L., Chhabra, P. S., Yee, L. D., Craven, J. S., Flagan, R. C., and Seinfeld, J. H.: Chemical

aging of m-xylene secondary organic aerosol: laboratory chamber study, *Atmos. Chem. Phys.*, 12, 151–167, 2012.

Matsui, H., Koike, M., Takegawa, N., Kondo, Y., Griffin, R. J., Miyazaki, Y., Yokouchi, Y., and Ohara, T.: Secondary organic aerosol formation in urban air: temporal variations and possible contributions from unidentified hydrocarbons, *J. Geophys. Res.-Atmos.*, 114, 2009.

Matsunaga, A. and Ziemann, P. J.: Gas-wall partitioning of organic compounds in a teflon film chamber and potential effects on reaction product and aerosol yield measurements, *Aerosol Sci. Technol.*, 44, 881–892, 2010.

McMurry, P. H. and Grosjean, D.: Gas and aerosol wall losses in teflon film smog chambers, *Environ. Sci. Technol.*, 19, 1176–1182, 1985.

Ng, N. L., Kroll, J. H., Chan, A. W. H., Chhabra, P. S., Flagan, R. C., and Seinfeld, J. H.: Secondary organic aerosol formation from *m*-xylene, toluene, and benzene, *Atmos. Chem. Phys.*, 7, 1-14, 2007.

Pankow, J. F.: An absorption model of gas/particle partitioning of organic compounds in the atmosphere, *Atmos. Environ.*, 28, 185–188, 1994.

Pathak, R., Donahue, N. M., and Pandis, S. N.; Ozonolysis of β-pinene: Temperature dependence of secondary organic aerosol mass fraction, *Environ. Sci. Technol.*, 42, 5081–5086, 2008.

Pierce, J. R., Engelhard, G. J., Hildebrandt, L., Weitkamp, E. A., Pathak, R. K., Donahue, N. M., Robinson, A. L., Adams, P. J., and Pandis, S. N.: Constraining particle evolution from wall losses, coagulation and condensation-evaporation in smog-chamber experiments: Optimal estimation based on size distribution measurements, *Aerosol Sci. Technol.*, 41, 1001-1015, 2008.

Pierce, J. R., Riipinen, I., Kulmala, M., Ehn, M., Petaja, T., Junninen, H., Worsnop, D. R., and Donahue, N. M.: Quantification of the volatility of secondary organic compounds in ultrafine particles during nucleation events, *Atmos. Chem. Phys.*, 11, 9019-9036, 2011.

Presto, A. A. and Donahue, N. M.: Investigation of α-pinene + ozone secondary organic aerosol formation at low total aerosol mass, *Environ. Sci. Technol.*, 40, 3536–3543, 2006.

Riipinen, I., Pierce, J. R., Donahue, N. M., and Pandis, S. N.: Equilibration time scales of organic aerosol inside thermodenuders: Evaporation kinetics versus thermodynamics, *Atmos. Environ.*, 44, 597–607, 2010.

Saleh, R., Donahue, N. M., and Robinson, A. L.: Time scales for gas-particle partitioning equilibration of secondary organic aerosol formed from alpha-pinene ozonolysis, *Environ. Sci. Technol.*, 47, 5588-5594, 2013.

Saukko, E., Lambe, A. T., Massoli, P., Koop, T., Wright, J. P., Croasdale, D. R., Pedernera, D. A., Onasch, T. B., Laaksonen, A., Davidovits, P., Worsnop, D. R., and Virtanen, A.: Humidity-dependent phase state of SOA particles from biogenic and anthropogenic precursors, *Atmos. Chem. Phys.*, 12, 7517-7529, 2012.

Seinfeld, J. H. and Pandis, S. N.: Atmospheric Chemistry and Physics: From Air Pollution to Climate Change, 2nd Edn. Wiley, Hoboken, N. J., 2006.

Shiraiwa, M. and Seinfeld, J. H.: Equilibration timescale of atmospheric secondary organic aerosol partitioning, *Geophys. Res. Lett.*, 39, L24801, 2012.

Stanier, C. O., Pathak, R. K., and Pandis, S. N.: Measurements of the volatility of aerosols from alpha-pinene ozonolysis, *Environ. Sci. Technol.*, 41, 2756-2763, 2007.

Trump, E. R. and Donahue, N. M.: Oligomer formation within secondary organic aerosols: equilibrium and dynamic considerations, *Atmos. Chem. Phys.*, 14, 3691-3701, 2014.

Vaden, T. D., Imre, D., Beranek, J., Shrivastava, M., and Zelenyuk, A.: Evaporation kinetics and phase of laboratory and ambient secondary organic aerosol, *P. Natl. Acad. Sci. USA*, 108, 2190-2195, 2011.

Virtanen, A., Joutsensaari, J., Koop, T., Kannosto, J., Yli-Pirilä, P., Leskinen, J., Mäkelä, J. M.,

Holopainen, J. K., Pöschl, U., Kulmala, M., Worsnop, D. R., and Laaksonen, A.: An amorphous solid state of biogenic secondary organic aerosol particles, *Nature*, 467, 824–827, 2010.

Volkamer, R., Jimenez, J. L., San Martini, F., Dzepina, K., Zhang, Q., Salcedo, D., Molina, L. T., Worsnop, D. R., and Molina, M. J.: Secondary organic aerosol formation from anthropogenic air pollution: rapid and higher than expected, *Geophys. Res. Lett.*, 33, 2006.

Zhang, X., Pandis, S. P., and Seinfeld, J. H.: Diffusion-limited versus quasi-equilibrium aerosol growth, *Aerosol Sci. Technol.*, 46, 874-885, 2012.

Zhang, X., Cappa, C. D., Jathar, S. H., McVay, R. C., Ensberg, J. J., Kleeman, M. J., and Seinfeld, J. H.: Influence of vapor wall-loss in laboratory chambers on yields of secondary organic aerosol, *P. Natl. Acad. Sci. USA*, 111, 5802–5807, doi:10.1073/pnas.1404727111, 2014.

parameter	definition	value
α_p	accommodation coefficient of vapor species on particle	varied
A/V	surface-area-to-volume ratio of the chamber	1.6 m^{-1}
α_{wall}	accommodation coefficient of vapor species on the wall	10^{-5}
C_i^*	saturation concentrations for species B–D	[10^1 10^0 10^{-1}] μg m^{-3}
C_w	equivalent wall organic aerosol concentration	10 mg m^{-3}
D_i	gas-phase diffusivity of species i	3x10^{-6} m^2 s^{-1}
G_A^0	initial parent VOC concentration	327 μg m^{-3} (40 ppb)
k_e	coefficient of eddy diffusion in chamber	0.015 s^{-1}
$k[\mathrm{OH}]_{A\rightarrow B}$	product of reaction rate constant and OH concentration	10^{-5} s^{-1}
$k_{wall,on}$	first-order vapor–wall deposition coefficient	1.7x10^{-4} s^{-1}
M_i	species molecular weight	200 g mol^{-1}
M_{init}	initially absorbing organic material in seed aerosol	0.01 μg m^{-3}
P	pressure	1x10^5 Pa
ρ	particle density	1700 kg m^{-3}
T	temperature	298 K

Table 2.1: Simulation parameters

case	initial particle concentration (cm^{-3})	mean particle diameter (nm)	initial particle surface area (μm^2 cm^{-3})	ratio of initial particle SA to wall SA
1	10,000	100	4.4x10^2	2.7x10^{-4}
2	20,000	100	8.7x10^2	5.3x10^{-4}
3	50,000	100	2.2x10^3	1.3x10^{-3}
4	100,000	100	4.4x10^3	2.7x10^{-3}
5	200,000	100	8.7x10^3	5.3x10^{-3}
6	400,000	100	1.7x10^4	1.1x10^{-2}
7	600,000	100	2.6x10^4	1.6x10^{-2}

Table 2.2: Assumed initial aerosol number distribution parameters

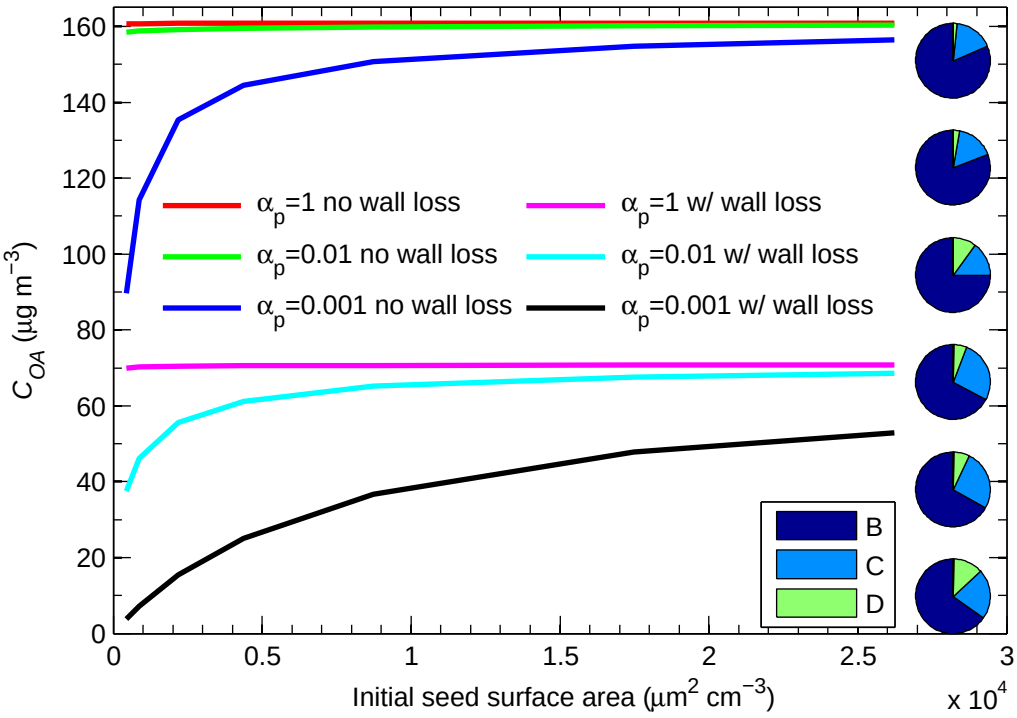

Figure 2.1: Final organic aerosol concentration C_{OA} after 20 h of simulation as a function of the initial seed surface area for simulations beginning with 40 ppb of parent VOC. Conditions for the simulations are given in Table 2.1 and 2.2. Different combinations of α_p and presence or absence of wall deposition are shown. The pie charts at the right show the product distribution at the end of the simulation at the highest seed surface area considered for each of the six simulations. The pie charts appear top to bottom in the same top-to-bottom order as the C_{OA} curves.

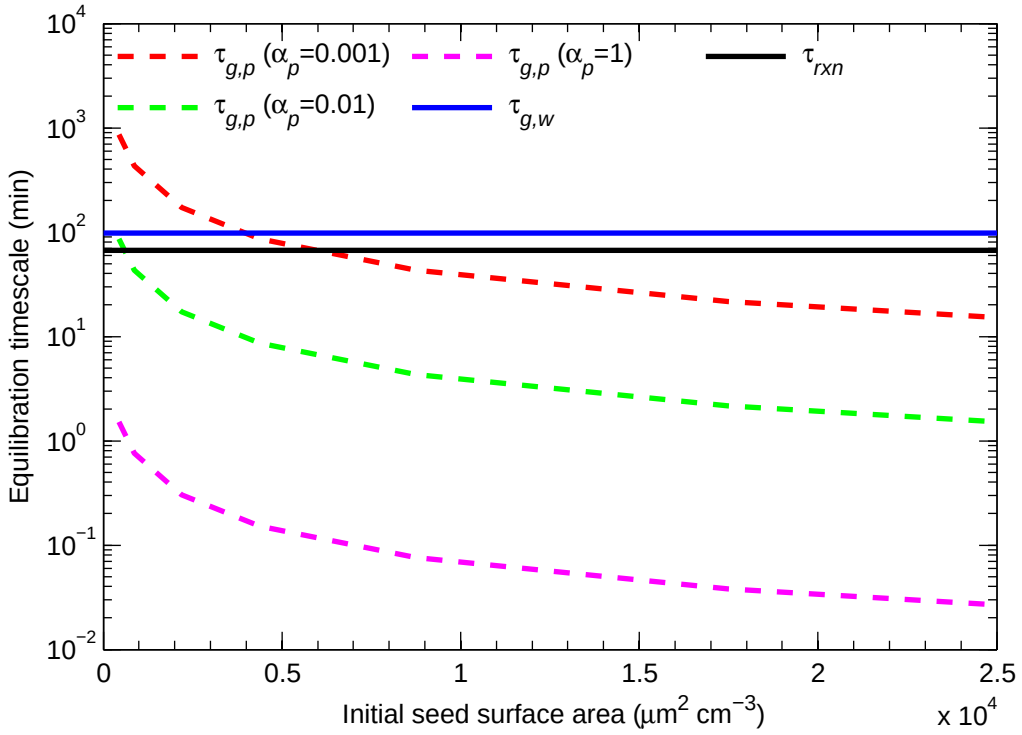

Figure 2.2: Equilibration time scale for gas–particle partitioning as a function of the initial seed surface area for different values of the vapor–particle accommodation coefficient, α_p. The equilibration time scale for gas–wall partitioning ($\tau_{g,w} = 1/k_{wall,on}$) and the time scale for reaction ($\tau_{rxn} = 1/(k[\mathrm{OH}]_{C\rightarrow D})$) are shown as horizontal lines as these time scales are independent of seed surface area.

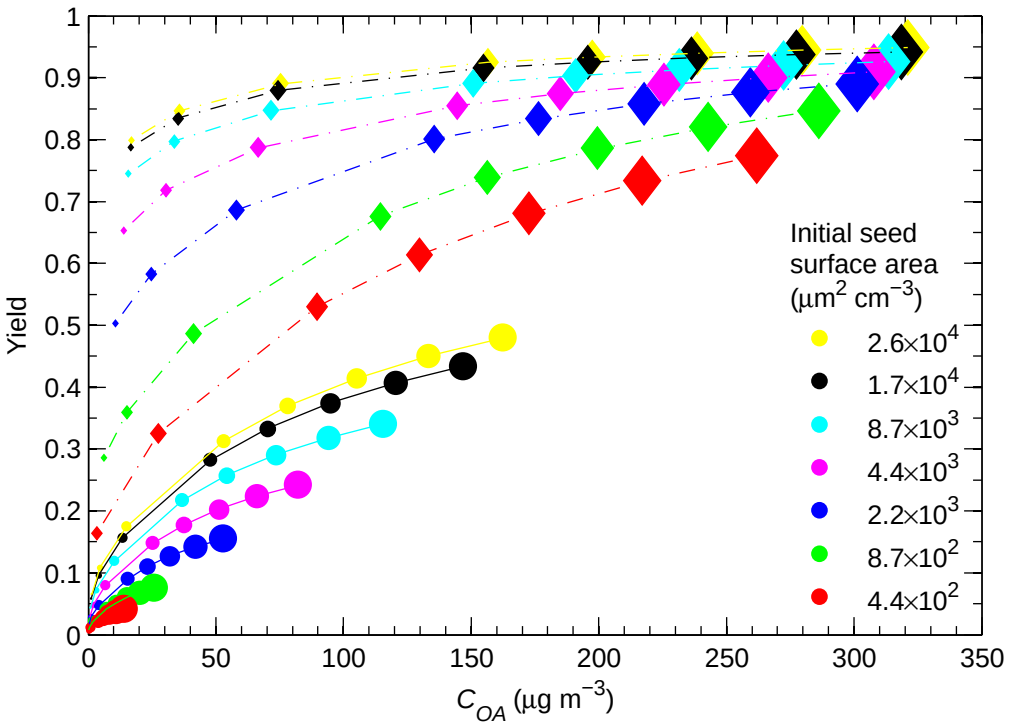

Figure 2.3: SOA yields after 20 h of simulation as a function of the final organic aerosol concentration C_{OA} for $\alpha_p = 0.001$. The points on the curve were generated by varying the initial parent VOC concentration G_A^0 with (circles) and without (diamonds) vapor–wall deposition. The size of the markers increases as G_A^0 increases and colors correspond to different values of the initial seed surface area. The lines were generated by fitting a two-product model to the datapoints.

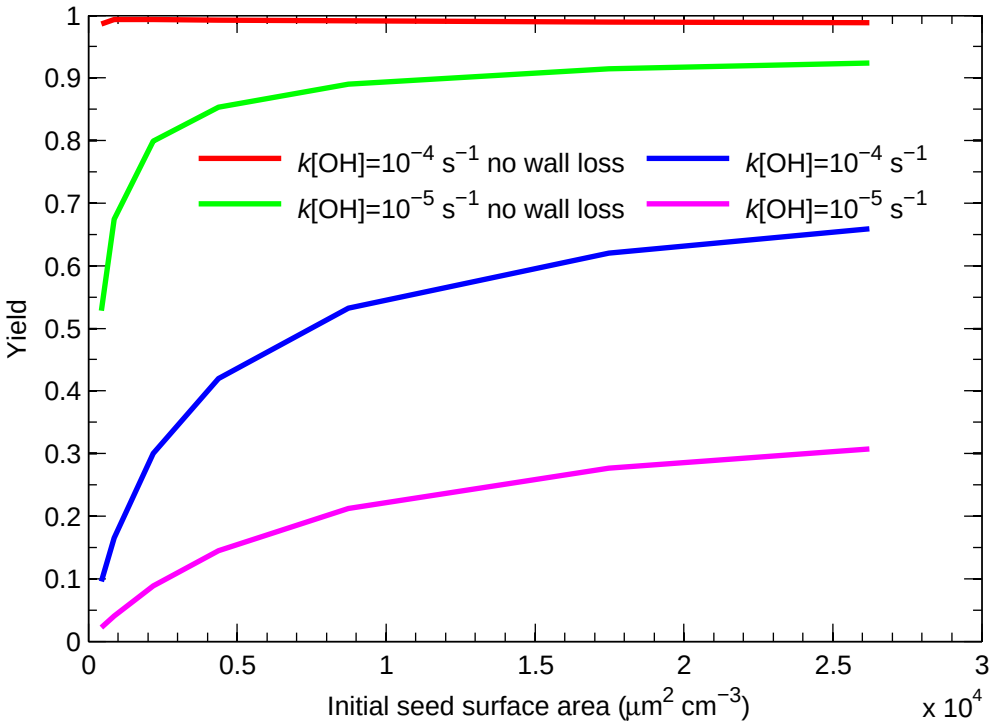

Figure 2.4: SOA yields after 20 h of simulation as a function of the initial seed surface area for simulations with $\alpha_p = 0.001$ for different values of $k[\mathrm{OH}]_{A\rightarrow B}$, in the presence and absence of wall deposition.

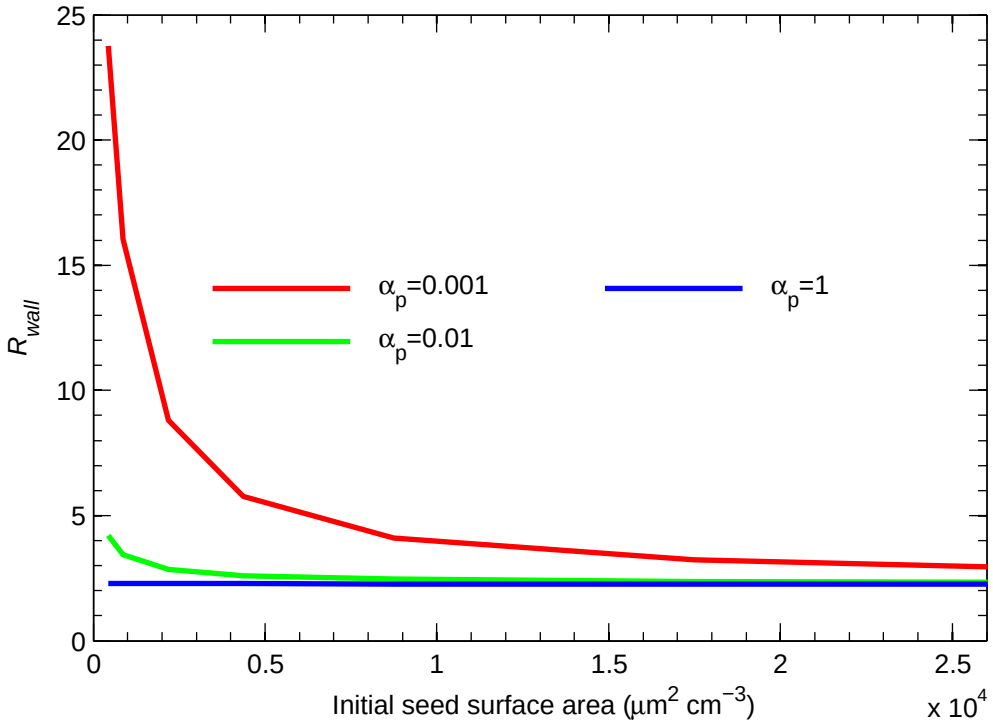

Figure 2.5: Wall deposition bias, $R_{wall} = Y^0/Y$, as a function of the initial seed surface area at different values of the vapor–particle accommodation coefficient α_p with an initial VOC mixing ratio of 40 ppb and $k[\mathrm{OH}]_{A\to B} = 10^{-5}$ s^{-1}.

Chapter 3

Influence of Seed Aerosol Surface Area and Oxidation Rate on Vapor-Wall Deposition and SOA Mass Yields: A Case Study with α-pinene Ozonolysis *

*Reproduced with permission from "Influence of Seed Aerosol Surface Area and Oxidation Rate on Vapor-Wall Deposition and SOA Mass Yields: A case study with α-pinene Ozonolysis" by Nah, T., McVay, R. C., Zhang, X., Boyd, C. M., Seinfeld, J. H., and Ng, N. L., *Atmospheric Chemistry and Physics Discussion*, doi:10.5194/acp-2016-269, 2016.

3.1 Abstract

Laboratory chambers, invaluable in atmospheric chemistry and aerosol formation studies, are subject to particle and vapor wall deposition, processes that need to be accounted for in order to accurately determine secondary organic aerosol (SOA) mass yields. Although particle wall deposition is reasonably well understood and usually accounted for, vapor wall deposition is less so. The effects of vapor wall deposition on SOA mass yields in chamber experiments can be constrained experimentally by increasing the seed aerosol surface area to promote the preferential condensation of SOA-forming vapors onto seed aerosol. Here, we study the influence of seed aerosol surface area and oxidation rate on SOA formation in α-pinene ozonolysis. The observations are analyzed using a coupled vapor-particle dynamics model to interpret the roles of gas-particle partitioning (quasi-equilibrium vs. kinetically-limited SOA growth) and α-pinene oxidation rate in influencing vapor wall deposition. We find that the SOA growth rate and mass yields are independent of seed surface area within the range of seed surface area concentrations used in this study. This behavior arises when the condensation of SOA-forming vapors is dominated by quasi-equilibrium growth. Faster α-pinene oxidation rates and higher SOA mass yields are observed at increasing O_3 concentrations for the same initial α-pinene concentration. When the α-pinene oxidation rate increases relative to vapor wall deposition, rapidly produced SOA-forming oxidation products condense more readily onto seed aerosol particles, resulting in higher SOA mass yields. Our results indicate that the extent to which vapor wall deposition affects SOA mass yields depends on the particular VOC system, and can be mitigated through the use of excess oxidant concentrations.

3.2 Introduction

Secondary organic aerosol (SOA), formed from the oxidation of volatile and intermediate volatility organic compounds (VOCs and IVOCs), contributes a significant fraction of the global organic aerosol burden (*Kanakidou et al.*, 2005; *Hallquist et al.*, 2009; *Tsigaridis et al.*, 2014). SOA formation studies, which are typically conducted in laboratory chambers in the presence of seed aerosol

particles, provide fundamental data that can be used to predict the rate of atmospheric SOA formation. An essential parameter of interest in laboratory chamber studies is the SOA mass yield (Y), which is defined as the ratio of mass concentration of SOA formed to mass concentration of parent hydrocarbon reacted ((ΔHC), $Y = \Delta Mo/\Delta HC$ (*Odum et al.*, 1996, 1997a,b)). The measured SOA mass yields can subsequently be applied in atmospheric models to predict regional and global organic aerosol burdens. In order to obtain accurate SOA mass yields from the evolving aerosol size distribution in chamber experiments, the loss of both particles and vapors to the chamber walls needs to be accurately accounted for (*Crump and Seinfeld*, 1981; *McMurry and Grosjean*, 1985; *McMurry and Rader*, 1985; *Cocker et al.*, 2001a; *Weitkamp et al.*, 2007; *Pierce et al.*, 2008; *Hildebrandt et al.*, 2009; *Loza et al.*, 2010; *Matsunaga and Ziemann*, 2010; *Loza et al.*, 2012; *Kokkola et al.*, 2014; *McVay et al.*, 2014; *Yeh and Ziemann*, 2014; *Zhang et al.*, 2014; *Yeh and Ziemann*, 2015; *Zhang et al.*, 2015a; *La et al.*, 2016).

The mechanisms by which particles in chambers deposit on chamber walls are reasonably well understood. Particles are transported to the boundary layer on the chamber walls via diffusion, gravitational settling, and electrostatic forces (*Crump and Seinfeld*, 1981; *McMurry and Grosjean*, 1985; *McMurry and Rader*, 1985; *Pierce et al.*, 2008). The rate at which particles are transported to the edge of the boundary layer is dictated primarily by mixing conditions in the chamber. An effective approach for characterizing particle wall loss involves measuring the size-dependent wall loss rates of polydisperse inert seed aerosol (e.g. ammonium sulfate particles) injected into the chamber during seed-only experiments (*Keywood et al.*, 2004; *Pierce et al.*, 2008). The observed particle number concentration decay in each size bin is then fitted to a first-order exponential decay from which the first-order wall loss coefficients are determined as a function of particle size. These wall loss coefficients are subsequently used to correct for size-dependent particle wall loss in actual SOA formation experiments.

Vapor-wall deposition mechanisms in chambers are not as well understood or accounted for as those for particles. The degree to which SOA-forming vapors deposit onto chamber walls is governed by the rate at which these gas-phase organic molecules are transported to the walls, the strength of

adherence of the organic molecule to the wall, and the extent of reversible vapor-wall partitioning (*Loza et al.*, 2010; *Matsunaga and Ziemann*, 2010; *Zhang et al.*, 2015a). For example, *Loza et al.* (2010) showed that the loss of 2,3-epoxy-1,4-butanediol, an isoprene oxidation product analogue, to walls in the Caltech chamber was essentially irreversible on short time scales but became reversible on longer time scales. In contrast, glyoxal, a common isoprene oxidation product, exhibited reversible vapor-wall partitioning over all time scales. Recent studies show that SOA mass yields measured in chamber experiments can be significantly underestimated due to wall deposition of SOA-forming vapors that would otherwise contribute to SOA growth (*McVay et al.*, 2014; *Zhang et al.*, 2014; *La et al.*, 2016). *Zhang et al.* (2014) found that chamber-derived SOA mass yields from toluene photooxidation may be underestimated by as much as a factor of four as a result of vapor wall loss. Consequently, the use of underestimated chamber-derived SOA mass yields in atmospheric models will lead to the underprediction of ambient SOA mass concentrations (*Cappa et al.*, 2016).

For the toluene photooxidation system, *Zhang et al.* (2014) showed that the measured SOA mass yields increased with increasing seed aerosol surface area, demonstrating that increasing the seed-to-chamber surface area ratio promoted the condensation of SOA-forming vapors onto seed aerosol particles. However, increasing the seed aerosol surface area to promote condensation of SOA-forming vapors onto seed aerosol particles may not be effective in all VOC oxidation systems. A modeling study by *McVay et al.* (2014) showed that the SOA mass yield depends on seed aerosol surface area only in cases where the condensation of SOA-forming vapors onto seed aerosol particles is kinetically limited (i.e., the timescale for gas-particle equilibrium is competitive with or greater than the timescale for reaction and vapor-wall deposition). In addition to the seed aerosol surface area, VOC oxidation rate may also play an important role in the effect of vapor wall loss on SOA formation. *Ng et al.* (2007) showed that the SOA mass yields from m-xylene photooxidation are dependent on the oxidation rate, with higher OH concentrations (hence faster oxidation rates) resulting in higher SOA mass yields. It was suggested that the oxidation rate effect could arise as a result of competition between growing particles and chamber walls for condensable VOC oxidation products (*Ng et al.*, 2007). However, *McVay et al.* (2016) reported similar SOA growth at low and high OH

concentrations in α-pinene photooxidation. Taken together, these studies show the importance of understanding how gas-particle partitioning and VOC oxidation rate impact vapor-wall deposition and SOA mass yields in laboratory chamber experiments.

In this study, we examine the influence of seed aerosol surface area and oxidation rate on SOA formation in α-pinene ozonolysis chamber experiments. α-pinene is the most abundant monoterpene, with global emissions estimated to be 66 Tg yr^{-1} (*Guenther et al.*, 2012). Ozonolysis is the major atmospheric oxidation pathway of α-pinene, and is estimated to account for reaction of ~46 % of emitted α-pinene (*Griffin et al.*, 1999; *Capouet et al.*, 2008). α-pinene ozonolysis, a major source of atmospheric SOA on both regional and global scales (*Kanakidou et al.*, 2005; *Hallquist et al.*, 2009; *Carlton et al.*, 2010; *Pye et al.*, 2010), has been the subject of numerous studies (*Hoffmann et al.*, 1997; *Griffin et al.*, 1999; *Cocker et al.*, 2001b; *Gao et al.*, 2004; *Presto et al.*, 2005; *Presto and Donahue*, 2006; *Pathak et al.*, 2007a,b; *Song et al.*, 2007; *Shilling et al.*, 2008; *Henry et al.*, 2012; *Ehn et al.*, 2014; *Kristensen et al.*, 2014; *Zhang et al.*, 2015b). Here, we measure the α-pinene SOA mass yield as a function of seed aerosol surface area concentration (0 to 3000 μm^2 cm^{-3}) and O_3 mixing ratio (100 vs. 500 ppb). These results are analyzed using a coupled vapor-particle dynamics model to evaluate the roles of gas-particle partitioning and VOC oxidation rate in influencing vapor-wall deposition effects on the measured SOA mass yields.

3.3 Experimental

3.3.1 Dark α-pinene Ozonolysis Experiments

Experiments were conducted in the Georgia Tech Environmental Chamber (GTEC) facility. Details of the dual chamber facility are provided elsewhere (*Boyd et al.*, 2015). Only one FEP Teflon chamber (volume 13 m^3) was used for the entirety of this study. Before each experiment, the chamber is flushed with dried, purified air for at least 36 h until the aerosol number concentration is <30 cm^{-3}. All experiments were conducted under dry conditions (< 5 % RH) at room temperature (25 °C). NO_x mixing ratios in these experiments are < 1 ppb. Experimental conditions are summarized in

Table 3.1.

22 ppm of cyclohexane (Sigma Aldrich, $\geq$ 99.9 %) was first injected into the chamber to act as an OH scavenger ($\sim$440 times the initial α-pinene concentration). After the cyclohexane concentration had stabilized in the chamber for 30 min, a known concentration ($\sim$50 ppb in all experiments) of α-pinene (Sigma Aldrich, $>$ 99 %) was injected into the chamber, followed by inorganic seed aerosol via atomization of an aqueous ammonium sulfate (AS) solution (in seeded experiments). To vary the seed aerosol surface area, different concentrations of AS solutions were used to generate seed aerosol particles in the seeded experiments. In the "low AS" experiments, a 0.015 M AS solution was used to generate seed particles, and the resulting initial total AS seed surface area concentration was $\sim$1000 μm^2 cm^{-3}. In the "high AS" experiments, a 0.05 M AS solution was used to generate seed aerosol particles, and the resulting initial total AS seed surface area concentration was $\sim$3000 μm^2 cm^{-3}. In selected experiments, no seed aerosol particles were introduced into the chamber and SOA was formed via nucleation. After the seed aerosol concentration in the chamber stabilized, O_3 (100 or 500 ppb), which was generated by passing purified air into a photochemical cell (Jelight 610), was introduced into the chamber. The start of O_3 injection into the chamber marked the beginning of the reaction (i.e., reaction time = 0 min). The initial α-pinene:O_3 molar ratio was fixed at approximately 1:2 and 1:10 in the 100 and 500 ppb O_3 experiments, respectively. O_3 was injected into the chamber for 13.5 and 54.25 min in the 100 and 500 ppb O_3 experiments, respectively, to achieve the desired O_3 concentrations. The O_3 injection times were established in separate experiments in which only O_3 was injected into the chamber.

The α-pinene and O_3 concentrations were measured by a Gas Chromatograph-Flame Ionization Detector (GC-FID, Agilent 7890A) and O_3 monitor (Teledyne T400), respectively. GC-FID measurements were taken 12 min apart. A High Resolution Time-of-Flight Aerosol Mass Spectrometer (HR-ToF-AMS, Aerodyne Research Inc.) was used to measure the aerosol elemental composition (*DeCarlo et al.*, 2006; *Canagaratna et al.*, 2015). Details on the operation of the HR-ToF-AMS and its data analysis are described elsewhere (*Canagaratna et al.*, 2015). Aerosol size distributions, number and volume concentrations were measured by a Scanning Mobility Particle Sizer (SMPS, TSI),

which consists of a Differential Mobility Analyzer (DMA, TSI 3081) and a Condensation Particle Counter (CPC, TSI 3775). For nucleation and low AS experiments, the measured aerosol size range was set to 14 to 686 nm diameter. For high AS experiments, the measured aerosol size range was set to 17 to 983 nm. Prior checks were made to confirm that no particles larger than 686 nm were detected in the nucleation and low AS experiments. The SOA mass concentrations reported in this study were measured using the SMPS. The SOA density was calculated from the ratio of the aerosol size distributions measured by the HR-ToF-AMS and the SMPS during nucleation experiments (*DeCarlo et al.*, 2004; *Bahreini et al.*, 2005).

3.3.2 Particle Wall Deposition Correction

Particle wall deposition needs to be accounted for to determine the SOA mass concentration in the chamber. Two limiting assumptions have traditionally been made regarding interactions between particles deposited on the chamber walls and suspended vapors when accounting for particle wall loss in the computation of SOA mass yields (*Weitkamp et al.*, 2007; *Hildebrandt et al.*, 2009; *Loza et al.*, 2012; *Zhang et al.*, 2014). The first case assumes that particles deposited on the walls cease to interact with suspended vapors, and therefore the SOA mass present on these deposited particles does not change after deposition (*Loza et al.*, 2012; *Zhang et al.*, 2014). Adding the SOA mass present on these deposited particles to that present on the suspended particles provides a lower bound of the total SOA mass concentration. In the second case, it is assumed that particles deposited on the walls continue to interact with suspended vapors as if these particles had remained suspended, and therefore the SOA mass present on these deposited particles increases at the same rate as those suspended (*Hildebrandt et al.*, 2009; *Weitkamp et al.*, 2007). Thus, this case provides an upper bound of the total SOA mass concentration due to the additional uptake of suspended vapors to wall-deposited particles. However, it must be kept in mind that the calculated SOA mass concentration can be underestimated even in the upper bound case since the calculation accounts neither for differences in the vapor-particle and vapor-wall interaction and transport timescales nor for the significantly larger amount of absorbing mass of the chamber walls (relative to the deposited particles) for suspended vapors (*McVay et al.*,

2014; *Zhang et al.*, 2014; *McVay et al.*, 2016).

In this study, we calculate SOA mass yields using the lower bound of the total SOA mass concentration obtained from SMPS measurements, which has been described in detail previously (*Loza et al.*, 2012), and will be reviewed briefly here. For each particle size bin i at each time increment Δt, the particle number distribution deposited on the wall ($n_{w,i,j}$) is:

$$n_{w,i,j} = n_{s,i,j}(1 - exp(-\beta_i \Delta t)) \tag{3.1}$$

where $n_{s,i,j}$ is the suspended particle number distribution in particle size bin i at time step j, Δt is the difference between time step j and time step $j + 1$, and β_i is the size-dependent first-order exponential wall loss rate obtained from seed-only experiments. The particle wall loss corrected number distribution ($n_{total,i,j}$) is obtained from the sum of the particle number distribution of deposited particles ($n_{w,i,j}$) and suspended particles ($n_{s,i,j}$):

$$n_{total,i,j} = n_{s,i,j} + n_{w,i,j} \tag{3.2}$$

Assuming spherical particles, the particle wall loss corrected volume concentration ($V_{total,j}$) is:

$$V_{total,j} = \sum_{i=1}^{m} \frac{n_{total,i,j}}{D_{p,i}\ln 10} \left(D_{p,i+} - D_{p,i-}\right) \frac{\pi}{6} D_{p,i}^3 \tag{3.3}$$

where m is the number of particle size bins, $D_{p,i+}$ and $D_{p,i-}$ are the upper and lower limits for size bin i, respectively, and $D_{p,i}$ is the median particle diameter for size bin i. The term $D_{p,i}\ln 10$ is needed to convert from a lognormal distribution. Figures B.1-B.4 and Table B.1 show results from the particle wall loss correction. To calculate the SOA mass concentration ($\Delta M_{o,j}$), the SOA density (ρ_{org}) is multiplied by the difference of the particle wall loss corrected volume concentration ($V_{total,j}$) and the initial seed volume concentration (V_{seed}):

$$\Delta M_{o,j} = \rho_{org} \left(V_{total,j} - V_{seed}\right) \tag{3.4}$$

The measured densities of the α-pinene SOA are 1.39 and 1.37 g cm^{-3} for the 100 and 500 ppb O_3 experiments, respectively, and are within the range (i.e., 1.19 to 1.52 g cm^{-3}) reported in previous α-pinene ozonolysis studies (*Bahreini et al.*, 2005; *Kostenidou et al.*, 2007; *Song et al.*, 2007; *Shilling et al.*, 2009).

3.4 Vapor–Particle Dynamics Model

A coupled vapor-particle dynamics model is used to evaluate the influence of seed aerosol surface area and oxidation rate on SOA formation in the α-pinene ozonolysis chamber experiments. This model is similar to that used in *McVay et al.* (2014), and will be briefly described here. Parameters from the experimental data (temperature, pressure, initial α-pinene concentration) are used as model inputs. The initial size distribution is set to that measured by the SMPS, with the exception of the two nucleation experiments. Because nucleation is not explicitly simulated, an approximation is used in which the smallest diameter bin is initialized with the total number of particles measured at the end of the experiment (see Table B.1). In each simulation, the decay of α-pinene, the consumption of O_3, the SOA mass concentration, and the SOA mass yield are calculated throughout the duration of the experiment. We assume a linear injection rate of O_3 based on the time required to inject the desired O_3 concentration. For example, O_3 is injected at a rate of 500/54.25 ppb min^{-1} for the first 54.25 min during the 500 ppb O_3 experiments. O_3 simultaneously decays by reaction with α-pinene at a rate constant of 9.4x10^{-17} cm^3 molec.$^{-1}$ s^{-1} (*Saunders et al.*, 2003). The O_3+α-pinene reaction is assumed to occur in a well-mixed chamber and produces five classes of first-generation products, which are grouped according to mass saturation concentrations, similar to the volatility basis set (*Donahue et al.*, 2006): $> 10^3$ (assumed to be completely volatile), 10^2, 10, 1 and 0.1 μg m^{-3}. Branching ratios between these products are optimized to fit the experimental data. These branching ratios cannot be compared directly to previously reported VBS parameters for α-pinene ozonolysis (e.g., *Henry et al.* (2012)) since VBS parameters are typically mass-based, while the branching ratios in the model are mole-based. Furthermore, the branching ratios here account for the influence of vapor wall deposition, while typical VBS parameters do not. We assume that these

five classes of products have molecular weights 168, 184, 192, 200 and 216 g mole^{-1} based on the group contribution method (*Donahue et al.*, 2011). The first-generation products are assumed not to undergo further reaction with O_3 upon formation.

The aerosol dynamics in the chamber obey the aerosol general dynamic equation (*Seinfeld and Pandis*, 2006):

$$\left(\frac{\partial n(D_p,t)}{\partial t}\right) = \left(\frac{\partial n(D_p,t)}{\partial t}\right)_{coag} + \left(\frac{\partial n(D_p,t)}{\partial t}\right)_{cond/evap} + \left(\frac{\partial n(D_p,t)}{\partial t}\right)_{wall\ loss} \tag{3.5}$$

Coagulation is not considered, since an alternative version of the model including coagulation showed no change in the predicted α-pinene ozonolysis SOA mass concentrations in simulations with and without coagulation. The change in particle number distribution due to particle wall loss is:

$$\left(\frac{\partial n(D_p,t)}{\partial t}\right)_{wall\ loss} = -\beta_j(D_p)n(D_p,t) \tag{3.6}$$

where, as noted in section 3.3.2, $\beta_j(D_p)$ is the size-dependent first-order wall loss rate coefficient obtained from fitting seed-only experiments. The rate at which vapor condenses onto a spherical aerosol particle is:

$$J_i = 2\pi D_i D_p (G_i - G_i^{eq}) F_{FS} \tag{3.7}$$

where G_i is the concentration of gas-phase species i, G_i^{eq} is the saturation concentration of gas-phase species i, D_i is the gas-phase molecular diffusivity (assumed to be 3x10^{-6} m^2 s^{-1} (*McVay et al.*, 2014)), and F_{FS} is the Fuchs-Sutugin correction for non-continuum gas-phase diffusion:

$$F_{FS} = \frac{0.75\alpha_p(1+\mathrm{Kn})}{\mathrm{Kn}^2 + \mathrm{Kn} + 0.283\mathrm{Kn}\alpha_p + 0.75\alpha_p} \tag{3.8}$$

where α_p is the vapor-particle mass accommodation coefficient, and Kn is the Knudsen number, $\mathrm{Kn} = 2\lambda_{AB}/D_p$. The vapor-particle mass accommodation coefficient accounts for any resistance

to vapor molecule uptake at the particle surface (e.g. surface accommodation and particle-phase diffusion limitations). λ_{AB} is the mean free path of the gas-phase species, which is:

$$\lambda_{AB} = 3D_i\sqrt{\frac{\pi M_i}{8RT}} \tag{3.9}$$

where R is the ideal gas constant, T is the temperature, and M_i is the molecular weight of diffusing gas-phase molecule i. For each particle size bin, Eqs. 3.7-3.9 are used to compute the flux of each gas-phase species to and from an aerosol particle, scaled by the particle number concentration in the size bin. The net rate of change for each gas-phase species due to evaporation or condensation is obtained from the total flux summed over all the particle size bins.

G_i^{eq} varies for each particle size bin because it depends on the mass concentration of species i and the total organic mass concentration in the size bin:

$$G_i^{eq} = \frac{A_i C_i^*}{\sum_k A_k + M_{init}} \tag{3.10}$$

where A_i is the concentration of species i in the particle phase, C_i^* is the saturation concentration of species i, $\sum_k A_k$ is the sum of all the species concentrations in the particle phase, and M_{init} is the mass concentration of any absorbing organic material initially present in the seed aerosol. To avoid numerical errors in Eq. 3.10 at the first time step, M_{init} is set to 0.01 μg m^{-3}.

The oxidation products of α-pinene ozonolysis are assumed to be subject to vapor-wall deposition, which is simulated using a first-order wall-loss coefficient (*McMurry and Grosjean*, 1985):

$$k_{wall,on} = \left(\frac{A}{V}\right)\frac{\frac{\alpha_{wall}\bar{c}}{4}}{1.0 + \frac{\pi}{2}\left[\frac{\alpha_{wall}\bar{c}}{4(k_e D_i)^{0.5}}\right]} \tag{3.11}$$

where A/V is the surface area-to-volume ratio of the chamber (estimated to be 2.5 m^{-1}), α_{wall} is the vapor-wall mass accommodation coefficient, and k_e is the eddy diffusion coefficient that describes mixing conditions in the chamber. Based on the measured size-dependent particle wall loss rates (method is described in *Zhang et al.* (2014)), k_e is estimated to be 0.03 s^{-1} for the GTEC chamber. Vapor-wall deposition is assumed to be reversible, and the rate constant of vapor desorption from

the chamber walls is:

$$k_{wall,off} = \frac{k_{wall,on}}{K_w C_w} = k_{wall,on}\left(\frac{C_i^* M_w \gamma_w}{C_w M_p \gamma_p}\right) \tag{3.12}$$

where C_w is the equivalent organic mass concentration in the wall (designated to treat gas-wall partitioning in terms of gas-particle partitioning theory and not necessarily representative of a physical layer of organic concentration on the wall (*Matsunaga and Ziemann*, 2010)), K_w is the gas-wall partitioning coefficient, M_w is the effective molecular weight of the wall material, γ_w is the activity coefficient of the species in the wall layer, M_p is the average molecular weight of organic species in the particle, and γ_p is the activity coefficient of the species in the particle. For simplicity, we assume that $M_w = M_p$ and $\gamma_w = \gamma_p$. C_w is set to 10 mg m^{-3} based on previous inferences by *Matsunaga and Ziemann* (2010). Sensitivity studies (not shown) show no change in model predictions when varying C_w above $C_w = 0.1$ mg m^{-3}.

In the initial version of the model, after all the α-pinene is consumed, vapor wall deposition was assumed to continue to deplete the gas-phase oxidation products and aerosol mass evaporates to maintain gas-particle equilibrium. SOA evaporation was not observed experimentally (i.e., the SOA mass concentration does not decrease significantly over time after peak SOA growth has been achieved in these chamber experiments (Fig. 3.2)). In order to represent these observations in the model, a first-order, particle-phase reaction is introduced by which aerosol species are converted into non-volatile absorbing organic mass with a timescale of τ_{olig}. This mechanism (which is not included in the model used in *McVay et al.* (2014)) is similar to that used by the sequential equilibrium partitioning model, in which aerosol is converted from an absorbing to non-absorbing, non-volatile phase in order to explain the inhibited diffusion and evaporation observed in α-pinene ozonolysis SOA (*Cappa and Wilson*, 2011). Although we assume here that the converted non-volatile aerosol mass still participates in partitioning, either mechanism invokes a particle-phase process to retard SOA evaporation.

Model parameters α_w, α_p, τ_{olig} and the branching ratios between the oxidation products are optimized to best-fit the predictions with the experimental observations. Specifically, model pre-

dictions are compared to experimental data: SOA mass concentration vs. reaction time, α-pinene concentration vs. reaction time, and O_3 concentration vs. reaction time. Figure B.6 compares reaction profiles of measured and modeled O_3 and α-pinene concentrations for the base model case. Sensitivity tests were also performed on each model parameter, shown in Figs. B.7-B.10. Table 3.2 summarizes the parameters used. While the optimized parameters provide a good fit to the data, we caution that the parameters are interconnected, and other fits may also be possible. We are confident that our conclusions derived using these parameters are robust.

3.5 Results

Figure 3.1 shows the size-dependent particle wall deposition coefficients inferred from seed-only deposition experiments. The initial total AS seed surface area concentration in the low AS-seed only and high AS-seed only experiments (which are conducted using 0.015 M AS and 0.05 M AS solutions, respectively) are similar to those used in the α-pinene ozonolysis experiments (i.e., $\sim$1000 and $\sim$3000 μm^2 cm^{-3}, respectively). While there are differences in the particle wall deposition coefficients from the low and high AS-seed only experiments, this difference is likely the result of uncertainties arising from the low particle number concentrations for the larger particles in the low AS-seed only experiment. As shown in Fig. 3.1, both sets of particle wall deposition coefficients generally fall within the range of those measured in routine monthly AS-seed only experiments conducted in the chamber.

The particle wall deposition corrected number concentration data provide a test of the appropriateness of the particle wall deposition correction. This is because the corrected number concentration should level off at a constant value (i.e., the initial particle number concentration), assuming no significant coagulation, when particle wall deposition is properly accounted for since the wall-deposited particle number distribution is added to the suspended particle number distribution during particle wall loss correction. We account for particle wall deposition in nucleation and low AS experiments using deposition coefficients determined from the low AS-seed only experiments, while particle deposition in high AS experiments is accounted for using coefficients determined from the high AS-seed

only experiments. Figures B.1 and B.2 show the particle wall deposition-corrected aerosol number and volume concentrations. Over all experiments, the particle wall deposition-corrected final particle number concentration (i.e., at the end of the reaction) is 9 to 17 % less than the initial particle number concentration for the low AS and high AS experiments (Table B.1), respectively, indicating that the particle wall deposition-corrected volume concentrations are slightly underestimated. It is currently unclear why the particle wall deposition-corrected final particle number concentrations are somewhat smaller than the initial particle number concentrations, though this could be due to variations in particle wall deposition rates in the AS-seed only and α-pinene ozonolysis experiments. As a sensitivity test, we used the average of the low AS-seed only and high AS-seed only particle wall deposition coefficients to account for particle wall deposition in all the experiments (Figs. B.3 and B.4). While there is a negligible difference in the particle wall deposition corrected volume concentrations (Figs. B.3 and B.4 vs. Figs. B.1 and B.2), a larger spread (1 to 22 %) exists in the difference between the initial and final particle number concentrations when the average particle wall deposition coefficients are used (Table B.1). Therefore, all subsequent nucleation and low AS data presented here are particle wall deposition-corrected using coefficients determined from the low AS-seed only experiments, and all high AS data are corrected using particle wall deposition coefficients determined from the high AS-seed only experiments.

Figure 3.2 shows the reaction profiles of the α-pinene ozonolysis experiments. SOA growth typically starts within 10 to 20 min of the start of the reaction. At either initial O_3 concentration, the molar ratio of O_3 reacted to α-pinene reacted is approximately 1:1 (i.e., 50 ppb α-pinene reacted with 50 ppb O_3), which indicates that O_3 reacts only with α-pinene and not its oxidation products. As anticipated, the α-pinene oxidation rates in the 100 ppb O_3 experiments are significantly slower than those in the 500 ppb O_3 experiments. Figures 3.2a-c show that peak SOA levels are typically reached at reaction time $\sim$300 to 350 min in the 100 ppb O_3 experiments, during which $\geq$ 95 % of the injected α-pinene has reacted. In contrast, all the α-pinene reacts within 80 to 90 min of the start of reaction in the 500 ppb O_3 experiments, and peak SOA levels are achieved at reaction time $\sim$100 min (Figs. 3.2d-f). These results indicate that the O_3 concentration dictates both the rate of

α-pinene oxidation and the time it takes to achieve peak SOA growth.

Figure 3.3 shows the time-dependent growth curves (SOA mass concentration vs. α-pinene reacted (*Ng et al.*, 2006)) for the 100 and 500 ppb O_3 experiments. Only SOA growth data up to SOA peak concentrations are shown. SOA growth essentially stops once all the α-pinene has reacted. This is expected, as α-pinene has only one double bond; the first step of α-pinene ozonolysis is rate-limiting and the first-generation products are condensable (*Ng et al.*, 2006; *Chan et al.*, 2007). The time-dependent SOA growth curves for experiments corresponding to different seed aerosol concentrations overlap for both low and high O_3 concentrations. This indicates that the initial AS seed surface area does not influence the SOA growth rate within the range of AS seed surface area concentration used. It is important to note that while it appears that the SOA growth rate is faster in the 100 ppb O_3 relative to the 500 ppb O_3 experiments based on the time-dependent growth curves shown in Fig. 3.3, this is not the case. Instead, the observed time-dependent growth curves can be explained by the higher concentration of α-pinene having reacted during the 10 to 20 min delay of SOA formation in the 500 ppb O_3 experiments compared to the 100 ppb O_3 experiments (Fig. 3.2).

Figure 3.4 shows the time-dependent SOA mass yields as a function of initial total AS seed surface area for the 100 and 500 ppb O_3 experiments. Regardless of the O_3 concentration, the SOA mass yields stay roughly constant despite the increase in AS seed surface area. This indicates that the surface area concentration of AS seed aerosol does not noticeably influence the partitioning of gas-phase α-pinene ozonolysis products to the particle phase within the range of AS seed surface area concentration used. Higher SOA mass yields are observed in the 500 ppb O_3 experiments, which indicates that the α-pinene oxidation rate controls the absolute amount of SOA formed. It is important to note that these conclusions are robust even when the average of the low AS-seed only and high AS-seed only particle wall loss coefficients are used to account for particle wall loss in all the experiments (Fig. B.5). The enhancement of SOA mass yields at higher O_3 concentrations and the lack of a SOA mass yield dependence on AS seed surface area (within the range of AS seed surface area concentration used in this study) will be discussed further in Section 3.6.

The α-pinene ozonolysis SOA mass yields obtained in this study are compared to those reported in previous studies in Fig. 3.5. Table B.2 lists the experimental conditions employed in these studies. To facilitate comparison between the different studies, all the SOA mass yield and concentration data (including this study) are adjusted to an organic density of 1.0 g cm^{-3}. As shown in Fig. 3.5, the SOA mass yields obtained at peak SOA growth in this study are generally consistent with those of previous studies where the chamber was operated in batch mode (that in this study).

The competition between the condensation of SOA-forming vapor to aerosol particles vs. to chamber walls is investigated using the coupled vapor-particle dynamics model described in Section 3. As noted earlier, optimal model values for α_p, α_w, τ_{olig} and the branching ratios between the oxidation products were determined for the 100 and 500 ppb O_3 experiments by comparing the observed and best-fit time-dependent SOA, α-pinene, and O_3 concentrations profiles (Figs. B.6-B.10). Sensitivity tests were performed for each parameter to establish that the set of optimal model values provide the best overall agreement with time-dependent SOA formation profiles observed for all experiments (Figs. B.7-B.10). Predictions from the coupled vapor-particle dynamics model show that the optimal parameters are: $\alpha_w = 10^{-6}$, $\alpha_p = 1$, $\tau_{olig} = 4$ h, branching ratios = 0.57, 0.35, 0.04, 0.015 and 0.025 for oxidation products with vapor pressures $> 10^3$, 10^2, 10, 1 and 0.1 μg m^{-3}, respectively. The best-fit $\alpha_w = 10^{-6}$ (Fig. B.7) corresponds to a first-order vapor-wall deposition rate constant ($k_{wall,on}$) of 10^{-4} s^{-1}. This $k_{wall,on}$ value is comparable to that reported by *Matsunaga and Ziemann* (2010) for a 8.2 m^3 chamber.

3.6 Discussion

α-pinene ozonolysis has been carried out at two O_3 mixing ratios (100 and 500 ppb) under varying AS seed aerosol surface area concentrations (0, ~1000 and ~3000 μm^2 cm^{-3}).

3.6.1 Seed Aerosol Surface Area Effect

Figure 3.3 shows that the time-dependent SOA growth curves for experiments with different seed area concentrations overlap at both O_3 concentrations, which indicates the AS seed surface area

does not affect the rate of SOA growth within the range of AS seed surface area concentration used in this study. This observation differs from findings by *Pathak et al.* (2007b) for the O_3+α-pinene system, who showed that even though the final SOA mass yields measured in the reaction of 7.3 ppb α-pinene with 1500 ppb O_3 were similar in their seeded and unseeded experiments, SOA growth was considerably slower in unseeded experiments compared to seeded experiments. The authors suggested that the slow SOA formation rate in their unseeded experiment was the result of SOA formation being limited by the mass transfer of semi-volatile oxidation products to newly formed particles (via nucleation) during the early stages of the experiment. These newly formed particles have a significantly smaller aerosol surface area for gas-particle partitioning as compared to that of seed aerosol particles in the seeded experiments. Consequently, the semi-volatile oxidation products accumulated in the gas phase during the early stages of the unseeded experiments, resulting in slower SOA growth compared to the seeded experiments. The observation that the presence of seed aerosol does not influence the SOA growth rate in the present study may be explained by the relatively high concentrations of α-pinene reacted and SOA mass loadings obtained. Previous studies have shown that the delay between the onset of VOC oxidation and SOA formation in unseeded experiments is most pronounced at low aerosol loadings (*Kroll et al.*, 2007). We note that the concentrations of α-pinene reacted and SOA mass loadings obtained in this study are significantly larger than those reported by *Pathak et al.* (2007b). Therefore, it is possible that due to the relatively large concentrations of α-pinene reacted in this study, substantial concentrations of gas-phase oxidation products are generated, which results in rapid partitioning into the particle phase even in the absence of seed aerosol. This is evident from the large increase in the particle number concentration during the early stages of the unseeded 100 and 500 ppb O_3 experiments, where the particle number concentration increased to $\sim$8000 and $\sim$10000 particles cm^3 during the first 45 min of the 100 and 500 ppb O_3 experiments, respectively (Fig. B.1a and B.2a). Thus, the SOA growth rates are not controlled by the presence of AS seed in this study.

Figure 3.4 shows that for both initial O_3 mixing ratios used, the time-dependent SOA mass yield is similar at any given AS seed surface area (see also Table 3.1). The absence of a SOA growth

dependence on the AS seed surface area is similar to observations reported by *McVay et al.* (2016) for the α-pinene photooxidation (OH-driven chemistry) system, but differ from those reported by *Zhang et al.* (2014) for the toluene photooxidation system in which the SOA mass yield increased with the surface area concentration of seed aerosol.

The best-fit $\alpha_p = 1$ (Fig. B.8) suggests the absence of significant limitations to vapor-particle mass transfer in the present α-pinene ozonolysis study, and that SOA formation is governed by quasi-equilibrium growth (*McVay et al.*, 2014), which occurs when SOA-forming vapors are produced at a rate that is significantly slower than that required to establish gas-particle equilibrium (*Shiraiwa et al.*, 2012; *Zhang et al.*, 2012). Moreover, the characteristic timescale to establish gas-particle equilibrium is less than those for reaction and vapor-wall deposition. When the vapor and particle phases maintain equilibrium, gas-particle equilibrium is controlled by the amount of organic matter in the VOC system. As a result, the rate of condensation of SOA-forming vapors is independent of the seed aerosol surface area (*McVay et al.*, 2014). The best-fit $\alpha_p = 1$ is within the approximate range of α_p coefficients determined from α-pinene ozonolysis SOA thermodenuder studies (α_p = 0.1) (*Saleh et al.*, 2013) and α-pinene photooxidation chamber studies (α_p = 0.1 or 1) (*McVay et al.*, 2016). Notably, this result differs markedly from that for toluene photooxidation (*Zhang et al.*, 2014), where α_p was determined to be 0.001, and for which, since the SOA mass yield was strongly dependent on the seed aerosol surface area, the condensation of SOA-forming vapors onto seed aerosol particles was kinetically limited (*McVay et al.*, 2014). Kinetically-limited SOA growth occurs when the timescale for gas-particle equilibrium is competitive with or exceeds the timescale for reaction and vapor wall deposition, and may reflect imperfect accommodation of gas-phase organics to the particle phase. The markedly different behavior of the α-pinene and toluene SOA systems could be due to differences in SOA volatility and aerosol physical phase state (*McVay et al.*, 2016).

3.6.2 Oxidation Rate Effect

At higher O_3 concentrations, the α-pinene oxidation rate increases, leading to higher SOA mass yields (the "oxidation rate effect"). This behavior was previously observed by *Ng et al.* (2007) for

the m-xylene photooxidation system, for which the oxidation rate effect was attributed to the loss of semi-volatile condensable products to chamber walls in competition with condensation onto seed particles to form SOA.

SOA formation from α-pinene ozonolysis is presumed to be driven by a range of semi- and low-volatility first-generation products arising from reaction of O_3 with the single C=C double bond (*Ng et al.*, 2006). These products are subject to two competing routes: condensation to particles to form SOA or deposition on the chamber walls. Each process can be represented in terms of a first-order rate constant: $k_{wall,on}$ and $k_{particle,on}$ (s^{-1}). The rate of vapor-wall deposition of condensable species A is then $k_{wall,on}$[A] (molec cm^{-3} s^{-1}) and the rate of condensation onto particles is $k_{particle,on}$[A] (molec cm^{-3} s^{-1}). Increasing the rate of reaction increases the concentration of [A], but the relative rates of vapor-wall deposition and condensation onto particles will remain the same. In general, however, both vapor-wall deposition and vapor-particle condensation are reversible processes (*McVay et al.*, 2014; *Zhang et al.*, 2014). The first-order rate constant for evaporation from the wall can be represented as *Matsunaga and Ziemann* (2010):

$$k_{wall,off} = k_{wall,on}\left(\frac{C_i^*}{C_w}\right) \tag{3.13}$$

where C_i^* is the saturation concentration and C_w is the assumed equivalent wall organic concentration. The rate of evaporation from particles is:

$$k_{particle,off} = k_{particle,on}\left(\frac{C_i^*}{C_{aer}}\right) \tag{3.14}$$

where C_{aer} is the organic aerosol concentration ($C_{aer} = \sum A_k + M_{init}$).

The difference between C_{aer} and C_w is the key to explaining the oxidation rate effect. At the beginning of the experiment, C_{aer} is very small because the inorganic seeds are essentially non-absorbing. Therefore, $k_{particle,off}$ is large, and the net SOA growth is small. In contrast, C_w is considered to be substantial (on the order of 10 mg m^{-3}) and to be essentially constant throughout the experiment (*Matsunaga and Ziemann*, 2010; *McVay et al.*, 2014; *Zhang et al.*, 2014). Model

predictions are insensitive to the value of C_w since, in any event, C_w is significantly larger than C_{aer} (*Zhang et al.*, 2014). Therefore, $k_{wall,off}$ is small at the beginning of the experiment and the net vapor wall loss rate is fast. As C_{aer} increases, the net SOA condensation rate increases relative to the net vapor wall loss rate. When the reaction rate increases corresponding to higher O_3 concentrations, C_{aer} grows more quickly because more condensable species are available to form SOA, and the net condensation rate increases more rapidly. Therefore, the observed oxidation rate effect is due to vapor wall deposition, and arises because vapor-particle and vapor-wall condensation are essentially reversible processes. This explanation is consistent with simulations varying the O_3 concentration in which all species are non-volatile (i.e., do not evaporate from the particles or the wall). In this case, no oxidation rate effect is observed as the O_3 concentration increases. The growth curves for different O_3 concentrations overlap, and the same yield is obtained regardless of O_3 concentration (Fig. B.11).

Sensitivity tests were performed to determine the point at which SOA formation is no longer influenced by the O_3 concentration. In these simulations, the initial α-pinene concentration is fixed at 48 ppb, while the O_3 concentration is varied from 75 to 1000 ppb. The rate of O_3 injection is assumed to remain constant as the O_3 concentration is increased to mimic the experimental protocol (i.e., O_3 injection time is increased to achieve higher O_3 concentrations). The O_3 injection rate used in these simulations is fixed at 500/54.25 ppb min^{-1}, which is the same as that used to analyze results from the 500 ppb O_3 experiments. Model predictions in Fig. B.12 show that the maximum SOA mass concentration increases with increasing O_3 concentration up to approximately 500 ppb O_3. Beyond this O_3 concentration, the SOA growth curves overlap and the maximum SOA mass concentration does not increase even when more O_3 is added. This plateau arises due to the lengthening time required to inject increasing amounts of O_3. More than 1 h is required to inject $>$ 500 ppb of O_3, and by this time, virtually all of the α-pinene has reacted. Increasing the O_3 concentration after all of the α-pinene has reacted does not lead to any changes in the SOA mass concentration. However, if a faster injection rate of O_3 is used, the oxidation rate effect will persist to higher O_3 concentrations (i.e., $>$ 500 ppb O_3) (Fig B.13). With a faster injection

rate, 500 ppb O_3 is injected before all of the α-pinene has reacted. Continuing to inject O_3 to a higher concentration (i.e., 750 ppb) will cause α-pinene to decay faster and SOA to grow faster than when the O_3 injection stops at 500 ppb. The oxidation rate effect is then apparent at higher O_3 concentrations. If, instead of using an injection rate of O_3, simulations are run using fixed initial O_3 (not possible experimentally), the rate effect persists to even higher O_3 concentrations. The relative increase in yield with increasing O_3 concentrations slows at very high O_3 concentrations because the rate of reaction becomes substantially faster than the vapor wall deposition rate, and there is less marginal effect to increasing the reaction rate.

3.6.3 Interplay of the Seed Aerosol Surface Area Effect and the Oxidation Rate Effect

In this study, we observe an oxidation rate effect but not a seed aerosol surface area effect. In *Zhang et al.* (2014), a seed aerosol surface area effect was observed, but the variation of the oxidation rate was not studied. A key aspect of vapor wall deposition is the potential interplay between the seed aerosol surface area effect and the oxidation rate effect. To examine this interplay in the α-pinene ozonolysis system, simulations were carried out by varying the seed aerosol surface area and the O_3 concentration simultaneously, while using the branching ratios, oligomerization rate, and vapor wall deposition rate parameters obtained in the present study. The initial α-pinene concentration was set to 50 ppb, and a fixed O_3 concentration was used in place of a linear injection. α_p was varied at 0.001, 0.01, and 1 in these simulations. Figure 3.6 shows the SOA mass yield at peak SOA growth as a function of both the seed aerosol surface area and O_3 concentration for $\alpha_p = 1$, 0.01, and 0.001. For $\alpha_p = 1$, the oxidation rate dominates: SOA mass yield increases significantly as O_3 concentration increases while the seed aerosol surface area has a negligible effect. For $\alpha_p = 0.01$, both effects can be observed in different regions: at low O_3 concentrations and high seed aerosol surface areas, the oxidation rate effect dominates; at low seed aerosol surface areas and high O_3 concentrations, the seed surface area dominates. At low seed aerosol surface areas and low O_3 concentrations, both effects are present. For $\alpha_p = 0.001$, the seed aerosol surface area effect dominates except at very

high seed aerosol surface areas. These observations show that the presence of an oxidation rate effect and/or seed aerosol surface area effect depends on a complex interplay of factors, such as α_p, the rate of hydrocarbon oxidation, and the amount of seed surface area present.

3.7 Implications

In this study, we systematically examine the roles of gas-particle partitioning and VOC oxidation rate in the presence of vapor-wall deposition in α-pinene ozonolysis. We show that despite the presence of vapor-wall deposition, SOA mass yields at peak SOA growth remain approximately constant regardless the seed aerosol surface area (within the range of AS seed surface area concentration used in this study). This observation is consistent with SOA formation in the α-pinene ozonolysis system being governed by quasi-equilibrium growth, for which there are no substantial limitations to vapor-particle mass transfer. This result was demonstrated in a previous modeling study which showed that increasing the seed-to-chamber surface area ratio will lead to increased SOA growth only in cases in which the condensation of SOA-forming vapors onto seed aerosol particles is kinetically limited as a result of imperfect accommodation of gas-phase organics to the particle phase (*McVay et al.*, 2014).

An important implication of this study is that diverting vapor-wall deposition in chamber studies via the addition of ever-increasing quantities of seed aerosol particles is not effective in VOC systems for which SOA formation is governed by quasi-equilibrium growth. This study also underscores the importance of accounting for particle wall deposition appropriately in chamber studies, to avoid erroneous conclusions regarding the role of gas-particle partitioning (quasi-equilibrium vs. kinetically-limited SOA growth) in influencing vapor wall loss in the VOC system.

We note that the present study shows that the SOA mass yield is independent of seed aerosol surface area concentration for values ranging from 0 to ~3000 μm^2 cm^{-3}. This corresponds to a seed-to-chamber surface area ratio of 0 to ~1x10^{-3}, which is substantially smaller than the range used by *Zhang et al.* (2014) to study the influence of vapor-wall deposition on toluene photooxidation SOA formation in the Caltech chamber (i.e., 0 to ~5x10^{-3}). It is possible that a SOA mass yield

dependence on the seed surface area may have become more apparent had a larger range of seed aerosol surface area (i.e., > 3000 $\mu m^2 cm^{-3}$), and hence a larger range of seed-to-chamber surface area ratio, been used here. One consideration is that coagulation may become increasingly important, and will need to be accounted for, when higher seed aerosol number concentrations (relative to those used in this study) are used (*Seinfeld and Pandis*, 2006; *Pierce et al.*, 2008). A detailed analysis of the effect of seed aerosol surface area concentrations > 3000 $\mu m^2 cm^{-3}$ on α-pinene ozonolysis SOA mass yields will be the subject of forthcoming work.

Higher SOA mass yields at peak SOA growth are observed in the present study when O_3 is increased from 100 to 500 ppb. This is because α-pinene is oxidized more quickly, which leads to gas-phase oxidation products being formed more rapidly, and consequently partitioning more quickly onto AS seed aerosol particles before they are lost to the chamber walls. Therefore, the oxidation rate effect (i.e., higher SOA mass yields as a result of faster hydrocarbon oxidation rates) is a consequence of vapor-wall deposition. An important implication of this study is that SOA mass yields can be affected by vapor-wall deposition in VOC systems that are not characterized by slow mass accommodation of gas-phase organics to the particle phase (*Zhang et al.*, 2014). Thus, this work demonstrates that the effect of vapor-wall deposition on SOA mass yields can be mitigated through the use of excess oxidant concentrations. It should be noted that the α-pinene ozonolysis SOA mass yields (absolute values) increased by 5 to 9 % when O_3 is increased from 100 to 500 ppb (for an initial α-pinene concentration of $\sim$50 ppb), where SOA formation is governed by quasi-equilibrium growth. In the absence of vapor-wall deposition, SOA mass yields are predicted by the model used here to approximately double from those observed experimentally. In contrast, *Zhang et al.* (2014) showed that the presence of vapor-wall deposition led to underestimation of SOA formation by factors as much as four in the toluene photooxidation system, where the condensation of SOA-forming vapors onto seed aerosol is kinetically limited. Taken together, these results indicate that the magnitude by which vapor-wall deposition affects SOA mass yields depends on the extent to which the VOC system is governed by kinetically-limited SOA condensational growth.

Given these observations of how gas-particle partitioning can influence the magnitude by which

vapor-wall deposition affects SOA mass yields, an overriding question is: what controls the gas-particle partitioning behavior of SOA formed in different VOC systems? α_p describes the overall mass transfer of vapor molecules into the particle phase (*McVay et al.*, 2014; *Zhang et al.*, 2014). Thus, α_p affects the vapor-particle equilibrium timescale, which, depending on the extent to which it is competitive with the timescales for reaction and vapor-wall deposition, determines whether SOA formation is governed by kinetically-limited or quasi-equilibrium growth. Markedly different α_p values could arise from the physical phase state of the SOA formed. As discussed by *McVay et al.* (2014, 2016), if the SOA formed exists in a semi-solid state (*Vaden et al.*, 2010; *Virtanen et al.*, 2010; *Cappa and Wilson*, 2011; *Vaden et al.*, 2011; *Virtanen et al.*, 2011; *Kuwata and Martin*, 2012; *Perraud et al.*, 2012; *Saukko et al.*, 2012; *Abramson et al.*, 2013; *Renbaum-Wolff et al.*, 2013), a low value of α_p might be expected owing to retarded surface accommodation and particle-phase diffusion (*Zaveri et al.*, 2014). Quantification of α_p is challenging experimentally, and reported α_p values for the same system can vary by several orders of magnitude (*Grieshop et al.*, 2007; *Stanier et al.*, 2007; *Vaden et al.*, 2011; *Miles et al.*, 2012; *Saleh et al.*, 2013). Therefore, α_p of SOA formed in different VOC systems need to be better constrained through a combination of experimental and modeling efforts.

The SOA mass yield from the ozonolysis of monoterpenes in the GEOS-CHEM chemical transport model (19 % at 10 μg m^{-3}) is currently based on that measured in α-pinene ozonolysis studies by *Shilling et al.* (2008) (*Pye et al.*, 2010). *Shilling et al.* (2008) measured these SOA mass yields in a teflon chamber operated in continuous-flow mode, as opposed to batch mode, which is how experiments in the present study and most of those shown in Fig. 3.5 and Table B.2 were conducted. While it is not possible to directly compare our results with those of *Shilling et al.* (2008) due to differences in SOA mass concentrations, the SOA mass concentrations and yields measured in the current study are generally consistent with those of previous batch chamber studies. The SOA mass yields at $\sim$10 μg m^{-3} SOA mass concentration measured by *Shilling et al.* (2008) are generally higher than those measured in chambers operated in batch mode (*Griffin et al.*, 1999; *Cocker et al.*, 2001b; *Presto et al.*, 2005; *Presto and Donahue*, 2006; *Pathak et al.*, 2007b) (Fig. 3.5). One

possible explanation for the higher SOA mass yields in the continuous-flow, steady state, mode is that the SOA-forming vapors are in equilibrium with the organic mass present on the chamber walls and seed aerosol, hence minimizing the irreversible loss of SOA-forming vapors to the chamber walls (*Shilling et al.*, 2008). However, the extent to which SOA mass yields obtained in a continuous-flow reactor are influenced by vapor wall loss is unclear. Using a continuous-flow reactor, *Ehn et al.* (2014) observed α-pinene ozonolysis SOA mass yields to increase with increasing seed aerosol surface area but required $\alpha_p = 1$ to fit the observed SOA growth. The observed vapor-wall deposition rate constant in their continuous-flow reactor (0.011 s^{-1}) is two orders of magnitude larger than that of the GTEC chamber (10^{-4} s^{-1}). The estimated timescales for gas-particle and gas-wall partitioning are also approximately equal in their continuous-flow reactor. This indicates that SOA condensational growth is kinetically limited in their continuous-flow reactor even at $\alpha_p = 1$ (*Ehn et al.*, 2014; *McVay et al.*, 2014), which suggests that SOA mass yields measured in their continuous-flow reactor may be significantly affected by vapor-wall deposition.

Previous studies on SOA formation from the OH and NO_3 oxidation of biogenic VOCs have similarly reported higher SOA mass yields in the presence of higher oxidant concentrations. For example, in the NO_3 oxidation of β-pinene, *Boyd et al.* (2015) reported SOA mass yields 10 to 30 % higher than those previously reported by *Fry et al.* (2009, 2014). In addition to differences in the experimental conditions of the two studies, *Boyd et al.* (2015) hypothesized that the higher SOA mass yields could also be a result of the higher NO_3 concentrations used in their study (which led to faster β-pinene oxidation rates) compared to those used by *Fry et al.* (2009, 2014). The oxidation rate effect was also observed in the m-xylene photooxidation system, where *Ng et al.* (2007) showed that the SOA mass yields were dependent on the m-xylene oxidation rate, with higher OH concentrations (and hence faster oxidation rates) resulting in higher SOA mass yields. Together, these studies show that faster hydrocarbon oxidation rates can alleviate the effects of vapor-wall deposition on SOA mass yields in different VOC systems.

This gives rise to the question: should chamber SOA experiments on different VOC systems be performed under as rapid oxidation conditions as possible (i.e., large oxidant concentrations) to

reduce the effects of vapor-wall deposition? A recent study by *McVay et al.* (2016) reported similar SOA growth under low and high OH levels for α-pinene photooxidation. The authors hypothesized that the autoxidation mechanism likely becomes a more important pathway at low OH levels (*Crounse et al.*, 2013), and thus contributes substantially to SOA growth. Therefore, it is possible that certain reaction pathways and mechanisms (which are important in the atmosphere) are biased when unusually high levels of oxidants are used in chamber experiments (e.g. autoxidation). Thus, this underscores the need to design chamber experiments that simultaneously mitigate the magnitude of vapor-wall deposition while ensuring that reaction conditions, and consequently reaction pathways and oxidation products, are atmospherically relevant.

Figures B.1 - B.13 and Tables B.1 - B.2 are provided in Appendix B.

Acknowledgements

This research was funded by NSF Grants 1455588 and AGS-1523500, and US Environmental Protection Agency STAR grant (Early Career) RD-83540301. This publication's contents are solely the responsibility of the grantee and do not necessarily represent the official views of the US EPA. Further, US EPA does not endorse the purchase of any commercial products or services mentioned in the publication. R.C. McVay was supported by a National Science Foundation Graduate Research Fellowship under Grant No. DGE-1144469.

Bibliography

Abramson, E., Imre, D., Beránek, J., Wilson, J. M., and Zelenyuk, A.: Experimental determination of chemical diffusion within secondary organic aerosol particles, *Phys. Chem. Chem. Phys.*, 15, 2983–2991, 2013.

Bahreini, R., Keywood, M. D., Ng, N. L., Varutbangkul, V., Gao, S., Flagan, R. C., Seinfeld, J. H., Worsnop, D. R., and Jimenez, J. L.: Measurements of Secondary Organic Aerosol from Oxidation of Cycloalkenes, Terpenes, and m-Xylene Using an Aerodyne Aerosol Mass Spectrometer, *Environ. Sci. Technol*, 39, 5674-5688, doi:10.1021/es048061a, 2005.

Boyd, C. M., Sanchez, J., Xu, L., Eugene, A. J., Nah, T., Tuet, W. Y., Guzman, M. I., and Ng, N. L.: Secondary organic aerosol formation from the β-pinene+NO3 system: effect of humidity and peroxy radical fate, *Atmos. Chem. Phys.*, 15, 7497-7522, doi:10.5194/acp-15-7497-2015, 2015.

Canagaratna, M. R., Jimenez, J. L., Kroll, J. H., Chen, Q., Kessler, S. H., Massoli, P., Hildebrandt Ruiz, L., Fortner, E., Williams, L. R., Wilson, K. R., Surratt, J. D., Donahue, N. M., Jayne, J. T., and Worsnop, D. R.: Elemental ratio measurements of organic compounds using aerosol mass spectrometry: characterization, improved calibration, and implications, *Atmos. Chem. Phys.*, 15, 253-272, doi:10.5194/acp-15-253-2015, 2015.

Capouet, M., Müller, J.-F., Ceulemans, K., Compernolle, S., Vereecken, L., and Peeters, J.: Modeling aerosol formation in alpha-pinene photo-oxidation experiments, *J. Geophys. Res.*, 113, D02308, doi:10.1029/2007JD008995, 2008.

Cappa, C. D. and Wilson, K. R.: Evolution of organic aerosol mass spectra upon heating: implications for OA phase and partitioning behavior, *Atmos. Chem. Phys.*, 11, 1895–1911, doi: 10.5194/acp-11-1895-2011, 2011.

Cappa, C. D., Jathar, S. H., Kleeman, M. J., Docherty, K. S., Jimenez, J. L., Seinfeld, J. H., and Wexler, A. S.: Simulating secondary organic aerosol in a regional air quality model using the

statistical oxidation model Part 2: Assessing the influence of vapor wall losses, *Atmos. Chem. Phys.*, 16, 3041-3059, doi:10.5194/acp-16-3041-2016, 2016.

Carlton, A. G., Bhave, P. V., Napelenok, S. L., Edney, E. D., Sarwar, G., Pinder, R. W., Pouliot, G. A., and Houyoux, M.: Model Representation of Secondary Organic Aerosol in CMAQv4.7, *Environ. Sci. Technol.*, 44, 8553-8560, doi:10.1021/es100636q, 2010.

Chan, A. W. H., Kroll, J. H., Ng, N. L., and Seinfeld, J. H.: Kinetic modeling of secondary organic aerosol formation: effects of particle- and gas-phase reactions of semivolatile products, *Atmos. Chem. Phys.*, 7, 4135-4147, 2007.

Cocker, D. R., Flagan, R. C., and Seinfeld, J. H.: State-of-the-art chamber facility for studying atmospheric aerosol chemistry, *Environ. Sci. Technol.*, 35, 2594-2601, doi:10.1021/es0019169, 2001a.

Cocker, D. R., Clegg, S. L., Flagan, R. C., and Seinfeld, J. H.: The effect of water on gas-particle partitioning of secondary organic aerosol. Part I: alpha-pinene/ozone system, *Atmos. Environ.*, 35, 6049-6072, doi:10.1016/s1352-2310(01)00404-6, 2001b.

Crounse, J. D., Nielsen, L. B., Jørgensen, S., Kjaergaard, H. G., and Wennberg, P. O.: Autoxidation of organic compounds in the atmosphere, *J. Phys. Chem. Lett.*, 4, 3513–3520, 2013.

Crump, J. G., and Seinfeld, J. H.: Turbulent Deposition and Gravitational Sedimentation of an Aerosol in a Vessel of Arbitrary Shape, *J. Aer. Sci.*, 12, 405-415, doi:10.1016/0021-8502(81)90036-7, 1981.

DeCarlo, P. F., Slowik, J. G., Worsnop, D. R., Davidovits, P., and Jimenez, J. L.: Particle morphology and density characterization by combined mobility and aerodynamic diameter measurements. Part 1: Theory, *Aerosol Sci. Technol.*, 38, 1185-1205, doi:10.1080/027868290903907, 2004.

DeCarlo, P. F., Kimmel, J. R., Trimborn, A., Northway, M. J., Jayne, J. T., Aiken, A. C., Gonin, M., Fuhrer, K., Horvath, T., Docherty, K. S., Worsnop, D. R., and Jimenez, J. L.: Field-deployable, high-resolution, time-of-flight aerosol mass spectrometer, *Analytical Chem.*, 78, 8281-8289, doi:10.1021/ac061249n, 2006.

Donahue, N. M., Robinson, A. L., Stanier, C. O., and Pandis, S. N.: Coupled partitioning, dilution, and chemical aging of semivolatile organics, *Environ. Sci. Technol.*, 40, 2635-2643, doi:10.1021/es052297c, 2006.

Donahue, N. M., Epstein, S. A., Pandis, S. N., and Robinson, A. L.: A two-dimensional volatility basis set: 1. organic-aerosol mixing thermodynamics, *Atmos. Chem. Phys.*, 11, 3303-3318, doi:10.5194/acp-11-3303-2011, 2011.

Ehn, M., Thornton, J. A., Kleist, E., Sipilä, M., Junninen, H., Pullinen, I., Springer, M., Rubach, F., Tillmann, R., Lee, B., Lopez-Hilfiker, F., Andres, S., Acir, I.-H., Rissanen, M., Jokinen, T., Schobesberger, S., Kangasluoma, J., Kontkanen, J., Nieminen, T., Kurtén, T., Nielsen, L. B., Jørgensen, S., Kjaergaard, H. G., Canagaratna, M., Maso, M. D., Berndt, T., Petäjä, T., Wahner, A., Kerminen, V.-M. Kulmala, M., Worsnop, D. R., Wildt, J., and Mentel, T. F.: A large source of low-volatility secondary organic aerosol, *Nature*, 506, 476–479, doi:10.1038/nature13032, 2014.

Fry, J. L., Kiendler-Scharr, A., Rollins, A. W., Wooldridge, P. J., Brown, S. S., Fuchs, H., Dube, W., Mensah, A., dal Maso, M., Tillmann, R., Dorn, H. P., Brauers, T., and Cohen, R. C.: Organic nitrate and secondary organic aerosol yield from NO3 oxidation of beta-pinene evaluated using a gas-phase kinetics/aerosol partitioning model, *Atmos. Chem. Phys.*, 9, 1431-1449, 2009.

Fry, J. L., Draper, D. C., Barsanti, K. C., Smith, J. N., Ortega, J., Winkler, P. M., Lawler, M. J., Brown, S. S., Edwards, P. M., Cohen, R. C., and Lee, L.: Secondary Organic Aerosol Formation and Organic Nitrate Yield from NO3 Oxidation of Biogenic Hydrocarbons, *Environ. Sci. Technol.*, 48, 11944-11953, doi:10.1021/es502204x, 2014.

Gao, S., Ng, N. L., Keywood, M., Varutbangkul, V., Bahreini, R., Nenes, A., He, J., Yoo, K. Y., Beauchamp, J. L., Hodyss, R. P., Flagan, R. C., and Seinfeld, J. H.: Particle phase acidity and oligomer formation in secondary organic aerosol, *Environ. Sci. Technol.*, 38, 6582–6589, 2004.

Grieshop, A. P., Donahue, N. M., and Robinson, A. L.: Is the gas-particle partitioning in alpha-

pinene secondary organic aerosol reversible?, *Geophys. Res. Lett.*, 34, doi:10.1029/2007GL029987, 2007.

Griffin, R. J., Cocker III, D. R., Flagan, R. C., and Seinfeld, J. H.: Organic aerosol formation from the oxidation of biogenic hydrocarbons, *J. Geophys. Res.*, 104, 3555–3567, 1999.

Guenther, A. B., Jiang, X., Heald, C. L., Sakulyanontvittaya, T., Duhl, T., Emmons, L. K., and Wang, X.: The Model of Emissions of Gases and Aerosols from Nature version 2.1 (MEGAN2.1): an extended and updated framework for modeling biogenic emissions, *Geosci. Model Dev.*, 5, 1471-1492, doi:10.5194/gmd-5-1471-2012, 2012.

Hallquist, M., Wenger, J. C., Baltensperger, U., Rudich, Y., Simpson, D., Claeys, M., Dommen, J., Donahue, N. M., George, C., Goldstein, A. H., Hamilton, J. F., Herrmann, H., Hoffmann, T., Iinuma, Y., Jang, M., Jenkin, M. E., Jimenez, J. L., Kiendler-Scharr, A., Maenhaut, W., McFiggans, G., Mentel, Th. F., Monod, A., Prévôt, A. S. H., Seinfeld, J. H., Surratt, J. D., Szmigielski, R., and Wildt, J.: The formation, properties and impact of secondary organic aerosol: current and emerging issues, *Atmos. Chem. Phys.*, 9, 5155–5236, doi:10.5194/acp-9-5155-2009, 2009.

Henry, K. M., Lohaus, T., and Donahue, N. M.: Organic Aerosol Yields from alpha-Pinene Oxidation: Bridging the Gap between First-Generation Yields and Aging Chemistry, *Environ. Sci. Technol.*, 46, 12347-12354, doi:10.1021/es302060y, 2012.

Hildebrandt, L., Donahue, N. M., and Pandis, S. N.: High formation of secondary organic aerosol from the photo-oxidation of toluene, *Atmos. Chem. Phys.*, 9, 2973-2986, 2009.

Hoffmann, T., Odum, J. R., Bowman, F., Collins, D., Klockow, D., Flagan, R. C., and Seinfeld, J. H.: Formation of organic aerosols from the oxidation of biogenic hydrocarbons, *J. Atmos. Chem.*, 26, 189–222, 1997.

Kanakidou, M., Seinfeld, J. H., Pandis, S. N., Barnes, I., Dentener, F. J., Facchini, M. C., Van Dingenen, R., Ervens, B., Nenes, A., Nielsen, C. J., Swietlicki, E., Putaud, J. P., Balkanski, Y.,

Fuzzi, S., Horth, J., Moortgat, G. K., Winterhalter, R., Myhre, C. E. L., Tsigaridis, K., Vignati, E., Stephanou, E. G., and Wilson, J.: Organic aerosol and global climate modelling: a review, *Atmos. Chem. Phys.*, 5, 1053-1123, 2005.

Keywood, M. D., Varutbangkul, V., Bahreini, R., Flagan, R. C., and Seinfeld, J. H.: Secondary organic aerosol formation from the ozonolysis of cycloalkenes and related compounds, *Geophys. Res. Lett.*, 38, 4157-4164, doi:10.1021/es035363o, 2004.

Kokkola, H., Yli-Pirilä, P., Vesterinen, M., Korhonen, H., Keskinen, H., Romakkaniemi, S., Hao, L., Kortelainen, A., Joutsensaari, J., Worsnop, D. R., Virtanen, A., and Lehtinen, K. E. J.: The role of low volatile organics on secondary organic aerosol formation, *Atmos. Chem. Phys.*, 14, 1689–1700, doi:10.5194/acp-14-1689-2014, 2014.

Kostenidou, E., Pathak, R. K., and Pandis, S. N.: An algorithm for the calculation of secondary organic aerosol density combining AMS and SMPS data, *Aerosol Sci. Technol.*, 41, 1002-1010, doi:10.1080/02786820701666270, 2007.

Kristensen, K., Cui, T., Zhang, H., Gold, A., Glasius, M., and Surratt, J. D.: Dimers in alpha-pinene secondary organic aerosol: effect of hydroxyl radical, ozone, relative humidity and aerosol acidity, *Atmos. Chem. Phys.*, 14, 4201-4218, doi:10.5194/acp-14-4201-2014, 2014.

Kroll, J. H., Chan, A. W. H., Ng, N. L., Flagan, R. C., and Seinfeld, J. H.: Reactions of semivolatile organics and their effects on secondary organic aerosol formation, *Environ. Sci. Technol.*, 41, 3545-3550, doi:10.1021/es062059x, 2007.

Kuwata, M. and Martin, S. T.: Phase of atmospheric secondary organic material affects its reactivity, *P. Natl. Acad. Sci. USA*, 109, 17354–17359, 2012.

La, Y. S., Camredon, M., Ziemann, P. J., Valorso, R., Matsunaga, A., Lannuque, V., Lee-Taylor, J., Hodzic, A., Madronich, S., and Aumont, B.: Impact of chamber wall loss of gaseous organic compounds on secondary organic aerosol formation: explicit modeling of SOA formation from

alkane and alkene oxidation, *Atmos. Chem. Phys.*, 16, 1417–1431, doi:10.5194/acp-16-1417-2016, 2016.

Loza, C. L., Chan, A. W., Galloway, M. M., Keutsch, F. N., Flagan, R. C., and Seinfeld, J. H.: Characterization of vapor wall loss in laboratory chambers, *Environ. Sci. Technol.*, 44, 5074–5078, 2010.

Loza, C. L., Chhabra, P. S., Yee, L. D., Craven, J. S., Flagan, R. C., and Seinfeld, J. H.: Chemical aging of m-xylene secondary organic aerosol: laboratory chamber study, *Atmos. Chem. Phys.*, 12, 151–167, 2012.

Matsunaga, A. and Ziemann, P. J.: Gas-wall partitioning of organic compounds in a teflon film chamber and potential effects on reaction product and aerosol yield measurements, *Aerosol Sci. Tech.*, 44, 881–892, 2010.

McMurry, P. H. and Grosjean, D.: Gas and aerosol wall losses in teflon film smog chambers, *Environ. Sci. Technol.*, 19, 1176–1182, 1985.

McMurry, P. H., and Rader, D. J.: Aerosol Wall Losses in Electrically Charged Chambers, *Aerosol Sci. Technol.*, 4, 249-268, doi:10.1080/02786828508959054, 1985.

McVay, R. C., Cappa, C. D., and Seinfeld, J. H.: Vapor-wall deposition in chambers: theoretical considerations, *Environ. Sci. Technol.*, 48, 10251–10258, 2014.

McVay, R. C., Zhang, X., Aumont, B., Valorso, R., Camredon, M., La, Y. S., Wennberg, P. O., and Seinfeld, J. H.: SOA formation from the photooxidation of α-pinene: systematic exploration of the simulation of chamber data, *Atmos. Chem. Phys.*, 16, 2785–2802, doi:10.5194/acp-16-2785-2016, 2016.

Miles, R. E. H., Reid, J. P., and Riipinen, I.: Comparison of Approaches for Measuring the Mass Accommodation Coefficient for the Condensation of Water and Sensitivities to Uncertainties in Thermophysical Properties, *J. Phys. Chem. A*, 116, 10810-10825, doi:10.1021/jp3083858, 2012.

Ng, N. L., Kroll, J. H., Keywood, M. D., Bahreini, R., Varutbangkul, V., Flagan, R. C., Seinfeld, J. H., Lee, A., and Goldstein, A. H.: Contribution of first- versus second-generation products to secondary organic aerosols formed in the oxidation of biogenic hydrocarbons, *Environ. Sci. Technol.*, 40, 2283–2297, 2006.

Ng, N. L., Kroll, J. H., Chan, A. W. H., Chhabra, P. S., Flagan, R. C., and Seinfeld, J. H.: Secondary organic aerosol formation from *m*-xylene, toluene, and benzene, *Atmos. Chem. Phys.*, 7, 3909–3922, doi:10.5194/acp-7-3909-2007, 2007.

Odum, J. R., Hoffman, T., Bowman, F., Collins, D., Flagan, R. C., and Seinfeld, J. H.: Gas/particle partitioning and secondary organic aerosol yields. *Environ. Sci. Technol.*, 30, 2580–2585, 1996.

Odum, J. R., Jungkamp, T. P. W., Griffin, R. J., Flagan, R. C., and Seinfeld, J. H.: The atmospheric aerosol-forming potential of whole gasoline vapor, *Science*, 276, 96-99, doi:10.1126/science.276.5309.96, 1997a.

Odum, J. R., Jungkamp, T. P. W., Griffin, R. J., Forstner, H. J. L., Flagan, R. C., and Seinfeld, J. H.: Aromatics, reformulated gasoline, and atmospheric organic aerosol formation, *Environ. Sci. Technol.*, 31, 1890-1897, doi:10.1021/es960535l, 1997b.

Pathak, R. K., Presto, A. A., Lane, T. E., Stanier, C. O., Donahue, N. M., and Pandis, S. N.: Ozonolysis of alpha-pinene: parameterization of secondary organic aerosol mass fraction, *Atmos. Chem. Phys.*, 7, 3811-3821, 2007a.

Pathak, R. K., Stanier, C. O., Donahue, N. M., and Pandis, S. N.: Ozonolysis of α-pinene at atmospherically relevant concentrations: Temperature dependence of aerosol mass fractions (yields), *J. Geophys. Res.*, 112, D03201, doi:10.1029/2006JD007436, 2007b.

Perraud, V., Bruns, E. A., Ezell, M. J., Johnson, S. N., Yu, Y., Alexander, M. L., Zelenyuk, A., Imre, D., Chang, W. L., Dabdub, D., Pankow, J., and Finlayson-Pitts, B. J.: Nonequilibrium atmospheric secondary organic aerosol formation and growth, *P. Natl. Acad. Sci. USA*, 109, 2836–2841, 2012.

Pierce, J. R., Engelhart, G. J., Hildebrandt, L., Weitkamp, E. A., Pathak, R. K., Donahue, N. M., Robinson, A. L., Adams, P. J., and Pandis, S. N.: Constraining particle evolution from wall losses, coagulation, and condensation-evaporation in smog-chamber experiments: Optimal estimation based on size distribution measurements, *Aerosol Sci. Technol.*, 42, 1001-1015, doi:10.1080/02786820802389251, 2008.

Presto, A. A., Huff Hartz, K. E., and Donahue, N. M.: Secondary organic aerosol production from terpene ozonolysis: 2. Effect of NO_x concentration, *Environ. Sci. Technol.*, 39, 7046–7054, 2005.

Presto, A. A. and Donahue, N. M.: Investigation of α-pinene + ozone secondary organic aerosol formation at low total aerosol mass, *Environ. Sci. Technol.*, 40, 3536–3543, 2006.

Pye, H. O. T., Chan, A. W. H., Barkley, M. P., and Seinfeld, J. H.: Global modeling of organic aerosol: the importance of reactive nitrogen (NO_x and NO_3), *Atmos. Chem. Phys.*, 10, 11261–11276, doi:10.5194/acp-10-11261-2010, 2010.

Renbaum-Wolff, L., Grayson, J. W., Bateman, A. P., Kuwata, M., Sellier, M., Murray, B. M., Shilling, J. E., Martin, S. T., and Bertram, A. K.: Viscosity of α-pinene secondary organic material and implications for particle growth and reactivity, *P. Natl. Acad. Sci. USA*, 110, 8014–8019, 2013.

Saleh, R., Donahue, N. M., and Robinson, A. L.: Time scales for gas-particle partitioning equilibration of secondary organic aerosol formed from alpha-pinene ozonolysis, *Environ. Sci. Technol.*, 47, 5588–5594, 2013.

Saukko, E., Lambe, A. T., Massoli, P., Koop, T., Wright, J. P., Croasdale, D. R., Pedernera, D. A., Onasch, T. B., Laaksonen, A., Davidovits, P., Worsnop, D. R., and Virtanen, A.: Humidity-dependent phase state of SOA particles from biogenic and anthropogenic precursors, *Atmos. Chem. Phys.*, 12, 7517-7529, doi:10.5194/acp-12-7517-2012, 2012.

Saunders, S. M., Jenkin, M. E., Derwent, R. G., and Pilling, M. J.: Protocol for the development of the Master Chemical Mechanism, MCM v3 (Part A): tropospheric degradation of non-aromatic volatile organic compounds, *Atmos. Chem. Phys.*, 3, 161-180, 10.5194/acp-3-161-2003, 2003.

Seinfeld, J. H. and Pandis, S. N.: Atmospheric Chemistry and Physics: From Air Pollution to Climate Change, 2nd Edn. Wiley, Hoboken, N. J., 2006.

Shilling, J. E., Chen, Q., King, S. M., Rosenoern, T., Kroll, J. H., Worsnop, D. R., McKinney, K. A., and Martin, S. T.: Particle mass yield in secondary organic aerosol formed by the dark ozonolysis of a-pinene, *Atmos. Chem. Phys.*, 8, 2073–2088, doi:10.5194/acp-8-2073-2008, 2008.

Shilling, J. E., Chen, Q., King, S. M., Rosenoern, T., Kroll, J. H., Worsnop, D. R., DeCarlo, P. F., Aiken, A. C., Sueper, D., Jimenez, J. L., and Martin, S. T.: Loading-dependent elemental composition of alpha-pinene SOA particles, *Atmos. Chem. Phys.*, 9, 771-782, 2009.

Shiraiwa, M. and Seinfeld, J. H.: Equilibration timescale of atmospheric secondary organic aerosol partitioning, *Geophys. Res. Lett.*, 39, L24801, 2012.

Song, C., Zaveri, R. A., Alexander, M. L., Thornton, J. A., Madronich, S., Ortega, J. V., Zelenyuk, A., Yu, X. Y., Laskin, A., and Maughan, D. A.: Effect of hydrophobic primary organic aerosols on secondary organic aerosol formation from ozonolysis of alpha-pinene, *Geophys. Res. Lett.*, 34, 5, doi:10.1029/2007gl030720, 2007.

Stanier, C. O., Pathak, R. K., and Pandis, S. N.: Measurements of the volatility of aerosols from alpha-pinene ozonolysis, *Environ. Sci. Technol.*, 41, 2756-2763, 2007.

Tsigaridis, K., Daskalakis, N., Kanakidou, M., Adams, P. J., Artaxo, P., Bahadur, R., Balkanski, Y., Bauer, S. E., Bellouin, N., Benedetti, A., Bergman, T., Berntsen, T. K., Beukes, J. P., Bian, H., Carslaw, K. S., Chin, M., Curci, G., Diehl, T., Easter, R. C., Ghan, S. J., Gong, S. L., Hodzic, A., Hoyle, C. R., Iversen, T., Jathar, S., Jimenez, J. L., Kaiser, J. W., Kirkevg, A., Koch, D., Kokkola, H., Lee, Y. H., Lin, G., Liu, X., Luo, G., Ma, X., Mann, G. W., Mihalopoulos, N., Morcrette, J. J., Mller, J. F., Myhre, G., Myriokefalitakis, S., Ng, N. L., O'Donnell, D., Penner, J. E., Pozzoli, L., Pringle, K. J., Russell, L. M., Schulz, M., Sciare, J., Seland, Ø., Shindell, D. T., Sillman, S., Skeie, R. B., Spracklen, D., Stavrakou, T., Steenrod, S. D., Takemura, T., Tiitta, P., Tilmes, S., Tost, H., van Noije, T., van Zyl, P. G., von Salzen, K., Yu, F., Wang, Z., Zaveri, R. A., Zhang, H.,

Zhang, K., Zhang, Q., and Zhang, X.: The AeroCom evaluation and intercomparison of organic aerosol in global models, *Atmos. Chem. Phys.*, 14, 10845-10895, doi:10.5194/acp-14-10845-2014, 2014.

Vaden, T. D., Song, C., Zaveri, R. A., Imre, D., and Zelenyuk, A.: Morphology of mixed primary and secondary organic particles and the adsorption of spectator organic gases during aerosol formation, *P. Natl. Acad. Sci. USA*, 107, 6658–6663, 2010.

Vaden, T. D., Imre, D., Beranek, J., Shrivastava, M., and Zelenyuk, A.: Evaporation kinetics and phase of laboratory and ambient secondary organic aerosol, *P. Natl. Acad. Sci. USA*, 108, 2190-2195, 2011.

Virtanen, A., Joutsensaari, J., Koop, T., Kannosto, J., Yli-Pirilä, P., Leskinen, J., Mäkelä, J. M., Holopainen, J. K., Pöschl, U., Kulmala, M., Worsnop, D. R., and Laaksonen, A.: An amorphous solid state of biogenic secondary organic aerosol particles, *Nature*, 467, 824–827, 2010.

Virtanen, A., Kannosto, J., Kuuluvainen, H., Arffman, A., Joutsensaari, J., Saukko, E., Hao, L., Yli-Pirilä, P., Tiitta, P., Holopainen, J. K., Keskinen, J., Worsnop, D. R., Smith, J. N., and Laaksonen, A.: Bounce behavior of freshly nucleated biogenic secondary organic aerosol particles, *Atmos. Chem. Phys.*, 11, 8759–8766, doi:10.5194/acp-11-8759-2011, 2011.

Weitkamp, E. A., Sage, A. M., Pierce, J. R., Donahue, N. M., and Robinson, A. L.: Organic aerosol formation from photochemical oxidation of diesel exhaust in a smog chamber, *Environ. Sci. Technol.*, 41, 6969-6975, doi:10.1021/es070193r, 2007.

Yeh, G. K. and Ziemann, P. J.: Alkyl nitrate formation from the reactions of C_8-C_{14} *n*-alkanes with OH radicals in the presence of NO_x: measured yields with essential corrections for gas-wall partitioning, *J. Phys. Chem. A.*, 118, 8147–8157, 2014.

Yeh, G. K. and Ziemann, P. J.: Gas-wall partitioning of oxygenated organic compounds: measurements, structure-activity relationships, and correlation with gas chromatographic retention factor, *Aerosol. Sci. Tech.*, 49, 727–738, 2015.

Zaveri, R. A., Easter, R. C., Shilling, J. E., and Seinfeld, J. H.: Modeling kinetic partitioning of secondary organic aerosol and size distribution dynamics: representing effects of volatility, phase state, and particle-phase reaction, *Atmos. Chem. Phys.*, 13, 5153–5181, 2014.

Zhang, X., Pandis, S. N., and Seinfeld, J. H.: Diffusion-Limited Versus Quasi-Equilibrium Aerosol Growth, *Aerosol Sci. Technol.*, 46, 874-885, doi:10.1080/02786826.2012.679344, 2012.

Zhang, X., Cappa, C. D., Jathar, S. H., McVay, R. C., Ensberg, J. J., Kleeman, M. J., and Seinfeld, J. H.: Influence of vapor wall-loss in laboratory chambers on yields of secondary organic aerosol, *P. Natl. Acad. Sci. USA*, 111, 5802–5807, doi:10.1073/pnas.1404727111, 2014.

Zhang, X., Schwantes, R. H., McVay, R. C., Lignell, H., Coggon, M. M., Flagan, R. C., and Seinfeld, J. H.: Vapor wall deposition in Teflon chambers, *Atmos. Chem. Phys.*, 15, 4197–4214, doi:10.5194/acp-15-4197-2015, 2015a.

Zhang, X., McVay, R. C., Huang, D. D., Dalleska, N. F., Aumont, B., Flagan, R. C., and Seinfeld, J. H.: Formation and evolution of molecular products in alpha-pinene secondary organic aerosol, *P. Natl. Acad. Sci. USA*, 112, 14168-14173, 10.1073/pnas.1517742112, 2015b.

Table 3.1: Experimental conditions and results for the α-pinene ozonolyis experiments

Experiment	Initial Seed Surface Area (μm^2 cm^{-3})	Initial [α-pinene][a] (μg m^{-3})	ΔM_0[b] (μg m^{-3})	SOA Mass Yield[c] (%)
100 ppb O_3 nucleation	0	290.2±23.2	62.0±1.2[d]	22.6±1.9
100 ppb O_3 low AS	1130	280.5±22.4	63.0±0.8[d]	23.3±1.9
100 ppb O_3 high AS	2700	238.7±19.1	50.6±1.6[d]	23.3±1.9
500 ppb O_3 nucleation	0	274.4±21.9	87.3±0.3[e]	31.8±2.5
500 ppb O_3 low AS	1300	264.9±21.2	75.7±0.6[e]	28.6±2.3
500 ppb O_3 high AS	2720	236.1±18.9	66.3±1.9[e]	28.1±2.4

[a]Concentration of α-pinene injected into the chamber. All the α-pinene reacted in the 500 ppb O_3 experiments, but not the 100 ppb O_3 experiments.

[b]Uncertainties in the peak SOA mass concentration (ΔM_0) are calculated from one standard deviation of the aerosol volume as measured by the scanning mobility particle sizer.

[c]SOA mass yields at peak SOA growth are reported.

[d]The SOA mass concentration is calculated using the density = 1.39 g cm^{-3} obtained from the 100 ppb O_3 nucleation experiment.

[e]The SOA mass concentration is calculated using the density = 1.37 g cm^{-3} obtained from the 500 ppb O_3 nucleation experiment.

Table 3.2: Coupled vapor–particle dynamics model parameters

Parameter	Definition	Value
α_p	Vapor-particle mass accommodation coefficient	1
α_w	Vapor-wall mass accommodation coefficient	10^{-6}
τ_{olig}	Timescale of oligomerization	4 h
C^*	Saturation vapor pressures and branching ratios of oxidation products	[0.57($>10^3$), 0.35 (10^2), 0.04(10), 0.015 (1) and 0.025(0.1)]
D_i	Gas-phase molecular diffusivity	3×10^{-6} m^2 s^{-1}
A/V	Surface area-to-volume ratio of the chamber	2.5 m^{-1}
C_w	Equivalent organic mass concentration in the wall	10 mg m^{-3}
k_e	Eddy diffusion coefficient	0.03 s^{-1}
M_i	Molecular weight of the diffusing gas-phase molecule i	168, 184, 192, 200 and 216 g mole^{-1}
M_{init}	Initially absorbing organic material in seed aerosol	0.01 μg m^{-3}
P	Pressure	1×10^5 Pa
T	Temperature	298 K
ρ_{seed}	Density of inorganic seed	1700 kg m^{-3}
ρ_{org}	Density of organic material on seed particle	1300 kg m^{-3}

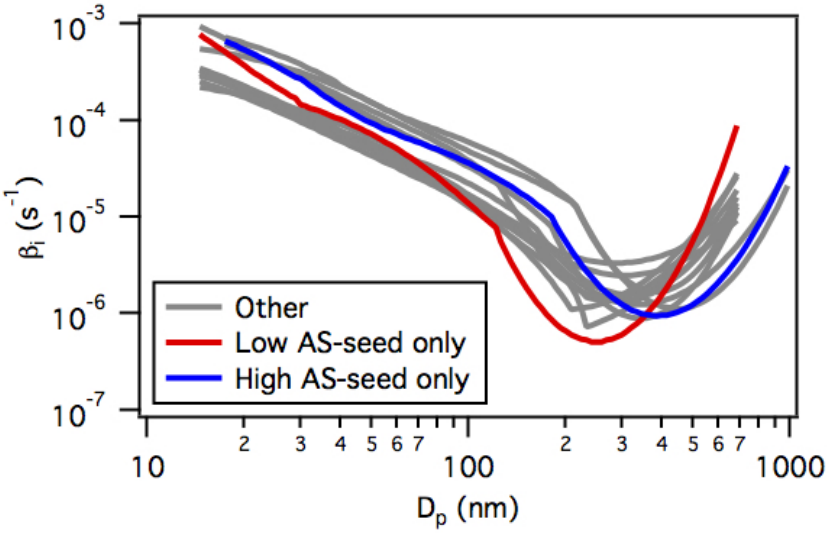

Figure 3.1: Particle wall deposition coefficients (β_i) measured during the low AS-seed only and high AS-seed only experiments in GTEC. Also shown are the particle wall deposition coefficients (labeled "Other") measured in previous routine monthly AS-seed only experiments in the chamber. These previous routine monthly AS-seed only experiments were performed using either a 0.008 M AS or a 0.1 M AS solution.

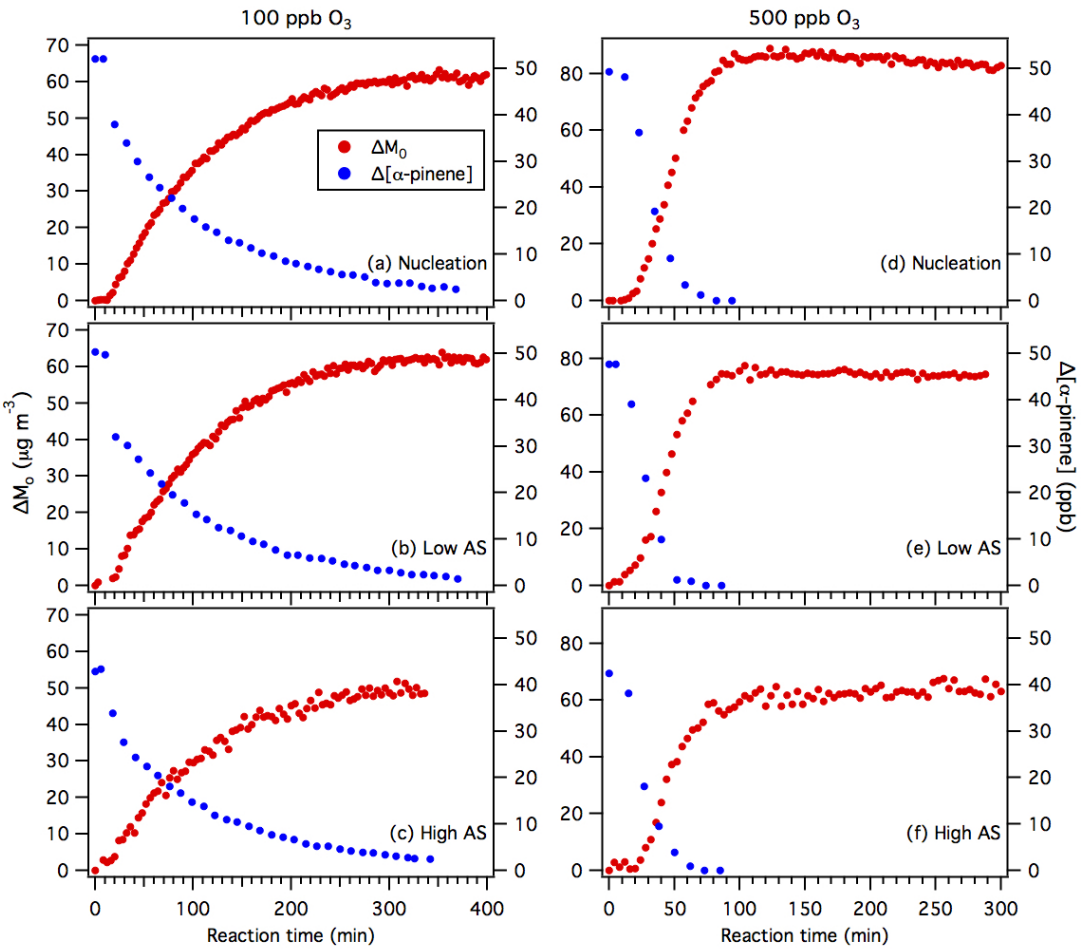

Figure 3.2: Reaction profiles of the α-pinene ozonolysis experiments. Panels (a), (b) and (c) show results from the nucleation, low AS and high AS 100 ppb O_3 experiments, respectively. Panels (d), (e) and (f) show results from the nucleation, low AS and high AS 500 ppb O_3 experiments, respectively. As explained in the main text, the SOA mass concentrations (ΔM_o) for the nucleation and low AS experiments are obtained using the particle wall rates obtained from the low AS-seed only experiments, while the SOA mass concentrations (ΔM_o) for the high AS-seed experiments are obtained using the particle wall rates obtained from the high AS-seed only experiments.

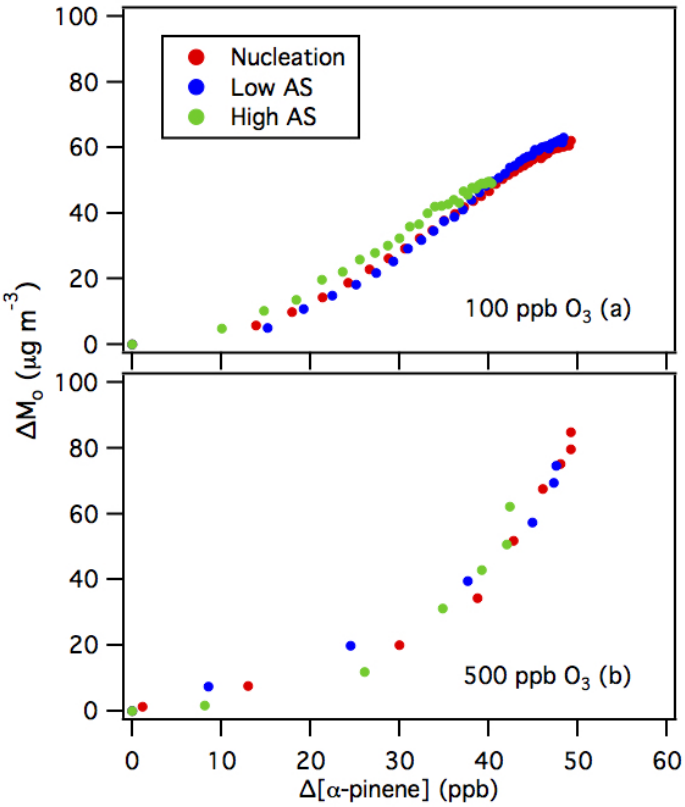

Figure 3.3: Time-dependent SOA growth curves for α-pinene ozonolysis. Panels (a) and (b) show 10 min-averaged results from the 100 ppb and 500 ppb O_3 experiments, respectively. Only SOA growth data up to the point of SOA peak growth are shown.

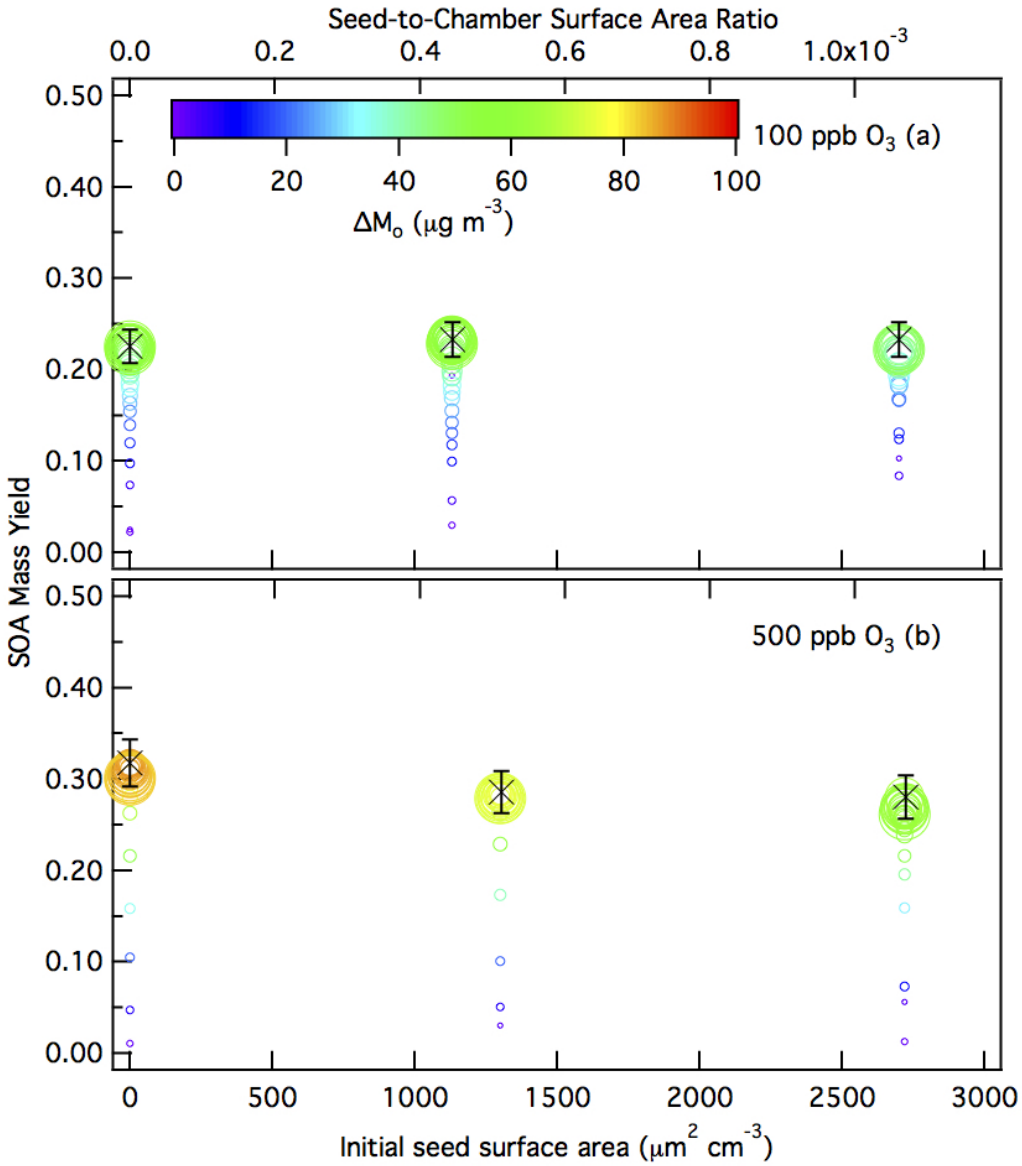

Figure 3.4: 10 min-averaged SOA mass yields over the course of an α-pinene ozonolysis experiment as a function of initial total AS seed surface area concentration for the (a) 100 ppb O_3 experiments, and (b) 500 ppb O_3 experiments. Symbol color indicates the SOA mass concentration and symbol size indicates the time after O_3 is injected into the chamber. The $\times$ symbols are the SOA mass yields at peak SOA growth obtained from the experimental data. The y-axis error bars represent the uncertainty in the SOA mass yield at peak SOA growth, which originates from the α-pinene injection and the aerosol volume concentration measured by the SMPS at peak SOA growth (one standard deviation).

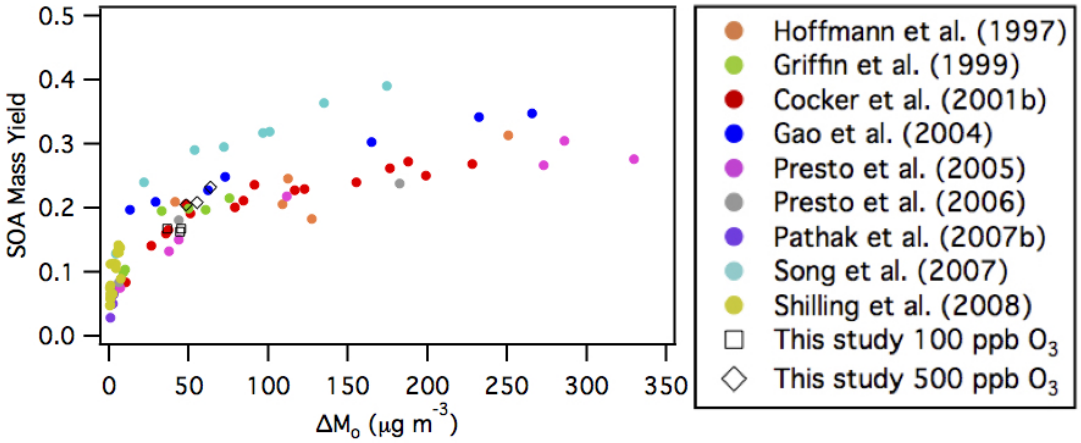

Figure 3.5: Comparison of SOA mass yields obtained in this study to those of previous dark α-pinene ozonolysis studies (Table B.2). The SOA mass yields and concentrations of majority of these previous studies (*Hoffmann et al.*, 1997; *Griffin et al.*, 1999; *Cocker et al.*, 2001b; *Gao et al.*, 2004; *Presto et al.*, 2005; *Presto and Donahue*, 2006; *Pathak et al.*, 2007b; *Song et al.*, 2007) were previously compiled by *Shilling et al.* (2008). Similar to *Shilling et al.* (2008), all the data shown here (including those reported in this study) have been adjusted using an organic density of 1.0 g cm^{-3}, and to 298 K using a temperature correction of 1.6 % per K, as recommended by *Pathak et al.* (2007b) to facilitate easier comparison among the different studies.

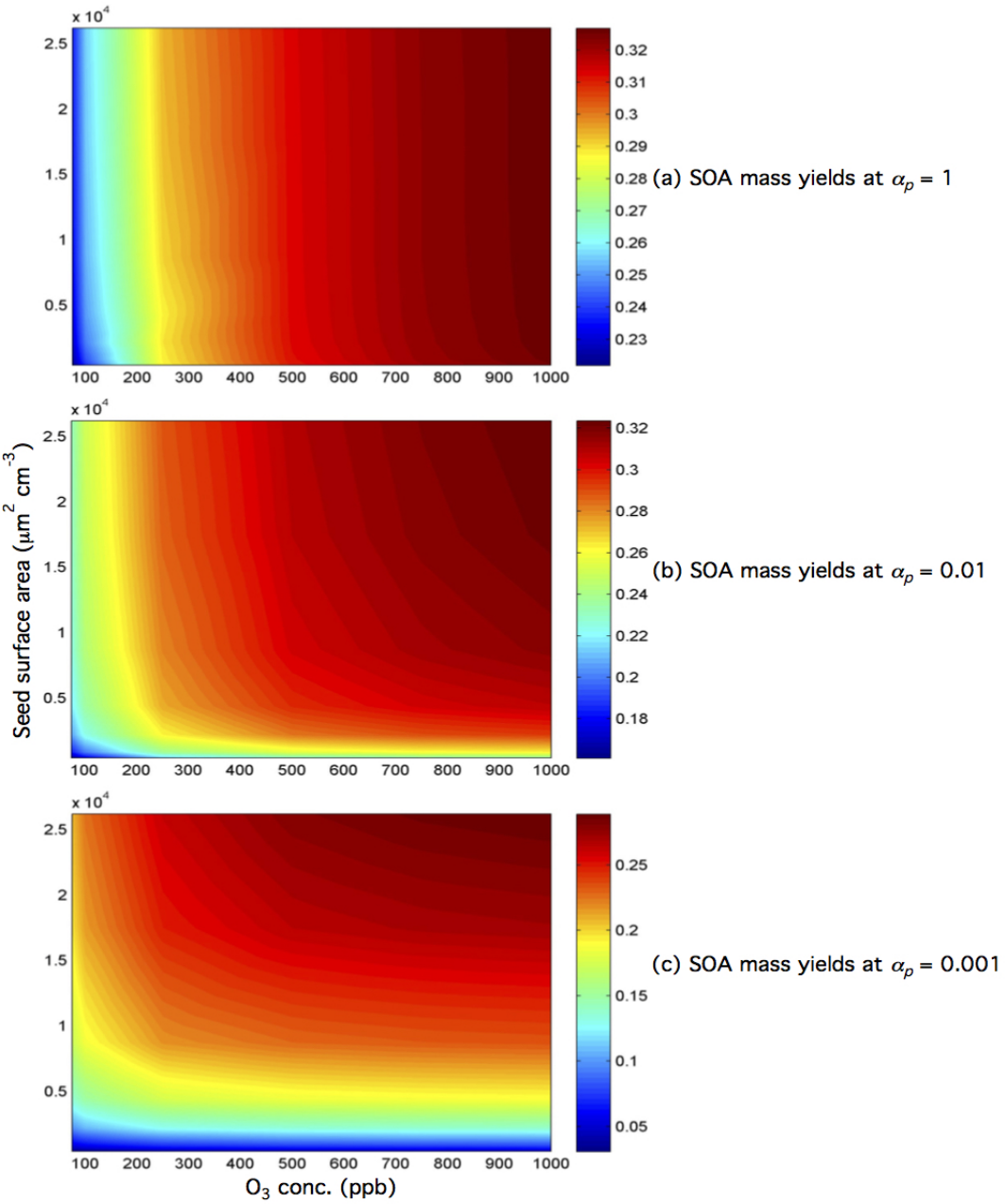

Figure 3.6: SOA mass yields at peak SOA growth as a function of both the seed surface area and O_3 concentration for $\alpha_p = 1$, 0.01, and 0.001. The SOA mass yields at peak SOA growth are indicated by colors and contours. Note that the color bars for panels (a), (b) and (c) have different SOA mass yield ranges. Simulations were carried out using the branching ratios, oligomerization rate, and vapor wall deposition rate parameters obtained in this study. The initial α-pinene concentration was set to 50 ppb, and a fixed O_3 concentration was used in place of a linear injection.

Chapter 4

SOA Formation from the Photooxidation of α-pinene: Systematic Exploration of the Simulation of Chamber Data *

*Reproduced with permission from "SOA formation from the photooxidation of α-pinene: systematic exploration of the simulation of chamber data" by McVay, R. C., Zhang, X., Aumont, B., Valorso, R., Camredon, M., La, Y. S., Wennberg, P. O., and Seinfeld, J. H., *Atmospheric Chemistry and Physics*, 16, 2785–2802, doi:10.5194/acp-16-2785-2016, 2016.

4.1 Abstract

Chemical mechanisms play an important role in simulating the atmospheric chemistry of volatile organic compound oxidation. Comparison of mechanism simulations with laboratory chamber data tests our level of understanding of the prevailing chemistry as well as the dynamic processes occurring in the chamber itself. α-Pinene photooxidation is a well-studied system experimentally, for which detailed chemical mechanisms have been formulated. Here, we present the results of simulating low-NO α-pinene photooxidation experiments conducted in the Caltech chamber with the Generator for Explicit Chemistry and Kinetics of Organics in the Atmosphere (GECKO-A) under varying concentrations of seed particles and OH levels. Unexpectedly, experiments conducted at low and high OH levels yield the same secondary organic aerosol (SOA) growth, whereas GECKO-A predicts greater SOA growth under high OH levels. SOA formation in the chamber is a result of a competition among the rates of gas-phase oxidation to low-volatility products, wall deposition of these products, and condensation into the aerosol phase. Various processes – such as photolysis of condensed-phase products, particle-phase dimerization, and peroxy radical autoxidation – are explored to rationalize the observations. In order to explain the observed similar SOA growth at different OH levels, we conclude that vapor wall loss in the Caltech chamber is likely of order $10^{-5}\,s^{-1}$, consistent with previous experimental measurements in that chamber. We find that GECKO-A tends to overpredict the contribution to SOA of later-generation oxidation products under high-OH conditions. Moreover, we propose that autoxidation may alternatively resolve some or all of the measurement–model discrepancy, but this hypothesis cannot be confirmed until more explicit mechanisms are established for α-pinene autoxidation. The key role of the interplay among oxidation rate, product volatility, and vapor–wall deposition in chamber experiments is illustrated.

4.2 Introduction

Secondary organic aerosol (SOA) contributes substantially to the tropospheric particle mass loading (*Jimenez et al.*, 2009), which in turns influences visibility, direct radiative forcing, cloud formation,

and human health (*Hallquist et al.*, 2009). Monoterpenes contribute significantly to global SOA formation, with an estimated emission rate of 100–130 $\mathrm{Tg\,C\,yr^{-1}}$ and SOA mass yield of 10–20 % (*Hoffmann et al.*, 1997; *Pye et al.*, 2010; *Guenther et al.*, 1995). Of the terpenes, α-pinene has the highest estimated emission rate of 34 $\mathrm{Tg\,C\,yr^{-1}}$ (*Pye et al.*, 2010). Numerous studies have examined SOA formation from both the OH oxidation and ozonolysis of α-pinene (*Hoffmann et al.*, 1997; *Griffin et al.*, 1999; *Kamens and Jaoui*, 2001; *Takekawa et al.*, 2003; *Presto et al.*, 2005a,b; *Ng et al.*, 2006; *Pathak et al.*, 2007; *Shilling et al.*, 2008; *Ng et al.*, 2007a; *Eddingsaas et al.*, 2012b). Ozonolysis is a more efficient route to α-pinene SOA than OH oxidation (*Griffin et al.*, 1999), and the ozonolysis path has received considerable attention. Fewer studies have examined SOA formation from OH oxidation of α-pinene, and even fewer studies have focused on low-NO conditions, under which most α-pinene is oxidized (*Nozière et al.*, 1999; *Ng et al.*, 2007a; *Claeys et al.*, 2009; *Eddingsaas et al.*, 2012a). However, nearly half of the global sink of α-pinene has been estimated to be reaction with OH (42 %); the remainder is oxidized predominantly by O_3, with only 12 % oxidized by NO_3 (*Capouet et al.*, 2008).

As in virtually all volatile organic compound (VOC) systems that lead to SOA, the OH oxidation of α-pinene is complex, and parts of the mechanism are still not fully characterized (*Peeters et al.*, 2001; *Vereecken et al.*, 2007; *Eddingsaas et al.*, 2012a,b). Theoretical and experimental work has indicated that heretofore unidentified alkoxy and peroxy isomerization channels may contribute substantially to SOA formation (*Peeters et al.*, 2001; *Capouet et al.*, 2004; *Vereecken et al.*, 2007; *Ehn et al.*, 2014; *Rissanen et al.*, 2014). Further evidence suggests that particle-phase dimerization reactions are also important to SOA growth in the α-pinene system, although most studies have focused on the ozonolysis path (*Gao et al.*, 2004a,b; *Lopez-Hilfiker et al.*, 2015). Condensed-phase photolysis has also been shown to affect SOA formation from α-pinene, although again the focus has been predominantly on SOA produced via ozonolysis (*Henry and Donahue*, 2012; *Donahue et al.*, 2012; *Epstein et al.*, 2014; *Wong et al.*, 2015). Uncertainty in the mechanism of SOA formation by photooxidation leads to uncertainty in global predictions of α-pinene SOA (*Pye et al.*, 2010).

Experiments in environmental chambers produce the basic data on the extent of SOA formation

from volatile organic compounds and provide a means to test our understanding of the underlying chemistry of SOA formation. Simulations with explicit chemical mechanisms provide a means to evaluate predictions of SOA formation using chamber observations made under a variety of conditions (*Capouet et al.*, 2008; *Valorso et al.*, 2011). The goal of the present work is to carry out such an evaluation for the α-pinene OH photooxidation system.

4.3 α-Pinene Photooxidation Mechanism

4.3.1 Gas-phase Oxidation

A near-explicit gas-phase oxidation mechanism for the oxidation of α-pinene was generated using the Generator for Explicit Chemistry and Kinetics of Organics in the Atmosphere (GECKO-A) (*Aumont et al.*, 2005; *Camredon et al.*, 2007). GECKO-A automatically assigns reactions and rate constants on the basis of experimental data and structure–activity relationships (SARs), producing chemical mechanisms far more detailed and explicit than can be written manually (*Aumont et al.*, 2005). As described in *Valorso et al.* (2011), a protocol is implemented in GECKO-A to reduce the number of species generated to meet computational limits while maintaining as much chemical detail as possible; for example, gas-phase chemistry is not generated for species with vapor pressures below 10^{-13} atm, and isomer substitution is allowed for position isomers for non-radical species formed with a maximum yield less than 2 % after two or more generations. Vapor pressures are estimated using the *Nannoolal et al.* (2008) method. Four generations of oxidation of α-pinene in GECKO-A (a generation encompassing reaction with an oxidant such as OH up to the formation of a stable product) yield 9×10^5 reactions and 1.8×10^5 species. SOA predictions for the base case are found not to be sensitive to the number of generations beyond three (sensitivity tests not shown).

OH oxidation of α-pinene proceeds predominantly via OH addition, with minor channels proceeding via hydrogen abstraction. An overview of the base mechanism in GECKO-A for the OH oxidation of α-pinene is shown in black in Fig. 4.1 and discussed in more detail in *Valorso et al.* (2011). Updates to this mechanism (shown in blue in Fig. 4.1) were added here based on recent

literature. *Vereecken et al.* (2007) proposed several non-traditional pathways in the OH oxidation of α-pinene based on quantum and theoretical chemical calculations. Species in Fig. 4.1 are labeled to be consistent with *Vereecken et al.* (2007). Species R1 is formed with 22 % yield by a prompt ring opening of the four-membered ring following initial OH addition to the double bond in α-pinene (*Peeters et al.*, 2001). A 40 : 60 ratio of *syn* vs. *anti* stereochemistry is estimated for species R1 (*Vereecken et al.*, 2007). The *anti* conformer is predicted to undergo a 1,6-hydrogen shift to form a peroxide, forming a radical stabilized by allyl resonance, R7. This reaction is predicted to dominate over all other peroxy reactions for the *anti* conformer even in high-NO conditions. The position of oxygen addition to the alkyl radical R7 is not well constrained. The branching ratio between addition at the secondary and tertiary sites has conservatively been predicted to be 50 : 50 (*Vereecken et al.*, 2007). *Vereecken et al.* (2007) calculate that the *syn* conformer of R1 will not only participate in traditional peroxy chemistry but will also undergo ring closure to form a six-membered ring, species R3. *Vereecken et al.* (2007) calculate a rate constant for this reaction of $2.6\,s^{-1}$ at 298 K. Species R2 in Fig. 4.1, formed from the reaction of the *syn* conformer of species R1 with NO and RO_2, is predicted to undergo a ring-closure reaction to form species R10. This reaction is predicted to dominate over acetone elimination and hydroxy formation, the previous pathways for R2 in GECKO-A (*Valorso et al.*, 2011). R10 adds oxygen and then participates in the usual peroxy reactions.

The HO_2 chemistry has also been updated in GECKO-A. The main reaction channel for reaction of alkyl peroxy radicals with HO_2 is formation of hydroperoxides. Recent evidence indicates that the reaction of some peroxy radicals with HO_2 can also lead to an alkoxy radical, regenerating OH (*Hasson et al.*, 2004; *Dillon and Crowley*, 2008; *Birdsall et al.*, 2010; *Eddingsaas et al.*, 2012a). This reaction is promoted by the presence of neighboring polar functional groups, which can stabilize the intermediate leading to the alkoxy through hydrogen bonding (*Hasson et al.*, 2005). This pathway has been added to GECKO-A for molecules with an oxygenated moiety in the α position to the peroxy radical. Estimates of the yield of the alkoxy for small acyl peroxy radicals range from 0.15 to 0.7 (*Hasson et al.*, 2004; *Dillon and Crowley*, 2008); however, branching ratios for the larger molecules in the α-pinene mechanism have not been determined. In light of this uncertainty, the

branching ratio between the hydroperoxide and the alkoxy has been assigned to 80 : 20 in GECKO-A.

Ozonolysis chemistry in GECKO-A does not explicitly include the Criegee biradicals formed from the addition of O_3 to the α-pinene double bond; rather the predicted products of the Criegee intermediates are directly assigned to the α-pinene ozonolysis reaction. This simplification overlooks potential reactions of the stabilized Criegee intermediates (SCIs) with water, alcohols, acids, carbonyls, etc. (*Ma et al.*, 2008; *Tobias and Ziemann*, 2001). Reaction of SCIs with water to form pinonaldehyde is thought to be significant (*Capouet et al.*, 2008), and a direct route to pinonaldehyde has been added in GECKO-A. The initial reaction step for ozonolysis is shown in Fig. C.1 in Appendix C. Furthermore, *Ma et al.* (2008) proposed several later-generation intramolecular isomerization reactions to form low-volatility acids. These reactions have been implemented in GECKO-A as a sensitivity test. Virtually no change in predicted SOA concentrations is observed when adding these reactions or when changing the branching ratios of the SCI products. Separate (not shown), purely ozonolysis simulations showed very little SOA formation, indicating potential missing pathways in the ozonolysis mechanism forming low-volatility products. Updating the ozonolysis mechanism should be the subject of future studies. The above updates constitute the base mechanism. Sensitivity tests applied on this base mechanism are addressed in the sections that follow.

4.3.2 Condensed-phase Photolysis

Photolysis of gas-phase compounds containing carbonyl, peroxide, or nitrate chromophores is included automatically within oxidation schemes generated by GECKO-A (*Aumont et al.*, 2005). For the simulations presented here, compound-specific photolysis rates are calculated using cross sections and quantum yields described in *Aumont et al.* (2005) and measured irradiance data in the Caltech chamber. Photolysis of condensed-phase compounds, recently shown to lead to rapid loss of α-pinene SOA (*Henry and Donahue*, 2012; *Donahue et al.*, 2012; *Epstein et al.*, 2014; *Wong et al.*, 2015), is included here as a possible reaction route. Because GECKO-A does not generate chemical reactions within the condensed phase, radical species produced by condensed-phase photolytic reac-

tions are assumed to be irreversibly lost and to not participate in subsequent chemistry (*Hodzic et al.*, 2015). This approximation likely represents an upper limit to the actual physical process since it does not account for recombination of fragments in the particle phase (*Henry and Donahue*, 2012; *Hodzic et al.*, 2015). Two methods of calculating condensed-phase photolysis rate constants were tested in *Hodzic et al.* (2015): (1) all photolabile compounds in the condensed phase are assigned the same empirically derived rate constant, and (2) the condensed-phase photolytic rate constant for each species is set to the corresponding gas-phase value. *Hodzic et al.* (2015) showed that the second method generally results in a greater loss of SOA. Therefore, assumption (2) is tested in the present simulations to evaluate the maximum possible impact of condensed-phase photolysis on overall SOA growth.

4.3.3 Particle-phase Dimerization

The importance of aerosol-phase dimerization and oligomerization reactions has been demonstrated (*Kalberer et al.*, 2004; *Gao et al.*, 2004a,b; *Tolocka et al.*, 2004; *Yee et al.*, 2013; *Shiraiwa et al.*, 2013; *Fahnestock et al.*, 2014). These include alcohol + carbonyl to form hemiacetals and acetals, hydroperoxide + carbonyl to form peroxyhemiacetals and peroxyacetals, carboxylic acid + alcohol to form esters, and aldehyde self-reactions to form aldols (*Ziemann and Atkinson*, 2012). *Shiraiwa et al.* (2013) modeled a generalized particle-phase reaction of an SVOC + carbonyl with a rate constant of $12\,\mathrm{M^{-1}\,s^{-1}}$ when fitting the observed evolution of the particle size distribution of dodecane SOA. In contrast, *Capouet et al.* (2008) modeled the formation of peroxyhemiacetals during α-pinene SOA formation using a rate constant of $0.06\,\mathrm{M^{-1}\,s^{-1}}$; they found that these reactions had a minor impact on SOA yield, except during ozonolysis with large VOC / NO_x ratios that led to high hydroperoxide yields.

In the present work, particle-phase dimerization reactions have been added to the GECKO-A α-pinene oxidation scheme for aldehydes, hydroperoxides, alcohols, and carboxylic acids. Three reaction pairings are considered: aldehyde + alcohol, aldehyde + hydroperoxide, and carboxylic acid + alcohol. As a first approximation, reactions are assumed to be irreversible and to form nonvolatile products.

The mass of dimers becomes part of the organic aerosol mass into which gas-phase species can partition. The rate constant is set to be the same for each dimerization reaction, and two values are tested: $12\,\mathrm{M^{-1}\,s^{-1}}$ (*Shiraiwa et al.*, 2013) and $0.01\,\mathrm{M^{-1}\,s^{-1}}$ (*Ziemann and Atkinson*, 2012). The rate constant is converted from liters of solution to volume of chamber air based on the amount of organic aerosol condensed at each time step.

4.4 Box Model for SOA Formation

Each α-pinene oxidation scheme generated for the different sensitivity tests is coupled to a box model describing the chemical dynamics within the chamber, including dynamic transport of vapors to the particle phase and to the chamber walls.

4.4.1 Vapor–Particle Transport

In previous versions of GECKO-A, instantaneous equilibrium partitioning is assumed to occur between the vapor and particle phases (*Camredon et al.*, 2007; *Lee-Taylor et al.*, 2015). As a more general treatment of vapor–particle transport, dynamic partitioning for mass transfer between the gas and the particle phase is implemented here as described in *La et al.* (2016), with a few modifications. Mass transfer to and from the particle is represented by

$$\left(\frac{\mathrm{d}G_i}{\mathrm{d}t}\right)_{\mathrm{gp}} = -k_{\mathrm{gp}}G_i + k_{\mathrm{pg}}P_i, \tag{4.1}$$

$$\left(\frac{\mathrm{d}P_i}{\mathrm{d}t}\right)_{\mathrm{pg}} = k_{\mathrm{gp}}G_i - k_{\mathrm{pg}}P_i, \tag{4.2}$$

where k_{gp} and k_{pg} are first-order rate constants for transport to and from the particle ($\mathrm{s^{-1}}$), and G_i and P_i are concentrations in the gas and particle phase, respectively. Mass transfer can be limited by gas-phase diffusion, interfacial accommodation, or particle-phase diffusion (e.g., *Mai et al.*, 2015). Particle-phase diffusion in GECKO-A is assumed to be sufficiently rapid that particles are well mixed. Recent studies have shown that the assumption of rapid particle-phase diffusion in SOA may not be accurate owing to semi-solid behavior (*Perraud et al.*, 2012; *Cappa and Wilson*,

2011; *Vaden et al.*, 2010, 2013; *Virtanen et al.*, 2010, 2011; *Kuwata and Martin*, 2012; *Saukko et al.*, 2012; *Abramson et al.*, 2013; *Renbaum-Wolff et al.*, 2013). Computationally, the gas–particle accommodation coefficient, α_{p}, is used to approximate resistances to gas–particle partitioning from surface accommodation and particle-phase diffusion (*Saleh et al.*, 2013). Therefore, the overall rate constant of mass transfer k_{gp} can be approximated as

$$\frac{1}{k_{\mathrm{gp}}} = \frac{1}{k_{\mathrm{diff}}} + \frac{1}{k_{\mathrm{int}}} \tag{4.3}$$

with $k_{\mathrm{diff}} = 4\pi D_{\mathrm{g}} r_{\mathrm{p}} C_{\mathrm{p}}$ and $k_{\mathrm{int}} = \alpha_{\mathrm{p}} \bar{c} \pi r_{\mathrm{p}}^2 C_{\mathrm{p}}$, where D_{g} is the species gas-phase diffusivity, r_{p} is the particle radius, C_{p} is the number of particles per unit volume of air, α_{p} is the gas–particle accommodation coefficient, and $\bar{c}$ is the gas-phase mean velocity (*Seinfeld and Pandis*, 2006). In the present work, the accommodation coefficient α_{p} is treated as a parameter that can be varied in order to produce the best fit to the observed SOA growth. In the model, a single particle size bin is used, so that all particles have the same radius. For all experiments except nucleation, the initial inorganic seed radius is set at 50 nm, and the initial number concentration is calculated from the measured initial seed surface area. GECKO-A does not currently include a mechanism for nucleation; therefore, for the nucleation experiment, an initial seed concentration of $10^4\,\mathrm{cm}^{-3}$ was assumed with an initial radius of 5 nm. The number concentration of particles C_{p} in the model remains unchanged over the course of the experiment as r_{p} grows owing to condensation of organic aerosol. Particle wall loss is not included in GECKO-A. SOA growth in the α-pinene system is essentially independent of seed surface area (discussed in the Results section); therefore, lack of particle wall loss in GECKO-A will not substantially affect SOA predictions. r_{p} is calculated at each time step as

$$r_{\mathrm{p}} = \left(\frac{3}{4\pi} \left(\frac{4}{3}\pi r_{\mathrm{p0}}^3 + \frac{M_{\mathrm{aer}} C_{\mathrm{aer}}}{N_A \rho_{\mathrm{OA}} C_{\mathrm{p}}} \right) \right)^{\frac{1}{3}}, \tag{4.4}$$

where r_{p0} is the initial inorganic seed radius, M_{aer} is the organic aerosol mean molecular weight, C_{aer} is the organic aerosol mass concentration ($\mathrm{molec\,cm}^{-3}$), and ρ_{OA} is the organic aerosol density ($1.32\,\mathrm{g\,cm}^{-3}$ for α-pinene SOA; *Ng et al.*, 2007a). Condensation to and evaporation from the particle

occurs until equilibrium is reached between the gas and particle phases (if ever). The gas-particle partitioning at equilibrium is assumed to follow Raoult's law; therefore the reverse rate constant for mass transfer from the particle to the gas phase is calculated from the relationship (*La et al.*, 2016)

$$\frac{k_{\mathrm{gp}}}{k_{\mathrm{pg}}} = \frac{RT}{P^{\mathrm{vap}}} \frac{C_{\mathrm{aer}}}{M_{\mathrm{aer}} \gamma_{\mathrm{aer}}}, \tag{4.5}$$

where R is the ideal gas constant, T is the temperature, P^{vap} is the species vapor pressure, and γ_{aer} is the activity coefficient in the particle phase (assumed to be 1).

4.4.2 Vapor–Wall Transport

Chamber data are affected by wall deposition of semi and low-volatility vapors (*Loza et al.*, 2010; *Matsunaga and Ziemann*, 2010; *Kokkola et al.*, 2014; *Yeh and Ziemann*, 2014, 2015; *Zhang et al.*, 2014, 2015; *Bian et al.*, 2015). Partitioning of vapor species between the gas phase and the chamber wall is based on the parameterization of *Matsunaga and Ziemann* (2010) and is implemented as described in *La et al.* (2016), with minor variations. Reported values for the rate of transport from the gas to the wall, k_{gw}, span several orders of magnitude in different chambers (*Matsunaga and Ziemann*, 2010; *Zhang et al.*, 2014, 2015; *Loza et al.*, 2010, 2014). Wall loss rates directly measured in the Caltech chamber are of order 10^{-5}–$10^{-6}\,\mathrm{s}^{-1}$ (*Zhang et al.*, 2015; *Loza et al.*, 2010, 2014), although *Zhang et al.* (2014) fit a wall loss rate of $10^{-4}\,\mathrm{s}^{-1}$ during toluene SOA experiments. Gas–wall equilibration timescales, $\tau_{\mathrm{g,w}}$, of order 10–100 min have consistently been measured in the $8.2\,\mathrm{m}^3$ chamber used by *Yeh and Ziemann* (2015). With $\tau_{\mathrm{g,w}} = 1/(k_{\mathrm{gw}} + k_{\mathrm{wg}})$ (*La et al.*, 2016), these timescales correspond to wall loss rates of 10^{-3}–$10^{-4}\,\mathrm{s}^{-1}$. The *Yeh and Ziemann* (2015) chamber is smaller than the Caltech chamber, 8.2 vs. $24\,\mathrm{m}^3$; however, the differences in measured wall loss rates are greater than expected if wall loss scales with the surface-to-volume ratio of the chamber. It has been suggested that rapid initial vapor wall loss could be difficult to distinguish from changes in concentration due to injection and mixing during the long fill period in the Caltech chamber (*Zhang et al.*, 2014; *Loza et al.*, 2014). Vapor species could potentially rapidly equilibrate with the wall and

be subsequently lost to the wall with a much slower uptake owing to relaxation of the Teflon polymer (*Yeh and Ziemann*, 2015). Sensitivity tests in the present work examine the extent to which these differences indicate significantly slower vapor wall loss in the Caltech chamber or arise from the procedure by which experimental measurements were carried out. Furthermore, *Zhang et al.* (2015) showed that k_{gw} may depend on the species' volatility; here we assume k_{gw} to be the same for all species in order to evaluate the order of magnitude of k_{gw} needed to fit the observations. The nominal value is set to $10^{-3}\,\mathrm{s}^{-1}$. As an additional sensitivity test, we implement the k_{gw} parameterization developed by *Zhang et al.* (2015) in which k_{gw} increases as species' volatility decreases. Transport between the gas phase and the wall is represented by the balance equations

$$\left(\frac{\mathrm{d}G_i}{\mathrm{d}t}\right)_{\mathrm{gw}} = -k_{\mathrm{gw}}\,G_i + k_{\mathrm{wg}}\,W_i, \tag{4.6}$$

$$\left(\frac{\mathrm{d}W_i}{\mathrm{d}t}\right)_{\mathrm{wg}} = k_{\mathrm{gw}}\,G_i - k_{\mathrm{wg}}\,W_i, \tag{4.7}$$

where k_{gw} and k_{wg} are first-order rate constants for transport to and from the wall, and W_i is the concentration in the wall layer. The reverse rate is calculated assuming gas–wall partitioning follows Raoult's law (*La et al.*, 2016):

$$\frac{k_{\mathrm{gw}}}{k_{\mathrm{wg}}} = \frac{RT}{P^{\mathrm{vap}}}\frac{C_{\mathrm{w}}}{M_{\mathrm{w}}\gamma_{\mathrm{w}}}, \tag{4.8}$$

where C_{w} is the equivalent overall organic mass concentration in the wall, M_{w} is the equivalent molar weight of the organic concentration in the wall, and γ_{w} is the activity coefficient in the Teflon film. Values of $C_{\mathrm{w}}/M_{\mathrm{w}}\gamma_{\mathrm{w}}$ must be determined experimentally from chamber observations (*Matsunaga and Ziemann*, 2010; *Zhang et al.*, 2015). In the present simulations, a nominal $C_{\mathrm{w}}/M_{\mathrm{w}}\gamma_{\mathrm{w}}$ value of $120\,\mu\mathrm{mol\,m}^{-3}$, the value determined by *Matsunaga and Ziemann* (2010) for 2-ketones, is used for all species except for α-pinene, for which $C_{\mathrm{w}}/M_{\mathrm{w}}\gamma_{\mathrm{w}} = 20\,\mu\mathrm{mol\,m}^{-3}$, the value determined by *Matsunaga and Ziemann* (2010) for alkenes. $C_{\mathrm{w}}/M_{\mathrm{w}}\gamma_{\mathrm{w}}$ is varied as a sensitivity test.

4.5 Experimental

Six α-pinene photooxidation experiments were conducted in the Caltech dual 24 m^3 environmental chambers at $\sim$ 298 K and $<$ 5 % RH (Table 4.1). Prior to each experiment, the Teflon chambers were flushed with purified, dry air for 24 h until the particle number concentration was $< 10\,cm^{-3}$ and volume concentration was $< 0.01\,\mu m^3\,cm^{-3}$. Hydrogen peroxide (H_2O_2) was used as the OH source by evaporating 113 µL of 50 wt % aqueous solution into the chamber with 5 L min^{-1} purified air for 110 min, resulting in an approximate starting H_2O_2 mixing ratio of 2 ppm. Experiments were conducted at low NO ($<$ 2 ppb). Heated 5 L min^{-1} of purified, dry air was flowed through a glass bulb containing liquid α-pinene into the chamber for 30 min, introducing $\sim$ 50 ppb α-pinene into the chamber. Ammonium sulfate (AS) seed aerosol was injected into the chamber by atomizing 0.015 or 0.1 M aqueous $(NH_4)_2SO_4$ solution into the chamber for 30 to 90 min, varying the initial AS concentration in order to vary the seed surface area (SA) available for condensation. After $\sim$ 1 h of mixing, photooxidation was initiated. Four of the experiments were performed using the full set of blacklights, for which the calculated $j_{NO_2} = 4 \times 10^{-3}\,s^{-1}$, with varying amounts of inorganic seed particles (Table 4.1). The remaining two experiments were performed using only 10 % of the available blacklights, for which the calculated $j_{NO_2} = 3.7 \times 10^{-4}\,s^{-1}$, again with varying amounts of inorganic seed particles.

Relative humidity (RH) and temperature were monitored via a Vaisala HMM211 probe. O_3 and NO_x mixing ratios were measured by a Horiba O_3 analyzer (APOA-360) and a Teledyne NO_x analyzer (T200), respectively. α-Pinene concentration was monitored by a gas chromatograph equipped with a HP-5 column (15 m $\times$ 0.53 mm ID $\times$ 1.5 µm thickness, Hewlett-Packard) coupled with flame ionization detector (GC/FID, Agilent 6890N). The size distribution and number concentration of seed particles and organic aerosols were characterized using a custom-built Scanning Mobility Particle Sizer (SMPS) consisting of a Differential Mobility Analyzer (DMA, TSI, 3081) coupled with a Condensation Particle Counter (CPC, TSI, 3010).

Measured volume distributions must be corrected for particle wall loss; the DMA measures the total volume of particles, which is a mixture of organic aerosol and inorganic seed. By accounting for

particle wall loss, the seed volume can be subtracted and the mass of SOA calculated. Two limiting assumptions have traditionally been made when correcting for particle wall loss (*Loza et al.*, 2014): in the lower bound, once deposited, particles are assumed to no longer interact with the vapor. The mass of SOA present on a particle at the moment of its deposition is added when calculating the total SOA. In the upper bound, deposited particles are assumed to continue growing at the same rate as suspended particles, and this SOA is similarly added to the total SOA. The upper bound can be viewed as an early approximation of vapor wall loss from a time when vapor wall loss was less well understood. However, this approximation does not account for the differing mechanisms of vapor–particle and vapor–wall transport, which is reflected in different timescales. Moreover, the absorbing mass of the wall, represented by the parameter C_{w}, is ~ 3 orders of magnitude higher than the mass of deposited particles (*Zhang et al.*, 2014). The upper bound is therefore less appropriate to use when vapor wall loss is accounted for separately, and thus the lower bound is used to correct the SOA data, using size-dependent wall loss rates measured in the Caltech chamber. Figure C.2 shows temporal plots of the experimental non-particle-wall-loss-corrected total volume and the total volume with both the upper and lower bound particle wall loss correction. (Gaps in the volume data resulted when the DMA was taken off-line briefly to clean the inlet.)

The initial concentrations of H_2O_2, NO_x, and O_3 in the chemical model were optimized to match the α-pinene decay and O_3 formation. The initial mixing ratio of H_2O_2 was optimized to be 2 ppm, yielding predicted OH levels of $\sim 2 \times 10^6$ molec cm^{-3} for the 100 % UV experiments and $\sim 2 \times 10^5$ molec cm^{-3} for the 10 % UV experiments. Although experiments were conducted under low-NO conditions, background levels of NO_x were observed in the chamber. Due to voltage interference in the NO_x measurements at such low values, it was not possible to determine the exact amount of NO_x present in the chamber. Therefore, the initial background concentration in the simulations was set to 0.1 ppb, split evenly between NO and NO_2. NO and NO_2 then evolve throughout the simulation according to the standard inorganic gas-phase reactions. Ozone formation was observed during the experiments, giving evidence of the presence of NO_2 in the chamber. Because any NO_2 initially present in the chamber is quickly photolyzed, a NO_x wall off-gassing rate of 2.5 ppt min^{-1} is

needed to match the observed ozone formation (e.g., *Valorso et al.*, 2011). Predicted SOA formation is not sensitive to the assumed NO_x off-gassing rate. An initial O_3 concentration was measured in the chamber; however, this was attributed to interference by H_2O_2 because α-pinene did not decay in the dark, as would have occurred in the presence of O_3. Therefore, the initial O_3 was set to zero in the model. Comparisons of measurements and model predictions for the decay of α-pinene and the evolution of O_3 are shown in Figs. C.3 and C.4 in Appendix C.

Figure C.5 shows the amount of α-pinene predicted to react with OH vs. O_3, using both the modeled and measured O_3 concentration. For the 100 % UV experiments, $\sim$2–3 % of the total α-pinene is predicted to react with O_3, using either the modeled or measured O_3 concentration. For the 10 % UV experiments, $\sim$20 % of the total α-pinene is predicted to react with O_3 using the modeled O_3 concentration. For experiment 141113, roughly the same amount of α-pinene is predicted to react with O_3 based on the measured O_3 concentration. However, for experiment 141125, because the model underpredicts the O_3 concentration, much more α-pinene is predicted to react with the measured O_3 concentration, $\sim$49 %.

4.6 Results

Experimental particle-wall-loss-corrected SOA growth curves as a function of reacted α-pinene are shown in Fig. 4.2 for the six photooxidation experiments. With the exception of the nucleation experiment, SOA growth is observed immediately upon irradiation, similar to *Ng et al.* (2007a). When presented as a function of reacted α-pinene, the growth curves essentially overlap, regardless of the UV level or the initial seed particle concentration. Overlap at two different UV intensities indicates that SOA growth is not very sensitive to the oxidation rate for these conditions. SOA yields (ratio of maximum mass of SOA formed to mass of α-pinene reacted) for these experiments range from 17 to 26 %, at the low end of the range of previously reported yields of 26–45 % for this system (*Ng et al.*, 2007a; *Eddingsaas et al.*, 2012b).

Figure 4.2 also shows predictions from the base GECKO-A mechanism for the six experiments. In the GECKO-A model, the two main parameters representing vapor–particle and vapor–wall

transport, α_p and k_{gw}, are set to nominal values of 1 and $10^{-3}\,s^{-1}$, respectively. $C_w/(M_w\gamma_w)$ is set to $120\,\mu mol\,m^{-3}$ for all species except α-pinene. These parameters give a good agreement for the 100 % UV experiments. Figure C.6 in Appendix C shows the effect of varying the vapor–particle accommodation coefficient α_p for different values of the vapor wall loss rate k_{gw}. $\alpha_p = 1$ or 0.1 yields almost identical SOA predictions for all experiments except nucleation. In the nucleation case, $\alpha_p = 0.1$ results in substantially less SOA predicted, which may result because nucleation is not treated explicitly in GECKO-A but instead approximated by initializing the particle concentration with particles of 5 nm radius. Lowering the value of α_p to 0.01 or 0.001 delays the onset of SOA formation for the 100 % UV experiments, which is not consistent with experimental observations. Lowering k_{gw} results in substantial overprediction of SOA for the 100 % UV experiments. For the 10 % UV experiments, all combinations of parameters underpredict the SOA. Figure C.7 in Appendix C shows the effect of varying $C_w/(M_w\gamma_w)$ for different values of the vapor wall loss rate k_{gw}. $C_w/(M_w\gamma_w)$ controls partitioning between the gas phase and the wall at equilibrium; therefore, variations in $C_w/(M_w\gamma_w)$ have more of an effect on SOA predictions when using a faster wall loss rate because equilibrium is approached sooner. The base $C_w/(M_w\gamma_w)$ and $k_{gw} = 10^{-3}\,s^{-1}$ give the best agreement for 100 % UV experiments; however, SOA for the 10 % UV experiments is still underpredicted. This discrepancy will be addressed subsequently. All subsequent simulations are conducted with $\alpha_p = 1$ and the base $C_w/(M_w\gamma_w)$.

The best-fit $\alpha_p = 1$ (and 0.1 for all experiments except nucleation) for the 100 % UV experiments suggests that there are no substantial limitations to vapor–particle mass transfer (*Mai et al.*, 2015). This conclusion is consistent with the experimental observation that the SOA growth in this system is virtually independent of the amount of seed surface area present; dependence of SOA growth on seed surface area occurs only with diffusion- or accommodation-limited vapor–particle mass transfer (*McVay et al.*, 2014). Optimal $\alpha_p = 1$ or 0.1 is consistent with *Saleh et al.* (2013), who determined accommodation coefficients of order 0.1 for α-pinene ozonolysis SOA. This result differs from that of *Zhang et al.* (2014), who observed toluene SOA formation to depend strongly on the seed surface area and consequently to adhere to a low $\alpha_p = 0.001$. The different behavior observed for α-pinene

and toluene SOA may reflect differences in SOA formation mechanisms; however, it is not possible to discern the reason for the difference based solely on the data at hand. If α-pinene SOA behaves as a semi-solid (*Perraud et al.*, 2012; *Cappa and Wilson*, 2011; *Vaden et al.*, 2010, 2013; *Virtanen et al.*, 2010, 2011; *Kuwata and Martin*, 2012; *Saukko et al.*, 2012; *Abramson et al.*, 2013; *Renbaum-Wolff et al.*, 2013), a lower α_{p} might be expected. However, if, once formed, SOA is converted into a glassy state through hydrogen bonding or oligomerization (*Cappa and Wilson*, 2011), SOA formation itself could still be characterized by a high α_{p}.

The observation that SOA growth is insensitive to oxidation rate (shown by the overlap of the growth curves in Fig. 4.2 for different UV exposures) is not consistent with predictions regarding the interplay of reaction rate and vapor wall loss: if the reaction rate increases relative to the vapor wall loss rate, successive generations of low-volatility species will be produced more quickly and will condense preferentially onto particles before their precursors are lost to the chamber walls, leading to a higher SOA yield (*Zhang et al.*, 2014; *McVay et al.*, 2014). Such behavior was observed experimentally by *Ng et al.* (2007b): higher SOA yields were observed in the aromatic system using HONO as an OH precursor than when only NO and NO_2 were present initially, leading to much lower OH levels. This "rate effect" was tentatively attributed by *Ng et al.* (2007b) to loss of semivolatile organics to the chamber walls, albeit at a time when the nature of vapor wall deposition was less well understood. A dependence of SOA growth on oxidation rate is also predicted by the base scenario in GECKO-A: the SOA levels are predicted to be substantially lower at 10 % UV owing to significant organic mass loss to the walls. A number of explanations can be advanced for the overlap of the growth curves at high and low UV, and these are systematically explored below.

4.6.1 Negligible or Slow Vapor Wall Loss

In the absence of vapor wall loss, the growth curves predicted by GECKO-A overlap at high and low UV (Fig. C.8 in Appendix C). Oxidation occurs more slowly under low UV owing to the decreased rate of generation of OH, but if condensable species or their precursors do not deposit on the walls, the same amount of SOA eventually forms. However, in the absence of vapor wall loss, GECKO-A

overpredicts SOA substantially for the high-UV experiments and slightly for the low-UV experiments.

At a low level of vapor wall loss, $k_{gw} = 10^{-5}\,s^{-1}$, the growth curves predicted by GECKO-A still essentially overlap (Fig. 4.3). A rate effect, in which the SOA yield depends on the rate of oxidation, is observed only if the rate of oxidation is slower than or competitive with other loss processes. The rate constant for the reaction of OH with α-pinene is $5.23 \times 10^{-11}\,cm^3\,molec^{-1}\,s^{-1}$ (*Atkinson and Arey*, 2003). OH concentrations predicted by GECKO-A of 2×10^6 and $2 \times 10^5\,molec\,cm^{-3}$ for the high- and low-UV experiments, respectively, give overall reaction rates of 10^{-4} and $10^{-5}\,s^{-1}$. (OH reaction rate constants for oxidized products will be slower than that for α-pinene, and the reaction rate slows in later generations.) A vapor wall loss characterized by $k_{gw} = 10^{-3}\,s^{-1}$ exceeds substantially either of these reaction rates, and thus at this wall deposition rate the effect of changing oxidation rate is strong. At a much slower wall loss, $k_{gw} = 10^{-5}\,s^{-1}$, the rate effect is less pronounced, leading to overlap of the growth curves predicted by GECKO-A. The absence of a rate effect in the experimental observations is consistent with a slower vapor wall loss rate, in accord with wall loss rates that have been measured previously in the Caltech chamber (*Loza et al.*, 2010, 2014; *Zhang et al.*, 2015).

With a vapor wall loss rate of $10^{-5}\,s^{-1}$, SOA predictions match the data fairly well at low UV, within $10\,\mu g\,m^{-3}$ of the final SOA concentration, but remain overpredicted by 80 to $200\,\mu g\,m^{-3}$ at high UV. Thus, a slow wall loss rate alone is not sufficient to reconcile the predictions at high and low UV. However, it is instructive to examine the contribution of different generations of reaction to SOA predictions with this slow vapor wall loss (Fig. 4.4). GECKO-A predicts that SOA will consist of almost entirely second-generation products. At the end of the experiment, simulations under high UV predict $\sim 100\,\mu g\,m^{-3}$ of second-generation products, as opposed to $\sim 50\,\mu g\,m^{-3}$ for low UV. Thus, reducing the contribution of second-generation products in high UV may result in closer model–data agreement for both high- and low-UV conditions at a slow vapor wall loss rate.

4.6.2 Overcontribution of Second- and Later-generation Species

As a sensitivity test, all OH reaction rate constants, except that of OH + α-pinene, are reduced by varying factors. Figure C.9 in Appendix C shows the impact of reducing the OH rate constants to 1, 10, and 50 % of the default values at a vapor wall loss rate of $10^{-5}\,s^{-1}$. A reduction to 10 % and a wall loss rate of $10^{-5}\,s^{-1}$ result in the best fit to both high- and low-UV experiments (Fig. 4.5), albeit with an overprediction up to 75 % for the high-UV experiments and a 20–40 % underprediction for the low-UV experiments. While this result does not necessarily suggest that reaction rate constants in GECKO-A are overpredicted by an order of magnitude, it does suggest that second- and higher-generation compounds may be primarily responsible for the model–measurement discrepancy at differing UV levels. An excess contribution of later-generation compounds to SOA in GECKO-A could be due to several factors: (1) overprediction of the OH reaction rate constants by the SARs, (2) assumed reaction pathways in GECKO-A, (3) underestimation of volatilities for later-generation species, or (4) significantly faster wall loss rate for later-generation products. Each of these possibilities is considered in turn.

OH reaction rate constants in GECKO-A are based on SARs from *Kwok and Atkinson* (1995) and subsequent updates, which have been shown to predict OH reaction rate constants within a factor of 2 for alkanes, alkenes, and diols but may be more uncertain for the complex and highly functionalized compounds in later generations of α-pinene oxidation (*Bethel et al.*, 2001). For example, *Bethel et al.* (2001) showed that OH rate constants for 1,2-hydroxyaldehydes are overestimated by factors of 3–4 using the established SARs. Although rate constants are likely not overpredicted by an order of magnitude as the simulations suggest, it is possible that uncertainties in the SARs for later-generation species may contribute to the overprediction of these products by GECKO-A.

SARs used to predict reaction pathways and branching ratios in GECKO-A are also prone to uncertainties. In the reaction of peroxy radicals with HO_2, the dominant pathway in GECKO-A is formation of the hydroperoxide (assumed branching ratio 80 %). α-Pinene hydroxy dihydroperoxide ($C_{10}H_{16}O_5$) is a second-generation compound formed via two such reactions with HO_2 that is predicted by GECKO-A to contribute significantly to SOA under the high-UV conditions. Fig-

ure C.10 in Appendix C shows that eliminating the mass of this compound from SOA predictions in the absence of vapor wall loss results in a much more significant decrease in SOA at high UV ($\sim 100\,\mu g\,m^{-3}$) than at low UV ($\sim 15\,\mu g\,m^{-3}$). α-Pinene hydroxy dihydroperoxide results from two successive OH reactions and is therefore formed more rapidly and in greater amounts at a higher OH level. α-Pinene hydroxy dihydroperoxide has been observed in the gas phase with an estimated 3 % yield (*Eddingsaas et al.*, 2012a). In the high-UV simulation, this compound is formed with $>30\,\%$ yield; therefore, it is likely that reaction pathways leading to this product are overrepresented in GECKO-A.

A second pathway for the reaction of peroxy radicals with HO_2 is formation of an alkoxy and regeneration of OH, added to GECKO-A with an uncertain branching ratio of 20 % and only for peroxy radicals with an oxygenated moiety in the α position. Simulations show that SOA predictions are not sensitive to the second assumption but are very sensitive to the assumed branching ratio for this reaction (Fig. 4.6). Increasing formation of the alkoxy leads to decreasing SOA formation, with a greater effect at high UV than at low UV. Uncertainty in this branching ratio in the α-pinene system could be a major factor leading to the high–low-UV discrepancy.

Finally, *Praske et al.* (2015) recently identified a third HO_2 reaction channel for peroxy radicals produced from methyl vinyl ketone (MVK): formation of a carbonyl and regeneration of OH and HO_2. In place of a hydroperoxide, which results from the standard HO_2 reaction channel, this reaction produces a ketone which has a higher vapor pressure and therefore forms less SOA. If this reaction occurs in the α-pinene system, the absence of this pathway in GECKO-A could contribute to SOA overprediction.

Volatilities in this version of GECKO-A are estimated using the *Nannoolal et al.* (2008) method, which is based on the Clausius–Clapeyron equation. Boiling points are estimated using the *Nannoolal et al.* (2004, 2008) method with some group contributions taken from *Compernolle et al.* (2010) (*Valorso et al.*, 2011). Limited experimental data exist for vapor pressures of semivolatile and low-volatility species, and uncertainty in vapor pressure estimation increases as vapor pressure decreases (*Valorso et al.*, 2011). Therefore, underprediction of vapor pressures for later-generation species

could lead to excess SOA. Indeed, *Valorso et al.* (2011) showed that significant uncertainties in SOA predictions result when using different methods for vapor pressure estimation. While the *Nannoolal et al.* (2008) method generally led to the highest volatilites and the lowest SOA predictions when compared to the *Myrdal and Yalkowsky* (1997) method and the SIMPOL-1 method from *Pankow and Asher* (2008), each of these methods estimates vapor pressures via a group contribution method (i.e., summing the contributions of all functional groups). If this approach is less accurate for compounds with many functional groups, the volatilities may be underpredicted and these species may be overpredicted in SOA.

A final possible explanation for the overprediction of higher-generation SOA species is that significantly faster vapor wall loss exists for these more functionalized species. *Zhang et al.* (2015) showed that vapor wall loss rates increase as compound vapor pressure decreases. They measured wall loss rates for primarily first-generation oxidation products to be 10^{-5}–$10^{-6}\,s^{-1}$ in the Caltech chambers. Implementing the k_{gw} parameterization developed by *Zhang et al.* (2015) in GECKO-A yields similar SOA predictions to those based on assuming a fixed $k_{gw} = 10^{-5}\,s^{-1}$ (with the exception of the nucleation experiment, in which the k_{gw} parameterization predicted more SOA than using a fixed $k_{gw} = 10^{-5}\,s^{-1}$). However, it is certainly possible that later generation, more functionalized compounds could exhibit significantly faster wall loss than predicted by the parameterization of *Zhang et al.* (2015). As one example, *Krechmer et al.* (2015) fit a wall loss rate of $3 \times 10^{-3}\,s^{-1}$ for a $C_5H_{10}O_5$ isoprene oxidation product in the Caltech chambers. If later-generation species in the α-pinene system exhibit markedly higher wall loss as well, SOA overprediction in GECKO-A will be reduced.

In summary, if GECKO-A overpredicts the contribution of later-generation species, the measurement–model discrepancy at differing UV levels could be reduced. Reducing the contribution of second-generation species also requires a slower vapor wall loss rate to fit the data, which is actually more consistent with those that have been measured in the Caltech chamber.

4.6.3 Condensed-phase Photolysis

If condensed-phase photolysis occurs in the chamber but is missing in GECKO-A, both the high–low-UV measurement–model discrepancy and the high wall loss rate needed to match the 100 % UV observations could potentially be explained. If condensed-phase photolysis is an efficient loss mechanism for SOA at 100 % UV, a lower vapor wall loss rate would be required in order to continue to fit experimental observations. Because condensed-phase photolysis would be less efficient at 10 % UV, at this slower wall loss rate the low-UV SOA predictions will increase in the direction of the observations. However, this effect is not seen in the simulations. Figure 4.7 shows the effect of condensed-phase photolysis, with the radicals produced assumed to be lost permanently. Two wall loss rates are shown: the default $k_{\mathrm{gw}} = 10^{-3}\,\mathrm{s}^{-1}$ and a slower $k_{\mathrm{gw}} = 10^{-4}\,\mathrm{s}^{-1}$. Only one high-UV experiment is shown, but the results are similar for all high-UV experiments. Moreover, condensed-phase photolysis has no effect on the low-UV predictions (not shown).

Under high-UV conditions, the assumed presence of condensed-phase photolysis leads to a slight reduction in SOA predictions at the end of the experiment, regardless of k_{gw}. Note that the current implementation of condensed-phase photolysis represents an upper limit: compounds in the condensed phase are taken to photolyze at the same rate as in the gas phase, and fragmentation products are lost permanently. The minor effect of this photolysis upper limit can be explained by comparing the wavelength-dependent photon flux of the chamber to absorption cross sections of species predicted to constitute the SOA (Fig. C.11 in Appendix C). *Wong et al.* (2015) found that the main absorption region of SOA produced by α-pinene ozonolysis corresponds to characteristic absorptions of carbonyl and peroxide functional groups and that the SOA absorption is strongest between 240 and 400 nm. Although products of α-pinene OH oxidation and ozonolysis differ, peroxide and carbonyl functional groups are generated during both (*Eddingsaas et al.*, 2012a). The photon flux in the Caltech chamber is less intense than the solar flux in this region, particularly for the wavelength region over which peroxides photolyze (Fig. S11). Because peroxides are expected to be abundant in α-pinene SOA (*Capouet et al.*, 2008; *Eddingsaas et al.*, 2012a), the effect of condensed-phase photolysis may be underrepresented in the Caltech chamber as compared to the

atmosphere.

The minor effect of condensed-phase photolysis in these simulations is consistent with the findings of *Hodzic et al.* (2015) that reduction in SOA from both gas-phase and condensed-phase photolysis for various systems, including α-pinene, is minor during the initial 10 h of a simulation but becomes substantial over a week of atmospheric ageing. Moreover, this result indicates that this process does not explain the high–low-UV measurement–model discrepancy. Even in the presence of condensed-phase photolysis, at a wall loss rate $k_{\mathrm{gw}} = 10^{-4}\,\mathrm{s}^{-1}$ a strong overprediction of SOA still exists at 100 % UV. Although condensed-phase photolysis is potentially important in the atmosphere on longer timescales (*Hodzic et al.*, 2015), it does not explain the low-UV measurement–model discrepancy of these experiments.

4.6.4 Autoxidation Chemistry

Autoxidation has been demonstrated to be important in SOA formation (*Crounse et al.*, 2013; *Ehn et al.*, 2014; *Rissanen et al.*, 2014; *Jokinen et al.*, 2014; *Mentel et al.*, 2015; *Rissanen et al.*, 2015). Formation of extremely low-volatility organic compounds (ELVOCs) via autoxidation has been observed from both the OH oxidation and ozonolysis of α-pinene, with higher yields observed from ozonolysis (*Ehn et al.*, 2014; *Jokinen et al.*, 2014). In autoxidation, a peroxy radical undergoes an intramolecular hydrogen abstraction to form a hydroperoxide, generating an alkyl radical which then adds oxygen to reform a peroxy radical. This pathway becomes important only when the rate of hydrogen abstraction is competitive with bimolecular reactions of the peroxy radicals with NO, HO_2, and RO_2 (*Crounse et al.*, 2013). Because lower UV intensities will lead to lower HO_2 and RO_2 concentrations, intramolecular hydrogen abstraction could potentially be favored under low UV. For the high-UV experiments, the predicted lifetime with HO_2 is $\sim$10 s; for the low-UV experiments it is $\sim$50 s, indicating that autoxidation may potentially be more important under low UV.

Moreover, during the low-UV experiments, 20–50 % of α-pinene reacts with O_3 instead of OH, compared to only 2–3 % for the high-UV experiments. As discussed previously, the ozonolysis mechanism in GECKO-A is likely incomplete and may be lacking pathways to SOA precursors, such

as autoxidation. Because autoxidation is much more efficient from the ozonolysis pathway than from the OH pathway (*Ehn et al.*, 2014; *Jokinen et al.*, 2014), more ELVOCs will likely be produced under low UV and will increase the amount of SOA formed. Furthermore, autoxidation could also explain the difference in SOA yield observed between the two low-UV experiments. Experiment 141125 has a higher yield than experiment 141113 and also has a higher observed O_3 concentration. ELVOC production was likely higher during this experiment owing to the increased fraction of α-pinene reacted via ozonolysis.

Autoxidation is observed to occur immediately upon oxidation (*Rissanen et al.*, 2015), indicating that it is likely a first-generation process. Second-generation species are predominantly responsible for the discrepancy in model predictions between high and low UV due to the difference in OH levels (Fig. 4.4). Unlike second-generation products, autoxidation products will not depend on the OH concentration and will not be produced more slowly under low UV. Therefore, adding autoxidation pathways will likely increase the fraction of SOA composed of first-generation products, which may lead to similar predictions for high and low UV.

However, explicit mechanisms and rate constants are still lacking for autoxidation in the α-pinene system, although they have been developed for simpler cycloalkenes (*Mentel et al.*, 2015; *Rissanen et al.*, 2015). A recent computational study found that the cyclobutyl ring in α-pinene must open in order for intramolecular hydrogen shifts to be competitive with the peroxy bimolecular sink reactions (*Kurtén et al.*, 2015). The currently accepted α-pinene ozonolysis mechanism does not include rapid opening of this ring. *Kurtén et al.* (2015) investigated several pathways to break this ring but found none that could explain all of the characteristics of observed ELVOCs from α-pinene. In the absence of explicit mechanisms, the effect of autoxidation cannot be fully tested. To approximate the effect, a $C_{10}H_{15}O_9$ species (an ELVOC predicted by *Kurtén et al.*, 2015) is added with a 7 % molar yield (based on the 6–8 % yield measured by *Ehn et al.*, 2014) as a direct product from the α-pinene + O_3 reaction. This addition has no effect on SOA concentrations for the high-UV experiments but increases the final SOA concentrations for the low-UV experiments by $\sim 10\,\mu g\,m^{-3}$ (not shown). However, adding this fixed ELVOC yield does not increase SOA predictions for low

UV at the beginning of the experiment, when no O_3 is present. Therefore, although autoxidation via ozonolysis is likely important towards the end of the low-UV experiments, other explanations are needed to reconcile the underprediction of SOA at the start of the experiment. Autoxidation via OH oxidation could potentially resolve part of this discrepancy, but no pathways or yields are yet available. Overall, autoxidation is a likely process to explain the measurement–model discrepancy at high and low UV but is in need of more study. The presence of significant autoxidation could furthermore lead to a different best-fit vapor wall loss rate.

4.6.5 Particle-phase Dimerization

If dimerization is more competitive with gas-phase fragmentation at the lower OH levels at 10 % lights, increased SOA growth could result. Figure 4.8 shows one 100 % UV and one 10 % UV experiment with two different values for the dimerization rate constant: $0.01\,M^{-1}\,s^{-1}$ (*Ziemann and Atkinson*, 2012; *Capouet et al.*, 2008) and $12\,M^{-1}\,s^{-1}$ (*Shiraiwa et al.*, 2013) using the same base $k_{gw} = 10^{-3}\,s^{-1}$. The $12\,M^{-1}\,s^{-1}$ rate constant results in significant SOA overprediction for both the 100 % and the 10 % UV experiments; the slower dimerization rate constant still results in an overprediction for the 100 % UV experiment but an underprediction at 10 % UV. For this rate constant, rapid vapor wall loss combined with the slower chemistry at low UV prevents significant SOA formation, despite dimerization. In the high-UV experiment, because gas-phase chemistry occurs faster relative to vapor wall loss, even a slower dimerization rate increases SOA predictions. While dimerization increases SOA predictions for low UV, it has the same effect at high UV. Therefore, dimerization in its current implementation in GECKO-A does not resolve the low-UV discrepancy without causing an SOA overprediction for high UV.

4.6.6 Enhanced Wall Loss at High UV

To recapitulate, using the base chemistry in GECKO-A, predictions agree with the high-UV experiments when using a relatively fast vapor wall loss rate of $10^{-3}\,s^{-1}$, and predictions approximately match the low-UV experiments when using a much slower wall loss rate of $10^{-5}\,s^{-1}$. This result

prompts the hypothesis that vapor wall loss could somehow be dependent on the UV level. The diffusion coefficient and the eddy diffusivity could change based solely on the UV level if a change in the UV level results in a temperature change in the chamber. The temperature of the chamber was $\sim 3\,\mathrm{K}$ higher for the high-UV experiments than for the low. Gas-phase diffusion coefficients are $\sim T^{3/2}$ (*Incropera et al.*, 2007). A 3 K temperature increase will result in an increase in the diffusion coefficient by only a factor of 1.015. The eddy diffusivity characterizes the degree of turbulent mixing in the chamber, which could be increased by temperature variations. When UV lights are turned on, the temperature in the chamber increases by 2–3 K and then gradually decreases to the original temperature from a well-controlled recirculating chilled-water system. This small fluctuation is not expected to cause a dramatic increase in turbulence in the chamber. Therefore, increase of vapor wall loss for high-UV experiments is deemed incapable of explaining the modeling discrepancy.

4.7 Atmospheric Implications

From the systematic analysis of the experiments and mechanism predictions (and in the absence of explicit autoxidation mechanisms), two hypotheses could explain some or all of the inability of the base case in GECKO-A to simulate both the high- and low-UV experiments. The first hypothesis is that later-generation species overcontribute to the SOA in GECKO-A. To compensate for this overcontribution necessitates the assumption of rapid vapor wall loss in order to fit the high-UV data; when extended to the low-UV experiments, this rapid wall loss results in significant SOA underprediction, since later-generation species are produced more slowly at the lower OH levels. This overcontribution could be the result of several possibilities, each of which has different implications for atmospheric SOA formation. If some reaction pathways are under- or misrepresented in GECKO-A, atmospheric predictions from GECKO-A may then overestimate SOA. If instead all reaction pathways in GECKO-A are realistic but the rates are simply overpredicted, these compounds may still form in the atmosphere but will be affected by competing processes such as dry and wet deposition and uptake into cloud particles (*Hodzic et al.*, 2014; *Mouchel-Vallon et al.*, 2013). If volatilities are too low in GECKO-A, atmospheric predictions will then be biased high. Finally, if

higher-generation species simply exhibit a faster wall loss, these compounds will be produced quickly in the atmosphere and will generate significant SOA.

This hypothesis implies that vapor wall loss in the Caltech chamber is likely slower than that of the base case assumed in GECKO-A. This slower wall loss is consistent with measurements in the Caltech chamber (*Loza et al.*, 2010, 2014; *Zhang et al.*, 2014) but is considerably slower than those measured in the $8\,m^3$ chamber used by *Yeh and Ziemann* (2015), 10^{-3}–$10^{-4}\,s^{-1}$. Differences in the size and operation of two chambers may contribute to the differences in measured wall loss rates.

The vapor wall loss implied by the present experiments results in an order of magnitude slower rate than that fit by *Zhang et al.* (2014) during toluene SOA photooxidation. This difference could potentially indicate differences between chemical systems or could also arise from the manner in which the modeling was performed: *Zhang et al.* (2014) used the Statistical Oxidation Model of *Cappa and Wilson* (2012) vs. the GECKO-A model used here. An implication of this difference is that the wall loss bias (the ratio of the yield predicted in the absence of vapor wall loss divided by the observed yield) for the α-pinene system is likely lower than the 1.6 predicted by *Zhang et al.* (2014). However, because we could not definitively fit here both the high- and low-UV experiments, we cannot calculate a corresponding wall loss bias.

The second hypothesis with the potential to explain the measurement–model discrepancy is autoxidation. Autoxidation from both the OH and ozonolysis pathway could be important during the low-UV experiments. Explicit mechanisms and rate constants are needed in order to test this hypothesis. If significant, the presence of autoxidation could change the vapor wall loss rate implied by these simulations.

Although other processes do not reconcile the high–low-UV model discrepancy, such processes may still be important. Condensed-phase photolysis, though not significant over the short timescale of chamber experiments, has been shown to potentially have a more significant effect in the atmosphere (*Hodzic et al.*, 2015). Particle-phase reactions have been shown to generate significant amounts of high-molecular weight, low-volatility species in the α-pinene system (*Docherty et al.*, 2005; *Lopez-Hilfiker et al.*, 2015; *Gao et al.*, 2004b), albeit more efficiently in ozonolysis (*Lopez-*

Hilfiker et al., 2015). Even if particle-phase dimerization is significant in this system, the assumed irreversible formation of dimers in GECKO-A may not accurately represent particle-phase reactions, which have been suggested to be reversible (*Ziemann and Atkinson*, 2012; *Trump and Donahue*, 2014).

Figures C.1–C.11 are provided in Appendix C.

Acknowledgements

This work was supported by National Science Foundation grant AGS-1523500. Renee C. McVay acknowledges support by a National Science Foundation Graduate Research Fellowship under grant no. DGE-1144469. Bernard Aumont acknowledges support from the French National Research Agency (ANR) under the MAGNIFY project (ANR-14-CE01-0010).

Bibliography

Abramson, E., Imre, D., Beránek, J., Wilson, J. M., and Zelenyuk, A.: Experimental determination of chemical diffusion within secondary organic aerosol particles, *Phys. Chem. Chem. Phys.*, 15, 2983–2991, 2013.

Atkinson, R. and Arey, J.: Atmospheric degradation of volatile organic compounds, *Chem. Rev.*, 103, 4605–4638, 2003.

Aumont, B., Szopa, S., and Madronich, S.: Modelling the evolution of organic carbon during its gas-phase tropospheric oxidation: development of an explicit model based on a self generating approach, *Atmos. Chem. Phys.*, 5, 2497–2517, doi:10.5194/acp-5-2497-2005, 2005.

Bethel, H. L., Atkinson, R., and Arey, J.: Kinetics and products of the reactions of selected diols with the OH radical, *Int. J. Chem. Kinet.*, 33, 310–316, 2001.

Bian, Q., May, A. A., Kreidenweis, S. M., and Pierce, J. R.: Investigation of particle and vapor wall-loss effects on controlled wood-smoke smog-chamber experiments, *Atmos. Chem. Phys.*, 15, 11027–11045, doi:10.5194/acp-15-11027-2015, 2015.

Birdsall, A. W., Andreoni, J. F., and Elrod, M. J.: Investigation of the role of bicyclic peroxy radicals in the oxidation mechanism of toluene, *J. Phys. Chem. A.*, 114, 10655–10663, 2010.

Camredon, M., Aumont, B., Lee-Taylor, J., and Madronich, S.: The SOA/VOC/NO_x system: an explicit model of secondary organic aerosol formation, *Atmos. Chem. Phys.*, 7, 5599–5610, doi: 10.5194/acp-7-5599-2007, 2007.

Cappa, C. D. and Wilson, K. R.: Evolution of organic aerosol mass spectra upon heating: implications for OA phase and partitioning behavior, *Atmos. Chem. Phys.*, 11, 1895–1911, doi: 10.5194/acp-11-1895-2011, 2011.

Cappa, C. D. and Wilson, K. R.: Multi-generation gas-phase oxidation, equilibrium partitioning, and the formation and evolution of secondary organic aerosol, *Atmos. Chem. Phys.*, 12, 9505–9528, doi:10.5194/acp-12-9505-2012, 2012.

Capouet, M., Peeters, J., Nozière, B., and Müller, J.-F.: Alpha-pinene oxidation by OH: simulations of laboratory experiments, *Atmos. Chem. Phys.*, 4, 2285–2311, doi:10.5194/acp-4-2285-2004, 2004.

Capouet, M., Müller, J.-F., Ceulemans, K., Compernolle, S., Vereecken, L., and Peeters, J.: Modeling aerosol formation in alpha-pinene photo-oxidation experiments, *J. Geophys. Res.*, 113, D02308, doi:10.1029/2007JD008995, 2008.

Claeys, M., Iinuma, Y., Szmigielski, R., Surratt, J. D., Blockhuys, F., Van Alsenoy, C., Boge, O., Siereau, B., Gomez-Gonzalez, Y., Vermeylen, R., Van der Veken, P., Shahgholi, M., Chan, A. W. H., Herrmann, H., Seinfeld, J. H., and Maenhaut, W.: Terpenylic acid and related compounds from the oxidation of alpha-pinene: implications for new particle formation and growth above forests, *Environ. Sci. Technol.*, 43, 6976–6982, 2009.

Compernolle, S., Ceulemans, K., and Müller, J.-F.: Technical Note: Vapor pressure estimation methods applied to secondary organic aerosol constituents from α-pinene oxidation: an intercomparison study, *Atmos. Chem. Phys.*, 10, 6271–6282, doi:10.5194/acp-10-6271-2010, 2010.

Crounse, J. D., Nielsen, L. B., Jørgensen, S., Kjaergaard, H. G., and Wennberg, P. O.: Autoxidation of organic compounds in the atmosphere, *J. Phys. Chem. Lett.*, 4, 3513–3520, 2013.

Dillon, T. J. and Crowley, J. N.: Direct detection of OH formation in the reactions of HO2 with $CH_3C(O)O_2$ and other substituted peroxy radicals, *Atmos. Chem. Phys.*, 8, 4877–4889, doi: 10.5194/acp-8-4877-2008, 2008.

Docherty, K. S., Wu, W., Lim, Y. B., and Ziemann, P. J.: Contributions of organic peroxides to secondary aerosol formed from reactions of monoterpenes with O_3, *Environ. Sci. Technol.*, 39, 4049–4059, 2005.

Donahue, N. M., Henry, K. M., Mentel, T. F., Kiendler-Scharr, A., Spindler, C., Bohn, B., Brauer, T., Dorn, H. P., Fuchs, H., Tillmann, R., Wahner, A., Saathoff, H., Naumann, K. H., Möhler, O., Leisner, T., Müller, L., Reinnig, M. C., Hoffmann, T., Salo, K., Hallquist, M., Frosch, M., Bilde, M., Tritscher, T., Barmet, P., Praplan, A. P., DeCarlo, P. F., Dommen, J., Prévôt, A. S., and Bal-

tensperger, U.: Aging of biogenic secondary organic aerosol via gas-phase OH radical reactions, *P. Natl. Acad. Sci. USA*, 21, 13503–13508, 2012.

Eddingsaas, N. C., Loza, C. L., Yee, L. D., Seinfeld, J. H., and Wennberg, P. O.: α-pinene photooxidation under controlled chemical conditions – Part 1: Gas-phase composition in low- and high-NO_x environments, *Atmos. Chem. Phys.*, 12, 6489–6504, doi:10.5194/acp-12-6489-2012, 2012a.

Eddingsaas, N. C., Loza, C. L., Yee, L. D., Chan, M., Schilling, K. A., Chhabra, P. S., Seinfeld, J. H., and Wennberg, P. O.: α-pinene photooxidation under controlled chemical conditions – Part 2: SOA yield and composition in low- and high-NO_x environments, *Atmos. Chem. Phys.*, 12, 7413–7427, doi:10.5194/acp-12-7413-2012, 2012b.

Ehn, M., Thornton, J. A., Kleist, E., Sipilä, M., Junninen, H., Pullinen, I., Springer, M., Rubach, F., Tillmann, R., Lee, B., Lopez-Hilfiker, F., Andres, S., Acir, I.-H., Rissanen, M., Jokinen, T., Schobesberger, S., Kangasluoma, J., Kontkanen, J., Nieminen, T., Kurtén, T., Nielsen, L. B., Jørgensen, S., Kjaergaard, H. G., Canagaratna, M., Maso, M. D., Berndt, T., Petäjä, T., Wahner, A., Kerminen, V.-M. Kulmala, M., Worsnop, D. R., Wildt, J., and Mentel, T. F.: A large source of low-volatility secondary organic aerosol, *Nature*, 506, 476–479, doi:10.1038/nature13032, 2014.

Epstein, S. A., Blair, S. L., and Nizkorodov, S. A.: Direct photolysis of α-pinene ozonolysis secondary organic aerosol: Effect on particle mass and peroxide content, *Environ. Sci. Technol.*, 48, 11251–11258, 2014.

Fahnestock, K. A. S., Yee, L. D., Loza, C. L., Coggon, M. M., Schwantes, R., Zhang, X., Dalleska, N. F., and Seinfeld, J. H.: Secondary organic aerosol composition from C_{12} alkanes, *J. Phys. Chem. A.*, 119, 4281–4297, 2014.

Gao, S., Ng, N. L., Keywood, M., Varutbangkul, V., Bahreini, R., Nenes, A., He, J., Yoo, K. Y., Beauchamp, J. L., Hodyss, R. P., Flagan, R. C., and Seinfeld, J. H.: Particle phase acidity and oligomer formation in secondary organic aerosol, *Environ. Sci. Technol.*, 38, 6582–6589, 2004a.

Gao, S., Keywood, M., Ng, N. L., Surratt, J., Varutbangkul, V., Bahreini, R., Flagan, R. C., and Seinfeld, J. H.: Low-molecular-weight and oligomeric components in secondary organic aerosol from the ozonolysis of cycloalkenes and α-pinene, *J. Phys. Chem. A.*, 108, 10147–10164, 2004b.

Griffin, R. J., Cocker III, D. R., Flagan, R. C., and Seinfeld, J. H.: Organic aerosol formation from the oxidation of biogenic hydrocarbons. *J. Geophys. Res.*, 104, 3555–3567, 1999.

Geunther, A., Hewitt, C. N., Erickson, D., Fall, R., Geron, C., Graedel, T., Harley, P., Klinger, L., Lerdau, M., Mckay, W. A., Pierce, T., Scholes, B., Seinbrecher, R., Tallamraju, R., Taylor, J., and Zimmerman, P.: A global model of natural volatile organic compound emissions, *J. Geophys. Res.*, 100, 8873–8892, 1995.

Hallquist, M., Wenger, J. C., Baltensperger, U., Rudich, Y., Simpson, D., Claeys, M., Dommen, J., Donahue, N. M., George, C., Goldstein, A. H., Hamilton, J. F., Herrmann, H., Hoffmann, T., Iinuma, Y., Jang, M., Jenkin, M. E., Jimenez, J. L., Kiendler-Scharr, A., Maenhaut, W., McFiggans, G., Mentel, Th. F., Monod, A., Prévôt, A. S. H., Seinfeld, J. H., Surratt, J. D., Szmigielski, R., and Wildt, J.: The formation, properties and impact of secondary organic aerosol: current and emerging issues, *Atmos. Chem. Phys.*, 9, 5155–5236, doi:10.5194/acp-9-5155-2009, 2009.

Hasson, A. S., Tyndall, G. S., and Orlando, J. J.: A product yield study of the reaction of HO_2 radicals with ethyl peroxy ($C_2H_5O_2$), acetyl peroxy ($CH_3C(O)O_2$), and acetonyl peroxy ($CH_3C(O)CH_2O_2$), *J. Phys. Chem. A.*, 108, 5979–5989, 2004.

Hasson, A. S., Kuwata, K. T., Arroyo, M. C., and Petersen, E. B.: Theoretical studies of the reaction of hydroperoxy radicals ($HO_2^{\cdot}$), with ethyl peroxy ($C_2H_5O_2^{\cdot}$), acetyl peroxy ($CH_3C(O)O_2^{\cdot}$) and acetonyl peroxy ($CH_3C(O)CH_2O_2^{\cdot}$) radicals, *J. Photoch. Photobio. A*, 176, 218–230, 2005.

Henry, K. M. and Donahue, N. M.: Photochemical aging of α-pinene secondary organic aerosol: Effects of OH radical sources and photolysis, *J. Phys. Chem. A.*, 116, 5932–5940, 2012.

Hodzic, A., Aumont, B., Knote, C., Lee-Taylor, J., Madronich, S., and Tyndall, G.: Volatility

dependence of Henry's law constants of condensable organics: application to estimate depositional loss of secondary organic aerosol, *Geophys. Res. Lett.*, 41, 4795–4804, 2014.

Hodzic, A., Madronich, S., Kasibhatla, P. S., Tyndall, G., Aumont, B., Jimenez, J. L., Lee-Taylor, J., and Orlando, J.: Organic photolysis reactions in tropospheric aerosols: effect on secondary organic aerosol formation and lifetime, *Atmos. Chem. Phys.*, 15, 9253–9269, doi: 10.5194/acp-15-9253-2015, 2015.

Hoffmann, T., Odum, J. R., Bowman, F., Collins, D., Klockow, D., Flagan, R. C., and Seinfeld, J. H.: Formation of organic aerosols from the oxidation of biogenic hydrocarbons, *J. Atmos. Chem.*, 26, 189–222, 1997.

Incropera, F. P., Dewitt, D. P., Bergman, T. L., and Lavine, A. S.: Fundamentals of Heat and Mass Transfer, 6th Edn., Wiley, Hoboken, NJ, 2007.

Jimenez, J. L., Canagaratna, M. R., Donahue, N. M., Prévôt, A. S., Zhang, Q., Kroll, J. H., DeCarlo, P. F., Allan, J. D., Coe, H., Ng, N. L., Aiken, A. C., Docherty, K. S., Ulbrich, I. M., Grieshop, A. P., Robinson, A. L., Duplissy, J., Smith, J. D., Wilson, K. R., Lanz, V. A., Hueglin, C., Sun, Y. L., Tian, J., Laaksonen, A., Raatikainen, T., Rautiainen, J., Vaattovaara, P., Ehn, M., Kulmala, M., Tomlinson, J. M., Collins, D. R., Cubison, M. J., Dunlea, E. J., Huffman, J. A., Onasch, T. B., Alfarra, M. R., Williams, P. I., Bower, K., Kondo, Y., Schneider, J., Drewnick, F., Borrmann, S., Weimer, S., Demerjian, K., Salcedo, D., Cottrell, L., Griffin, R., Takami, A., Miyoshi, T., Hatakeyama, S., Shimono, A., Sun, J. Y., Zhang, Y. M., Dzepina, K., Kimmel, J. R., Sueper, D., Jayne, J. T., Herndon, S. C., Trimborn, A. M., Williams, L. R., Wood, E. C., Middlebrook, A. M., Kolb, C. E., Baltensperger, U., and Worsnop, D. R.: Evolution of organic aerosols in the atmosphere, *Science*, 326, 1525–1529, 2009.

Jokinen, T., Sipilä, M., Richters, S., Kerminen, V.-M., Paasonen, P., Stratmann, F., Worsnop, D., Kulmala, M., Ehn, M., Herrmann, H., and Berndt, T.: Rapid autoxidation forms highly oxidized RO_2 radicals in the atmosphere, *Angew. Chem. Int. Edit.*, 53, 14596–14600, 2014.

Kalberer, M., Paulsen, D., Sax, M., Steinbacher, M., Dommen, J., Prévôt, A. S. H., Fisseha, R., Weingartner, E., Frankevich, V., Zenobi, R., and Baltensperger, U.: Identification of polymers as major components of atmospheric organic aerosols, *Science*, 303, 1659–1662, 2004.

Kamens, R. and Jaoui, M.: Modeling aerosol formation from α-pinene + NO_x in the presence of natural sunlight using gas-phase kinetics and gas-particle partitioning theory, *Environ. Sci. Technol.*, 35, 1394–1405, 2001.

Kokkola, H., Yli-Pirilä, P., Vesterinen, M., Korhonen, H., Keskinen, H., Romakkaniemi, S., Hao, L., Kortelainen, A., Joutsensaari, J., Worsnop, D. R., Virtanen, A., and Lehtinen, K. E. J.: The role of low volatile organics on secondary organic aerosol formation, *Atmos. Chem. Phys.*, 14, 1689–1700, doi:10.5194/acp-14-1689-2014, 2014.

Krechmer, J. E., Coggon, M. M., Massoli, P., Nguyen, T. B., Crounse, J. D., Hu, W., Day, D. A., Tyndall, G. S., Henze, D. V., Rivera-Rios, J. C., Nowak, J. B., Kimmel, J. R., Mauldin III, R. L., Stark, H., Jayne, J. T., Sipilä, M., Junninen, H., St. Clair, J. M., Zhang, X., Feiner, P. A., Zhang, L., Miller, D. O., Brune, W. H., Keutsch, F. N., Wennberg, P. O., Seinfeld, J. H., Worsnop, D. R., Jimenez, J. L., and Canagaratna, M. R.: Formation of low volatility organic compounds and secondary organic aerosol from isoprene hydroxyhydroperoxide low-NO oxidation, *Environ. Sci. Technol.*, 49, 10330–10339, 2015.

Kurtén, T., Rissanen, M. P., Mackeprang, K., Thornton, J. A., Hyttinen, N., Jørgensen, S., Ehn, M., and Kjaergaard, H. G.: Computational study of hydrogen shifts and ring-opening mechanisms in α-pinene ozonolysis products, *J. Phys. Chem. A.*, 119, 11366–11375, 2015.

Kuwata, M. and Martin, S. T.: Phase of atmospheric secondary organic material affects its reactivity, *P. Natl. Acad. Sci. USA*, 109, 17354–17359, 2012.

Kwok, E. S. C. and Atkinson, R.: Estimation of hydroxyl radical reaction rate constants for gas-phase organic compounds using a structure–reactivity relationship: an update, *Atmos. Environ.*, 29, 1685–1695, 1995.

La, Y. S., Camredon, M., Ziemann, P. J., Valorso, R., Matsunaga, A., Lannuque, V., Lee-Taylor, J., Hodzic, A., Madronich, S., and Aumont, B.: Impact of chamber wall loss of gaseous organic compounds on secondary organic aerosol formation: explicit modeling of SOA formation from alkane and alkene oxidation, *Atmos. Chem. Phys.*, 16, 1417–1431, doi:10.5194/acp-16-1417-2016, 2016.

Lee-Taylor, J., Hodzic, A., Madronich, S., Aumont, B., Camredon, M., and Valorso, R.: Multiday production of condensing organic aerosol mass in urban and forest outflow, *Atmos. Chem. Phys.*, 15, 595–615, doi:10.5194/acp-15-595-2015, 2015.

Lopez-Hilfiker, F. D., Mohr, C., Ehn, M., Rubach, F., Kleist, E., Wildt, J., Mentel, Th. F., Carrasquillo, A. J., Daumit, K. E., Hunter, J. F., Kroll, J. H., Worsnop, D. R., and Thornton, J. A.: Phase partitioning and volatility of secondary organic aerosol components formed from α-pinene ozonolysis and OH oxidation: the importance of accretion products and other low volatility compounds, *Atmos. Chem. Phys.*, 15, 7765–7776, doi:10.5194/acp-15-7765-2015, 2015.

Loza, C. L., Chan, A. W., Galloway, M. M., Keutsch, F. N., Flagan, R. C., and Seinfeld, J. H.: Characterization of vapor wall loss in laboratory chambers, *Environ. Sci. Technol.*, 44, 5074–5078, 2010.

Loza, C. L., Craven, J. S., Yee, L. D., Coggon, M. M., Schwantes, R. H., Shiraiwa, M., Zhang, X., Schilling, K. A., Ng, N. L., Canagaratna, M. R., Ziemann, P. J., Flagan, R. C., and Seinfeld, J. H.: Secondary organic aerosol yields of 12-carbon alkanes, *Atmos. Chem. Phys.*, 14, 1423–1439, doi:10.5194/acp-14-1423-2014, 2014.

Ma, Y., Russell, A. T., and Marston, G.: Mechanisms for the formation of secondary organic aerosol components from the gas-phase ozonolysis of α-pinene, *Phys. Chem. Chem. Phys.*, 10, 4294–4312, 2008.

Mai, H., Shiraiwa, M., Flagan, R. C., and Seinfeld, J. H.: Under what conditions can equilibrium gas-particle partitioning be expected to hold in the atmosphere?, *Environ. Sci. Technol.*, 49, 11485–11491, 2015.

Matsunaga, A. and Ziemann, P. J.: Gas-wall partitioning of organic compounds in a teflon film chamber and potential effects on reaction product and aerosol yield measurements, *Aerosol Sci. Tech.*, 44, 881–892, 2010.

McVay, R. C., Cappa, C. D., and Seinfeld, J. H.: Vapor-wall deposition in chambers: theoretical considerations, *Environ. Sci. Technol.*, 48, 10251–10258, 2014.

Mentel, T. F., Springer, M., Ehn, M., Kleist, E., Pullinen, I., Kurtén, T., Rissanen, M., Wahner, A., and Wildt, J.: Formation of highly oxidized multifunctional compounds: autoxidation of peroxy radicals formed in the ozonolysis of alkenes – deduced from structure–product relationships, *Atmos. Chem. Phys.*, 15, 6745–6765, doi:10.5194/acp-15-6745-2015, 2015.

Mouchel-Vallon, C., Bräuer, P., Camredon, M., Valorso, R., Madronich, S., Herrmann, H., and Aumont, B.: Explicit modeling of volatile organic compounds partitioning in the atmospheric aqueous phase, *Atmos. Chem. Phys.*, 13, 1023–1037, doi:10.5194/acp-13-1023-2013, 2013.

Myrdal, P. B. and Yalkowsky, S. H.: Estimating pure component vapor pressures of complex organic molecules, *Ind. Eng. Chem. Res.*, 36, 2494–2499, 1997.

Nannoolal, Y., Rarey, J., Ramjugernath, D., and Cordes, W.: Estimation of pure component properties: Part 1. Estimation of the normal boiling point of non-electrolyte organic compounds via group contributions and group interactions, *Fluid Phase Equilibr.*, 226, 45–63, 2004.

Nannoolal, Y., Rarey, J., and Ramjugernath, D.: Estimation of pure component properties: Part 3: Estimation of the vapor pressure of non-electrolyte organic compounds via group contribution and group interactions, *Fluid Phase Equilibr.*, 269, 117–133, 2008.

Ng, N. L., Kroll, J. H., Keywood, M. D., Bahreini, R., Varutbangkul, V., Flagan, R. C., Seinfeld, J. H., Lee, A., and Goldstein, A. H.: Contribution of first- versus second-generation products to secondary organic aerosols formed in the oxidation of biogenic hydrocarbons, *Environ. Sci. Technol.*, 40, 2283–2297, 2006.

Ng, N. L., Chhabra, P. S., Chan, A. W. H., Surratt, J. D., Kroll, J. H., Kwan, A. J., McCabe, D. C., Wennberg, P. O., Sorooshian, A., Murphy, S. M., Dalleska, N. F., Flagan, R. C., and Seinfeld, J. H.: Effect of NOx level on secondary organic aerosol (SOA) formation from the photooxidation of terpenes, *Atmos. Chem. Phys.*, 7, 5159–5174, doi:10.5194/acp-7-5159-2007, 2007a.

Ng, N. L., Kroll, J. H., Chan, A. W. H., Chhabra, P. S., Flagan, R. C., and Seinfeld, J. H.: Secondary organic aerosol formation from *m*-xylene, toluene, and benzene, *Atmos. Chem. Phys.*, 7, 3909–3922, doi:10.5194/acp-7-3909-2007, 2007b.

Nozière, B., Barnes, I., and Becker, K. H.: Product study and mechanisms of the reactions of α-pinene and of pinonaldehyde with OH radicals, *J. Geophys. Res.*, 104, 645–656, 1999.

Pankow, J. F. and Asher, W. E.: SIMPOL.1: a simple group contribution method for predicting vapor pressures and enthalpies of vaporization of multifunctional organic compounds, *Atmos. Chem. Phys.*, 8, 2773–2796, doi:10.5194/acp-8-2773-2008, 2008.

Pathak, R. K., Stanier, C. O., Donahue, N. M., and Pandis, S. N.: Ozonolysis of α-pinene at atmospherically relevant concentrations: Temperature dependence of aerosol mass fractions (yields), *J. Geophys. Res.*, 112, D03201, doi:10.1029/2006JD007436, 2007.

Peeters, J., Vereecken, L., and Fantechi, G.: The detailed mechanism of the OH-initiated atmospheric oxidation of α-pinene: A theoretical study, *Phys. Chem. Chem. Phys.*, 3, 5489–5504, 2001.

Perraud, V., Bruns, E. A., Ezell, M. J., Johnson, S. N., Yu, Y., Alexander, M. L., Zelenyuk, A., Imre, D., Chang, W. L., Dabdub, D., Pankow, J., and Finlayson-Pitts, B. J.: Nonequilibrium atmospheric secondary organic aerosol formation and growth, *P. Natl. Acad. Sci. USA*, 109, 2836–2841, 2012.

Praske, E., Crounse, J. D., Bates, K. H., Kurtén, T., Kjaergaard, H. G., and Wennberg, P. O.: Atmospheric fate of methyl vinyl ketone: peroxy radical reactions with NO and HO_2, *J. Phys. Chem.*, 119, 4562–4572, 2015.

Presto, A. A., Huff Hartz, K. E., and Donahue, N. M.: Secondary organic aerosol production from terpene ozonolysis: 1. Effect of UV radiation, *Environ. Sci. Technol.*, 39, 7036–7045, 2005a.

Presto, A. A., Huff Hartz, K. E., and Donahue, N. M.: Secondary organic aerosol production from terpene ozonolysis: 2. Effect of NO_x concentration, *Environ. Sci. Technol.*, 39, 7046–7054, 2005b.

Pye, H. O. T., Chan, A. W. H., Barkley, M. P., and Seinfeld, J. H.: Global modeling of organic aerosol: the importance of reactive nitrogen (NO_x and NO_3), *Atmos. Chem. Phys.*, 10, 11261–11276, doi:10.5194/acp-10-11261-2010, 2010.

Renbaum-Wolff, L., Grayson, J. W., Bateman, A. P., Kuwata, M., Sellier, M., Murray, B. M., Shilling, J. E., Martin, S. T., and Bertram, A. K.: Viscosity of α-pinene secondary organic material and implications for particle growth and reactivity, *P. Natl. Acad. Sci. USA*, 110, 8014–8019, 2013.

Rissanen, M. P., Kurtén, T., Sipilä, M., Thornton, J. A., Kangasluoma, J., Sarnela, N., Junninen, H., Jørgensen, S., Schallhart, S., Kajos, M. K., Taipale, R., Springer, M., Mentel, T. F., Ruuskanen, T., Petäjä, T., Worsnop, D. R., Kjaergaard, H. G., and Ehn, M.: The formation of highly oxidized multifunctional products in the ozonolysis of cyclohexene, *J. Am. Chem. Soc.*, 136, 15596–15606, 2014.

Rissanen, M. P., Kurtén, T., Sipilä, M., Thornton, J. A., Kausiala, O., Garmash, O., Kjaergaard, H. G., Petäjä, T., Worsnop, D. R., Ehn, M., and Kulmala, M.: Effects of chemical complexity on the autoxidation mechanisms of endocyclic alkene ozonolysis products: from methylcyclohexenes toward understanding α-pinene, *J. Phys. Chem.*, 119, 4633–4650, 2015.

Saleh, R., Donahue, N. M., and Robinson, A. L.: Time scales for gas-particle partitioning equilibration of secondary organic aerosol formed from alpha-pinene ozonolysis, *Environ. Sci. Technol.*, 47, 5588–5594, 2013.

Saukko, E., Lambe, A. T., Massoli, P., Koop, T., Wright, J. P., Croasdale, D. R., Pedernera, D. A., Onasch, T. B., Laaksonen, A., Davidovits, P., Worsnop, D. R., and Virtanen, A.: Humidity-

dependent phase state of SOA particles from biogenic and anthropogenic precursors, *Atmos. Chem. Phys.*, 12, 7517–7529, doi:10.5194/acp-12-7517-2012, 2012.

Seinfeld, J. H. and Pandis, S. N.: Atmospheric Chemistry and Physics: From Air Pollution to Climate Change, 2nd Edn. Wiley, Hoboken, N. J., 2006.

Shilling, J. E., Chen, Q., King, S. M., Rosenoern, T., Kroll, J. H., Worsnop, D. R., McKinney, K. A., and Martin, S. T.: Particle mass yield in secondary organic aerosol formed by the dark ozonolysis of a-pinene, *Atmos. Chem. Phys.*, 8, 2073–2088, doi:10.5194/acp-8-2073-2008, 2008.

Shiraiwa, M., Yee, L. D., Schilling, K. A., Loza, C. L., Craven, J. S., Zuen, A., Ziemann, P. J., and Seinfeld, J. H.: Size distribution dynamics reveal particle-phase chemistry in organic aerosol formation, *P. Natl. Acad. Sci. USA.*, 110, 11746–11750, 2013.

Takekawa, H., Minoura, H., and Yamazaki, S.: Temperature dependence of secondary organic aerosol formation by photo-oxidation of hydrocarbons, *Atmos. Environ.*, 37, 3413–3424, 2003.

Tobias, H. J. and Ziemann, P. J.: Kinetics of the gas-phase reactions of alcohols, aldehydes, carboxylic acids, and water with the C13 stabilized Criegee intermediate formed from ozonolysis of 1-tetradecene, *J. Phys. Chem. A.*, 105, 6129–6135, 2001.

Tolocka, M. P., Jang, M., Ginter, J. M., Cox, F. J., Kamens, R. M., and Johnston, M. V.: Formation of oligomers in secondary organic aerosol, *Environ. Sci. Technol.*, 38, 1428–1434, 2004.

Trump, E. R. and Donahue, N. M: Oligomer formation within secondary organic aerosols: equilibrium and dynamic considerations, *Atmos. Chem. Phys.*, 14, 3691–3701, doi: 10.5194/acp-14-3691-2014, 2014.

Vaden, T. D., Song, C., Zaveri, R. A., Imre, D., and Zelenyuk, A.: Morphology of mixed primary and secondary organic particles and the adsorption of spectator organic gases during aerosol formation, *P. Natl. Acad. Sci. USA*, 107, 6658–6663, 2010.

Vaden, T. D., Imre, D., Beránek, J., Shrivastava, M., and Zelenyuk, A.: Evaporation kinetics and

phase of laboratory and ambient secondary organic aerosol, *P. Natl. Acad. Sci. USA*, 108, 2190–2195, 2011.

Valorso, R., Aumont, B., Camredon, M., Raventos-Duran, T., Mouchel-Vallon, C., Ng, N. L., Seinfeld, J. H., Lee-Taylor, J., and Madronich, S.: Explicit modelling of SOA formation from a-pinene photooxidation: sensitivity to vapour pressure estimation, *Atmos. Chem. Phys.*, 11, 6895–6910, doi:10.5194/acp-11-6895-2011, 2011.

Vereecken, L., Müller, J.-F., and Peeters, J.: Low-volatility poly-oxygenates in the OH-initiated atmospheric degradation of *alpha*-pinene: impact of non-traditional peroxy radical chemistry, *Phys. Chem. Chem. Phys.*, 9, 5241–5248, 2007.

Virtanen, A., Joutsensaari, J., Koop, T., Kannosto, J., Yli-Pirilä, P., Leskinen, J., Mäkelä, J. M., Holopainen, J. K., Pöschl, U., Kulmala, M., Worsnop, D. R., and Laaksonen, A.: An amorphous solid state of biogenic secondary organic aerosol particles, *Nature*, 467, 824–827, 2010.

Virtanen, A., Kannosto, J., Kuuluvainen, H., Arffman, A., Joutsensaari, J., Saukko, E., Hao, L., Yli-Pirilä, P., Tiitta, P., Holopainen, J. K., Keskinen, J., Worsnop, D. R., Smith, J. N., and Laaksonen, A.: Bounce behavior of freshly nucleated biogenic secondary organic aerosol particles, *Atmos. Chem. Phys.*, 11, 8759–8766, doi:10.5194/acp-11-8759-2011, 2011.

Wong, J. P. S., Zhou, S., and Abbatt, P. D.: Changes in secondary organic aerosol composition and mass due to photolysis: relative humidity dependence, *J. Phys. Chem. A.*, 119, 4309–4316, 2015.

Yee, L. D., Craven, J. S., Loza, C. L., Schilling, K. A., Ng, N. L., Canagaratna, M. R., Ziemann, P. J., Flagan, R. C., and Seinfeld, J. H.: Effect of chemical structure on secondary organic aerosol formation from C_{12} alkanes, *Atmos. Chem. Phys.*, 13, 11121–11140, doi:10.5194/acp-13-11121-2013, 2013.

Yeh, G. K. and Ziemann, P. J.: Alkyl nitrate formation from the reactions of C_8-C_{14} *n*-alkanes with OH radicals in the presence of NO_x: measured yields with essential corrections for gas-wall partitioning, *J. Phys. Chem. A.*, 118, 8147–8157, 2014.

Yeh, G. K. and Ziemann, P. J.: Gas-wall partitioning of oxygenated organic compounds: measurements, structure-activity relationships, and correlation with gas chromatographic retention factor, *Aerosol. Sci. Tech.*, 49, 727–738, 2015.

Zhang, X., Cappa, C. D., Jathar, S. H., McVay, R. C., Ensberg, J. J., Kleeman, M. J., and Seinfeld, J. H.: Influence of vapor wall-loss in laboratory chambers on yields of secondary organic aerosol, *P. Natl. Acad. Sci. USA*, 111, 5802–5807, doi:10.1073/pnas.1404727111, 2014.

Zhang, X., Schwantes, R. H., McVay, R. C., Lignell, H., Coggon, M. M., Flagan, R. C., and Seinfeld, J. H.: Vapor wall deposition in Teflon chambers, *Atmos. Chem. Phys.*, 15, 4197–4214, doi:10.5194/acp-15-4197-2015, 2015.

Ziemann, P. J. and Atkinson, R.: Kinetics, products, and mechanisms of secondary organic aerosol formation, *Chem. Soc. Rev.*, 41, 6582–6605, 2012.

Table 4.1: Initial conditions for photooxidation experiments.

Expt.	Desc.	T (K)	RH (%)	HC_0 (ppb)	Initial Seed Surface Area ($\mu m^2\,cm^{-3}$)	Duration (min)
141007	Nucleation	300	$< 5\,\%$	51	0	300
141016	Low SA	300	$< 5\,\%$	56	1.7×10^3	534
141028	Med SA	300	$< 5\,\%$	53	3.2×10^3	233
141118	High SA	298	$< 5\,\%$	51	3.4×10^3	410
141113	10 % UV, Low SA	297	$< 5\,\%$	53	9.9×10^2	1070
141125	10 % UV, Med SA	297	$< 5\,\%$	49	2.4×10^3	1160

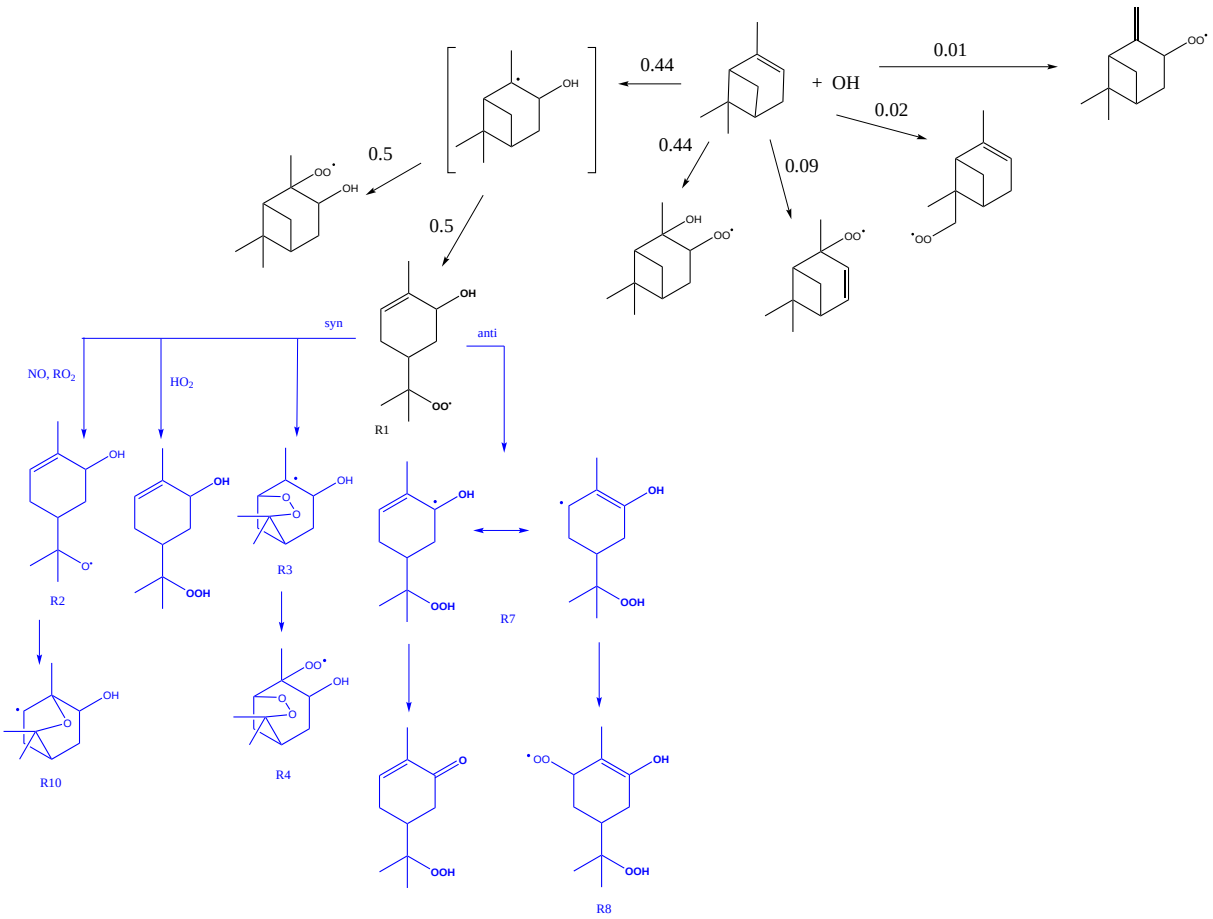

Figure 4.1: Overview of the α-pinene + OH oxidation mechanism in GECKO-A. Reactions in black are those originally implemented in *Valorso et al.* (2011). Additions to this mechanism are shown in blue. Species are labeled to be consistent with *Vereecken et al.* (2007). All subsequent chemistry is generated in GECKO-A according to the standard protocols in GECKO-A.

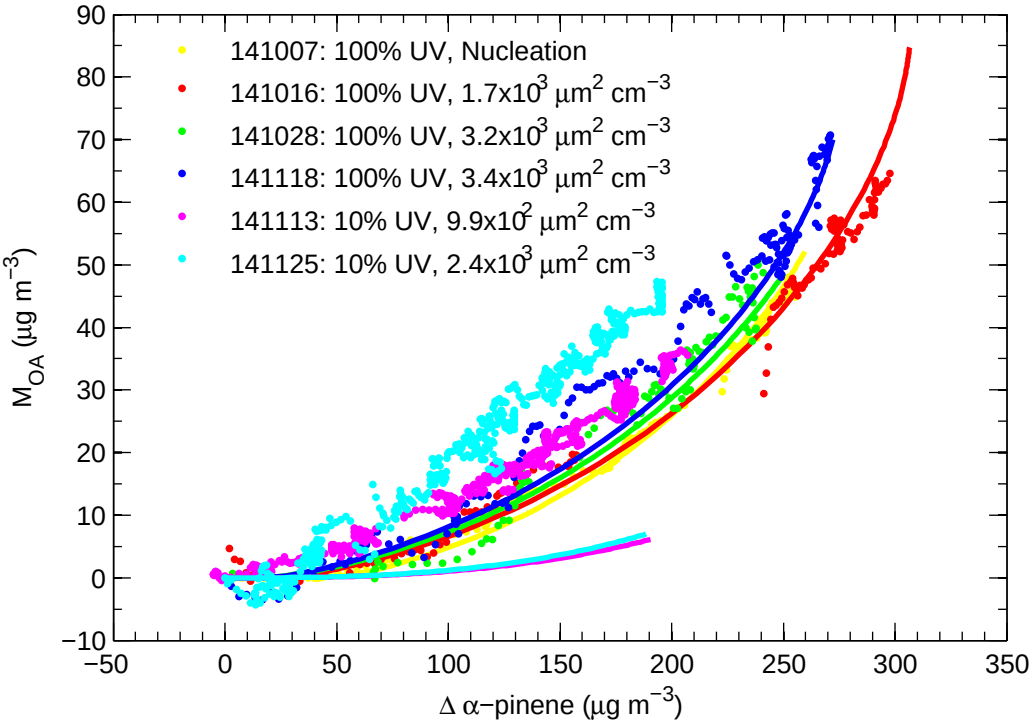

Figure 4.2: Mass of SOA, M_{OA}, as a function of reacted α-pinene. Experimental data are shown with filled circles, with colors corresponding to individual experiments (see Table 4.1), and have been corrected for particle wall loss (see text). Predictions using the default GECKO-A are shown as solid lines with the colors corresponding to the different experiments. In GECKO-A, the vapor–particle accommodation coefficient is set to $\alpha_{\mathrm{p}} = 1$ and the vapor wall loss rate is set to $k_{\mathrm{gw}} = 10^{-3}\,\mathrm{s}^{-1}$.

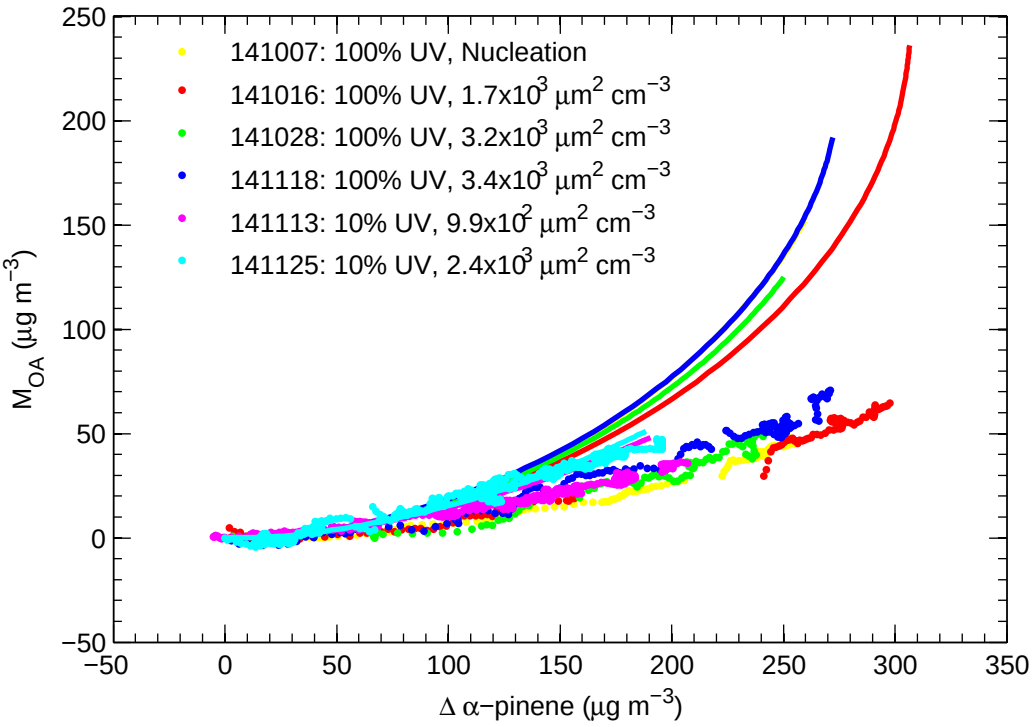

Figure 4.3: Mass of SOA as a function of reacted α-pinene. Experimental data are shown as filled circles. Solid lines correspond to GECKO-A predictions using a vapor wall loss rate $k_{\mathrm{gw}} = 10^{-5}\,\mathrm{s}^{-1}$.

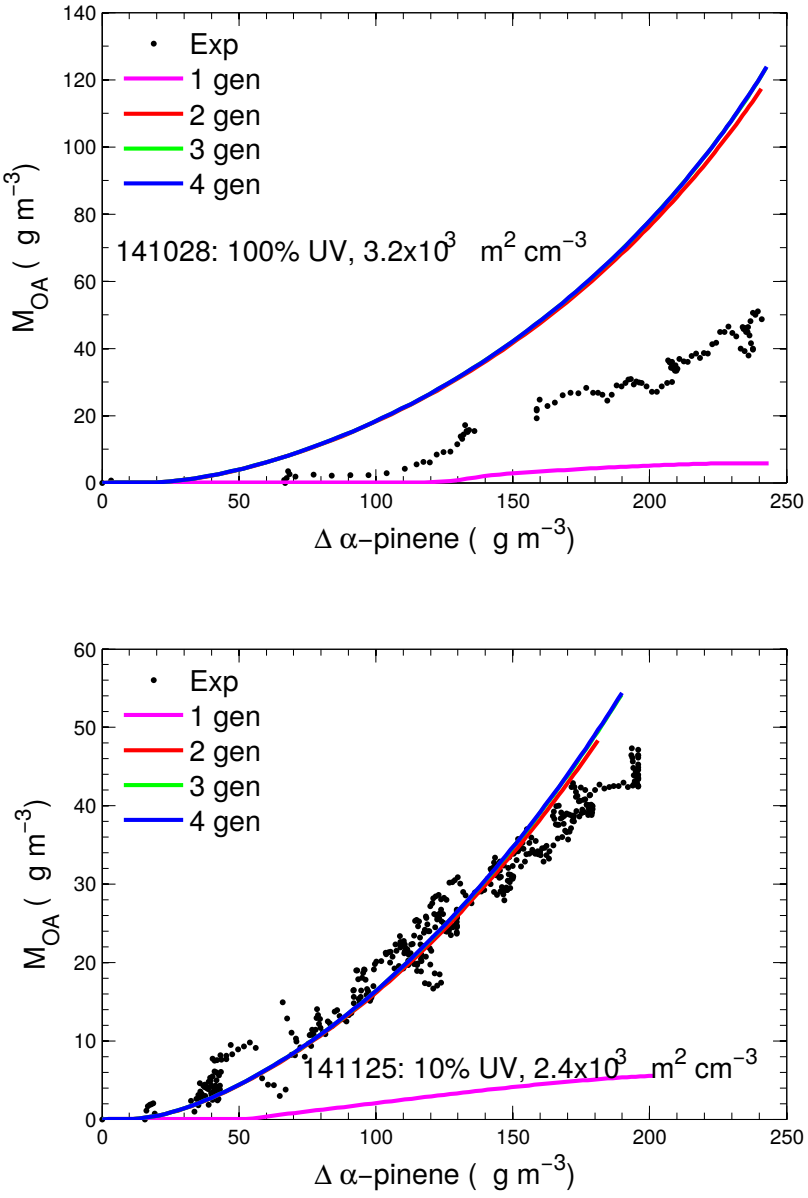

Figure 4.4: Mass of SOA as a function of reacted α-pinene. Experimental data are shown with filled circles. Solid lines correspond to GECKO-A predictions from different generations of reaction using a vapor wall loss rate $k_{\mathrm{gw}} = 10^{-5}\,\mathrm{s}^{-1}$, where a generation corresponds to reaction with an oxidation such as OH up to formation of a stable product.

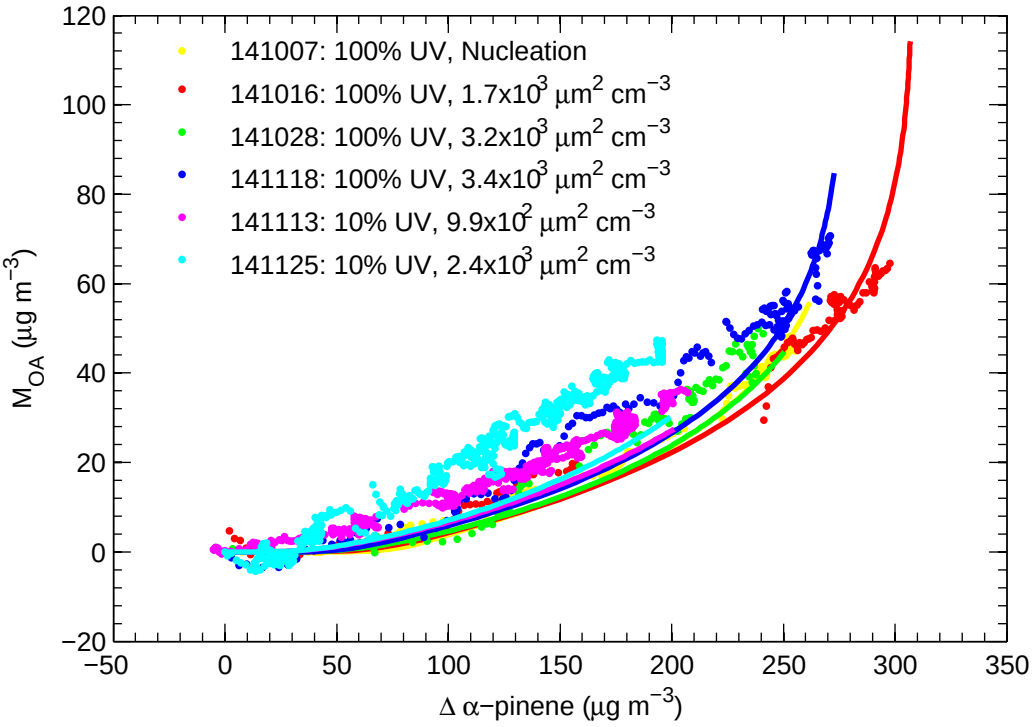

Figure 4.5: Mass of SOA as a function of reacted α-pinene. Experimental data are shown with filled circles. Solid lines display GECKO-A predictions when using OH reaction rate constants that have been reduced to 10 % of their default values (with the exception of α-pinene + OH) and $k_{\mathrm{gw}} = 10^{-5}\,\mathrm{s}^{-1}$.

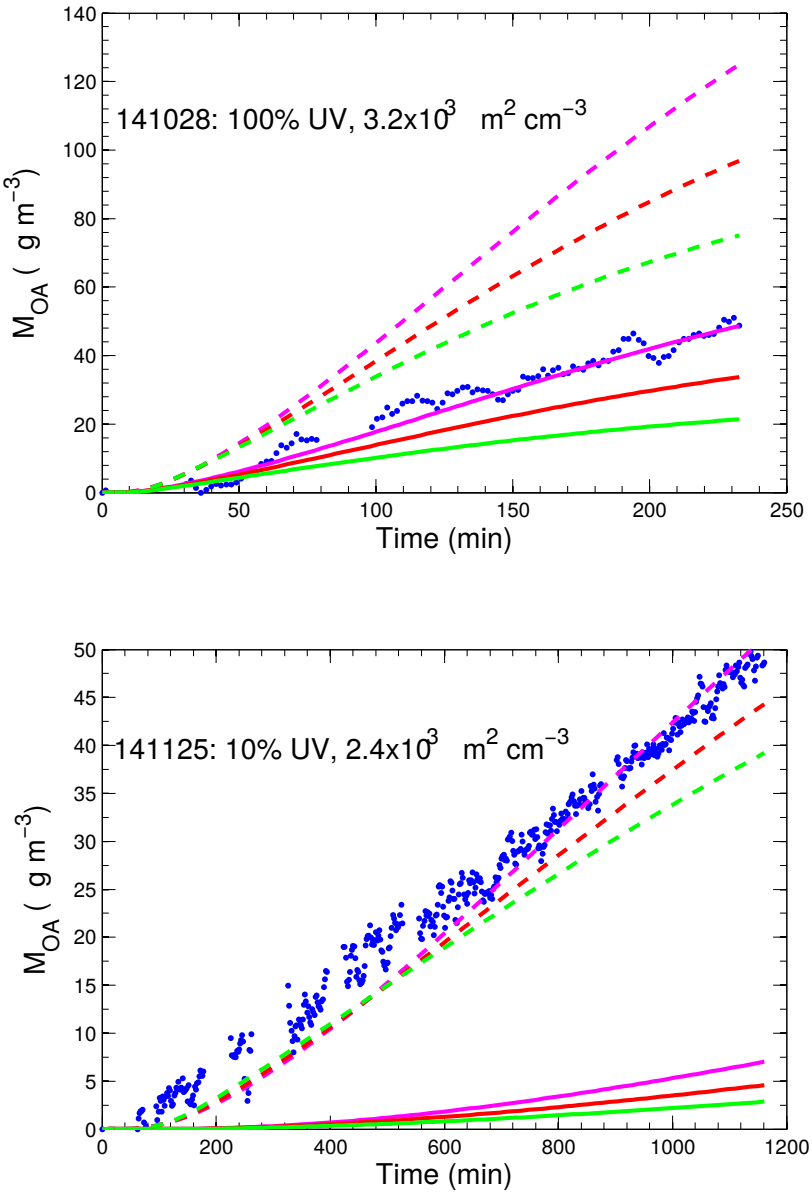

Figure 4.6: Mass of SOA as a function of time for one 100 % UV and one 10 % UV experiment. Experimental data are shown with filled circles. Lines show GECKO-A predictions when varying the branching ratio for the $RO_2 + HO_2$ reaction with differing vapor wall loss rates. Solid lines show predictions with $k_{gw} = 10^{-3}\,s^{-1}$, and dashed lines show predictions with $k_{gw} = 10^{-5}\,s^{-1}$. Pink lines show the base case predictions, in which the branching between formation of the hydroperoxide and the alkoxy from $RO_2 + HO_2$ is 80 : 20. For the red lines, the branching ratio is 50 : 50, and for the green, it is 25 : 75.

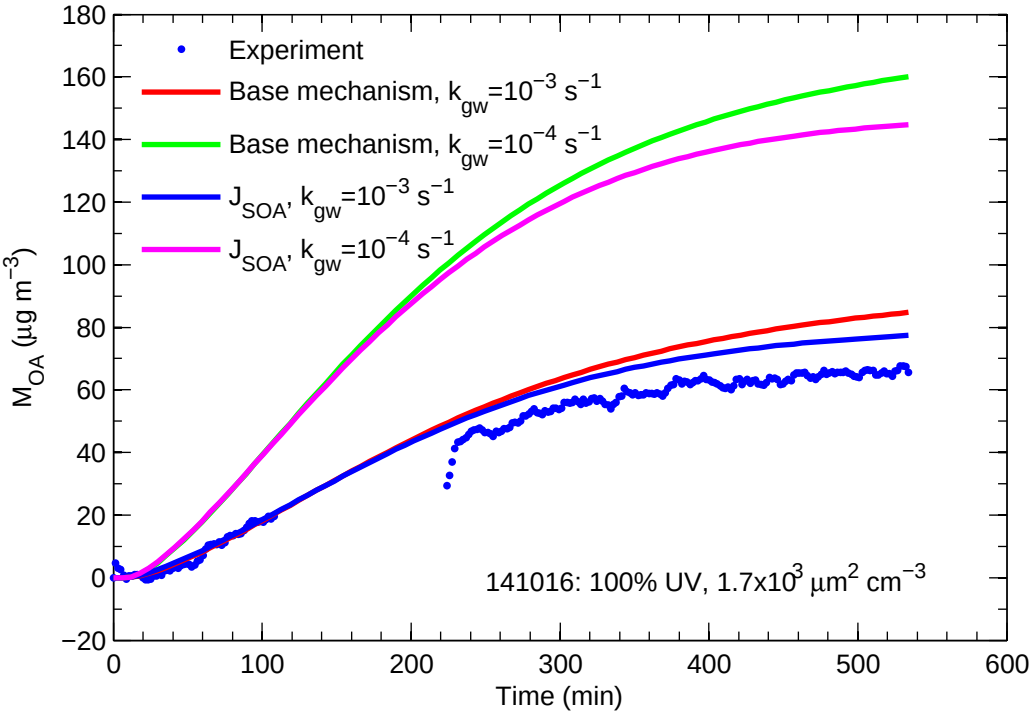

Figure 4.7: Mass of SOA as a function of time for one 100 % UV experiment. Experimental data are shown with filled circles. Solid lines show GECKO-A predictions with and without condensed-phase photolysis with two different vapor wall loss rates.

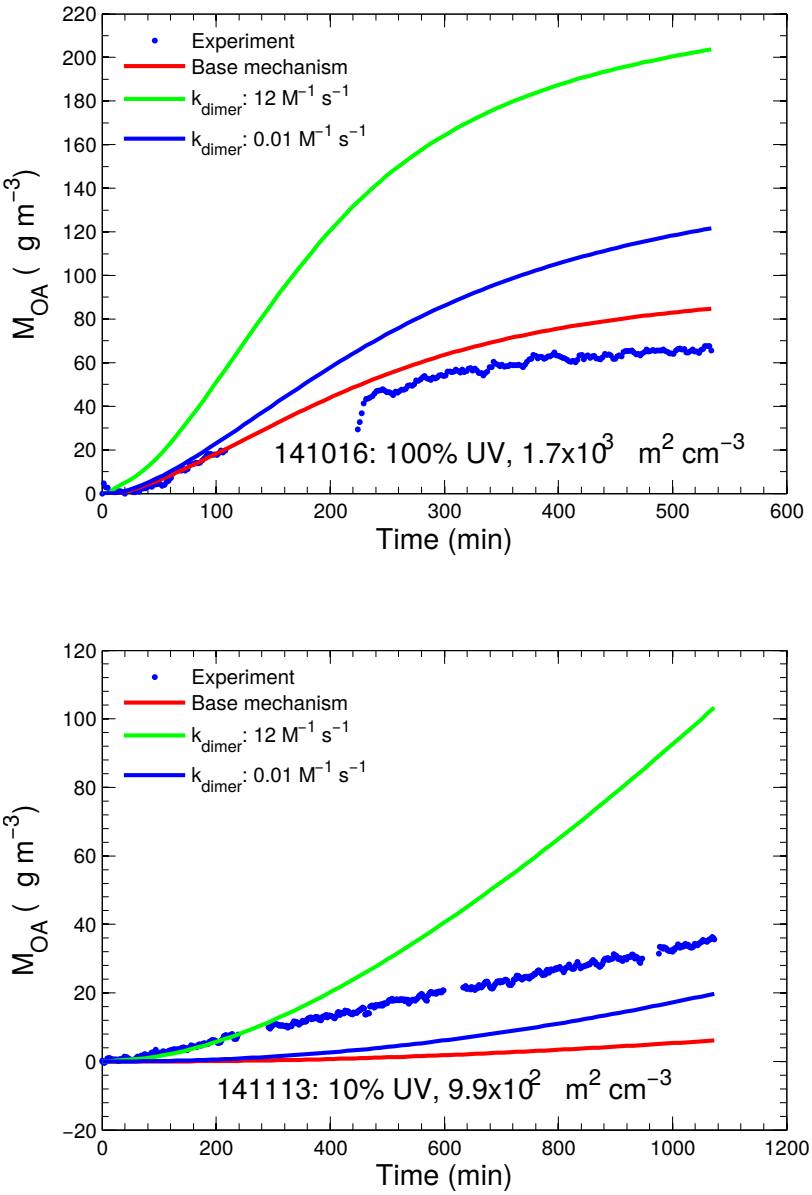

Figure 4.8: Mass of SOA as a function of time for one 100 % UV experiment and one 10 % experiment. Experimental data are shown with filled circles. Solid lines show GECKO-A predictions for the base case and then with two values of a condensed-phase dimerization rate constant, all simulations using $k_{\mathrm{gw}} = 10^{-3}\,\mathrm{s}^{-1}$.

Chapter 5

Conclusions and Future Work

The effect of vapor wall deposition on SOA yields measured in chambers is complex. Chapter 2 shows that the effect of vapor wall deposition depends on the relative time scales of the gas-phase oxidation rate, the rate of gas–particle mass transfer, and the rate of gas–wall mass transfer. Changing either the gas-phase oxidation rate, by changing the oxidant concentration, or the rate of gas–particle mass transfer, by changing the concentration of seed particles, can affect the influence of vapor wall deposition and thus affect the observed yield. Simulations show that changing the rate of gas–particle mass transfer by increasing the seed particle concentration affects the measured SOA yield only in instances in which SOA formation is kinetically limited arising from slow accommodation of organic species into the particle phase. This effect is observed experimentally for the toluene system, as discussed in Appendix D. For systems with kinetically limited SOA formation, increasing the concentration of seed particles lessens the influence of vapor wall deposition by promoting faster condensation onto particles and thereby increases the observed SOA yield.

Chapter 3 applies the model developed in Chapter 2 to α-pinene ozonolysis experiments in which an effect on the SOA yield is observed when changing the oxidation rate but not when changing the concentration of seed particles. Model simulations show that the absence of an effect of changing the seed particle concentration is consistent with SOA formation being governed by quasi-equilibrium growth, in which gas–particle equilibrium is established much faster than the rate of change of the gas-phase concentration. In contrast to the toluene system of Appendix D, for α-pinene ozonolysis and other systems governed by quasi-equilibrium growth, increasing the concentration of seed particles is not an effective way to mitigate the influence of vapor wall deposition. The observed effect of oxidation rate on SOA yield arises due to the presence of vapor wall deposition: gas-phase oxidation products are produced more quickly and condense preferentially onto seed particles before being lost to the walls. Therefore, for α-pinene ozonolysis, increasing the oxidation rate is the most effective way to mitigate the influence of vapor wall deposition. Model sensitivity studies show that the presence of an oxidation rate effect and/or seed particle effect depends on a complex interplay of factors, such as α_p (the vapor–particle accommodation coefficient), the rate of hydrocarbon oxidation, and the concentration of seed particles. Depending on the relative time scales of the

oxidation rate and the rate of gas–particle mass transfer, increasing either the oxidation rate or the seed particle concentration or both can be effective in mitigating the effect of vapor wall deposition in depressing the measured SOA yield.

Appendix D shows that the toluene system is characterized by kinetically limited SOA formation, and therefore an effect on SOA yield is observed when increasing the seed particle concentration. However, variation of the oxidation rate was not studied. Experiments in which the oxidation rate and seed particle concentration are varied simultaneously during toluene SOA experiments would be useful to determine how best to mitigate the effects of vapor wall deposition for this system. Similar experiments should be carried out for other precursors.

In addition to conducting experiments that minimize the effect of vapor wall deposition, it is necessary to use models to correct SOA yields for this effect, as is done in Appendix D. However, a complication to attempting to correct chamber-derived SOA yields for vapor wall deposition is the still-debated magnitude of the vapor wall deposition rate. In Appendix E, vapor wall deposition rates for individual species are directly measured in the Caltech chamber to be of order 10^{-5}–10^{-6} s^{-1}. However, wall deposition rates of 10^{-3}–10^{-4} s^{-1} have been observed in other chambers (*Yeh and Ziemann*, 2015; *Matsunaga and Ziemann*, 2010; *Krechmer et al.*, 2016), with the differences in these rates too great to be explained merely by differences in the surface-to-volume ratios of the chambers. Furthermore, the behavior of vapor wall deposition is very different between that measured in Appendix E and *Krechmer et al.* (2016). In Appendix E, slow continuous vapor decay is observed, with no equilibration with the wall. In *Krechmer et al.* (2016), rapid vapor decay followed by vapor–wall equilibration is observed. Both studies measured vapor wall deposition rates of individual species formed in situ in chambers; however, there are important differences in how the experiments were carried out that could explain the differences in measured rates. In Appendix E, oxidation products were generated via photooxidation that lasted for one hour, while *Krechmer et al.* (2016) generated products with only 10 s of photooxidation. If during the one hour of photooxidation in Appendix E, individual species saturate in the wall layer, slower wall deposition may be observed after lights are turned off because the concentrations in the wall are closer to equilibrium. Furthermore, different

instruments are used in the two studies to monitor vapor decay: the study in Appendix E used a CF_3O^- CIMS while *Krechmer et al.* (2016) used a NO_3^- or I^- CIMS. Differences between the CIMS, especially in the inlet region, could contribute to the discrepancies in measured wall deposition rates. To resolve these discrepancies, more experiments are needed to measure vapor wall deposition rates of individual compounds. Both possible causes for the discrepancy, experimental protocol and CIMS differences, should be examined: experiments should be conducted in the Caltech chamber using the protocol of *Krechmer et al.* (2016) and, if possible, using a NO_3^- or I^- CIMS. If indeed the CIMS is found to be the source of the discrepancy, a computer model should be developed for the Caltech CF_3O^- CIMS to better understand the behavior of vapor species within the CIMS.

Chapter 4 explores how the assumed magnitude of the vapor wall deposition rate can greatly affect conclusions drawn from comparisons between simulations and experiments. α-pinene+OH SOA experiments were carried out at different seed particle concentrations (changing the rate of gas–particle mass transfer) and different UV intensities (changing the oxidation rate). The experimentally-observed SOA yield is not affected when changing either the rate of gas–particle mass transfer or the oxidation rate. Simulations are performed using the detailed model GECKO-A which predict that changing the oxidation rate should drastically affect the SOA yield. Two alternative hypotheses are advanced to explain this discrepancy depending on the assumed magnitude of the vapor wall deposition rate. If vapor wall loss in the Caltech chamber is of order 10^{-5} s^{-1}, GECKO-A greatly overpredicts SOA during high UV experiments, likely due to an overprediction of second-generation products. However, if instead vapor wall loss in the Caltech chamber is of order 10^{-3} s^{-1}, GECKO-A greatly underpredicts SOA during low UV experiments, possibly due to the absence of autoxidation pathways in the α-pinene mechanism. As the conclusions from this study will be drastically different depending on the order of magnitude of the vapor wall deposition rate, it is of paramount importance to resolve the discrepancy between different measurements of this rate.

Bibliography

Krechmer, J. E., Pagonis, D., Ziemann, P. J., and Jimenez, J. L.: Quantification of gas–wall partitioning in Teflon environmental chambers using rapid bursts of low-volatility oxidized species generated *in-situ*, *Environ. Sci. Technol.*, doi:10.1021/acs.est.6b00606, 2016.

Matsunaga, A. and Ziemann, P. J.: Gas-wall partitioning of organic compounds in a teflon film chamber and potential effects on reaction product and aerosol yield measurements, *Aerosol Sci. Tech.*, 44, 881–892, 2010.

Yeh, G. K. and Ziemann, P. J.: Gas-wall partitioning of oxygenated organic compounds: measurements, structure-activity relationships, and correlation with gas chromatographic retention factor, *Aerosol. Sci. Tech.*, 49, 727–738, 2015.

Appendix A

Supplemental Material for Chapter 2

A.0.1 Comparison to *Zhang et al.* (2014)

The SOA growth data from *Zhang et al.* (2014) can be plotted similarly to Figure 2.3 to observe the competing effects of kinetic limitations and vapor wall deposition. The yields over the course of each toluene low-NO_x photooxidation experiment in *Zhang et al.* (2014) are shown as circles in Figure A.2 as a function of C_{OA} for different seed surface areas. The lines in Figure A.2 are yields calculated using the SOM model with parameters fit to the experimental data at each surface area but in the absence of vapor wall deposition (see *SI* of *Zhang et al.* (2014) for more details). Yields over the course of one representative experiment from *Ng et al.* (2007) are shown as diamonds for comparison. The measured yields from *Zhang et al.* (2014) quickly reach a plateau with respect to C_{OA}, indicating that the SOA formed via the low-NO_x pathway is essentially nonvolatile for $C_{OA} > 10\ \mu g\ m^{-3}$. These yield curves clearly diverge at different surface areas, due to both vapor wall deposition and kinetic growth limitations. Yields calculated in the absence of vapor wall deposition diverge into separate curves solely as a result of kinetic limitations on particle growth. These yields are higher than the measured yields because species that would have otherwise condensed to the walls are able to partition to particles. The model presented here qualitatively reproduces this behavior, Figure A.3. To match the nonvolatile behavior observed in the low-NO_x case of *Zhang et al.* (2014), the saturation concentrations of species B through D are all decreased to $10^{-3}\ \mu g\ m^{-3}$. The magnitudes of the yields clearly differ from *Zhang et al.* (2014), but the general behavior is reproduced.

Yields over the course of each toluene high-NO_x photooxidation experiment in *Zhang et al.* (2014) are shown in Figure A.4, circles representing observed yields and lines representing calculated yields from the SOM model in the absence of vapor wall deposition. Although the yield curves as a function of C_{OA} do diverge slightly, the effect is much less pronounced than in the low-NO_x case. Furthermore, the yields do not reach a plateau with respect to C_{OA}. To match this observed behavior, Figure A.5, the saturation concentrations of species B through D are set as $[10^3\ 10^1\ 10^{-1}]\ \mu g\ m^{-3}$. The reaction rate constants are set as $k[OH]_{A\rightarrow B} = k[OH]_{B\rightarrow C} = 5x10^{-5}\ s^{-1}$ and $k[OH]_{C\rightarrow D} = 5x10^{-4}\ s^{-1}$. These parameters do not necessarily represent volatilities or rates of the toluene high-NO_x experiments in *Zhang et al.* (2014), but merely to show that the present model

can reproduce the general behavior.

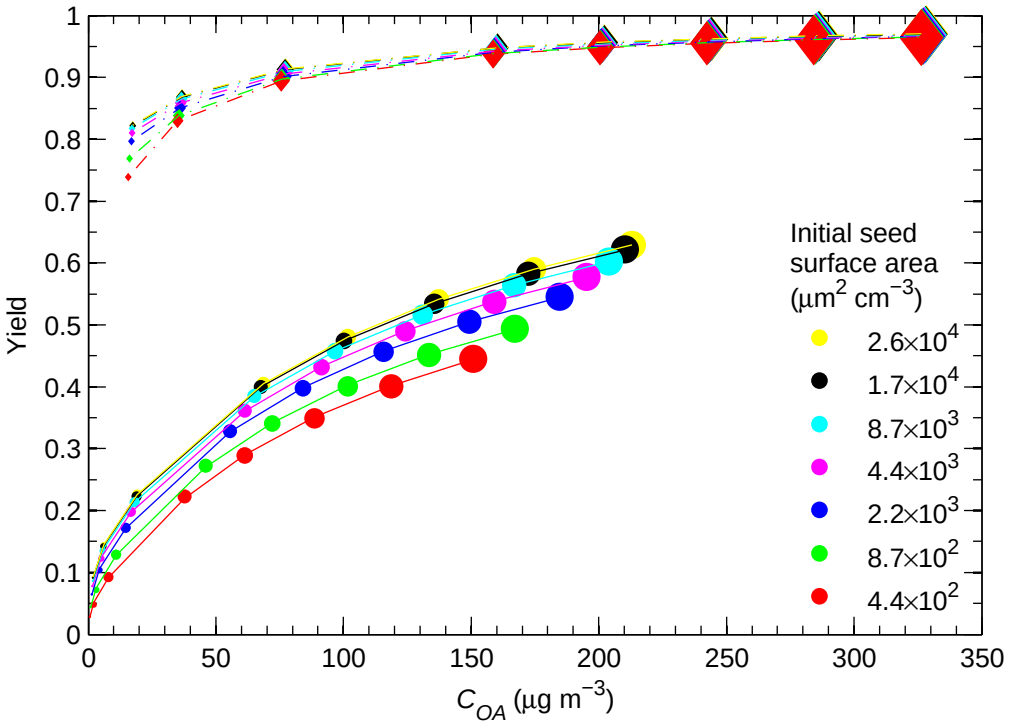

Figure A.1: SOA yields after 20 h of simulation as a function of the final organic aerosol concentration C_{OA} for $\alpha_p = 0.01$. The points on the curve were generated by varying the initial parent VOC concentration G_{A0} with (circles) and without (diamonds) vapor wall deposition. The size of the markers increases as G_{A0} increases and colors correspond to different values of the initial seed surface area. The lines were generated by fitting a two-product model to the datapoints.

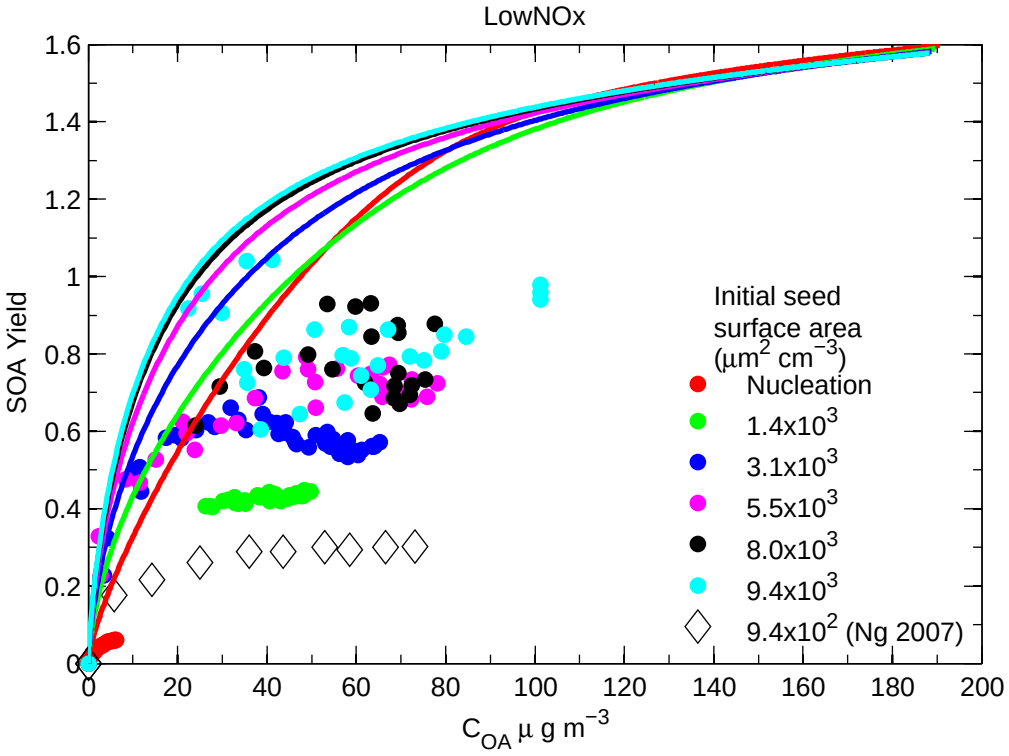

Figure A.2: SOA yields over the course of each toluene low-NO_x photooxidation experiment in *Zhang et al.* (2014) as a function of C_{OA} for different seed surface areas are shown as circles. Lines are yields calculated using the SOM model with wall deposition turned off (see *SI* of *Zhang et al.* (2014) for more details). Yields over the course of one representative experiment from *Ng et al.* (2007) are shown as diamonds for comparison.

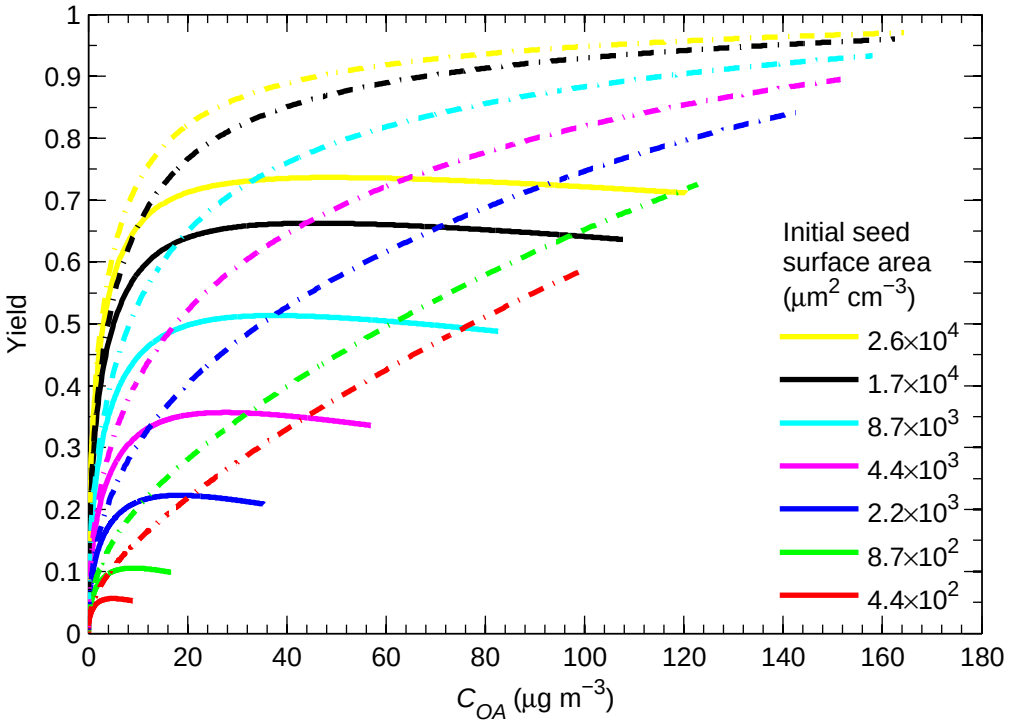

Figure A.3: SOA yields are shown as a function of C_{OA} over the course of a simulation using the present model, with $C^*_{B-D} = 10^{-3}$ μ g m^{-3} and $\alpha_p = 0.001$. Yields are calculated in the presence (solid lines) and absence (dashed lines) of vapor wall deposition. Different initial seed surface areas are shown using different colors.

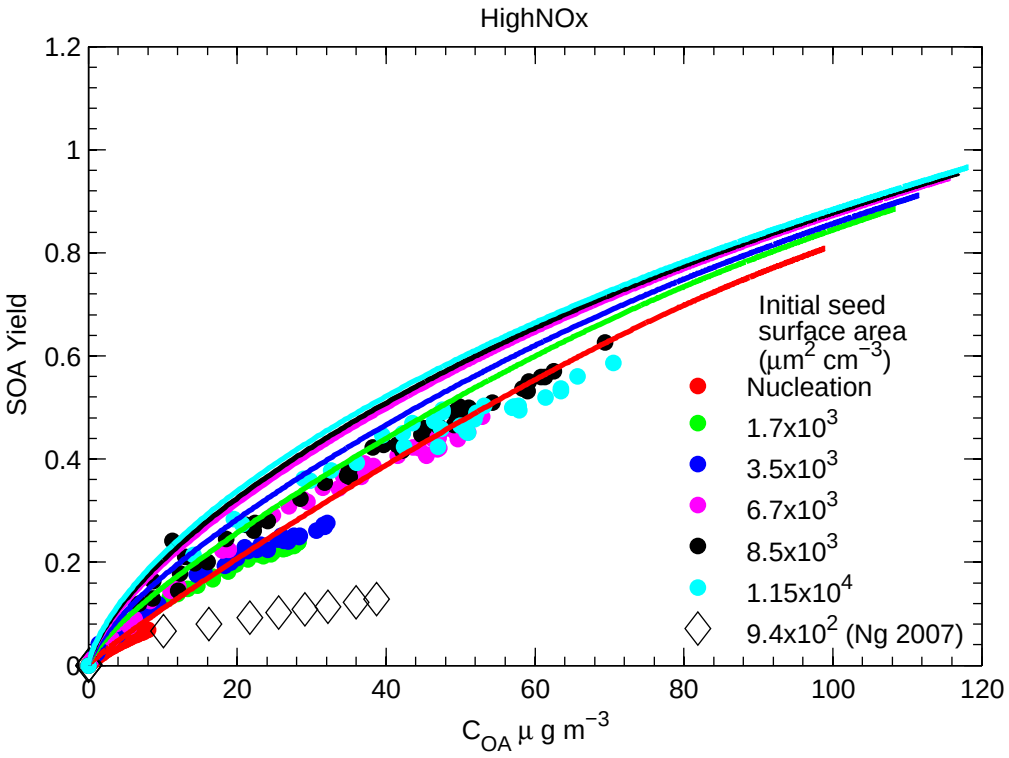

Figure A.4: SOA yields over the course of each toluene high-NO_x photooxidation experiment in *Zhang et al.* (2014) as a function of C_{OA} for different seed surface areas are shown as circles. Lines are yields calculated using the SOM model with wall deposition turned off (see *SI* of *Zhang et al.* (2014) for more details). Yields over the course of one representative experiment from *Ng et al.* (2007) are shown as diamonds for comparison.

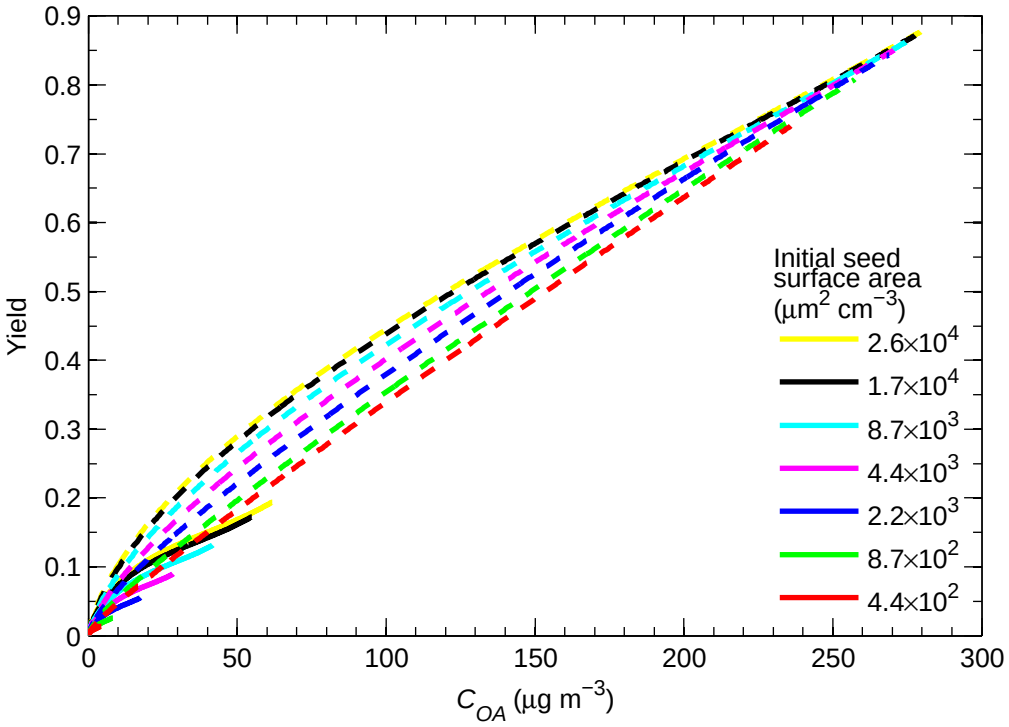

Figure A.5: SOA yields are shown as a function of C_{OA} over the course of a simulation using the present model, with $C_i^* = [10^3\ 10^1\ 10^{-1}]$ μg m^{-3}, $k[\mathrm{OH}]_{A\rightarrow B} = k[\mathrm{OH}]_{B\rightarrow C} = 5\mathrm{x}10^{-5}$ s^{-1} and $k[\mathrm{OH}]_{C\rightarrow D} = 5\mathrm{x}10^{-4}$ s^{-1}, and $\alpha_p = 0.001$. Yields are calculated in the presence (solid lines) and absence (dashed lines) of vapor wall deposition. Different initial seed surface areas are shown using different colors.

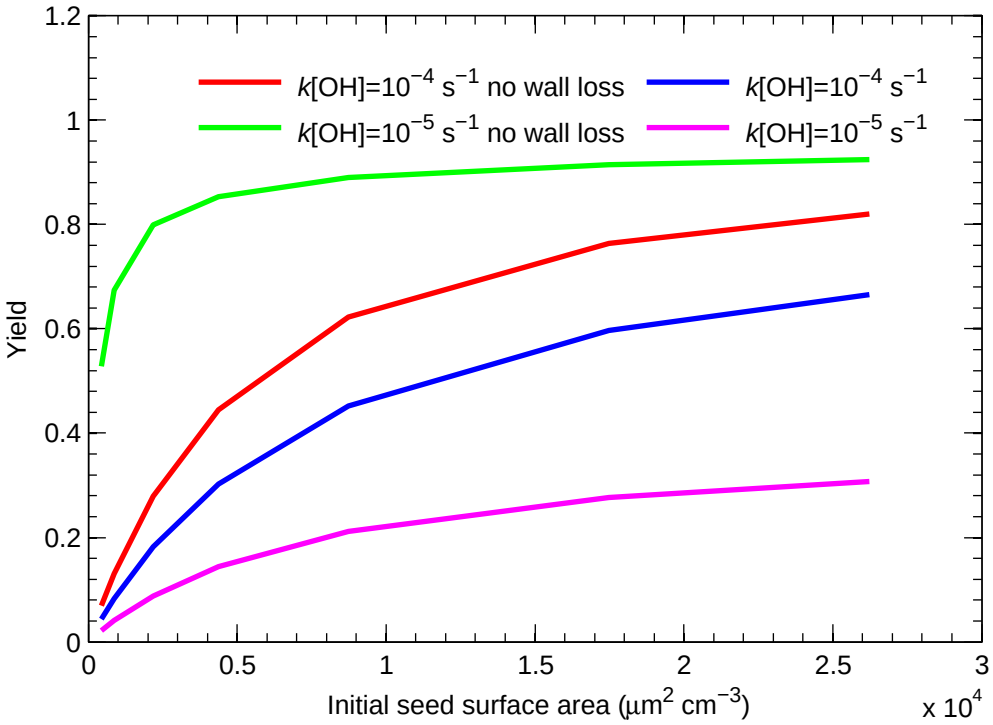

Figure A.6: SOA yields after an equivalent amount of OH exposure (20 h for $k[\mathrm{OH}]_{A\rightarrow B} = 10^{-5}$ s^{-1} and 2 h for $k[\mathrm{OH}]_{A\rightarrow B} = 10^{-4}$ s^{-1}) as a function of the final organic aerosol concentration C_{OA} for simulations with $\alpha_p = 0.001$ for different values of $k[\mathrm{OH}]_{A\rightarrow B}$, with and without vapor wall deposition.

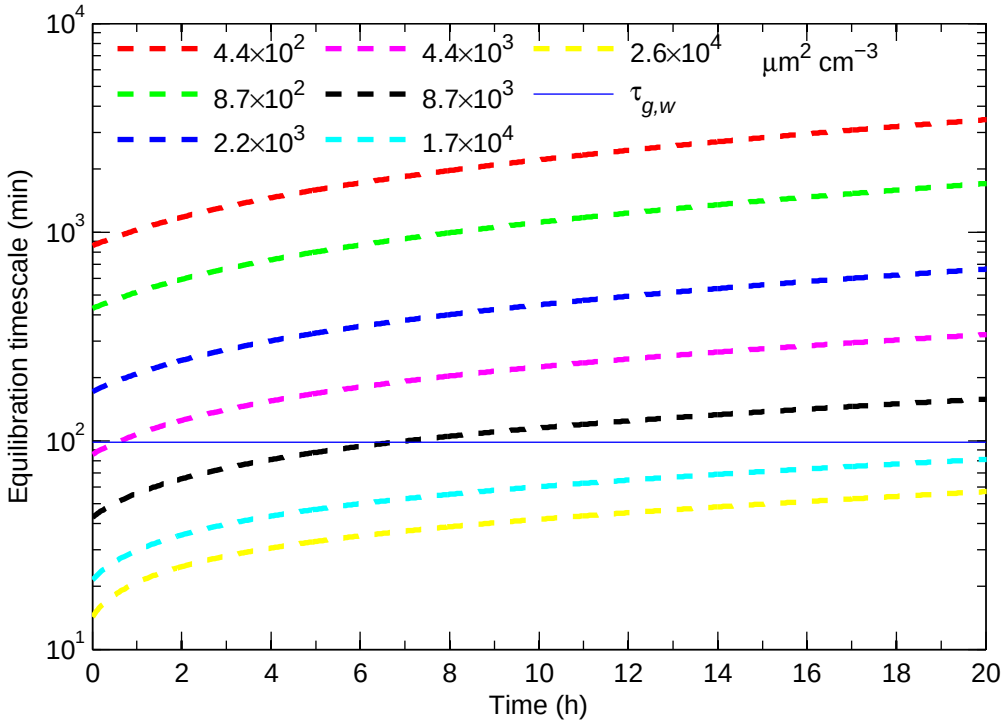

Figure A.7: Time evolution of equilibration timescale for gas-particle partitioning $\tau_{g,p}$ for different initial seed surface areas. The equilibration timescale for gas-wall partitioning ($\tau_{g,w} = 1/k_{wall,on}$) is shown as a horizontal line because this timescale does not change with time.

Bibliography

Ng, N. L., Kroll, J. H., Chan, A. W. H., Chhabra, P. S., Flagan, R. C., and Seinfeld, J. H.: Secondary organic aerosol formation from *m*-xylene, toluene, and benzene, *Atmos. Chem. Phys.*, 7, 1-14, 2007.

Zhang, X., Cappa, C. D., Jathar, S. H., McVay, R. C., Ensberg, J. J., Kleeman, M. J., and Seinfeld, J. H.: Influence of vapor wall-loss in laboratory chambers on yields of secondary organic aerosol, *P. Natl. Acad. Sci. USA*, 111, 5802–5807, doi:10.1073/pnas.1404727111, 2014.

Appendix B

Supplemental Material for Chapter 3

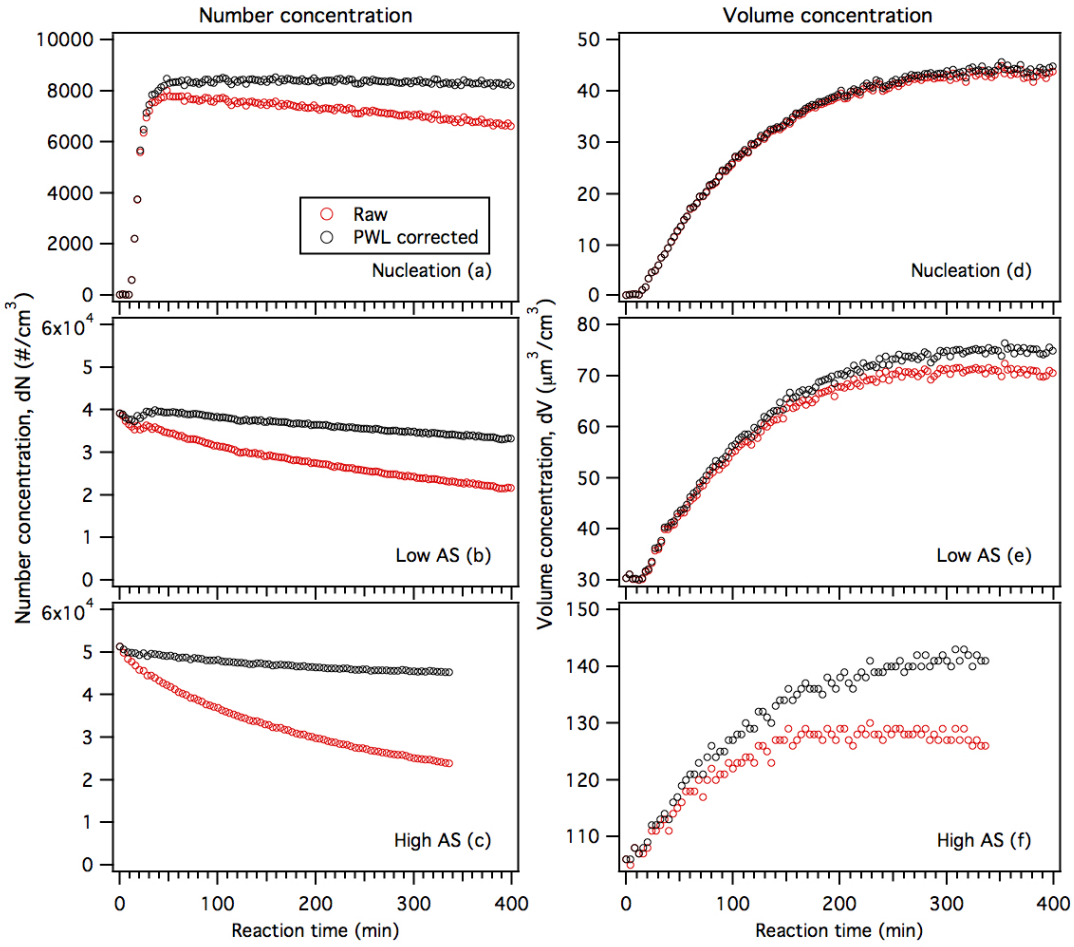

Figure B.1: Raw and particle wall loss (PWL) corrected number and volume concentration data for the 100 ppb O_3 experiments. Raw nucleation (panels a and d) and low AS (panels b and e) data are particle wall loss corrected using particle wall loss rates determined from the low AS-seed only experiments. Raw high AS (panels c and f) data are particle wall loss corrected using particle wall loss rates determined from the high AS-seed only experiments.

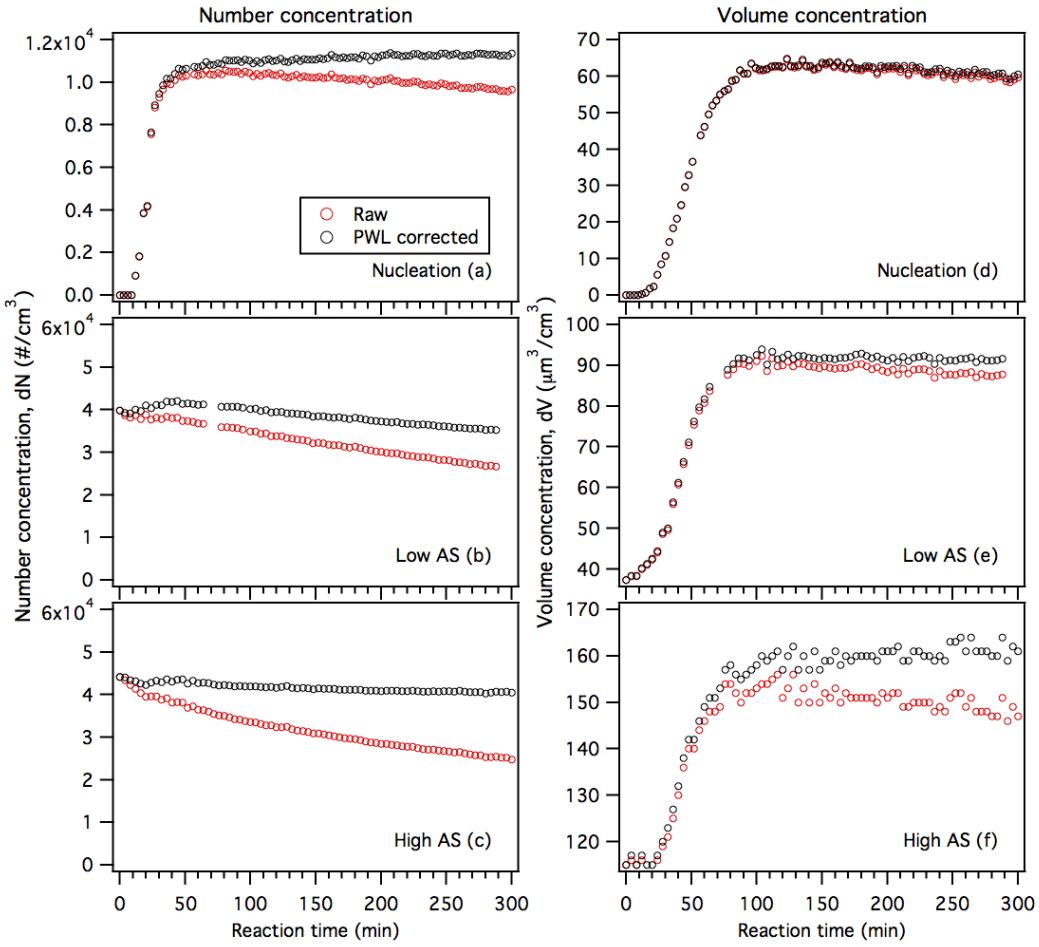

Figure B.2: Raw and particle wall loss (PWL) corrected number and volume concentration data for the 500 ppb O_3 experiments. Raw nucleation (panels a and d) and low AS (panels b and e) data are particle wall loss corrected using particle wall loss rates determined from the low AS-seed only experiments. Raw high AS (panels c and f) data are particle wall loss corrected using particle wall loss rates determined from the high AS-seed only experiments.

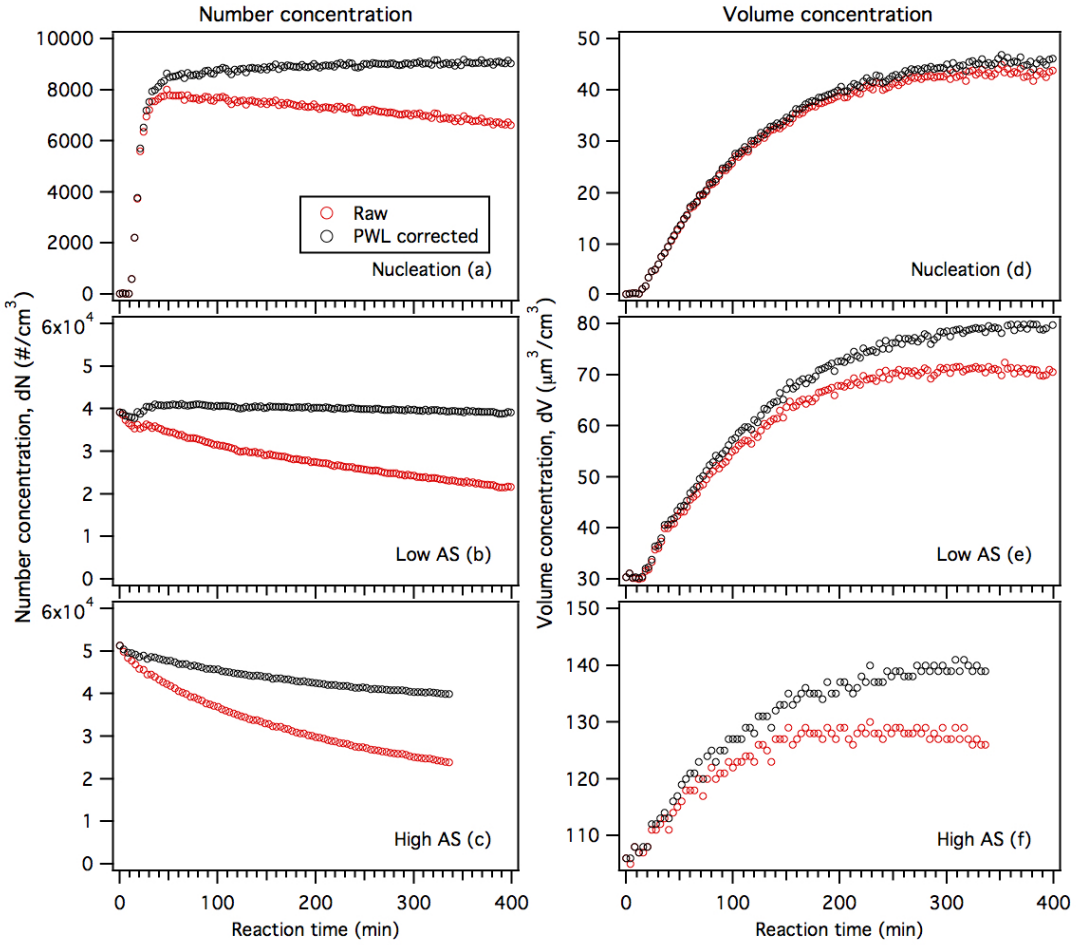

Figure B.3: Raw and particle wall loss (PWL) corrected number and volume concentration data for the 100 ppb O_3 experiments. All the raw data are particle wall loss corrected using the average particle wall loss rates (i.e. average of the particle wall loss rates obtained from low AS-seed only and high-AS seed only experiments).

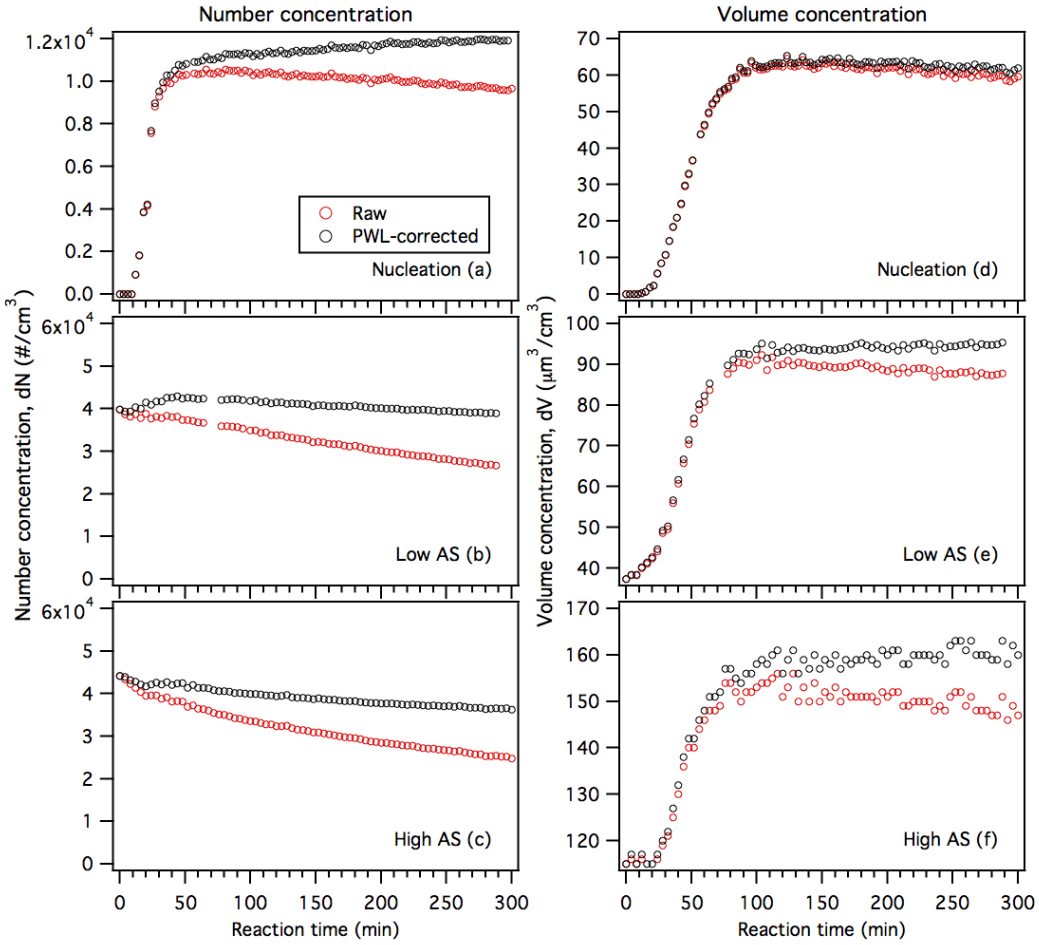

Figure B.4: Raw and particle wall loss (PWL) corrected number and volume concentration data for the 500 ppb O_3 experiments. All the raw data are particle wall loss corrected using the average particle wall loss rates (i.e. average of the particle wall loss rates obtained from low AS-seed only and high-AS seed only experiments).

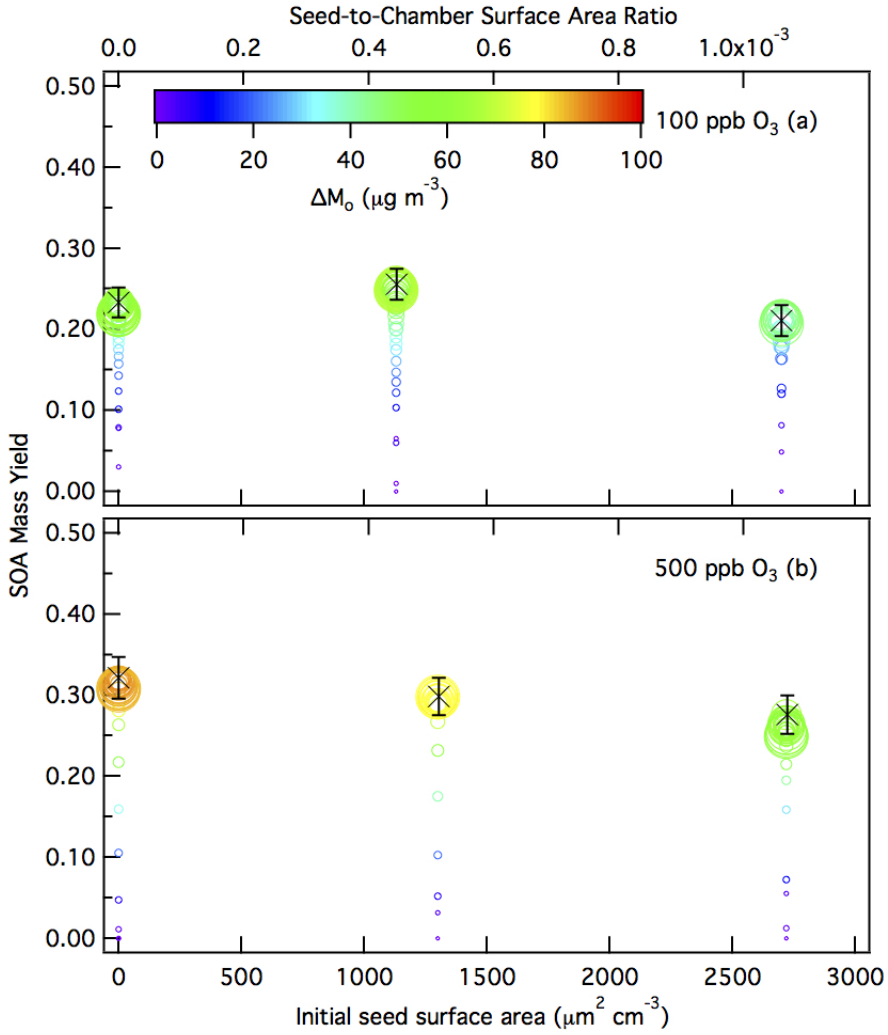

Figure B.5: 10 min-averaged SOA mass yields over the course of an α-pinene ozonolysis experiment as a function of initial total AS seed surface area concentration for the (a) 100 ppb O_3 experiments, and (b) 500 ppb O_3 experiments. Here, all the data have been particle wall loss corrected using the average particle wall loss rates (i.e. average of the particle wall loss rates obtained from low AS-seed only and high-AS seed only experiments). Symbol color indicates the SOA mass concentration and symbol size indicates the time after O_3 is injected into the chamber. The $\times$ symbols are the SOA mass yields at peak SOA growth. The y-axis error bars represent the uncertainty in the peak SOA mass yield, which originates from the α-pinene injection and the aerosol volume concentration measured by the SMPS at peak SOA growth (one standard deviation). As discussed in the main text, the use of average particle wall loss rates for particle wall loss correction does not change the conclusions of this work: 1) SOA mass yields are enhanced at higher O_3 concentrations, and 2) there is a lack of a SOA mass yield dependence on the seed surface area within the range of AS seed surface area concentration used in this study.

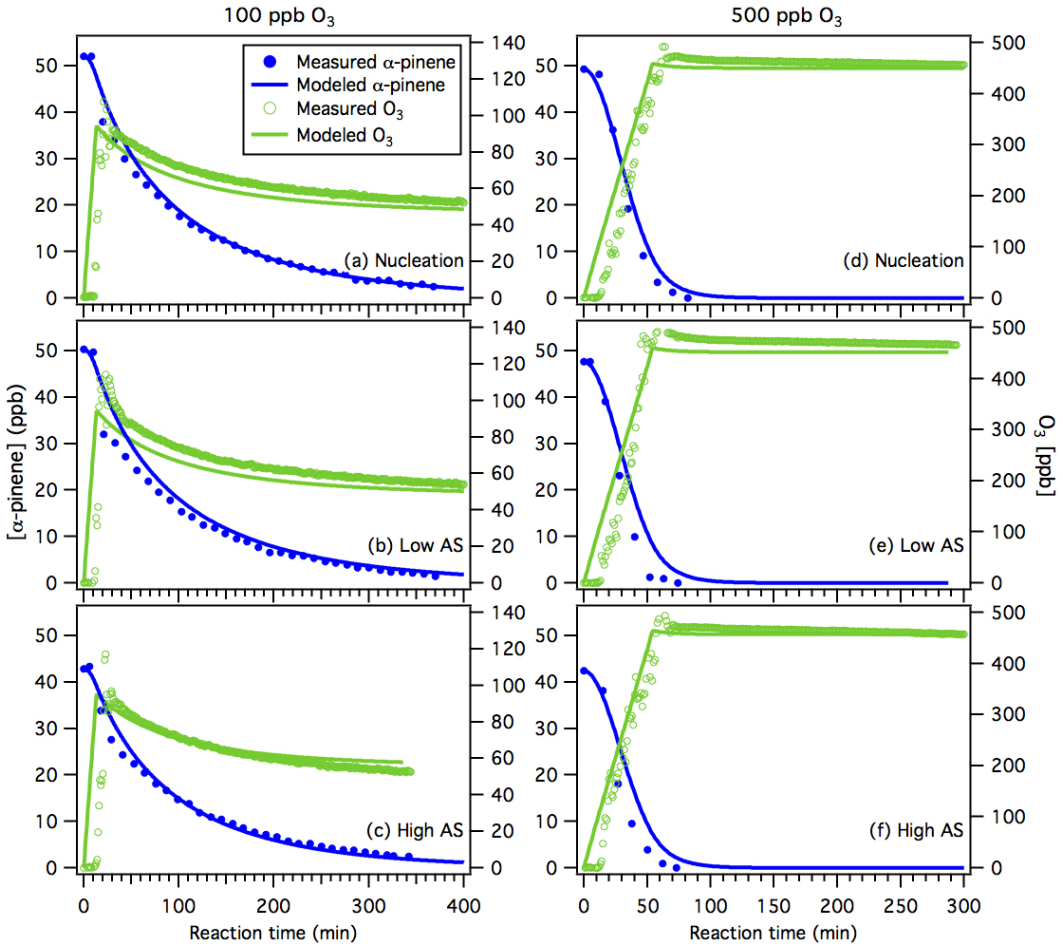

Figure B.6: Reaction profiles of the measured and modeled O_3 and α-pinene concentration in the α-pinene ozonolysis experiments. Panels (a), (b) and (c) show results from the nucleation, low AS and high AS 100 ppb O_3 experiments, respectively. Panels (d), (e) and (f) show results from the nucleation, low AS and high AS 500 ppb O_3 experiments, respectively. The blue lines that fit the α-pinene concentration measurements and the green lines that fit the O_3 concentration measurements are model simulation results that come from the coupled vapor-particle dynamics model using the optimal model values: $\alpha_p = 1$, $\alpha_w = 10^{-6}$, $\tau_{olig} = 4$ h, branching ratios = 0.57, 0.35, 0.04, 0.015 and 0.025 for oxidation products with vapor pressures $> 10^3$, 10^2, 10, 1 and 0.1 μg m^{-3}, respectively (described in the main text).

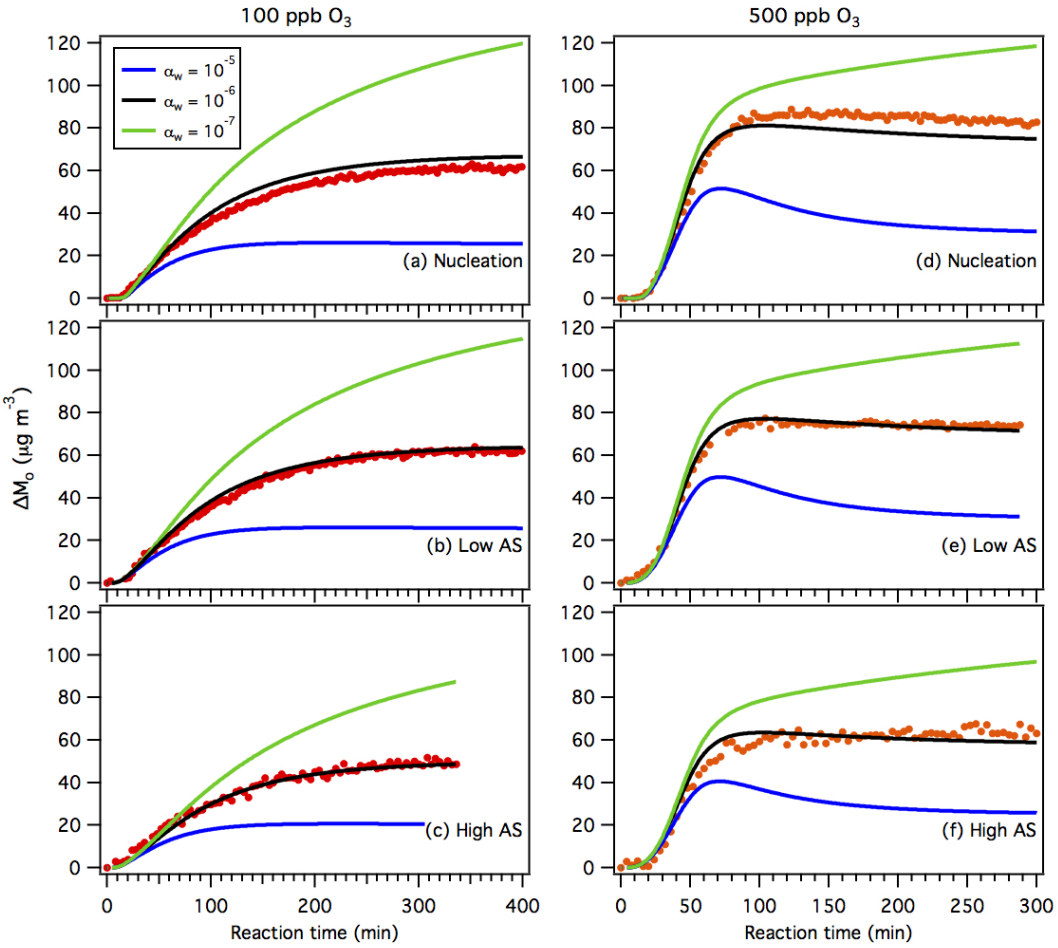

Figure B.7: Results of sensitivity tests performed for α_w.

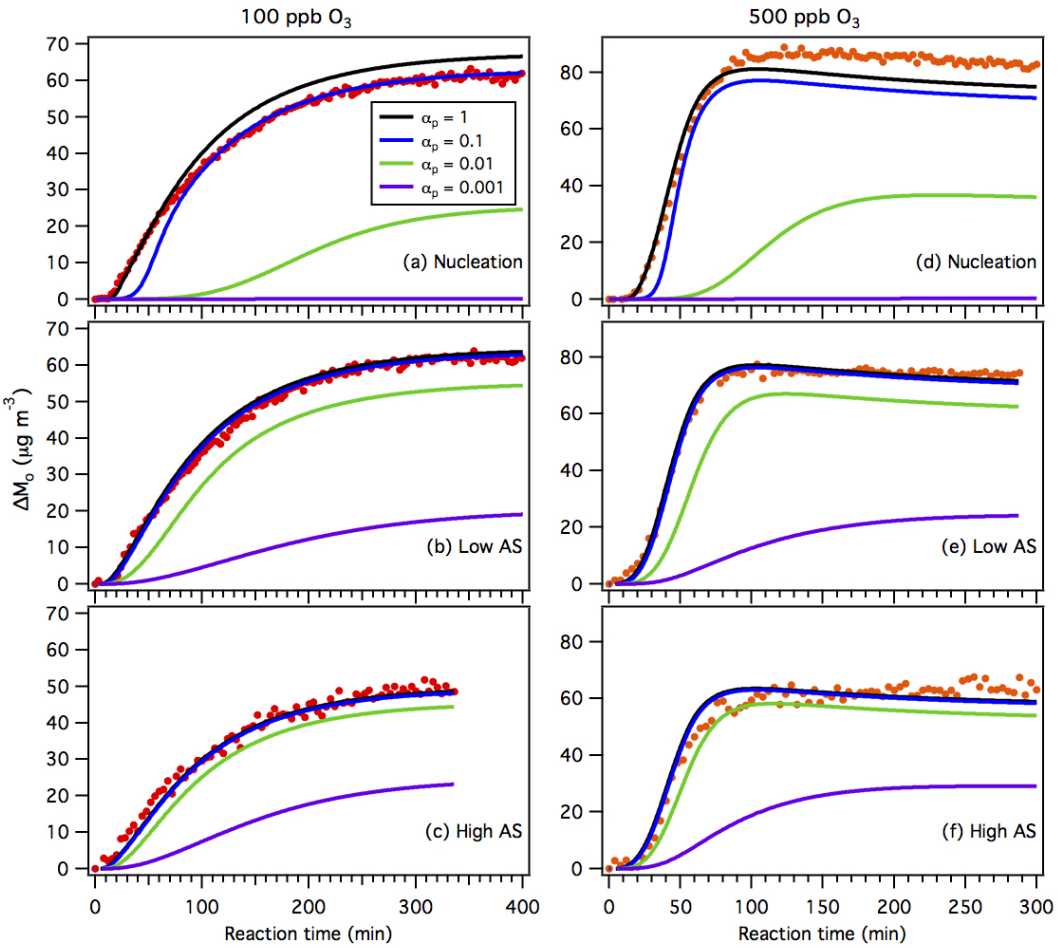

Figure B.8: Results of sensitivity tests performed for α_p. Note that for all experiments except the two nucleation experiments, $\alpha_p = 1$ and $\alpha_p = 0.1$ give identical results.

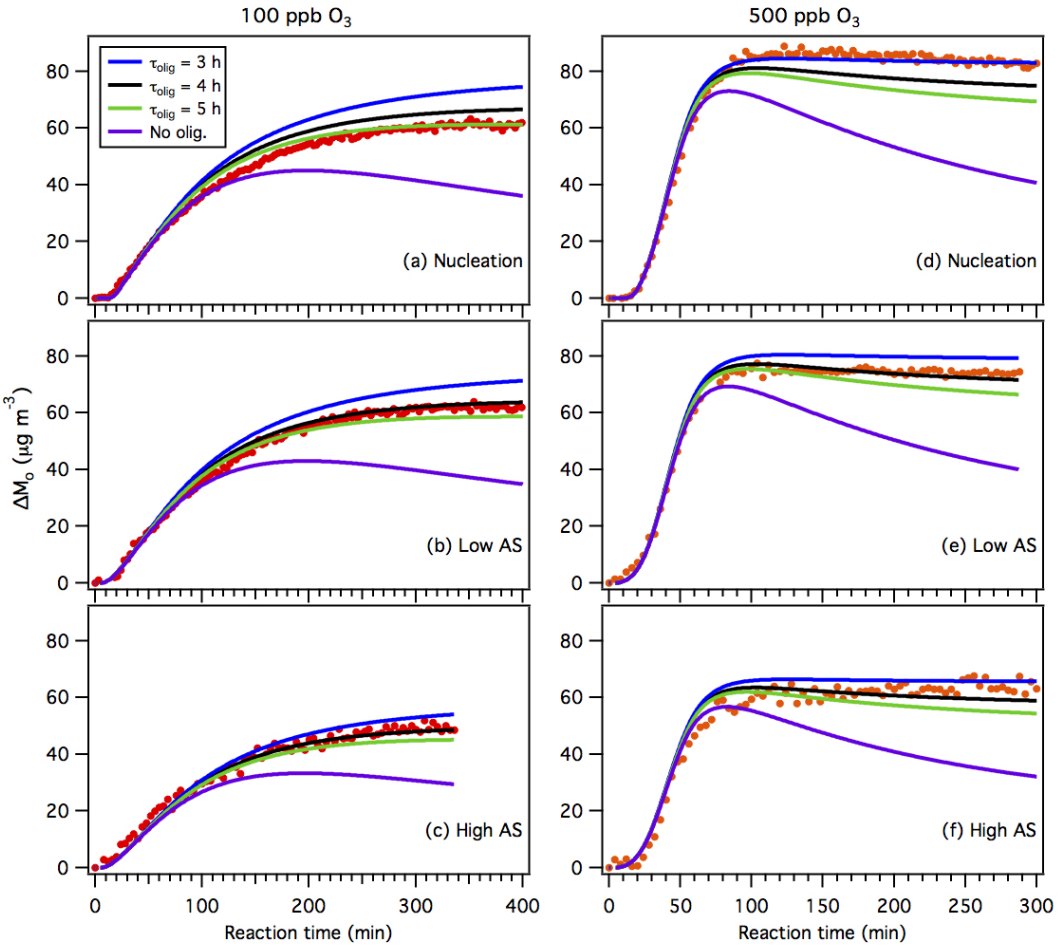

Figure B.9: Results of sensitivity tests performed for τ_{olig}.

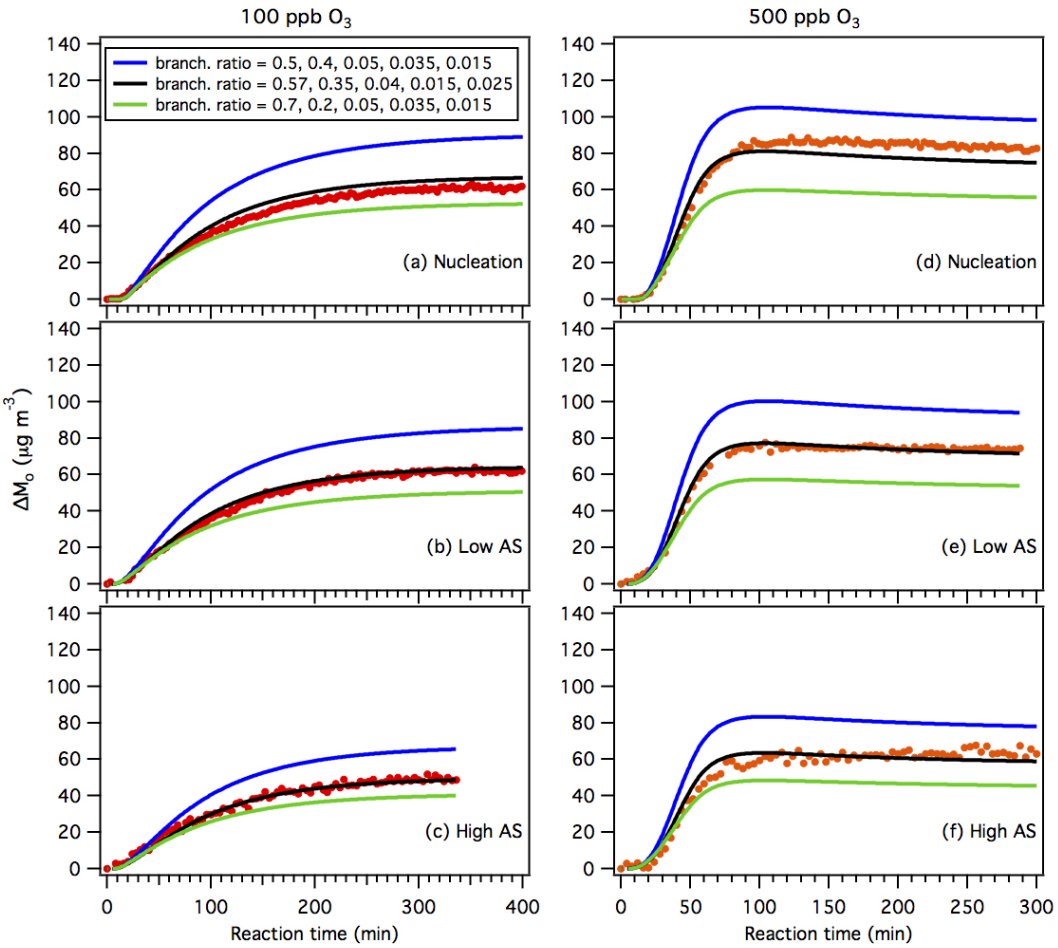

Figure B.10: Results of sensitivity tests performed for the branching ratios of oxidation products with vapor pressures $> 10^3$, 10^2, 10, 1 and 0.1 μg m^{-3}.

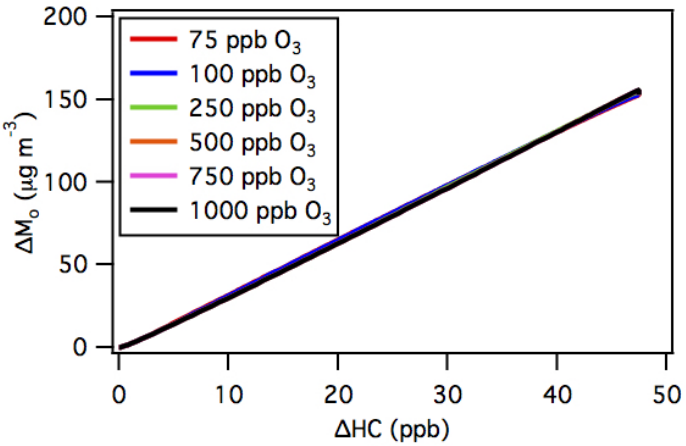

Figure B.11: Results from the coupled vapor-particle dynamics model showing how SOA mass concentration (ΔM_o) changes as a function of reacted α-pinene at different O_3 concentrations, assuming all the α-pinene oxidation products are non-volatile. In these model simulation runs, the initial α-pinene concentration is fixed at 48 ppb, while the O_3 concentration is varied from 75 to 1000 ppb. The O_3 injection rate used in these model simulation runs is 500/54.25 ppb min^{-1}.

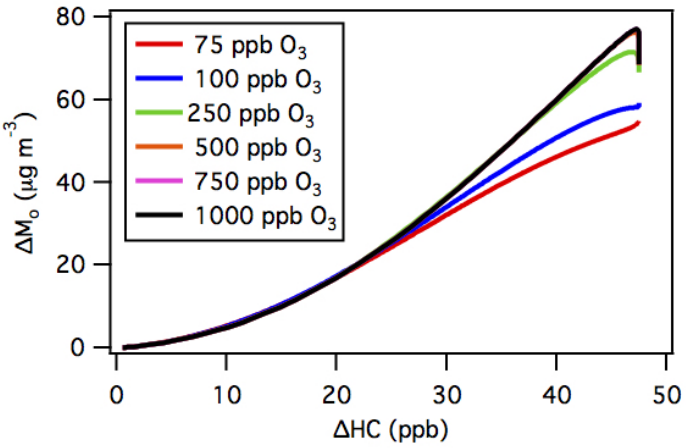

Figure B.12: Predictions from the coupled vapor-particle dynamics model showing time-dependent growth curves for SOA formation from α-pinene ozonolysis at different O_3 concentrations. In these model simulation runs, the initial α-pinene mixing ratio is fixed at 48 ppb, while the O_3 mixing ratio is increased from 75 to 1000 ppb. In the model, the O_3 injection rate is assumed to be fixed at 500/54.25 ppb min^{-1}, and the injection time is increased to achieve the desired O_3 concentration (i.e., 75, 100, 250, 500, 750 or 1000 ppb) in the chamber. The predicted ΔM_o decreased slightly at the end of the experiment at the higher O_3 concentrations (250, 500, 750 and 1000 ppb) due to SOA evaporation. It is important to note that SOA evaporation is predicted at high O_3 concentrations in the coupled vapor-particle dynamics model, but not observed in chamber experiments.

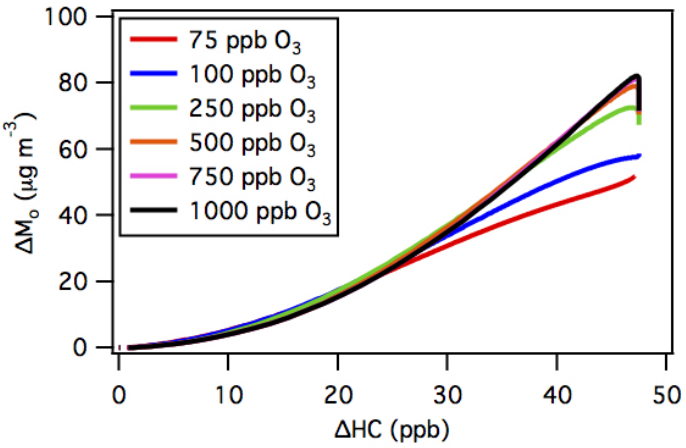

Figure B.13: Results from the coupled vapor-particle dynamics model showing how SOA mass concentration (ΔM_o) changes as a function of reacted α-pinene at different O_3 concentrations. In these model simulation runs, the initial α-pinene concentration is fixed at 48 ppb, while the O_3 concentration is varied from 75 to 1000 ppb. Here, the O_3 injection rate is five times faster that the base rate used in the model. The base rate is 500/54.25 ppb min^{-1}, similar to the rate used to analyze results from the 500 ppb O_3 experiments. As discussed in the main text, the oxidation rate effect persists at a higher O_3 concentration when a faster O_3 injection rate is used. It is important to note that SOA evaporation is predicted at high O_3 concentrations in the coupled vapor-particle dynamics model, but not observed in chamber experiments.

Table B.1: Initial and particle wall loss corrected final number concentrations[a]

Experiment	Initial Number Concentration	Final Number Concentration[b]	% Change[c]	Final Number Concentration[d]	% Change[c]
100 ppb O_3 nucleation	23	8222	3.5×10^4	9152	3.9×10^4
100 ppb O_3 low AS	39119	32553	-16.8	38689	-1.1
100 ppb O_3 high AS	51254	45280	-11.7	39889	-22.2
500 ppb O_3 nucleation	1	11303	1.6×10^6	11974	1.7×10^6
500 ppb O_3 low AS	39800	35216	-11.5	38905	-2.2
500 ppb O_3 high AS	44196	40191	-9.1	35189	-20.4

[a]Particle number concentrations (dN).

[b]The data shown here correspond to those shown in Figs. B.1 and B.2. The nucleation and low AS data have been particle wall loss corrected using particle wall loss rates determined from the low AS-seed only experiments. The high AS data have been particle wall loss corrected using particle wall loss rates determined from the high AS-seed only experiments.

[c]$\%\ \text{Change} = \frac{(\textit{Difference between initial and particle wall loss corrected final number concentration})}{\textit{Initial number concentration}} \times 100\%$

[d]The data shown here correspond to those shown in Figs. B.3 and B.4. All the data have been particle wall loss corrected using the average particle wall loss rates (i.e. average of the particle wall loss rates obtained from low AS-seed only and high-AS seed only experiments).

Table B.2: Comparison of experimental conditions used in this work with those of previous dark α-pinene ozonolysis studies. The SOA mass yields and concentrations of these studies are shown Fig. B.6.

Study	Temperature (K)	RH (%)	Seed	OH Scavenger	O_3 (ppb)	ΔHC (ppb)
Cocker et al. (2001)[a]	301.2-302.9	<2, 39-49.2	None, $(NH_4)_2SO_4$ and NH_4HSO_4	2-butanol	130-600	22.6-212.3
Gao et al. (2004)[b]	293	55	$MgSO_4$	cyclohexane	24-270	12-135
Griffin et al. (1999)	303.3-309.9	5	$(NH_4)_2SO_4$	2-butanol	67-260	16.7-65
Hoffmann et al. (1997)	289.3-322.1	N.A.	$(NH_4)_2SO_4$	None	210-327	38-154.1
Pathak et al. (2007b)	288-313	<10	None, $(NH_4)_2SO_4$	2-butanol	750-3100	3.7-8.5
Presto et al. (2005)[c]	295	<10	None	2-butanol	160-605	15-210
Presto et al. (2006)[d]	295	<10	None	2-butanol	260-350	13.4-135
Shilling et al. (2008)[e]	298	40	$(NH_4)_2SO_4$	1- and 2-butanol	50, 300, 535	0.3-22.8
Song et al. (2007)[f]	300.6-301.7	<2	None	cyclohexane	46-369	5.9-81.1
This study	298	<5	$(NH_4)_2SO_4$	cyclohexane	100, 500	42.4-52.1

[a]Data collected using aqueous seed aerosol is excluded from our analysis.

[b]Data collected using acidic seed aerosol is excluded from our analysis.

[c]Only dark experiments in which [α-pinene]/[NO_x] > 15 are used in our analysis.

[d]Only dark α-pinene ozonolysis experiments are used in our analysis.

[e]Data collected in batch mode and continuous-flow mode are used in our analysis.

[f]Data collected using organic seed aerosol is excluded from our analysis.

Appendix C

Supplemental Material for Chapter 4

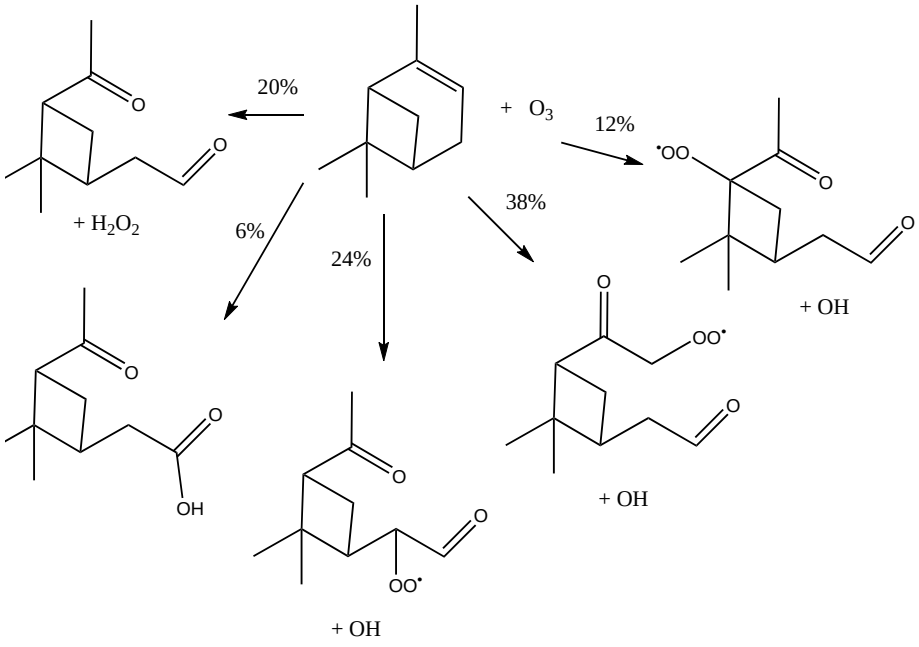

Figure C.1: Overview of the α-pinene + O_3 initial reaction step in GECKO-A. All subsequent chemistry is generated according to the standard protocols in GECKO-A.

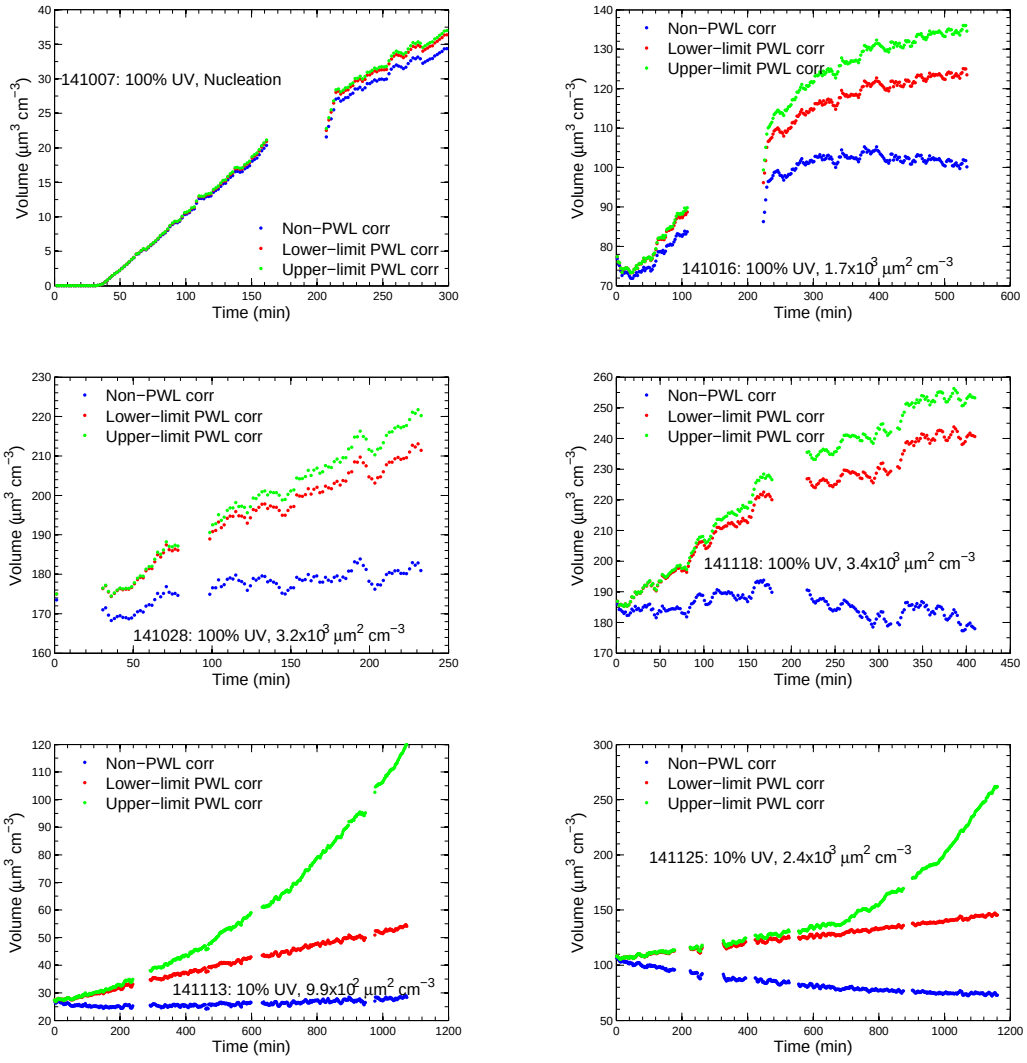

Figure C.2: Caption on next page.

Figure C.2: Total particle volume as a function of time, non-particle wall loss corrected (blue data points) and using two different corrections for particle wall loss. Red data points have been corrected with the lower bound assumption, in which deposited particles are assumed to not interact with vapor, and the mass of SOA present on a particle at the moment of its deposition is added to the total SOA. Green data points have been corrected with the upper bound assumption, in which deposited particles continue to grow via condensation at the same rate as suspended particles. The dramatic increase in the upper bound towards the end of the low UV experiments is likely an artifact of how the upper bound is calculated. The Aerosol Parameter Model (*Pierce et al.*, 2008) is used to constrain the rate of condensation to particles by fitting the DMA size distribution at each time step, and this condensation rate is then applied to deposited particles. At the end of the low UV experiments, only 11% of the initial total number of particles remain suspended, as opposed to 30-40% for the high UV experiments. SOA growth in the α-pinene system is not seed surface area dependent (discussed in the Results section), and condensation to suspended particles will not decrease due to the decreased number. Therefore, at the end of the low UV experiments, the condensation rate per suspended particle is very large. With the upper bound correction, the deposited particles then grow with the same high condensation rate, despite the fact that transport to deposited particles will be slower than transport to suspended particles. The upper bound is likely a substantial overestimation for these experiments.

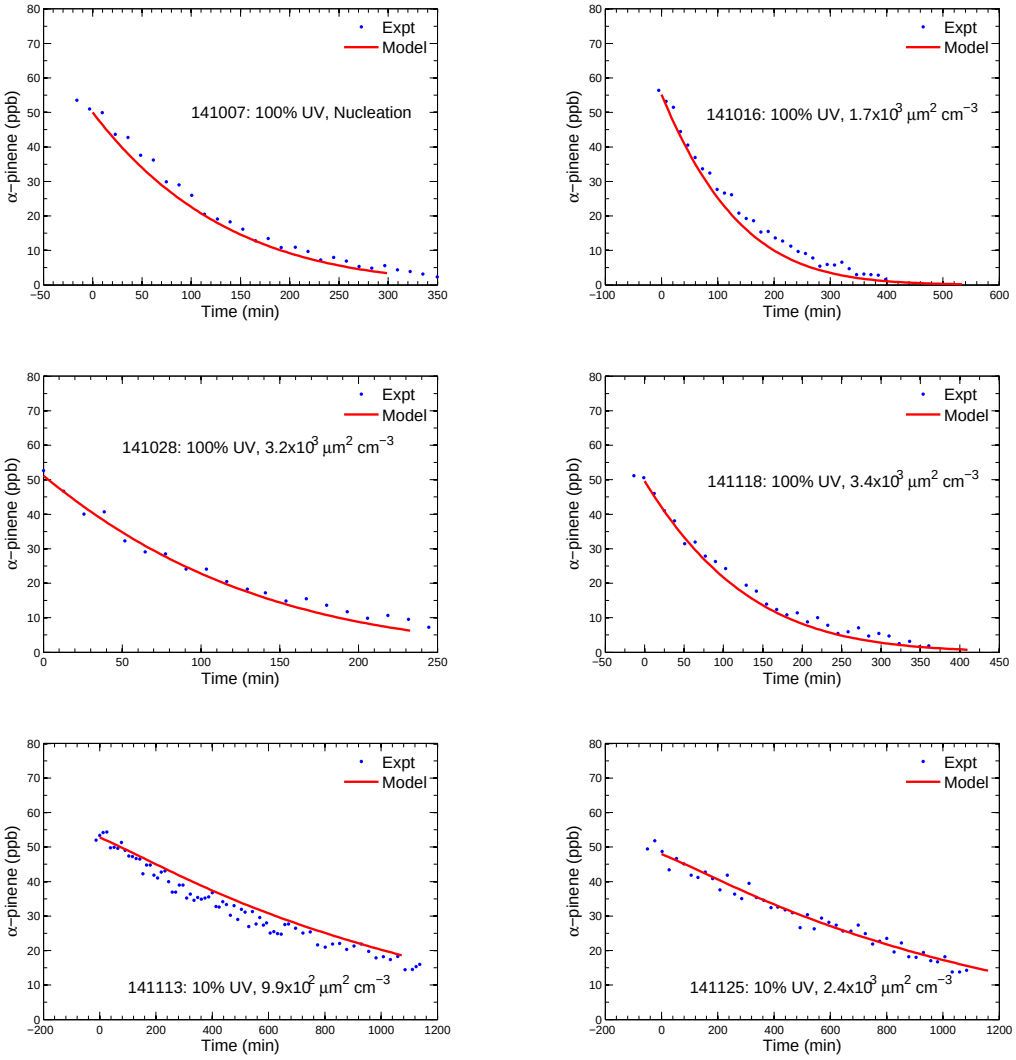

Figure C.3: Decay of α-pinene as a function of time for the six different photooxidation experiments. Experimental datapoints are shown with blue data points, and GECKO-A predictions are shown with solid red lines.

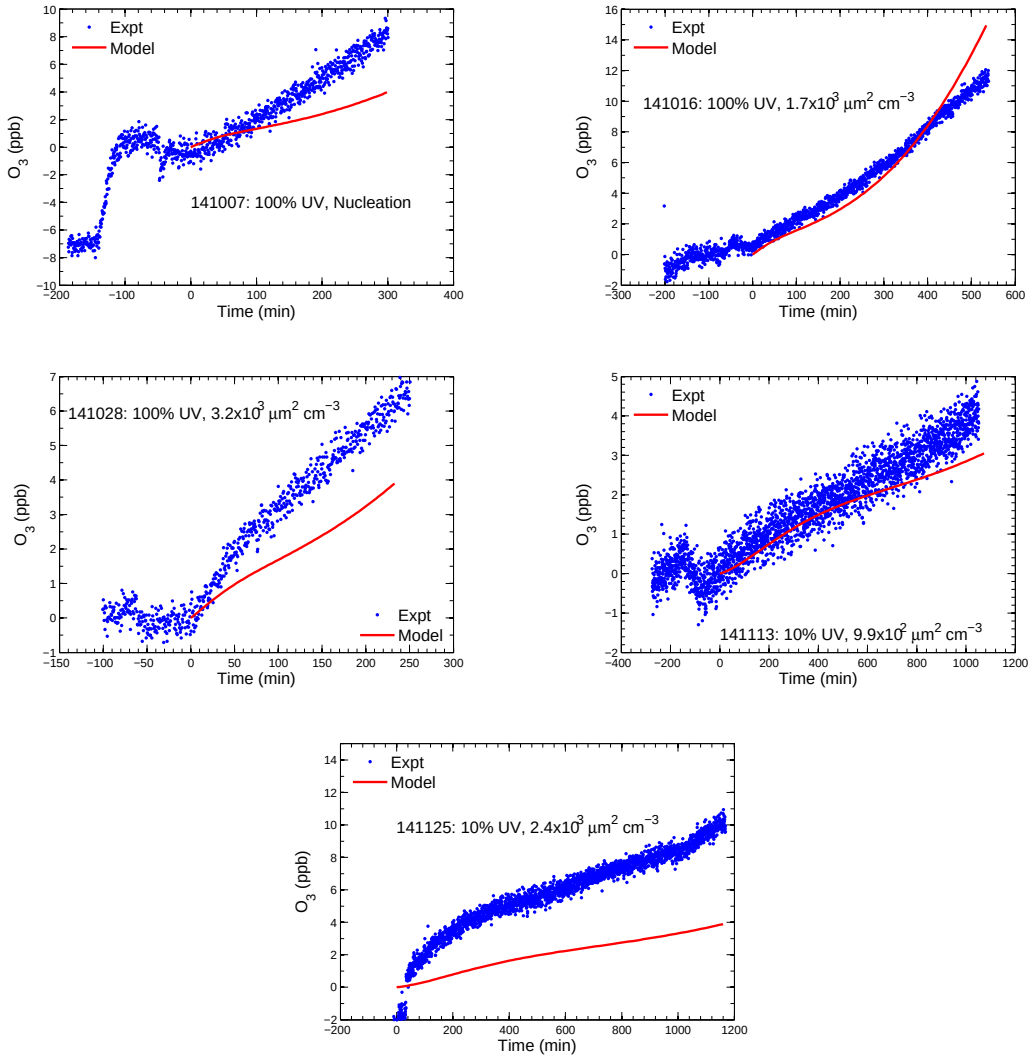

Figure C.4: O_3 formation as a function of time for five of the six experiments. The O_3 analyzer malfunctioned during one of the experiments (not shown). Because α-pinene was not observed to decay before lights were turned on, the initial O_3 concentration was assumed to be zero. Therefore, the experimental O_3 measurements have been normalized to the measured value at time zero (lights on). A NO_x wall off-gassing rate of 2.5 ppt min^{-1} was optimized to match the observed O_3 formation. Although predicted O_3 concentrations do not correspond exactly to O_3 observations, SOA was not affected by changing the NO_x wall off-gassing rate.

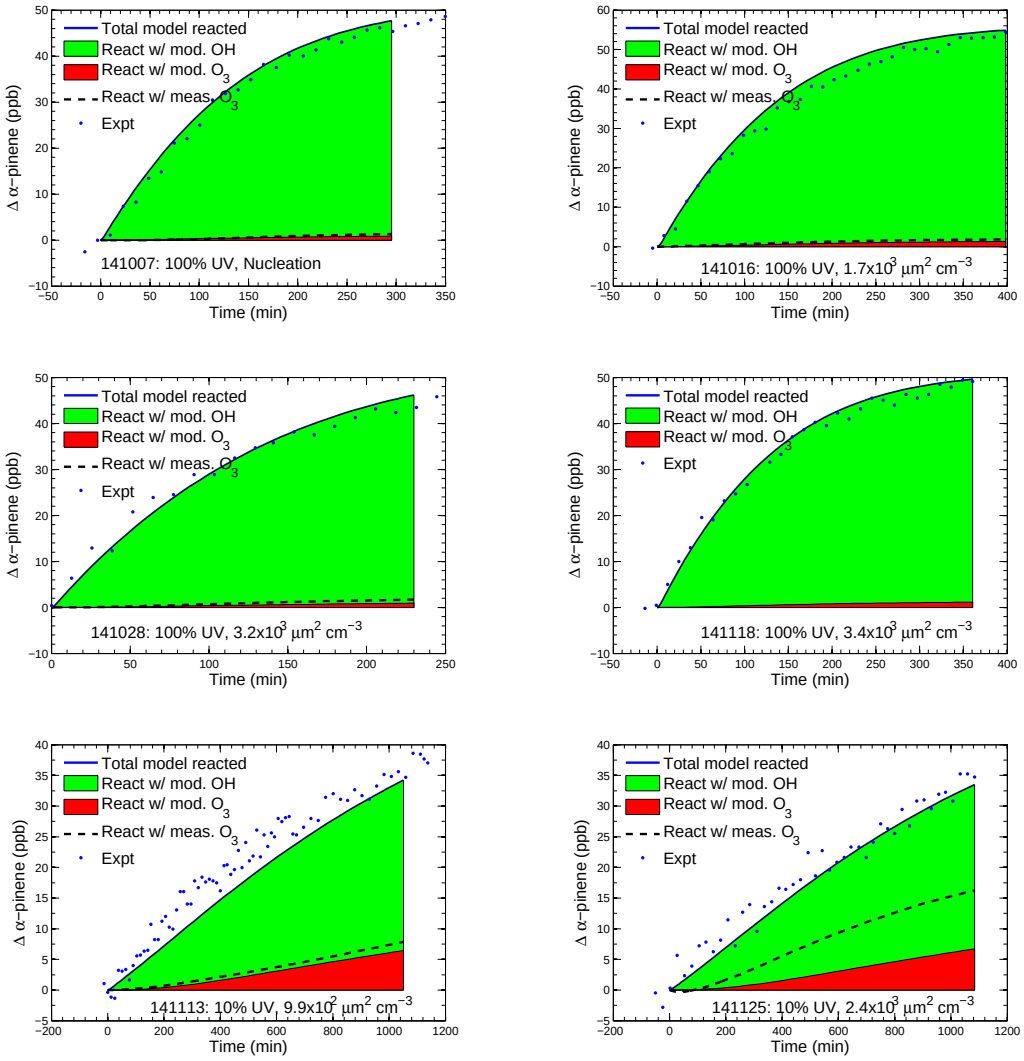

Figure C.5: Amount of α-pinene predicted to be reacted with OH versus O_3, for both modeled and measured O_3 concentrations. The solid blue line shows the total α-pinene reacted. The green area shows the amount reacted with OH based on the modeled OH concentration. The red area shows the amount reacted with O_3 based on the modeled O_3 concentration. The dashed black line shows the amount predicted to have reacted with the measured O_3 concentration. Because the O_3 monitor malfunctioned during experiment 141118, the dashed line is not shown for this experiment.

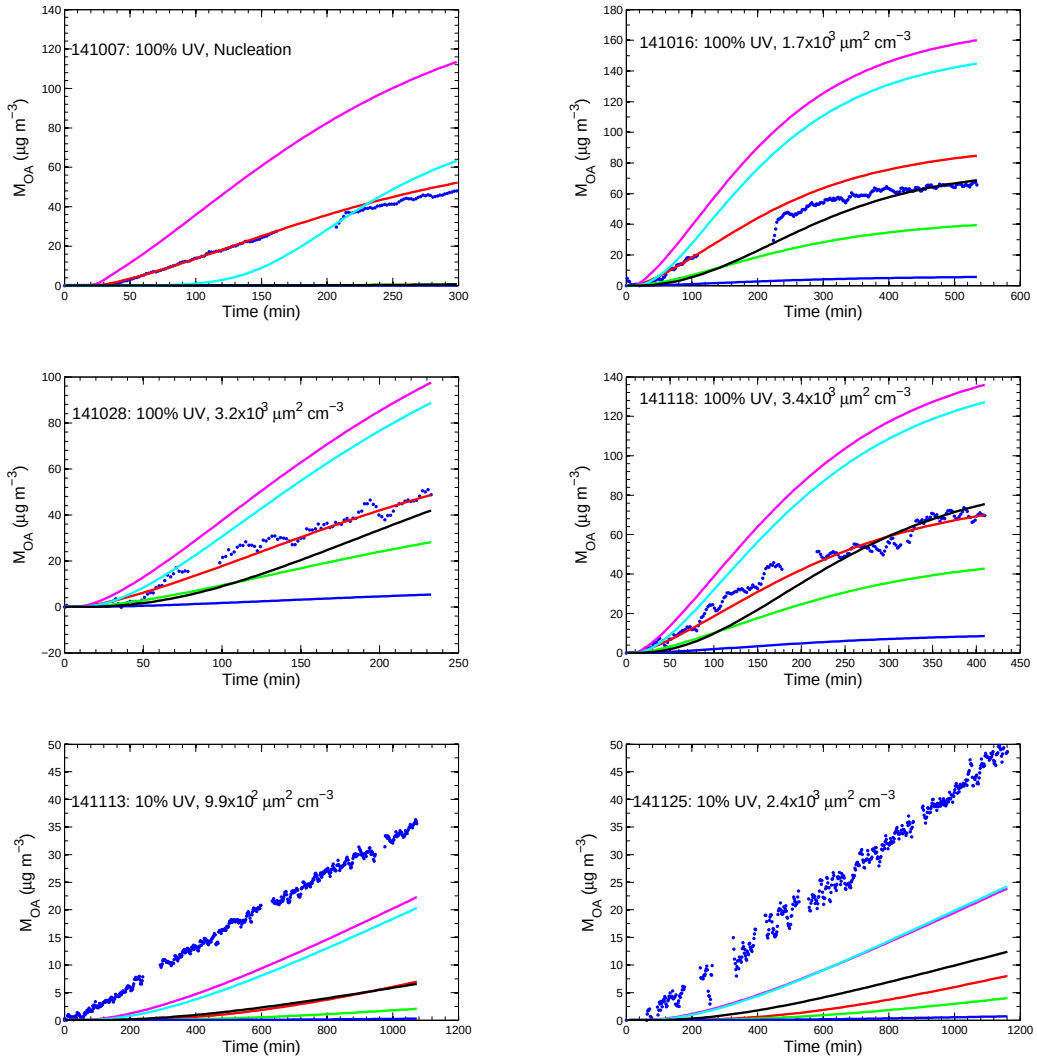

Figure C.6: Mass of organic aerosol as a function of time. Experimental measurements are shown with blue data points. GECKO-A predictions are shown for different combinations of the vapor-particle accommodation coefficient α_p and the vapor-wall loss rate k_{gw}: Red line: α_p=1 and k_{gw} = 10^{-3} s^{-1}; green line: α_p=0.01 and k_{gw} = 10^{-3} s^{-1}; blue line: α_p=0.001 and k_{gw} = 10^{-3} s^{-1}; pink line: α_p=1 and k_{gw} = 10^{-4} s^{-1}; cyan line: α_p=0.01 and k_{gw} = 10^{-4} s^{-1}; black line: α_p=0.001 and k_{gw} = 10^{-4} s^{-1}. α_p=0.1 is not shown; this value gives almost identical predictions to α_p=1 with the exception of the nucleation experiment, in which significantly less SOA is predicted. For the 100% UV experiments, decreasing α_p delays the onset of SOA formation which is not consistent with the observations. Lowering the wall loss rate to 10^{-4} s^{-1} for the 100% UV experiments results in significant overprediction of SOA for all α_p except α_p = 0.001. Although this combination yields an ending SOA similar to that of the experiment, the shape of the curve does not agree with experimental observations. Based on these sensitivity tests, α_p = 1 and k_{gw} = 10^{-3} s^{-1} were determined to provide the best fit for the 100% UV experiments. All of the combinations shown result in significant underprediction for the 10% UV experiments.

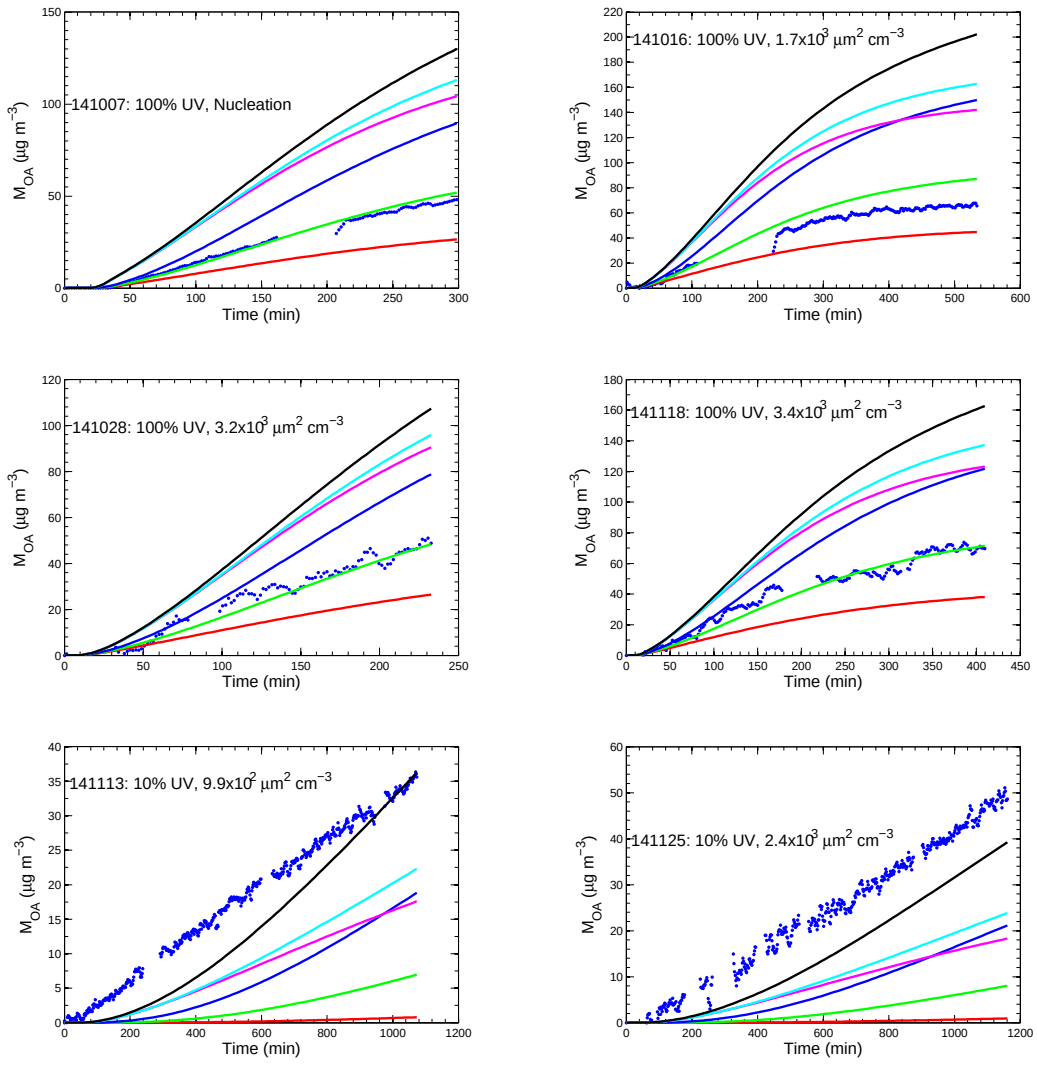

Figure C.7: Mass of organic aerosol as a function of time. Experimental measurements are shown with blue data points. GECKO-A predictions are shown for different combinations of $C_w/(M_w\gamma_w)$ and the vapor-wall loss rate k_{gw}: Red line: $C_w/(M_w\gamma_w)$x10 and $k_{gw} = 10^{-3}$ s^{-1}; green line: base $C_w/(M_w\gamma_w)$ and $k_{gw} = 10^{-3}$ s^{-1}; blue line: $C_w/(M_w\gamma_w)$x0.1 and $k_{gw} = 10^{-3}$ s^{-1}; magenta line: $C_w/(M_w\gamma_w)$x10 and $k_{gw} = 10^{-4}$ s^{-1}; cyan line: base $C_w/(M_w\gamma_w)$ and $k_{gw} = 10^{-4}$ s^{-1}; and black line: $C_w/(M_w\gamma_w)$x0.1 and $k_{gw} = 10^{-4}$ s^{-1}.

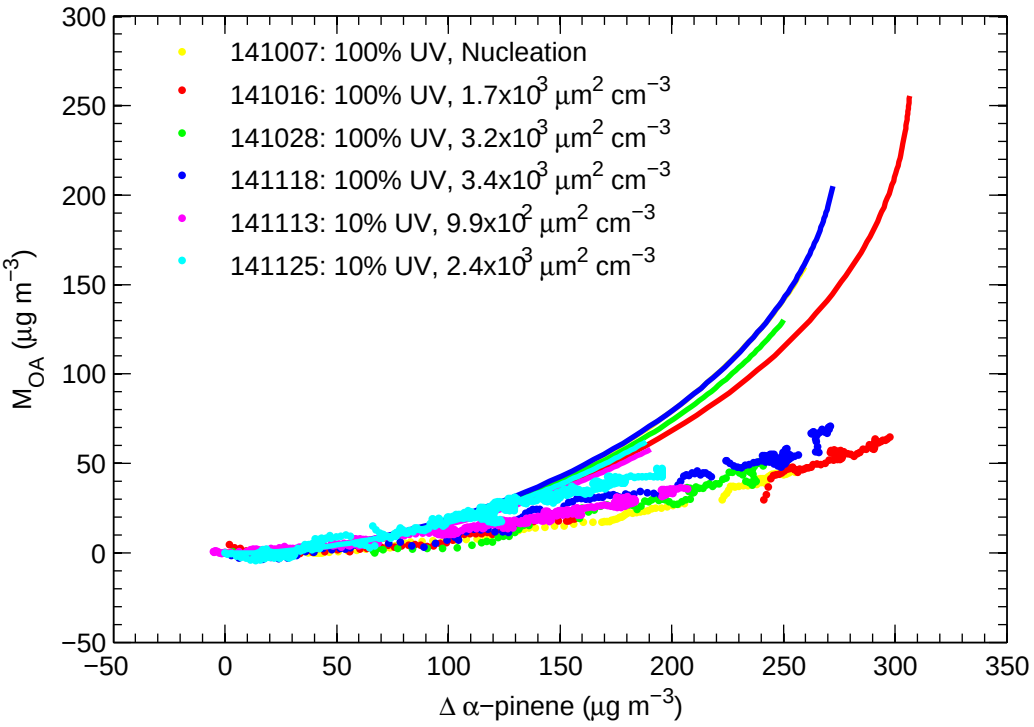

Figure C.8: Mass of SOA as a function of reacted α-pinene. Experimental data are shown with filled data points. Solid lines correspond to GECKO-A predictions in the absence of vapor wall loss.

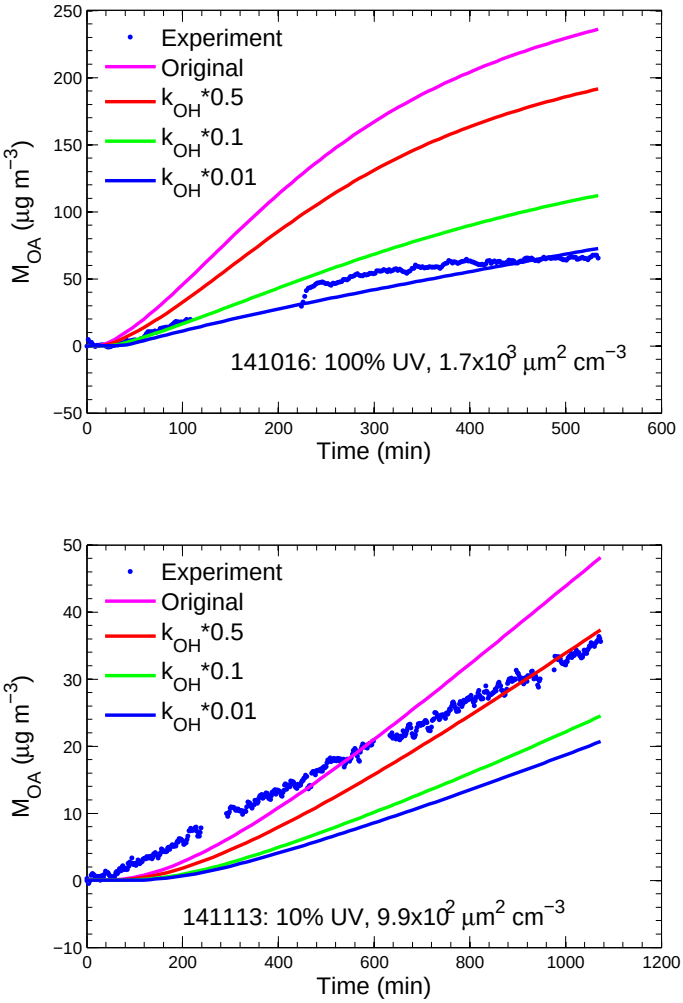

Figure C.9: Mass of SOA as a function of time for one high UV and one low UV experiment. Solid lines show GECKO-A predictions with $k_{gw} = 10^{-5}$ s^{-1} and the second and later-generation OH reaction rate constants reduced by varying factors: pink line: no reduction in OH reaction rate constants; red line: OH reaction rate constants reduced to 50% of default values; green line: OH reaction rate constants reduced to 10% of default values; blue line: OH reaction rate constants reduced to 1% of default values.

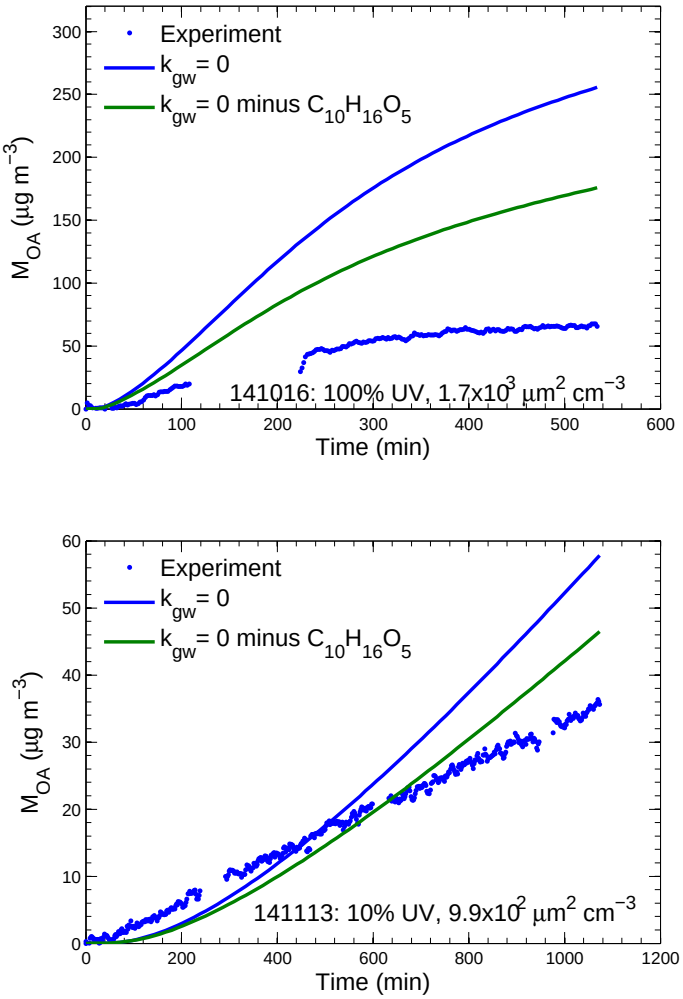

Figure C.10: Mass of SOA as a function of time for one high UV experiment and one low UV experiment. GECKO-A predictions simulated with no vapor wall loss are shown by the solid blue line. The green line shows the result of subtracting the α-pinene hydroxy dihydroperoxide, $C_{10}H_{16}O_5$, from the predictions shown with the blue line.

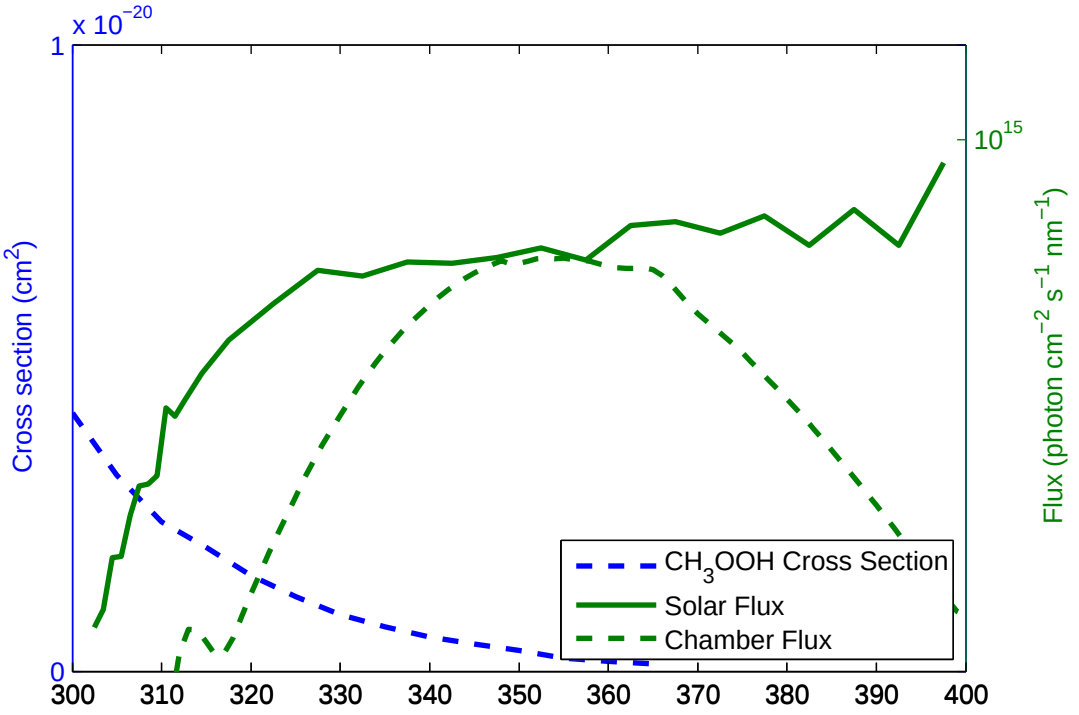

Figure C.11: Absorption cross-section of methyl hydroperoxide as a function of wavelength (*Sander et al.*, 2011) compared to photon fluxes of both the sun (*Seinfeld and Pandis*, 2006) and the Caltech chamber.

Bibliography

Pierce, J. R., Engelhart, G. J., Hildebrandt, L., Weitkamp, E. A., Pathak, R. K., Donahue, N. M., Robinson, A. L., Adams, P. J., and Pandis, S. N.: Constraining particle evolution from wall losses, coagulation, and condensation-evaporation in smog-chamber experiments: optimal estimation based on size distribution measurements, *Aer. Sci. Technol.*, 42, 1001–1015, 2008.

Sander, S. P.; Abbatt, J.; Barker, J.R.; Burkholder, J.B.; Friedl, R. R.; Golden, D. M.; Huie, R. E.; Kolb, C. E.; Kurylo, M. J.; Moortgat, G. K.; Orkin, V. L.; Wine, P. H. Chemical Kinetics and Photochemical Data for Use in Atmospheric Studies, Evaluation No. 17. *JPL Publication 10-6*, Jet Propulsion Laboratory, Pasadena, http://jpldataeval.jpl.nasa.gov, 2011.

Seinfeld, J. H., Pandis, S. N. *Atmospheric chemistry and physics: from air pollution to climate change*, 2nd ed. Wiley: Hoboken, N.J., 2006.

Appendix D

Influence of vapor wall loss in laboratory chambers on yields of secondary organic aerosol *

*Reproduced with permission from "Influence of vapor wall loss in laboratory chambers on yields of secondary organic aerosol" by Zhang, X., Cappa, C. D., Jathar, S. H., McVay, R. C., Ensberg, J. J., Kleeman, M. J., and Seinfeld, J. H., *Proceedings of the National Academy of Sciences*, 111, 5802–5807, doi:10.1073/pnas.1404727111, 2014.

Influence of vapor wall loss in laboratory chambers on yields of secondary organic aerosol

Xuan Zhang[a,1], Christopher D. Cappa[b,1,2], Shantanu H. Jathar[b], Renee C. McVay[c], Joseph J. Ensberg[c], Michael J. Kleeman[b], and John H. Seinfeld[a,c,2]

[a]Division of Engineering and Applied Science, California Institute of Technology, Pasadena, CA 91125; [b]Department of Civil and Environmental Engineering, University of California, Davis, CA 95616; and [c]Division of Chemistry and Chemical Engineering, California Institute of Technology, Pasadena, CA 91125

Contributed by John H. Seinfeld, March 12, 2014 (sent for review January 6, 2014)

Secondary organic aerosol (SOA) constitutes a major fraction of submicrometer atmospheric particulate matter. Quantitative simulation of SOA within air-quality and climate models—and its resulting impacts—depends on the translation of SOA formation observed in laboratory chambers into robust parameterizations. Worldwide data have been accumulating indicating that model predictions of SOA are substantially lower than ambient observations. Although possible explanations for this mismatch have been advanced, none has addressed the laboratory chamber data themselves. Losses of particles to the walls of chambers are routinely accounted for, but there has been little evaluation of the effects on SOA formation of losses of semivolatile vapors to chamber walls. Here, we experimentally demonstrate that such vapor losses can lead to substantially underestimated SOA formation, by factors as much as 4. Accounting for such losses has the clear potential to bring model predictions and observations of organic aerosol levels into much closer agreement.

Most of the understanding concerning the formation of secondary organic aerosol (SOA) from atmospheric oxidation of volatile organic compounds (VOCs) over the past 30 y has been developed from data obtained in laboratory chambers (1). SOA is a major component of particulate matter smaller than 1 μm (2) and consequently has important impacts on regional and global climate and human health and welfare. Accurate simulation of SOA formation and abundance within 3D models is critical to quantifying its atmospheric impacts. Measurements of SOA formation in laboratory chambers provide the basis for the parameterizations of SOA formation (3) in regional air-quality models and global climate models (4). A number of studies indicate that ambient SOA concentrations are underpredicted within models, often substantially so, when these traditional parameterizations are used (e.g., 5, 6). Some of this bias has been attributed to missing SOA precursors in emissions inventories, such as so-called intermediate volatility organic compounds, to ambient photochemical aging of semivolatile compounds occurring beyond that in chamber experiments (7) or to aerosol water/cloud processing (8). The addition of a more complete spectrum of SOA precursors into models has not, however, closed the measurement/prediction gap robustly. For example, recent analysis of organic aerosol (OA) concentrations in Los Angeles revealed that observed OA levels, which are dominated by SOA, exceed substantially those predicted by current atmospheric models (9), in accord with earlier findings in Mexico City (10).

Here, we demonstrate that losses of SOA-forming vapors to chamber walls during photooxidation experiments can lead to substantial and systematic underestimation of SOA. Recent experiments have demonstrated that losses of organic vapors to the typically Teflon walls of a laboratory chamber can be substantial (11), but the effects on SOA formation have not yet been quantitatively established. In essence, the walls serve as a large reservoir of equivalent OA mass that compete with the particulate SOA for SOA-forming compounds.

Toluene Photooxidation Experiments

The effect of vapor wall loss on SOA formation has been comprehensively assessed based on results from a series of 18-h toluene photooxidation experiments conducted in the California Institute of Technology (Caltech) environmental chamber under both high- and low-NO_x conditions (*SI Appendix, Toluene Photooxidation Experiments* and Table S1). Toluene is a component of motor vehicle emissions and an important SOA precursor (1). Initial [VOC]/[NO_x] ratios were 5.4 ± 0.3 ppbC/ppb, similar to current conditions in Los Angeles. In these experiments, the ratio of initial seed particle surface area (*SA*) to chamber wall *SA* was systematically varied by changing the concentration and diameter of $(NH_4)_2SO_4$ seed aerosol and keeping all other conditions the same [i.e., hydroxyl radical (OH) and toluene concentration]. In this manner, the influence of seed *SA* on SOA formation can be isolated.

Fig. 1 shows the observed time-dependent SOA yields, defined as the mass of SOA formed per mass of VOC reacted, determined from the evolution of the particle size distributions (*SI Appendix*, Fig. S1) as a function of initial seed *SA* for the high- and low-NO_x experiments. The SOA concentrations have been corrected for physical deposition of particles to the walls (*SI Appendix, Particle Wall Loss Correction*), which is the appropriate correction to use here as our analysis explicitly accounts for loss of vapors to the walls, discussed further below. Except for the unseeded experiment, the SOA yield for each low-NO_x

Significance

Atmospheric secondary organic aerosol (SOA) has important impacts on climate and air quality, yet models continue to have difficulty in accurately simulating SOA concentrations. Nearly all SOA models are tied to observations of SOA formation in laboratory chamber experiments. Here, a comprehensive analysis of new experimental results demonstrates that the formation of SOA in laboratory chambers may be substantially suppressed due to losses of SOA-forming vapors to chamber walls, which leads to underestimates of SOA in air-quality and climate models, especially in urban areas where anthropogenic SOA precursors dominate. This analysis provides a time-dependent framework for the interpretation of laboratory chamber experiments that will allow for development of parameterized models of SOA formation that are appropriate for use in atmospheric models.

Author contributions: X.Z., C.D.C., J.J.E., and J.H.S. designed research; X.Z. performed research; C.D.C., S.H.J., R.C.M., and M.J.K. analyzed data; and C.D.C. and J.H.S. wrote the paper.

The authors declare no conflict of interest.

Freely available online through the PNAS open access option.

[1]X.Z. and C.D.C. contributed equally to this work.

[2]To whom correspondence may be addressed. E-mail: cdcappa@ucdavis.edu or seinfeld@caltech.edu.

This article contains supporting information online at www.pnas.org/lookup/suppl/doi:10.1073/pnas.1404727111/-/DCSupplemental.

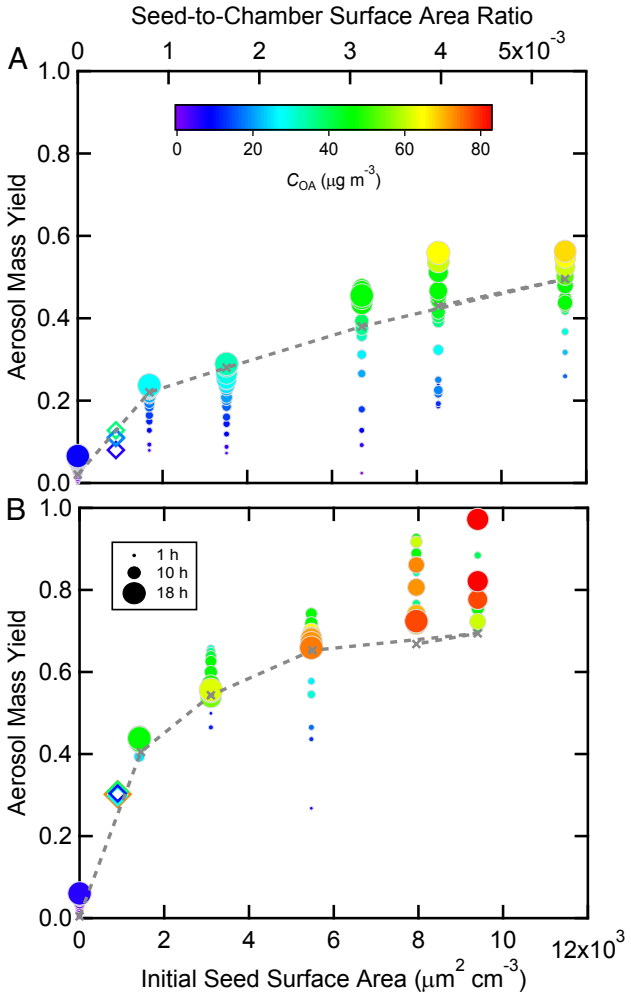

Fig. 1. Hourly averaged lower bound SOA yields over the course of a toluene photooxidation experiment as a function of initial ammonium sulfate seed surface area for (*A*) high-NO_x and (*B*) low-NO_x conditions. Symbol color indicates the SOA mass concentration and symbol size the time after lights were turned on. The filled circles are from the current experiments and the open diamonds from ref. 21. The dashed gray line and × are the end-of-experiment yields from the optimized best-fit SOM simulations.

experiment is reasonably constant with time (from 4 to 18 h) and C_{OA} at any given *SA*. For each high-NO_x experiment there is a clear increase in the yield with C_{OA} and time. The toluene SOA yield at a given C_{OA} is generally lower for high-NO_x than for low-NO_x conditions at a comparable initial seed *SA*. These differences in the time-dependent yields indicate differences in the chemical pathways leading to SOA formation between low- and high-NO_x conditions. Most importantly, the absolute amount of SOA formed for the same initial conditions increases with seed *SA*, consistent with refs. 12 and 13, with an indication of a plateau being reached at the highest seed *SA*. The SOA formed in the unseeded experiments is particularly small. Typical laboratory chamber experiments use initial seed $SA < 10^3$ μm^2 cm^{-3}, which corresponds to seed-to-wall ratios of $<1 \times 10^{-3}$ in most chambers. These experiments definitively demonstrate that SOA yields vary with seed *SA*. This variability may partially explain some of the differences in SOA yields reported in the literature.

SOA Modeling and the Influence of Vapor Wall Loss

The increase in yield with seed *SA* is consistent with loss of vapors to the chamber walls, and likely results from an increase in the rate of mass transfer of vapor species to the particles relative to the walls. Quantitative understanding of the role of vapor wall loss is necessary to characterize the extent to which SOA yields in chamber experiments are underestimated relative to the atmosphere. The loss of "extremely low volatility" organic compounds to chamber walls has recently been implicated as important for understanding SOA formation for a different chemical system, α-pinene + O_3 (13, 14). The competition between vapor condensation to particles versus to chamber walls is quantitatively examined here using a time-dependent, parameterizable model of SOA formation, the statistical oxidation model (SOM; refs. 15, 16; *SI Appendix, The Statistical Oxidation Model*). The SOM accounts for vapor wall losses based on observations showing that wall losses of semivolatile species in Teflon chambers are reversible (11). Such wall loss is modeled dynamically and depends on the equivalent OA mass of the chamber walls (C_w, mg m^{-3}), the first-order vapor wall loss rate coefficient (k_w, s^{-1}), and the vapor saturation concentration of compounds *i* (C_i^*, μg m^{-3}). k_w reflects the combined effects of turbulent mixing in the chamber, molecular diffusion of vapor molecules through the near-wall boundary layer, and any penetration into chamber walls. k_w is likely to be chamber specific, as the extent of turbulent mixing depends on specific chamber operating conditions, but is reasonably independent of compound identity (11). Values of k_w for a range of gases were estimated in one study (17) to range from $\sim 2 \times 10^{-5}$ to 10^{-3} s^{-1}, corresponding to timescales of many hours to 10 min. The largest k_w values are appropriate only for chambers with active mixing, which the Caltech chamber does not have (*SI Appendix, Vapor Wall Loss*). Observations (11) suggest that C_w varies somewhat with compound identity, ranging from ~2 to 24 mg m^{-3}, compared with chamber OA concentrations that are usually 1–3 orders of magnitude smaller; a value of 10 mg m^{-3} is used here as the base case. Gas-particle partitioning is modeled dynamically assuming absorptive partitioning, including correction for noncontinuum effects and imperfect accommodation, the latter of which is characterized by the mass-accommodation coefficient, α. The accommodation coefficient reflects the overall transfer of vapor molecules into the particle bulk, and is likely dependent on the chemical makeup of both the vapor and particle phases and processes that occur at the particle surface. This formulation is more general than most previous analyses of SOA formation in environmental chambers, which typically assume instantaneous gas-particle equilibrium.

Optimal values for k_w and α have been determined for the sets of low- and high-NO_x experiments by comparing observed and simulated best-fit time-dependent C_{OA} profiles for a wide range of k_w and α. The k_w/α pair that provides for the best overall agreement with the time-dependent SOA formation observed across all experiments at a given NO_x condition, excluding the nucleation experiments, is considered the optimal solution (Fig. 2 *A* and *B*) (*SI Appendix, Optimizing k_w and α* and Fig. S3). For low-NO_x experiments, the optimal $k_w = 2.5 \times 10^{-4}$ s^{-1} and $\alpha = 2 \times 10^{-3}$. The independently determined values for high-NO_x experiments are similar: $k_w = 2.5 \times 10^{-4}$ s^{-1} and $\alpha = 1 \times 10^{-3}$. The simulations provide good overall agreement with the observed seed *SA* dependence only for a combination of a small α and a k_w on the order of 10^{-4} s^{-1}, indicating that both parameters are important to describing chamber SOA formation. (It should be noted that a reasonable fit for an individual experiment can be obtained for many k_w/α pairs, including when instantaneous gas-particle equilibrium is assumed, i.e., when $\alpha = 1$. This is not meant to imply that the absolute values of these parameters are not important, but that only in analyzing the combined datasets

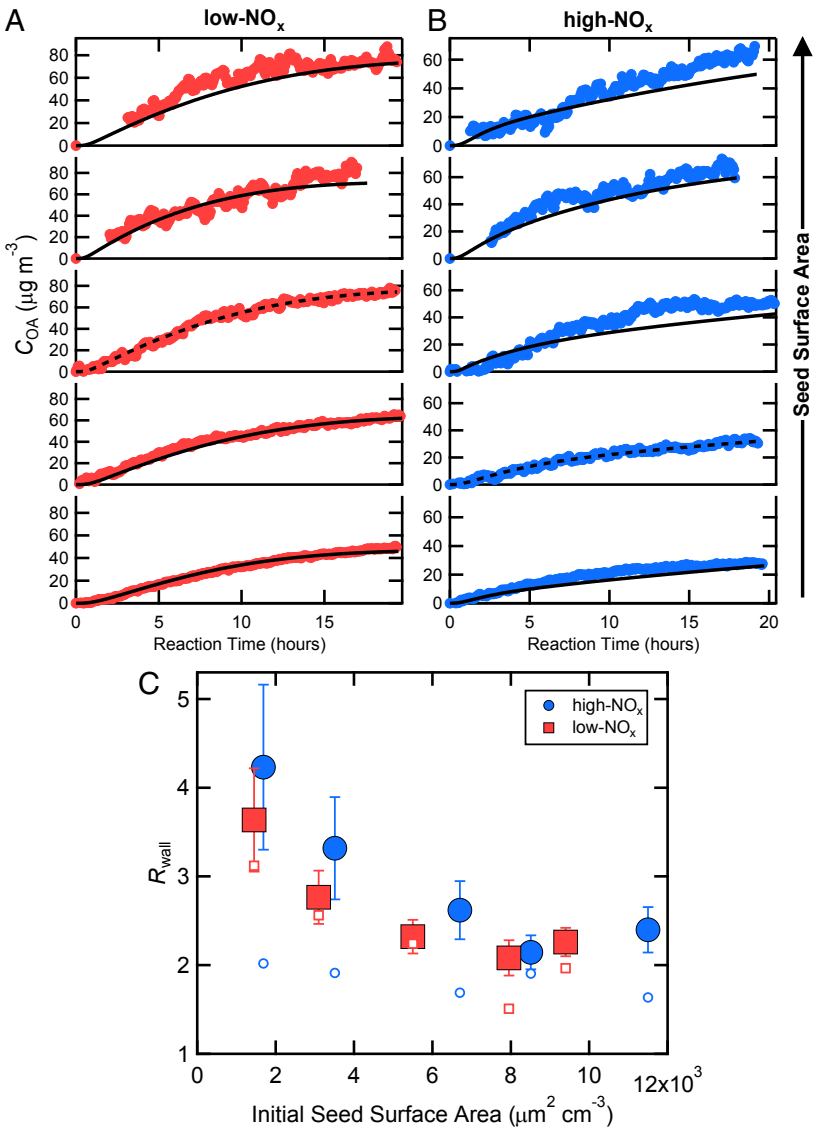

Fig. 2. Observed (points) and simulated (lines) SOA concentrations for each photochemical oxidation experiment performed for different initial inorganic seed surface area for (*A*) low-NO_x and (*B*) high-NO_x conditions. The dashed lines indicate the experiment to which the SOM was explicitly fit, and the solid lines indicate simulation results based on those fits. (*C*) The wall loss bias factor, R_{wall}, as a function of seed surface area. Filled symbols use the optimal k_w/α pair and the corresponding best-fit SOM parameters determined from *A* and *B*. Open symbols assume $\alpha = 1$ and each experiment was individually fit using the optimal k_w. The error bars indicate the 1σ SD in R_{wall} for each experiment over the period when $C_{OA} > 0.5$ μg m^{-3}.

at multiple seed *SA* can optimal k_w and α values be uniquely established.) The determined optimal k_w values are consistent with theoretical estimates (*SI Appendix, Vapor Wall Loss* and Fig. S4) and some observations (11), but larger than some previous observations in the Caltech chamber (18), most likely reflecting the limited time resolution of those observations, which might not have allowed for separation of filling and mixing of the chamber from wall loss, but potentially also reflecting differences between chemical systems.

The small optimal α values required to reproduce the observed seed *SA* dependence likely reflect mass-transfer limitations within the particle phase, which can occur for highly viscous SOA particles (19). When $\alpha \sim 10^{-3}$, mass accommodation is relatively slow and the vapors and particles cannot be assumed to be in instantaneous equilibrium. The timescale associated with reaching gas-particle equilibrium ($\tau_{g\text{-}p,eqm}$) varies with seed *SA* and size (*SI Appendix, Gas-Particle Partitioning Timescales* and Fig. S5). Given $\alpha = 10^{-3}$, $\tau_{g\text{-}p,eqm}$ ranges from ~230 min for the smallest seed *SA* to only ~30 min for the largest seed *SA*. Thus, at the smallest seed *SA* $\tau_{g\text{-}p,eqm}$ is similar to the timescale determined for gas wall loss ($1/k_w = 67$ min) and the influence of gas wall loss is more pronounced.

Importantly, loss of condensable vapors to the chamber walls leads to a low bias in the observed SOA formed even for the experiments with the highest seed *SA*. To quantitatively assess this bias, simulations have been performed using the best-fit SOM parameters determined for the optimal k_w/α pair above, but with $k_w = 0$ (no wall loss). The ratio $R_{wall} = C_{SOA}(k_w = 0)/C_{SOA}(k_{w,optimal})$ has been calculated for each experiment and quantifies the bias in the SOA yield due to traditionally unaccounted for vapor wall losses. The magnitude of R_{wall} depends on the experiment considered, decreasing with increasing seed

SA and reaching a plateau at large seed *SA* (Fig. 2*C*). For the seeded experiments, R_{wall} averaged over the period when $C_{OA} > 0.5$ μg m^{-3} varied from 3.6 (±0.6) to 2.1 (±0.2) for low NO_x and from 4.2 (±0.9) to 2.1 (±0.2) for high NO_x in going from lowest to highest seed *SA*, and where the uncertainties are 1 SD over the averaging period. These ratios correspond to end-of-experiment corrected mass yields of 1.6 (low NO_x) and 0.93 (high NO_x), substantially exceeding the values currently used in chemical transport models for toluene (~0.47 for low NO_x and ~0.12 for high NO_x; ref. 4). Given an O:C ratio for toluene + OH SOA of ~0.7 (20), the carbon yields would be 0.94 (low NO_x) and 0.55 (high NO_x). [The calculated end of experiment O:C are 0.67 (low NO_x) and 0.91 (high NO_x).] This implies that ~6% and ~55% of the product carbon mass remains in the gas phase for low- and high-NO_x conditions, respectively. The oxidation process is a balance between functionalization and fragmentation. In the absence of fragmentation, the carbon yield would asymptote to 100%. The low-NO_x carbon yield in the absence of vapor wall loss is close to 100% and the SOA yield is approximately independent of the total OA mass, which together indicate that fragmentation plays only a minor role. Fragmentation is comparably more important under high-NO_x conditions.

Interestingly, R_{wall} values similar to those determined for the optimal k_{wall}/α pair are obtained when vapor wall loss is accounted for (i.e., $k_w \neq 0$) but when it is assumed that $\alpha = 1$ (i.e., that gas-particle equilibration is effectively instantaneous) during fitting of each individual experiment (Fig. 2*C*). This indicates that the magnitude of α is not key to fitting of an individual experiment, but when the experiments are taken together as a combined dataset α is indeed key to matching the observed dependence on seed surface area. Related, α is not key to there being an influence of vapor wall loss on the overall SOA yield, which is controlled more so by the magnitude of k_w, although at lower seed *SA* for a given k_w, the derived R_{wall} increases as α decreases. The finding that large R_{wall} values are obtained even when $\alpha = 1$ indicates that the general conclusions here regarding vapor wall loss are robust with respect to knowledge of α. This is important because other chemical systems might not exhibit as slow mass accommodation but could still be affected by vapor wall loss. Clearly, loss of condensable vapors to the chamber walls can suppress SOA yields relative to those that are relevant for the atmosphere.

Dependence on Experimental Conditions

For a given chamber, the extent to which vapor wall loss affects SOA yield will depend on the combination of (*i*) the rate of oxidation and duration of a given experiment, (*ii*) the precursor VOC concentration, (*iii*) the particular chemical pathways associated with oxidation of a given species, i.e., the precursor identity, and (*iv*) the seed *SA*. This is illustrated for the toluene low-NO_x system by carrying out a series of 18-h simulations where [OH] is varied from 1 to 100 × 10^6 molecules cm^{-3} and $[toluene]_{initial}$ from 1 to 900 ppb for a seed $SA = 1{,}000$ μm^2 cm^{-3} using the SOM parameters and optimal k_w/α determined above. The calculated R_{wall} varies with oxidant and precursor concentration (actually, VOC loss rate), with smaller R_{wall} when oxidation is faster and at larger precursor VOC concentration (Fig. 3 and *SI Appendix*, Fig. S6). (Note that these calculations do not account for differences that might result from changes in the relative importance of $RO_2 + HO_2$ versus $RO_2 + RO_2$ reactions as $[VOC]_{initial}$ and [OH] are varied.) Such "rate effects" have been observed for SOA produced in aromatic systems (21). The seed *SA* dependence is substantially reduced when the $[VOC]_{initial}$ is large, especially at high [OH]. Overall, these dependencies, along with differences in the initial seed *SA*, may help explain some of the differences (and similarities) in historical aerosol yields measured in different chambers.

Vapor Losses and Sensitivity to C_w

The observed time-dependent C_{OA} to which the SOM was fit were corrected to account for physical deposition of the particles to the walls. Loss of vapors, excluding growth of suspended

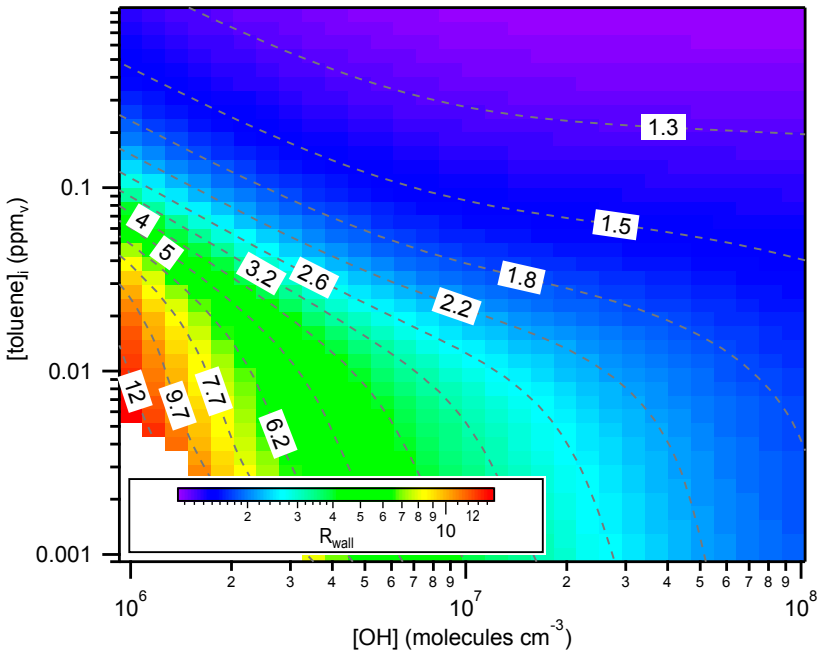

Fig. 3. Calculated SOA yield bias as a function of initial toluene concentration and OH concentration when $k_w = 2.5 \times 10^{-4}$ s^{-1} and $C_w = 10$ mg m^{-3}. The R_{wall} values for a given [toluene] and [OH] are indicated by colors and contours, and are averaged over the period when $C_{SOA} > 0.5$ μg m^{-3} to the end of an experiment at 18 h. Results are based on the optimal fit of the SOM to the low-NO_x experiments.

particles, was separately accounted for assuming that the vapors continuously interact with the Teflon chamber walls, with C_w = 10 mg m^{-3} (11). Some previous studies (22, 23) have alternatively assumed that vapors interact only with particles that have deposited to the walls during that experiment, as opposed to with the walls directly, and further that the timescales associated with partitioning between vapors and suspended or wall-deposited particles are the same (*SI Appendix, Particle Wall-Loss Correction*). In this alternative scenario, the effective C_w is time dependent (and zero at the start of an experiment) and related to the suspended particle concentration and the particle wall loss rate. Most chamber experiments aim to limit the extent of particle deposition, and thus it is reasonable to assume that, in general, the concentration of wall-deposited particles is less than the suspended particle concentration. Further, most modern experiments limit the observed C_{OA} to < 0.1 mg m^{-3}, and thus the effective C_w in this alternative case will be substantially smaller than when vapors are assumed to partition into the chamber walls.

It is therefore useful to examine the dependence of the calculated R_{wall} on the assumed C_w, where an assumed C_w < ~0.1 mg m^{-3} corresponds approximately to the wall-deposited particle alternative scenario (22, 23). This has been done for the low-NO$_x$ experiments where the SOM was fit to the observations for different assumed C_w, with good fits obtained for all C_w. Above C_w = 0.2 mg m^{-3} (= 200 μg m^{-3}) the calculated R_{wall} is constant. Below 0.2 mg m^{-3} the calculated R_{wall} falls off, reaching a second plateau at small C_w that is still above unity (Fig. 4). The plateaus at high and low C_w result from the best-fit SOM parameters varying with C_w to compensate for the differing amounts of loss of vapors to the walls and still maintaining the same suspended C_{OA} time profile (*SI Appendix*, Fig. S7). Because measurements demonstrate that vapors are lost directly to Teflon walls (11), this indicates that when vapor wall loss is accounted for assuming that the vapors interact only with wall-deposited particles, the extent of the vapor loss is underestimated. That R_{wall} is constant above C_w = 0.2 mg m^{-3} demonstrates that our conclusions are robust with respect to the assumption regarding the exact value of C_w.

Consideration of Historical Experiments

To estimate the potential influence of vapor wall losses for systems other than toluene, we calculated SOA yield biases for a variety of other VOCs (16, 20, 21, 23, 24) (*SI Appendix, Fitting of Historical Chamber Data*). It should be noted that the experimental conditions in the historical experiments are not identical to those for the toluene experiments, especially for high-NO$_x$ conditions (*SI Appendix, Historical Experiments*). Although k_w for a given chamber is reasonably independent of the precursor compound, α may depend on the precursor identity. The results for the toluene experiments indicate that smaller α values generally correspond to larger R_{wall}. Therefore, a conservative, likely lower-bound estimate of R_{wall} has been obtained for each precursor assuming that α = 1 during fitting and using $k_w = 1 \times 10^{-4}$ s^{-1} (instead of 2.5×10^{-4}) to account for potential differences in the chamber used for these historical experiments (*SI Appendix*, Figs. S8–S10). The use of a smaller k_w will decrease R_{wall}, all other factors being equal. Calculated R_{wall} values range from as small as 1.1 to as large as 4.1 (Table 1 and *SI Appendix*, Fig. S11). The typically smaller values for the high-NO$_x$ vs. low-NO$_x$ experiments reflect the much shorter reaction timescales and higher oxidant and NO$_x$ concentrations in the historical high-NO$_x$ experiments, compared with the current experiments with toluene. Evidently, the extent to which vapor wall loss will have influenced historical experiments is variable, yet potentially substantial and deserving of further investigation through new experiments and consideration of other datasets. Importantly, the results here indicate that quantitative analysis of SOA formation in chambers

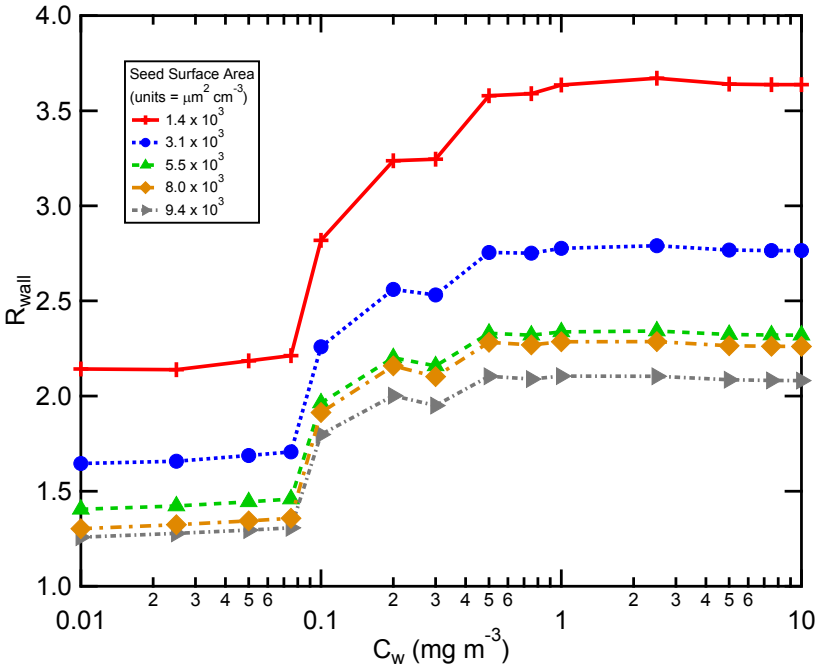

Fig. 4. Calculated vapor wall loss bias, R_{wall}, as a function of the effective wall mass concentration, C_w, for the low-NO$_x$ toluene photooxidation experiments at varying initial seed surface area. For each C_w, the SOM was fit to the experiment with seed surface area = 5.5×10^3 μm^2 cm^{-3} using $k_w = 2.5 \times 10^{-4}$ s^{-1} and $\alpha = 2 \times 10^{-3}$. The determined best-fit SOM parameters were then used to simulate SOA formation for the experiments performed at other seed concentrations but assuming the same C_w.

Table 1. Average biases in SOA yields due to vapor wall losses for various VOCs under low- and high-NO_x conditions

VOC*	Low-NO_x R_{wall}[†]	High-NO_x R_{wall}[†]
Toluene[‡] (this study)	2.1–3.6	2.1–4.2
n-dodecane (16)	4.1 ± 0.8[¶]	1.16 ± 0.08
2-methylundecane (16)	3.7 ± 0.5	1.4 ± 0.2
Cyclododecane (16)	3.0 ± 0.3	1.10 ± 0.05
Hexylcyclohexane (16)	2.4 ± 0.3	1.16 ± 0.07
Toluene (21)	1.9 ± 0.4	1.13 ± 0.06
Benzene (21)	1.8 ± 0.4	1.25 ± 0.1
M-xylene (21)	1.8 ± 0.4	1.2 ± 0.1
M-xylene (23)	1.6 ± 0.3	
Naphthalene (24)	1.2 ± 0.1	1.2 ± 0.1
α-pinene + OH (20)	1.6 ± 0.3	1.3 ± 0.1
Isoprene + OH (20)	3.1 ± 1.3	2.2 ± 0.5

*For all VOC's except toluene (this study), $k_w = 1 \times 10^{-4}$ s^{-1} and $\alpha = 1$. For toluene (this study), $k_w = 2.5 \times 10^{-4}$ s^{-1} and $\alpha = 0.002$ (low NO_x) or 0.001 (high NO_x).

[†]Calculated for the period when $C_{SOA} > 0.5$ μg m^{-3} through the end of a given experiment.

[‡]For toluene, the reported R_{wall} indicate the range of values determined at different initial seed *SA*.

[¶]Uncertainties are 1σ over the averaging period.

requires use of an explicitly time-dependent model that accounts for the simultaneous and competing condensation of vapors onto particles versus onto the chamber walls, representing a major shift from most historical analyses, which did not take time explicitly into account.

Implications

Our results show that the effect of vapor wall loss on SOA yields can be substantial. If reported SOA yields are low by factors of ~1.1–4.2, as our results suggest they may be, then SOA concentrations simulated in 3D models will be correspondingly low. Although the analysis presented here for the toluene SOA system needs to be comprehensively expanded to other main classes of SOA precursors, beyond the assessment above, it is likely that a lack of proper accounting for vapor wall losses that suppress chamber-derived SOA yields contribute substantially to the underprediction of ambient SOA concentrations in atmospheric models.

Materials and Methods

Chamber Experiments. Toluene photooxidation experiments were carried out in the new 24-m^3 Teflon environmental reaction chambers at Caltech. Liquid toluene was evaporated into the chamber to achieve a concentration of ~38 ppb gas-phase mixing ratio (= 143 μg m^{-3}). Hydroxyl radicals were generated from photolysis of H_2O_2 either with (high NO_x) or without (low NO_x) addition of NO to the chamber. Dried ammonium sulfate seed particles were added via atomization of an aqueous solution of ammonium sulfate solution until the desired seed concentration was obtained. The toluene, seed particles, H_2O_2 and NO_x were allowed to mix in the chamber for 1 h, after which time the black lights were turned on to initiate H_2O_2 photolysis. Particle number size distributions were measured using a cylindrical differential mobility analyzer coupled to a condensation particle counter. More details are available in the *SI Appendix*.

SOA Modeling. The statistical oxidation model (15) was used to analyze the experimental observations. The SOM simulates the multigenerational gas-phase oxidation of a precursor VOC that has N_C carbon atoms and N_O oxygen atoms as reactions cause the precursor and product species to functionalize, increasing N_O, and/or fragment, decreasing N_C. Addition of oxygen atoms leads to a decrease in vapor pressure, which drives condensation of the gas-phase species. Mass transfer between the gas and particle phases is treated dynamically. The parameters that describe functionalization, fragmentation, and the decrease in vapor pressure upon oxygen addition are adjusted by fitting to the experimental observations of time-dependent SOA formation. More details are provided in the *SI Appendix*.

ACKNOWLEDGMENTS. We thank Alma Hodzic, Julia Lee-Taylor, Sasha Madronich (National Center for Atmospheric Research), Paul Ziemann (University of Colorado Boulder), Paul Wennberg (Caltech), Manabu Shiraiwa (Max Planck Institut für Chemie), and Anthony Wexler (University of California, Davis) for useful discussions. This work was supported by the National Science Foundation Grants ATM-1151062 and AGS-1057183, Department of Energy Grant DE-SC 0006626, and the California Air Resources Board Contract 12-312.

1. Odum JR, Jungkamp TPW, Griffin RJ, Flagan RC, Seinfeld JH (1997) The atmospheric aerosol-forming potential of whole gasoline vapor. *Science* 276(5309):96–99.
2. Jimenez JL, et al. (2009) Evolution of organic aerosols in the atmosphere. *Science* 326(5959):1525–1529.
3. Odum JR, et al. (1996) Gas/particle partitioning and secondary organic aerosol yields. *Environ Sci Technol* 30(8):2580–2585.
4. Carlton AG, et al. (2010) Model representation of secondary organic aerosol in CMAQv4.7. *Environ Sci Technol* 44(22):8553–8560.
5. Heald CL, et al. (2005) A large organic aerosol source in the free troposphere missing from current models. *Geophys Res Lett* 32:L18809.
6. Volkamer R, et al. (2006) Secondary organic aerosol formation from anthropogenic air pollution: Rapid and higher than expected. *Geophys Res Lett* 33:L17811, 10.1029/2006GL026899.
7. Robinson AL, et al. (2007) Rethinking organic aerosols: Semivolatile emissions and photochemical aging. *Science* 315(5816):1259–1262.
8. Ervens B, Turpin BJ, Weber RJ (2011) Secondary organic aerosol formation in cloud droplets and aqueous particles (aqSOA): A review of laboratory, field and model studies. *Atmos Chem Phys* 11(21):11069–11102.
9. Ensberg JJ, et al. (2013) Emission factor ratios, SOA mass yields, and the impact of vehicular emissions on SOA formation. *Atmos Chem Phys* 14:2383–2397.
10. Dzepina K, et al. (2011) Modeling the multiday evolution and aging of secondary organic aerosol during MILAGRO 2006. *Environ Sci Technol* 45(8):3496–3503.
11. Matsunaga A, Ziemann PJ (2010) Gas-wall partitioning of organic compounds in a Teflon film chamber and potential effects on reaction product and aerosol yield measurements. *Aerosol Sci Technol* 44(10):881–892.
12. Kroll JH, Chan AWH, Ng NL, Flagan RC, Seinfeld JH (2007) Reactions of semivolatile organics and their effects on secondary organic aerosol formation. *Environ Sci Technol* 41(10):3545–3550.
13. Ehn M, et al. (2014) A large source of low-volatility secondary organic aerosol. *Nature* 506(7489):476–479.
14. Kokkola H, et al. (2014) The role of low volatile organics on secondary organic aerosol formation. *Atmos Chem Phys* 14(3):1689–1700.
15. Cappa CD, Wilson KR (2012) Multi-generation gas-phase oxidation, equilibrium partitioning, and the formation and evolution of secondary organic aerosol. *Atmos Chem Phys* 12:9505–9528.
16. Cappa CD, et al. (2013) Application of the Statistical Oxidation Model (SOM) to secondary organic aerosol formation from photooxidation of C12 alkanes. *Atmos Chem Phys* 13:1591–1606.
17. McMurry PH, Grosjean D (1985) Gas and aerosol wall losses in Teflon film smog chambers. *Environ Sci Technol* 19(12):1176–1182.
18. Loza CL, et al. (2013) Secondary organic aerosol yields of 12-carbon alkanes. *Atmos Chem Phys Discuss* 13(8):20677–20727.
19. Shiraiwa M, et al. (2013) Size distribution dynamics reveal particle-phase chemistry in organic aerosol formation. *Proc Natl Acad Sci USA* 110(29):11746–11750.
20. Chhabra PS, et al. (2011) Elemental composition and oxidation of chamber organic aerosol. *Atmos Chem Phys* 11(17):8827–8845.
21. Ng NL, et al. (2007) Secondary organic aerosol formation from m-xylene, toluene, and benzene. *Atmos Chem Phys* 7(14):3909–3922.
22. Hildebrandt L, Donahue NM, Pandis SN (2009) High formation of secondary organic aerosol from the photo-oxidation of toluene. *Atmos Chem Phys* 9(9):2973–2986.
23. Loza CL, et al. (2012) Chemical aging of m-xylene secondary organic aerosol: Laboratory chamber study. *Atmos Chem Phys* 12(1):151–167.
24. Chan AWH, et al. (2009) Secondary organic aerosol formation from photooxidation of naphthalene and alkylnaphthalenes: Implications for oxidation of intermediate volatility organic compounds (IVOCs). *Atmos Chem Phys* 9(9):3049–3060.

Supporting Information for Influence of vapor wall-loss in laboratory chambers on yields of secondary organic aerosol

Xuan Zhang, Christopher D. Cappa, Shantanu Jathar, Renee C. McVay, Joseph J. Ensberg, Michael J. Kleeman, and John H. Seinfeld

correspondence to: cdcappa@ucdavis.edu or seinfeld@caltech.edu

This file includes:

Section 1. Materials and Methods

The Supplementary information contains an overview of the new and historical chamber experiments (S1.1), optimization of k_w and α (S1.2), the statistical oxidation model (S1.3), the treatment of vapor wall loss within the SOM and a discussion of vapor-particle equilibrium timescales (S1.4), and the fitting of historical chamber data (S1.5).

S1.1. Experiments

S1.1.1. Toluene Photooxidation Experiments

Toluene SOA formation experiments were conducted in the new Caltech dual 24-m^3 Environmental Chambers, in which the temperature (T) and relative humidity (RH) are automatically controlled. Prior to each experiment, the Teflon chambers were flushed with clean, dry air for 24 h until the particle number concentration < 10 cm^{-3} and volume concentration < 0.01 μm^3 cm^{-3}. Ammonium sulfate (AS) seed aerosol was injected into the chamber by atomizing 0.015 or 0.1 M aqueous $(NH_4)_2SO_4$ solution into the chamber for 30 to 120 min. The resulting total AS seed surface area ranged from ~ 1×10^3 μm^2 cm^{-3} up to ~ 1×10^4 μm^2 cm^{-3}, and the corresponding particle-to-wall surface area ratio ranged from ~ 1×10^{-3} to 7×10^{-3}. Hydrogen peroxide (H_2O_2) was used for the OH source by evaporating 120 μL of 50% wt aqueous solution into the chamber with 5 L min^{-1} of purified air for ~ 100 min, resulting in an approximate starting H_2O_2 concentration of 2.0 ppm. 3 μL toluene (Sigma-Aldrich, 99.8% purity) was injected into a glass bulb, which was connected into the Teflon chamber. 5 L min^{-1} of purified air flowed through the glass bulb into the chamber for ~ 15 min, introducing ~ 40 ppb toluene into the chamber. For experiments at elevated NO_x (i.e. high-NO_x conditions) NO and NO_2 were added to the chamber at the start of a given experiment until the concentrations were ~17 ppb and 30 ppb, respectively. The initial [VOC]/[NO_x] in the high-NO_x experiments ranged from 4.8-6.0 ppbC/ppb. After ~ 90 min mixing, photooxidation was initiated by irradiating the chamber with black lights with output wavelength ranging from 300 to 400 nm. The irradiation leads to photolysis of H_2O_2 to produce OH radicals with an approximately constant concentration throughout the entire experiment. Temperature and relative humidity of all experiments were ~298 K and ~3%,

respectively. The initial O_3 concentration was below detection limit in all experiments. H_2O_2 exerts an interference on the O_3 detection, increasing the O_3 monitor readout by ~ 2-3 ppb in the current study. NO was continuously injected into the chamber over the course of each experiment at 80 ppb h^{-1} for the first 2.5 h of reaction, then 50 ppb h^{-1} for the next 4.5 h of reaction, and then 30 ppb h^{-1} for the remainder of the reaction. Experimental conditions (e.g. [VOC], seed surface area, [NO_x]) for each experiment are reported in Table S1.

A suite of instruments was used to monitor toluene SOA formation and evolution. T, RH, NO, NO_x and O_3 were continuously monitored. Toluene concentration was monitored using a gas chromatograph with flame ionization detector (GC/FID, Agilent 6890N), equipped with a HP-5 column (15 m × 0.53 mm ID × 1.5 μm thickness, Hewlett-Packard). Particle size distribution and number concentration were measured by a cylindrical differential mobility analyzer (DMA; TSI Model 3081) coupled to a condensation particle counter (TSI Model 3010). The DMA was operated in a closed system with a recirculating sheath and excess flow of 2.67 L min^{-1} and a 5.4 : 1 ratio of sheath to aerosol flow rate. The column voltage was scanned from 15 to 9850 V over 45 s.

S1.1.2. Historical Experiments

All the other SOA formation experiments used in SOM optimal fitting were carried out in the Caltech dual 28-m^3 Environmental Chamber. Details of experimental protocols can be found in (1-6). Experimental conditions are reported in Tables S2 and S3 and differences in methodology from the above toluene photooxidation experiments are highlighted below. An identical suite of instrumentation was used as in the toluene photooxidation experiments. The historical experiments typically had seed *SA* around 1-2 x 10^3 cm^{-3}, corresponding to the lowest seeded experiments in the toluene photooxidation experiments. The majority of the historical low-NO_x experiments examined in this study used similar methods and conditions as the new toluene experiments, i.e. used H_2O_2 as the OH source. The experimental procedures associated with the high-NO_x experiments differed from the new toluene experiments. Specifically, for the historical high-NO_x experiments the primary OH source was HONO photolysis, as opposed to H_2O_2 photolysis. This has the practical implication of leading to reaction conditions where (i) the OH concentration is initially ~O(10^7 molecules cm^{-3}) and decays rapidly over a period of ~1-3 hours and (ii) the initial [VOC]/[NO_x] ratio tends to be much smaller compared to the current experiments. Thus, the timescales of SOA

formation during the historical high-NO_x experiments were, in general, very different than for the toluene photooxidation experiments: rapid formation over approximately 1-2 hours vs. continuous formation over 18 hours. For high-NO_x experiments, NO_x was added prior to the lights being turned on both from the HONO injection, which introduces some NO_2, and from addition of NO. Additional NO was produced upon photolysis of HONO. Typical initial NO_x concentrations were on the order of 500 ppb, corresponding to initial [VOC]/[NO_x] of ~0.5 ppbC/ppb (Table S3).

S1.1.3. Particle Wall-Loss Correction

Particle wall losses during an experiment must be accounted for. Two limiting assumptions have been made for the interactions between those particles that have deposited on the wall and suspended vapors in determining the corrected suspended SOA concentrations (5, 7, 8). In one case, particles deposited on the wall are assumed to cease interaction with the suspended vapors and no loss of vapors to the walls is accounted for. This case gives the lower bound of the total organic mass concentration, since particles remain the same size as at the moment they deposited on the wall for the remainder of the experiment. SOA concentrations determined from this case are used for the primary analysis in the manuscript, which is appropriate because vapor loss to the walls is treated separately. In the second limiting case, particles deposited on the wall are assumed to continue to interact with the suspended vapors as if they had remained suspended, with the wall-bound particles assumed to grow at the same rate as suspended particles in the chamber. The corrected SOA concentrations in this case are larger than in the first case because of the additional uptake of vapors to wall-bound particles. This case provides an upper-bound on the actual SOA formed under the assumption that the vapors interact with wall-bound particles, but not the Teflon walls (5, 7, 8). However, traditional application of this second case does not account for the substantially differing timescales of gas-particle vs. gas-wall transport, nor does it account for loss of vapors to the chamber walls and the substantially larger amount of effective absorbing mass of the walls (C_w) compared to the deposited particles. Compared with C_w (10 mg m^{-3}), which is assumed as a constant from the onset of the experiment, the total organic mass deposited on the chamber wall over the course of 18 h photooxidation is ~ 3 orders of magnitude lower. As such, this “upper bound” can underestimate the actual SOA formation,

as it accounts for only a subset of the overall vapor wall-loss correction. Nonetheless, the "upper bound" corrected results are provided for reference to previous experiments.

For either case, the Aerosol Parameter Estimation (APE) model (9), derived on the basis of the aerosol general dynamic equation (10), is employed to calculate these two limits. The suspended particle population evolves as a result of three processes: coagulation, condensation, and wall-loss. The change of suspended particle number-size distribution due to coagulation is well constrained. The size-dependent wall loss rate is determined by experimentally monitoring the decay of dry inert $(NH_4)_2SO_4$ particles assuming first-order kinetics. The condensation rate is the only free parameter in the model, which can be obtained by optimal fitting of the APE model predictions to the DMA measured particle size distribution at each time step. Once the condensation rate values are estimated, they can be applied to parameterize the growth of particles on the walls due to condensation of gaseous vapor and deposition of suspended particles. A factor that describes the extent of interactions between deposited particles and suspended vapors is applied when summing aerosol masses in the chamber core and on the walls. A value of 0 for this factor corresponds to no condensation to deposited particles. A value of 1 for this factor corresponds to the case where the condensation rate of gaseous vapors to deposited particles is the same as those suspended. The primary analysis in this work utilizes the corrected particle mass under the assumption of no condensation to deposited particles because vapor wall loss is treated separately. The evolution of the wall-loss corrected particle size distributions is shown for each experiment in Fig. S1 for the lower limit case. The time-dependent aerosol growth, from which the aerosol yield can be calculated, is shown for each experiment in Fig. S2 for both limiting cases.

S1.2. Optimizing k_w and α

The optimal values of k_w and α were determined using the general procedure as outlined below. There were a total of 6 experiments conducted for each NO_x condition, 5 with seed aerosol and 1 without. Only the seeded experiments are considered in the optimization method because of difficulties associated with specification of nucleation. The SOM was fit to one of these 5 seeded experiments for a variety of k_w and α values. For each k_w/α pair a set of best-fit SOM parameters (i.e. ΔLVP, m_{frag} and the P_{func} array) were determined. Specifically,

the experiments with seed SA = 5.5 x 10^3 μm^2 cm^{-3} (low-NO_x) and SA = 3.5 x 10^3 μm^2 cm^{-3} (high-NO_x) were used for fitting. These best-fit SOM parameters and the associated k_w/α pair were then used to simulate SOA formation for the other 4 seeded experiments. Reduced goodness of fit metric (χ^2_{red}) values were calculated for each experiment as:

$$\chi^2_{red} = \frac{1}{n-6-1}\sum\left(\frac{C_{OA,obs}(t)-C_{OA,model}(t)}{\sigma_{OA,obs}(t)}\right)^2 \quad \text{(S1)}$$

where n is the number of data points per experiment, 6 is the number of model degrees of freedom and $\sigma_{OA,obs}$ is the uncertainty in the observations. For each experiment, the minimum χ^2_{red} across all k_w/α pairs was determined, and the set of χ^2_{red} values for each experiment was normalized by the minimum in that set. Normalization ensures that the different experiments carry equal weight in the next step. The composite χ^2_{red} across all seeded experiments was then determined as:

$$\chi^2_{red,composite}(k_w,\alpha) = \sum_{i=1}^{5}\chi^2_{red,norm,i}(k_w,\alpha) \quad \text{(S2)}$$

where the sum is over the normalized χ^2_{red} for all seeded experiments. Smaller values of the composite χ^2_{red} indicate overall better agreement across all of the seeded experiments for a given set of best-fit SOM parameters, k_w and α. A contour diagram of the calculated composite χ^2_{red} as a function of k_w and α (Fig. S3) illustrates that only certain combinations of k_w and α provide for good agreement across all experiments. There is almost no seed effect when $\alpha > 0.1$, and therefore the overall agreement is poor no matter what k_w is used. As α is lowered, a seed effect becomes evident. However, only when α is O(10^{-3}) and k_w is O(10^{-4}) can overall good agreement with all experiments be obtained. Since the k_w and α values were not determined from a specific fitting algorithm, we refer to the values that provide for best agreement as the "optimal" values rather than "best fit" values. These are: k_w = 2.5 x 10^{-4} s^{-1} and α = 2 x 10^{-3} for low-NO_x experiments and k_w = 2.5 x 10^{-4} s^{-1} and α = 1 x 10^{-3} for high-NO_x experiments.

S1.3. The Statistical Oxidation Model

The SOM simulates the oxidation of a given hydrocarbon as a trajectory through a 2-D grid of carbon and oxygen atoms in which "species" are considered particular carbon/oxygen combinations (e.g. $C_{12}O_4$). Specific rules define the movement through this space, describing the probability that a reaction leads to functionalization or fragmentation, how many oxygen atoms are added per reaction, and the decrease in vapor pressure that occurs upon addition of a single oxygen atom. SOM effectively simulates the multi-generational chemistry that characterizes photooxidation experiments. Full details are provided in (6, 11). The fragmentation probability (P_{frag}) depends on the oxygen content of the reacting species and is parameterized as:

$$P_{frag} = \left(\frac{N_O}{N_C}\right)^{m_{frag}} \quad \text{(S3)}$$

where m_{frag} is an adjustable parameter, and N_O and N_C are the number of oxygen and carbon atoms comprising an SOM species, respectively. The P_{frag} is always constrained to be ≤ 1. (Recently, a "bug" in the SOM code was found related to how the fragmentation was being treated. Rather than the probability of fragmentation depending on the oxygen content of the reacting species, it was being determined based on the oxygen content of the product species. This has now been fixed. The SOM was originally written in the IGOR programming language. The SOM has now been independently implemented in Fortan using the framework outlined in (11) and the IGOR and Fortan versions produce equivalent results, suggesting that no further "bugs" of this sort exist. The best-fit SOM parameters for the alkanes differ from those reported in (6) as a result of this update and because vapor wall-loss has been included.)

The functionalization probability (P_{func}) describes the likelihood of adding 1, 2, 3 or 4 oxygen atoms per reaction, and each can be adjusted independently, subject to the constraint that they are positive and must sum to 1. The decrease in vapor pressure (or more specifically, in the log of the saturation concentration, C^*, in μg m^{-3}) per oxygen added is referred to as ΔLVP, and ranges from ~0.7 to 2.5, depending on the type of functional group added. Thus, there are

6 total adjustable (tunable) parameters in the base model: (i) fragmentation, (ii) volatility decrease per oxygen added and (iii-vi) oxygen addition probability. For this study, heterogeneous OH reactions are not simulated.

The reaction rate coefficient matrix associated with reactions of product species with OH radicals has been updated from the original SOM on the basis of comparison with output from the GECKO-A model for simulations of the outflow from Mexico City (12). The reaction rate coefficient of the parent hydrocarbon with OH, k_{OH} (cm^3 $molecules^{-1}$ s^{-1}), is specified to be consistent with literature results, e.g. for toluene k_{OH} = 5.2 x 10^{-12} cm^3 $molecules^{-1}$ s^{-1}. For all other species within the SOM grid, the k_{OH} are determined referenced to the reaction rate coefficient for species with the same number of carbon atoms but zero oxygen atoms as:

$$\log\left(k_{OH,base}\right) = A_1 + A_2 \times N_C^{A_3} \quad \text{(S4)}$$

and where A_1 = -15.103, A_2 =-3.9481, and A_3 = -0.79796. For a given N_C, the k_{OH} is temperature dependent and varies with N_O as

$$k_{OH}(T) = k_{OH,base} \times T^2 \times exp\left(-1 \times \frac{E_a}{8.314 \times T}\right) \times \left[1 + \frac{b_1}{\sigma\sqrt{2\pi}} \exp\left(-\frac{1(ln(N_O+0.01)-ln(b_2))^2}{2\sigma^2}\right)\right] \quad \text{(S5)}$$

and where the variables b_1, b_2, and σ are functions of N_C, with

$$\sigma(N_C \leq 15) = 0.0214 \times N_C + 0.5238;\ \ \sigma(N_C > 15) = -0.115 \times N_C + 2.695\ , \quad \text{(S6)}$$

$$b_1 = -0.2583 \times N_C + 5.8944\ , \quad \text{(S7)}$$

And

$$b_2(N_C \leq 15) = 0.0314 \times N_C + 0.9871\,;\, b_2(N_C > 15) = 0.25 \times N_C - 2.183\,. \quad \text{(S8)}$$

Within the SOM gas-particle partitioning is treated through the framework of absorptive partitioning theory (13), in which compounds partition between the gas and particle phases according to their Raoult's Law adjusted vapour pressures. Unlike in previous usages of the SOM, which assumed instantaneous gas-particle equilibrium, the SOM here treats gas-particle mass transfer dynamically. The net flux of molecules to/from the particle is calculated at each timestep as:

$$\frac{\partial C_{OA,i}}{dt} = 4\pi D_{gas,i} R_p N_p F_{FS}\left(C^{\infty}_{gas,i} - \chi_i C^*_i\right) \quad \text{(S9)}$$

where $D_{\mathrm{gas,i}}$ is the gas-phase diffusivity, R_{p} is particle radius, N_{p} is particle number concentration, F_{FS} is the Fuchs-Sutugin correction for noncontinuum mass transfer, $C^{\infty}_{gas,i}$ is the gas-phase concentration, χ_{i} is the mass fraction and C^*_i is the saturation concentration of species *i*. The entire SOA mass is considered absorbing in the calculation of χ_{i}. It is assumed that $D_{\mathrm{gas,i}}$ varies with molecular weight (*MW*) and is equal to $D_{\mathrm{CO2}}(\mathrm{MW_{CO2}}/\mathrm{MW_i})$, with D_{CO2} = 1.38 x 10^{-5} $\mathrm{m^2\ s^{-1}}$. The Fuchs-Sutugin correction is equal to:

$$F_{FS} = \frac{0.75\alpha(1+Kn)}{Kn^2+Kn+0.283\cdot Kn\cdot\alpha+0.75\alpha} \quad \text{(S10)}$$

where α is the mass accommodation coefficient onto particles and *Kn* is the Knudsen number, defined as:

$$Kn = \lambda / R_p \quad \text{(S11)}$$

and λ is the gas mean free path, which is equal to:

246

247 $$\lambda_i = 3 \cdot \frac{D_{gas,i}}{\bar{c}_i} \quad \text{(S12)}$$

248

249 with $\bar{c}_i$ equal to the root mean square speed of the gas, which is equal to:

250

251 $$\bar{c}_i = \left(\frac{8N_A kT}{\pi MW_i}\right)^{\frac{1}{2}} \quad \text{(S13)}$$

252

253 with N_A = Avagadro's number, k = the Boltzmann constant and T = temperature. The results
254 obtained with the dynamic partitioning SOM are equivalent to those obtained using the
255 instantaneous equilibrium assumption when $\alpha > 0.1$ and with seed aerosols present. It should
256 be noted that α as used in Eqn. S8 represents the net mass transfer and can include resistances
257 both in the gas-phase and at the particles surface. Full accommodation of vapors into the bulk
258 particle can be limited by diffusion within the particles when particles are highly viscous (14).
259 The dynamic SOM utilized here uses monodisperse particles with a size equal to the number
260 mean diameter and the number concentration adjusted to give the desired initial seed surface
261 area (*SA*). Although the ideal model would use the actual seed size distribution as input, we
262 have established that for particle diameters larger than ~ 50 nm the model results are
263 sufficiently insensitive to the selected particle diameter for a fixed seed *SA*. As such, the
264 results here are not limited by the simplification of using monodisperse particles. Nucleation
265 is not explicitly simulated by the SOM. Therefore, dynamic SOM calculations for the
266 nucleation experiments have been carried out assuming an initial seed size of 5 nm and a seed
267 concentration equal to that observed at the end of the experiment. Given that there is
268 substantial uncertainty associated with this assumption the nucleation experiments have not
269 been quantitatively assessed.

270

S1.4. Vapor Wall-Loss

Loss of vapors to the chamber walls is simulated as a first-order process, characterized by the first-order wall-loss coefficient k_w (s^{-1}). Vapor wall-losses are assumed to be reversible, characterized by the gas-wall partitioning coefficient, K_w, which is dependent upon compound vapor pressure,

$$K_w = \frac{RT}{M_w \gamma_w P_{sat}} \quad \text{(S14)}$$

where R is the ideal gas constant, T is temperature (assumed 298 K), M_w is the effective molecular weight of the wall material, γ_w is the activity coefficient, and P_{sat} is the saturation concentration of the species of interest. It is convenient to use the saturation concentration, C^* ($\mu g\ m^{-3}$), instead of the saturation vapor pressure, where

$$C^* = \frac{1}{K_p} = \frac{M_p \gamma_p P_{sat}}{RT} \quad \text{(S15)}$$

with K_p the gas-particle partitioning coefficient, M_p the average molecular weight of the organic species comprising the particles and γ_p is the activity coefficient. The rate coefficient for transfer of gas-phase species onto the walls is given as $k_{w,on}$ while that for evaporation from the walls is given as $k_{w,off}$. The $k_{w,on}$ is specified as a model input parameter (and is equivalent to the k_w in the main text). The $k_{w,off}$ is obtained from detailed balance as:

$$k_{w,off} = \frac{k_{w,on}}{K_w C_w} = k_{w,on}\left(\frac{C^* M_w \gamma_w}{C_w M_p \gamma_p}\right) \quad \text{(S16)}$$

and where C_w is the equivalent wall OA concentration ($\mu g\ m^{-3}$). If one makes the simple assumption that $M_w = M_p$ and $\gamma_w = \gamma_p$, then C_w can be viewed as an effective concentration that accounts for differences in molecular weight and activity between the particles and walls.

297 The C_w must therefore be estimated from experiments. Matsunaga and Ziemann (15) report a
298 range of C_w values that are constant within a given class of molecules (e.g. ketones vs.
299 alkanes), with C_w = 2, 4, 10 and 24 mg m^{-3} for alkanes, alkenes, alcohols and ketones. For all
300 reported simulations here it has been assumed that C_w = 10 mg m^{-3}. Results are reasonably
301 insensitive to the choice of C_w over the previously determined range because $C_w >> C_{OA}$. The
302 sensitivity of our results to the assumed C_w is discussed further below in Section S1.4.3.

303 It is assumed that $k_{w,on}$ is not dependent on compound identity. Consequently, the $k_{w,off}$ terms
304 vary with compound identity, specifically with C^*.

305 The value of $k_{w,on}$ can be estimated from consideration of just the gas-phase transport terms
306 within a chamber. McMurry and Grosjean (16) report an expression for $k_{w,on}$,

307

308 $$k_{w,on} = \left(\frac{A}{V}\right)\frac{\left(\frac{\alpha_w \bar{c}}{4}\right)}{1.0+\left(\frac{\pi}{2}\right)\left[\frac{\alpha_w \bar{c}}{4\left(k_e D_{gas}\right)^{0.5}}\right]} \quad \text{(S17)}$$

309

310 where A/V is the surface to volume ratio of the chamber (equal to $6/L$ for a square chamber,
311 and where L is the length of one side), α_w is the mass accommodation coefficient of vapors
312 onto the chamber walls, $\bar{c}$ is the mean thermal speed of the molecules, k_e is the coefficient of
313 eddy diffusion, and D_{gas} is the molecular diffusivity. It should be noted that α_w is not
314 necessarily equal to α for uptake onto particles. For the type of molecules here, D_{gas} is ~3 x
315 10^{-6} m^2 s^{-1} and $\bar{c}$ ~ 200 m s^{-1}. This leaves k_e and α_w as the two key unknowns. Values of $k_{w,on}$
316 have been calculated as a function of k_e for α_w ranging from 10^{-7} to 1, where 1 is perfect
317 accommodation. k_e values from 10^{-3} s^{-1} to 1 s^{-1} have been used, which corresponds to mixing
318 timescales of 17 min to 1 s (Fig. S4). McMurry and Grosjean (16) reported values for their
319 actively mixed chambers of 0.02 s^{-1} (60 m^3 chamber) and 0.12 s^{-1} (4 m^{-3} chamber). Since the
320 Caltech chamber is not actively mixed it is expected that the characteristic k_e value is
321 considerably smaller.

322 The value of k_e for the Caltech chamber is estimated based on observed size-dependent
323 deposition rates of particles in the chamber. The minimum in the k_w for particles as a function
324 of size is dependent upon k_e. This minimum occurs at a diameter of ~350 nm for the 24 m^{-3}

Caltech chamber and at ~250 nm for the 28 m^{-3} chamber (5). For particles in a cubic chamber the k_w is related to the eddy diffusion coefficient through the equation (17):

$$k_w = \frac{1}{L}\left[\frac{8\sqrt{k_e D}}{\pi} + v \cdot \coth\left(\frac{x}{2}\right)\right] \quad \text{(S18)}$$

where v is the particle terminal settling velocity (m s^{-1}) and x is defined as:

$$x = \frac{\pi v}{2\sqrt{k_e D}} \quad \text{(S19)}$$

From Eqn. S5, k_w has been calculated as a function of particle diameter and the k_e value adjusted until the minimum occurs at 250 nm or 350 nm. The required k_e in the 24 m^3 chamber is 0.075 s^{-1} and in the 28 m^3 chamber is 0.015 s^{-1}, similar to the values reported by McMurry and Grosjean for 60 m^3 (k_e = 0.12 s^{-1}) and 4 m^3 (k_e = 0.02 s^{-1}) chambers (16). Therefore, it is expected that the *maximum* k_w ~ 6.0 x 10^{-4} s^{-1} for the 24 m^3 chamber and ~ 3 x 10^{-4} for the 28 m^3 chamber from consideration of Fig. S4. Since the accommodation coefficient for the condensing species on the Teflon chamber walls is not known, it is not possible to definitively put a lower bound on the k_w. However, the experimental results of Matsunaga and Ziemann (15) clearly demonstrate that vapors are taken up to their chamber walls quite rapidly, and they estimate that $\alpha_w \sim 10^{-5}$, which suggests that k_w ~ 3 x 10^{-4} s^{-1} (24 m^3) or ~ 2 x 10^{-4} s^{-1} (28 m^3). This theoretical estimate is in very good agreement with the optimal k_w (= 2 x 10^{-4} s^{-1}) for the 24 m^3 chamber.

Loza et al. (18) report observations of vapor wall-loss rates for two compounds: 2,3-epoxy-1,4-butanediol (BEPOX) and glyoxal. BEPOX is the butadiene derivative of an epoxydiol of isoprene. The uptake of both compounds to the chamber walls was observed to depend strongly on RH and whether a "new" or "old" chamber was used, with the measured values ranging from ~2-7 x 10^{-5} s^{-1} (18). Such new vs. old dependence was not observed by Matsunaga and Ziemann (15), who investigated wall-losses of alkanes, alkenes, 2-ketones and 2-alcohols. This suggests that the mechanism involved in the uptake of BEPOX and glyoxal

was somewhat different than that for the hydrocarbons considered by Matsunaga and Ziemann (15), or may alternatively indicate complications associated with capturing fast initial decay during the fill period in the much larger Caltech chamber. Such fill and mixing complications likely also explain the strong differences between the wall-loss rate coefficients for 2-dodecanol determined by Loza et al. (19) and Matsunaga and Ziemann (15). Since the vapor uptake to the Teflon chamber walls is reversible, care must be taken in the interpretation of observed wall-loss rates. Only measurements made in the very early stages of uptake will correspond directly to the first-order wall-loss rate coefficient, since as the system approaches equilibrium net vapor uptake will slow. As such, we suggest that the estimates of k_w using the α from Matsunaga and Ziemann (15) may be more relevant to the current study given the nature of the compounds involved.

S1.4.1. Gas-Particle Partitioning Timescales

The timescale associated with reaching gas-particle equilibrium varies with seed *SA*, and for a distribution is approximately:

$$\tau_{g-p} \sim \left(2\pi N_p \overline{D_p} D_{gas} \bar{F}_{FS}\right)^{-1} \quad \text{(S20)}$$

where N_p is the particle number concentration, $\overline{D_p}$ is the number mean diameter, D_{gas} is the gas-phase diffusivity and $\bar{F}_{FS}$ is the correction to the mass transfer flux due to noncontinuum effects and imperfect accommodation given in Eqn. S8. Values for τ_{g-p} have been calculated for the low-NO_x experiments based on the initial seed number concentration and mean diameter as a function of α (Fig. S5), using D_{gas} = 1 x 10^{-5} m^2 s^{-1} and λ = 150 nm. The τ_{g-p} vary approximately inversely with α. The optimal α was determined to be $\alpha \sim 0.002$, corresponding to an optimal k_w = 2 x 10^{-4} s^{-1}, or a lifetime with respect to wall loss of $\tau_w = 1/k_w$ = 83 min. The τ_{g-p} for the experiment with the smallest seed concentration (1.4 x 10^3 μm^2 cm^{-3}) when α = 0.001 is 230 min, very similar to τ_w. As seed *SA* increases, the τ_{g-p} decrease to ~30 min for the highest seed *SA*. This difference in the relative values of τ_{g-p} vs. τ_w explains why the seed effect is seen most strongly when seed *SA* is less than ~ 3 x 10^3 μm^2 cm^{-3}, because this is the point at which the two timescales become highly competitive. Similarly, it

helps to explain why larger values of α do not lead to a noticeable seed *SA* dependence; when $\alpha > 0.1$ the $\tau_{g\text{-}p} = 2$ min for the experiment with the smallest seed *SA*.

S1.4.2. Dependence on VOC and OH concentrations

Calculations were performed to determine the magnitude of the wall-loss bias (R_{wall}) as a function of the initial [toluene] and [OH] based on the best-fit of the SOM to the low-NO_x set of experiments. Fig. S6 shows the variation in the end of experiment SOA concentration as a function of initial toluene and OH, and corresponds to the results shown in Fig. 3 in the main text.

S1.4.3. Sensitivity to C_w

As discussed in the main text, the sensitivity of our results to the assumed C_w is has been established by performing fits to the observations for varying values of C_w, from 0.01 to 10 mg m^{-3} for the suite of low-NO_x toluene photooxidation experiments (c.f. Fig. 4). Here, it was assumed that $k_w = 2 \times 10^{-4}$ s^{-1} and $\alpha = 2 \times 10^{-3}$, consistent with the optimized values determined in the main text. Good fits are obtained over the entire range of C_w. Above C_w = 0.2 mg m^{-3} (= 200 μg m^{-3}) the calculated wall-loss bias, R_{wall}, is constant. Below 0.2 mg m^{-3} the calculated R_{wall} falls off, reaching a second plateau at small C_w that is still above unity. The best-fit SOM parameters vary systematically with C_w (Fig. S7), apparently compensating for the varying levels of vapor wall-loss.

S1.5. Fitting of Historical Chamber Data

Beyond the toluene experiments, which are the focus of the manuscript, best-fit SOM parameters have been determined for a suite of historical photooxidation experiments conducted using a variety of other precursor compounds, both under low- and high-NO_x conditions. The historical experiments were all carried out in the prior 28 m^3 Caltech chamber. Experimental conditions are given in Tables S2 and S3. Fitting of the SOM to the observations is performed for these experiments assuming that $k_w = 1 \times 10^{-4}$ s^{-1}, $\alpha = 2 \times 10^{-3}$ and $C_w = 10$ mg m^{-3}. The results are relatively insensitive to C_w when varied over the range 2-24 mg m^{-3}, as discussed above. The value of k_w for the historical chamber is estimated to be slightly smaller than the optimal value determined for the new 24 m^3 chamber based on

411 consideration of the size-dependent particle wall-loss rates, as discussed in Section S1.4. Best
412 fit SOM parameters for low-NO_x and high-NO_x conditions are given in Table S4. Wall-loss
413 bias values were calculated in the same manner as for the toluene experiments. Experimental
414 data and simulation results are shown in Fig. S8-9.

415

416 S1.6. References

417 1. Chan AWH*, et al.* (2009) Secondary organic aerosol formation from photooxidation
418 of naphthalene and alkylnaphthalenes: implications for oxidation of intermediate
419 volatility organic compounds (IVOCs). *Atmos. Chem. Phys.* 9(9):3049-3060.

420 2. Chhabra PS, Flagan RC, & Seinfeld JH (2010) Elemental analysis of chamber organic
421 aerosol using an aerodyne high-resolution aerosol mass spectrometer. *Atmos. Chem.*
422 *Phys.* 10(9):4111-4131.

423 3. Ng NL*, et al.* (2007) Secondary organic aerosol formation from m-xylene, toluene,
424 and benzene. *Atmos. Chem. Phys.* 7(14):3909-3922.

425 4. Chhabra PS*, et al.* (2011) Elemental composition and oxidation of chamber organic
426 aerosol. *Atmos. Chem. Phys.* 11(17):8827-8845.

427 5. Loza CL*, et al.* (2012) Chemical aging of m-xylene secondary organic aerosol:
428 laboratory chamber study. *Atmos. Chem. Phys.* 12(1):151-167.

429 6. Cappa CD*, et al.* (2013) Application of the Statistical Oxidation Model (SOM) to
430 secondary organic aerosol formation from photooxidation of C12 Alkanes. *Atmos.*
431 *Chem. Phys.* 13:1591-1606.

432 7. Hildebrandt L, Donahue NM, & Pandis SN (2009) High formation of secondary
433 organic aerosol from the photo-oxidation of toluene. *Atmos. Chem. Phys*. 9(9):2973-
434 2986.

435 8. Weitkamp EA, Sage AM, Pierce JR, Donahue NM, & Robinson AL (2007) Organic
436 aerosol formation from photochemical oxidation of diesel exhaust in a smog chamber.
437 *Environmental Science & Technology* 41(20):6969-6975.

438 9. Pierce JR*, et al.* (2008) Constraining Particle Evolution from Wall Losses,
439 Coagulation, and Condensation-Evaporation in Smog-Chamber Experiments: Optimal
440 Estimation Based on Size Distribution Measurements. *Aerosol Science and*
441 *Technology* 42(12):1001-1015.

442 10. Seinfeld, J. H. and Pandis, S. N.: Atmospheric chemistry and physics: From air
443 pollution to climate change, Wiley, New Jersey, 612pp., 2006

444 11. Cappa CD & Wilson KR (2012) Multi-generation gas-phase oxidation, equilibrium
445 partitioning, and the formation and evolution of secondary organic aerosol. *Atmos.*
446 *Chem. Phys.* 12:9505-9528.

12. Lee-Taylor J, *et al.* (2011) Explicit modeling of organic chemistry and secondary organic aerosol partitioning for Mexico City and its outflow plume. *Atmospheric Chemistry and Physics* 11(24):13219-13241.

13. Pankow JF (1994) An absorption-model of the gas aerosol partitioning involved in the formation of secondary organic aerosol. *Atmos. Environ.* 28(2):189-193.

14. Shiraiwa M, *et al.* (2013) Size distribution dynamics reveal particle-phase chemistry in organic aerosol formation. *Proc. Nat. Acad. Sci.*

15. Matsunaga A & Ziemann PJ (2010) Gas-Wall Partitioning of Organic Compounds in a Teflon Film Chamber and Potential Effects on Reaction Product and Aerosol Yield Measurements. *Aerosol Sci. Technol.* 44(10):881-892.

16. McMurry PH & Grosjean D (1985) Gas and aerosol wall losses in Teflon film smog chambers. *Environ. Sci. Technol.* 19(12):1176-1182.

17. Crump JG & Seinfeld JH (1981) Turbulent deposition and gravitational sedimentation of an aerosol in a vessel of arbitrary shape. *J Aerosol Sci* 12(5):405-415.

18. Loza CL, *et al.* (2010) Characterization of Vapor Wall Loss in Laboratory Chambers. *Environ. Sci. Technol.* 44(13):5074-5078.

19. Loza CL, *et al.* (2013) Secondary organic aerosol yields of 12-carbon alkanes. *Atmos. Chem. Phys. Discuss.* 13(8):20677-20727.

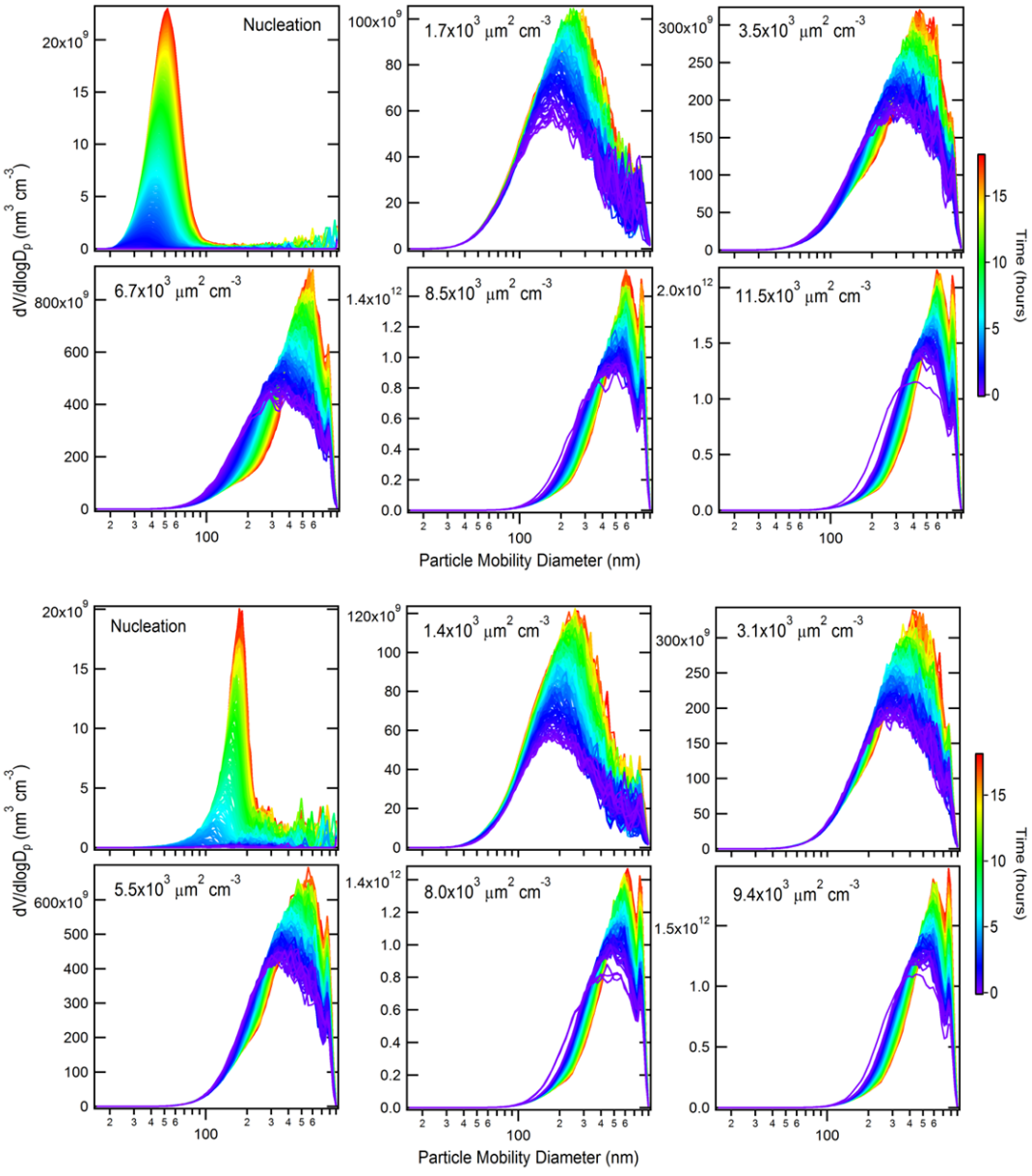

Fig. S1: Time-dependent volume distributions ($dV/dlogD_p$) of AS seed and organic aerosols after 0 - 18 h of photoxidation of toluene under (top panels) high-NO_x and (bottom panels) low-NO_x conditions. Distributions are colored according to the time after lights were turned on. The lower bound wall-loss correction is used here. For the experiments at higher seed *SA*, the influence of coagulation on the particle evolution is evident.

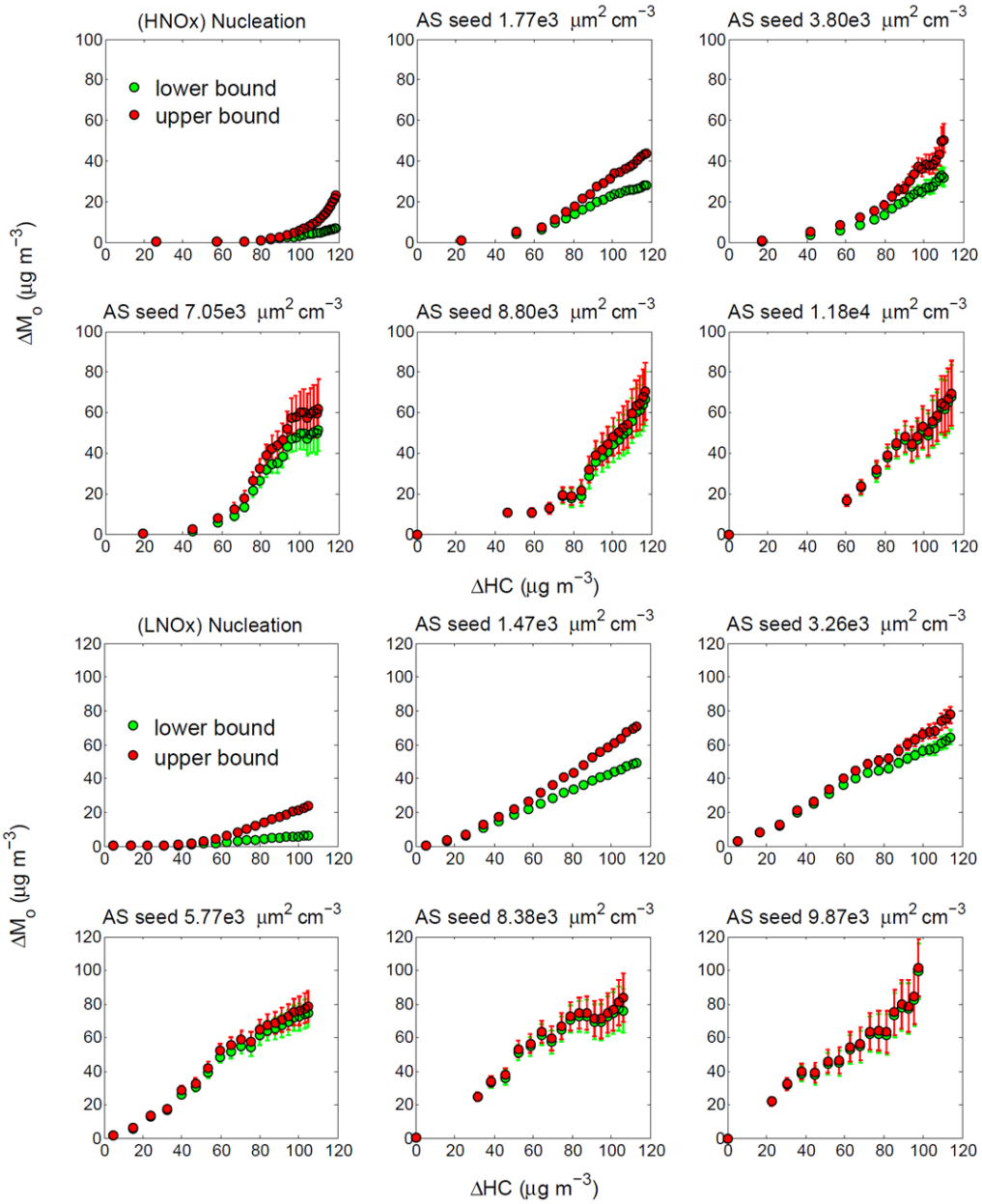

Fig. S2: Time-dependent SOA growth curves for toluene photooxidation under high-NO_x (HNO_x) and low-NO_x (LNO_x) conditions. Error bars come from the 95% confidence interval associated with determining the size-dependent first-order wall-loss rate for dry inert ammonium sulfate ($(NH_4)_2SO_4$) particles.

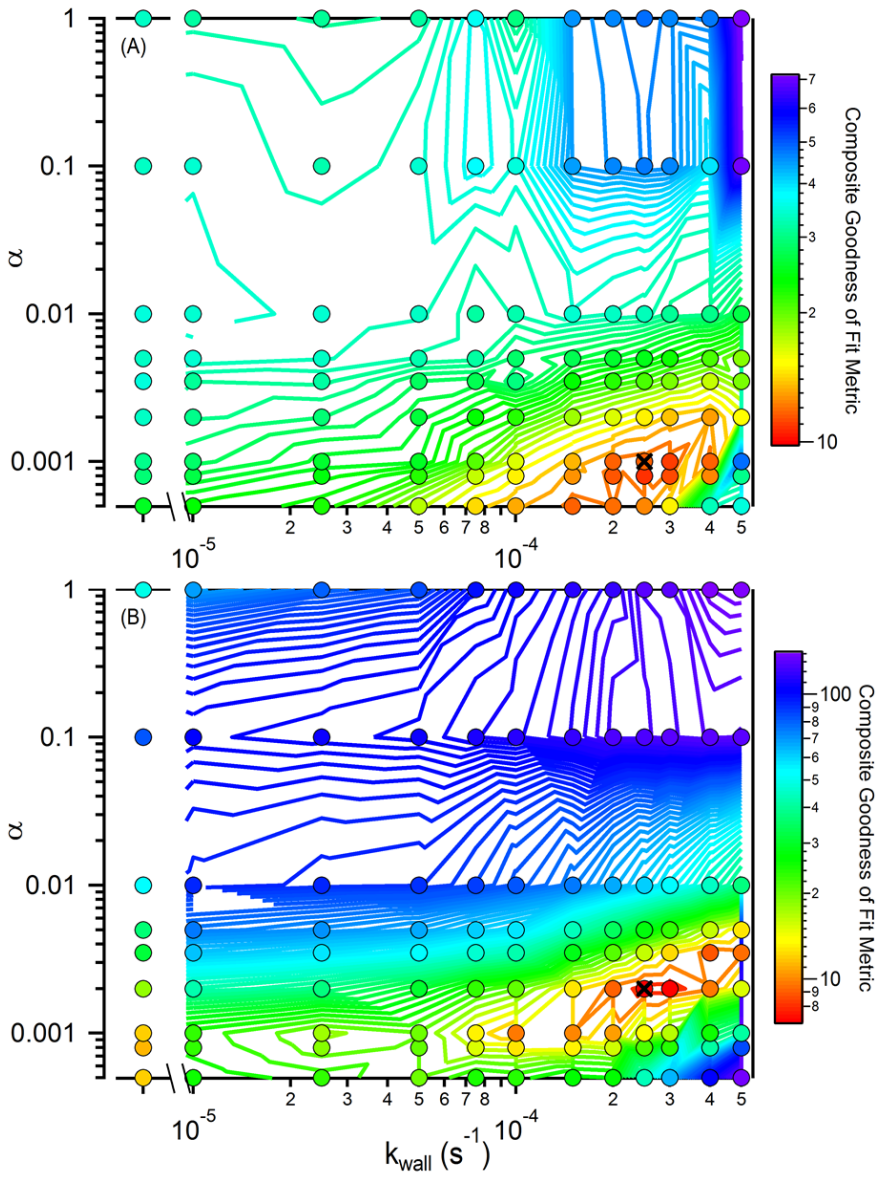

Fig. S3: Calculated composite reduced chi-square values for (A) high-NO_x and (B) low-NO_x toluene experiments as a function of the mass accommodation coefficient, α, and the first order wall-loss rate coefficient, k_w. The colors indicate the magnitude of the calculated composite reduced goodness of fit metric, with the contours based on the circles. The black x indicates the optimal value: $k_w = 2.5 \times 10^{-4}$ s^{-1} and $\alpha = 1 \times 10^{-3}$ (high-NO_x) and $k_w = 2.5 \times 10^{-4}$ s^{-1} and $\alpha = 2 \times 10^{-3}$ (low-NO_x).

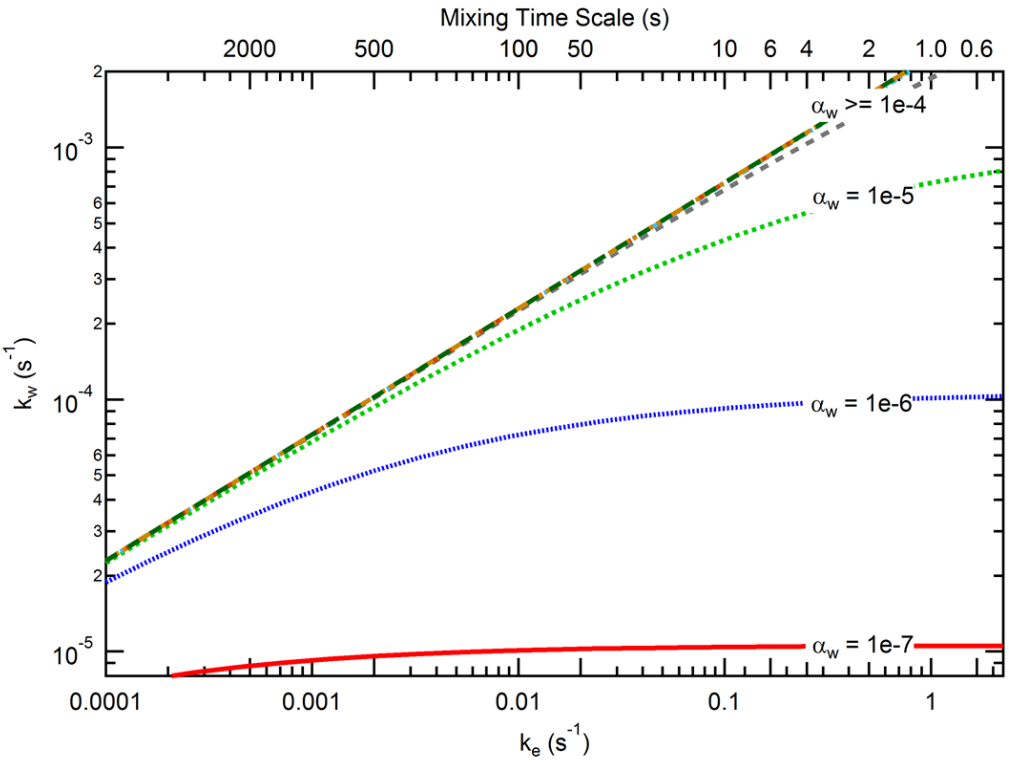

Fig. S4: Calculated wall-loss coefficients k_w as a function of the coefficient of eddy diffusion, k_e, which characterizes the state of turbulent diffusion in the chamber, for different values of the mass accommodation coefficient onto the walls, α_w. The top axis shows the time-scales corresponding to the eddy diffusion coefficients.

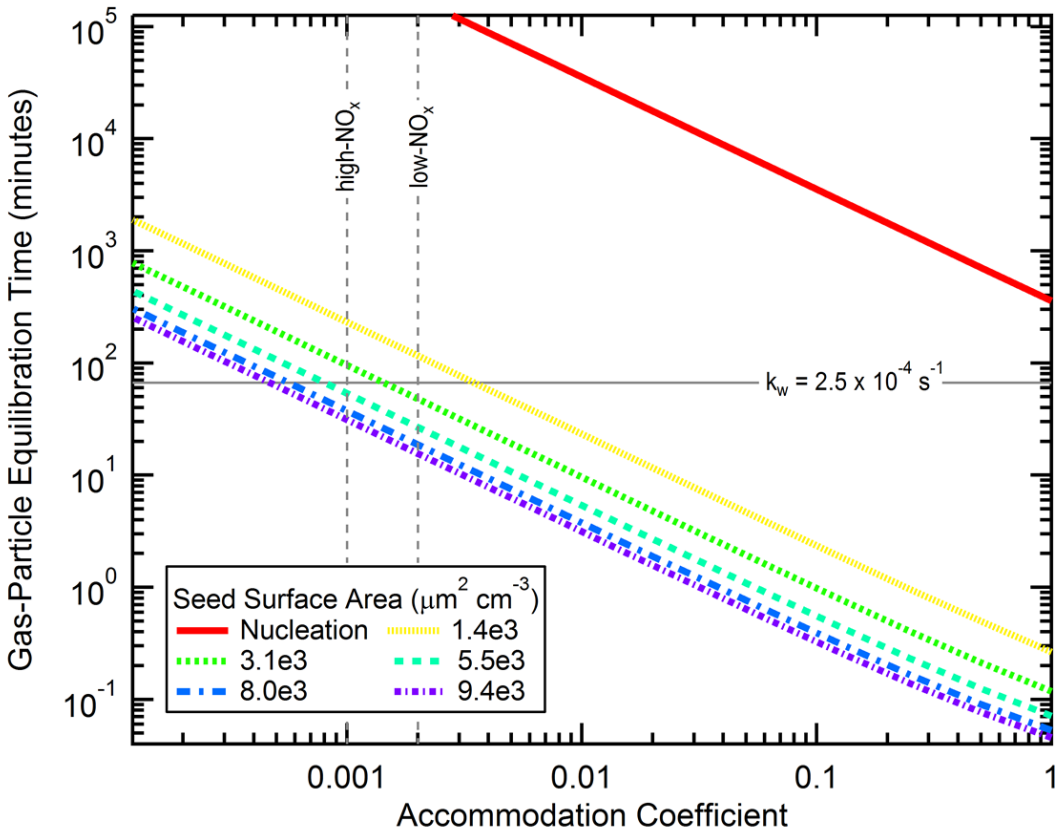

Fig. S5: Calculated gas-particle equilibration time as a function of the gas-particle mass accommodation coefficient, α, for different seed surface areas corresponding to the low-NO_x experiments. The horizontal gray line indicates the timescale associated with vapour wall-loss for k_w = 2.5 x 10^{-4} s^{-1}. The vertical dashed gray lines indicate the optimal values of α determined here for the high- and low-NO_x toluene systems. For the nucleation experiments, it is assumed that the particles are 10 nm diameter.

505

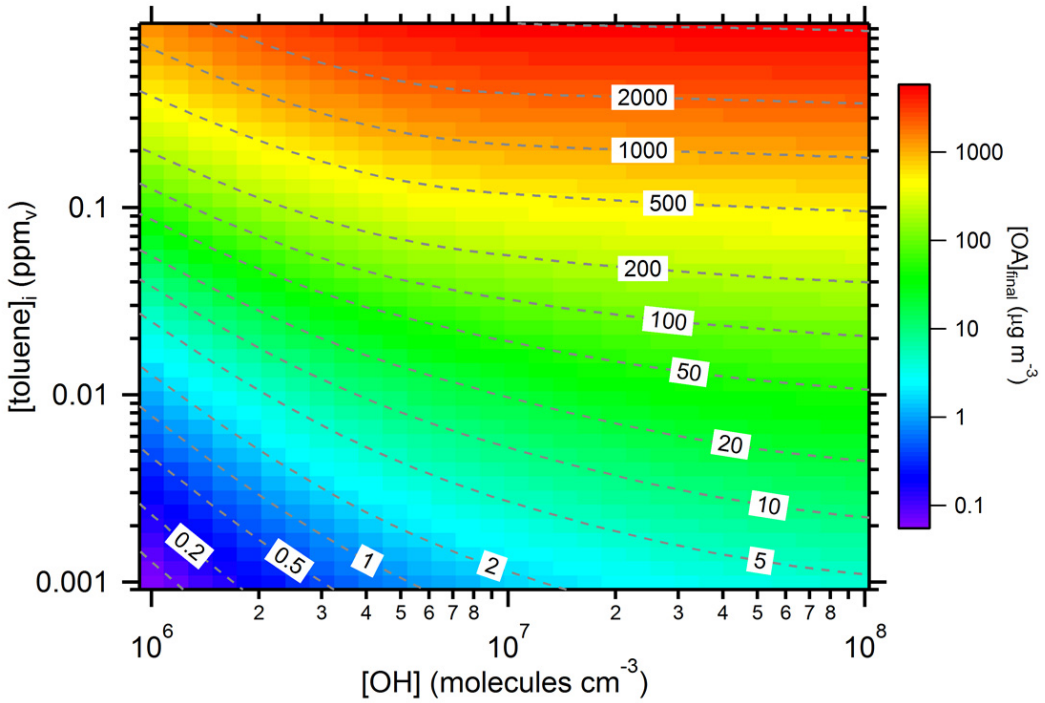

506

507 **Fig. S6:** Calculated end-of-experiment SOA mass concentrations corresponding to the results
508 shown in Figure 3. The SOA concentration is shown as a function of initial toluene
509 concentration and OH concentration when k_w = 2.5 x 10^{-4} s^{-1} and C_w = 10 mg m^{-3}. The SOA
510 concentrations for a given [toluene] and [OH] are indicated by colors and contours. Results
511 are based on the optimal fit of the SOM to the low-NO_x experiments.
512

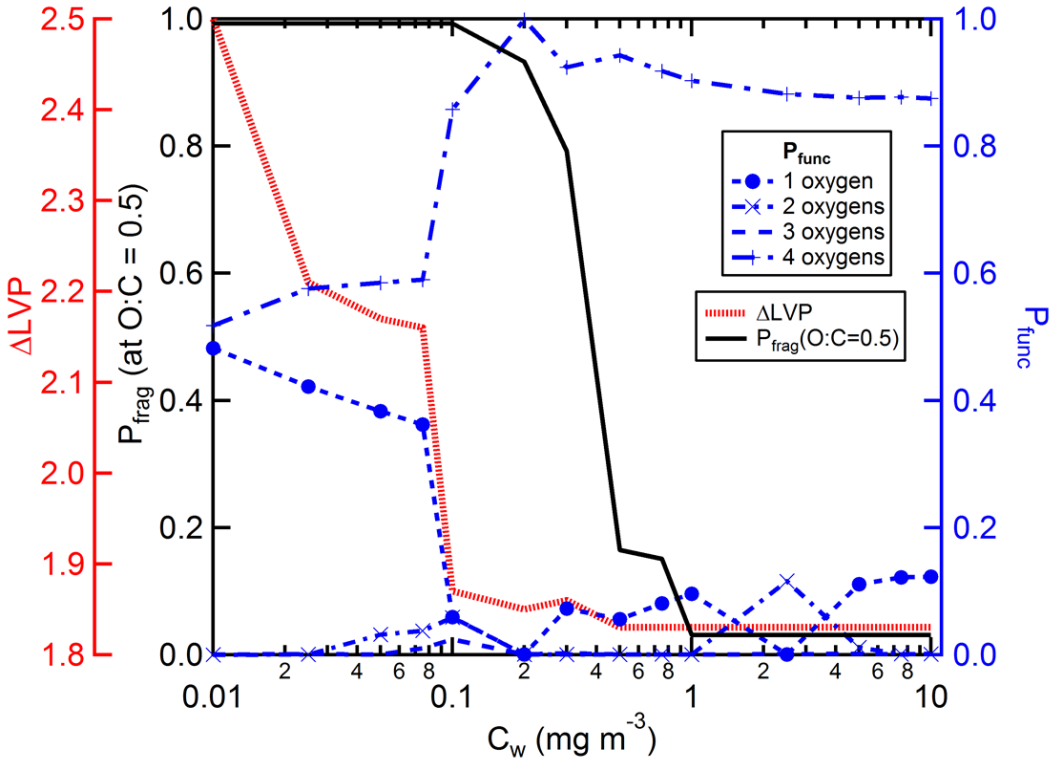

Fig. S7: The best-fit SOM parameters determined at each C_w corresponding to the results shown in Fig. 4 in the main text. The fragmentation probabilities, P_{frag}, were calculated from the best-fit m_{frag} values and Eqn. S3 using O:C = 0.5. ΔLVP corresponds to the decrease in vapor saturation concentration per oxygen added and P_{func} corresponds to the probability of adding 1, 2, 3 or 4 oxygen atoms per reaction.

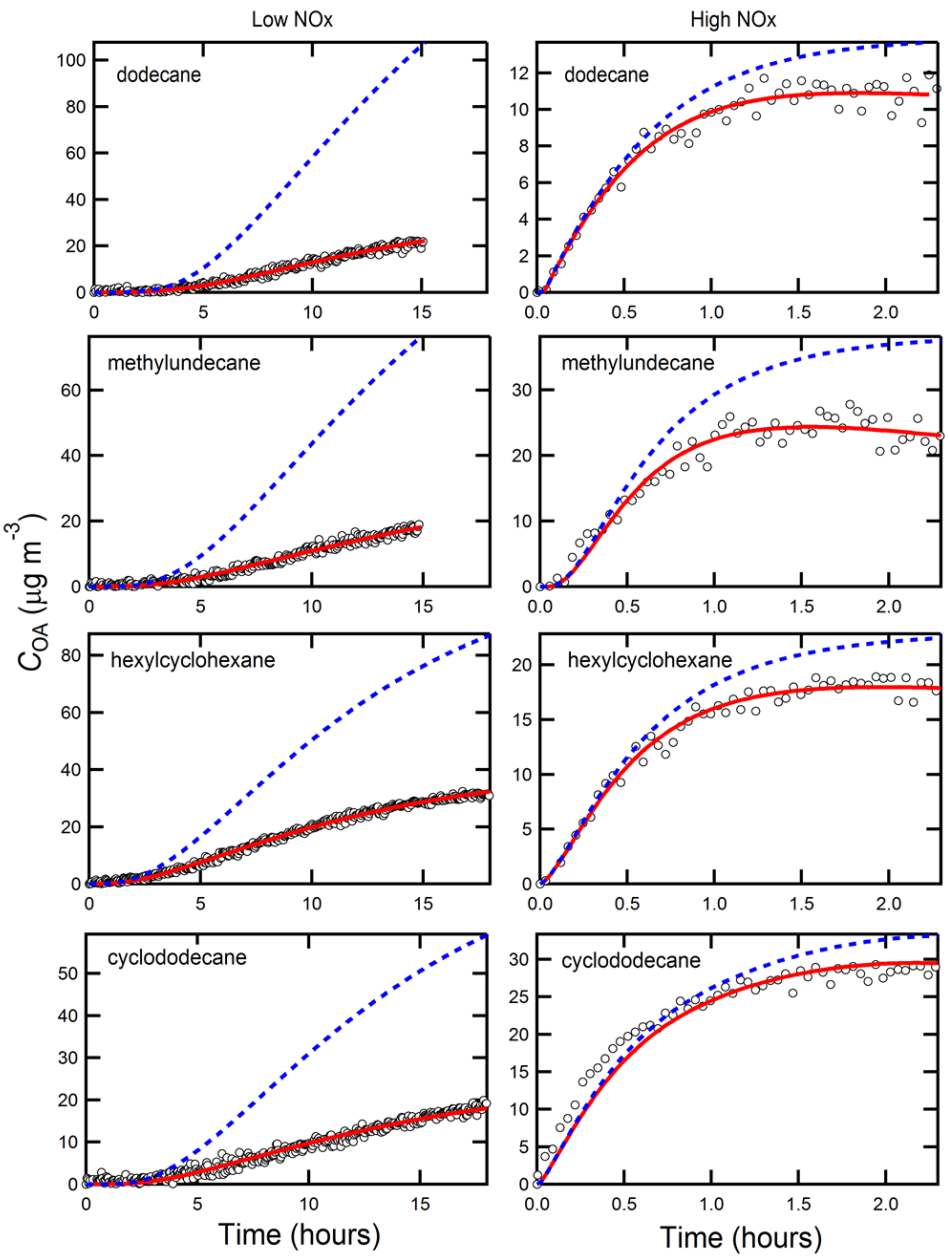

Fig. S8: Results from historical low (left panels) and high (right panels) NO_x SOA formation experiments for alkane photooxidation (open circles). The solid red lines are best-fit SOM results when wall losses are accounted for assuming that k_w = 1 x 10^{-4}, α = 1 and C_w = 10 µg m^{-3}. The blue dashed lines are the simulated SOA concentrations when wall-loss is turned off, but the SOM parameters determined from the best-fit with wall-loss on are retained.

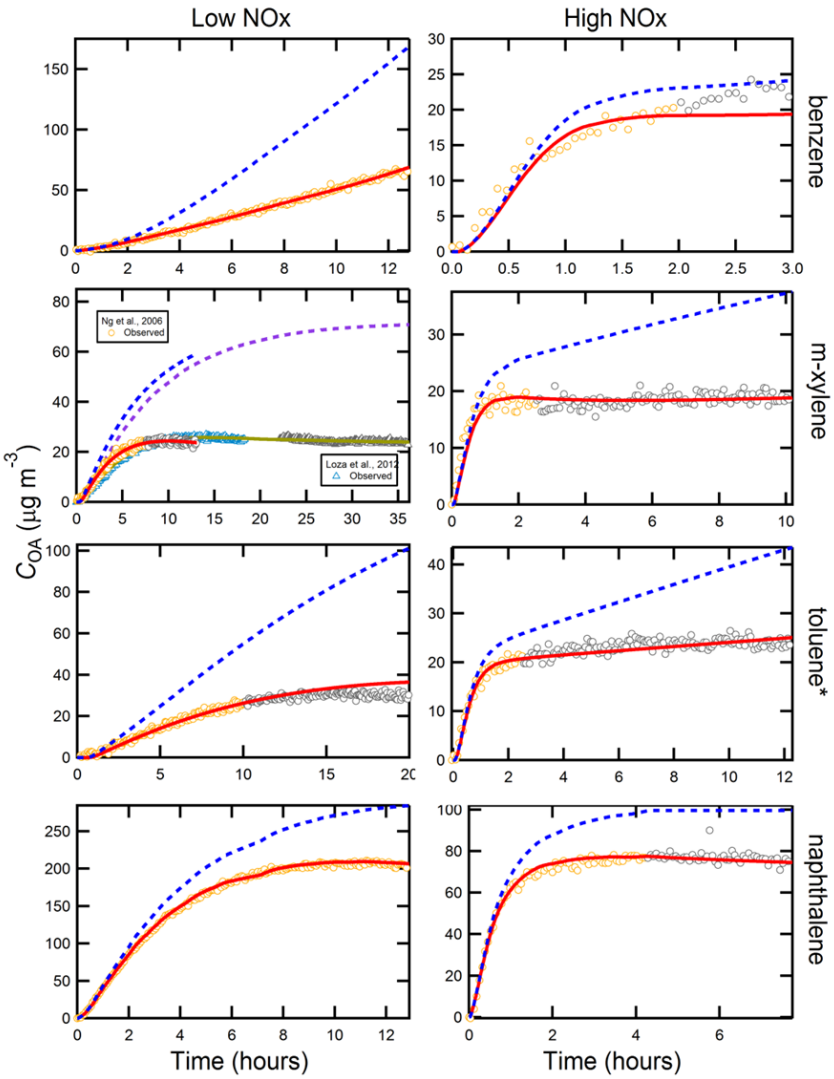

Fig. S9: Same as Fig. S3, but for aromatics. Importantly, the toluene experimental results are from Ng et al. (3), not from the current set of experiments. For each experiment, data collected over the full experiment time is shown. However, the SOM fitting has been restricted to the periods shown as colors other than gray (orange or blue). The gray points are data that were collected, but not used in fitting. These data have been excluded to be consistent with the range of data considered in Ng et al. (3) and Chan et al. (1), where 2-product fits have been performed. For m-xylene, low-NO_x, fits to data from Ng et al. (3) and Loza et al. (5) are shown separately.

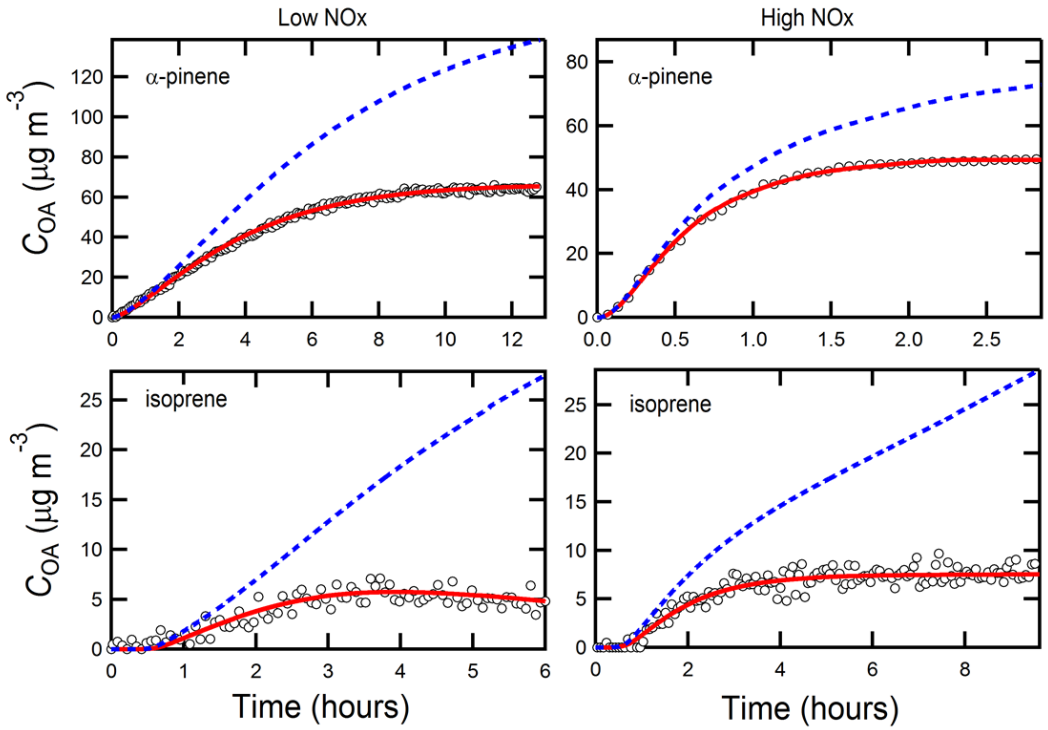

Fig. S10: Same as Fig. S8, but for α-pinene (4) and isoprene (4) photooxidation.

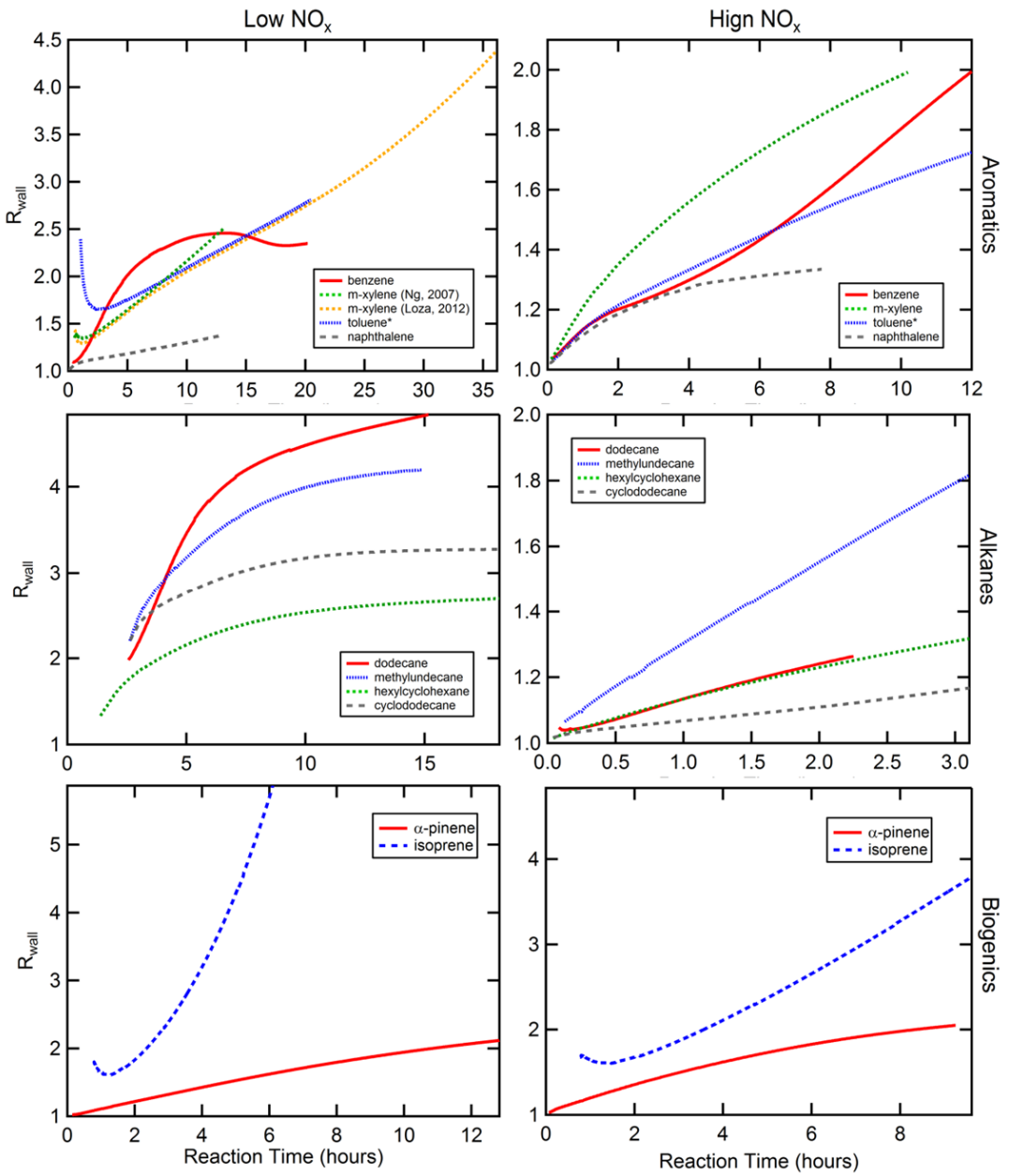

Fig. S11: Calculated time-dependent R_{wall} values for historical experiments based on the results shown in Fig. S8 - Fig. S10. Results are grouped according to species type and NO_x level. Left panels are low-NO_x and right panels high-NO_x results. Note that the toluene results in the top panels are based on data presented in Ng et al. (3), not from the current set of experiments. Results are shown for m-xylene, low-NO_x for two separate experimental data sets: Ng et al. (3) and Loza et al. (5). The presented results are limited to the period where $C_{OA} > 0.5$ µg m^{-3}.

Table S1. Experimental conditions for toluene SOA photooxidation experiments in the 24 m^3 Caltech chamber.

	Exp. (#)	$[HC]_0$ (ppb)	$[NO]_0$ (ppb)	$[NO_2]_0$ (ppb)	Initial [VOC]/[NO_x] (ppbC/ppb)	Additional NO injection	Initial seed surface area (μm^2 cm^{-3})	Initial surface area ratio (Aerosol/Wall)
High NO_x	1	~36.8	~ 19.0	~ 34.4	4.8	yes	~ 0	~ 0
	2	~38.7	~ 19.6	~ 32.2	5.2	yes	1.69×10^3	8.57×10^{-4}
	3	~37.9	~ 15.5	~ 34.9	5.3	yes	3.51×10^3	1.88×10^{-3}
	4	~37.9	~ 17.5	~ 31.7	5.4	yes	6.70×10^3	3.32×10^{-3}
	5	~38.2	~ 13.1	~ 31.5	6.0	yes	8.51×10^3	4.83×10^{-3}
	6	~38.7	~ 16.8	~ 35.3	5.2	yes	1.15×10^4	5.72×10^{-3}
Low NO_x	1	~33.9	< DL[c]	< DL	--	--	~ 0	~ 0
	2	~37.6	< DL	< DL	--	--	1.41×10^3	1.03×10^{-3}
	3	~37.3	< DL	< DL	--	--	3.10×10^3	2.13×10^{-3}
	4	~36.8	< DL	< DL	--	--	5.47×10^3	4.07×10^{-3}
	5	~38.7	< DL	< DL	--	--	7.95×10^3	5.17×10^{-3}
	6	~37.9	< DL	< DL	--	--	9.41×10^3	6.70×10^{-3}

[a] Detection limits (DL) for O_3, NO, and NO_2 are 0.5 ppb, 0.4 ppb, and 0.4 ppb, respectively.

Table S2. Conditions for low-NO_x experiments in the 28 m^3 Caltech chamber.

VOC	Ref	Date [mm/dd/yy]	$[VOC]_0$ (ppb)	$[NO_x]_0$ (ppb)	Initial $[VOC]/[NO_x]$ (ppbC/ppb)	$[OH]^a$ (molecules/cm^3)	% Yield at C_{OA} = 10 μg m^{-3}	k_{OH} (cm^3 $molecules^{-1}$ s^{-1})
n-dodecane	(6)	03/16/11	34.0	<2	--	$2.5x10^6$	6.1	$1.34x10^{-11}$
methylundecane	(6)	02/25/11	28.1	<2	--	$2.4x10^6$	7.2	$1.34x10^{-11}$
cyclododecane	(6)	02/23/11	9.8	<2	--	$2.7x10^6$	17.2	$1.34x10^{-11}$
hexylcyclohexane	(6)	03/21/11	15.6	<2	--	$3.0x10^6$	15.4	$1.34x10^{-11}$
benzene	(3)	11/04/06	414	<2	--	$3x10^6$	23.8	$1.22x10^{-12}$
toluene[c]	(3)	10/24/06	52.7	<2	--	$3.3x10^6$	26.7	$5.63x10^{-12}$
m-xylene[d]	(3)	10/27/06	19.3	<2	--	$3x10^6$	28.2	$2.31x10^{-11}$
m-xylene[d]	(5)	10/11/10	29.2	<2	--	$2.5x10^6$	21.4	$2.31x10^{-11}$
naphthalene	(1, 2)	08/13/08	31.5	2	--	$2x10^6$	19.0	$2.44x10^{-11}$
α-pinene	(4)	06/02/10	66.2	<2	--	$3x10^6$	36.8	$5.3x10^{-10}$
isoprene	(4)	02/25/09	49	<2	--	$2x10^6$	4.3[b]	$1x10^{-10}$

[a] Average over the experiment
[b] Maximum yield, since maximum C_{OA} < 10 μg m^{-3}.
[c] From historical experiments by Ng et al. (2007), not the current set of experiments.
[d] m-xylene data are available from two independent sets of experiments.

Table S3. Conditions for high-NO_x experiments in the 28 m^3 Caltech chamber.

VOC	Ref.	Date [mm/dd/yy]	$[VOC]_0$ (ppb)	$[NO]_0$ & $[NO_2]_0$ (ppb)	Initial $[VOC]/[NO_x]$ (ppbC/ppb)	$[OH]^a$ (molecules/cm^3)	% Yield at C_{OA} = 10 μg m^{-3}	k_{OH} (cm^3 $molecules^{-1}$ s^{-1})
n-dodecane	(6)	05/12/11	32.2	343/--	1.13	$4.5x10^7$	6.2	$1.34x10^{-11}$
methylundecane	(6)	03/01/11	72.4	366/--	2.37	$3.3x10^7$	5.1	$1.34x10^{-11}$
cyclododecane	(6)	05/23/11	13.8	362/--	0.46	$2.7x10^7$	38.3	$1.34x10^{-11}$
hexylcyclohexane	(6)	03/22/11	22.1	320/--	0.83	$4.1x10^7$	12.3	$1.34x10^{-11}$
benzene	(3)	01/15/07	336	83/86	11.9	$3.2x10^7$	15.6	$1.22x10^{-12}$
toluene[c]	(3)	10/14/06	138	373/568	1.03	$3.6x10^7$	8.3	$5.63x10^{-12}$
m-xylene	(3)	10/05/06	89.8	469/474	0.76	$4.2x10^7$	3.9	$2.31x10^{-11}$
naphthalene	(1, 2)	08/14/08	48.6	404/171	0.85	$2.5x10^7$	11.2	$2.44x10^{-11}$
α-pinene	(4)	06/03/10	44.9	446/398	0.53	$1.4x10^7$	9.5	$5.3x10^{-11}$
isoprene	(4)	04/04/09	268	535/402	1.43	$6.6x10^6$	1.0[b]	$1x10^{-11}$

[a] For all high-NOx experiments HONO was used as the OH source. The [OH] was not constant in time, but decreased rapidly from the start of the experiment by at least an order of magnitude. The [OH] derived from the first [VOC] measurement after the lights were turned on is given here.
[b] Maximum yield, since maximum C_{OA} < 10 μg m^{-3}.
[c] From historical experiments by Ng et al. (2007), not the current set of experiments.

Table S4. Derived SOM parameters for the experiments when vapor wall-loss is accounted for (assuming C_w = 10 μg m^{-3}).

VOC[a]	Fragmentation	ΔLVP	P1	P2	P3	P4	χ^2_{red} [b]
		Low NO_x					
toluene (this study)	5	1.83	0.123	0.001	0.002	0.875	1.74
n-dodecane (6)	0.671	1.58	0.977	0.016	0.003	0.004	1.47
methylundecane (6)	0.433	1.92	0.997	0.000	0.001	0.002	1.33
cyclododecane (6)	1.56	1.90	0.994	0.000	0.001	0.005	1.73
hexylcyclohexane (6)	0.78	1.84	0.885	0.106	0.001	0.008	0.56
benzene[c] (3)	0.01	2.29	0.284	0.000	0.644	0.072	0.42
toluene[c] (3)	0.01	1.88	0.001	0.001	0.727	0.271	1.36
m-xylene[c] (3)	0.245	1.96	0.000	0.085	0.836	0.079	0.57
m-xylene[c] (5)	0.069	1.88	0.285	0.000	0.613	0.101	0.20
naphthalene (1, 2)	0.072	1.76	0.382	0.027	0.431	0.161	0.04
α-pinene (4)	0.151	1.91	0.262	0.619	0.075	0.044	0.19
isoprene (4)	0.01	2.23	0.000	0.146	0.826	0.028	1.61
		High NO_x					
toluene (this study)	1.02	1.42	0.000	0.000	1.000	0.000	1.10
n-dodecane (6)	0.188	1.45	0.963	0.000	0.001	0.036	0.07
methylundecane (6)	0.188	1.12	0.263	0.277	0.455	0.005	0.61
cyclododecane (6)	0.01	1.69	0.664	0.002	0.004	0.33	0.64
hexylcyclohexane (6)	0.153	1.75	0.832	0.086	0.055	0.028	0.14
benzene[c] (3)	0.912	1.47	0.105	0.001	0.893	0.001	1.15
m-xylene[c] (3)	0.18	1.54	0.000	0.000	1.000	0.000	0.64
toluene[c] (3)	0.039	1.46	0.001	0.001	0.906	0.094	1.13
naphthalene[c] (1, 2)	0.64	1.41	0.835	0.001	0.002	0.162	0.17
α-pinene (4)	0.080	1.81	0.193	0.694	0.101	0.012	0.04
isoprene (4)	0.322	2.23	0.679	0.321	0.000	0.000	0.79

[a] The toluene experiments from this study were conducted in the 24 m^3 Caltech chamber (i.e. "new" experiments) and simulated using k_w = 2.5 x 10^{-4} s^{-1} and the experimentally-determined optimal α (~2 x 10^{-3}). All other experiments, including the toluene experiments from (3) were conducted in the 28 m^3 Caltech chamber (i.e. "historical" experiments") and simulated using k_w = 1 x 10^{-4} s^{-1} and α = 1.

[b] The reduced χ^2 associated with the best fit.

[c] Fits were performed over the ranges shown in Fig. S9.

Appendix E

Vapor Wall Deposition in Teflon Chambers *

*Reproduced with permission from "Vapor wall deposition in Teflon chambers" by Zhang, X., Schwantes, R. H., McVay, R. C., Lignell, H., Coggon, M. M., Flagan, R. C., and Seinfeld, J. H., *Atmospheric Chemistry and Physics*, 15, 4197–4214, doi:10.5194/acp-15-4197-2015, 2015.

Atmos. Chem. Phys., 15, 4197–4214, 2015
www.atmos-chem-phys.net/15/4197/2015/
doi:10.5194/acp-15-4197-2015

Atmospheric Chemistry and Physics
Open Access

Vapor wall deposition in Teflon chambers

X. Zhang[1], R. H. Schwantes[1], R. C. McVay[2], H. Lignell[2], M. M. Coggon[2], R. C. Flagan[1,2], and J. H. Seinfeld[1,2]

[1]Division of Engineering and Applied Science, California Institute of Technology, Pasadena, CA, USA
[2]Division of Chemistry and Chemical Engineering, California Institute of Technology, Pasadena, CA, USA

Correspondence to: J. H. Seinfeld (seinfeld@caltech.edu)

Received: 23 September 2014 – Published in Atmos. Chem. Phys. Discuss.: 24 October 2014
Revised: 7 February 2015 – Accepted: 25 March 2015 – Published: 23 April 2015

Abstract. Teflon chambers are ubiquitous in studies of atmospheric chemistry. Secondary organic aerosol (SOA) formation can be underestimated, owing to deposition of SOA-forming vapors to the chamber wall. We present here an experimental protocol and a model framework to constrain the vapor–wall interactions in Teflon chambers. We measured the wall deposition rates of 25 oxidized organic compounds generated from the photooxidation of isoprene, toluene, α-pinene, and dodecane in two chambers that had been extensively used and in two new unused chambers. We found that the extent of prior use of the chamber did not significantly affect the sorption behavior of the Teflon films. Among the 25 compounds studied, the maximum wall deposition rate is exhibited by the most highly oxygenated and least volatile compounds. By optimizing the model output to the observed vapor decay profiles, we identified that the dominant parameter governing the extent of wall deposition of a compound is its wall accommodation coefficient ($\alpha_{w,i}$), which can be correlated through its volatility with the number of carbons and oxygens in the molecule. By doing so, the wall-induced deposition rate of intermediate/semi-volatile organic vapors can be reasonably predicted based on their molecular constituency. The extent to which vapor wall deposition impacts measured SOA yields depends on the competition between uptake of organic vapors by suspended particles and the chamber wall. The timescale associated with vapor wall deposition can vary from minutes to hours depending on the value of $\alpha_{w,i}$. For volatile and intermediate volatility organic compounds (small $\alpha_{w,i}$), gas-particle partitioning will dominate wall deposition for typical particle number concentrations in chamber experiments. For compounds characterized by relatively large $\alpha_{w,i}$, vapor transport to particles is suppressed by competition with the chamber wall even with perfect particle accommodation.

1 Introduction

Understanding of the mechanism and extent of secondary organic aerosol (SOA) formation from oxidation of volatile organic compounds (VOCs) has been derived largely from experiments in Teflon chambers. Chamber-measured SOA yields (mass of SOA formed per mass of VOC reacted) have been widely parameterized into regional/global atmospheric models, and chemical mechanisms leading to SOA formation and aging have been derived based on the gas/particle-phase identification of intermediate/semi/low-volatility compounds generated in controlled chamber experiments. An unavoidable consequence of the use of an environmental chamber is interaction of vapors and particles with the chamber wall. It has been recently established that SOA formation can be substantially underestimated due to deposition of SOA-forming vapors to the chamber wall rather than growing particles (Zhang et al., 2014a).

Chamber-wall-induced decay of organic vapors was reported 30 years ago. Grosjean (1985) and McMurry and Grosjean (1985) measured wall deposition rates of several volatile organic compounds in a chamber constructed from Fluorinated ethylene propylene (FEP) Teflon film. The lifetime of the VOCs, with respect to wall deposition, was found generally to exceed ~ 15 h. Loza et al. (2010) found that deposition of the isoprene oxidation product surrogate, 2,3-epoxy-1,4-butanediol (BEPOX), and glyoxal to the FEP Teflon chamber wall is reversible on sufficiently long timescales. On the contrary, rapid reversible gas–wall partitioning of *n*-alkanes, 1-alkenes, 2-alcohols, 2-ketones, monoacids, and 1,2-diols was universally observed by Matsunaga and Ziemann (2010) and Yeh and Ziemann (2014). Following the same experimental protocol, Kokkola et al. (2014) measured that the equilibrium fractions of

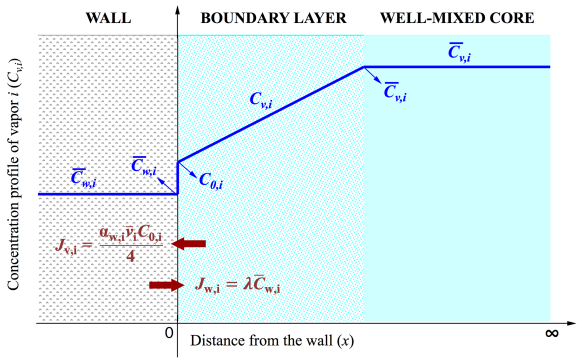

Figure 1. Theoretical framework representing the vapor–wall interactions. Concentrations of organic vapor i in the well-mixed core, in the boundary layer, over the surface of the chamber wall, and in the chamber wall are denoted by $\bar{C}_{\mathrm{v},i}$, $C_{\mathrm{v},i}$, $C_{0,i}$, $\bar{C}_{\mathrm{w},i}$, respectively. Vapor fluxes at the gas–wall interface are denoted by $J_{\mathrm{v},i}$ and $J_{\mathrm{w},i}$.

nopinone and pinanediol on the wall of a 4 m^3 FEP Teflon chamber are on average 0.4 and 0.8, respectively.

The extent to which vapors and the chamber wall interact is reflected by properties such as the gas-phase transport rate of organic molecules, affinity of the wall for various organic molecules, the degree of reversibility of the vapor–wall partitioning, and the equilibrium solubility of organic vapors in the wall. Organic materials generated in chamber experiments can deposit on the chamber wall to form a coating that can act as the primary absorbing medium, or the Teflon film itself could act as the absorbing medium, in a process akin to the sorption of small molecules by organic polymers. While measurement of vapor wall deposition rates for the thousands of organic molecules that are produced from the oxidation of SOA precursor VOCs is not presently possible, empirical expressions that represent the deposition rates of organic vapors as a function of general molecular properties would be highly useful.

A prime goal of characterizing vapor wall deposition in a chamber is to understand its impact on SOA formation and evolution. We present here an experimental protocol to constrain the nature of organic vapor wall deposition in Teflon chambers. We measured wall-induced dark decay rates of 25 intermediate/semi-volatility organic vapors, which span a range of volatilities and oxidation states, in both unused and previously used chambers constructed with FEP Teflon film. A temperature ramping program (298–318 K) was implemented to study the reversibility of vapor–wall partitioning. A model framework is developed to describe interactions between organic vapors and the chamber wall following the theories for particle wall deposition and gas-particle partitioning. We address the following questions in the present study. (1) What is the physicochemical nature of the chamber wall? (2) What are the key parameters that characterize the vapor–wall interactions and how can these values be determined? (3) How can one predict the wall deposition rate of a specific compound based on its molecular properties?

2 Vapor wall deposition – theory

Figure 1 depicts the steady-state concentration profiles of an organic compound i in the well-mixed core of the chamber ($\bar{C}_{\mathrm{v},i}$), in the boundary layer adjacent to the wall ($C_{\mathrm{v},i}$), at the wall surface ($C_{0,i}$), and in the chamber wall ($\bar{C}_{\mathrm{w},i}$). Vapor molecules in the well-mixed core of a chamber are transported through a boundary layer adjacent to the wall by a combination of molecular and turbulent diffusion. The transport rate depends on both the molecular properties of the individual organic compound (as characterized by the molecular diffusion coefficient, D_i), as well as the extent of turbulent mixing in the chamber (as characterized by the coefficient of eddy diffusion, K_{e}). As vapor molecules encounter the chamber wall, the fraction of those encounters that lead to uptake is represented by the accommodation coefficient ($\alpha_{\mathrm{w},i}$), and molecules rebound with a probability of $1-\alpha_{\mathrm{w},i}$. The accommodation coefficient depends, in principle, on the nature of the wall surface as well as the compound chemical composition. It is worth emphasizing that $\alpha_{\mathrm{w},i}$ characterizes imperfect wall accommodation of the gas–wall interface. Molecules deposited on the wall may re-evaporate at a rate that depends on their concentration in the wall. In order to represent this process, we note that, at equilibrium, the flux arriving from the gas phase ($J_{\mathrm{v},i}$) and the evaporation flux from the wall ($J_{\mathrm{w},i}$) are equal. Thus, the evaporative flux from the wall ($J_{\mathrm{w},i}$) can be expressed as a function of the accommodation coefficient ($\alpha_{\mathrm{w},i}$), as described in Eqs. (7)–(9) later.

A conservation balance on $\bar{C}_{\mathrm{v},i}$, the concentration of vapor i in the well-mixed core of a chamber that is subject only to the deposition process, is given by

$$\frac{d\bar{C}_{\mathrm{v},i}}{\mathrm{d}t} = -k_{\mathrm{w,depo},i}\bar{C}_{\mathrm{v},i} + k_{\mathrm{w,evap},i}\bar{C}_{\mathrm{w},i}, \quad (1)$$

where $k_{\mathrm{w,depo},i}$ (s^{-1}) is the deposition rate coefficient to the wall, $k_{\mathrm{w,evap},i}$ (s^{-1}) is the evaporation rate coefficient from the wall, and $\bar{C}_{\mathrm{w},i}$ is the concentration of vapor i that has accumulated on the chamber wall. The dynamic behavior of $\bar{C}_{\mathrm{w},i}$ is described by a corresponding balance:

$$\frac{d\bar{C}_{\mathrm{w},i}}{\mathrm{d}t} = -k_{\mathrm{w,evap},i}\bar{C}_{\mathrm{w},i} + k_{\mathrm{w,depo},i}\bar{C}_{\mathrm{v},i}\,. \quad (2)$$

Note that $\bar{C}_{\mathrm{w},i}$ is assumed to be zero at the onset of vapor i generation, ultimately reaching equilibrium with $\bar{C}_{\mathrm{v},i}$.

2.1 Vapor flux arriving from the gas phase ($J_{\mathrm{v},i}$)

For a chamber that is relatively well mixed, transport to the wall occurs by molecular and turbulent diffusion across a thin boundary layer, of thickness δ, adjacent to the chamber wall.

The flux due to molecular diffusion is given by $-D_i \nabla C_{\mathrm{v},i}$, where $C_{\mathrm{v},i}$ is the local vapor i concentration in the boundary layer and D_i is its molecular diffusivity. The turbulent diffusion flux is expressed as $-D_\mathrm{e} \nabla C_{\mathrm{v},i}$, where D_e is the eddy diffusivity. One can invoke the Prandtl mixing length expression near a wall, $D_\mathrm{e} = K_\mathrm{e} x^2$, where x is the distance from the wall, and K_e is the coefficient of eddy diffusion (Corner and Pendlebury, 1951; Crump and Seinfeld, 1981). Owing to the small value of δ, a quasi-steady state condition exists in the boundary layer, and the concentration of vapor i within the boundary layer, $0 \le x \le \delta$, is governed by

$$\frac{d}{\mathrm{d}x}\left[(K_\mathrm{e}x^2 + D_i)\frac{dC_{\mathrm{v},i}}{\mathrm{d}x}\right] = 0. \tag{3}$$

Introducing the dimensionless variable z by setting $x = (D_i/K_\mathrm{e})^{1/2} z$, Eq. (3) becomes

$$\left(z^2+1\right)\frac{d^2 C_{\mathrm{v},i}}{\mathrm{d}z^2} + 2z\frac{\mathrm{d}C_{\mathrm{v},i}}{\mathrm{d}z} = 0, \tag{4}$$

subject to the boundary conditions,

$$x = 0 (z = 0) \rightarrow C_{\mathrm{v},i} = C_{0,i},$$

$$x = \delta (z = (K_\mathrm{e}/D_i)^{1/2}\delta) \rightarrow C_{\mathrm{v},i} = \bar{C}_{\mathrm{v},i},$$

where $C_{0,i}$ and $\bar{C}_{\mathrm{v},i}$ are concentrations of vapor i over the wall surface and in the well-mixed core of the chamber, respectively. Note that the accommodation coefficient for particles on the wall was assumed to be unity in previous theoretical studies (e.g., Crump and Seinfeld, 1981; McMurry and Grosjean, 1985), meaning that particles that encounter the wall will lead to 100 % uptake. This assumption is reasonable, especially if particles are in a quasi-liquid state. On the other hand, the accommodation coefficient for vapors on the wall ($\alpha_{\mathrm{w},i}$) is likely less than unity, and the steady-state concentration is then nonzero at the chamber wall surface. The solution of Eq. (4) expressed in the original variables is

$$\begin{aligned} C_{\mathrm{v},i} &= C_{0,i} + (\bar{C}_{\mathrm{v},i} - C_{0,i})\frac{\tan^{-1}\left[(K_\mathrm{e}/D_i)^{1/2}x\right]}{\tan^{-1}\left[(K_\mathrm{e}/D_i)^{1/2}\delta\right]} \\ &\approx C_{0,i} + (\bar{C}_{\mathrm{v},i} - C_{0,i})\frac{\tan^{-1}\left[(K_\mathrm{e}/D_i)^{1/2}x\right]}{\pi/2}. \end{aligned} \tag{5}$$

Physically, turbulent diffusion dominates molecular diffusion at the outer edge of the boundary layer, so that $(K_\mathrm{e}/D_i)^{1/2}\delta \gg 1$.

The vapor flux arriving from the gas phase to the wall surface ($J_{\mathrm{v},i}$) is derived from the kinetic theory of gases:

$$J_{\mathrm{v},i} = \frac{\alpha_{\mathrm{w},i}\bar{v}_i C_{0,i}}{4}, \tag{6}$$

where $\bar{v}_i$ is the species mean thermal speed.

2.2 Vapor flux leaving from the wall due to evaporation ($J_{\mathrm{w},i}$)

Without loss of generality, vapor wall deposition can be assumed to be reversible. The flux of molecules i that evaporate from the wall back to the gas phase ($J_{\mathrm{w},i}$) depends on the concentration of i in the wall ($\bar{C}_{\mathrm{w},i}$). So we can write $J_{\mathrm{w},i}$ as a function of $\bar{C}_{\mathrm{w},i}$:

$$J_{\mathrm{w},i} \propto \bar{C}_{\mathrm{w},i} \text{ or } J_{\mathrm{w},i} = \lambda \bar{C}_{\mathrm{w},i}, \tag{7}$$

where λ is simply a quantity that reflects the positive correlation between $J_{\mathrm{w},i}$ and $\bar{C}_{\mathrm{w},i}$. If the gas and wall phases are at equilibrium, then

$$J_{\mathrm{v},i,(\mathrm{eq})} = J_{\mathrm{w},i,(\mathrm{eq})}. \tag{8}$$

Therefore,

$$\lambda = \frac{\alpha_{\mathrm{w},i}\bar{v}_i C_{0,\mathrm{i,eq}}}{4\bar{C}_{\mathrm{w},i,\mathrm{eq}}} = \frac{\alpha_{\mathrm{w},i}\bar{v}_i}{4H_i}, \tag{9}$$

where H_i is the Henry's law constant of organic species i. Substitution of Eq. (9) into Eq. (7) gives

$$J_{\mathrm{w},i} = \frac{\alpha_{\mathrm{w},i}\bar{v}_i \bar{C}_{\mathrm{w},i}}{4H_i}. \tag{10}$$

If applying vapor–particle partitioning theory here, Eq. (10) can be rewritten as

$$J_{\mathrm{w},i} = \frac{\alpha_{\mathrm{w},i}\bar{v}_i \bar{C}_{\mathrm{w},i}}{4K_{\mathrm{w},i}C_\mathrm{w}}, \tag{11}$$

where $K_{\mathrm{w},i}$ is vapor–wall partition coefficient (Matsunaga and Ziemann, 2010):

$$K_{\mathrm{w},i} = \frac{RT}{p^0_{\mathrm{L},i}\gamma_i \bar{M}_\mathrm{w}}, \tag{12}$$

and where $p^0_{\mathrm{L},i}$ is the vapor pressure of compound i as a liquid. We calculate $p^0_{\mathrm{L},i}$ by the average of two group contribution methods, "SIMPOL.1" developed by Pankow and Asher (2008) and "EVAPORATION" developed by Compernolle et al. (2011). γ_i, the activity coefficient in the wall layer on a mole fraction basis, is assumed to be unity here, R is the gas constant, T is temperature, and $\bar{M}_\mathrm{w}$ is the average molecular weight of the absorbing organic material on the wall, which, following Matsunaga and Ziemann (2010), is assumed to be $250\,\mathrm{g\,mol^{-1}}$. C_w ($\mathrm{g\,m^{-3}}$) is an assumed equivalent mass of absorbing organic material on the chamber wall (Matsunaga and Ziemann, 2010). It can be regarded as characterizing the equilibrium solubility of individual organic molecules in FEP Teflon polymer and, possibly, in other organic materials deposited on the wall. When $C_\mathrm{w} \rightarrow \infty$, the wall presents essentially an absorbing medium of infinite extent, and vapor wall deposition is ultimately an irreversible process. Note,

however, that the concept of an "equivalent absorbing organic mass" does not necessarily imply that an actual layer of organic material exists on the chamber wall. C_w might well represent the accumulation of deposited organic material from previous chamber experiments, or it could reflect the absorption properties of FEP film itself. We will return to the nature of C_w shortly.

Since the gas–wall interface is presumed to have no thickness, the net flux across the interface results from the concentration gradient,

$$D_i \left.\frac{dC_{v,i}}{dx}\right|_{x=0} = J_{v,i} - J_{w,i} = \frac{\alpha_{w,i}\bar{v}_i C_{0,i}}{4} - \frac{\alpha_{w,i}\bar{v}_i \bar{C}_{w,i}}{4K_{w,i}C_w}. \quad (13)$$

Note that when equilibrium is established, the net flux becomes zero and the concentration gradient no longer exists at the gas–wall interface. The LHS of Eq. (13) is based on Fick's law of diffusion and leads to Eq. (5). In this way, the quantity $C_{0,i}$ is expressed as a function of $\bar{C}_{v,i}$ and $\bar{C}_{w,i}$. Therefore, the conservation equation for the change in the concentration of vapor i in the well-mixed core of the chamber owing to wall deposition is given by

$$\frac{d\bar{C}_{v,i}}{dt} = \left(\frac{A}{V}\right)\left(\frac{\alpha_{w,i}\bar{v}_i/4}{\pi\alpha_{w,i}\bar{v}_i/8(D_i K_e)^{1/2}+1}\right)\left(\frac{\bar{C}_{w,i}}{K_{w,i}C_w} - \bar{C}_{v,i}\right), \quad (14)$$

where A and V are the surface area and volume of the chamber, respectively. A rewrite of Eq. (14) gives

$$k_{w,depo,i} = \left(\frac{A}{V}\right)\left(\frac{\alpha_{w,i}\bar{v}_i/4}{\pi\alpha_{w,i}\bar{v}_i/8(D_i K_e)^{1/2}+1}\right), \quad (15a)$$

$$k_{w,evap,i} = \frac{k_{w,depo,i}}{K_{w,i}C_w}. \quad (15b)$$

3 Vapor wall deposition – experiment

Experiments were conducted in the Caltech dual 24 m^3 Fluorinated ethylene propylene (FEP) Teflon chambers that are suitable for pristine (low-NO) and polluted (high-NO) conditions (Zhang and Seinfeld, 2013; Fahnestock et al., 2014; Loza et al., 2014). Figure 2 shows a schematic of the experimental protocol used to measure deposition of organic vapors to the chamber wall. Oxidized organic vapors were generated via photooxidation of four parent VOCs, isoprene, toluene, α-pinene, and dodecane, in the absence of seed aerosol. Once a sufficient amount of oxidized products is formed with none or limited aerosol formation via nucleation, irradiation is ceased, and the ensuing wall-induced dark decay of the array of oxidation products is monitored by chemical ionization mass spectrometry (CIMS). Following this period, the chambers were heated to investigate the extent to which vapor–wall partitioning is reversible. These experiments were carried out in two chambers that had been used in past SOA

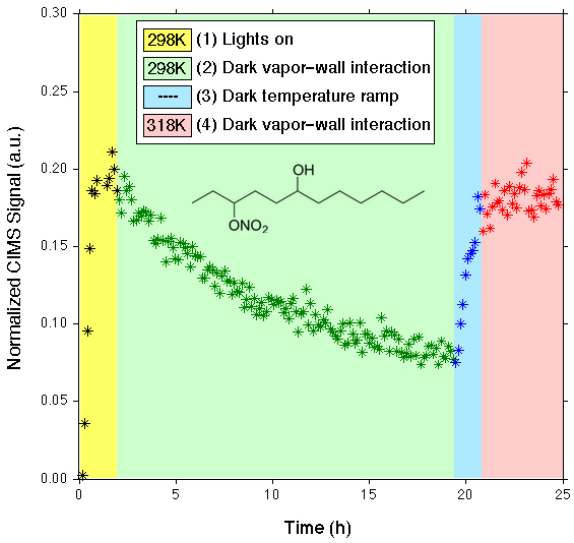

Figure 2. Example of the experimental procedure to assess vapor wall deposition using 3-nitrooxy-6-dodecanol ($m/z = (-)332$): period (1) organic oxidation product generation; period (2) vapor wall deposition at 298 K in the dark; period (3) chamber temperature ramp from 298 to 318 K; and Period (4) temperature held at 318 K in the dark.

studies. Two control experiments were also conducted in two unused 24 m^3 Teflon chambers using identical experimental protocols, see Table 1.

Vapor molecules representing SOA products were generated directly via VOC photooxidation, as opposed to the external injection of commercially available chemical standards. In this manner, uncertainty in the initial vapor concentration due to filling and mixing is avoided. In order to generate a spectrum of oxidized compounds characterized by a combination of different carbon numbers and types of functional groups, isoprene, toluene, α-pinene, and dodecane were chosen as the parent VOCs. Prior to each experiment, the Teflon chambers were flushed with purified dry air for 12 h at 45 °C, then "conditioned" by UV irradiation for 24 h in the presence of 2 ppm H_2O_2, followed by purging with purified dry air for $\sim$ 4 days at 25 °C. Experiments were carried out under conditions in which the peroxy radicals formed from the initial OH reaction with the parent hydrocarbon react either primarily with NO (so-called high-NO) or HO_2 and RO_2 (so-called low-NO). For low-NO conditions, hydrogen peroxide (H_2O_2) was used as the OH source by evaporating 120 µL of 50 % wt aqueous solution into the chamber with 5 L min^{-1} of purified air for $\sim$ 110 min, resulting in an approximate starting H_2O_2 mixing ratio of 2.0 ppm. For high-NO conditions, nitrous acid (HONO) was used as the OH source by dropwise addition of 15 mL of 1 wt% $NaNO_2$ into 30 mL of 10 wt% H_2SO_4 in a glass bulb and introduced into the chambers with 5 L min^{-1} of purified air

Table 1. Experimental conditions for production of oxidized organic vapors.

	Exp.#	Lights on (h)	Lights off (h)	T program[a] (K [h–h])	OH source	VOC	HC_0 (ppb)	$(NO)_0$ (ppb)	$(NO_2)_0$ (ppb)	Maximum Particle conc. ($\mu g\,m^{-3}$)	FEP Bag condition
high-NO	1	∼ 1	∼ 24.2	298 [0–17.6] 318 [19.9–25.2]	HONO	α-pinene	∼ 30	242	458	∼ 0.4	used
	2	∼ 1	∼ 24.2	298 [0–17.6] 318 [19.9–25.2]	HONO	α-pinene	∼ 30	229	371	∼ 0.3	unused
	3	∼ 1	∼ 23.8	298 [0–17.3] 318 [20.9–24.8]	HONO	dodecane	∼ 50	275	556	∼ 2.1	used
	4	∼ 2	∼ 23	298 [0–17.3] 318 [20.8–25]	HONO	isoprene	∼ 200	243	460	∼ 0.2	used
low-NO	5	∼ 1	∼ 24.2	298 [0–17.8] 318 [20.3–25.2]	H_2O_2	α-pinene	∼ 30	< DL	< DL	∼ 1.2	used
	6	∼ 1	∼ 24.2	298 [0–17.8] 318 [20.3–25.2]	H_2O_2	α-pinene	∼ 30	< DL	< DL	∼ 1.1	unused
	7	∼ 7	∼ 21.6	298 [0–20.6] 318 [22–28.6]	H_2O_2	dodecane	∼ 50	< DL	< DL	∼ 0.0	used
	8	∼ 5	∼ 24.7	298 [0–21.3] 318 [24.7–29.7]	H_2O_2	toluene	∼ 100	< DL	< DL	∼ 0.1	used

[a] The temperature is controlled at 298 K for the first ∼ 20 h of the experiment, including ∼ 1–7 h irradiation and ∼ 13–16 h darkness, and then ramped up to 318 K within ∼ 3 h and held for ∼ 4–6 h.

for ∼ 40 min. Ozone formation is substantially limited in the presence of a high concentration of HONO, and NO_3 formation is negligible. A measured volume of hydrocarbon (isoprene/toluene/α-pinene/dodecane) was injected via a syringe into a glass bulb, which was connected to the Teflon chamber. Heated 5 L min^{-1} of purified air flowed through the glass bulb into the chamber for 20 min, introducing 25–200 ppb of hydrocarbon into the chamber. After ∼ 60 min mixing, photooxidation was initiated by irradiating the chamber with black lights with output wavelength ranging from 300 to 400 nm. Over the course of the irradiation period, the maximum particle mass concentration formed via nucleation ranged from 0.3 to 2 $\mu g\,m^{-3}$, corresponding to a particle surface area to chamber wall area ratio of $< 10^{-5}$. Under these conditions, the surface area of particles present in the chamber is sufficiently low that partitioning of organic vapors onto particles is negligible. After ∼ 1–7 h of reaction, UV lights were turned off and the decay of oxidation products due to wall deposition was monitored for ∼ 13–16 h at 25 °C. The chamber temperature was then ramped up to 45 °C during the remaining ∼ 4–6 h of the experiment with other conditions held constant.

Gas-phase organic compounds were monitored using a custom-modified Varian 1200 triple-quadrupole CIMS (Crounse et al., 2006; Paulot et al., 2009). In negative-mode operation, CF_3O^- was used as the reagent ion to cluster with analytes [R] with strong fluorine affinity such as hydroperoxide, producing $[R{\bullet}CF_3O]^-$ or $m/z = [M + 85]^-$, where M is the molecular weight of the analyte. For more strongly acidic species [X], the transfer product, $[X_{[H]}{\bullet}HF]^-$ or $m/z = [M+19]^-$, is formed during ionization. Carboxylic acids tend to have contributions to both the transfer and cluster products, in which case the trace with higher signal-to-noise ratio is considered. Prior to each experiment, the purified air in the chamber was sampled, and this is subtracted off as the CIMS background signal. The background signal is fairly consistent between the masses and over time. However, this background subtraction does not guarantee that the background for every m/z signal is absolutely zero, as noted in Fig. 3 that the CIMS background for certain ions is hovering around zero. Identification of products by CIMS from the photooxidation of isoprene, α-pinene, and dodecane in our laboratory has been previously reported (Paulot et al., 2009; Eddingsaas et al., 2012; Yee et al., 2012; Zhang et al., 2014b).

4 Absorbing organic mass on the chamber wall (C_w)

Figure 3 shows the continuous dark decay of the 25 organic vapors generated from the photooxidation of isoprene, toluene, α-pinene, and dodecane under high/low-NO conditions. In contrast to the behavior in Fig. 3, Matsunaga and Ziemann (2010) and Yeh and Ziemann (2014) observed rapid equilibrium established within less than an hour for vapor wall losses of n-alkanes, 1-alkenes, 2-alcohols, 2-ketones, monoacids, and 1,2-diols in both 1.7 and 5.9 m^3 Teflon chambers. The organic vapor generation period in the present study ranges from 1 to 7 h, thus precluding the possibility of observing more rapid partitioning that may have occurred. In view of this, we carried out one vapor wall deposition experiment in the α-pinene+OH low-NO system, with the

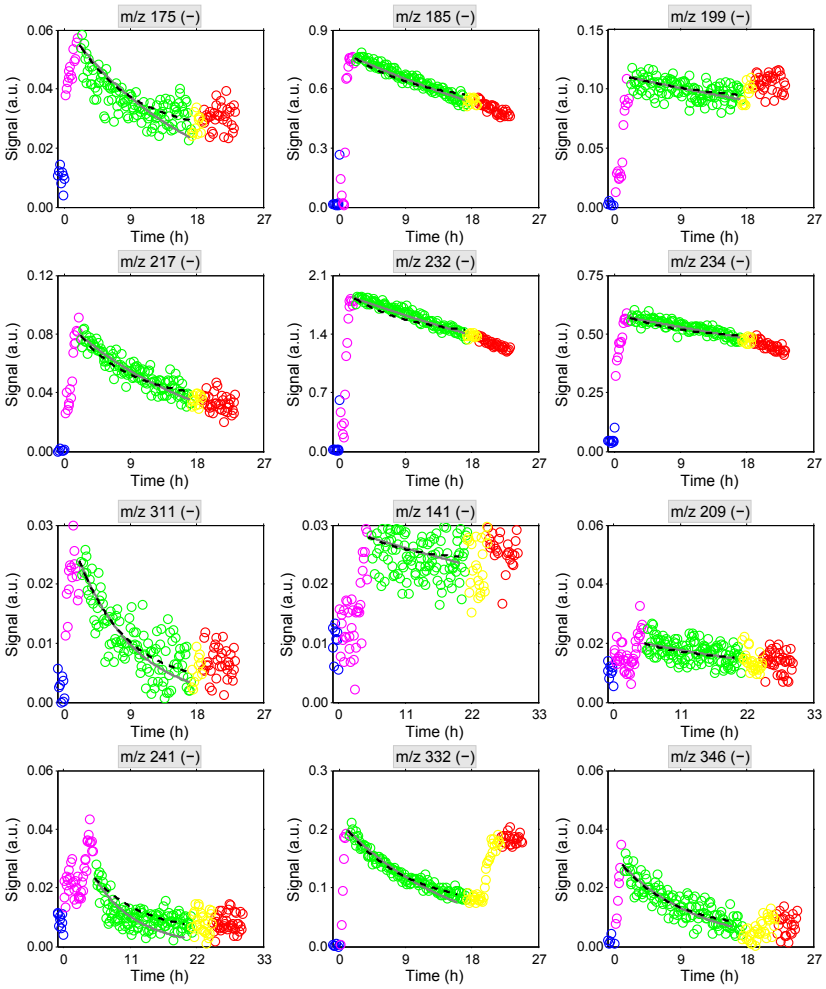

Figure 3.

experimental procedures identical to those in Sect. 3, but with lights on for only 10 min. We also increased the initial mixing ratios of α-pinene and OH radical precursor H_2O_2 to 1 and 4 ppm, respectively, in order to generate sufficient organic vapor CIMS signals during the short irradiation period. Prompt formation of two ions, m/z 269 (–) and m/z 285 (–), was observed on the CIMS after 10 min of photochemistry. These are assigned to be two first-generation products, pinonic acid ($C_{10}H_{16}O_3$) and pinonic peroxy acid ($C_{10}H_{16}O_4$), respectively (see Table 2 for the proposed chemical structures). Owing to the short photochemical reaction timescale, the other four possible products in Table 2 were not found in this experiment. Figure 3 (bottom panel) shows the wall induced dark decay of m/z 269 (–) and m/z 285 (–) at 298 K. The best-fit first-order decay rates lie within the same order of magnitude as those reported in Table 2, i.e., $7.61 \times 10^{-6}\,s^{-1}$ vs. $8.95 \times 10^{-6}\,s^{-1}$ for m/z 269 (–) and $1.67 \times 10^{-6}\,s^{-1}$ vs. $2.98 \times 10^{-6}\,s^{-1}$ for m/z 285 (–). No rapid vapor wall loss was found immediately after lights off, and the deposition rates for both ions were pretty consistent over the course of $\sim$ 15 h dark decay. Note that m/z 285 (–), although having a higher molecular weight, decays more slowly than m/z 269 (–). We will demonstrate later that the wall-induced decay rate depends inversely on the vapor pressure, which is a function of the molecule size and functionalities. The addition of a carboxylic acid group, as in m/z 269 (–), leads to a greater decrease in volatility than that resulting from the addition of a peroxy carboxylic acid group, as in m/z 285 (–). Our observations for these two compounds are consistent with the observed behavior of the other 23 compounds. There are three considerations regarding equipment setup and experimental protocol that potentially contribute to the differences between the present study and Ziemann and co-worker's work: (1) chamber size and depletion rate; (2) mixing status, i.e.,

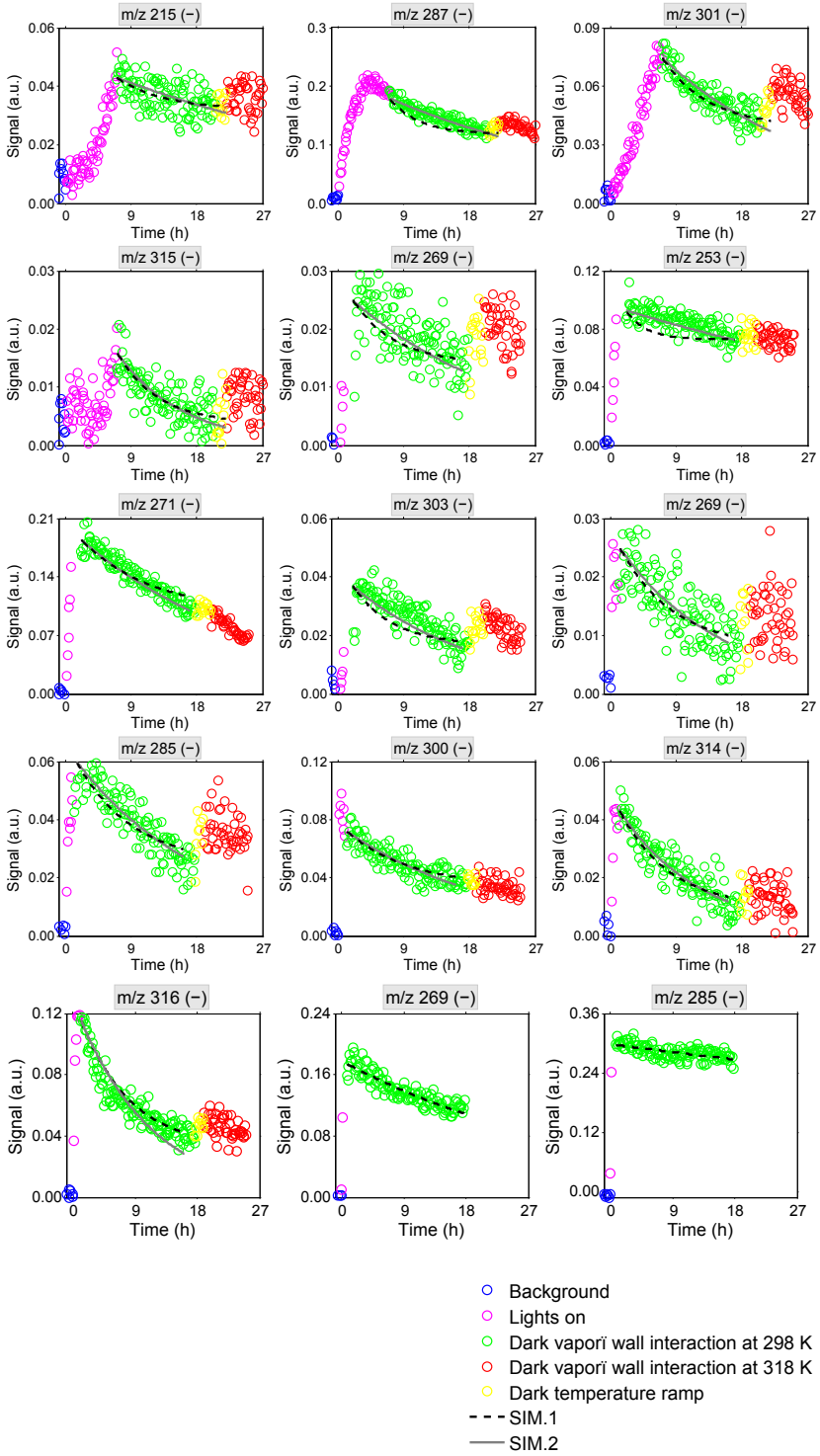

Figure 3. CIMS traces of oxidized organic vapors generated from the photooxidation of isoprene, toluene, α-pinene and dodecane under high/low-NO conditions over the four chamber periods in Fig. 2. Colored circles represent CIMS measured normalized signals during background (blue), vapor generation (magenta), vapor wall deposition at 298 K (green), temperature ramp (yellow), and vapor re-evaporation at 318 K (red). Black dashed lines and gray solid lines represent the simulated deposition rates generated from SIM.1 and SIM.2, respectively.

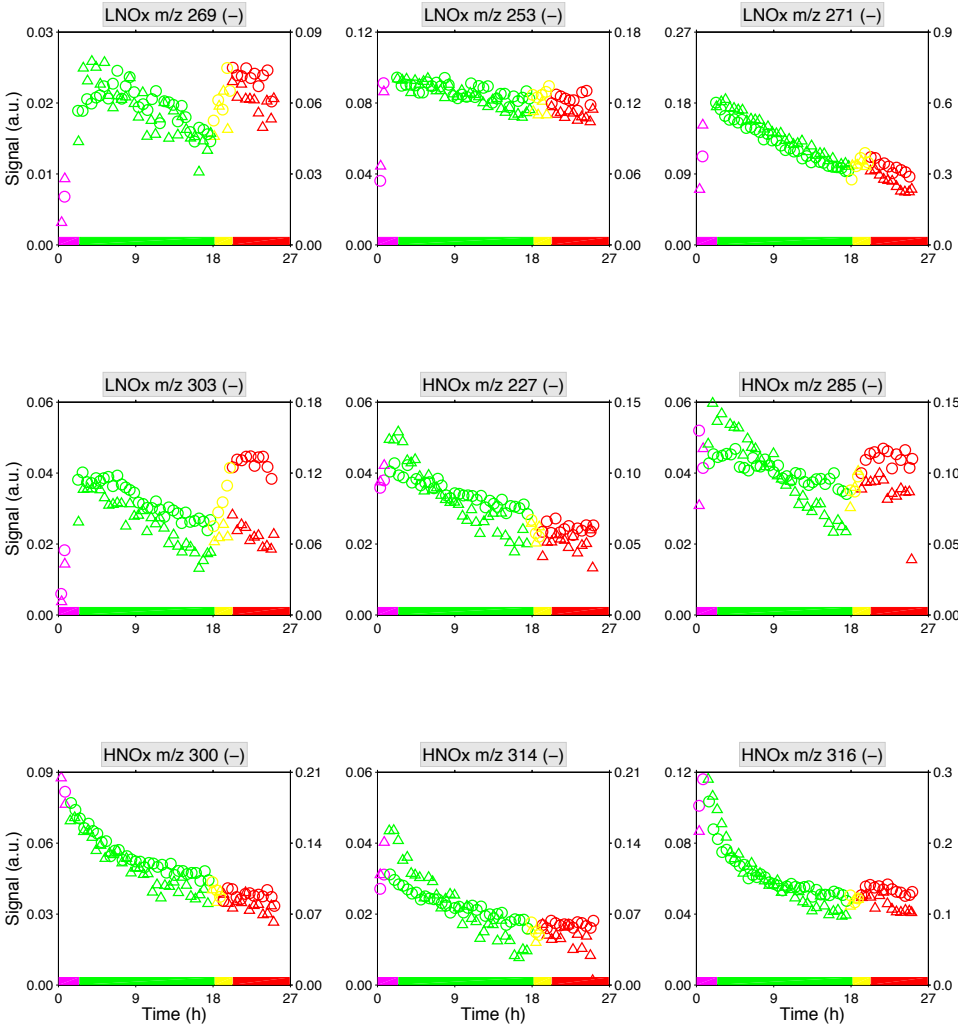

Figure 4. Comparison of vapor–wall interactions for α-pinene + OH products under controlled experimental conditions in used (triangle) vs. unused (circle) Teflon chambers. 30-min averaged data are shown here for clarity. Colored bands denote successive experimental periods: vapor generation (magenta), vapor wall deposition at 298 K (green), temperature ramp (yellow), and vapor re-evaporation at 318 K (red).

actively mixed vs. static; and (3) definition of the starting point of the gas-phase vapor concentration.

When the chamber temperature was increased from 25 to 45 °C, with all the other experimental conditions held constant, the concentrations of most compounds in the chamber increased to a minor degree relative to the initial peak signal, reflecting modest desorption of vapors from the chamber wall. As noted earlier, the chamber wall (in the used chambers) might actually be coated with organic materials from previous experiments, or the FEP Teflon film itself may act as an absorbing medium. In view of the uncertain nature of the wall itself, two control experiments were also conducted in the unused dual 24 m^3 FEP Teflon chambers with identical protocols: see Table 1. Organic vapor deposition and evaporation rates between unused and used chambers are compared in Fig. 4. For all the α-pinene photooxidation products studied here, their interaction with the wall in the unused chambers is in general agreement with that in the used chambers, except for a few oxidation products generated under high-NO conditions. The fact that these particular compounds exhibit slightly higher deposition rates in used chambers might be due to the heterogeneous chemistry on the wall catalyzed by nitric acid, a product from the NO_x-O_3 photochemical cycle. Overall, we conclude that the extent to which chambers have been previously used is not a significant factor in the sorption behavior of the FEP Teflon films.

The equivalent absorbing organic mass parameter (C_w/g m^{-3}) is estimated using equilibrium partitioning

Table 2. Best-fit values of vapor–wall accommodation coefficient ($\alpha_{w,i}$) and calculated equivalent absorbing organic mass (C_w) on the chamber wall for vapors with structure proposed based on the CIMS measurement.

Observed m/z	Molecular weight	Chemical formula	Proposed structure	Vapor pressure (atm @ 298 K)[a]	Vapor wall deposition rate $k_{w,i}$ (s^{-1})[b]	$\alpha^c_{w,i}$	C_w ($g\,m^{-3}$)[d]	Formation mechanism
269 (–)	184	$C_{10}H_{16}O_3$	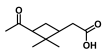	9.64×10^{-8}	$(8.95 \pm 2.55) \times 10^{-6}$	$(9.15 \pm 2.63) \times 10^{-8}$	$(6.59 \pm 3.43) \times 10^{-4}$	α-pinene + OH (low-NO_x) Eddingsaas et al. (2012)
285 (–)	200	$C_{10}H_{16}O_4$	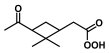	1.05×10^{-6}	$(2.98 \pm 1.14) \times 10^{-6}$	$(3.24 \pm 1.20) \times 10^{-8}$	$(5.90 \pm 3.65) \times 10^{-3}$	
253 (–)	168	$C_{10}H_{16}O_2$		6.79×10^{-6}	$(4.40 \pm 0.70) \times 10^{-6}$	$(4.31 \pm 0.68) \times 10^{-8}$	$(4.57 \pm 2.45) \times 10^{-3}$	
257 (–)	172	$C_9H_{16}O_3$	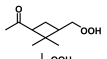	2.65×10^{-6}	$(3.19 \pm 3.13) \times 10^{-6}$	$(3.12 \pm 3.07) \times 10^{-8}$	$(6.31 \pm 4.98) \times 10^{-3}$	
271 (–)	186	$C_{10}H_{18}O_3$		5.14×10^{-8}	$(1.09 \pm 0.06) \times 10^{-5}$	$(1.15 \pm 0.07) \times 10^{-7}$	$(5.56 \pm 3.86) \times 10^{-5}$	
303 (–)	218	$C_{10}H_{18}O_5$		1.56×10^{-10}	$(1.32 \pm 0.19) \times 10^{-5}$	$(1.49 \pm 0.22) \times 10^{-7}$	$(1.12 \pm 1.19) \times 10^{-6}$	
227 (–)	142	$C_7H_{10}O_3$		1.24×10^{-5}	$(1.63 \pm 0.50) \times 10^{-5}$	$(1.52 \pm 0.15) \times 10^{-7}$	$(1.01 \pm 0.91) \times 10^{-2}$	α-pinene + OH (high-NO_x) Eddingsaas et al. (2012)
269 (–)	184	$C_{10}H_{16}O_3$		3.48×10^{-9}	$(1.94 \pm 0.30) \times 10^{-5}$	$(1.97 \pm 0.32) \times 10^{-7}$	$(2.80 \pm 1.02) \times 10^{-5}$	
285 (–)	200	$C_{10}H_{16}O_4$		6.32×10^{-11}	$(1.51 \pm 0.15) \times 10^{-5}$	$(1.62 \pm 0.16) \times 10^{-7}$	$(3.83 \pm 3.11) \times 10^{-7}$	
300 (–)	215	$C_{10}H_{17}O_4N$		1.53×10^{-7}	$(1.19 \pm 0.13) \times 10^{-5}$	$(1.34 \pm 0.14) \times 10^{-7}$	$(1.79 \pm 0.06) \times 10^{-4}$	
314 (–)	229	$C_{10}H_{15}O_5N$	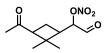	1.52×10^{-7}	$(2.31 \pm 0.21) \times 10^{-5}$	$(2.94 \pm 0.26) \times 10^{-7}$	$(1.14 \pm 0.10) \times 10^{-3}$	
316 (–)	231	$C_{10}H_{17}O_5N$	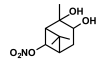	9.03×10^{-10}	$(1.85 \pm 0.14) \times 10^{-5}$	$(2.19 \pm 0.17) \times 10^{-7}$	$(5.36 \pm 9.85) \times 10^{-6}$	
215 (–)	130	$C_7H_{14}O_2$	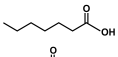	1.98×10^{-5}	$(5.27 \pm 1.74) \times 10^{-6}$	$(4.50 \pm 1.49) \times 10^{-8}$	$(3.10 \pm 0.55) \times 10^{-2}$	Dodecane + OH (low-NO_x) Yee et al. (2012)
285 (–)	200	$C_{12}H_{24}O_2$	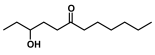	3.58×10^{-7}	$(1.32 \pm 0.44) \times 10^{-5}$	$(1.42 \pm 0.46) \times 10^{-7}$	$(3.50 \pm 0.81) \times 10^{-3}$	
287 (–)	202	$C_{12}H_{26}O_2$	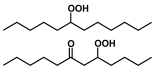	1.21×10^{-6}	$(8.25 \pm 0.67) \times 10^{-6}$	$(8.79 \pm 0.73) \times 10^{-8}$	$(2.81 \pm 1.92) \times 10^{-3}$	
301 (–)	216	$C_{12}H_{24}O_3$		1.30×10^{-7}	$(1.19 \pm 0.13) \times 10^{-5}$	$(1.35 \pm 0.15) \times 10^{-7}$	$(8.39 \pm 7.24) \times 10^{-4}$	
315 (–)	230	$C_{12}H_{22}O_4$	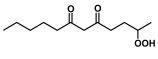	1.56×10^{-8}	$(2.68 \pm 0.49) \times 10^{-5}$	$(3.17 \pm 0.61) \times 10^{-7}$	$(1.79 \pm 2.15) \times 10^{-4}$	
332 (–)	247	$C_{12}H_{25}O_4N$	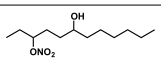	2.17×10^{-8}	$(1.55 \pm 0.07) \times 10^{-5}$	$(1.86 \pm 0.09) \times 10^{-7}$	$(3.93 \pm 0.46) \times 10^{-4}$	Dodecane + OH (high-NO_x) Zhang et al. (2014b)
346 (–)	261	$C_{12}H_{23}O_5N$	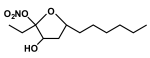	4.46×10^{-9}	$(2.33 \pm 0.25) \times 10^{-5}$	$(2.91 \pm 0.33) \times 10^{-7}$	$(1.87 \pm 0.21) \times 10^{-5}$	

Table 2. Continued.

Observed m/z		Molecular weight	Chemical formula	Proposed structure	Vapor pressure (atm @ 298 K)[a]	Vapor wall deposition rate $k_{w,i}$ (s^{-1})[b]	$\alpha^c_{w,i}$	C_w ($g\,m^{-3}$)[d]	Formation mechanism
141	(–)	122	$C_7H_6O_2$		5.30×10^{-6}	$(2.04 \pm 1.88) \times 10^{-6}$	$(1.68 \pm 1.35) \times 10^{-8}$	$(1.13 \pm 0.07) \times 10^{-2}$	toluene + OH ($low\text{-}NO_x$) MCM v3.2
209	(–)	124	$C_7H_8O_2$		4.89×10^{-5}	$(5.78 \pm 1.93) \times 10^{-6}$	$(4.82 \pm 1.62) \times 10^{-8}$	$(7.03 \pm 1.42) \times 10^{-2}$	
241	(–)	156	$C_7H_8O_4$		4.00×10^{-6}	$(2.04 \pm 0.40) \times 10^{-5}$	$(1.95 \pm 0.39) \times 10^{-7}$	$(2.66 \pm 0.71) \times 10^{-2}$	
175	(–)	90	$C_3H_6O_3$		2.21×10^{-4}	$(9.68 \pm 1.51) \times 10^{-6}$	$(6.90 \pm 1.08) \times 10^{-8}$	$(3.03 \pm 1.10) \times 10^{-1}$	
185	(–)	100	$C_5H_8O_2$		1.73×10^{-4}	$(6.58 \pm 0.30) \times 10^{-6}$	$(4.93 \pm 0.22) \times 10^{-8}$	$(7.70 \pm 2.01) \times 10^{-2}$	isoprene + OH ($high\text{-}NO_x$) Paulot et al. (2009)
199	(–)	114	$C_5H_6O_3$		8.17×10^{-6}	$(2.46 \pm 0.81) \times 10^{-6}$	$(1.96 \pm 0.64) \times 10^{-8}$	$(1.23 \pm 0.31) \times 10^{-2}$	
217	(–)	132	$C_5H_8O_4$		2.70×10^{-7}	$(1.40 \pm 0.11) \times 10^{-5}$	$(1.22 \pm 0.10) \times 10^{-7}$	$(1.15 \pm 0.60) \times 10^{-4}$	
232	(–)	147	$C_5H_9O_4N$		2.34×10^{-5}	$(5.24 \pm 0.24) \times 10^{-6}$	$(4.76 \pm 0.22) \times 10^{-8}$	$(1.78 \pm 0.42) \times 10^{-3}$	
234	(–)	149	$C_4H_7O_5N$	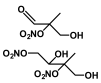	3.93×10^{-6}	$(3.23 \pm 1.30) \times 10^{-6}$	$(2.97 \pm 0.28) \times 10^{-8}$	$(5.16 \pm 1.36) \times 10^{-4}$	
311	(–)	226	$C_5H_{10}O_8N_2$	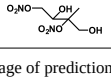	1.15×10^{-9}	$(3.10 \pm 0.45) \times 10^{-5}$	$(3.66 \pm 0.54) \times 10^{-7}$	$(8.27 \pm 1.24) \times 10^{-6}$	

[a] Vapor pressures are estimated from the average of predictions from the two group contribution methods, "SIMPOL.1" (Pankow and Asher, 2008) and "EVAPORATION" (Compernolle et al., 2011).
[b] The vapor wall deposition rate ($k_{w,i}$) is calculated by Eq. (22b).
[c] The accommodation coefficient ($\alpha_{w,i}$) is calculated via optimal fitting of Eq. (22b) to the CIMS measured vapor decay rate assuming first-order kinetics and irreversible gas–wall partitioning.
[d] C_w is calculated from the combination of Eqs. (16) and (17) as an equation set.

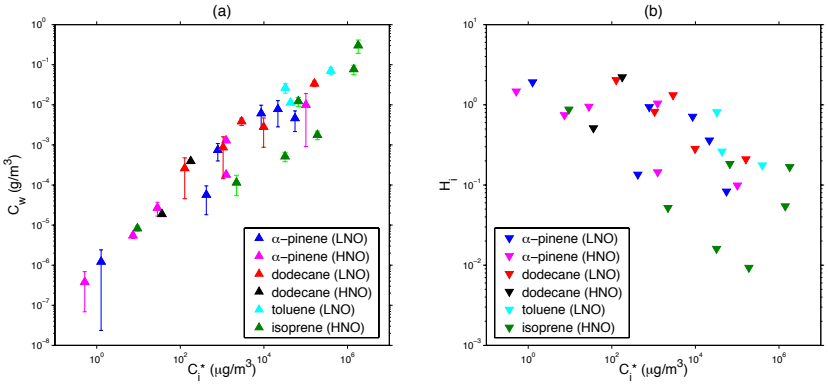

Figure 5. Inferred total amount of **(a)** equivalent absorbing organic mass on the chamber wall, C_w ($g\,m^{-3}$), and **(b)** dimensionless Henry's law constants, H_i, as a function of saturation concentration, C_i^* ($\mu g\,m^{-3}$). Estimated vapor pressures of organic compounds studied here are obtained from the average of predictions from the two group contribution methods, "SIMPOL.1" (Pankow and Asher, 2008) and "EVAPORATION" (Compernolle et al., 2011). The uncertainty bars give the upper and lower limits of C_w values derived from Eq. (12), together with Eqs. (16) and (17), when either "EVAPORATION" or "SIMPOL.1" is used to estimate vapor pressures.

theory. We show in the Supplementary Materials that this theory is suitable for C_w estimation after ~ 18 h of wall-induced vapor decay. The ratio of the concentration of vapor i in the wall phase ($\bar{C}_{w,i}$) to that in the gas phase ($\bar{C}_{v,i}$) is expressed as a function of the corresponding gas–wall partitioning coefficient ($K_{w,i}$) and the total amount of equivalent absorbing organic mass on the chamber wall (C_w). Ideally, C_w can be obtained if the initial total concentration ($\bar{C}_{tot,i}$) and equilibrium gas-phase concentration ($\bar{C}_{v,i}$) of vapor i can be measured by CIMS. However, since the fraction of organic compound i in the chamber wall at the onset of vapor wall deposition is unknown, we estimate C_w via the combination of equilibrium partitioning expressions at two

different temperatures, e.g., 298 and 318 K:

$$\frac{\bar{C}_{\mathrm{w},i@298\,\mathrm{K}}}{\bar{C}_{\mathrm{v},i@298\,\mathrm{K}}} = \frac{\bar{C}_{\mathrm{tot},i} - \bar{C}_{\mathrm{v},i@298\,\mathrm{K}}}{\bar{C}_{\mathrm{v},i@298\,\mathrm{K}}} = K_{\mathrm{w},i\,@298\,\mathrm{K}} C_{\mathrm{w}}, \quad (16)$$

$$\frac{\bar{C}_{\mathrm{w},i@318\,\mathrm{K}}}{\bar{C}_{\mathrm{v},i@318\,\mathrm{K}}} = \frac{\bar{C}_{\mathrm{tot},i} - \bar{C}_{\mathrm{v},i@318\,\mathrm{K}}}{\bar{C}_{\mathrm{v},i@318\,\mathrm{K}}} = K_{\mathrm{w},i\,@318\,\mathrm{K}} C_{\mathrm{w}}, \quad (17)$$

where $\bar{C}_{\mathrm{tot},i}$ is the total initial concentration of vapor i, $\bar{C}_{\mathrm{v},i@298/318\,\mathrm{K}}$ is the gas-phase concentration (as indicated by the normalized CIMS signal with unit "a.u.") of vapor i at 298/318 K, and $K_{\mathrm{w},i\,@T}$ is the corresponding partitioning coefficient at temperature T, see Eq. (12). In this manner, both $\bar{C}_{\mathrm{tot},i}$ and C_{w} can be calculated by solving the equation set (16) and (17). Note that the product $K_{\mathrm{w},i\,@T} C_{\mathrm{w}}$ is dimensionless, so that the normalized CIMS signal can be directly substituted into Eqs. (16) and (17) as the actual gas-phase concentration of organic vapor i. In the calculation, $\bar{C}_{\mathrm{v},i@298\,\mathrm{K}}$ and $\bar{C}_{\mathrm{v},i@318\,\mathrm{K}}$ were obtained by taking a 30 min average of the first-order extrapolation of the normalized CIMS signals at 298 and 318 K, respectively, during the temperature ramping period. The estimated C_{w} values vary by approximately 5 orders of magnitude and exhibit a strong dependence on the volatility of the organics, as shown in Table 2 and Fig. 5a. We will address subsequently why the C_{w} values span such a wide range.

5 Vapor sorption into FEP Teflon films

It is instructive to consider possible mechanisms of organic vapor interactions with Teflon films. Dual sorption mechanisms in glassy polymers have been identified: ordinary dissolution and microvoid-filling (Meares, 1954; Paul, 1979; Paterson et al., 1999; Tsujita, 2003; Kanehashi and Nagai, 2005). From the point of view of solubility behavior, organic polymers such as FEP Teflon may be idealized as high molecular weight organic liquids (Vieth et al., 1966). The polymer rubbery state is hypothesized to represent a thermodynamic equilibrium liquid state within which gas solubility obeys Henry's law. The glassy state, on the other hand, is considered to comprise two components: a hypothetical liquid state and a solid state, the latter containing a distribution of microvoids/holes that act to immobilize a portion of the penetrant molecules when the polymer is below its glass transition temperature ($T_{\mathrm{g}} = 339$ K for FEP, Kim and Smith, 1990). The overall solubility of a gas molecule in a glassy polymer has been expressed by (Barrer et al., 1958; Michaels et al., 1963; Vieth et al., 1966; Kanehashi and Nagai, 2005):

$$C = C_{\mathrm{H}} + C_{\mathrm{L}} = k_{\mathrm{H}} p + \frac{C'_{\mathrm{L}} b p}{1 + b p}, \quad (18)$$

where C is the total vapor concentration in the glassy polymer, C_{H} is the concentration based on Henry's law dissolution, C_{L} is the concentration based on Langmuir sorption, k_{H} is the Henry's law constant, p is the partial pressure in the gas phase, C'_{L} is the hole saturation constant, and b is the hole affinity constant. If $bp \ll 1$, Eq. (18) reduces to

$$C = (k_{\mathrm{H}} + C'_{\mathrm{L}} b)\, p. \quad (19)$$

The condition of $bp \ll 1$ holds in the present situation because the partial pressures of organic vapors generated in the chamber are $< 10^{-7}$ atm, and the derived hole affinity constants for small organic molecules are $< 1\,\mathrm{atm}^{-1}$ in glassy polymers (Vieth et al., 1966; Sada et al., 1988; Kanehashi and Nagai, 2005). If Eq. (18) holds for the equilibrium sorption behavior of organic vapors by FEP films, then the dimensionless form of the effective Henry's law constant (H_i) can be expressed as a function of the partitioning coefficient of vapor i ($K_{\mathrm{w},i}$) and total absorbing organic mass on the chamber wall (C_{w}):

$$H_i = \frac{\bar{C}_{\mathrm{w},i}}{\bar{C}_{\mathrm{v},i}} = K_{\mathrm{w},i} C_{\mathrm{w}} \propto (k_{\mathrm{H}} + C'_{\mathrm{L}} b). \quad (20)$$

As shown in Fig. 5b, the derived Henry's law constants (H_i) for the organic oxidation products span approximately 2 orders of magnitude and depend inversely on saturation concentrations ($C_i^*/\mu\mathrm{g\,m}^{-3}$). This behavior suggests that organic vapor solubility in FEP films increases with decreasing volatility, i.e., increasing carbon number and functionalization. This behavior provides a qualitative explanation for the wide range of C_{w} values calculated for the 25 organic vapors studied here. Although the solubility of low volatility vapors in the FEP Teflon film is relatively high (large H_i), the total equivalent absorbing organic mass on the wall required for gas–wall partitioning can still be low (small C_{w}) because low volatility compounds tend to partition preferentially in the wall phase (large $K_{\mathrm{w},i}$). As illustrated in Fig. 5b, the dimensionless Henry's law constant of $m/z = (-)303$, a product from α-pinene low-NO photochemistry, is ~ 20 times larger than that of $m/z = (-)185$, a product from isoprene + OH under high-NO conditions. The vapor pressure of $m/z = (-)303$, however, is ~ 6 orders of magnitude lower than that of $m/z = (-)185$. As a result, the C_{w} value for $m/z = (-)303$ is ~ 5 orders of magnitude smaller than that for $m/z = (-)185$. One infers that the equivalent absorbing organic mass on the chamber wall derived earlier is not constant but specific to individual organic compounds, i.e., a function of volatility and solubility in FEP Teflon polymer. We will show that C_{w} is not the most dominant parameter, so the assumption of a single value for C_{w}, does not invalidate the usefulness of the theory.

6 Accommodation coefficient on the chamber wall ($\alpha_{\mathrm{w},i}$)

One key parameter that emerges from the theory of vapor wall deposition, the total equivalent absorbing organic mass (C_{w}), can be calculated based on equilibrium gas–wall partitioning at two different temperatures. From this information,

we can estimate the other key parameter, the accommodation coefficient ($\alpha_{w,i}$), by optimal fitting of the solution of Eq. (14) to CIMS measured organic vapor decay at 298 K:

$$\frac{d\bar{C}_{v,i}}{dt} = \left(\frac{A}{V}\right)\left(\frac{\alpha_{w,i}\bar{v}_i/4}{\pi\alpha_{w,i}\bar{v}_i/8(D_iK_e)^{1/2}+1}\right) \cdot \left(\frac{\bar{C}_{tot,i}-\bar{C}_{v,i}}{K_{w,i}C_w} - \bar{C}_{v,i}\right). \quad (21)$$

Note that Eq. (21) is simply Eq. (14) in which $\bar{C}_{w,i}$ has been replaced with $(\bar{C}_{tot,i} - \bar{C}_{v,i})$. Thus, Eq. (21) constitutes a linear ODE system with the one unknown (estimable) parameter, $\alpha_{w,i}$. The Levenberg–Marquardt method implemented in MATLAB's "System Identification Toolbox" was used for the nonlinear minimization at each time step of its solution. The best-fit $\alpha_{w,i}$ value obtained was then substituted into Eq. (21) to give the simulated temporal profile of the organic vapor i. Simulation results (SIM.1) are shown in Fig. 3.

The other limit of wall behavior is that of irreversible gas–wall partitioning ($C_w \to \infty$). In this case, the accommodation coefficient $\alpha_{w,i}$ is the sole governing parameter and Eq. (14) can be simplified as

$$\frac{d\bar{C}_{v,i}}{dt} = -\left(\frac{A}{V}\right)\left(\frac{\alpha_{w,i}\bar{v}_i/4}{\pi\alpha_{w,i}\bar{v}_i/8(D_iK_e)^{1/2}+1}\right)\bar{C}_{v,i}. \quad (22a)$$

The overall wall loss rate of organic vapor i ($k_{w,i}$) is therefore

$$k_{w,i} = \left(\frac{A}{V}\right)\left(\frac{\alpha_{w,i}\bar{v}_i/4}{\pi\alpha_{w,i}\bar{v}_i/8(D_iK_e)^{1/2}+1}\right). \quad (22b)$$

Results for irreversible gas–wall partitioning (SIM.2) are shown in Fig.. 3.

Simulations using both reversible (SIM.1) and irreversible (SIM.2) vapor wall deposition expressions match the experimental data. Outputs from SIM.1 tend to level off, whereas those from SIM.2 exhibit a continuous decreasing trend at the end of $\sim$ 18 h of vapor decay. The extent of agreement between observations and simulations depends on the nature of vapor wall deposition: most organic vapors in the Caltech Teflon chambers exhibit a continuous decay. The agreement between SIM.1 and SIM.2 indicates that the estimated C_w values are sufficiently large so that the wall-induced vapor deposition in the Caltech chamber can be treated as an irreversible process ($C_w \to \infty$) within a relatively long timescale (< 18 h).

Overall, results from the two simulations indicate that $\alpha_{w,i}$ is the more influential parameter than C_w in describing the wall-induced deposition of semi-volatile organic vapors. The significance of $\alpha_{w,i}$ is 2-fold: first, the accommodation coefficient for the desorption of organic molecules from the gas–wall interface equals that for the adsorption/uptake process, which together influence the time needed to establish equilibrium; and second, diffusion in the chamber wall is not considered in the theoretical framework; consequently, the best-fit $\alpha_{w,i}$ will reflect the mass transfer resistance in both the gas–wall interface and the chamber wall layer. We suggest that the vapor wall deposition of individual compounds can be adequately parameterized through the accommodation coefficient $\alpha_{w,i}$ as the single dominant variable. As shown in Table 2 and Fig. 6, for the compounds studied here, estimated values of $\alpha_{w,i}$ span approximately 2 orders of magnitude (10^{-8}–10^{-6}) and depend inversely on volatility, implying that more highly functionalized compounds dissolve more easily in FEP Teflon film. The correlation of $\alpha_{w,i}$ with the average carbon oxidation state (OS_C), however, is not strong due to the fact that vapor pressures of molecules, although highly oxidized, are not necessarily low.

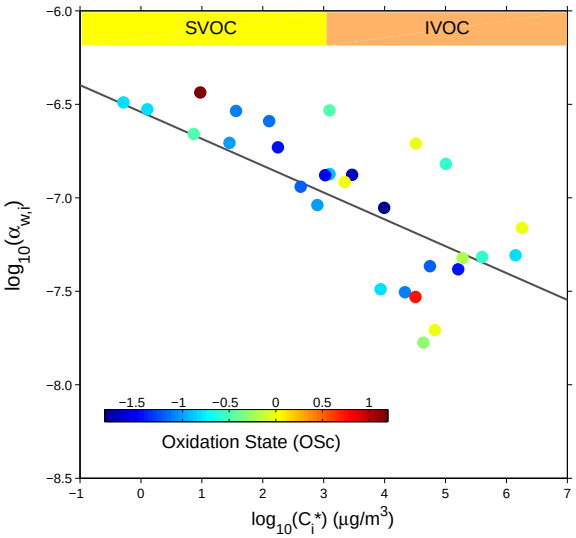

Figure 6. Inferred accommodation coefficients of organic oxidation products on the chamber wall ($\log_{10}(\alpha_{w,i})$) as a function of saturation concentrations ($\log_{10}(C_i^*)$) and average carbon oxidation state (OS_C). Colored filled circles represent the best-fit $\alpha_{w,i}$ assuming irreversible gas–wall partitioning. The black solid line represents the linear regression of $\log_{10}(\alpha_{w,i})$ vs. $\log_{10}(C_i^*)$ for all compounds.

7 Characterizing chamber vapor wall deposition rate

The wall-induced deposition of the 25 organic compounds investigated in the present study can be sufficiently represented by a single parameter, the wall accommodation coefficient ($\alpha_{w,i}$), which is observed to exhibit a strong inverse dependence on C_i^* (Fig. 6). It is possible to formulate an empirical expression for $\alpha_{w,i}$ as a function of C_i^*, a parameter that can be estimated by vapor pressure prediction models.

Linear regression was performed on $\log_{10}\alpha_{w,i}$ vs. $\log_{10}C_i^*$ for the 25 organic vapors studied:

$$\log_{10}\alpha_{w,i} = -0.1919 \times \log_{10}C_i^* - 6.32. \quad (23)$$

We employ a group-contribution expression for $\log_{10}C_i^*$ as a function of carbon number (n_C^i) and oxygen number (n_O^i) developed by Donahue et al. (2011):

$$\log_{10}C_i^* = \left(n_C^0 - n_C^i\right)b_C - n_O^i b_O - 2\frac{n_C^i n_O^i}{n_C^i + n_O^i}b_{CO}, \quad (24)$$

where n_C^0 is the carbon number of $1\,\mu g\,m^{-3}$ alkane ($n_C^0 = 28.0483$), b_C is the carbon–carbon interaction term ($b_C = 0.4015$), b_O is the oxygen–oxygen interaction term ($b_O = 2.3335$), and b_{CO} is the carbon–oxygen nonideality term ($b_{CO} = -0.4709$). Best-fit values of n_C^0, b_C, b_O, and b_{CO} are obtained by optimal fitting Eq. (24) to the saturation concentrations of 110 species, including C_5-C_{14} *n*-alkanes, C_5-C_{14} carbonyls, C_5-C_{14} di-carbonyls, C_5-C_{14} alcohols, C_5-C_{14} diols, C_5-C_{14} carboxylic acids, C_5-C_{14} di-carboxylic acids, C_5-C_{14} peroxides, C_5-C_{14} di-peroxides, C_5-C_{14} nitrates, and C_5-C_{14} di-nitrates. Vapor pressures of these species are estimated by taking the average of predictions from the two group contribution methods, "SIMPOL.1" and "EVAPORATION".

Combining Eqs. (22), (23), and (24), the vapor wall deposition rate of any intermediate/semi/low-volatility compound ($k_{w,i}/s^{-1}$) can be ultimately related to its carbon and oxygen numbers. This vapor wall loss rate estimation approach, although simplified, proves to be quite useful considering the limited knowledge of the chemical structures of the thousands of ions detected by mass spectrometry during an experiment. The proper guess of a molecular formula would be able to constrain the wall-induced decay rate of each ion, and thus provide information to better understand its formation and removal dynamics. In this way, one can reasonably constrain the wall-induced organic vapor deposition rate based on only two measurable or predictable properties, volatility and the extent of oxygenation.

As shown in Fig. 7, within a certain volatility range, $k_{w,i}$ increases with decreasing C_i^*, implying that highly functionalized compounds tend to deposit on the chamber wall more efficiently. The maximum value of vapor wall deposition rate is eventually approached for highly oxygenated and extremely low-volatility compounds (which, of course, are precisely those compounds that are most prone to form SOA). Revisiting Eq. (22) reveals that the deposition rate of organic vapors is limited either by gas phase transport (molecular diffusion and turbulent mixing) or wall surface accommodation. For extremely small $\alpha_{w,i}$ (large C_i^*), $k_{w,i}$ becomes

$$k_{w,i} = \left(\frac{A}{V}\right)\left(\frac{\alpha_{w,i}\bar{v}_i}{4}\right). \quad (25)$$

In this case, the organic vapor wall deposition rate is governed by the chamber wall accommodation process. On the other hand, if $\alpha_{w,i}$ is sufficiently large (small C_i^*), $k_{w,i}$ is approximately given by

$$k_{w,i} = \frac{\pi}{2}\left(\frac{A}{V}\right)(D_i K_e)^{1/2}. \quad (26)$$

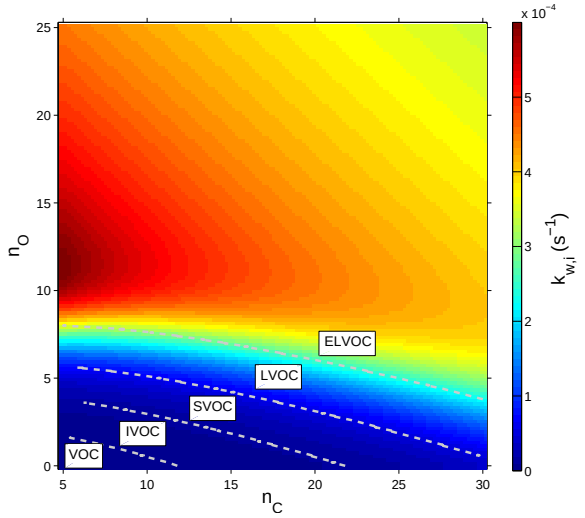

Figure 7. Predicted vapor wall deposition rate ($k_{w,i}/s^{-1}$) of organic compounds in a Teflon chamber as a function of carbon number (n_C) and oxygen number (n_O).

In this case, the vapor wall deposition rate is ultimately controlled by the mixing state in the chamber. Equation (26) provides an expression for the upper limit of vapor wall deposition rate in a chamber, which is a manifestation of the extent of turbulent mixing in the chamber. One can determine which process is the limiting step in governing the overall wall deposition rate by referring to Eqs. (25) and (26). The threshold value of $\alpha_{w,i}$, at which gas phase transport (molecular diffusion and turbulence mixing) and wall surface accommodation contribute equally to the vapor wall deposition rate, is 6.8×10^{-6} in the Caltech chamber.

8 Impact of vapor wall deposition on SOA yields

The extent to which vapor wall deposition impacts measured SOA yields depends on the competition between uptake of organic vapors by suspended particles and the chamber wall. The timescale ($\tau_{g/p,i}$) associated with establishing equilibrium gas-particle partitioning is governed by three transport processes: diffusion of vapor molecules from the bulk gas phase to the surface of the particle, uptake of vapor molecules by the particle surface, and diffusion of molecules in the bulk particle phase. Depending on a given situation, any of these three transport processes can be the limiting step in determining the overall equilibrium partitioning timescale. Here we represent the diffusional transport processes across the gas-particle interface and in the particle phase itself by a single parameter, the accommodation coefficient of organic vapors on the particle ($\alpha_{p,i}$). In doing so, the mass transfer resistances at the gas-particle interface and in the particle phase are reflected by the single parameter $\alpha_{p,i}$, and the timescale

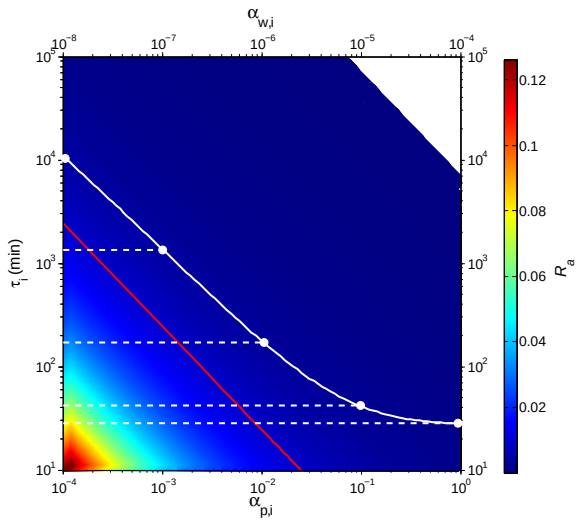

Figure 8. Comparison of estimated gas-particle equilibration timescale ($\tau_{g/p,i}$) as a function of the gas-particle mass accommodation coefficient ($\alpha_{p,i}$, lower x axis) and the ratio of total particle surface area to the chamber wall area (R_a, color bar), and vapor wall deposition timescale ($\tau_{g/w,i}$) as a function of gas–wall mass accommodation coefficient ($\alpha_{w,i}$, upper x axis). The red solid line represents the gas-particle equilibration time for a typical chamber experiment with seed surface area of $\sim 1 \times 10^{-3}$ µm^2 cm^{-3}. White solid and dashed lines define the region where $\tau_{g/p,i} \cong \tau_{g/w,i}$. For example, the top dashed white line is a collection of data points for which the equality $\tau_{g/p,i} = \tau_{g/w,i} = 1.3 \times 10^3$ min holds. $\tau_{g/w,i}$ is calculated by substituting $\alpha_{w,i} = 10^{-7}$ into Eqs. (22), (23), and (24). $\tau_{g/p,i}$ is calculated from Eq. (27) by varying $\alpha_{p,i}$ (10^{-4}–10^{-3}) and R_a (0.01–0.02).

to achieve gas-particle partitioning following a small perturbation of the condensing species in the gas phase is given by (Seinfeld and Pandis, 2006):

$$\tau_{g/p,i} = (2\pi N_p \bar{D}_p D_i f(Kn, \alpha_{p,i}))^{-1}, \quad (27)$$

where N_p is the total number concentration of suspended particles, $\bar{D}_p$ is the number mean particle diameter, $Kn (= 2\lambda/D_p)$ is the Knudsen number, and $f(Kn, \alpha_{p,i})$ is the correction factor for noncontinuum diffusion and imperfect accommodation (Seinfeld and Pandis, 2006).

Figure 8 shows the predicted $\tau_{g/p,i}$ as a function of: (1) the ratio of total particle surface area to chamber wall area (R_a) and (2) $\alpha_{p,i}$. The red solid line represents $\tau_{g/p,i}$ for a typical chamber experiment with seed surface area of ~ 1000 µm^2 cm^{-3}. In this case, equilibrium vapor–particle partitioning is established within a few minutes in the presence of perfect accommodation of organic vapors onto particles ($\alpha_{p,i} = 1$) or when a sufficiently large concentration of suspended particles is present (e.g., $C_{OA} > 10^5$ µg m^{-3} when $\alpha_{p,i} < 10^{-4}$).

By analogy with the treatment of gas-particle partitioning, the time scale associated with vapor–wall interactions is presumably governed by gas-phase diffusion of vapor molecules to the wall through a boundary layer adjacent to the wall, uptake of vapor molecules at the wall surface, and, potentially, diffusion of molecules in the wall. Again, a single parameter, the accommodation coefficient on the wall ($\alpha_{w,i}$), is employed to represent the latter two processes. Thus, the vapor wall deposition timescale is given by

$$\tau_{g/w,i} = k_{w,i}^{-1}. \quad (28)$$

The white solid line in Fig. 8 represents the predicted $\tau_{g/w,i}$, covering a range of several minutes to several hours, as a function of the vapor accommodation coefficient on the chamber wall ($\alpha_{w,i}$). The region to the left of the white solid line is that in which $\tau_{g/w,i}$ and $\tau_{g/p,i}$ are competitive. For low $\alpha_{w,i}$ (e.g., $< 10^{-8}$), $\tau_{g/w,i}$ is comparable to $\tau_{g/p,i}$ only if the vapor has a low accommodation coefficient on the particles ($\alpha_{p,i} < 10^{-4}$) or if a relatively small concentration of particles is present in the chamber ($R_a < 10^{-4}$). For $\alpha_{w,i} > 10^{-4}$, $\tau_{g/w,i}$ is estimated to be of the order of several minutes and, as a result, vapor transport to particles is suppressed by competition with the chamber wall, even with perfect particle accommodation ($\alpha_{p,i} = 1$) or high particle concentrations ($R_a > 10^{-2}$).

Overall, in the region (confined by the white solid and dash lines in Fig. 8) where gas–wall partitioning is competitive with gas-particle partitioning, it is necessary to account for vapor wall deposition when deriving SOA yields from chamber experiments. The theoretical framework developed in this study suggests that the area of this region is ultimately controlled by the accommodation coefficient of organic vapors on particles ($\alpha_{p,i}$) vs. the chamber wall ($\alpha_{w,i}$).

9 Conclusions

The wall-induced decay of organic vapors is the result of coupled physical processes involving transport of organic vapors from the well-mixed core of a chamber to its wall by molecular and turbulent diffusion, uptake of organic molecules by the Teflon film, and re-evaporation from the wall. The wall-induced dark decay of 25 intermediate/semi-volatility organic compounds generated from the photochemistry of four parent hydrocarbons was monitored in the Caltech dual 24 m^3 FEP Teflon chambers. The extent to which organic vapors and the chamber wall interact was found to be similar in used vs. unused Teflon chambers. Based on this observation, one concludes that the Teflon film itself acts as an effective sorption medium, and organic materials deposited from past chamber experiments, if they indeed exist, do not significantly impact the sorption behavior of organic molecules. Reversibility in gas–wall partitioning was observed: evaporation of all 25 compounds that had deposited on the wall

during an 18 h deposition period occurred when the chamber temperature was increased from 25 to 45 °C.

Based on a derived model that describes the dynamics of vapor deposition on the chamber wall, a single parameter, the accommodation coefficient ($\alpha_{w,i}$), emerges to govern the extent of the vapor–wall mass transfer process. Moreover, $\alpha_{w,i}$ exhibits a strong dependence on the molecular properties, such as vapor pressure and oxidation state, of the 25 organics studied. We present an empirical expression for $\alpha_{w,i}$ as a function of the compound vapor pressure, thus affording the possibility to predict the wall deposition rate of intermediate/semi/non-volatility compounds in a Teflon chamber based on their molecular constituency.

Previous studies have observed the chemical transformation of δ-hydroxycarbonyls to substituted dihydrofurans on the chamber wall (Lim and Ziemann, 2005, 2009; Zhang et al., 2014b), suggesting the potential occurrence of heterogeneous reactions on the chamber wall surface. While the extent to which heterogeneous transformations proceed can be potentially represented through the accommodation coefficient, the occurrence of wall-induced chemistry adds another dimension of complexity in predicting vapor wall deposition rates.

Quantifying the impact of vapor wall deposition on the chamber-derived SOA yield is the next step in assessing the effect of vapor wall deposition of SOA formation and evolution. Future studies will be directed at (1) experiments to determine the accommodation coefficients of organic vapors on particles for a variety of SOA systems, and (2) state-of-art SOA predictive models that describe the dynamics of vapor–wall and vapor–particle interactions to estimate the fraction of organic vapor fluxes transported to the suspended particles vs. the chamber wall.

Appendix A

A (m^2):	Total surface area of the chamber wall
$\alpha_{p,i}$ (dimensionless):	Accommodation coefficient of organic vapor i on particles
$\alpha_{w,i}$ (dimensionless):	Accommodation coefficient of organic vapor i on the chamber wall
$C_{0,i}$ ($g\,m^{-3}$):	Concentration of organic vapor i over the gas–wall interface
C_i^* ($g\,m^{-3}$):	Saturation concentration of organic vapor i
$\bar{C}_{tot,i}$ ($g\,m^{-3}$):	Total concentration of organic vapor i in the chamber
$\bar{C}_{v,i}$ ($g\,m^{-3}$):	Concentration of organic vapor i in the well-mixed core of the chamber
$C_{v,i}$ ($g\,m^{-3}$):	Local concentration of organic vapor i in the boundary layer adjacent to the wall
$\bar{C}_{w,i}$ ($g\,m^{-3}$):	Concentration of organic vapor i that has accumulated on the chamber wall
C_w ($g\,m^{-3}$):	Equivalent mass of absorbing organic material on the chamber wall
$\bar{D}_p$ (m):	Number mean particle diameter
D_e ($m^2\,s^{-1}$):	Eddy diffusivity
D_i ($m^2\,s^{-1}$):	Molecular diffusivity of organic vapor i
δ (m):	Thickness of the boundary layer adjacent to the wall
H_i (dimensionless):	Henry's law constant of organic compound i
$J_{v,i}$ ($g\,m^{-2}\,s^{-1}$):	Vapor flux arriving at the gas–wall interface
$J_{w,i}$ ($g\,m^{-2}\,s^{-1}$):	Vapor flux evaporating from the wall
K_e (s^{-1}):	Eddy diffusion coefficient
$K_{w,i}$ ($m^3\,g^{-1}$):	Gas–wall partitioning coefficient
$k_{w,depo,i}$ (s^{-1}):	Deposition rate coefficient to the wall
$k_{w,evap,i}$ (s^{-1}):	Evaporation rate coefficient from the wall
$\bar{M}_w$ ($g\,mol^{-1}$):	Average molecular weight of the absorbing organic material on the wall
N_p (m^{-3}):	Total number concentration of suspended particles
$p_{L,i}^0$ (atm):	Vapor pressure of organic compound i as a liquid
γ_i (dimensionless):	Activity coefficient in the wall layer on a mole fraction basis
$\bar{v}_i$ ($m\,s^{-1}$):	Mean thermal speed
V (m^3):	Total volume of the chamber

The Supplement related to this article is available online at doi:10.5194/acp-15-4197-2015-supplement.

Acknowledgements. This study was supported by NOAA Climate Program Office AC4 program, award # NA13OAR4310058 and State of California Air Resources Board agreement 13-321.

Edited by: V. F. McNeill

References

Barrer, R. M., Barrie, J. A., and Slater, J.: Sorption and diffusion in ethyl cellulose. Part III. Comparison between ethyl cellulose and rubber, J. Polym. Sci., 27, 177–197, 1958.

Compernolle, S., Ceulemans, K., and Müller, J.-F.: EVAPORATION: a new vapour pressure estimation methodfor organic molecules including non-additivity and intramolecular interactions, Atmos. Chem. Phys., 11, 9431–9450, doi:10.5194/acp-11-9431-2011, 2011.

Corner, J. and Pendlebury, E. D.: The coagulation and deposition of a stirred aerosol, P. Phys. Soc. Lond. B., 64, 645–654, 1951.

Crounse, J. D., McKinney, K. A., Kwan, A. J., and Wennberg, P. O.: Measurement of gas-phase hydroperoxides by chemical ionization mass spectrometry, Anal. Chem., 78, 6726–6732, 2006.

Crump, J. G. and Seinfeld, J. H.: Turbulent deposition and gravitational sedimentation of an aerosol in a vessel of arbitrary shape, J. Aerosol. Sci., 12, 405–415, 1981.

Donahue, N. M., Epstein, S. A., Pandis, S. N., and Robinson, A. L.: A two-dimensional volatility basis set: 1. organic-aerosol mixing thermodynamics, Atmos. Chem. Phys., 11, 3303–3318, doi:10.5194/acp-11-3303-2011, 2011.

Eddingsaas, N. C., Loza, C. L., Yee, L. D., Seinfeld, J. H., and Wennberg, P. O.: α-pinene photooxidation under controlled chemical conditions – Part 1: Gas-phase composition in low- and high-NO_X environments, Atmos. Chem. Phys., 12, 6489–6504, doi:10.5194/acp-12-6489-2012, 2012.

Fahnestock, K. A. S., Yee, L. D., Loza, C. L., Coggon, M. M., Schwantes, R., Zhang, X., Dalleska, N. F., and Seinfeld, J. H.: Secondary Organic Aerosol Composition from C_{12} Alkanes, J. Phys. Chem. A., published online, doi:10.1021/jp501779w, 2014.

Grosjean, D.: Wall loss of gaseous-pollutants in outdoor Teflon chambers, Environ. Sci. Technol., 19, 1059–1065, 1985.

Kanehashi, S. and Nagai, K.: Analysis of dual-mode model parameters for gas sorption in glassy polymers, J. Membrane. Sci., 253, 117–138, 2005.

Kim, C. S. and Smith, T. L.: An improved method for measuring the thermal coefficient of linear expansion of flexible polymer-films, J. Polym. Sci. Pol. Phys., 28, 2119–2126, 1990.

Kokkola, H., Yli-Pirilä, P., Vesterinen, M., Korhonen, H., Keskinen, H., Romakkaniemi, S., Hao, L., Kortelainen, A., Joutsensaari, J., Worsnop, D. R., Virtanen, A., and Lehtinen, K. E. J.: The role of low volatile organics on secondary organic aerosol formation, Atmos. Chem. Phys., 14, 1689–1700, doi:10.5194/acp-14-1689-2014, 2014.

Lim, Y. B. and Ziemann, P. J.: Products and mechanism of secondary organic aerosol formation from reactions of n-alkanes with OH radicals in the presence of NO_x, Environ. Sci. Technol., 39, 9229–9236, 2005.

Lim, Y. B. and Ziemann, P. J.: Effects of molecular structure on aerosol yields from OH radical-initiated reactions of linear, branched, and cyclic alkanes in the presence of NO_x, Environ. Sci. Technol., 43, 2328–2334, 2009.

Loza, C. L., Chan, A. W. H., Galloway, M. M., Keutsch, F. N., Flagan, R. C., and Seinfeld, J. H.: Characterization of vapor wall loss in laboratory chambers, Environ. Sci. Technol., 44, 5074–5078, 2010.

Loza, C. L., Craven, J. S., Yee, L. D., Coggon, M. M., Schwantes, R. H., Shiraiwa, M., Zhang, X., Schilling, K. A., Ng, N. L., Canagaratna, M. R., Ziemann, P. J., Flagan, R. C., and Seinfeld, J. H.: Secondary organic aerosol yields of 12-carbon alkanes, Atmos. Chem. Phys., 14, 1423–1439, doi:10.5194/acp-14-1423-2014, 2014.

Matsunaga, A. and Ziemann, P. J.: Gas-wall partitioning of organic compounds in a Teflon film chamber and potential effects on reaction product and aerosol yield measurements, Aerosol. Sci. Tech., 44, 881–892, 2010.

McMurry, P. H. and Grosjean, D.: Gas and aerosol wall losses in Teflon film smog chambers, Environ. Sci. Technol., 19, 1176–1182, 1985.

Meares, P.: The diffusion of gases through polyvinyl acetate, J. Am. Chem. Soc., 76, 3415–3422, 1954.

Michaels, A. S., Barrie, J. A., and Vieth, W. R.: Solution of gases in polyethylene terephthalate, J. Appl. Phys., 34, 1–13, 1963.

Pankow, J. F. and Asher, W. E.: SIMPOL.1: a simple group contribution method for predicting vapor pressures and enthalpies of vaporization of multifunctional organic compounds, Atmos. Chem. Phys., 8, 2773–2796, doi:10.5194/acp-8-2773-2008, 2008.

Paterson, R., Yampol'skii, Y., Fogg, P. G. T., Bokarev, A., Bondar, V., Ilinich, O., and Shishatskii, S.: IUPAC-NIST solubility data series 70. Solubility of gases in glassy polymers, J. Phys. Chem. Ref. Data, 28, 1255–1450, 1999.

Paul, D. R.: Gas sorption and transport in glassy-polymers, Ber. Bunsen. Phys. Chem., 83, 294–302, 1979.

Paulot, F., Crounse, J. D., Kjaergaard, H. G., Kroll, J. H., Seinfeld, J. H., and Wennberg, P. O.: Isoprene photooxidation: new insights into the production of acids and organic nitrates, Atmos. Chem. Phys., 9, 1479–1501, doi:10.5194/acp-9-1479-2009, 2009.

Sada, E., Kumazawa, H., Xu, P., and Nishigaki, M.: Mechanism of gas permeation through glassy polymer-films, J. Membrane Sci., 37, 165–179, 1988.

Seinfeld, J. H. and Pandis, S. N.: Atmospheric chemistry and physics : from air pollution to climate change (2nd Edn.), John Wiley & Sons, Inc., Hoboken, NJ, 2006.

Tsujita, Y.: Gas sorption and permeation of glassy polymers with microvoids, Prog. Polym. Sci., 28, 1377–1401, 2003.

Vieth, W. R., Tam, P. M., and Michaels, A. S.: Dual sorption mechanisms in glassy polystyrene, J. Colloid. Interf. Sci., 22, 360–370, 1966.

Yee, L. D., Craven, J. S., Loza, C. L., Schilling, K. A., Ng, N. L., Canagaratna, M. R., Ziemann, P. J., Flagan, R. C., and Seinfeld, J. H.: Secondary organic aerosol formation from low-NO_x photooxidation of dodecane: Evolution of multigeneration gas-

phase chemistry and aerosol composition, J. Phys. Chem. A., 116, 6211–6230, 2012.

Yeh, G. K. and Ziemann, P. J.: Alkyl nitrate formation from the reactions of C8-C14 n-alkanes with OH radicals in the presence of NOx: meausred yields with essential corections for gas-wall partitioning, J. Phys. Chem. A, 118, 8147–8157, 2014.

Zhang, X. and Seinfeld, J. H.: A functional group oxidation model (FGOM) for SOA formation and aging, Atmos. Chem. Phys., 13, 5907–5926, doi:10.5194/acp-13-5907-2013, 2013.

Zhang, X., Cappa, C. D., Jathar, S. H., McVay, R. C., Ensberg, J. J., Kleeman, M. J., and Seinfeld, J. H.: Influence of vapor wall loss in laboratory chambers on yields of secondary organic aerosol, P. Natl. Acad. Sci. USA, 111, 5802–5807, 2014a.

Zhang, X., Schwantes, R. H., Coggon, M. M., Loza, C. L., Schilling, K. A., Flagan, R. C., and Seinfeld, J. H.: Role of ozone in SOA formation from alkane photooxidation, Atmos. Chem. Phys., 14, 1733–1753, doi:10.5194/acp-14-1733-2014, 2014b.

Appendix F

Formation and Evolution of Molecular Products in α-pinene Secondary Organic Aerosol *

*Reproduced with permission from "Formation and evolution of molecular products in α-pinene secondary organic aerosol" by Zhang, X., McVay, R.C., Huang, D. D., Dalleska, N., Aumont, B., Flagan, R. C., and Seinfeld J. H., *Proceedings of the National Academy of Sciences*, 112, 14168–14173, doi:10.1073/pnas.1517742112, 2015.

Formation and evolution of molecular products in α-pinene secondary organic aerosol

Xuan Zhang[a], Renee C. McVay[b], Dan D. Huang[c], Nathan F. Dalleska[a], Bernard Aumont[d], Richard C. Flagan[a,b], and John H. Seinfeld[a,b,1]

[a]Division of Engineering and Applied Science, California Institute of Technology, Pasadena, CA 91125; [b]Division of Chemistry and Chemical Engineering, California Institute of Technology, Pasadena, CA 91125; [c]Department of Chemical and Biomolecular Engineering, Hong Kong University of Science and Technology, Hong Kong, China; and [d]Laboratoire Interuniversitaire des Systèmes Atmosphériques, UMR CNRS 7583, Université Paris Est Créteil and Université Paris Diderot, 94010 Créteil, France

Contributed by John H. Seinfeld, September 30, 2015 (sent for review September 4, 2015; reviewed by Thorsten Hoffmann and Murray V. Johnston)

Much of our understanding of atmospheric secondary organic aerosol (SOA) formation from volatile organic compounds derives from laboratory chamber measurements, including mass yield and elemental composition. These measurements alone are insufficient to identify the chemical mechanisms of SOA production. We present here a comprehensive dataset on the molecular identity, abundance, and kinetics of α-pinene SOA, a canonical system that has received much attention owing to its importance as an organic aerosol source in the pristine atmosphere. Identified organic species account for ∼58–72% of the α-pinene SOA mass, and are characterized as semivolatile/low-volatility monomers and extremely low volatility dimers, which exhibit comparable oxidation states yet different functionalities. Features of the α-pinene SOA formation process are revealed for the first time, to our knowledge, from the dynamics of individual particle-phase components. Although monomeric products dominate the overall aerosol mass, rapid production of dimers plays a key role in initiating particle growth. Continuous production of monomers is observed after the parent α-pinene is consumed, which cannot be explained solely by gas-phase photochemical production. Additionally, distinct responses of monomers and dimers to α-pinene oxidation by ozone vs. hydroxyl radicals, temperature, and relative humidity are observed. Gas-phase radical combination reactions together with condensed phase rearrangement of labile molecules potentially explain the newly characterized SOA features, thereby opening up further avenues for understanding formation and evolution mechanisms of α-pinene SOA.

secondary organic aerosol | particulate matter | air quality | climate

Secondary organic aerosol (SOA), comprising a large number of structurally different organic oxygenates, is a dominant constituent of submicrometer atmospheric particulate matter (1). Molecular characterization of SOA has been a major research goal in atmospheric chemistry for several decades (2), owing to the importance of organic aerosol in air quality and Earth's energy budget. Both biogenic (e.g., isoprene, monoterpenes) and anthropogenic (e.g., aromatics, large alkanes) organic compounds are well-established precursors to SOA. Knowledge of the SOA molecular composition is crucial for elucidation of its underlying formation mechanisms.

The most abundant monoterpene in the troposphere is α-pinene (3). The oxidation of α-pinene by ozone has become a canonical SOA system (4–12). Identification of multifunctional particle-phase products has been reported, including monomers with carboxylic acid moieties (4, 6) and high-molecular-weight compounds (7, 8, 12), although molecular structures and formation pathways of oligomers remain uncertain (5). Recently, a class of extremely low-volatility gas-phase organic compounds (ELVOCs) has been identified as an important component in the α-pinene ozonolysis chemistry (13). Identification of the ELVOCs in the particle phase and elucidation of the mechanism of their formation remain key missing pieces in closing the α-pinene SOA system (14).

We report here, for the first time, to our knowledge, time-resolved molecular characterization of the abundance, formation, and evolution of organic species in α-pinene-derived SOA. Identified classes of species account for (∼58–72) ± (∼34–39)% of the overall α-pinene SOA mass, with volatilities spanning from the semivolatile to extremely low-volatility range and molecular structures characterized as multifunctionalized monomers and dimers. These organic species exhibit distinct characteristics in terms of oxidation states, chemical structures, initial growth rates, evolution patterns, and responses to variations in temperature (T), relative humidity (RH), and oxidant type.

Results and Discussion

Distribution of α-pinene SOA Constituents. The α-pinene-derived SOA was generated in the Caltech Environmental Chamber; see *Materials and Methods*. The Particle-into-Liquid Sampler (PILS) integrated with Ultra Performance Liquid Chromatography/Electrospray Ionization Quadrupole Time-of-Flight Mass Spectrometry (UPLC/ESI-Q-ToFMS) is used to characterize temporal profiles of particulate molecular constituents (15). A spectrum of monomers and dimers, with molecular formulas $C_{8–10}H_{12–16}O_{3–6}$ and $C_{14–19}H_{24–28}O_{5–9}$, respectively, is observed in α-pinene SOA. Chemical structure elucidation of these organic molecules is based on the interpretation of chromatographic and spectrometric behaviors of the corresponding ions upon electrospray ionization (*SI Appendix*, *Molecular Structure Elucidation*). Based on the fragmentation pattern of the relevant parent ions upon collision-induced dissociation in MS/MS spectra, monomers are generally (di)-carboxylic acids. Ester-containing

Significance

Secondary organic aerosol (SOA) plays a pivotal role in climate and air quality. Characterizing the molecular makeup of SOA has been a major research goal for several decades, yet the chemical dynamics of most anthropogenic and biogenic SOA systems remain poorly resolved. We report here the time-resolved molecular characterization of SOA derived from the canonical α-pinene system, one of the most abundant biogenic emissions in the troposphere. We reveal distinct features of SOA components in terms of molecular structure, abundance, growth rates, evolution patterns, and responses to variations in temperature, relative humidity, and oxidant type. Our findings provide a comprehensive analysis of processes governing α-pinene SOA formation and aging.

Author contributions: X.Z., R.C.F., and J.H.S. designed research; X.Z., D.D.H., and N.F.D. performed research; X.Z., R.C.M., and B.A. analyzed data; and X.Z. and J.H.S. wrote the paper.

Reviewers: T.H., Johannes Gutenberg University; and M.V.J., University of Delaware.

The authors declare no conflict of interest.

[1]To whom correspondence should be addressed. Email: seinfeld@caltech.edu.

This article contains supporting information online at www.pnas.org/lookup/suppl/doi:10.1073/pnas.1517742112/-/DCSupplemental.

structures are prevalent in dimers, with $C_8H_{11}O_4$ (*m/z* 171) and $C_9H_{13}O_4$ (*m/z* 185) as primary building blocks.

Fig. 1 summarizes identified gas- and particle-phase products mapped onto the carbon number versus oxidation state ($n_C - OS_C$) space at the point when >99% α-pinene is consumed during ozonolysis in the absence of an OH scavenger at 298 K and <5% relative humidity. Products with mass saturation concentration (C*) in the range of $<3 \times 10^{-4}$, 3×10^{-4} to 0.3, 0.3–300, and 300 to 3×10^6 μg m^{-3} are designated as extremely low-volatility, low-volatility, semivolatile, and intermediate-volatility organic compounds (ELVOCs, LVOCs, SVOCs, and IVOCs), respectively. A number of monomers in the SVOC category ($C_8H_{12}O_4$, $C_8H_{14}O_5$, $C_9H_{14}O_3$, $C_9H_{14}O_4$, $C_{10}H_{16}O_3$, and $C_{10}H_{16}O_4$) are detected both in gas and particle phases. Two monomers ($C_{10}H_{14}O_5$ and $C_{10}H_{16}O_6$) fall in the LVOC range, whereas all of the dimers are categorized as ELVOCs. At the completion of the oxidation of α-pinene, mass concentrations of individual oxidation products, represented by the size of the circular symbols in Fig. 1, range from ~0.1 μg m^{-3} to ~26 μg m^{-3} and account for 58 ± 34% of the total organic particulate mass. The mean carbon oxidation state of the identified SOA molecular constituents (−0.68 ± 0.27) agrees essentially identically with the average level derived from the Aerosol Mass Spectrometer (AMS) measurement (−0.72 ± 0.43). Note that the monomer and dimer units have comparable O:C ratios.

Fig. 2 shows the temporal profiles of the three volatility categories, characterized as the mass loading and fraction (Fig. 2 *A* and *C*), as well as the growth dynamics of individual species (Fig. 2 *B* and *D*). At first glance, SVOC products dominate the α-pinene SOA, whereas the LVOC and ELVOC products in total account for less than 45% of the overall organic mass. The growth rates of ELVOCs are comparable to or even exceed those for SVOCs and LVOCs. As α-pinene oxidation proceeds, ELVOC production is inhibited, whereas SVOC and LVOC accumulation is favored. By examining the growth dynamics of individual oxidation products, key processes that significantly contribute to α-pinene SOA formation and evolution can be deduced. Prompt formation of ELVOCs at the beginning of the ozonolysis of α-pinene is crucial to initiate organic particle growth. The observation that most ELVOC dimers grow faster than SVOCs and LVOCs indicates that there is no intrinsic kinetic barrier to the ELVOC dimer formation (16). The role of aging in the α-pinene SOA evolution is reflected, to a certain degree, by the slow but continuous growth of LVOCs over the 4-h course of an experiment.

Effect of Temperature, Relative Humidity, and Oxidant. Current understanding regarding the effect of temperature on SOA yield is that lower temperature favors partitioning into the particle phase and hence enhances organic aerosol production owing to decreasing compound vapor pressure. For instance, mass fractions of terpenylic acid ($C_8H_{12}O_4$), pinalic acid ($C_9H_{14}O_3$), pinic acid ($C_9H_{14}O_4$), oxopinonic acid ($C_{10}H_{14}O_4$), and hydroxy-pinonic acid ($C_{10}H_{16}O_4$), increase by 33%, 119%, 10%, 59%, and 111%, respectively, after 3 h of reaction (>99% of α-pinene is consumed) when the chamber temperature is decreased from 25 °C to 12 °C; see Fig. 3 and *SI Appendix*, Fig. S6. The particle-phase mass fractions of most dimers, on the other hand, decrease at lower temperature, indicating that additional pathways that are temperature-sensitive

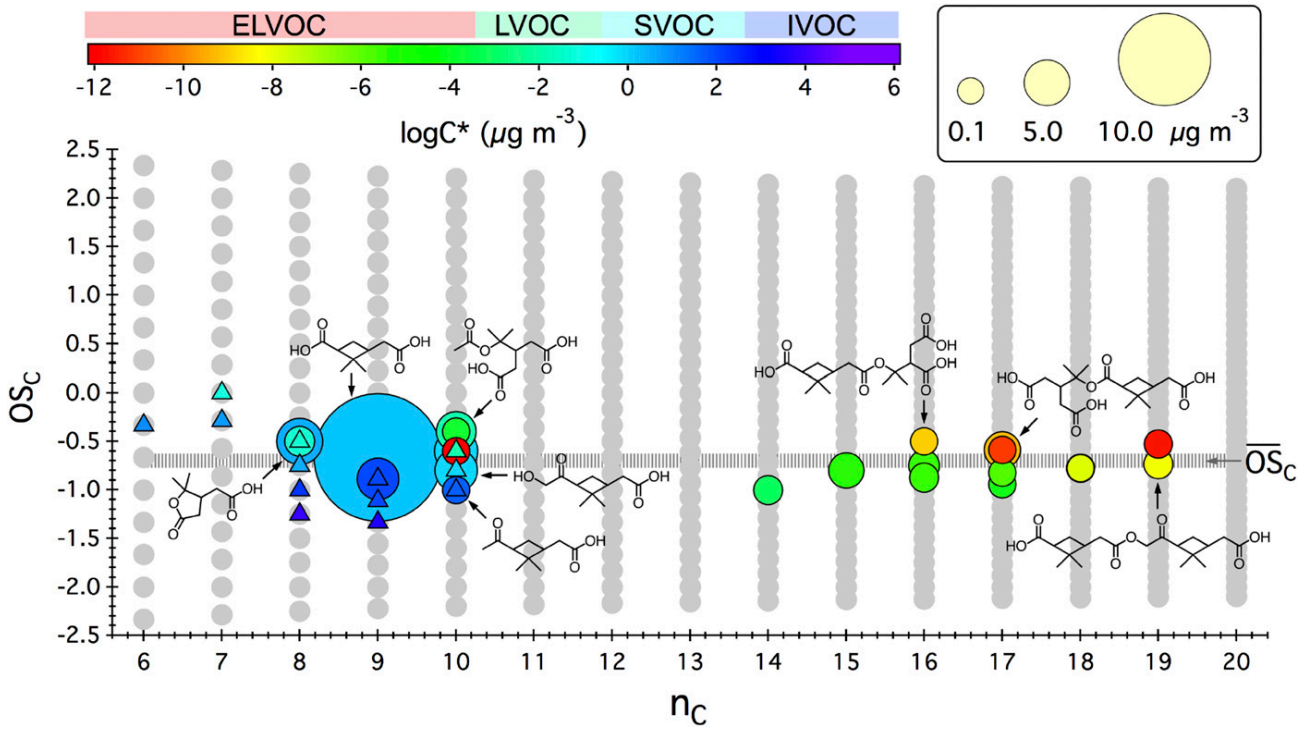

Fig. 1. Distribution of gas/particle-phase products from the ozonolysis of α-pinene in the absence of an OH scavenger in the oxidation state versus carbon number ($OS_C - n_C$) space. The gray circles represent all possible combinations of OS_C and n_C for stable organic molecules. Experimental details are given in *SI Appendix*, Table S1. Chemical structures of particle-phase species, as denoted by filled circles, are given in *SI Appendix*, Table S2. Here, structures are shown only for compounds that have been reported in the literature. Particle-phase mass concentration of each compound (micrograms per cubic meter), as denoted by the marker size, is a 5-min average quantification at the point when >99% of α-pinene is consumed via reaction with O_3 and, to a lesser extent, OH radicals. Molecular formulas and potential structures of gas-phase species, as denoted by filled triangles, are given in *SI Appendix*, Table S3. The average carbon oxidation state ($\overline{OS_C}$) derived from AMS measurement is represented by the horizontal gray line. The saturation mass concentration of each species (log C*) is estimated via an empirical model developed by Donahue et al. (34).

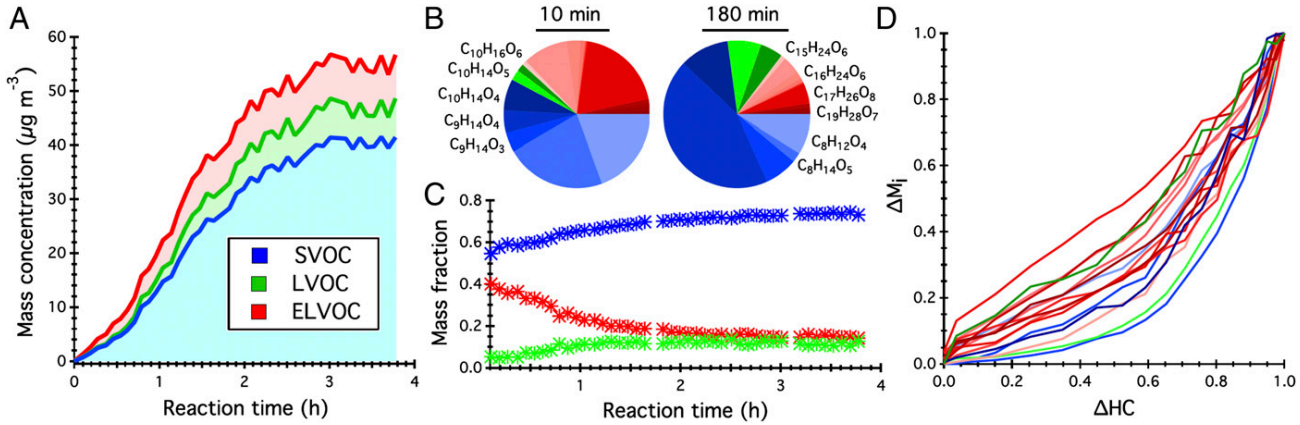

Fig. 2. Temporal profiles of identified organic molecules lumped as SVOCs (blue hues), LVOCs (green hues), and ELVOCs (red hues) in α-pinene SOA. (*A*) Particle-phase mass concentration of three volatility categories as a function of reaction time. (*B*) A 2D pie chart representing the mass fraction of 23 molecules in the particle phase after 10 min and 180 min of α-pinene reaction with O_3. Note that molecular formulas are shown for compounds with mass fractions exceeding 5%. (*C*) Mass fraction of three volatility categories in the particle phase as a function of reaction time. (*D*) Growth rates of individual species in the particle phase, defined as the ratio of the mass of each species normalized by its highest mass value to the reacted mass of α-pinene normalized by its highest mass value after ~83 min of reaction.

govern dimer production other than purely gas–particle partitioning. We discuss this observation in more detail subsequently.

The impact of RH on the growth and evolution of individual oxidation products is shown in Fig. 3 and *SI Appendix*, Fig. S7. As RH increases, SOA yield increases slightly, potentially as a result of decreasing the particle-phase diffusion timescale and the mean molecular weight of the organic particulate matter. Prompt and significant increase in the mass concentration of certain compounds in the aerosol is also observed, potentially a result of enhanced reactive uptake of hydrophilic compounds and/or reactions involving water. However, the presence of liquid water can lead to a decrease in the mass yield of certain products. As shown in *SI Appendix*, Fig. S7, the continuous dynamics observed for species $C_{10}H_{16}O_6$ (*m/z* 231) and $C_{19}H_{29}O_9$ (*m/z* 399) over the course of SOA formation reflects the competition between production and removal pathways governing the accumulation of these two compounds in the particle phase.

Significant differences in the product distribution and abundances are observed in the SOA generated from the O_3-initiated vs. OH-initiated oxidation of α-pinene. The identities of carboxylic acid monomers in both systems are quite similar; see *SI Appendix*, Fig. S1. Gas-phase products with peroxide functionalities are prevalent in the OH system (*SI Appendix*, Table S3), which is expected because the RO_2 + HO_2 pathway is dominant under the current experimental conditions. Importantly, none of the covalent ester dimers is observed in the OH system, although the major building blocks, i.e., $C_8H_{11}O_4$ (*m/z* 171) and $C_9H_{13}O_4$ (*m/z* 185), are still present. This provides strong evidence that these dimers are not a product of particle-phase esterification (17).

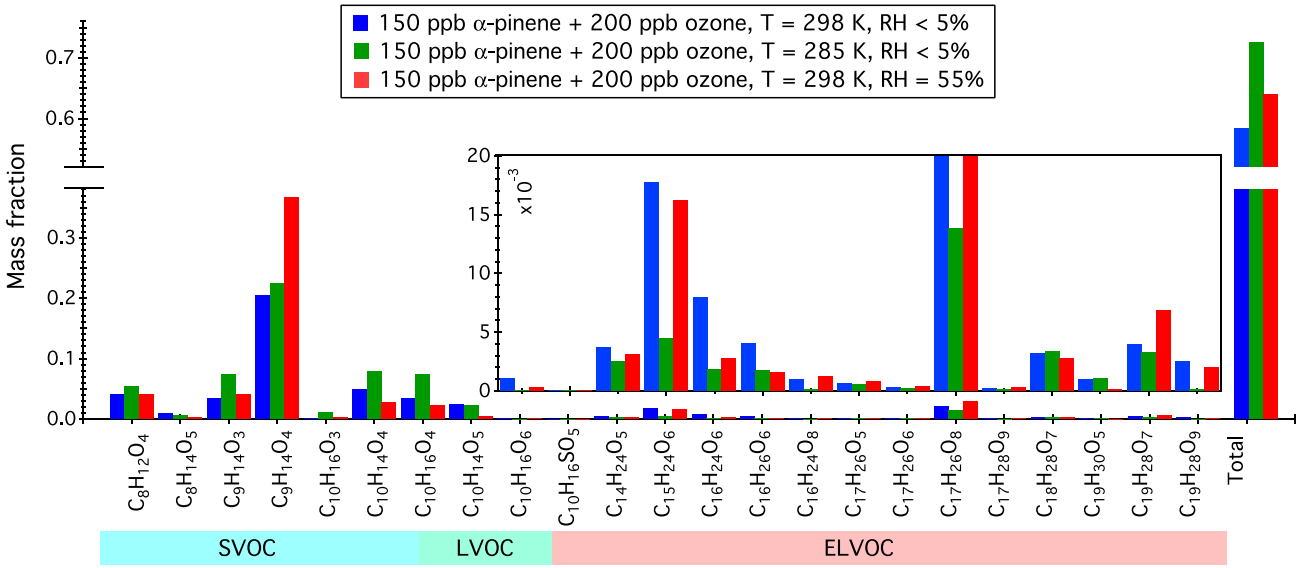

Fig. 3. Effect of temperature and relative humidity on the mass fraction of particle-phase components (defined as the ratio of PILS + UPLC/ESI-Q-ToFMS characterized mass concentration of individual species to the SMPS measured total particulate organic mass) when >99% α-pinene is reacted (predominantly with O_3). Corresponding temporal profiles of these compounds are given in *SI Appendix*, Figs. S6 and S7.

Mechanism of Extremely Low-Volatility Dimer Formation. We propose that a combination of two well-established mechanisms, that is, combination of acetylperoxy radicals yielding diacyl peroxides and their subsequent decomposition in the condensed phase after partitioning, is an important pathway for the production of ELVOC dimers. This mechanism is illustrated for the product, $C_{17}H_{26}O_6$ (*m/z* 325), in Fig. 4*A*. Addition of ozone to the double bond of α-pinene produces two carbonyl-substituted Criegee biradicals, which either are collisionally stabilized or isomerize via 1,4-H-shift, yielding an alkenoxy radical ($C_{10}H_{15}O_4$·). The $C_{10}H_{15}O_4$· radical reacts further with an RO_2 radical and undergoes subsequent 1,7-H shift, due to the presence of a labile H atom at the aldehydic carbon, producing an acetylperoxy radical ($C_9H_{13}O_5$·). The homogeneous recombination of two $C_9H_{13}O_5$· radicals via elimination of O_2 produces a covalently bound diacyl peroxide. Note that this reaction pathway was proposed as a radical chain termination step from oxidation of aldehydes in both gas and liquid phases (18, 19). The covalent dimer homologs have been observed in the gas phase from the ozonolysis of α-pinene ranging from ∼500 parts per trillion (ppt) to ∼30 parts per billion (ppb) (13, 20). Alternatively, the $C_9H_{13}O_5$· radical reacts with RO_2/HO_2, yielding pinic acid.

The decomposition of diacyl peroxides in the condensed phase generally proceeds through the formation of ion/radical pair intermediates, which undergo decarboxylation, with an ester as a primary product, as well as carboxylic acids and alcohols (21–27). The ester yield could be increased markedly by increasing the solvent polarity and the addition of common ions (25–27). The e-folding lifetime of diacyl peroxides with respect to the first-order decomposition ranges from essentially instantaneous to several hours at room temperature (23, 24, 27), and the decomposition rate is accelerated with increasing solvent polarity and temperature (22–24, 27). Based on measurement of decomposition rates of secondary/tertiary alkyl and phenyl diacyl peroxides in pure organic solvents (e.g., acetone), we expect that the decomposition of diacyl peroxide homologs produced in the α-pinene+O_3 system proceeds rapidly (shorter than the SOA formation timescale) in the organic, water, and ammonium sulfate aerosol mixture.

Processes Altering the α-pinene SOA Nature. The gas-phase production of diacyl peroxides via acetylperoxy radical self/cross-combination and its subsequent decomposition upon solvation can rationalize a series of important experimental observations. First, it has been suggested that the highly functionalized and extremely low-volatility vapors (O:C > 0.7) produced via the gas-phase autooxidation of peroxy radicals contribute, on average, >10% of the total α-pinene SOA and dominate the organic mass at the onset of the SOA growth (13). However, the AMS measured average O:C ratio ranges from ∼0.45 to ∼0.55 over the entire course of α-pinene SOA formation; see *SI Appendix*, Fig. S5. This indicates that processes involving the loss of oxygen significantly alter the oxygenated nature of compounds contributing to α-pinene SOA. Here the $RO_2 + RO_2 \rightarrow ROOR$ reaction and decomposition of diacyl peroxides result in a net loss of four oxygen atoms, substantially decreasing the O:C ratio of the ELVOC dimer produced in the particle phase. Second, as shown in Fig. 3 and *SI Appendix*, Figs. S6 and S7, the yield of ester dimers increases as the aerosol water content and temperature increase, providing further evidence that the decomposition of diacyl peroxide is temperature and solvent polarity sensitive, consistent with previous observations (24–27). Third, none of the ELVOC dimers is observed from the OH-initiated oxidation of α-pinene, although the monomeric building blocks, such as pinic acid, are present in the OH system. This demonstrates that traditionally cited particle-phase esterification is not important in dimer production. It is also consistent with the general α-pinene degradation chemistry in the gas phase, where the diacyl peroxide precursors, acetylperoxy radicals, are one of the major products from the ozonolysis vinylhydroperoxide channel, but rather limited from the OH oxidation pathway (6). Additionally, the mass fraction of the ELVOC dimers decreases significantly as the ozonolysis reaction proceeds (Fig. 2 *B* and *C*), because the continuous production of free radicals enhances their collision probability, thus decreasing the lifetime of free radicals and inhibiting the isomerization channel. Fourth, gas-phase production coupled with gas–particle partitioning cannot completely explain the observed behavior of pinic acid, which is the dominant monomeric product and

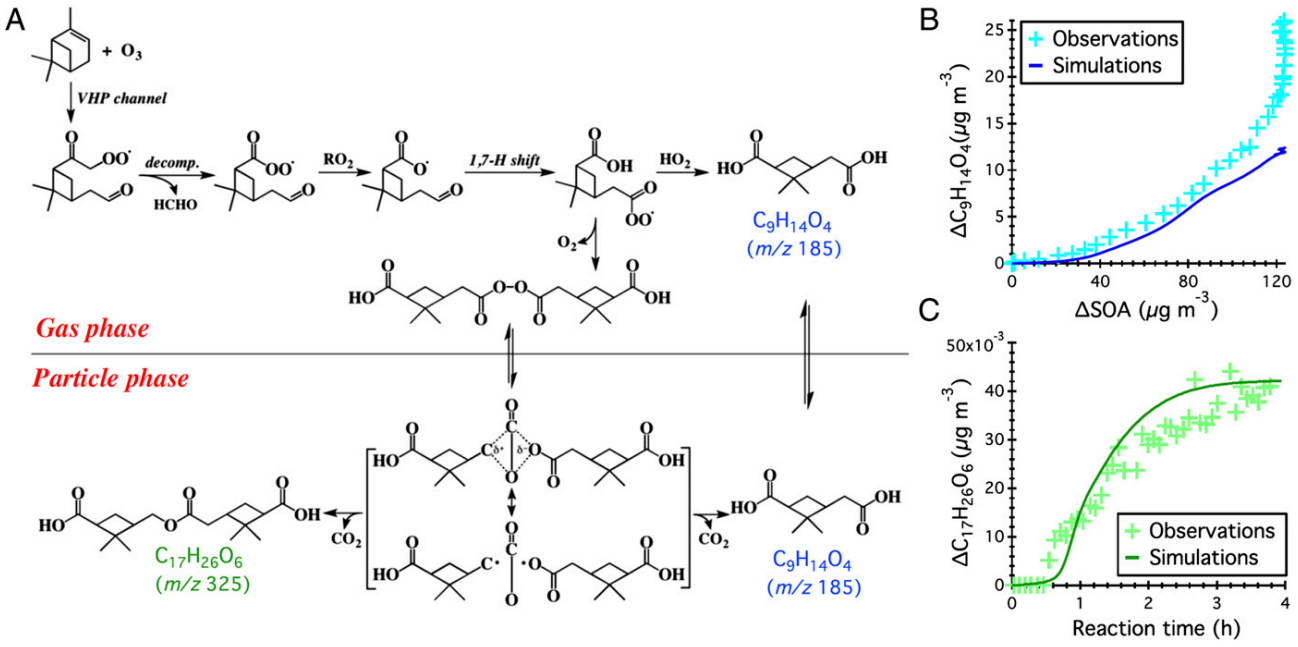

Fig. 4. (*A*) Proposed gas- and particle-phase mechanism for the formation of the dimer $C_{17}H_{26}O_6$ and pinic acid ($C_9H_{14}O_4$). Model simulations (solid line) and experimental observations (plus sign) of the growth dynamics of (*B*) $C_9H_{14}O_4$ and (*C*) $C_{17}H_{26}O_6$.

accounts for up to ~23% of the overall α-pinene SOA mass. As shown in Fig. 4*B* and *SI Appendix*, Fig. S8, a continuous growth of pinic acid is observed after >99% of α-pinene is consumed, indicating an additional production pathway, which will be discussed in *SOA Formation Kinetics in the a-pinene System*.

SOA Formation Kinetics in the α-pinene System. Successive chemical reactions yielding one covalent ester dimer ($C_{17}H_{26}O_6$), as listed in *SI Appendix*, Table S4, are incorporated into the Vapor–Particle Dynamics Model, which accounts for a series of comprehensive processes during SOA formation in chamber experiments (*SI Appendix*, *Vapor–Particle Dynamics Model*). By adjusting free parameters in the model framework, simulation of the temporal profile of the $C_{17}H_{26}O_6$ ester dimer agrees well with the experimental observation (see Fig. 4*C*), confirming that the mechanism involving diacyl peroxide as an intermediate is a plausible explanation for the formation of the identified ELVOC dimers in α-pinene SOA. Optimal molar yield of the $C_{18}H_{26}O_8$ diacyl peroxide from $C_9H_{13}O_5\cdot$ radical combination is 2%. Despite a small yield, the irreversible partitioning of diacyl peroxides onto aerosols makes these species an important contributor to α-pinene SOA. The best-fit first-order decomposition rate of the $C_{18}H_{26}O_8$ diacyl peroxide in the condense phase is 10^{-1} s^{-1}. This timescale needs to be rather short to match the rapid growth of the $C_{17}H_{26}O_6$ ester dimer in the particle phase.

Although our model framework captures the observed rapid growth of the $C_{17}H_{26}O_6$ ester dimer in the particle phase, the predicted pinic acid concentration is up to ~50% lower than that measured; see Fig. 4*B*. This is expected because, in the current mechanism, only one diacyl peroxide decomposition reaction is considered, whereas 14 structurally different ELVOC dimers are identified. Note that the model captures the initial growth trend of pinic acid, reflecting the role of gas-phase production coupled with gas–particle partitioning. The later gap between simulations and observations potentially represents an upper bound of the contribution of diacyl peroxide decomposition to pinic acid formation. Although other potential reaction channels for the continuous production of pinic acid may exist, the fact that the pinic acid concentration continues to increase after α-pinene is consumed strongly suggests an additional particle-phase production pathway.

Optimal fitting of model simulations to the observed temporal profiles of individual particulate species yields the effective vapor–particle accommodation coefficient ($\alpha_{p,i}$). Here "effective" indicates that $\alpha_{p,i}$ represents gas–particle interfacial mass transfer as well as particle bulk phase diffusion. The best-fit value of $\alpha_{p,i}$ ranges from 0.01 to 0.1, indicative of rather slow diffusion in the particle phase, which is consistent with recent observations reporting a semisolid phase state of α-pinene SOA (28). This provides insights into the limiting timescale that ultimately controls the aerosol growth.

To assess the effect of the relatively high experimental α-pinene mixing ratio of 150 ppb, we simulated the $C_{17}H_{26}O_6$ ester dimer formation under more atmospherically relevant mixing ratios of 10 ppb α-pinene and 20 ppb O_3. The predicted dimer yield increases by ~6 times at ~30 μg m^{-3} total SOA mass loadings (*SI Appendix*, Fig. S9). Although the timescale with respect to the decomposition of diacyl peroxide depends on ambient conditions (e.g., RH and T), changes in initial reactant concentrations impact the lifetime of free radicals. At low α-pinene levels, the longer lifetime of radicals favors the isomerization pathway and consequently leads to enhanced ELVOC dimer production.

Atmospheric Implications

The identified SVOC/LVOC monomers and ELVOC dimers, with carboxylic acids and esters as the prevalent functionalities, are found to account for a significant fraction of total α-pinene SOA mass (~58–72%). The remaining carbon mass likely comprises highly oxidized multifunctional organic compounds (HOMs) that have been successfully characterized in the gas phase, with an O:C ratio of >0.7 and a molar yield of 7% (13). HOMs production is ultimately controlled by two competing processes, i.e., RO_2 autooxidation via H shift vs. reaction with RO_2/HO_2. The initial α-pinene mixing ratio in the present chamber experiment was ~150 ppb, which favors RO_2 radical combination rather than self-isomerization, compared with more atmospherically relevant conditions (a few parts per billion). This increase in α-pinene level is estimated to lead to a negligible to moderate decrease in HOMs yield (*SI Appendix*, Fig. S10). The PILS+UPLC/ESI-Q-ToFMS technique used here is sensitive to relatively polar compounds, whereas the HOMs are mostly carbonyl-/peroxide-containing compounds. That these HOMs might undergo rapid chemical transformation after partitioning into particles is supported by the AMS measured average O:C ratio of α-pinene SOA, ranging from 0.45 to 0.55 over the course of 4-h ozonolysis.

Prompt and significant production of the covalent ester dimers accounts for up to 40% of the α-pinene SOA mass at the early stage of particle growth. We propose these dimers are produced from the particle-phase decomposition of diacyl peroxide, which has been suggested as an important nucleating agent of aerosol formed from reactions of cyclic alkenes and ozone (29). Although the role of organic peroxides in SOA production in pristine atmospheres has been recognized, their actual characterization in aerosols is attended by substantial difficulties due to their thermally labile nature. We provide here indirect evidence for the abundance of organic peroxides and their rapid transformation to covalent esters upon solvation in organic aerosol mixtures. Significant and continuous production of SVOC monomers underscores the importance of gas-phase photochemistry coupled with gas–particle partitioning, as well as particle-phase reaction pathways, e.g., diacyl peroxide decomposition. Although the importance of accretion reactions in oligomer formation has been widely acknowledged, the role of rapid rearrangement/decomposition of large labile molecules in SOA growth and evolution is established here.

Materials and Methods

Experiments were carried out in the 24-m^3 Teflon reactor in the Caltech Environmental Chamber. The α-pinene (~150 ppb) was oxidized by O_3 (~200 ppb) or OH radicals (~2×10^6 molecules cm^{-3}) in the presence of ammonium sulfate seed particles at concentrations of NO_x typical of pristine conditions. The ozonolysis experiments were conducted in the absence of an OH scavenger, resulting in an initial OH molar yield of 0.74 (30). As a consequence, ~20% of the α-pinene mass is expected to react with OH, and first-generation ozonolysis products are subject to oxidation by OH as well; see *SI Appendix*, *Chamber Experiments*. The gas-phase composition of oxidation products was monitored by a Chemical Ionization Mass Spectrometer. The particle size distribution and number concentration were characterized using a custom-built Scanning Mobility Particle Sizer (SMPS). The particle-phase elemental composition was measured by an Aerodyne High Resolution Time-of-Flight AMS; see *SI Appendix*, *Instrument Operation and Data Analysis Protocols*.

Temporal profiles of α-pinene SOA components were characterized by using the PILS+UPLC/ESI-Q-ToFMS technique (15). The overall PILS collection efficiency toward α-pinene-derived SOA is estimated to be >85%, based on an empirical correlation of water solubility and average O:C ratio of the aerosol ensemble (15). The time resolution of the PILS+UPLC/ESI-Q-ToFMS technique is 5 min, thus providing information on the particle-phase dynamics during ~4 h of SOA formation experiments. Mass concentrations of organic molecules in the particle phase (micrograms per cubic meter) are calculated based on mass conservation balance upon phase transfer (*SI Appendix*, *Particle-Phase Components Mass Concentration Retrieval*). The negative ESI sensitivity of pinonic acid product in the PILS collected liquid sample is calculated based on the counts/concentration calibration curve of a commercially available standard (98% purity; Sigma-Aldrich). Owing to the lack of authentic standards, the relative ionization efficiency of other identified products toward that of *cis*-pinonic acid in the ESI negative mode

is calculated using a linear model with the acid dissociation constant at logarithmic scale (pK_a) of individual compounds, pH of the mobile phase, and weighted average positive sigma of different molecules as the input (31). These three parameters are computed using the Conductor-like Screening Model for Real Solvents (32) implemented into the Amsterdam Density Functional (ADF 2014.07) molecular modeling suite (33). Computational details are given in *SI Appendix, Electrospray Ionization Efficiency Estimation*.

ACKNOWLEDGMENTS. We thank John Crounse and Paul Wennberg for useful discussions. This work was supported by National Science Foundation Grant AGS-1523500.

1. Jimenez JL, et al. (2009) Evolution of organic aerosols in the atmosphere. *Science* 326(5959):1525–1529.
2. Hallquist M, et al. (2009) The formation, properties and impact of secondary organic aerosol: Current and emerging issues. *Atmos Chem Phys* 9(14):5155–5236.
3. Guenther A, et al. (1995) A global model of natural volatile organic compound emissions. *J Geophys Res* 100(D5):8873–8892.
4. Claeys M, et al. (2009) Terpenylic acid and related compounds from the oxidation of α-pinene: Implications for new particle formation and growth above forests. *Environ Sci Technol* 43(18):6976–6982.
5. Hall WA, Johnston MV (2011) Oligomer content of α-pinene secondary organic aerosol. *Aerosol Sci Technol* 45(1):37–45.
6. Jenkin ME, Shallcross DE, Harvey JN (2000) Development and application of a possible mechanism for the generation of *cis*-pinic acid from the ozonolysis of α- and β-pinene. *Atmos Environ* 34(18):2837–2850.
7. Kristensen K, et al. (2014) Dimers in α-pinene secondary organic aerosol: Effect of hydroxyl radical, ozone, relative humidity and aerosol acidity. *Atmos Chem Phys* 14(8): 4201–4218.
8. Muller L, Reinnig MC, Warnke J, Hoffmann T (2008) Unambiguous identification of esters as oligomers in secondary organic aerosol formed from cyclohexene and cyclohexene/α-pinene ozonolysis. *Atmos Chem Phys* 8(5):1423–1433.
9. Pathak RK, et al. (2007) Ozonolysis of α-pinene: Parameterization of secondary organic aerosol mass fraction. *Atmos Chem Phys* 7(14):3811–3821.
10. Presto AA, Donahue NM (2006) Investigation of α-pinene + ozone secondary organic aerosol formation at low total aerosol mass. *Environ Sci Technol* 40(11):3536–3543.
11. Shilling JE, et al. (2009) Loading-dependent elemental composition of α-pinene SOA particles. *Atmos Chem Phys* 9(3):771–782.
12. Yasmeen F, et al. (2010) Terpenylic acid and related compounds: Precursors for dimers in secondary organic aerosol from the ozonolysis of α- and β-pinene. *Atmos Chem Phys* 10(19):9383–9392.
13. Ehn M, et al. (2014) A large source of low-volatility secondary organic aerosol. *Nature* 506(7489):476–479.
14. Mutzel A, et al. (2015) Highly oxidized multifunctional organic compounds observed in tropospheric particles: A field and laboratory study. *Environ Sci Technol* 49(13): 7754–7761.
15. Zhang X, et al. (2015) Time-resolved molecular characterization of organic aerosols by PILS + UPLC/ESI-Q-TOFMS. *Atmos Environ*, 10.1016/j.atmosenv.2015.08.049.
16. Heaton KJ, Dreyfus MA, Wang S, Johnston MV (2007) Oligomers in the early stage of biogenic secondary organic aerosol formation and growth. *Environ Sci Technol* 41(17):6129–6136.
17. DePalma JW, Horan AJ, Hall WA, Johnston MV (2013) Thermodynamics of oligomer formation: Implications for secondary organic aerosol formation and reactivity. *Phys Chem Chem Phys* 15(18):6935–6944.
18. Clinton NA, Kenley RA, Traylor TG (1975) Autoxidation of acetaldehyde. 3. Oxygen-labeling studies. *J Am Chem Soc* 97(13):3757–3762.
19. McDowell CA, Sifniades S (1963) Oxygen-18 tracer evidence for termination mechanism in photochemical oxidation of acetaldehyde. *Can J Chem* 41(2):300–307.
20. Rissanen MP, et al. (2015) Effects of chemical complexity on the autoxidation mechanisms of endocyclic alkene ozonolysis products: From methylcyclohexenes toward understanding α-pinene. *J Phys Chem A* 119(19):4633–4650.
21. Cooper RA, Ward HR, Lawler RG (1972) Mechanistic implications of chemically induced dynamic nuclear polarization spectra derived from radical-pair interactions in aliphatic diacyl peroxide decompositions. *J Am Chem Soc* 94(2):545–552.
22. Lamb RC, Pacifici JG, Ayers PW (1965) Organic peroxides. 4. Kinetics and products of decompositions of cyclohexaneformyl and isobutyryl peroxides. BDPA as a free-radical scavenger. *J Am Chem Soc* 87(17):3928–3935.
23. Leffler JE, More AA (1972) Decomposition of bicyclo [2.2.2]-1-formyl and pivaloyl peroxides. *J Am Chem Soc* 94(7):2483–2487.
24. Linhardt RJ, Murr BL (1979) Mechanism of decomposition for diacyl peroxides and related carboxy inversion compounds in aqueous acetone. *Tetrahedron Lett* 20(12): 1007–1010.
25. Linhardt RJ, Murr BL, Montgomery E, Osby J, Sherbine J (1982) Mechanism for diacyl peroxide decomposition. *J Org Chem* 47(12):2242–2251.
26. Taylor KG, Govindan CK, Kaelin MS (1979) Radical and ionic reaction pathways in the thermal decomposition of diacyl peroxides. *J Am Chem Soc* 101(8):2091–2099.
27. Walling C, Waits HP, Milovanovic J, Pappiaonnou CG (1970) Polar and radical paths in decomposition of diacyl peroxides. *J Am Chem Soc* 92(16):4927–4932.
28. Kidd C, Perraud V, Wingen LM, Finlayson-Pitts BJ (2014) Integrating phase and composition of secondary organic aerosol from the ozonolysis of α-pinene. *Proc Natl Acad Sci USA* 111(21):7552–7557.
29. Ziemann PJ (2002) Evidence for low-volatility diacyl peroxides as a nucleating agent and major component of aerosol formed from reactions of ozone with cyclohexene and homologous compounds. *J Phys Chem A* 106(17):4390–4402.
30. Aumont B, Szopa S, Madronich S (2005) Modelling the evolution of organic carbon during its gas-phase tropospheric oxidation: Development of an explicit model based on a self generating approach. *Atmos Chem Phys* 5(9):2497–2517.
31. Kruve A, Kaupmees K, Liigand J, Leito I (2014) Negative electrospray ionization via deprotonation: Predicting the ionization efficiency. *Anal Chem* 86(10):4822–4830.
32. Klamt A (1995) Conductor-like screening model for real solvents: A new approach to the quantitative calculation of solvation phenomena. *J Phys Chem* 99(7):2224–2235.
33. Pye CC, Ziegler T, van Lenthe E, Louwen JN (2009) An implementation of the conductor-like screening model of solvation within the Amsterdam density functional package - Part II. COSMO for real solvents. *Can J Chem* 87(7):790–797.
34. Donahue NM, Epstein SA, Pandis SN, Robinson AL (2011) A two-dimensional volatility basis set: 1. Organic-aerosol mixing thermodynamics. *Atmos Chem Phys* 11(7):3303–3318.

Supporting Information

Formation and Evolution of Molecular Products in α-Pinene Secondary Organic Aerosol

Xuan Zhang[a], Renee C. McVay[b], Dan D. Huang[c], Nathan F. Dalleska[a],

Bernard Aumont[d], Richard C. Flagan[a,b], John H. Seinfeld[a,b]

[a] Division of Engineering and Applied Science, California Institute of Technology, Pasadena, CA 91125, USA

[b] Division of Chemistry and Chemical Engineering, California Institute of Technology, Pasadena, CA 91125, USA

[c] Department of Chemical and Biomolecular Engineering, Hong Kong University of Science and Technology, Hong Kong, China

[d] Laboratoire Interuniversitaire des Systèmes Atmosphériques (LISA), UMR CNRS 7583, Université Paris Est Créteil et Université Paris Diderot, 94010 Créteil, France

To whom correspondence should be addressed: seinfeld@caltech.edu

This file includes:

S1. Chamber Experiments

α-pinene SOA formation experiments were conducted in the Caltech dual 24-m^3 Environmental Chamber, in which the temperature (T) and relative humidity (RH) are automatically controlled. Prior to each experiment, the Teflon chambers were flushed with purified, dry air for 24 h until the particle number concentration < 10 cm^{-3} and volume concentration < 0.01 μm^3 cm^{-3}. For humid experiments, the Teflon chamber was humidified to ~50% by passing purified air through a Nafion membrane humidifier (FC200, Permapure LLC) that is kept wet by recirculation of 27 °C ultra-pure water (18 MΩ, Millipore Milli-Q). Seed aerosols were injected into the chamber by atomizing 0.015 M aqueous ammonium sulfate (AS) solution to provide sufficient surface area for partition of products. For humid experiments, a custom-built wet-wall denuder was employed to generate hydrated ammonium sulfate seed aerosol. 15 μL α-pinene (Sigma-Aldrich, 98% purity) was injected into a glass bulb, which was connected into the Teflon chamber via a 1/4″ O.D. Teflon tubing. Heated 5 L min^{-1} of purified, dry air flowed through the glass bulb into the chamber for 30 min, introducing ~150 ppb α-pinene into the chamber. For dark ozonolysis experiments, O_3 was introduced into the chamber by flowing 5 L min^{-1} dry, purified air through an ozone generator (EMMET). For photooxidation experiments, hydrogen peroxide (H_2O_2) was used for the OH source by evaporating 113 μL of 50 wt % aqueous solution into the chamber with 5 L min^{-1} purified air for ~110 min, resulting in an approximate starting H_2O_2 mixing ratio of 2 ppm. After ~1 h mixing, photooxidation was initiated by irradiating the chamber with black lights with output wavelength ranging from 300 to 400 nm.

Relative Humidity and temperature were monitored via a Vaisala HMM211 probe. O_3 and NO_x mixing ratios were measured by a Horiba O_3 analyzer (APOA-360) and a Teledyne NO_x analyzer (T200), respectively. α-pinene concentration was monitored by a gas chromatograph equipped with a HP-5 column (15 m × 0.53 mm ID × 1.5 μm thickness, Hewlett-Packard) coupled with flame ionization detector (GC/FID, Agilent 6890N). In addition, a suite of instruments was used to investigate gas- and particle-phase chemistry, see Section S2.

S2. Instrument Operation and Data Analysis Protocols

S2.1 Chemical Ionization Mass Spectrometer (CIMS)

The gas-phase products from α-pinene+O_3/OH reaction were monitored using a custom-modified Varian 1200 triple-quadrupole Chemical Ionization Mass Spectrometer (CIMS). In negative mode operation, CF_3O^- was used as the reagent ion to cluster with an analyte such as hydroperoxide or acid [R], producing $[R{\cdot}CF_3O]^-$ or *m/z* $[M+85]^-$, where M is the molecular weight of the analyte. For more strongly acidic species [H·X], the transfer product, $[H{\cdot}X{\cdot}F]^-$ or *m/z* $[M+19]^-$, is formed during ionization. Carboxylic acids tend to have contributions to both the transfer and cluster product, in which case the overall signal of a compound is considered as the sum of the two product signals.

S2.2 Scanning Mobility Particle Sizer (SMPS)

The size distribution and number concentration of seed particles and organic aerosols were characterized using a custom-built Scanning Mobility Particle Sizer (SMPS) consisting of a Differential Mobility Analyzer (DMA, TSI, 3081) coupled with a Condensation Particle Counter (CPC, TSI, 3010). The DMA was operated in a closed system with a recirculating sheath and excess flow of 2.67 L min^{-1} and a 5.4 : 1 ratio of sheath to aerosol flow rate. The column voltage was scanned from 15 to 9850 V over 45 s. More details on the SMPS operation are given by Loza et al. (1) and Zhang et al. (2). Particle wall loss is not accounted for in the derivation of the overall SOA volume and mass, in order to directly compare with the mass concentration of individual products detected in the suspended particles in the chamber. For a typical ozonolysis experiment conducted at 298 K and < 5% RH, the initial AS seed volume is ~70 μm^3 cm^{-3}, and the initial AS seed number distribution spans from ~20 nm to ~600 nm, with a median diameter of ~80 nm. Growth driven by gas-phase chemistry and gas-particle partitioning occurs primarily on large particles and, as a result, the number median diameter shifts to ~200 nm after ~5 h of reaction.

S2.3 Aerosol Mass Spectrometer (AMS)

Real-time particle mass spectra were collected continuously by an Aerodyne High Resolution Time-of-Flight Aerosol Mass Spectrometer (AMS). All AMS data were

processed with "Squirrel", the ToF-AMS Unit Resolution Analysis Toolkit (http://cires.colorado.edu/jimenez-group/ToFAMSResources /ToFSoftware/index. html), in Igor Pro Version 6.36 (Wavemetrics, Lake Oswego, OR). The ToF-AMS High Resolution Analysis software tool PIKA (Peak Integration by Key Analysis) was employed for high-resolution analysis. Interference of chamber air on the particulate spectrum was corrected by adjusting parameters in the fragmentation table based on the "filter run" (AMS is collecting chamber air with a particle filter in-line) before each experiment. The Improved-Ambient method has been updated in the elemental ratio calculation algorithm (3). The derived average O:C ratios of SOA from α-pinene+O_3 reaction at 298K and < 5% RH range from ~0.45 to ~0.50, which is ~50% higher than that estimated by the traditional routine (4).

S2.4 Particle-into-Liquid Sampler (PILS)

Chamber generated α-pinene SOA was sampled through a 1 μm cut size impactor with a flow rate of 12.5 L min^{-1}, and passed successively through individual acid and base gas denuders and an organic carbon denuder to remove inorganic and organic vapors. A steam flow generated at 100 °C is adiabatically mixed with the cooler aerosol flow in a condensation chamber, creating a high water supersaturation environment in which particles grow sufficiently large (D_p > 1 μm) for collection by inertial impaction onto a quartz plate. Impacted particles are transported to a debubbler by a washing flow (0.15 mL min^{-1}) comprising 50% water and 50% isopropanol. The sampled liquid is delivered into vials held on a rotating carousel. Under the current configuration, a 5-min time resolution can be achieved for the characterization of particle-phase dynamics. In this way, a total of 72 liquid samples were collected for an experiment with approximately 6 h duration.

S2.5 Ultra Performance Liquid Chromatography / Electrospray Ionization Quadrupole Time-of-Flight Mass Spectrometry (UPLC/ESI-Q-ToFMS)

PILS collected liquid samples were analyzed by a WATERS ACQUITY UPLC I-Class System, coupled with a Quadrupole Time-of-Flight Mass Spectrometer (Xevo G2-S QToF) and equipped with an Electrospray Ionization (ESI) source. Sample temperature was kept at 4 °C. An ACUITY BEH C_{18} column (2.1 × 50 mm) was used to separate the

particle-phase product generated from α-pinene reaction with OH/O_3. The 12-min eluent program is: (0 – 2.0 min) 100% A (0.1% v/v formic acid in 99% v/v water and 1% v/v acetonitrile); (2.0 – 10.2 min) 10% A and 90% B (acetonitrile); and (10.2 – 12 min) 100% A. The total flow rate is 0.3 mL min^{-1} and the injection volume is 10 μL. The column temperature was kept at 30 °C. Optimum electrospray conditions are: 2.0 kV capillary voltage, 40 V sampling cone, 80 V source offset, 120 °C source temperature, 500 °C desolvation temperature, 30 L h^{-1} cone gas, and 650 L h^{-1} desolvation gas. Negative ion mass spectra were acquired over a mass range of 40 – 1000 Da. MS/MS spectra were obtained by applying a collision energy ramping program starting from 15 eV to 50 eV over one MS scan in the collision cell. Accurate masses were corrected by a lock spray of leucine encephalin (*m/z* 556.2771 $[M+H]^+$). Data were acquired and processed using the MassLynx v4.1 software.

S3. Characterization of Monomers and Dimers in α-pinene SOA

S3.1 Molecular Structure Elucidation

SI Appendix, Figure S1 (A–C) shows the UPLC/(–)ESI-Q-ToFMS base peak chromatograms (BPCs) for the PILS collected SOA sample (5-min duration) when > 99% α-pinene is consumed via reaction with O_3 at 298 K + 5% RH, 298 K + 50% RH, and 285 K + 5% RH respectively. The dominant ions include *m/z* 213 (retention time, RT 3.81 min), *m/z* 197 (RT 3.86 min), *m/z* 171 (RT 3.96 min), *m/z* 199 (RT 4.07 min), *m/z* 185 (RT 4.35 min), *m/z* 357 (RT 5.32 min), *m/z* 299 (RT 5.78 min) and *m/z* 367 (RT 5.98 min). They are produced in the negative mode of electrospray ionization by the loss of a hydrogen atom from the parent molecule ($[M–H]^-$). The ions at *m/z* 171, *m/z* 185, *m/z* 197, and *m/z* 199 appear in the BPCs of SOA samples generated from the OH-initiated oxidation of α-pinene as well, see *SI Appendix, Figure S1 (D)*, whereas ions at higher mass-to-charge ratio (*m/z* 213, *m/z* 299, *m/z* 357, and *m/z* 367) were not observed over the course of the photooxidation experiment. In addition to the ions that are apparently present on the BPCs, a series of less abundant ions with the mass-to-charge ratio ranging from ~150 to ~400 were also characterized, as listed in *SI Appendix, Table S2*. It is worth noting that each ion we present here has a distinct retention time due to its unique

interactions with the LC column, thus confirming that they are actual α-pinene SOA products instead of artifacts generated in the ESI process.

Molecular structure elucidation of each ion listed in *SI Appendix, Table S2* is based on the first-order (–) ESI mass spectra and fragmentation characteristics in the MS/MS spectra. *SI Appendix, Figure S2* shows the extracted ion chromatograph (EIC), as well as (–) ESI MS and MS/MS spectra for each ion. The major peak on the *m/z* 183 (RT 4.96 min) EIC is assigned to pinonic acid based on comparison of its chromatographic and mass spectrometric behavior with that of commercial available standard *cis*-pinonic acid (Sigma-Aldrich, 98% purity). The MS/MS product spectrum of *m/z* 183 reveals a major peak at *m/z* 139 due to the neutral loss of CO_2 (44 u), see *SI Appendix, Figure S2 (H)*. Similar fragmentation patterns were also observed for ions at *m/z* 169, 171, 185, 189, 197, and 199, as shown in *SI Appendix, Figure S2 (G3, C3, F3, A3, B3, and D3)*. They are assigned to pinalic acid, terpenylic acid, pinic acid, diaterpenylic acid, oxopinonic acid, and hydroxypinonic acid, respectively, consistent with previous studies (5-15). Note that neutral loss of CO_2 has been demonstrated as an abundant dissociation pathway of deprotonated carboxylic acid upon collision induced dissociation (16). The *m/z* 171 EIC shows a dominant peak at retention time (RT) 3.96 min, which is assigned to terpenylic acid, as well as a small shoulder peak at RT 4.07 min, which is assigned to norpinic acid, based on comparison with LC/MS data reported in literature (12). The major peak in the *m/z* 199 EIC is attributed to hydroxypinonic acid, based on the *m/z* 199 → *m/z* 182 (loss of OH) → *m/z* 155 (loss of CO_2) product ion MS/MS spectrum. The weak shoulder peak in the *m/z* 199 EIC likely corresponds to an isobaric compound of hydroxypinonic acid due to the presence of different product ions upon collision. The *m/z* 231 EIC contains five peaks. Of these, the dominant peak (RT 4.12 min) is assigned to diaterpenylic acid acetate based on its fragmentation pattern in the MS/MS spectrum: the two major ions *m/z* 171 and *m/z* 153 result from the neutral loss of CH_3COOH and H_2O molecules, respectively. The ion at *m/z* 247, which has been observed previously (17), is assigned to a molecular formula $C_{10}H_{16}O_5S$. The MS/MS spectrum of the parent ion at *m/z* 247 reveals a major product peak at *m/z* 97 (HSO_4^-), suggesting it contains a sulfate ester structure.

A number of dimers were observed in the mass range between *m/z* 300 and *m/z* 400. Accurate mass measurement suggests they are the extremely low volatility organic compounds (ELVOC) with molecular formula $C_{14\text{-}19}H_{24\text{-}28}O_{6\text{-}9}$. Of these, covalent dimers of the ester type, i.e., pinyl-diaterebyl ester, pinyl-diaterpenyl ester, and pinonyl-pinyl ester, have been proposed for *m/z* 343 (RT 5.45 min), 357, and 367, respectively (8, 9, 12-15). As shown in *SI Appendix, Figure S2 (J3–L3)*, the MS/MS spectra of these ions are in good agreement with previously published results: the collision-induced dissociation of *m/z* 343 (RT 5.45 min) results in *m/z* 157 and *m/z* 185; the collision-induced dissociation of *m/z* 357 results in *m/z* 185 and *m/z* 171; and the collision-induced dissociation of *m/z* 367 results in *m/z* 199 and *m/z* 185. These product ions are produced via the scission of the C–O bond in the ester structure or the C–O bond between the secondary/tertiary carbon and the alcoholic oxygen; see the fragmentation pattern sketched in *SI Appendix, Figure S3*. Further fragmentation of *m/z* 185 produces the *m/z* 141 product ion by the loss of CO_2, which is comparable to that observed for the deprotonated pinic acid $[M–H]^-$. Similarly, further fragmentation of *m/z* 171 produces the *m/z* 127 product ion, which is comparable to that observed for the deprotonated diaterpenylic acid $[M–H]^-$. It is worth noting that there are four major peaks in the *m/z* 343 EIC in *SI Appendix, Figure S2 (I)*. The first peak (RT 3.96) has been attributed to a non-covalent dimer of terpenylic acid, which is produced in the electrospray process (9). The second peak (RT 5.05) is most likely an ester of terpenylic acid and diaterpenylic acid: collision-induced dissociation of this ion results in the formation of *m/z* 213, *m/z* 187, *m/z* 171, and *m/z* 127 ions, see *SI Appendix, Figure S3* for the fragmentation mechanism. The third peak (RT 5.32) co-elutes with the *m/z* 357 ion, indicating that this peak might be formed in the electrospray process (loss of CH_2) other than representing an actual product from the reaction of α-pinene with ozone.

In addition to the dimers (*m/z* 343, *m/z* 357, and *m/z* 367) that have been previously reported, a number of ions with mass to charge ratio of 300 – 400 (u) are newly identified here, including *m/z* 271 (RT 6.45 min), *m/z* 299 (RT 5.78 min), *m/z* 309 (RT 5.70 min), *m/z* 311 (RT 5.80 min), *m/z* 313 (RT 6.08 min), *m/z* 325 (RT 6.01 min), *m/z* 337 (RT 6.19 min), *m/z* 355 (RT 5.62 min), *m/z* 375 (RT 5.90 min), and *m/z* 399 (RT 5.88 min). They are assigned to molecular formulas of $C_{14}H_{24}O_5$, $C_{15}H_{24}O_6$, $C_{17}H_{26}O_5$, $C_{16}H_{24}O_6$,

$C_{16}H_{26}O_6$, $C_{17}H_{26}O_6$, $C_{18}H_{26}O_6$, $C_{18}H_{28}O_7$, $C_{17}H_{28}O_9$, and $C_{19}H_{28}O_9$, respectively, with estimated errors less than ± 10 ppm, as shown in *SI Appendix, Table S2*. Close inspection of their MS/MS spectra reveals that two ions, *m/z* 185 and *m/z* 171, are the major fragments produced upon collision-induced dissociation of the parent ions, see *SI Appendix, Figure S3 (M3 – V3)*. Further, the *m/z* 185 → *m/z* 167 (loss of H_2O) → *m/z* 141 (loss of CO_2) and *m/z* 171 → *m/z* 127 (loss of CO_2) fragmentation patterns, which are typical for dicarboxylic acid monoanions, are commonly observed across all ions. This indicates that pinic acid and diaterpenylic acid, or their isobaric isomers, are important monomeric building blocks for these dimers.

S3.2 Quantification

S3.2.1 Particle-Phase Components Mass Concentration Retrieval

Chamber generated α-pinene SOA was collected by PILS, which operates with a duty cycle of 5 min, and then analyzed off-line by UPLC/ESI-Q-ToFMS in the negative mode. For each experiment with approximately 6 h duration (*SI Appendix, Table S1*), a total of 72 liquid samples were collected in order to capture the dynamics of individual particle-phase components during the early stage of particle growth and SOA aging. It is worth noting that the liquid column separation prior to the electrospray ionization process precludes ionization suppression caused by potential interfering compounds mixed with the analyte, thus facilitating molecular-level quantification of particle-phase components. For any given species *i*, its particle-phase mass concentration, $C_{p,i}$ (μg m^{-3}), in the chamber is given by:

$$C_{p,i} = \frac{1000 \cdot R_i \cdot Q_l \cdot DF \cdot \rho_l}{IE_i \cdot Q_g \cdot CE_{PILS}} \quad \text{(S1)}$$

where 1000 is the unit conversion factor, R_i is the ESI-Q-ToFMS response towards the ion ($[M-H]_i^-$) produced via deprotonation of compound *i* in the negative mode, Q_l is the liquid sampling flow rate (1.5 mL min^{-1}), *DF* is the dilution factor that accounts for the water vapor condensation on the PILS impactor wall, ρ_l is the density of collected liquid, which is assumed to be the density of the washing flow (0.893 g cm^{-3}), which is composed of 50% Milli-Q water and 50% isopropyl alcohol, Q_g is the gas sampling flow

rate (12.5 L min^{-1}), IE_i is the electrospray ionization efficiency (sensitivity) of compound *i,* and CE_{PILS} is the collection efficiency of PILS for α-pinene+O_3 derived SOA. Here a collection efficiency of 0.8–0.9 is used based on a linear relationship between CE_{PILS} and the particulate average O:C ratio developed in our recent studies (18).

S3.2.2 Electrospray Ionization Efficiency Estimation

The ESI process proceeds via the ion evaporation mechanism in the case of low molecular weight compounds (19, 20). The electrospray conditions and molecular structures of analytes govern the ionization efficiency. Since the ESI-MS operation parameters are controlled consistently in the present study, the ionization efficiency of individual products identified here is expected to depend strongly on their physicochemical properties, such as molecule size, pK_a value, hydrophobicity, surface activity, etc. (21). The ionization efficiency of pinonic acid is obtained directly from the counts/concentration calibration curve of commercially available *cis*-pinonic acid standard (Sigma-Aldrich, 98% purity). The ionization efficiency of other products identified in *SI Appendix, Table S2* is estimated based on a linear model developed by Kruve et al. (22):

$$\log RIE_i = (1.04\pm0.34) + (2.23\pm0.34)\cdot\alpha_i + (-0.51\pm0.04)\cdot WAPS_i\cdot 10^5 \quad \text{(S2)}$$

where RIE_i is the relative ionization efficiency of compound *i* relative to benzoic acid via deprotonation in the negative mode, α_i is the degree of ionization for compound *i*, which is calculated based on its pK_a and the pH of the aqueous phase, and $WAPS_i$ (weighted average positive sigma) is a parameter defined as the weighted mean of positive sigma (σ) values divided by the ion surface area (23):

$$WAPS = \frac{\int_{\sigma=0}^{\infty} \sigma \cdot p(\sigma) \cdot d\sigma}{A \int_{\sigma=0}^{\infty} p(\sigma) \cdot d\sigma} \quad \text{(S3)}$$

where σ is the polarization charge density on the ion surface, $p(\sigma)$ is the probability function of σ (sigma profile), and A is the surface area of the anion.

COnductor-like Screening MOdel for Real Solvents (COSMO-RS) method (24) implemented into the Amsterdam Density Functional (ADF 2014.07) molecular modeling suite (25) was used for calculating pK_a of individual compounds dissolved in

water/acetonitrile mixture, as well as generating the sigma profiles needed for calculating the *WAPS* parameter. First, 18 molecules were chosen from *SI Appendix, Table S2* and the proper structure and connectivity of each molecule was drawn in three dimensions in the ADF tool. Different conformations were considered and the conformers with lowest energy were adopted. Next, the molecular geometries were optimized at the TZP level with the Becke-Perdew (BP) Generalized Gradient Approximation (GGA) density functional. By doing so, the ideal-gas phase-equilibrium geometry for each molecule can be obtained. Second, a COSMO calculation was carried out on all species using the ADF input files to calculate the screening charges mapped on the cavity surface surrounding the molecule in the condensed phase. Here, hydrogen bonding was taken into account, which is particularly necessary for large molecules so that the monoanion adopts a 'coiled' conformation placing the ionized carboxyl group with a labile hydrogen atom in close proximity. It is worth noting that the atomic radii for the four elements, i.e., carbon, hydrogen, oxygen, and sulfur, have been included and optimized in the COSMO-RS approach. Finally, using the calculated charge density distribution, we can calculate the charge delocalization in the species, as represented by the parameter *WAPS*.

The aqueous pK_a of each compound, denoted as ${}^{w}_{w}pK_a$, was calculated based on its free energy of dissociation in water (ΔG^*_{diss}). The cluster-continuum approach in the COSMO-RS model was employed to compute the ΔG^*_{diss} values. It has been recommended that the cluster-continuum approach can predict the aqueous pK_a for strong to moderately weak acids with reasonable accuracy (26). Molecules that have two or more equivalent sites for deprotonation (e.g., dicarboxylic acids) were not taken into account, so the predicted aqueous pK_a values are only for the dissociation of the first proton (pK_{a1}). Here it is not necessary to predict pK_{a2} since di-anions were not observed during the electrospray ionization of dicarboxylic acids. It is important to note that when an analyte elutes from the LC column, the solvent composition for this particular analyte depends on the eluent program: the volume fraction of acetonitrile in the water/acetonitrile solvent mixture increases linearly from ~20% to ~50% from retention time 3.6 min to retention time 7.2 min. To account for the explicit solvent molecules, we applied a linear model developed by Espinosa et al. (27). In this way, the pK_a value of an

analyte in the water/acetonitrile mixture (${}^{s}_{s}pK_a$) can be accurately predicted from its corresponding pK_a value in water (${}^{w}_{w}pK_a$), with standard deviation less than 0.3 pK_a unit:

$$ {}^{s}_{s}pK_a = a_s \times {}^{w}_{w}pK_a + b_s \quad \text{(S4)} $$

where a_s is related to difference between specific solvation interactions, which depend on the solvent and family of compounds, and b_s is related to the difference in basicities, dielectric constants, and specific solvation interactions of the solute between the organic solvent, which is acetonitrile here, and water. Specific values used for a_s and b_s in this study are referred to Table 2 in the original paper.

The pH of the LC solvent, i.e., acetonitrile/water mixture, was directly measured using a digital pH meter (VWR Scientific Model 8010), with its electrode calibrated with standard aqueous buffers. The pH obtained herein is denoted as ${}^{s}_{w}pH$, namely, pH measured in acetonitrile/water mixture and referred to water as standard state. The 'δ' factor is applied to convert ${}^{s}_{w}pH$ to ${}^{s}_{s}pH$, i.e., pH measured in acetonitrile/water mixture and referred to the same acetonitrile/water mixture as standard state, with standard deviation less than 0.02 pH unit (28):

$$ {}^{s}_{s}pH = {}^{s}_{w}pH - \delta \quad \text{(S5)} $$

Here the 'δ' term represents the primary medium effect and the difference between the liquid-junction potentials of the electrode system in solvent mixture and water. Specific values used for δ in this study are referred to Equation (10) in the original paper.

Finally, the degree of ionization for each analyte (α) in the LC mobile phase (v/v % acetonitrile/water) can be calculated given the estimated ${}^{s}_{s}pK_a$ value for each compound and the ${}^{s}_{s}pH$ of the mobile phase:

$$ \alpha = \frac{10^{-{}^{s}_{s}pK_a}}{10^{-{}^{s}_{s}pK_a} + 10^{-{}^{s}_{s}pH}} \quad \text{(S6)} $$

SI Appendix, Figure S4 shows the COSMO-RS computed sigma profiles for 6 negative ions (*m/z* 171, 183, 231, 247, 357, and 367) identified in this study. The sigma profile presents the probability distribution of a molecular surface segment that has a specific charge density (29). For each ion, its sigma profile contains 90 segments, 0.0089

e/Å^2 wide, in the range of -0.04 e/Å^2 to 0.04 e/Å^2. Given the sigma profiles, we can calculate the weighted average positive sigma (*WAPS*) via Equation (S3). The smaller the *WAPS* value, the more delocalized the charge in the anion. The effect of charge delocalization on the electrospray ionization efficiency can be explained by the charge to charge repulsion occurring on the ESI droplet (22). The more delocalized the charge in the anion, the more charge to charge repulsion occurs between ions, the more likely ions evaporates from the ESI droplet, and as a result, the higher ionization efficiency of the parent molecule. It can be seen that the calculated relative ionization efficiency towards *cis*-pinonic acid standard (*RIE*) strongly depends on the *WAPS* parameter. For example, the *RIE* of *m/z* 367 is ~7 times higher than that for *cis*-pinonic acid, given the corresponding *WAPS* values of 2.58×10^{-5} and 4.25×10^{-5}, respectively. The effect of the pK_a parameter on the ionization efficiency lies in the abundance of ionizable components in the droplets. A straightforward illustration would be that strong acids tend to completely dissociate in the aqueous solution and present as the conjugate base ($HA \rightarrow H^+ + A^-$). As a result, compounds with relatively low pK_a values tend to give a high response in the ESI negative mode. For example, the *RIE* of *m/z* 247, which represents a sulfate ester, is approximately two orders magnitude higher than that for *cis*-pinonic acid.

S3.2.3 Uncertainty Analysis

Uncertainties in the PILS particle sampling technique arise mainly from variation of the collected liquid volume due to the existence of air bubbles. We have estimated in the PILS+UPLC/ESI-Q-ToFMS methodology study that this uncertainty is less than ±11% (16). Next, we need to evaluate the uncertainties that arise from the electrospray ionization efficiency calculation. Since we have used a linear model that is developed based on optimal fitting of the predicted ionization efficiency to the corresponding measurements, we focus on the resulting uncertainties by employing this linear model to predict the *RIE* of the identified species. While we acknowledge uncertainties from the prediction of thermodynamic properties of molecules using the COSMO-RS software, it is important to note that these uncertainties have been incorporated in the linear model. *SI Appendix, Table S2* gives the predicted *RIE* of each product identified from the α-pinene SOA system relative to that of the *cis*-pinonic acid standard as well as the corresponding

uncertainties. It can be seen that the parameter, *WAPS*, contributes to most of the simulation uncertainties, whereas uncertainty resulting from the pK_a parameter is insignificant. This is due to the LC conditions employed in this study: most products are not dissociated at pH of 2–3 and are present in molecular form in the mobile phase prior to ESI.

S4. Vapor-Particle Dynamics Model

A modified version of the Vapor-Particle Dynamics Model was used to simulate the proposed mechanism for the $C_{17}H_{26}O_6$ ester dimer formation during the ozonolysis of α-pinene. Details of the model can be found in the original paper (30), and only an overview and the additional modifications are presented here. The model simulates gas/condensed-phase reactions, condensation/evaporation of gas-phase compounds to produce organic aerosol, particle-wall deposition, and vapor-wall interactions in a well-mixed laboratory chamber. A moving-bin version of the model is used to represent the single distribution of the chamber aerosol, and coagulation is neglected.

The gas- and particle-phase reactions simulated are given in *SI Appendix, Table S4*. These reactions are not intended to represent the full mechanism for the ozonolysis of α-pinene but rather involve species only contributing to the formation of the $C_{17}H_{26}O_6$ ester dimer. The particle-phase decomposition of the diacyl peroxide to form the ester is added to the mechanism, which did not originally include particle-phase reactions. Reactions G01 through G10 are taken from MCMv3.2 (http://mcm.leeds.ac.uk/MCM). The rate constants for G07 and G10 were changed to 5×10^{-12} cm^3 $molec^{-1}$ s^{-1} based on the mean of primary, secondary, and tertiary RO_2 reaction rate constants (31). The rate constants and molar product yields for reactions G11, P01, and P02 were optimized in order to match the observed particle-phase concentration of the $C_{17}H_{26}O_6$ ester dimer. Because the model does not simulate inorganic chemistry or the full α-pinene ozonolysis mechanism, O_3, OH, HO_2, and RO_2 concentrations are needed as inputs (no OH scavenger was used during the experiment, and thus the ozonolysis of α-pinene generates OH as a coproduct). The O_3 concentration was measured experimentally. This experimental curve was fit to a fourth-order Gaussian function and used in the model to determine the O_3 concentration at each moment in time. OH, HO_2, and RO_2 concentrations were not measured

experimentally. Therefore, concentrations for these species were predicted using the Generator for Explicit Chemistry and Kinetics of Organics in the Atmosphere (GECKO-A) (32) using the corresponding experimental conditions (154 ppb α-pinene, 200 ppb O_3, zero NO_x, 298 K, and < 5% RH) as the input. The OH, HO_2, and RO_2 curves generated by GECKO-A were also fit to fourth-order Gaussian functions which were then implemented in the model. For simulations with initial mixing ratios of 10 ppb α-pinene + 20 ppb O_3, concentrations of reactants and free radicals were predicted by GECKO-A as well.

The two stable gas-phase species, pinic acid ($C_9H_{14}O_4$) and the diacyl peroxide ($C_{18}H_{26}O_8$), condense onto both seed particles and the chamber walls. The rate of condensation onto particles is controlled by the vapor-particle accommodation coefficient. The optimal vapor-particle accommodation coefficient was determined separately for each of the two compounds in order to match the observed particle-phase concentration. An accommodation coefficient of 0.01 was determined for pinic acid, and an accommodation coefficient of 0.1 was determined for the diacyl peroxide. The vapor pressures of pinic acid and the diacyl peroxide are listed in *SI Appendix, Table S4*. The organic aerosol concentration was measured experimentally using the SMPS. The 2-Product model was fit to the observed ΔM_o (the total organic aerosol mass produced) vs. ΔHC (the mass of hydrocarbon reacted) curve and was then used to predict the SOA yield at low organic mass loadings.

Condensation onto the chamber walls is treated as an equilibration process, characterized by an effective organic concentration in the walls (C_w), which is set to 10 mg m^{-3} (33). The vapor wall loss rates for the two condensable species, pinic acid and the diacyl peroxide, were predicted using the empirical expression derived by Zhang et al. (34) relating the vapor-wall accommodation to the species vapor pressure. The predicted wall loss rates are listed in *SI Appendix, Table S4*. The initial size distribution of the inorganic seed particles is lognormal with a standard deviation of 1.5 and a number concentration determined experimentally using the SMPS. Particle wall losses were implemented using the diameter-dependent wall loss rates measured experimentally in the Caltech chamber. The quantities of pinic acid and diacyl peroxide that condensed on

particles that subsequently deposited on the chamber walls are considered lost from the simulation.

References:

1. Loza CL, et al. (2014) Secondary organic aerosol yields of 12-carbon alkanes. *Atmos Chem Phys* 14(3):1423-1439.
2. Zhang X, et al. (2014) Role of ozone in SOA formation from alkane photooxidation. *Atmos Chem Phys* 14(3):1733-1753.
3. Canagaratna, et al. (2015) Elemental ratio measurements of organic compounds using aerosol mass spectrometry: characterization, improved calibration, and implications. Atmos. Chem. Phys. 15, 253-272, 2015.
4. Chhabra PS, Flagan RC, Seinfeld JH (2010) Elemental analysis of chamber organic aerosol using an aerodyne high-resolution aerosol mass spectrometer. *Atmos Chem Phys* 10(9):4111-4131.
5. Jenkin ME, Shallcross DE, Harvey JN (2000) Development and application of a possible mechanism for the generation of cis-pinic acid from the ozonolysis of alpha- and beta-pinene. *Atmos Environ* 34(18):2837-2850.
6. Jaoui M, Kamens RM (2001) Mass balance of gaseous and particulate products analysis from alpha-pinene/NOx/air in the presence of natural sunlight. *J Geophys Res-Atmos* 106(D12):12541-12558.
7. Ma Y, Russell AT, Marston G (2008) Mechanisms for the formation of secondary organic aerosol components from the gas-phase ozonolysis of alpha-pinene. *Phys Chem Chem Phys* 10(29):4294-4312.
8. Muller L, Reinnig MC, Warnke J, Hoffmann T (2008) Unambiguous identification of esters as oligomers in secondary organic aerosol formed from cyclohexene and cyclohexene/alpha-pinene ozonolysis. *Atmos Chem Phys* 8(5):1423-1433.
9. Claeys M, et al. (2009) Terpenylic acid and related compounds from the oxidation of alpha-pinene: implications for new particle formation and growth above forests. *Environ Sci Technol* 43(18):6976-6982.
10. Camredon M, et al. (2010) Distribution of gaseous and particulate organic composition during dark alpha-pinene ozonolysis. *Atmos Chem Phys* 10(6):2893-2917.
11. Gao YQ, Hall WA, Johnston MV (2010) Molecular composition of monoterpene secondary organic aerosol at low mass loading. *Environ Sci Technol* 44(20):7897-7902.

12. Yasmeen F, et al. (2010) Terpenylic acid and related compounds: precursors for dimers in secondary organic aerosol from the ozonolysis of alpha- and beta-pinene. *Atmos Chem Phys* 10(19):9383-9392.

13. Kristensen K, et al. (2013) Formation and occurrence of dimer esters of pinene oxidation products in atmospheric aerosols. *Atmos Chem Phys* 13(7):3763-3776.

14. Kristensen K, et al. (2014) Dimers in alpha-pinene secondary organic aerosol: effect of hydroxyl radical, ozone, relative humidity and aerosol acidity. *Atmos Chem Phys* 14(8):4201-4218.

15. Witkowski B, Gierczak T (2014) Early stage composition of SOA produced by alpha-pinene/ozone reaction: alpha-acyloxyhydroperoxy aldehydes and acidic dimers. *Atmos Environ* 95:59-70.

16. Bandu ML, Watkins KR, Bretthauer ML, Moore CA, Desaire H (2004) Prediction of MS/MS data. 1. a focus on pharmaceuticals containing carboxylic acids. *Anal Chem* 76(6):1746-1753.

17. Liggio J, Li SM (2006) Reactive uptake of pinonaldehyde on acidic aerosols. *J Geophys Res-Atmos* 111(D24).

18. Zhang X, et al. (2015) Time-resolved molecular characterization of organic aerosols by PILS + UPLC/ESI-Q-TOFMS. *Atmos Environ* 10.1016/j.atmosenv.2015.08.049.

19. Enke CG (1997) A predictive model for matrix and analyte effects in electrospray ionization of singly-charged ionic analytes. *Anal Chem* 69(23):4885-4893.

20. Kebarle P (2000) Gas phase ion thermochemistry based on ion-equilibria From the ionosphere to the reactive centers of enzymes. *Int J Mass Spectrom* 200(1-3):313-330.

21. Oss M, Kruve A, Herodes K, Leito I (2010) Electrospray ionization efficiency scale of organic compounds. *Anal Chem* 82(7):2865-2872.

22. Kruve A, Kaupmees K, Liigand J, Leito I (2014) Negative electrospray ionization via deprotonation: predicting the ionization efficiency. *Anal Chem* 86(10):4822-4830.

23. Kaupmees K, Kaljurand I, Leito I (2010) Influence of water content on the acidities in acetonitrile. quantifying charge delocalization in anions. *J Phys Chem A* 114(43):11788-11793.

24. Klamt A (1995) Conductor-like screening model for real solvents - a new approach to the quantitative calculation of solvation phenomena. *J Phys Chem-Us* 99(7):2224-2235.

25. Pye CC, Ziegler T, van Lenthe E, Louwen JN (2009) An implementation of the conductor-like screening model of solvation within the Amsterdam density functional package - Part II. COSMO for real solvents. *Can J Chem* 87(7):790-797.

26. Eckert F, Diedenhofen M, Klamt A (2010) Towards a first principles prediction of pK(a): COSMO-RS and the cluster-continuum approach. *Mol Phys* 108(3-4):229-241.

27. Espinosa S, Bosch E, Roses M (2002) Retention of ionizable compounds in high-performance liquid chromatography - 14. acid-base pK values in acetonitrile-water mobile phases. *J Chromatogr A* 964(1-2):55-66.

28. Espinosa S, Bosch E, Roses M (2000) Retention of ionizable compounds on HPLC. 5. pH scales and the retention of acids and bases with acetonitrile-water mobile phases. *Anal Chem* 72(21):5193-5200.

29. Mullins E, et al. (2006) Sigma-profile database for using COSMO-based thermodynamic methods. *Ind Eng Chem Res* 45(12):4389-4415.

30. McVay RC, Cappa CD, Seinfeld JH (2014) Vapor-wall deposition in chambers: theoretical considerations. *Environ Sci Technol* 48(17):10251-10258.

31. Orlando JJ, Tyndall GS (2012) Laboratory studies of organic peroxy radical chemistry: an overview with emphasis on recent issues of atmospheric significance. *Chem Soc Rev* 41(19):6294-6317.

32. Aumont B, Szopa S, Madronich S (2005) Modelling the evolution of organic carbon during its gas-phase tropospheric oxidation: development of an explicit model based on a self generating approach. *Atmos Chem Phys* 5:2497-2517.

33. Zhang X, et al. (2014) Influence of vapor wall loss in laboratory chambers on yields of secondary organic aerosol. *P Natl Acad Sci USA* 111(16):5802-5807.

34. Zhang X, et al. (2015) Vapor wall deposition in Teflon chambers. *Atmos Chem Phys* 15(8):4197-4214.

35. Crounse JD, Nielsen LB, Jorgensen S, Kjaergaard HG, Wennberg PO (2013) Autoxidation of organic compounds in the atmosphere. *J Phys Chem Lett* 4(20):3513-3520.

36. Rissanen MP, et al. (2014) The formation of highly oxidized multifunctional products in the ozonolysis of cyclohexene. *J Am Chem Soc* 136(44):15596-15606.

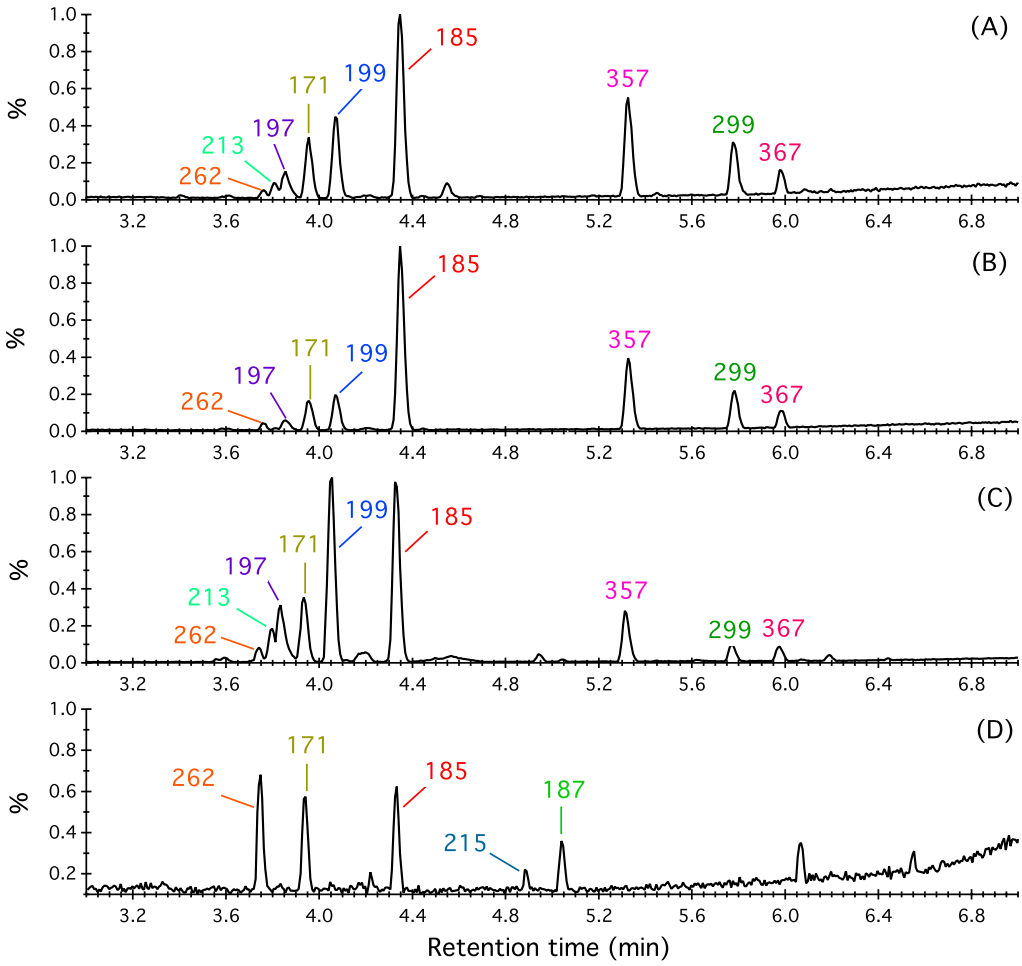

Figure S1. UPLC/(–)ESI-Q-ToFMS base peak chromatographs (BPCs) of particle-phase constituents produced from (A) dark ozonolysis of α-pinene at 298 K and 5% RH; (B) dark ozonolysis of α-pinene at 298 K and 50% RH; (C) dark ozonolysis of α-pinene at 285 K and 5% RH; and (D) OH-initiated oxidation of α-pinene at 298 K and 5% RH. The numbers listed next to each peak correspond to the respective $[M–H]^-$ ions generated in the ESI negative mode. Ions at *m/z* 171, 199, and 185 correspond to terpenylic acid, OH-pinonic acid, and pinic acid, respectively. These three monomers are detected in SOA from both OH-initiated and O_3-initiated oxidation of α-pinene.

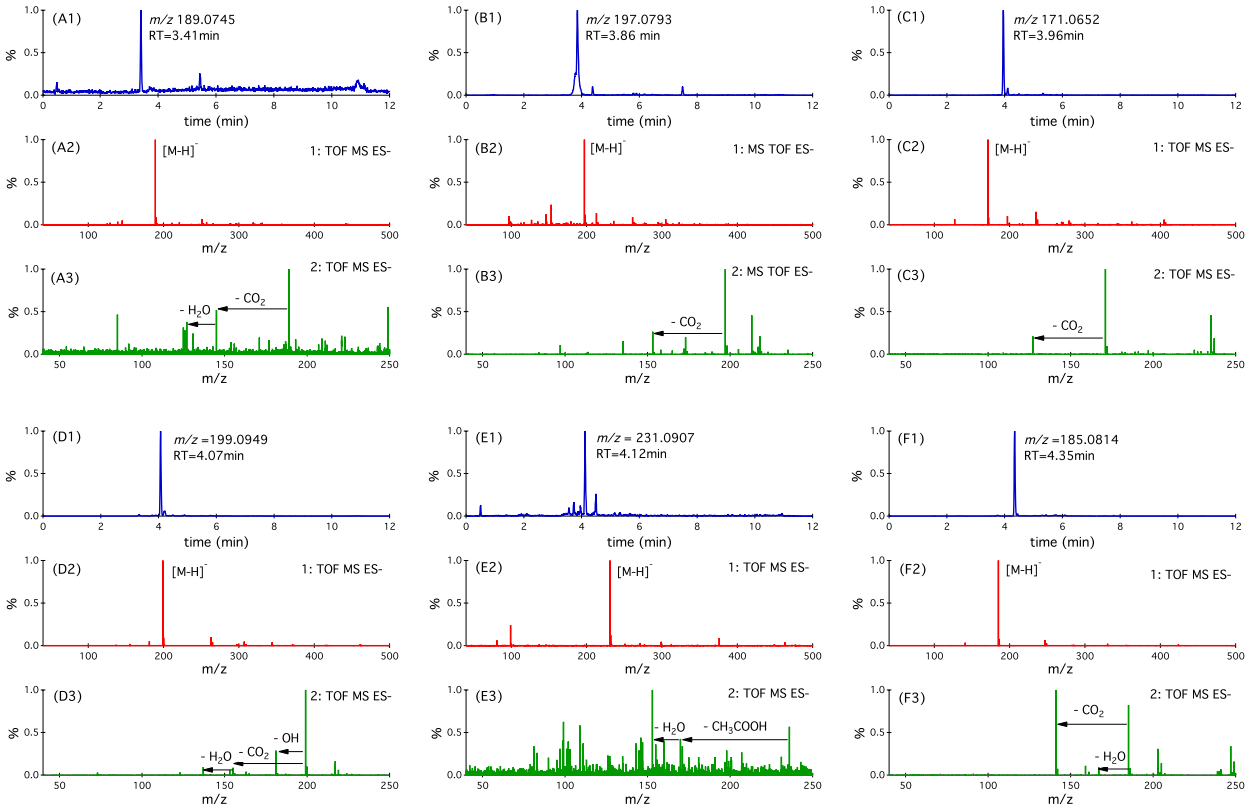
(A1)
m/z 189.0745
RT=3.41min
(A2)
[M-H]-
1: TOF MS ES-
(A3)
2: TOF MS ES-
- H2O
- CO2
(B1)
m/z 197.0793
RT=3.86 min
(B2)
[M-H]-
1: MS TOF ES-
(B3)
2: MS TOF ES-
- CO2
(C1)
m/z 171.0652
RT=3.96min
(C2)
[M-H]-
1: TOF MS ES-
(C3)
2: TOF MS ES-
- CO2
(D1)
m/z =199.0949
RT=4.07min
(D2)
[M-H]-
1: TOF MS ES-
(D3)
2: TOF MS ES-
- H2O
- CO2
- OH
(E1)
m/z = 231.0907
RT=4.12min
(E2)
[M-H]-
1: TOF MS ES-
(E3)
2: TOF MS ES-
- H2O
- CH3COOH
(F1)
m/z =185.0814
RT=4.35min
(F2)
[M-H]-
1: TOF MS ES-
(F3)
2: TOF MS ES-
- CO2
- H2O
%
time (min)
m/z

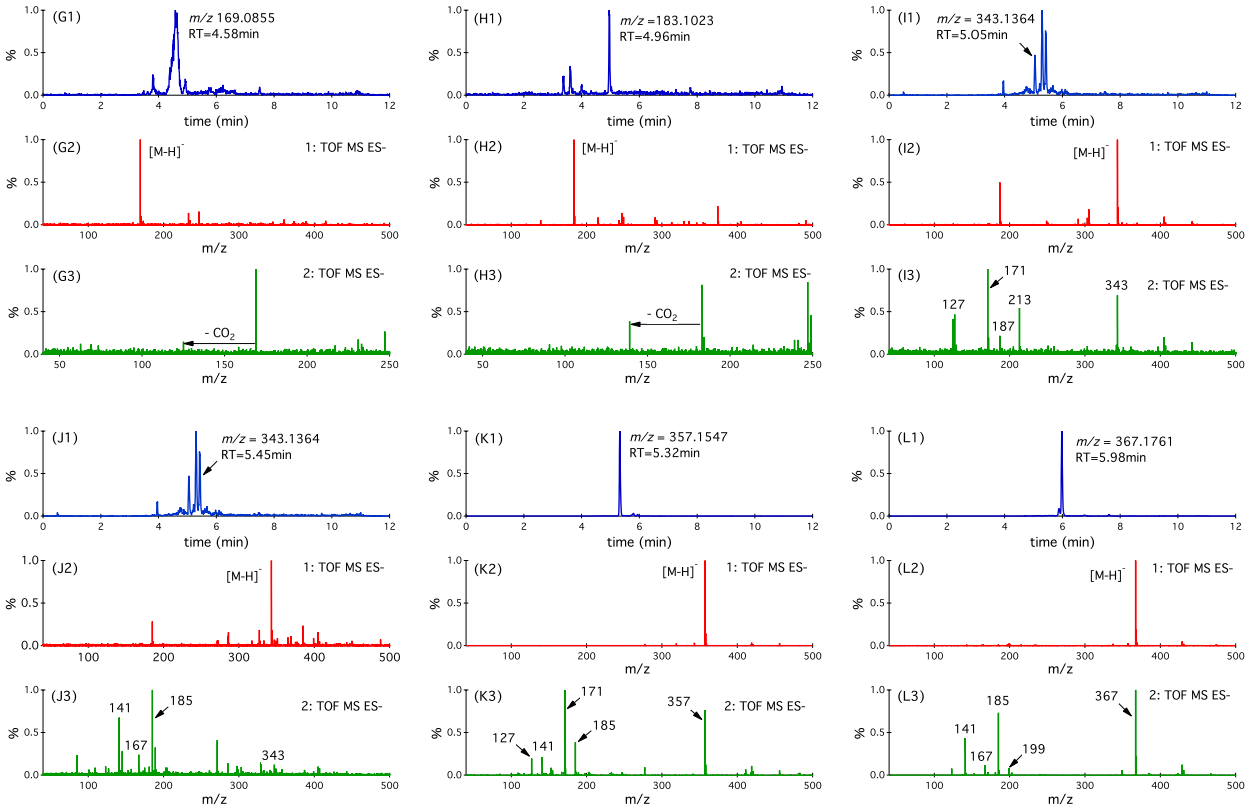
(G1)
m/z 169.0855
RT=4.58min
time (min)
(G2)
[M-H]-
1: TOF MS ES-
m/z
(G3)
2: TOF MS ES-
- CO2
m/z
(H1)
m/z =183.1023
RT=4.96min
time (min)
(H2)
[M-H]-
1: TOF MS ES-
m/z
(H3)
2: TOF MS ES-
- CO2
m/z
(I1)
m/z = 343.1364
RT=5.05min
time (min)
(I2)
[M-H]-
1: TOF MS ES-
m/z
(I3)
171
127
213
343
187
2: TOF MS ES-
m/z
(J1)
m/z = 343.1364
RT=5.45min
time (min)
(J2)
[M-H]-
1: TOF MS ES-
m/z
(J3)
141
185
167
343
2: TOF MS ES-
m/z
(K1)
m/z = 357.1547
RT=5.32min
time (min)
(K2)
[M-H]-
1: TOF MS ES-
m/z
(K3)
171
357
127
141
185
2: TOF MS ES-
m/z
(L1)
m/z = 367.1761
RT=5.98min
time (min)
(L2)
[M-H]-
1: TOF MS ES-
m/z
(L3)
185
367
141
167
199
2: TOF MS ES-
m/z

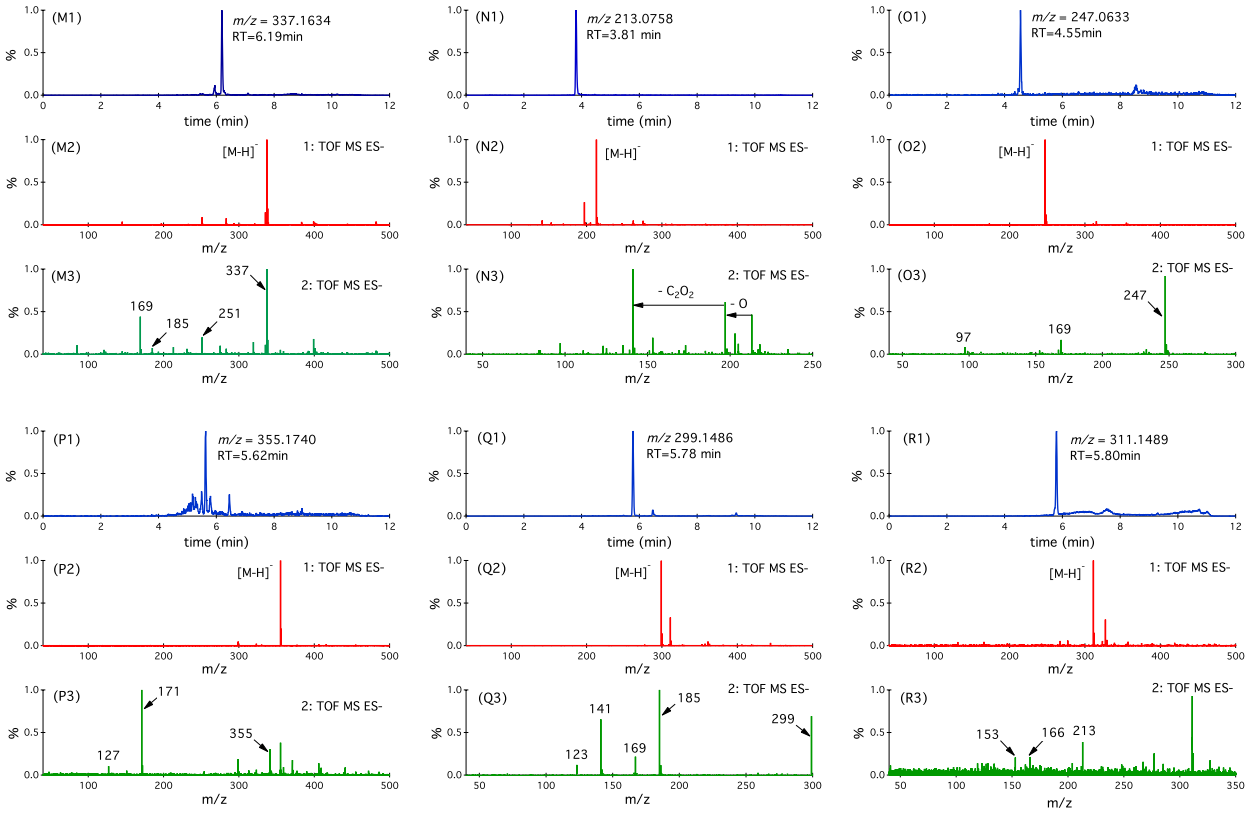
(M1)
m/z = 337.1634
RT=6.19min
time (min)
(M2)
[M-H]-
1: TOF MS ES-
m/z
(M3)
337
169
185
251
2: TOF MS ES-
m/z
(N1)
m/z 213.0758
RT=3.81 min
time (min)
(N2)
[M-H]-
1: TOF MS ES-
m/z
(N3)
- C2O2
- O
2: TOF MS ES-
m/z
(O1)
m/z = 247.0633
RT=4.55min
time (min)
(O2)
[M-H]-
1: TOF MS ES-
m/z
(O3)
247
97
169
2: TOF MS ES-
m/z
(P1)
m/z = 355.1740
RT=5.62min
time (min)
(P2)
[M-H]-
1: TOF MS ES-
m/z
(P3)
171
127
355
2: TOF MS ES-
m/z
(Q1)
m/z 299.1486
RT=5.78 min
time (min)
(Q2)
[M-H]-
1: TOF MS ES-
m/z
(Q3)
141
185
299
123
169
2: TOF MS ES-
m/z
(R1)
m/z = 311.1489
RT=5.80min
time (min)
(R2)
[M-H]-
1: TOF MS ES-
m/z
(R3)
153
166
213
2: TOF MS ES-
m/z

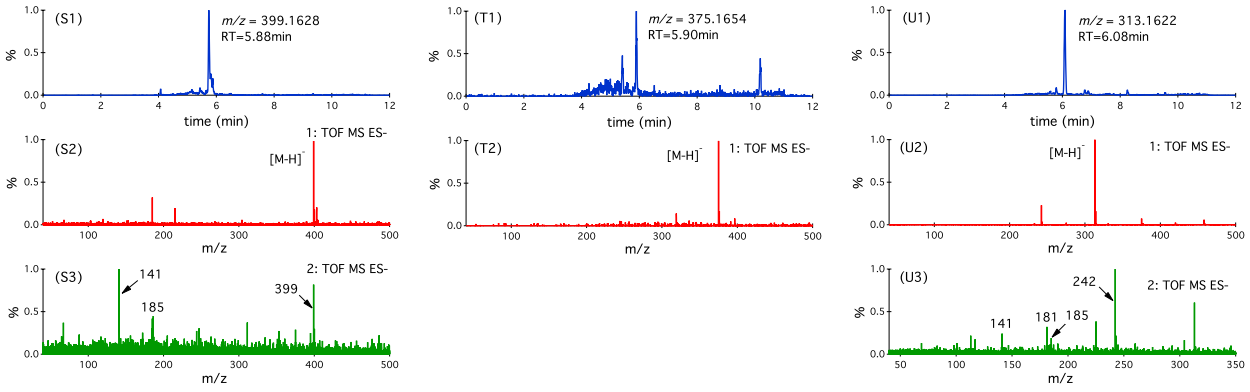

Figure S2. UPLC/(–)ESI-Q-ToFMS chromatographs and mass spectra of particle-phase constituents produced from the dark reaction of ~150 ppb α-pinene with ~200 ppb O_3 at 298 K and 5% RH. Corresponding molecular formula and chemical structures are proposed in *SI Appendix, Table S2*. Subplot (A1–V1): The extracted ion chromatograph (EIC) for each product identified with distinct retention time; Subplot (A2–V2): Corresponding mass spectra for the chromatographic peaks shown in A1–V1. Ions are detected in the negative mode by the loss of one hydrogen atom ($[M–H]^-$); and Subplot (A3–V3): Corresponding MS/MS spectra for the product ions generated from the collision-induced dissociation of the parent ions in A2–V2.

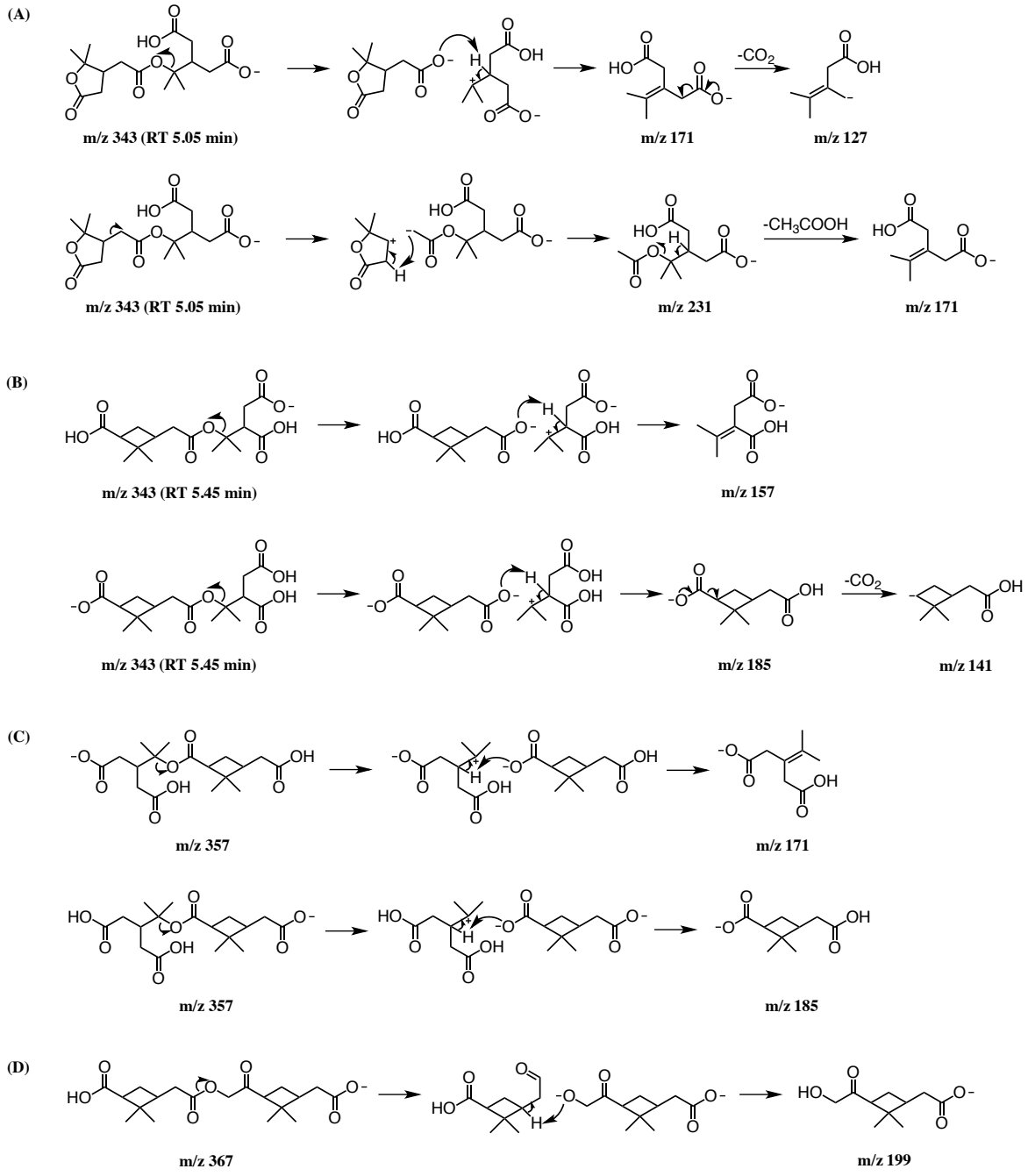

Figure S3. Fragmentation pathways of negative ions at m/z 343, m/z 357, and m/z 367 examined by collision induced dissociation (CID).

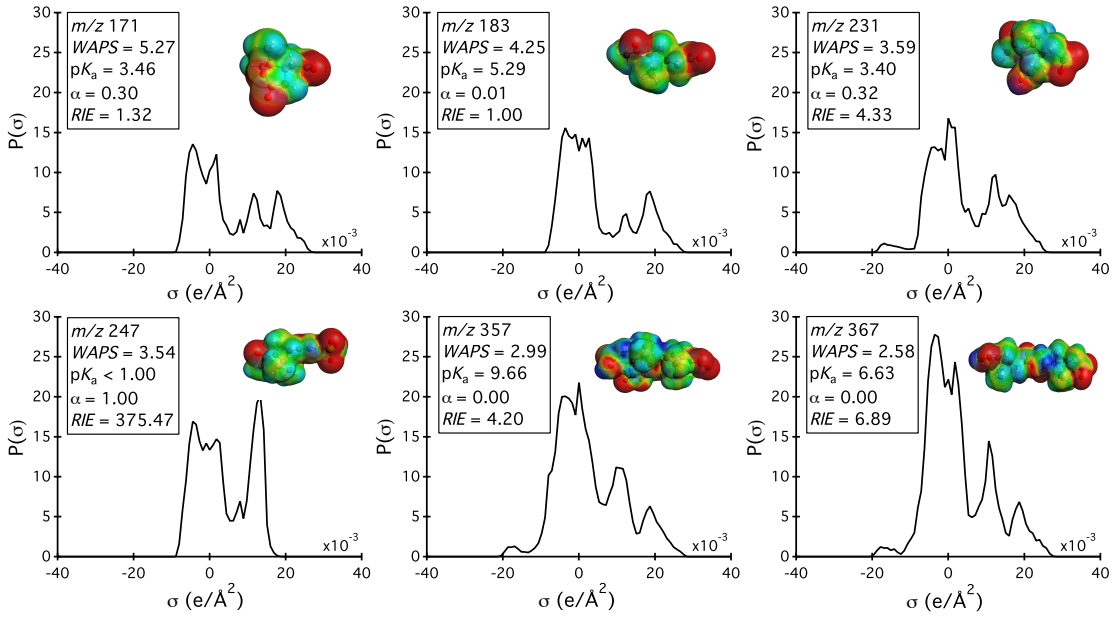

Figure S4. Sigma profiles of negative ions ($[M–H]^-$) at *m/z* 171, 183, 231, 247, 357, and 367. The structure of each ion is shown in the format of the COSMO charge density on a COSMO surface visualized with ADFview. Note that the red color represents positive COSMO charge density (the underlying molecular charge is negative), and the blue color represents negative COSMO charge density (the underlying molecular charge is positive). The calculated *WAPS* ($\times 10^5$), ${}^{s}_{s}pK_a$, degree of ionization (α), and relative ionization efficiency (RIE_i) to pinonic acid are also shown for each ion.

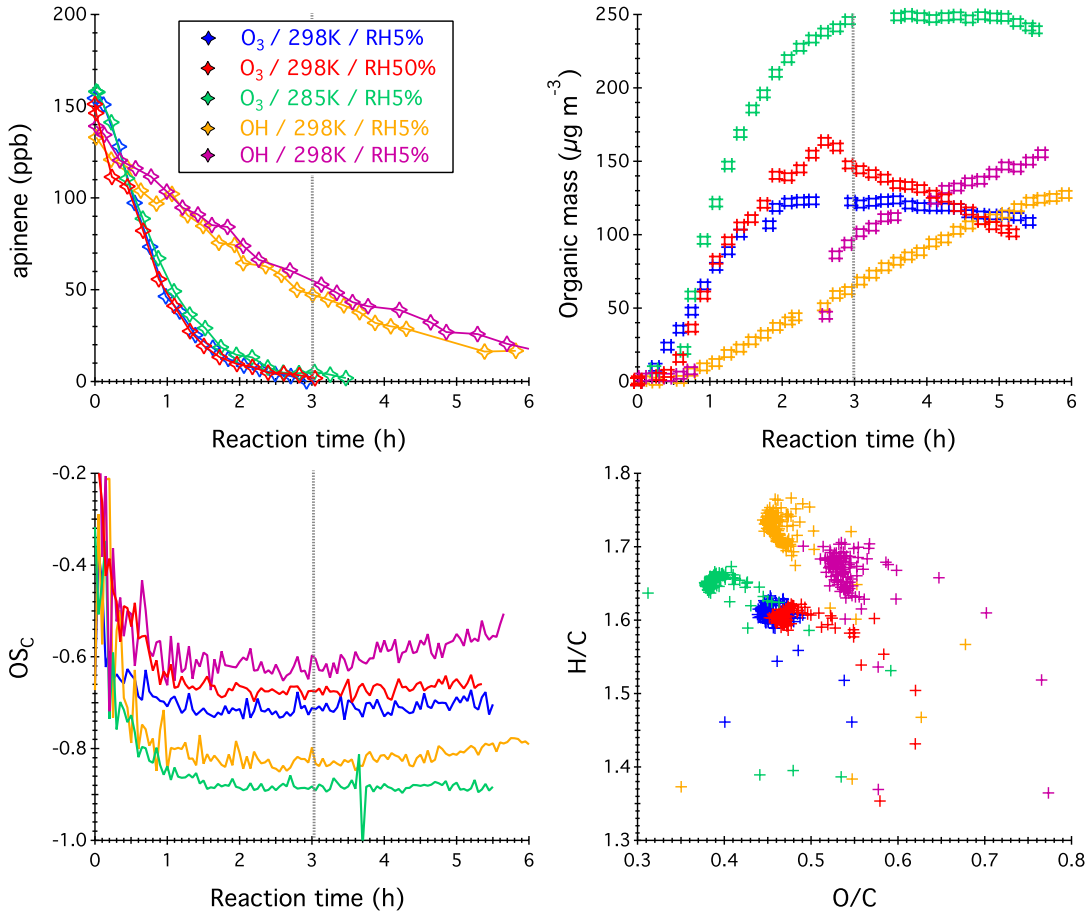

Figure S5. Organic mass concentration and molecular composition of α-pinene SOA. Experimental conditions are listed in *SI Appendix, Table S1*. The gray dashed lines denote the 5-min average time period at which the SOA chemical composition measured by PILS+UPLC/(–)ESI-Q-ToFMS is shown in Figure 1 and Figure 2. (A) GC-FID measured decay of α-pinene due to reaction with O_3 and OH. (B) DMA measured overall organic mass growth. Note that particle wall loss is not applied here in order to directly compare with the total mass of PILS collected suspended particle via the sum of individual compounds. (C) AMS measured average O:C and H:C ratios of α-pinene SOA in the van Krevelen diagram. (D) Progression of the derived oxidation state ($OS_C = 2 \times O/C - H/C$) of α-pinene SOA.

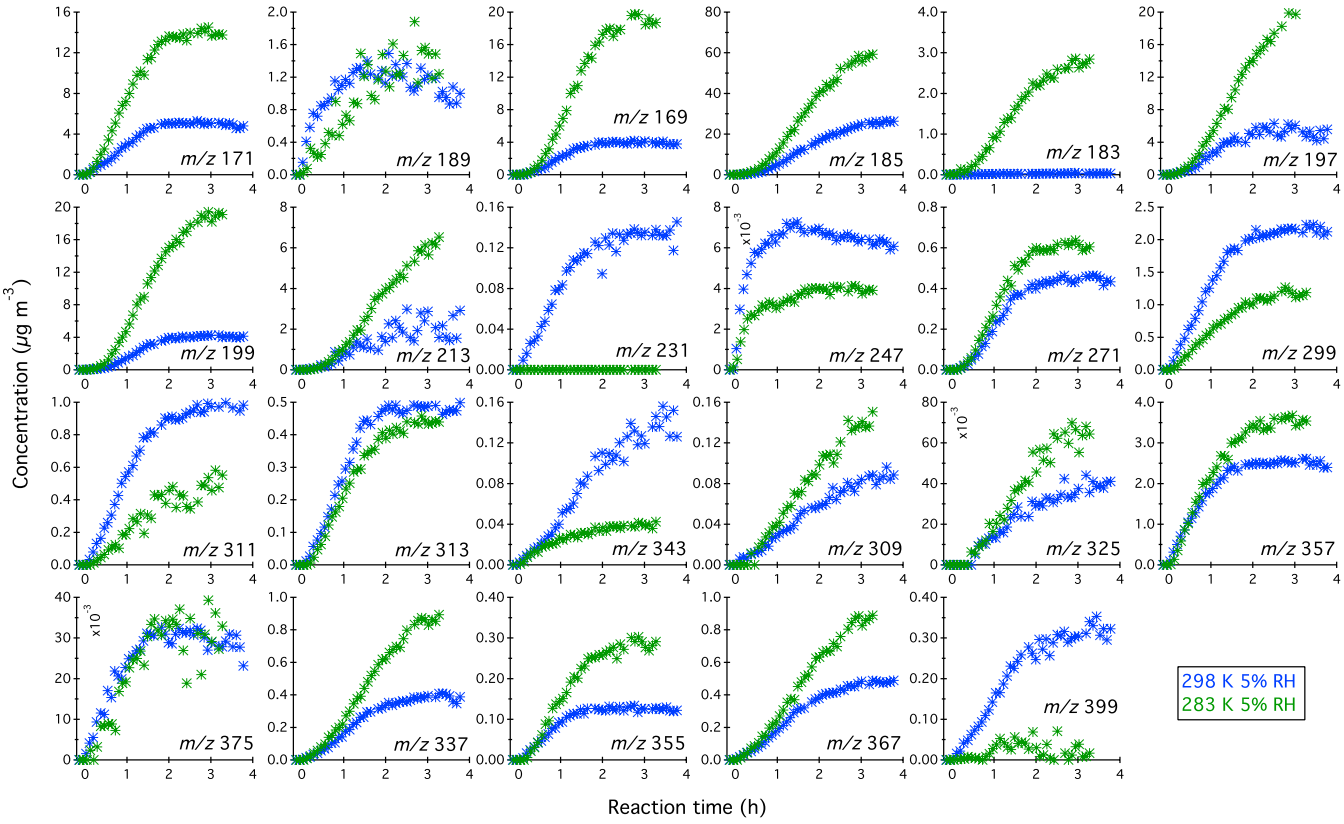

Figure S6. Temporal profiles of α-pinene+O_3 products in the particle phase: temperature effect.

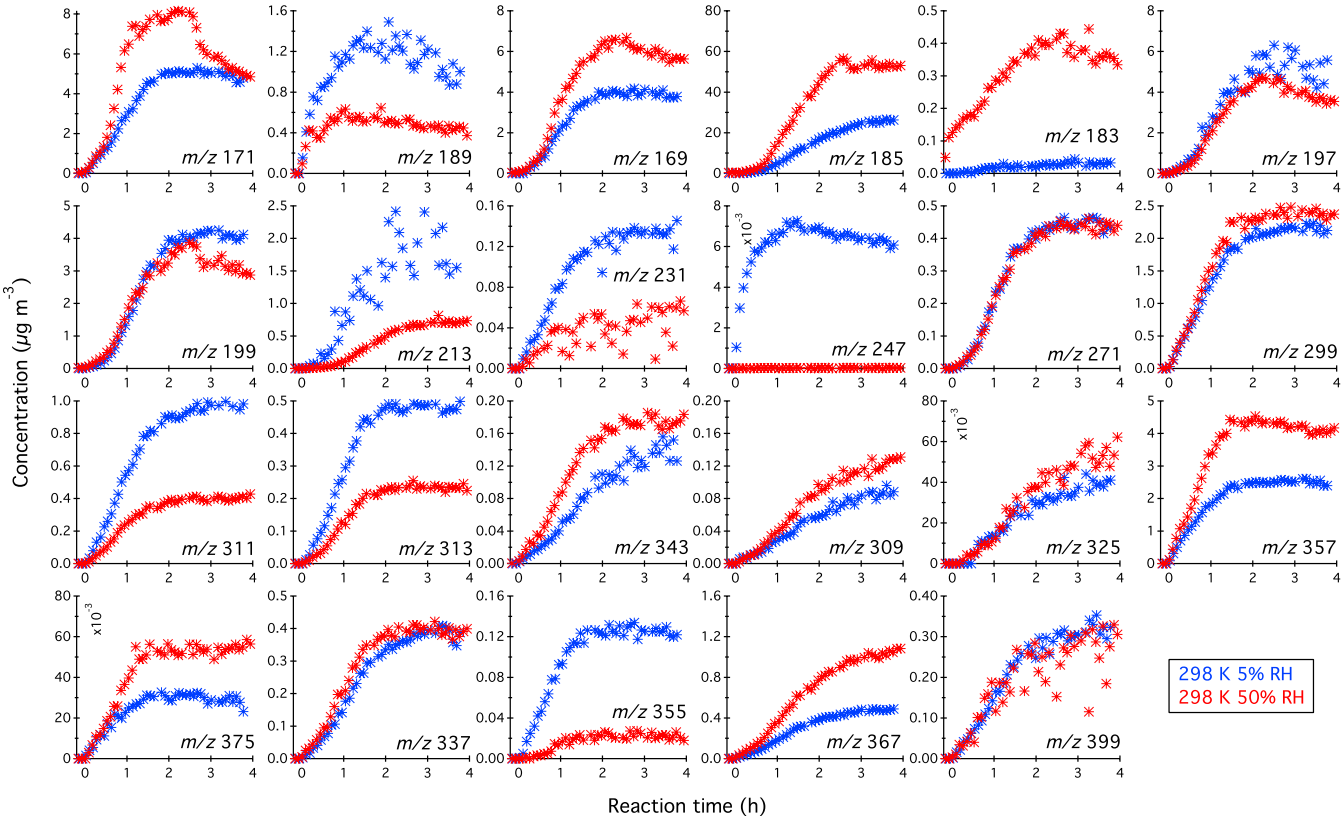

Figure S7. Temporal profiles of α-pinene+O_3 products in the particle phase: relative humidity effect.

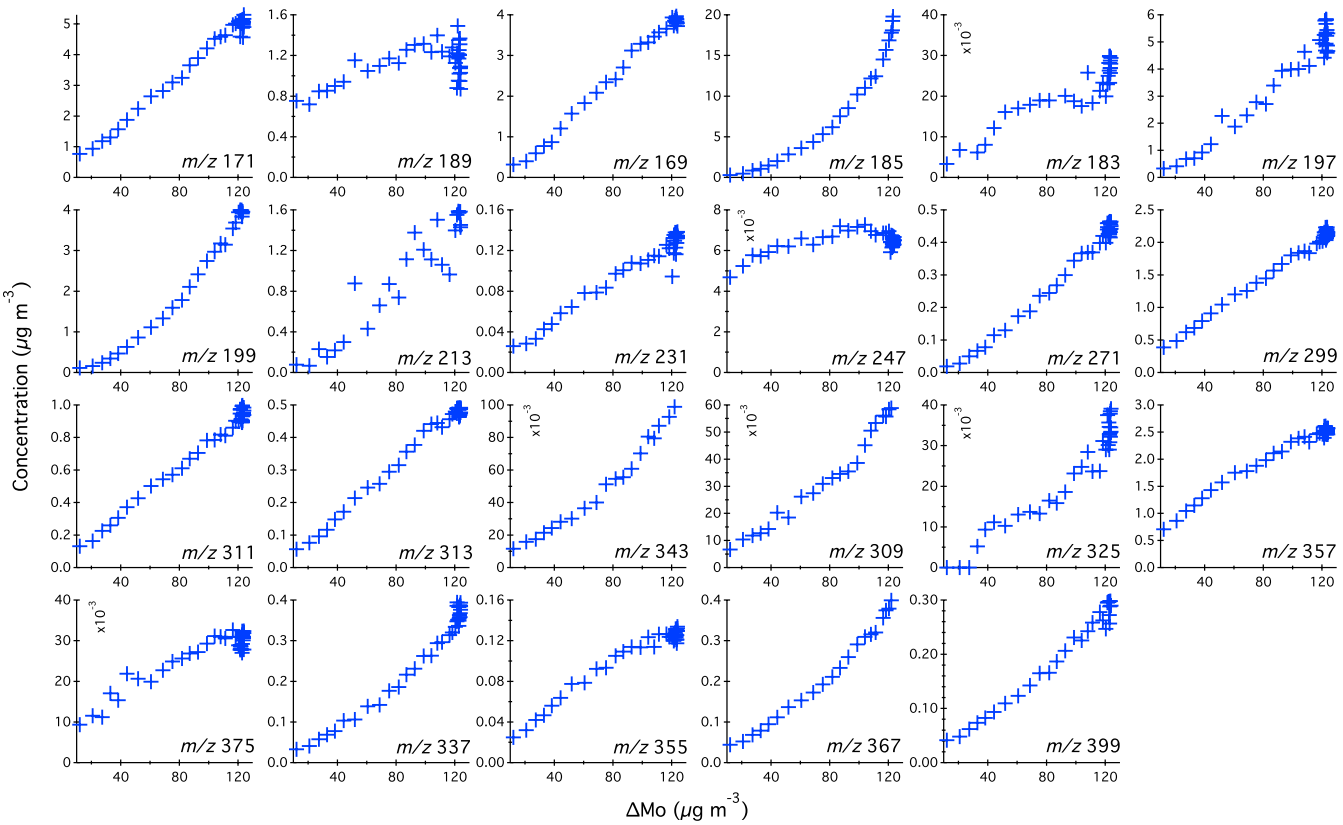

Figure S8. Temporal profiles of α-pinene+O_3 products in the particle phase as a function of total SOA mass.

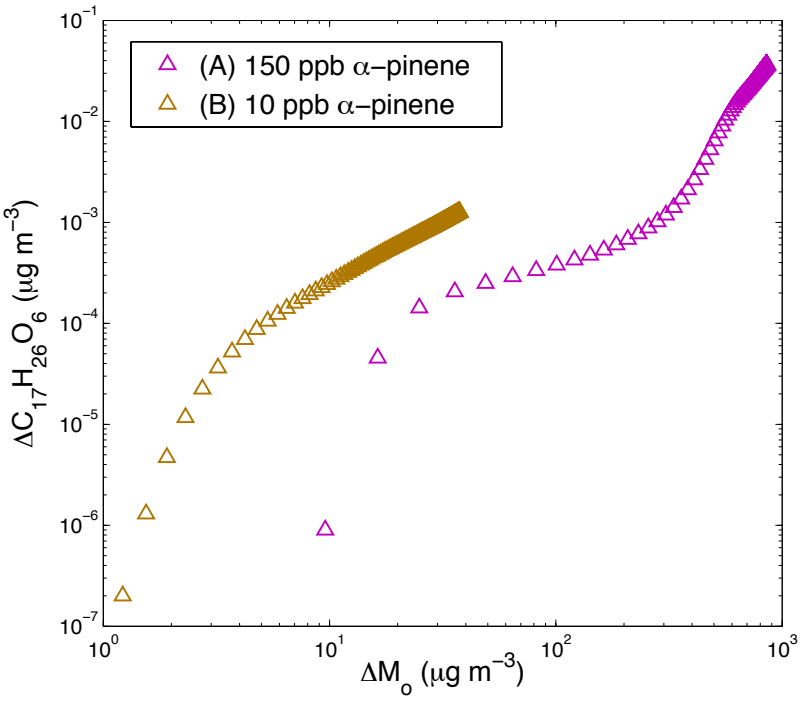

Figure S9. Simulated growth of the $C_{17}H_{26}O_6$ ester dimer in the particle phase under different initial conditions: (A) 150 ppb α-pinene + 200 ppb O_3 and (B) 10 ppb α-pinene + 20 ppb O_3.

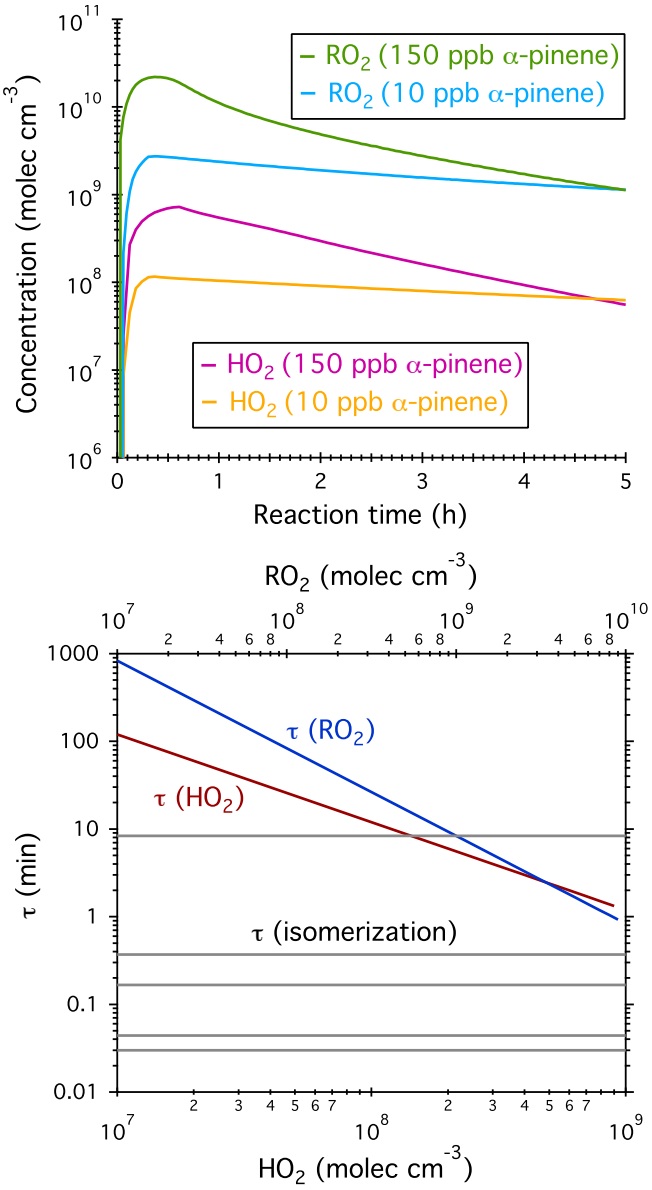

Figure S10. (Upper panel) GECKO-A simulated concentration profiles of RO_2 and HO_2 radicals under initial conditions of 150 ppb α-pinene + 200 ppb O_3 and 10 ppb α-pinene + 20 ppb O_3, respectively. (Lower panel) Estimated lifetimes of RO_2 radical with respect to self/cross combination with RO_2, reaction with HO_2, and H-shift isomerization. The RO_2+RO_2 and RO_2+HO_2 reaction rate constants are obtained from *SI Appendix, Table S4*. The isomerization reaction rate constants are from Crounse et al. (35) and Rissanen et al. (36). It can be seen that by increasing the initial α-pinene mixing ratio from 10 ppb to 150 ppb, the peak RO_2 and HO_2

concentrations are ~9.6 and 5.5 times higher, respectively. The corresponding lifetime of RO_2 with respect to reactions with RO_2/HO_2 decrease by less than an order of magnitude. This change is not sufficient to perturb the dynamics of overall RO_2 chemistry. In other words, the RO_2 isomerization channel is not completely shut down when α-pinene increases from 10 ppb to 150 ppb.

Table S1. Summary of experimental conditions.

Exp. #	T_0 (K)	RH_0 (%)	$[HC]_0$ (ppb)	$[NO_x]_0$ (ppb)	$[O_3]_0$ (ppb)	Oxidants	Seed Aerosol	Initial Seed vol. (μm^3 cm^{-3})	Maximum SOA yield [b]
1	298±2	< 5	154	< DL[a]	~ 200	O_3	$(NH_4)_2SO_4$ Neutral/Dry	73	0.16
2	285±2	< 5	154	< DL	~ 200	O_3	$(NH_4)_2SO_4$ Neutral/Dry	69	0.28
3	298±2	55±2	157	< DL	~ 200	O_3	$(NH_4)_2SO_4$ Neutral/Wet	129	0.21
4	298±2	< 5	133	< DL	~ 3	OH	$(NH_4)_2SO_4$ Neutral/Dry	106	0.29
5	298±2	46±1	139	< DL	~ 3	OH	$(NH_4)_2SO_4$ Neutral/Wet	107	0.31

[a] Detection limits (DL) for O_3, NO, and NO_2 are 0.5 ppb, 0.4 ppb, and 0.4 ppb, respectively. H_2O_2 has an interference on the O_3 detection, increasing the O_3 monitor readout by ~ 2-3 ppb in the current study.
[b] Yield is defined as the mass of organic aerosols produced divided by the mass of hydrocarbon reacted.

Table S2. α-pinene SOA constituents measured by PILS + UPLC/ESI-Q-ToFMS. Chemical standards are available for pinonic acid ($C_{10}H_{16}O_3$). Note that symbols '#' and '∗' denote products generated solely from α-pinene+O_3 and α-pinene+OH reactions, respectively.

Compound (Reference)	Observed *m/z* (–)	RT (min)	*RIE* (Uncertainties)	Molecular formula (error / ppm)	Proposed structure from literatures and this study
Diaterpenylic acid (9, 12, 13, 15) #	189.0745 $[M-H]^-$	3.41	0.65 (± 40.29%)	$C_8H_{14}O_5$ (-9.5 ppm)	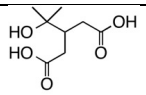
Oxopinonic acid (6) #	197.0793 $[M-H]^-$	3.86	0.99 (± 45.79%)	$C_{10}H_{14}O_4$ (-10.7 ppm)	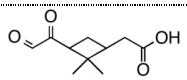
Terpenylic acid (9, 12, 13, 15)	171.0652 $[M-H]^-$	3.96	1.32 (± 65.93%)	$C_8H_{12}O_4$ (-2.9 ppm)	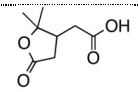
OH-pinonic acid (5, 6, 7, 10, 13, 15)	199.0949 $[M-H]^-$	4.07	2.49 (± 78.04%)	$C_{10}H_{16}O_4$ (-10.5 ppm)	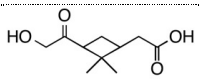
Diaterpenylic acid acetate (9, 12)	231.0907 $[M-H]^-$	4.12	4.32 (± 131.99%)	$C_{10}H_{16}O_6$ (-10.4 ppm)	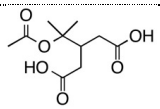
Pinic acid (5, 6, 7, 10, 13, 15)	185.0814 $[M-H]^-$	4.35	0.73 (± 41.90%)	$C_9H_{14}O_4$ (0 ppm)	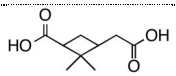
Pinalic acid (5, 6, 7, 10) #	169.0855 $[M-H]^-$	4.58	0.54 (± 38.62%)	$C_9H_{14}O_3$ (-5.9 ppm)	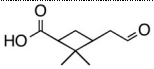
Pinonic acid (5, 6, 7, 10, 13, 15)	183.1023 $[M-H]^-$	4.96	1.00	$C_{10}H_{16}O_3$ (1.1 ppm)	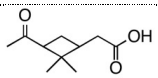
Pinyl-diaterebyl ester (13, 14, 15) #	343.1364 $[M-H]^-$	5.45	5.81 (± 133.49%)	$C_{16}H_{24}O_8$ (-8.5 ppm)	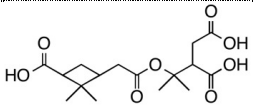
Pinyl-diaterpenyl ester (11, 12, 13, 14, 15) #	357.1547 $[M-H]^-$	5.32	4.19 (± 94.40%)	$C_{17}H_{26}O_8$ (-0.6 ppm)	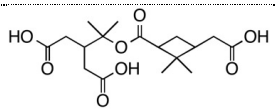
Pinonyl-pinyl ester (8, 13, 14, 15) #	367.1761 $[M-H]^-$	5.98	6.88 (± 162.94%)	$C_{19}H_{28}O_7$ (1.1 ppm)	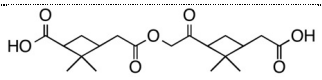
— #	213.0758 $[M-H]^-$	3.81	1.38 (± 51.30%)	$C_{10}H_{14}O_5$ (-2.3 ppm)	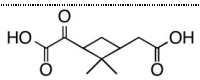
— #	247.0633 $[M-H]^-$	4.55	375.47 (± 56.10%)	$C_{10}H_{16}O_5S$ (-2.8 ppm)	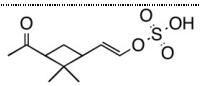
Terpenyl-diaterpenyl ester #	343.1364 $[M-H]^-$	5.05	5.07 (± 116.51%)	$C_{16}H_{24}O_8$ (-8.5 ppm)	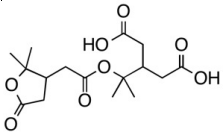

— [#]	355.1740 $[M-H]^-$	5.62	6.69 (± 155.94%)	$C_{18}H_{28}O_7$ (-4.8 ppm)	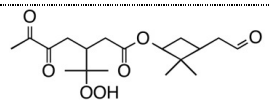
— [#]	309.1708	5.70	As *m/z* 325	$C_{17}H_{26}O_5$ (1.9 ppm)	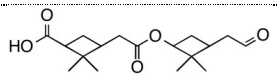
— [#]	299.1486 $[M-H]^-$	5.78	As *m/z* 357	$C_{15}H_{24}O_6$ (-3.0 ppm)	—
— [#]	311.1489 $[M-H]^-$	5.80	As *m/z* 313	$C_{16}H_{24}O_6$ (-1.9 ppm)	—
— [#]	399.1628 $[M-H]^-$	5.88	As *m/z* 343	$C_{19}H_{28}O_9$ (-6.8 ppm)	—
— [#]	375.1654 $[M-H]^-$	5.90	7.05 (± 169.00%)	$C_{17}H_{28}O_9$ (-0.3 ppm)	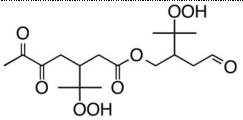
— [#]	325.1646 $[M-H]^-$	6.01	5.58 (± 129.54%)	$C_{17}H_{26}O_6$ (-1.5 ppm)	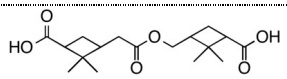
— [#]	313.1622 $[M-H]^-$	6.08	51.64 (± 106.93%)	$C_{16}H_{26}O_6$ (-9.3 ppm)	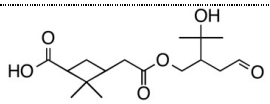
— [#]	337.1634 $[M-H]^-$	6.19	As *m/z* 367	$C_{18}H_{26}O_6$ (-5.0 ppm)	—
— [#]	271.1564 $[M-H]^-$	6.45	As *m/z* 325	$C_{14}H_{24}O_5$ (7.0 ppm)	—

References: (5) Jenkin et al., 2000; (6) Jaoui and Kamens, 2001; (7) Ma et al., 2008; (8) Müller et al., 2008; (9) Claeys et al., 2009; (10) Camredon et al., 2010; (11) Gao et al., 2010; (12) Yasmeen et al., 2010; (13) Kristensen et al., 2013; (14) Kristensen et al., 2014; (15) Witkowski and Gierczak, 2014.

Table S3. CIMS ions that represent gas-phase products generated from ozonolysis and OH-initiated oxidation of α-pinene. Note that symbols '#' and '∗' denote products generated solely from α-pinene+O_3 and α-pinene+OH reactions, respectively.

Molecular weight	Molecular formula	Observed m/z (−)	Proposed structure
116	$C_4H_4O_4$	135 & 201	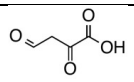
142	$C_8H_{14}O_2$	227	
146	$C_6H_{10}O_4$	231	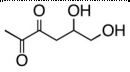
156	$C_8H_{12}O_3$	175 & 241	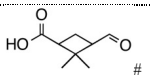
	$C_9H_{16}O_2$	241	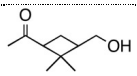
158	$C_7H_{10}O_4$	243	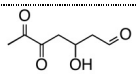
	$C_8H_{14}O_3$	243	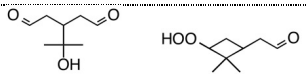
		177 & 243	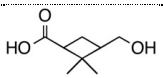
168	$C_{10}H_{16}O_2$	253	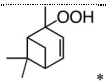
170	$C_9H_{14}O_3$	189 & 255	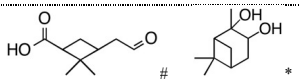
172	$C_9H_{16}O_3$	191&257	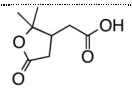
		257	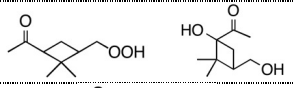
174	$C_7H_{10}O_5$	259	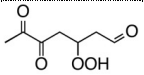
	$C_8H_{14}O_4$	259	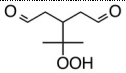
		193 & 259	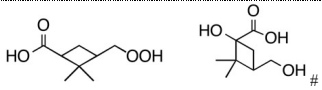
184	$C_{10}H_{16}O_3$	203 & 269	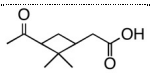
		269	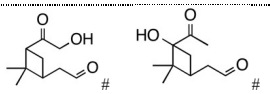

186	$C_9H_{14}O_4$	271	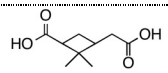
188	$C_{10}H_{20}O_3$	273	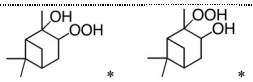
190	$C_8H_{14}O_5$	209 & 275	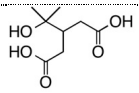
198	$C_{10}H_{14}O_4$	217	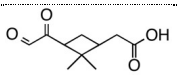
200	$C_{10}H_{16}O_4$	219 & 285	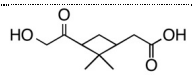
		285	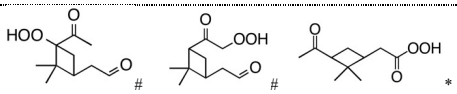
216	$C_{10}H_{16}O_5$	301	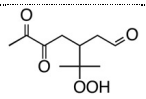
218	$C_{10}H_{18}O_5$	303	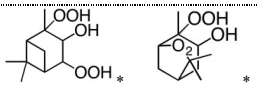

Table S4. Gas- and particle-phase reactions incorporated in simulations. 'G' and 'P' denotes gas-phase and particle-phase reactions, respectively. Acronyms of each species are consistent with those used in MCMv3.2. Concentrations of OH, HO_2, and RO_2 radicals are predicted by GECKO-A using the corresponding experimental conditions (154 ppb α-pinene, 200 ppb O_3, zero NO_x, 298 K, and < 5% RH) as the input.

No.	Reactants	Products			Reaction rate constant (cm^3 $molec^{-1}$ s^{-1})
		Name	Structure	Vapor pressure Vapor wall loss rate	
G01	APINENE + O3	0.6 × APINOOA	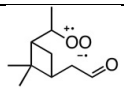	---	$6.3 \times 10^{-16} \times \exp(-580/Temp)$
G02	APINENE + OH	Products	---	---	$1.2 \times 10^{-11} \times \exp(440/Temp)$
G03	APINOOA	0.45 × C109O2	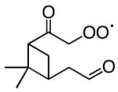	---	10^6
G04	C109O2 + RO2	0.9 × C109O	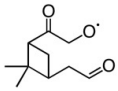	---	2×10^{-12}
G05	C109O	0.8 × C89CO3	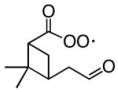	---	10^6
G06	C89CO3 + HO2	0.44 × C89CO2	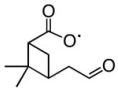	---	$5.2 \times 10^{-13} \times \exp(980/Temp)$
G07	C89CO3 + RO2	0.7 × C89CO2	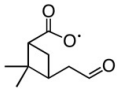	---	5×10^{-12}
G08	C89CO2	0.8 × C811CO3	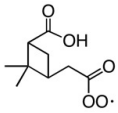	---	10^6
G09	C811CO3 + HO2	0.15 × PINIC	see Fig. 4	9.92×10^{-10} atm 1.88×10^{-5} s^{-1}	$5.2 \times 10^{-13} \times \exp(980/Temp)$
G10	C811CO3 + RO2	0.3 × PINIC	see Fig. 4	9.92×10^{-10} atm 1.88×10^{-5} s^{-1}	5×10^{-12}
G11	2 × C811CO3	0.02 × DIACYLPER	see Fig. 4	8.13×10^{-16} atm 4.36×10^{-4} s^{-1}	5×10^{-12}
G12	PINIC + OH	Products	---	---	7.3×10^{-12}
P01	DIACYLPER	0.5 × ESTER	see Fig. 4	2.62×10^{-12} atm 2.22×10^{-4} s^{-1}	1×10^{-1} (s^{-1})
P02	DIACYLPER	0.5 × PINIC	see Fig. 4	9.92×10^{-10} atm 1.88×10^{-5} s^{-1}	1×10^{-1} (s^{-1})

Appendix G

Isoprene Mechanism

A semi-explicit mechanism for isoprene was developed in a collaborative effort as part of the Environmental Science and Engineering 172 class. The mechanism, given in the following pages, is in a format suitable for use with the Kinetic Preprocessor (KPP) tool. The accompanying table gives the names of the species in the mechanism according to our naming convention along with the corresponding MCM name (where available). Terminal species with no subsequent chemistry are shown in the table with bolded italics.

G.1 Naming Scheme

Names of most species are based on precursor names (ISOP for isoprene, MVK for methyl vinyl ketone, MACR for methacrolein, etc.) that have the same carbon structure. Attached to the precursor name are any additional functional groups, each functional group immediately preceded by the carbon number that the functional group is attached to, in order of ascending location (i.e., functional groups attached to carbon 1 precede functional groups attached to carbon 2). Carbon numbers are those assigned to isoprene. E or Z or c (cis) or t (trans) are attached to the end of the name when appropriate to designate stereoisomers. A Stabilized Criegee Intermediate (SCI) is designated by "ci" before the precursor name and "OO" following. An energetically hot radical is designated by a lowercase "x" at the end of the name. Any functional groups included within the precursor molecule (e.g., ISOP) are not included within the name. Abbreviations for different functional groups are shown in the following table:

Carbonyl	CO
Nitrate	N
Hydroxy	OH
Hydroperoxy	OOH
Epoxide	##O (where ## are the two carbon numbers that the epoxide is attached to)
Alkoxy	O
Peroxy	OO
Double bond	##_ (where ## are the two carbon numbers that the double bond is attached to)

Abbreviations for common species that do not follow this naming convention (such as GLYOX for glyoxal) are also given in the table following the mechanism.

As an example of the naming scheme, an isoprene hydroxyhydroperoxide with the peroxy group attached to carbon #3 and the alcohol group attached to carbon #4 would be named ISOP3OOH4OH. The double bond is not included in the name because this double bond is present in isoprene (the precursor molecule).

G.2 Photolysis Rates

Photolysis rates for photolytic reactions included in the mechanism are the rates calculated when the sun is directly overhead. When input into a box model, this rate can then be scaled with the sunlight intensity at a particular time of day. These rates are multiplied in the mechanism by the variable "SUN" to denote this.

G.3 Lumping of Isomers

In some cases, isomers are lumped to reduce the number of species required. For example, in the NO_3 oxidation section, in some cases the peroxy radicals formed from OH oxidation of the first generation nitrates are lumped together as explained in *Schwantes et al.* (2015).

G.4 Ozone Chemistry

Ozone chemistry is not included (other than an overview of the ozonolysis of isoprene), but will be important for internal hydrogens.

G.5 Simulations

Simulations were carried out using the enclosed mechanism while holding the OH, HO_2, and NO concentrations constant. Maximum sunlight intensity was assumed (i.e., SUN = 1). The temperature was set to 298 K and the relative humidity to 30%. The initial isoprene concentration was set to 30 ppb, and the constant OH concentration was set to 1×10^6 molec cm^{-3}. NO and HO_2 concen-

trations were varied separately in order to investigate the product distributions at different relative concentrations. Product distributions were examined at 6.4 h, when 90% of the initial isoprene had reacted. Figures G.1-G.3 show the distribution of carbon among the most abundant products as a function of NO for three different fixed HO_2 concentrations. Figure G.4 shows distribution of carbon among the most abundant products as a function of HO_2 for a fixed NO concentration. Figure G.5 shows the fractional amount of MVK, MACR, and two 5-carbon hydroxyl carbonyl isomers as a function of NO for a fixed HO_2 concentration.

```
//OH Oxidation of Isoprene************************************************

ISOP + OH = ISOP1OHc : 2.7e-11*exp(390/TEMP)*0.64*0.5;

ISOP + OH = ISOP1OHt : 2.7e-11*exp(390/TEMP)*0.64*0.5;

ISOP + OH = ISOP4OHc : 2.7e-11*exp(390/TEMP)*0.36*0.7;

ISOP + OH = ISOP4OHt : 2.7e-11*exp(390/TEMP)*0.36*0.3;

//Reversible Addition of O2

ISOP4OHt + O2 = ISOP1OO4OHt : 0.357e-12/1.5/1.3;

ISOP4OHt + O2 = ISOP3OO4OH : 0.741e-12;

ISOP4OHc + O2 = ISOP1OO4OHc : 0.23e-12;

ISOP4OHc + O2 = ISOP3OO4OH : 0.741e-12;

ISOP1OHc + O2 = ISOP1OH4OOc : 0.244e-12/1.3;

ISOP1OHc + O2 = ISOP1OH2OO : 0.724e-12;

ISOP1OHt + O2 = ISOP1OH4OOt : 0.298e-12;

ISOP1OHt + O2 = ISOP1OH2OO : 0.724e-12;

ISOP1OO4OHt = ISOP4OHt :

0.357e-12/1.5/1.3/(exp(-((-53.1+34.8)-(416.5-(571.1))/1000*TEMP*0.239006)

/0.0019872/TEMP)/2.6867e19*2.0188/2./1.5*1.3*10);

ISOP3OO4OH = ISOP4OHt :

0.741e-12/(exp(-((-57.1+34.8)-(401.3-(571.1))/1000*TEMP*0.239006)/0.0019872

/TEMP)/2.6867e19*2.3967/2*1.3);

ISOP1OO4OHc = ISOP4OHc :

0.230e-12/(exp(-((-54.7+34.5)-(392.2-(565.8))/1000.*TEMP*0.239006)

/0.0019872/TEMP)/2.6867e19*0.8951*1.3/2.*1.3);

ISOP3OO4OH = ISOP4OHc :

0.741e-12/(exp(-((-57.1+34.5)-(401.3-(565.8))/1000.*TEMP*0.239006)

/0.0019872/TEMP)/2.6867e19*10.1089/10/2.*1.3);

ISOP1OH4OOc = ISOP1OHc :
```

0.244e-12/1.3/(exp(-((-55.5+35.7)-(394.7-(564.0))/1000*TEMP*0.239006)

/0.0019872/TEMP)/2.6867e19*0.5696/1.5);

ISOP1OH2OO = ISOP1OHc :

0.724e-12/(exp(-((-57.1+35.7)-(388.9-(564.0))/1000.*TEMP*0.239006)

/0.0019872/TEMP)/2.6867e19*20.3636/7*3/3.*3*3);

ISOP1OH4OOt = ISOP1OHt :

0.298e-12/(exp(-((-53.3+35.8)-(420.8-(567.4))/1000.*TEMP*0.239006)

/0.0019872/TEMP)/2.6867e19*1.5540*1.3*3/1.15/1.5/1.2);

ISOP1OH2OO = ISOP1OHt :

0.724e-12/(exp(-((-57.1+35.8)-(388.9-(567.4))/1000.*TEMP*0.239006)

/0.0019872/TEMP)/2.6867e19*2.9040*3);

// RO2 + NO

// 1 OH Addition Channels

//Beta isomer

ISOP1OH2OO + NO = NO2 + MVK + HO2 + HCHO : 8.8e-12*0.87;

ISOP1OH2OO + NO = ISOP1OH2N : 8.8e-12*0.13;

//Delta isomers

ISOP1OH4OOc + NO = NO2 + HO2 + ISOP1CO4OH : 8.8e-12*0.87*0.4;

ISOP1OH4OOc + NO = NO2 + ISOP1CO2OO3OOH4OH : 8.8e-12*0.87*0.6;

ISOP1OH4OOc + NO = ISOP1OH4Nc : 8.8e-12*0.13;

ISOP1OH4OOt + NO = NO2 + HO2 + ISOP1CO4OH : 8.8e-12*0.87*0.4;

ISOP1OH4OOt + NO = NO2 + ISOP1CO2OO3OOH4OH : 8.8e-12*0.87*0.6;

ISOP1OH4OOt + NO = ISOP1OH4Nt : 8.8e-12*0.13;

ISOP1CO2OO3OOH4OH + NO = NO2 + MGLYOX + HOCH2CHO + OH : 8.8e-12*0.87;

ISOP1CO2OO3OOH4OH + NO = ISOP1CO2N3OOH4OH : 8.8e-12*0.13;

ISOP1CO2OO3OOH4OH = MVK3OOH4OH + CO + OH : 0.5;

ISOP1CO2OO3OOH4OH + HO2 = ISOP1CO2OOH3OOH4OH : 2.91e-13*exp(1300/TEMP)*0.706;

// 4 OH Addition Channels

//Beta isomer

ISOP3OO4OH + NO = NO2 + MACR + HO2 + HCHO : 8.8e-12*0.87;

ISOP3OO4OH + NO = ISOP3N4OH : 8.8e-12*0.13;

//Delta isomers

ISOP1OO4OHc + NO = NO2 + HO2 + ISOP1OH4CO : 8.8e-12*0.87*0.4;

ISOP1OO4OHc + NO = NO2 + ISOP1OH2OOH3OO4CO : 8.8e-12*0.87*0.6;

ISOP1OO4OHc + NO = ISOP1N4OHc : 8.8e-12*0.13;

ISOP1OO4OHt + NO = NO2 + HO2 + ISOP1OH4CO : 8.8e-12*0.87*0.4;

ISOP1OO4OHt + NO = NO2 + ISOP1OH2OOH3OO4CO : 8.8e-12*0.87*0.6;

ISOP1OO4OHt + NO = ISOP1N4OHt : 8.8e-12*0.13;

ISOP1OH2OOH3OO4CO + NO = NO2 + GLYOX + CH3COCH2OH + OH : 8.8e-12*0.87;

ISOP1OH2OOH3OO4CO + NO = ISOP1OH2OOH3N4CO : 8.8e-12*0.13;

ISOP1OH2OOH3OO4CO = MACR1OH2OOH + CO + OH : 0.5;

ISOP1OH2OOH3OO4CO + HO2 = ISOP1OH2OOH3OOH4CO : 2.91e-13*exp(1300/TEMP)*0.706;

//RO2 + Peroxy Radical

//Self Reactions

ISOP1OH2OO + ISOP1OH2OO = MVK + MVK + HO2 + HO2 + HCHO + HCHO : 6.92e-14;

ISOP3OO4OH + ISOP3OO4OH = MACR + MACR + HO2 + HO2 + HCHO + HCHO :

5.74e-12*0.8;

ISOP3OO4OH + ISOP3OO4OH = ISOP3CO4OH + ISOP3OH4OH : 5.74e-12*0.2;

//Cross Reactions

ISOP1OH2OO + ISOP3OO4OH = MVK + MACR + HO2 + HO2 + HCHO + HCHO : 3.08e-12

*0.9;

ISOP1OH2OO + ISOP3OO4OH = ISOP1OH2OH + ISOP3CO4OH : 3.08e-12*0.1;

ISOP1OH2OO + ISOP1OO4OHc = MVK + HO2 + HCHO + ISOP1O4OHc : 2.49e-12*0.805;

ISOP1OH2OO + ISOP1OO4OHc = ISOP1OH2OH + ISOP1CO4OH : 2.49e-12*(1-0.805);

ISOP1OH2OO + ISOP1OO4OHt = MVK + HO2 + HCHO + ISOP1O4OHt : 2.49e-12*0.805;

ISOP1OH2OO + ISOP1OO4OHt = ISOP1OH2OH + ISOP1CO4OH : 2.49e-12*(1-0.805);

ISOP1OH2OO + ISOP1OH4OOc = MVK + HO2 + HCHO + ISOP1OH4Oc : 2.49e-12*0.805;

ISOP1OH2OO + ISOP1OH4OOc = ISOP1OH2OH + ISOP1OH4CO : 2.49e-12*(1-0.805);

ISOP1OH2OO + ISOP1OH4OOt = MVK + HO2 + HCHO + ISOP1OH4Ot : 2.49e-12*0.805;

ISOP1OH2OO + ISOP1OH4OOt = ISOP1OH2OH + ISOP1OH4CO : 2.49e-12*(1-0.805);

ISOP3OO4OH + ISOP1OO4OHc = MACR + HO2 + HCHO + ISOP1O4OHc : 3.94e-12*0.705;

ISOP3OO4OH + ISOP1OO4OHc = ISOP3OH4OH + ISOP1CO4OH : 3.94e-12*(1-0.705)*0.5;

ISOP3OO4OH + ISOP1OO4OHc = ISOP1OH4OH + ISOP3CO4OH : 3.94e-12*(1-0.705)*0.5;

ISOP3OO4OH + ISOP1OO4OHt = MACR + HO2 + HCHO + ISOP1O4OHt : 3.94e-12*0.705;

ISOP3OO4OH + ISOP1OO4OHt = ISOP3OH4OH + ISOP1CO4OH : 3.94e-12*(1-0.705)*0.5;

ISOP3OO4OH + ISOP1OO4OHt = ISOP1OH4OH + ISOP3CO4OH : 3.94e-12*(1-0.705)*0.5;

ISOP3OO4OH + ISOP1OH4OOc = MACR + HO2 + HCHO + ISOP1OH4Oc : 3.94e-12*0.705;

ISOP3OO4OH + ISOP1OH4OOc = ISOP3OH4OH + ISOP1OH4CO : 3.94e-12*(1-0.705)*0.5;

ISOP3OO4OH + ISOP1OH4OOc = ISOP1OH4OH + ISOP3CO4OH : 3.94e-12*(1-0.705)*0.5;

ISOP3OO4OH + ISOP1OH4OOt = MACR + HO2 + HCHO + ISOP1OH4Ot : 3.94e-12*0.705;

ISOP3OO4OH + ISOP1OH4OOt = ISOP3OH4OH + ISOP1OH4CO : 3.94e-12*(1-0.705)*0.5;

ISOP3OO4OH + ISOP1OH4OOt = ISOP1OH4OH + ISOP3CO4OH : 3.94e-12*(1-0.705)*0.5;

ISOP1OH2OO + CH3OO = MVK + CH3O + HO2 + HCHO : 2.00e-12*0.5;

ISOP1OH2OO + CH3OO = ISOP1OH2OH + HCHO : 2.00e-12*0.5;

ISOP3OO4OH + CH3OO = MACR + CH3O + HO2 + HCHO : 2.00e-12*0.5;

ISOP3OO4OH + CH3OO = ISOP3OH4OH + HCHO : 2.00e-12*0.25;

ISOP3OO4OH + CH3OO = ISOP3CO4OH + CH3OH : 2.00e-12*0.25;

//Alkoxy decomposition

ISOP1OH4Oc = HO2 + ISOP1CO4OH : 1e6*0.4;

ISOP1OH4Oc = ISOP1CO2OO3OOH4OH : 1e6*0.6;

ISOP1OH4Ot = HO2 + ISOP1CO4OH : 1e6*0.4;

ISOP1OH4Ot = ISOP1CO2OO3OOH4OH : 1e6*0.6;

ISOP1O4OHc = HO2 + ISOP1OH4CO : 1e6*0.4;

ISOP1O4OHc = ISOP1OH2OOH3OO4CO : 1e6*0.6;

ISOP1O4OHt = HO2 + ISOP1OH4CO : 1e6*0.4;

ISOP1O4OHt = ISOP1OH2OOH3OO4CO : 1e6*0.6;

ISOP1CO4OH + OH = MVK3OH4OH + CO + OH : 1e-10;

ISOP1OH4CO + OH = MACR1OH2OOH + HO2 + CO : 1e-10;

//RO2 + HO2 Radical

HO2 + ISOP1OH2OO = ISOP1OH2OOH + O2 : 2.22e-13*exp(1300/TEMP)*(1-0.063);

HO2 + ISOP1OH2OO = MVK + OH + HO2 + HCHO : 2.22e-13*exp(1300/TEMP)*0.063;

HO2 + ISOP3OO4OH = ISOP3OOH4OH + O2 : 2.22e-13*exp(1300/TEMP)*(1-0.063);

HO2 + ISOP3OO4OH = MACR + OH + HO2 + HCHO : 2.22e-13*exp(1300/TEMP)*0.063;

HO2 + ISOP1OO4OHc = ISOP1OOH4OH + O2 : 2.22e-13*exp(1300/TEMP);

HO2 + ISOP1OO4OHt = ISOP1OOH4OH + O2 : 2.22e-13*exp(1300/TEMP);

HO2 + ISOP1OH4OOc = ISOP1OH4OOH + O2 : 2.22e-13*exp(1300/TEMP);

HO2 + ISOP1OH4OOt = ISOP1OH4OOH + O2 : 2.22e-13*exp(1300/TEMP);

//Peroxy Isomerization

//1,6-H shift

ISOP1OH4OOc = ISOP1CO4OOHc + HO2 : 0.6*0.333;

ISOP1OH4OOc = CHOCH2OOH + MGLYOX + OH : 0.6*0.333;

ISOP1OH4OOc = MVK3OOH4OOH + CO + OH : 0.6*0.333;

ISOP1OO4OHc = ISOP1OOH4COc + HO2 : 2.5*0.333;

ISOP1OO4OHc = HPAC + GLYOX + OH : 2.5*0.333;

ISOP1OO4OHc = MACR1OOH2OOH + CO + OH : 2.5*0.333;

//1,5-H shift

ISOP1OH2OO = HCHO + OH + MVK : 8.94e10*exp(-9746/TEMP);

ISOP3OO4OH = MACR + OH + HCHO : 1.31e11*exp(-9752/TEMP);

//MVK

MVK + OH = MVK3OO4OH : 2.6e-12*exp(610/TEMP)*0.76;

MVK + OH = MVK3OH4OO : 2.6e-12*exp(610/TEMP)*0.24;

//HO2 Chemistry

MVK3OO4OH + HO2 = CH3CO3 + HOCH2CHO + OH: 1.8178e-13*exp(1300/TEMP)*0.48;

MVK3OO4OH + HO2 = MVK3CO4OH + OH + HO2: 1.8178e-13*exp(1300/TEMP)*0.34;

MVK3OO4OH + HO2 = MVK3OOH4OH: 1.8178e-13*exp(1300/TEMP)*0.18;

MVK3OH4OO + HO2 = MVK3OH4OOH: 1.8178e-13*exp(1300/TEMP)*0.83;

MVK3OH4OO + HO2 = MGLYOX + HCHO: 1.8178e-13*exp(1300/TEMP)*0.17;

MVK3OOH4OH = CH3CO3 + HOCH2CHO + OH : SUN*3e-5;

//NO Chemistry

MVK3OO4OH + NO = CH3CO3 + HOCH2CHO + OH + NO2: 2.7e-12*exp(360/TEMP)*0.97;

MVK3OO4OH + NO = MVK3N4OH : 2.7e-12*exp(360/TEMP)*0.03;

MVK3OH4OO + NO = MGLYOX + HCHO + HO2: 2.7e-12*exp(360/TEMP)*0.93;

MVK3OH4OO + NO = MVK3OH4N: 2.7e-12*exp(360/TEMP)*0.07;

MVK3N4OH = CH3CO3 + HOCH2CHO + NO2 : SUN*6.46e-5;

MVK3OH4N = CH3CO3 + ETHLN + HO2 : SUN*4.21e-5;

//MACR

MACR + OH = MACR1OH2OO : 8.0e-12*exp(380/TEMP)*0.53;

MACR + OH = MACR1OO2OH : 8.0e-12*exp(380/TEMP)*0.02;

MACR + OH = MACR3OO : 8.0e-12*exp(380/TEMP)*0.45;

//HO2 Chemistry

MACR1OH2OO + HO2 = MACR1OH2OOH : 1.5e-11*0.41;

MACR1OH2OO + HO2 = CH3COCH2OH + CO + HO2 + OH + O2 : 1.5e-11*0.59*0.86;

MACR1OH2OO + HO2 = MGLYOX + HCHO + OH + O2 : 1.5e-11*0.59*0.14;

MACR1OO2OH + HO2 = MACR1OOH2OH : 2.0e-11*0.83;

MACR1OO2OH + HO2 = MGLYOX + HCHO + HO2 + OH + O2 : 2.0e-11*0.17;

MACR3OO + HO2 = MACR3OOH : 5.2e-13*exp(980/TEMP)*0.40;

MACR3OO + HO2 = CH3CHCH2 + O2 + CO2 + OH + OH + O2 : 5.2e-13*exp(980/TEMP)

*0.40;

MACR3OO + HO2 = MACR3OH + O3 : 5.2e-13*exp(980/TEMP)*0.20;

//NO Chemistry

MACR1OH2OO + NO = CH3COCH2OH + CO + HO2 + NO2 : 2.7e-12*exp(360/TEMP)*0.94

*0.86;

MACR1OH2OO + NO = MGLYOX + HCHO + NO2 : 2.7e-12*exp(360/TEMP)*0.94*0.14;

MACR1OH2OO + NO = MACR1OH2N : 2.7e-12*exp(360/TEMP)*0.06;

MACR1OO2OH + NO = MGLYOX + HCHO + HO2 + NO2 : 2.7e-12*exp(360/TEMP)*0.94;

MACR1OO2OH + NO = MACR1N2OH : 2.7e-12*exp(360/TEMP)*0.06;

MACR3OO + NO = CH3CHCH2 + OH + O2 + CO2 + NO2 : 8.7e-12*exp(290/TEMP);

MACR3OO + NO2 + M = MPAN + M : KC0*KC1*FC/(KC0+KC1) ;

MPAN + M = MACR3OO + NO2 + M : KP0*KP1*FP/(KP0+KP1) ;

//Isomerization Chemistry

MACR1OH2OO = CH3COCH2OH + CO + OH : 2.9e7*exp(-5297/TEMP);

MACR1OO2OH = HPAC + CO + HO2 : 20;

//MPAN

MPAN + OH = MPAN1OHx : 3e-11;

MPAN1OHx = MPAN1OH2OO : 1e7;

MPAN1OHx = HMMLx : 4e9;

MPAN1OHx = MPAN1OH: 8.18e7;

MPAN1OH = HMMLx: 1e3;

MPAN1OH = MPAN1OH2OO : 1e7;

HMMLx = HMML + NO3 : 1E8*0.75;

HMMLx = CH3COCH2OH + CO + NO3 : 1E8*0.25;

HMPPN + OH = MPAN1OH : 5E-12;

MPAN1OH2OO + NO = MPAN1OH2O + NO2: 9.E-12*0.75;

MPAN1OH2OO + NO = MPAN1OH2N : 9.E-12*0.25;

MPAN1OH2OO + HO2 = MPAN1OH2OOH : 1.4E-11*0.1;

MPAN1OH2OO + HO2 = MPAN1OH2O + OH : 1.4E-11*0.9;

MPAN1OH2O = CH3COCH2OH + CO2 + NO3 : 1E8*0.4;

MPAN1OH2O = HO2 + HCHO + CH3COCOON : 1E8*0.6;

//ISOPOOH

//OH Addition

ISOP1OH2OOH + OH = ISOP1OH23O4OHt: 1.7e-11*exp(390/TEMP)*0.85*0.67;

ISOP1OH2OOH + OH = ISOP1OH23O4OHc: 1.7e-11*exp(390/TEMP)*0.85*0.33;

ISOP3OOH4OH + OH = ISOP1OH23O4OHt : 3.0e-11*exp(390/TEMP)*0.85*0.68;

ISOP3OOH4OH + OH = ISOP1OH23O4OHc : 3.0e-11*exp(390/TEMP)*0.85*0.32;

ISOP1OOH4OH + OH = ISOP12O3OH4OH + OH : 2e-10;

ISOP1OH4OOH + OH = ISOP1OH2OOH3OH4CO + OH : 2e-10;

ISOP1OH2OOH + OH = ISOP1OH2OOH3OH4OO: 1.7e-11*exp(390/TEMP)*0.05;

ISOP1OH2OOH3OH4OO + NO = HOCH2CHO + CH3COCH2OH: 2.7e-12*exp(360/TEMP);

ISOP1OH2OOH3OH4OO + HO2 = ISOP1OH2OOH3OH4OOH: 2.9e-13*exp(1300/TEMP);

ISOP3OOH4OH + OH = ISOP1OO2OH3OOH4OH : 3.0e-11*exp(390/TEMP)*0.10;

ISOP1OO2OH3OOH4OH + NO = CH3COCH2OH + HOCH2CHO : 2.7e-12*exp(360/TEMP)*0.7;

ISOP1OO2OH3OOH4OH + NO = CH3COCH2OH + CHOCH2OOH : 2.7e-12*exp(360/TEMP)*0.3;

ISOP1OO2OH3OOH4OH + HO2 = ISOP1OOH2OH3OOH4OH: 2.9e-13*exp(1300/TEMP);

ISOP1OH2OOH + OH = ISOP1OH2OOH3OO4OH: 1.7e-11*exp(390/TEMP)*0.10;

ISOP1OH2OOH3OO4OH + NO = HOCH2CHO + CH3COCH2OH: 2.7e-12*exp(360/TEMP);

ISOP1OH2OOH3OO4OH + HO2 = ISOP1OH2OOH3OOH4OH: 2.9e-13*exp(1300/TEMP);

ISOP3OOH4OH + OH = ISOP1OH2OO3OOH4OH: 3.0e-11*exp(390/TEMP)*0.05;

ISOP1OH2OO3OOH4OH + NO = CH3COCH2OH + HOCH2CHO: 2.7e-12*exp(360/TEMP);

ISOP1OH2OO3OOH4OH + HO2 = ISOP1OH2OOH3OOH4OH: 2.9e-13*exp(1300/TEMP);

//OH Abstraction

ISOP1OH2OOH + OH = ISOP1OH2OO : 4.6e-12*exp(200/TEMP);

ISOP1OH2OOH + OH = ISOP1CO2OOH : 1.5e-12*exp(200/TEMP)*0.5;

ISOP1OH2OOH + OH = ISO1OH12O : 1.5e-12*exp(200/TEMP)*0.5;

ISOP3OOH4OH + OH = ISOP3OO4OH : 2.1e-12*exp(200/TEMP);

ISOP3OOH4OH + OH = ISOP3CO4OH : 2.0e-12*exp(200/TEMP)*0.32;

ISOP3OOH4OH + OH = ISOP3OOH4CO : 2.0e-12*exp(200/TEMP)*0.68;

//Photolysis

ISOP1OH2OOH = MVK + HCHO + HO2 + OH : SUN*6.5e-6; //Photolysis rate for MHP with sun directly overhead

ISOP3OOH4OH = MACR + HCHO + HO2 + OH : SUN*6.5e-6; //Photolysis rate for MHP with sun directly overhead

//IEPOX

//cis

ISOP1OH23O4OHc + OH = CH3COCH2OH + GLYOX + OH: 0.08*1.52e-11;

ISOP1OH23O4OHc + OH = HOCH2CHO + MGLYOX + OH: 0.17*1.52e-11;

ISOP1OH23O4OHc + OH = ISOP1OH23O4CO + H2O + HO2: 0.21*1.52e-11;

ISOP1OH23O4OHc + OH = MVK3OH4OH + OH + CO: 0.41*1.52e-11;

ISOP1OH23O4OHc + OH = MACR2OH3OH + OH + CO: 0.05*1.52e-11;

ISOP1OH23O4OHc + OH = CH3COCOCH2OH + OH + HCHO: 0.08*1.52e-11;

//trans

ISOP1OH23O4OHt + OH = CH3COCH2OH + GLYOX + OH: 0.16*0.98e-11;

ISOP1OH23O4OHt + OH = HOCH2CHO + MGLYOX + OH: 0.14*0.98e-11;

ISOP1OH23O4OHt + OH = ISOP1OH23O4CO + H2O + HO2: 0.18*0.98e-11;

ISOP1OH23O4OHt + OH = MVK3OH4OH + OH + CO: 0.36*0.98e-11;

ISOP1OH23O4OHt + OH = MACR2OH3OH + OH + CO: 0.09*0.98e-11;

ISOP1OH23O4OHt + OH = CH3COCOCH2OH + OH + HCHO: 0.07*0.98e-11;

//MVK3OH4OH

MVK3OH4OH + OH = CH3COCHOHCHO + HO2 : 0.4*1.10e-11;

MVK3OH4OH + OH = CH3COCOCH2OH + HO2 : 0.6*1.10e-11;

//MACR2OH3OH

MACR2OH3OH + OH = MACR2OH3CO + HO2 : 0.16*3.0e-11;

MACR2OH3OH + OH = CH3COCH2OH + OH + CO2 : 0.84*3.0e-11;

//HPALD

//OH Chemistry

ISOP1CO4OOHc + OH = OH + CO + MVK3OH4OOH : 5e-11;

ISOP1OOH4COc + OH = HO2 + CO + MACR1OOH2OOH : 5e-11;

//Photolysis

ISOP1CO4OOHc = OH + OH + CO + MVKENOL : SUN*4.3e-4; //Photolysis rate with sun directly overhead

ISOP1OOH4COc = OH + OH + CO + MACRENOL : SUN*4.3e-4; //Photolysis rate with sun directly overhead

//Hydroxynitrates

//OH addition to 1,2 ISOPN

ISOP1OH2N + OH = ISOP1OH2N3OO4OH: 0.7*3e-12;

ISOP1OH2N + OH = ISOP1OH2N3OH4OO: 0.3*3e-12;

//NO channel for 1,2ISOPN-OH-OO adduct

ISOP1OH2N3OH4OO + NO = ISOP1OH2N3OH4N: 0.3*8.5e-11;

ISOP1OH2N3OH4OO + NO = MACR1OH2N + HO2 + HCHO + NO2: 0.7*8.5e-11;

ISOP1OH2N3OO4OH + NO = MACR1OH2N + HO2 + HCHO + NO2: 0.75*8.5e-11;

ISOP1OH2N3OO4OH + NO = ISOP1OH2N3N4OH: 0.15*8.5e-11;

ISOP1OH2N3OO4OH + NO = GLYOX + NO2 + NO2 + HO2 + CH3COCH2OH : 0.1*8.5e-11;

ISOP1OH2N3OO4OH = ISOP1CO2N3OOH4OH + HO2 : 0.1;

//HO2 channel for 1,2 ISOPN-OH-OO adduct

ISOP1OH2N3OH4OO + HO2 = ISOP1OH2N3OH4OOH: 0.5*1.6e-11;

ISOP1OH2N3OH4OO + HO2 = MACR1OH2N + HO2 + OH + O2 + HCHO : 0.5*1.6e-11;

ISOP1OH2N3OO4OH + HO2 = MACR1OH2N + HO2 + OH + O2 + HCHO : 0.45*1.6e-11;

ISOP1OH2N3OO4OH + HO2 = ISOP1OH2N3OOH4OH: 0.45*1.6e-11;

ISOP1OH2N3OO4OH + HO2 = GLYOX + CH3COCH2OH + HO2 + OH + O2 + NO2: 0.1

*1.6e-11;

//OH addition to 3,4, ISOPN

ISOP3N4OH + OH = ISOP1OH2OO3N4OH: 0.9*4e-12;

ISOP3N4OH + OH = ISOP1OO2OH3N4OH: 0.1*4e-12;

//NO channel

ISOP1OH2OO3N4OH + NO = MVK3N4OH + HO2 + NO2 + HCHO: 0.74*8.5e-11;

ISOP1OH2OO3N4OH + NO = ISOP1OH2N3N4OH: 0.15*8.5e-11;

ISOP1OH2OO3N4OH + NO = GLYOX + HO2 + NO2 + NO2 + CH3COCH2OH: 0.11*8.5e-11;

ISOP1OO2OH3N4OH = ISOP1OOH2OH3N4CO + HO2: 0.01;

ISOP1OO2OH3N4OH + NO = ISOP1N2OH3N4OH: 0.35*8.5e-11;

ISOP1OO2OH3N4OH + NO = MVK3N4OH + HO2 + NO2 + HCHO: 0.65*8.5e-11;

//HO2 Channel

ISOP1OH2OO3N4OH + HO2 = MVK3N4OH + HO2 + OH + O2 + HCHO: 0.74*1.6e-11;

ISOP1OH2OO3N4OH + HO2 = ISOP1OH2OOH3N4OH: 0.15*1.6e-11;

ISOP1OH2OO3N4OH + HO2 = GLYOX + CH3COCH2OH + HO2 + OH + NO2 + O2: 0.11

*1.6e-11;

ISOP1OO2OH3N4OH + HO2 = ISOP1OOH2OH3N4OH: 0.35*1.6e-11;

ISOP1OO2OH3N4OH + HO2 = MVK3N4OH + HO2 + OH + O2 + HCHO: 0.65*1.6e-11;

//Ozonolysis of Isoprene**

ISOP + O3 = MACR + ciCH2OO : 1.3e-17*(0.41);

ISOP + O3 = MVK + ciCH2OO : 1.3e-17*(0.17);

ISOP + O3 = OH : 1.3e-17*(0.28);

ISOP + O3 = ciMVKOO : 1.3e-17*(0.007);

ISOP + O3 = ciMACROO : 1.3e-17*(0.006);

ISOP + O3 = HO2 : 1.3e-17*(0.16);

ISOP + O3 = HCHO + CO2 + HCHO + CO + CH3OO : 1.3e-17*0.407;

//Reactions of SCI

ciCH2OO + SO2 = H2SO4 : 2e-11;

ciCH2OO + HCOOH = HPMF : 5.6e-11;

ciCH2OO + H2O = HMHP : 0.9e-15*(0.73);

ciCH2OO + H2O = HCOOH : 0.9e-15*(0.21);

ciCH2OO + H2O = HCHO : 0.9e-15*(0.06);

ciCH2OO + H2O = H2O2 : 0.9e-15*(0.06);

ciCH2OO + H2Od = HMHP : 0.8e-12*(0.4);

ciCH2OO + H2Od = HCOOH : 0.8e-12*(0.54);

ciCH2OO + H2Od = HCHO : 0.8e-12*(0.06);

ciCH2OO + H2Od = H2O2 : 0.8e-12*(0.06);

ciCH2OO + O3 = HCHO : 1.0e-12*(0.7);

ciMACROO + H2O = MACR3OHOOH : 1e-15;

ciMVKOO + H2O = MVK2OH2OOH : 1e-15;

//NO3 Oxidation of Isoprene**********

//Isoprene + NO3

ISOP + NO3 = ISOP1N2OO : 3.15E-12*exp(-450/TEMP)*0.42;

ISOP + NO3 = ISOP3OO4N : 3.15E-12*exp(-450/TEMP)*0.045;

ISOP + NO3 = ISOP1N4OO : 3.15E-12*exp(-450/TEMP)*0.45;

ISOP + NO3 = ISOP1OO4N : 3.15E-12*exp(-450/TEMP)*0.085;

//RO2 + HO2

ISOP1N2OO + HO2 = ISOP1N2OOH : 2.91E-13*exp(1300/TEMP)*0.706*0.47;

ISOP1N2OO + HO2 = MVK + OH + HCHO + NO2 : 2.91E-13*exp(1300/TEMP)

*0.706*0.53;

ISOP1N4OO + HO2 = ISOP1N4OOH : 2.91E-13*exp(1300/TEMP)*0.706;

ISOP3OO4N + HO2 = ISOP3OOH4N : 2.91E-13*exp(1300/TEMP)*0.706*0.735;

ISOP3OO4N + HO2 = MACR + OH + HCHO + NO2 : 2.91E-13*exp(1300/TEMP)

*0.706*0.265;

ISOP1OO4N + HO2 = ISOP1OOH4N : 2.91E-13*exp(1300/TEMP)*0.706;

//RO2 + Dominant RO2

ISOP1N2OO + ISOP1N4OO = ISOP1N4CO + ISOP1N2OH : 2.49E-12*0.77*0.5;

ISOP1N2OO + ISOP1N4OO = MVK + HCHO + NO2 + ISOP1N4O : 2.49E-12*0.77*0.5;

ISOP1N2OO + ISOP1N4OO = ISOP1N2O + ISOP1N4O : 2.49E-12*0.195;

ISOP1N2OO + ISOP1N4OO = ISOP1N2OOISOP1N4 : 2.49E-12*0.035;

ISOP1N4OO + ISOP1N4OO = ISOP1N4CO + ISOP1N4OHc : 3.9E-12*0.77*0.4;

ISOP1N4OO + ISOP1N4OO = ISOP1N4CO + ISOP1N4OHt : 3.9E-12*0.77*0.6;

ISOP1N4OO + ISOP1N4OO = ISOP1N4O + ISOP1N4O : 3.9E-12*0.195;

ISOP1N4OO + ISOP1N4OO = ISOP1N4OOISOP1N4 : 3.9E-12*0.035;

ISOP3OO4N + ISOP1N4OO = ISOP3OH4N + ISOP1N4CO : 3.94E-12*0.77*0.5;

ISOP3OO4N + ISOP1N4OO = MACR + HCHO + NO2 + ISOP1N4O : 3.94E-12*0.77*0.5;

ISOP3OO4N + ISOP1N4OO = ISOP3O4N + ISOP1N4O : 3.94E-12*0.195;

ISOP3OO4N + ISOP1N4OO = ISOP3OO4NISOP1N4 : 3.94E-12*0.035;

ISOP1OO4N + ISOP1N4OO = ISOP1CO4N + ISOP1N4OHc : 3.29E-12*0.77*0.5

*0.4;

ISOP1OO4N + ISOP1N4OO = ISOP1CO4N + ISOP1N4OHt : 3.29E-12*0.77*0.5*

0.6;

ISOP1OO4N + ISOP1N4OO = ISOP1OH4Nc + ISOP1N4CO : 3.29E-12*0.77*0.5

*0.4;

ISOP1OO4N + ISOP1N4OO = ISOP1OH4Nt + ISOP1N4CO : 3.29E-12*0.77*0.5

*0.6;

ISOP1OO4N + ISOP1N4OO = ISOP1O4N + ISOP1N4O : 3.29E-12*0.195;

ISOP1OO4N + ISOP1N4OO = ISOP1OO4NISOP1N4 : 3.29E-12*0.035;

//RO2 + CH3OO

ISOP1N2OO + CH3OO= HCHO + ISOP1N2OH : 1.6E-13*0.71*0.5;

ISOP1N2OO + CH3OO= MVK + HCHO + NO2 + CH3O : 1.6E-13*0.71*0.5;

ISOP1N2OO + CH3OO= ISOP1N2O + CH3O : 1.6E-13*0.29;

ISOP1N4OO + CH3OO = ISOP1N4CO + CH3OH : 1.2E-12*0.71*0.5;

ISOP1N4OO + CH3OO = ISOP1N4OHc + HCHO : 1.2E-12*0.71*0.5*0.4;

ISOP1N4OO + CH3OO = ISOP1N4OHt + HCHO : 1.2E-12*0.71*0.5*0.6;

ISOP1N4OO + CH3OO = ISOP1N4O + CH3O : 1.2E-12*0.29;

ISOP3OO4N + CH3OO = ISOP3OH4N + HCHO : 1.4E-12*0.71*0.5;

ISOP3OO4N + CH3OO = MACR + HCHO + NO2 + CH3O : 1.4E-12*0.71*0.5;

ISOP3OO4N + CH3OO = ISOP3O4N + CH3O : 1.4E-12*0.29;

ISOP1OO4N + CH3OO = ISOP1CO4N + CH3OH : 9.8E-13*0.71*0.5;

ISOP1OO4N + CH3OO = ISOP1OH4Nc + HCHO : 9.8E-13*0.71*0.5*0.4;

ISOP1OO4N + CH3OO = ISOP1OH4Nt + HCHO : 9.8E-13*0.71*0.5*0.6;

ISOP1OO4N + CH3OO = ISOP1O4N + CH3O : 9.8E-13*0.29;

//RO2 + CH3CO3

ISOP1N2OO + CH3CO3= MVK + HCHO + NO2 + CH3COO : 1.1E-12;

ISOP1N4OO + CH3CO3= ISOP1N4O + CH3COO : 7.9E-12;

ISOP3OO4N + CH3CO3 = MACR + HCHO + NO2 + CH3COO : 9.6E-12;

ISOP1OO4N + CH3CO3 = ISOP1O4N + CH3COO : 6.7E-12;

//RO2 + NO

ISOP1N2OO + NO = MVK + HCHO + NO2 + NO2 : 2.7E-12*exp(360/TEMP)*0.86;

ISOP1N2OO + NO = ISOP1N2N : 2.7E-12*exp(360/TEMP)*0.14;

ISOP1N4OO + NO = ISOP1N4O + NO2 : 2.7E-12*exp(360/TEMP)*0.86;

ISOP1N4OO + NO = ISOP1N4N : 2.7E-12*exp(360/TEMP)*0.14;

ISOP3OO4N + NO = MACR + HCHO + NO2 + NO2 : 2.7E-12*exp(360/TEMP)*0.86;

ISOP3OO4N + NO = ISOP3N4N : 2.7E-12*exp(360/TEMP)*0.14;

ISOP1OO4N + NO = ISOP1O4N + NO2 : 2.7E-12*exp(360/TEMP)*0.86;

ISOP1OO4N + NO = ISOP1N4N : 2.7E-12*exp(360/TEMP)*0.14;

//RO2 + NO3

ISOP1N2OO + NO3 = MVK + HCHO + NO2 + NO2 : 2.3E-12;

ISOP1N4OO + NO3 = ISOP1N4O + NO2 : 2.3E-12;

ISOP3OO4N + NO3 = MACR + HCHO + NO2 + NO2 : 2.3E-12;

ISOP1OO4N + NO3 = ISOP1O4N + NO2 : 2.3E-12;

//RO = decompose or react with O2

ISOP1N4O + O2 = ISOP1N4CO + HO2 : 2.5E-14*exp(-300/TEMP);

ISOP1O4N + O2 = ISOP1CO4N + HO2 : 2.5E-14*exp(-300/TEMP);

//1,5 H-shift

ISOP1N4O = ISOP1N25_3OO4OH : 3E5;

ISOP1N25_3OO4OH + NO3 = ISOP1N25_3O4OH + NO2 : 2.3E-12;

ISOP1N25_3OO4OH + NO = ISOP1N25_3O4OH + NO2 : 2.7E-12*exp(360

/TEMP);

ISOP1N25_3O4OH + O2 = ISOP1N25_3CO4OH + HO2 : 2.5E-14*exp(-300

/TEMP);

ISOP1N25_3OO4OH + HO2 = ISOP1N25_3OOH4OH : 2.91E-13*exp(1300/TEMP)

*0.706;

ISOP1N25_3OO4OH + ISOP1N4OO = ISOP1N25_3CO4OH + ISOP1N4OHc : 3.94E-12*

0.77*0.5*0.4;

ISOP1N25_3OO4OH + ISOP1N4OO = ISOP1N25_3CO4OH + ISOP1N4OHt : 3.94E-12*

0.77*0.5*0.6;

ISOP1N25_3OO4OH + ISOP1N4OO = ISOP1N25_3OH4OH + ISOP1N4CO : 3.94E-12*

0.77*0.5;

ISOP1N25_3OO4OH + ISOP1N4OO = ISOP1N25_3O4OH + ISOP1N4O : 3.94E-12*

0.195;

ISOP1N25_3OO4OH + ISOP1N4OO = ISOP1N25_3OO4OHISOP1N4 : 3.94E-12*

0.035;

ISOP1N25_3OO4OH + CH3OO = ISOP1N25_3OH4OH + HCHO : 1.4E-12*0.71*0.5;

ISOP1N25_3OO4OH + CH3OO = ISOP1N25_3CO4OH + CH3OH : 1.4E-12*0.71*0.5;

ISOP1N25_3OO4OH + CH3OO = ISOP1N25_3O4OH + CH3O : 1.4E-12*0.29;

ISOP1N25_3OO4OH + CH3CO3 = ISOP1N25_3O4OH + CH3COO : 9.6E-12;

//INP + OH

ISOP1N2OOH + OH = ISOP1N23O4OH : 4.2E-11*0.484;

ISOP1N2OOH + OH = ISOPNOOHOHOO_b1 : 4.2E-11*0.276;

ISOP1N2OOH + OH = ISOPNOOHOHOO_b2 : 4.2E-11*0.24;

ISOP1N4OOH + OH = ISOP1N2OH34O : 1.1E-10*0.201;

ISOP1N4OOH + OH = ISOPNOOHOHOO_d1 : 1.1E-10*0.109;

ISOP1N4OOH + OH = ISOPNOOHOHOO_d2 : 1.1E-10*0.6;

ISOP1N4OOH + OH = ISOP12O3OH4OOH + NO2 : 1.1E-10*0.09;

ISOP3OOH4N + OH = ISOP1OH23O4N : 4.2E-11*0.615;

ISOP3OOH4N + OH = ISOPNOOHOHOO_b1 : 4.2E-11*0.35;

ISOP3OOH4N + OH = ISOPNOOHOHOO_b2 : 4.2E-11*0.035;

ISOP1OOH4N + OH = ISOP12O3OH4N : 1.1E-10*0.447;

ISOP1OOH4N + OH = ISOPNOOHOHOO_d1 : 1.1E-10*0.243;

ISOP1OOH4N + OH = ISOPNOOHOHOO_d2 : 1.1E-10*0.27;

ISOP1OOH4N + OH = ISOP1OOH2OH34O + NO2 : 1.1E-10*0.04;

ISOP1N2OOH + OH = ISOP1N2OO + HO2 : 6.9E-12;

ISOP1N4OOH + OH = ISOP1N4OO + HO2 : 6.9E-12;

ISOP3OOH4N + OH = ISOP3OO4N + HO2 : 6.9E-12;

ISOP1OOH4N + OH = ISOP1OO4N + HO2 : 6.9E-12;

//ISOPNOOHOHOO_b1

ISOPNOOHOHOO_b1 + HO2 = ISOPNOOHOHOOH : 2.91E-13*exp(1300/TEMP)

*0.706*0.27;

ISOPNOOHOHOO_b1 + HO2 = OH + MACR1N2OOH + HCHO + HO2 : 2.91E-13*exp(1300

/TEMP)*0.706*0.13;

ISOPNOOHOHOO_b1 + HO2 = OH + MVK3OOH4N + HCHO + HO2 : 2.91E-13*exp(1300

/TEMP)*0.706*0.02;

ISOPNOOHOHOO_b1 + HO2 = OH + CH3COCH2OH + ETHLN + OH : 2.91E-13*exp(1300

/TEMP)*0.706*0.09;

ISOPNOOHOHOO_b1 + HO2 = OH + PROPNN + HOCH2CHO + OH : 2.91E-13*exp(1300

/TEMP)*0.706*0.49;

ISOPNOOHOHOO_b1 + NO = ISOPNOOHOHN : 2.7E-12*exp(360/TEMP)*0.04;

ISOPNOOHOHOO_b1 + NO = NO2 + MACR1N2OOH + HCHO + HO2 : 2.7E-12

*exp(360/TEMP)*0.17;

ISOPNOOHOHOO_b1 + NO = NO2 + MVK3OOH4N + HCHO + HO2 : 2.7E-12*exp(360

/TEMP)*0.03;

ISOPNOOHOHOO_b1 + NO = NO2 + CH3COCH2OH + ETHLN + OH : 2.7E-12*exp(360

/TEMP)*0.11;

ISOPNOOHOHOO_b1 + NO = NO2 + PROPNN + HOCH2CHO + OH : 2.7E-12*exp(360

/TEMP)*0.65;

//ISOPNOOHOHOO_b2

ISOPNOOHOHOO_b2 + HO2 = ISOPNOOHOHOOH : 2.91E-13*exp(1300/TEMP)*

0.706*0.27;

ISOPNOOHOHOO_b2 + HO2 = OH + MACR1N2OOH + HCHO + HO2 : 2.91E-13*exp(1300

/TEMP)*0.706*0.72;

ISOPNOOHOHOO_b2 + HO2 = OH + MVK3OOH4N + HCHO + HO2 : 2.91E-13*exp(1300

/TEMP)*0.706*0.01;

ISOPNOOHOHOO_b2 + NO = ISOPNOOHOHN : 2.7E-12*exp(360/TEMP)*0.04;

ISOPNOOHOHOO_b2 + NO = NO2 + MACR1N2OOH + HCHO + HO2 : 2.7E-12*exp(360 /TEMP)*0.94;

ISOPNOOHOHOO_b2 + NO = NO2 + MVK3OOH4N + HCHO + HO2 : 2.7E-12*exp(360 /TEMP)*0.02;

//ISOPNOOHOHOO_d1

ISOPNOOHOHOO_d1 + HO2 = ISOPNOOHOHOOH : 2.91E-13*exp(1300/TEMP)* 0.706*0.27;

ISOPNOOHOHOO_d1 + HO2 = OH + MACR1N2OH + HCHO + OH : 2.91E-13*exp(1300 /TEMP)*0.706*0.11;

ISOPNOOHOHOO_d1 + HO2 = OH + MVK3OH4N + HCHO + OH : 2.91E-13*exp(1300 /TEMP)*0.706*0.04;

ISOPNOOHOHOO_d1 + HO2 = OH + HPAC + ETHLN + HO2 : 2.91E-13*exp(1300 /TEMP)*0.706*0.17;

ISOPNOOHOHOO_d1 + HO2 = OH + PROPNN + HPETHNL + HO2 : 2.91E-13*exp(1300 /TEMP)*0.706*0.41;

ISOPNOOHOHOO_d1 + NO = ISOPNOOHOHN : 2.7E-12*exp(360/TEMP)*0.04;

ISOPNOOHOHOO_d1 + NO = NO2 + MACR1N2OH + HCHO + OH : 2.7E-12*exp(360 /TEMP)*0.14;

ISOPNOOHOHOO_d1 + NO = NO2 + MVK3OH4N + HCHO + OH : 2.7E-12*exp(360 /TEMP)*0.06;

ISOPNOOHOHOO_d1 + NO = NO2 + HPAC + ETHLN + HO2 : 2.7E-12*exp(360 /TEMP)*0.23;

ISOPNOOHOHOO_d1 + NO = NO2 + PROPNN + HPETHNL + HO2 : 2.7E-12*exp(360 /TEMP)*0.53;

//ISOPNOOHOHOO_d2

ISOPNOOHOHOO_d2 + HO2 = ISOPNOOHOHOOH : 2.91E-13*exp(1300/TEMP)*

0.706*0.27;

ISOPNOOHOHOO_d2 + HO2 = OH + PROPNN + HPETHNL + HO2 : 2.91E-13*exp(1300 /TEMP)*0.706*0.67;

ISOPNOOHOHOO_d2 + HO2 = OH + HPAC + ETHLN + HO2 : 2.91E-13*exp(1300 /TEMP)*0.706*0.06;

ISOPNOOHOHOO_d2 + NO = ISOPNOOHOHN : 2.7E-12*exp(360/TEMP)*0.04;

ISOPNOOHOHOO_d2 + NO = NO2 + HPAC + ETHLN + HO2 : 2.7E-12*exp(360 /TEMP)*0.08;

ISOPNOOHOHOO_d2 + NO = NO2 + PROPNN + HPETHNL + HO2 : 2.7E-12*exp(360 /TEMP)*0.88;

//INHE + OH

ISOP1N23O4OH + OH = NO2 + ISOP1OH23O4CO : 1.25E-11*0.6;

ISOP1N23O4OH + OH = OH + CO + NO2 + CH3COCOCH2OH : 1.25E-11*0.1;

ISOP1N23O4OH + OH = HO2 + ISOP1N23O4CO : 1.25E-11*0.1;

ISOP1N23O4OH + OH = OH + CO + MACR1N2OH : 1.25E-11*0.1;

ISOP1N23O4OH + OH = OH + GLYOX + PROPNN : 1.25E-11*0.1;

ISOP1OH23O4N + OH = OH + MGLYOX + ETHLN : 1.25E-11*0.2;

ISOP1OH23O4N + OH = OH + CO + MVK3OH4N : 1.25E-11*0.2;

ISOP1OH23O4N + OH = ISOP1CO23O4N + HO2 : 1.25E-11*0.2;

ISOP1OH23O4N + OH = OH + HCHO + CH3COCOCH2N : 1.25E-11*0.1;

ISOP1OH23O4N + OH = ISOP1OH23O4CO + NO2 : 1.25E-11*0.3;

ISOP1N2OH34O + OH = NO2 + ISOP1CO2OH34O : 8.4E-12;

ISOP12O3OH4N + OH = NO2 + ISOP12O3OH4CO : 8.4E-12*0.3;

ISOP12O3OH4N + OH = CH3COCH2OH + CO2 + NO2 + OH + HCHO : 8.4E-12*0.7;

//ICN

ISOP1N4CO + OH = PROPNN + OH + CO + CO : 2E-11;

ISOP1CO4N + OH = MVK3OH4N + CO + OH : 2E-11;

ISOP1N4CO + OH = ISOP12O3OH4CO + NO2 : 1.1E-10*0.09;

ISOP1N4CO + OH = ISOPCONOHOO_d1 : 1.1E-10*0.31;

ISOP1N4CO + OH = ISOPCONOHOO_d2 : 1.1E-10*0.6;

ISOP1CO4N + OH = ISOP1CO2OH34O + NO2 : 1.1E-10*0.04;

ISOP1CO4N + OH = ISOPCONOHOO_d2 : 1.1E-10*0.27;

ISOP1CO4N + OH = ISOPCONOHOO_d1 : 1.1E-10*0.69;

ISOPCONOHOO_d2 = MACR1N2OOH + CO + HO2 : 20*0.86;

ISOPCONOHOO_d2 = MVK3OOH4N + CO + HO2 : 20*0.14;

ISOPCONOHOO_d1 = MACR1N2OOH + CO + OH : 2.9e7*exp(-5297/TEMP)*0.56;

ISOPCONOHOO_d1 = MVK3OOH4N + CO + OH : 2.9e7*exp(-5297/TEMP)*0.44;

ISOPCONOHOO_d1 + HO2 = ISOPCONOHOOH : 2.91E-13*exp(1300/TEMP)*0.706*0.27;

ISOPCONOHOO_d1 + HO2 = MVK3OH4N + OH + HO2 + CO : 2.91E-13*exp(1300
/TEMP)*0.706*0.07;

ISOPCONOHOO_d1 + HO2 = MACR1N2OH + OH + HO2 + CO : 2.91E-13*exp(1300
/TEMP)*0.706*0.08;

ISOPCONOHOO_d1 + HO2 = OH + HO2 + MGLYOX + ETHLN : 2.91E-13*exp(1300
/TEMP)*0.706*0.25;

ISOPCONOHOO_d1 + HO2 = OH + HO2 + PROPNN + GLYOX : 2.91E-13*exp(1300
/TEMP)*0.706*0.32;

ISOPCONOHOO_d1 + NO = ISOPCONOHN : 2.7E-12*exp(360/TEMP)*0.04;

ISOPCONOHOO_d1 + NO = MVK3OH4N + NO2 + HO2 + CO : 2.7E-12*exp(360
/TEMP)*0.09;

ISOPCONOHOO_d1 + NO = MACR1N2OH + NO2 + HO2 + CO : 2.7E-12*exp(360
/TEMP)*0.11;

ISOPCONOHOO_d1 + NO = NO2 + HO2 + MGLYOX + ETHLN : 2.7E-12*exp(360
/TEMP)*0.34;

ISOPCONOHOO_d1 + NO = NO2 + HO2 + PROPNN + GLYOX : 2.7E-12*exp(360

/TEMP)*0.43;

//IHN + OH

ISOP1N2OH + OH = ISOPNOHOHOO_b : 4.2E-11;

ISOP1N4OHc + OH = ISOP12O3OH4OH : 1.1E-10*0.69*0.13;

ISOP1N4OHc + OH = ISOP1N2OO3OH4OH : 1.1E-10*0.69*0.87;

ISOP1N4OHc + OH = ISOP1N2OH3OO4OH : 1.1E-10*0.31;

ISOP1N4OHt + OH = ISOP12O3OH4OH : 1.1E-10*0.69*0.13;

ISOP1N4OHt + OH = ISOP1N2OO3OH4OH : 1.1E-10*0.69*0.87;

ISOP1N4OHt + OH = ISOP1N2OH3OO4OH : 1.1E-10*0.31;

ISOP3OH4N + OH = ISOPNOHOHOO_b : 4.2E-11;

ISOP1OH4Nc + OH = ISOP1OH2OH34O : 1.1E-10*0.31*0.13;

ISOP1OH4Nc + OH = ISOP1OH2OH3OO4N : 1.1E-10*0.31*0.87;

ISOP1OH4Nc + OH = ISOP1OH2OO3OH4N : 1.1E-10*0.69;

ISOP1OH4Nt + OH = ISOP1OH2OH34O : 1.1E-10*0.31*0.13;

ISOP1OH4Nt + OH = ISOP1OH2OH3OO4N : 1.1E-10*0.31*0.87;

ISOP1OH4Nt + OH = ISOP1OH2OO3OH4N : 1.1E-10*0.69;

ISOP1N2OO3OH4OH + HO2 = ISOP1N2OOH3OH4OH : 2.91E-13*exp(1300/TEMP)

*0.706*0.27;

ISOP1N2OO3OH4OH + HO2 = OH + HO2 + PROPNN + HOCH2CHO : 2.91E-13*exp(1300

/TEMP)*0.706*0.73;

ISOP1N2OH3OO4OH + HO2 = ISOP1N2OH3OOH4OH : 2.91E-13*exp(1300/TEMP)

*0.706*0.27;

ISOP1N2OH3OO4OH + HO2 = MACR1N2OH + HCHO + HO2 + OH : 2.91E-13*exp(1300

/TEMP)*0.706*0.73*0.21;

ISOP1N2OH3OO4OH + HO2 = OH + HO2 + PROPNN + HOCH2CHO : 2.91E-13*exp(1300

/TEMP)*0.706*0.73*0.79;

ISOP1OH2OH3OO4N + HO2 = ISOP1OH2OH3OOH4N : 2.91E-13*exp(1300/TEMP)

*0.706*0.27;

ISOP1OH2OH3OO4N + HO2 = OH + HO2 + CH3COCH2OH + ETHLN : 2.91E-13*exp(1300 /TEMP)*0.706*0.73;

ISOP1OH2OO3OH4N + HO2 = ISOP1OH2OOH3OH4N : 2.91E-13*exp(1300/TEMP) *0.706*0.27;

ISOP1OH2OO3OH4N+ HO2 = MVK3OH4N + HCHO + HO2 + OH : 2.91E-13*exp(1300 /TEMP)*0.706*0.73*0.21;

ISOP1OH2OO3OH4N + HO2 = OH + HO2 + CH3COCH2OH + ETHLN : 2.91E-13* exp(1300/TEMP)*0.706*0.73*0.79;

ISOP1N2OO3OH4OH + NO = ISOP1N2N3OH4OH : 2.91E-13*exp(1300/TEMP)*0.706*0.04;

ISOP1N2OO3OH4OH + NO = NO2 + HO2 + PROPNN + HOCH2CHO : 2.91E-13*exp(1300 /TEMP)*0.706*0.96;

ISOP1N2OH3OO4OH + NO = ISOP1N2OH3N4OH : 2.91E-13*exp(1300/TEMP)*0.706*0.04;

ISOP1N2OH3OO4OH + NO = MACR1N2OH + HCHO + HO2 + NO2 : 2.91E-13*exp(1300 /TEMP)*0.706*0.96*0.21;

ISOP1N2OH3OO4OH + NO = NO2 + HO2 + PROPNN + HOCH2CHO : 2.91E-13*exp(1300 /TEMP)*0.706*0.96*0.79;

ISOP1OH2OH3OO4N + NO = ISOP1OH2OH3N4N : 2.91E-13*exp(1300/TEMP)*0.706*0.04;

ISOP1OH2OH3OO4N + NO = NO2 + HO2 + CH3COCH2OH + ETHLN : 2.91E-13*exp(1300 /TEMP)*0.706*0.96;

ISOP1OH2OO3OH4N + NO = ISOP1OH2N3OH4N : 2.91E-13*exp(1300/TEMP)*0.706*0.04;

ISOP1OH2OO3OH4N+ NO = MVK3OH4N + HCHO + HO2 + NO2 : 2.91E-13*exp(1300 /TEMP)*0.706*0.96*0.21;

ISOP1OH2OO3OH4N + NO = NO2 + HO2 + CH3COCH2OH + ETHLN : 2.91E-13 *exp(1300/TEMP)*0.706*0.96*0.79;

ISOPNOHOHOO_b + HO2 = ISOPNOHOHOOH : 2.91E-13*exp(1300/TEMP)*0.706*0.27;

ISOPNOHOHOO_b + HO2 = MVK3OH4N + HCHO + HO2 + OH : 2.91E-13*exp(1300

/TEMP)*0.706*0.17;

ISOPNOHOHOO_b + HO2 = OH + HO2 + CH3COCH2OH + ETHLN : 2.91E-13*exp(1300

/TEMP)*0.706*0.56;

ISOPNOHOHOO_b + NO = ISOPNOHOHN : 2.7E-12*exp(360/TEMP)*0.04;

ISOPNOHOHOO_b + NO = MVK3OH4N + HCHO + HO2 + NO2 : 2.7E-12*exp(360

/TEMP)*0.23;

ISOPNOHOHOO_b + NO = NO2 + HO2 + CH3COCH2OH + ETHLN : 2.7E-12*exp(360

/TEMP)*0.74;

Common name	**Our name**	**MCM Name**
Isoprene	ISOP	C5H8
cis-OH-isoprene-adduct 1 addition	ISOP1OHc	CISOPA
trans-OH- isoprene-adduct 1 addition	ISOP1OHt	TISOPA
cis-OH- isoprene-adduct 4 addition	ISOP4OHc	CISOPC
trans-OH- isoprene-adduct 1 addition	ISOP4OHt	TISOPC
trans-(4,1)-ISOPOO	ISOP1OO4OHt	ISOPCO2
cis-(4,1)-ISOPOO	ISOP1OO4OHc	CISOPCO2
cis-(1,4)-ISOPOO	ISOP1OH4OOc	CISOPAO2
trans-(1,4)-ISOPOO	ISOP1OH4OOt	ISOPAO2
(1,2)-ISOPOOH	ISOP1OH2OOH	ISOPBOOH
(4,3)-ISOPOOH	ISOP3OOH4OH	ISOPDOOH
trans-beta-IEPOX	ISOP1OH23O4OHt	IEPOXB
cis-beta-IEPOX	ISOP1OH23O4OHc	IEPOXB
	ISOP12O3OH4OH	IEPOXC
(1,2)-ISOPOO	ISOP1OH2OO	ISOPBO2
(4,3)-ISOPOO	ISOP3OO4OH	ISOPDO2
	ISOP3CO4OH	HCOC5
	ISO1OH12O	
Dihydroperoxy diol	***ISOP1OH2OOH3OH4OOH***	
HPALD from (1,2)-ISOPOOH	***ISOP1CO2OOH***	
HPALD from (4,3)-ISOPOOH	***ISOP3OOH4CO***	
HPALD from cis-(1,4)-ISOPOO	ISOP1CO4OOHc	C5HPALD1
HPALD from cis-(4,1)-ISOPOO	ISOP1OOH4COc	C5HPALD2
Hydroperoxyacetone	***HPAC***	HYPERACET
	MVK3OOH4OOH	
	MACR1OOH2OOH	
Methacrolein	MACR	MACR
Formaldehyde	***HCHO***	HCHO
Methyl vinyl ketone	MVK	MVK
	MVK3OO4OH	HMVKBO2
	MVK3OH4OO	HMVKAO2
	MVK3OOH4OH	HMVKBOOH
	MVK3OH4OOH	HMVKAOOH
Glycolaldehyde	***HOCH2CHO***	HOCH2CHO
Methylglyoxal	***MGLYOX***	MGLYOX
Peroxyacetyl (PA)	CH3CO3	CH3CO3
	MVK3OH4N	HMVKANO3
Hydroxyacetone (HAC)	***CH3COCH2OH***	ACETOL
Glyoxal	***GLYOX***	GLYOX
	MVK3OH4OH	HO12CO3C4
	MACR2OH3OH	MACROH
	CH3COCOCH2OH	BIACETOH
	MVKENOL	HMVK
	MACRENOL	HMAC
(1,2) isoprene diol	***ISOP1OH2OH***	ISOPBOH

(3,4) isoprene diol	***ISOP3OH4OH***	ISOPDOH
	ISOP1O4OHc	CISOPCO
	ISOP1CO4OH	HC4CCHO
	ISOP1O4OHt	CISOPCO
	ISOP1OH4Oc	CISOPAO
	ISOP1OH4Ot	ISOPAO
	ISOP1OH4CO	HC4ACHO
	ISOP1OH4OH	ISOPAOH
	ISOP1OOH4OH	ISOPCOOH
	ISOP1OH4OOH	ISOPAOOH
	ISOP1OH2OOH3OH4CO	
Methyl peroxy radical	CH3OO	CH3O2
Methoxy radical	***CH3O***	CH3O
Methanol	***CH3OH***	CH3OH
	MACR1OH2OO	MACRO2
	MACR1OO2OH	MACROHO2
	MACR3OO	MACO3
	MACR1OH2OOH	MACROOH
	MACR1OOH2OH	MACROHOOH
	MACR3OOH	MACO3H
	CH3CHCH2	
Methacrylic acid	***MACR3OH***	MACO2H
	MACR1OH2N	
	MACR1N2OH	
Methacryloyl peroxynitrate	MPAN	MPAN
	ISOP1OH2OOH3OH4OO	
	ISOP1OO2OH3OOH4OH	
	ISOP1OOH2OH3OOH4OH	
	MVK3CO4OH	
	MVK3N4OH	MVKNO3
	ISOP1OH23O4CO	
C1 Stabilized Criegee	ciCH2OO	CH2OOE
C4 Stabilized Criegee, structure MACR	ciMACROO	MACROOA
C4 Stabilized Criegee, structure MVK	ciMVKOO	MVKOOA
Formic acid	HCOOH	HCOOH
Hydroxymethyl hydroperoxide	***HMHP***	
Hydroperoxy methyl formate	***HPMF***	CHOOCH2OOH
Water dimer	H2Od	
	ISOP1N2OO	
	ISOP1N4OO	NISOPO2
	ISOP3OO4N	
	ISOP1OO4N	
	ISOP1N2OOH	
	ISOP1N4OOH	NISOPOOH
	ISOP3OOH4N	
	ISOP1OOH4N	
	ISOP1N2OH	
	ISOP3OH4N	

	ISOP1N2O	
	ISOP1N4O	NISOPO
	ISOP3O4N	
	ISOP1O4N	
	ISOP1N2OOISOP1N4	
	ISOP1N4OOISOP1N4	
	ISOP3OO4NISOP1N4	
	ISOP1OO4NISOP1N4	
	ISOP1N4CO	NC4CHO
	ISOP1CO4N	
	ISOP1N2N	
	ISOP1N4N	NISOPNO3
	ISOP3N4N	
	ISOP1N25_3OO4OH	
	ISOP1N25_3OOH4OH	
	ISOP1N25_3OH4OH	
	ISOP1N25_3CO4OH	
	ISOP1N25_3O4OH	
	ISOP1N23O4OH	
	ISOP1OH23O4N	
	ISOP1N2OH34O	
	ISOP12O3OH4N	
	ISOP12O3OH4OOH	
	ISOP1OOH2OH34O	
Acetate anion	CH3COO	
	ISOP1N25_3OO4OHISOP1N4	
Propanone nitrate	***PROPNN***	NOA
	MACR1N2OOH	
Hydroperoxyethanal	***HPETHNL***	
	ISOPNOOHOHOO_b1	
	ISOPNOOHOHOO_b2	
	ISOPNOOHOHOO_d1	
	ISOPNOOHOHOO_d2	
	ISOPNOOHOHOOH	
	ISOPNOOHOHN	
	ISOP12O3OH4CO	
	ISOP1CO2OH34O	
	ISOPCONOHOO_d1	
	ISOPCONOHOO_d2	
	ISOPCONOHOOH	
	ISOPCONOHN	
	ISOP12O3OH4OH	
	ISOPNOHOHOO_b	
	ISOPNOHOHOOH	
	ISOPNOHOHN	
	ISOP1OH2N	ISOPBNO3

	ISOP3N4OH	ISOPDNO3
	ISOP1OH2N3OO4OH	INB1O2
	ISOP1OH2N3OH4OO	INB2O2
	ISOP1OH2N3N4OH	INB1NO3
	ISOP1CO2N3OOH4OH	C526NO3
	ISOP1OH2N3OH4OOH	INB2OOH
	ISOP1OH2OO3OH4N	INAO2
	ISOP1OOH2OH3N4OH	
	ISOP1OH2OOH3N4OH	
	ISOP1OH4Nc	ISOPANO3
	ISOP1OH4Nt	ISOPANO3
	ISOP1N4OHc	ISOPCNO3
	ISOP1N4OHt	ISOPCNO3
	ISOP1OH2OH3OO4N	
	ISOP1OH2N3OH4N	INANO3
	ISOP1OH2N3OOH4OH	INB1OOH
	ISOP1OH2OO3N4OH	INDO2
	ISOP1N2OH3N4OH	INCNO3
	ISOP1OO2OH3N4OH	
	ISOP1OOH2OH3N4CO	
Energetically hot alkyl radical of MPAN	MPAN1OHx	
	MPAN1OH2OO	
Energetically hot HMML (hydroxymethyl methyl-α-lactone)	HMMLx	
Stabilized alkyl radical of MPAN	MPAN1OH	
Hydroxymethyl methyl-α-lactone	***HMML***	HMML
	MPAN1OH2O	
	MPAN1OH2N	
	MPAN1OH2OOH	
2-oxopropanoyl peroxynitrate	***CH3COCOON***	
3-hydroxy-2-methylpropanoyl peroxynitrate	HMPPN	
	CHOCH2OOH	HCOCH2OOH
	ISOP1OH2OOH3OO4OH	
	ISOP1OH2OOH3OOH4OH	
	ISOP1OH2OO3OOH4OH	
	MVK3OOH4N	
Ethanal nitrate	***ETHLN***	NO3CH2CHO
	MACR2OH3CO	
	CH3COCHOHCHO	
1-Hydroperoxy-2-methyl-2-propen-1-ol	***MACR3OHOOH***	
2-Hydroperoxy-3-buten-2-ol	***MVK2OH2OOH***	
	ISOP1N23O4CO	

	ISOP1CO23O4N	
	CH3COCOCH2N	
	ISOP1N2OO3OH4OH	
	ISOP1N2OH3OO4OH	INCO2
	ISOP1OH2OH34O	
	ISOP1N2OOH3OH4OH	
	ISOP1N2OH3OOH4OH	INCOOH
	ISOP1OH2OH3OOH4N	
	ISOP1OH2OOH3OH4N	INAOOH
	ISOP1N2N3OH4OH	
	ISOP1OH2OH3N4N	
	ISOP1CO2OO3OOH4OH	C526O2
	ISOP1CO2OOH3OOH4OH	C526OOH
	ISOP1OH2OOH3OO4CO	C527O2
	ISOP1OH2OOH3N4CO	C527NO3
	ISOP1OH2OOH3OOH4CO	C527OOH

Species in ***bolded italics*** have no subsequent chemistry in model.

Bibliography

Schwantes, R. H., Teng, A. P., Nguyen, T. B., Coggon, M. M., Crounse, J. D., St. Clair, J. M., Zhang, X., Schilling, K. A., Seinfeld, J. H., and Wennberg, P. O.: Isoprene NO3 Oxidation Products from the RO2 + HO2 Pathway, *J. Phys. Chem. A.*, 119, 10158–10171, 2015.

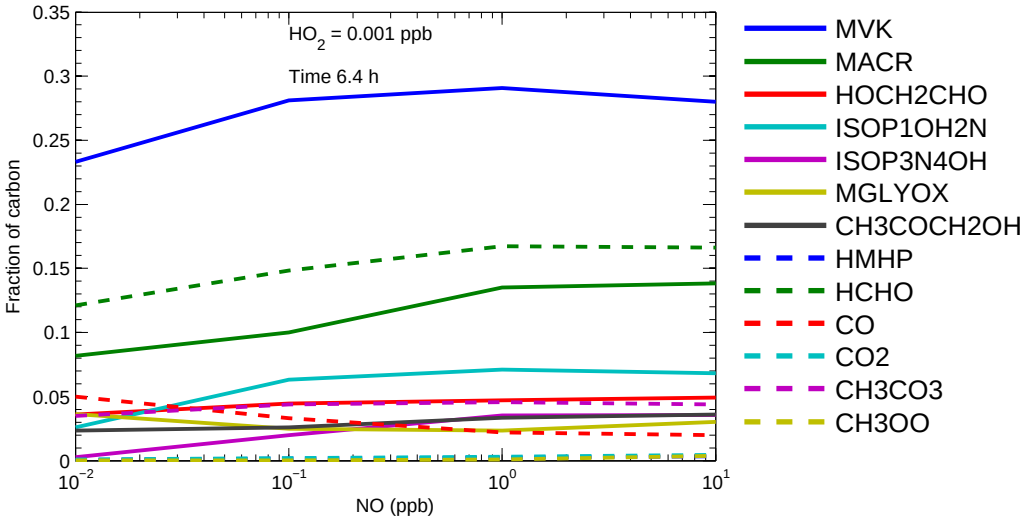

Figure G.1: The most abundant species as a function of fixed NO concentrations, with a fixed HO_2 concentration of 0.001 ppb. Species concentrations are expressed as fractions of the total reacted carbon (species concentrations in molec cm^{-3} are multiplied by the number of carbon atoms in the species, and this quantity is divided by the concentration of isoprene reacted multiplied by 5). Concentrations are shown at 6.4 h, when 90% of the initial isoprene has reacted. See text for initial conditions of the simulations.

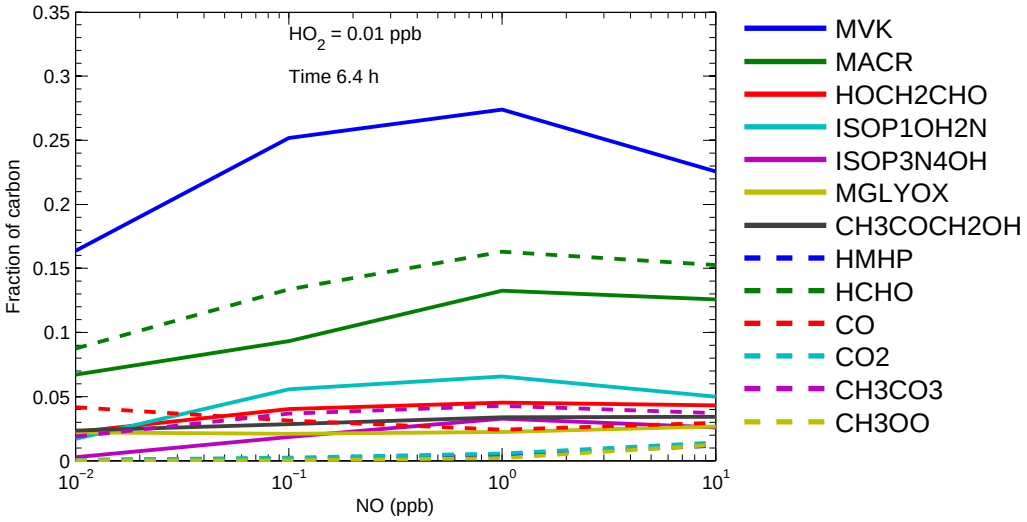

Figure G.2: The most abundant species as a function of fixed NO concentrations, with a fixed HO_2 concentration of 0.01 ppb. Species concentrations are expressed as fractions of the total reacted carbon (species concentrations in molec cm^{-3} are multiplied by the number of carbon atoms in the species, and this quantity is divided by the concentration of isoprene reacted multiplied by 5). Concentrations are shown at 6.4 h, when 90% of the initial isoprene has reacted. See text for initial conditions of the simulations.

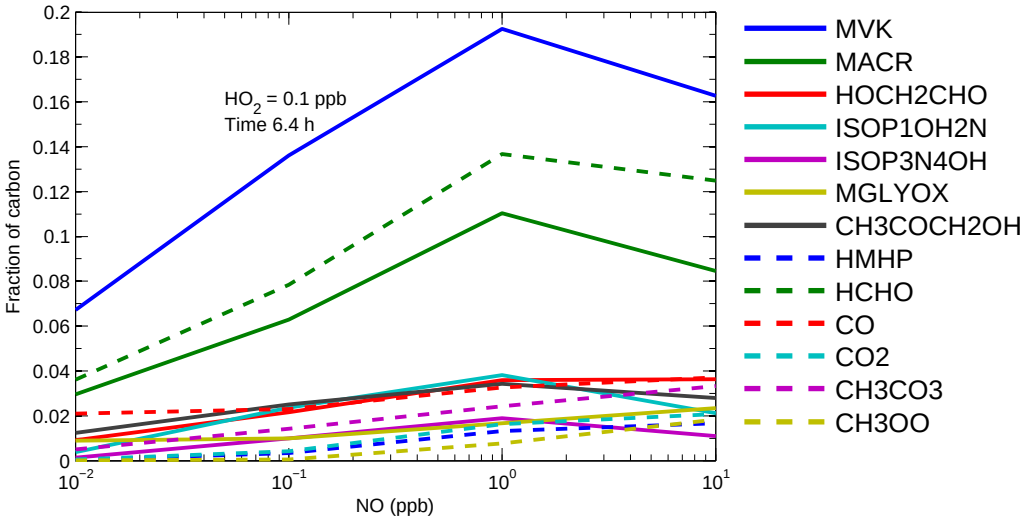

Figure G.3: The most abundant species as a function of fixed NO concentrations, with a fixed HO_2 concentration of 0.1 ppb. Species concentrations are expressed as fractions of the total reacted carbon (species concentrations in molec cm^{-3} are multiplied by the number of carbon atoms in the species, and this quantity is divided by the concentration of isoprene reacted multiplied by 5). Concentrations are shown at 6.4 h, when 90% of the initial isoprene has reacted. See text for initial conditions of the simulations.

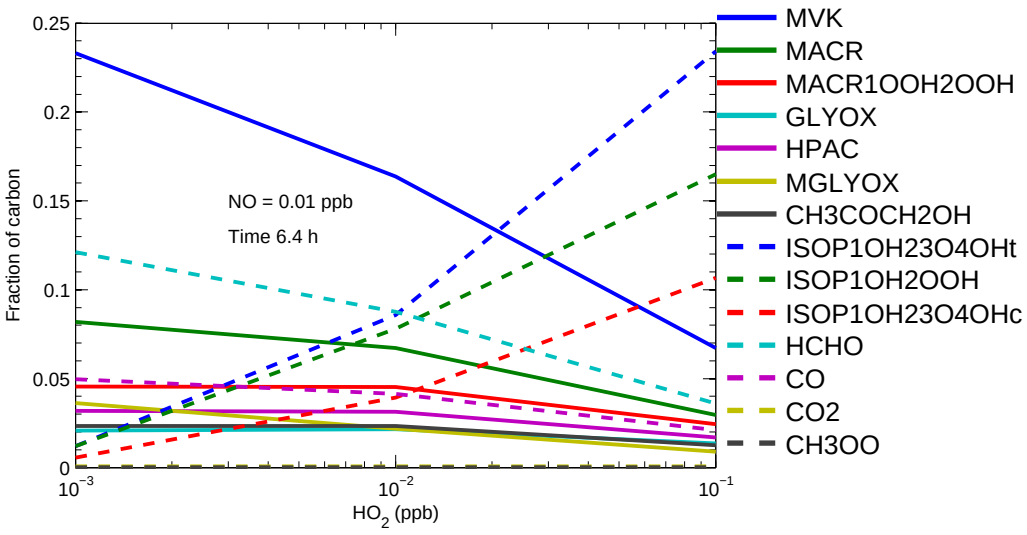

Figure G.4: The most abundant species as a function of fixed HO_2 concentrations, with a fixed NO concentration of 0.1 ppb. Species concentrations are expressed as fractions of the total reacted carbon (species concentrations in molec cm^{-3} are multiplied by the number of carbon atoms in the species, and this quantity is divided by the concentration of isoprene reacted multiplied by 5). Concentrations are shown at 6.4 h, when 90% of the initial isoprene has reacted. See text for initial conditions of the simulations.

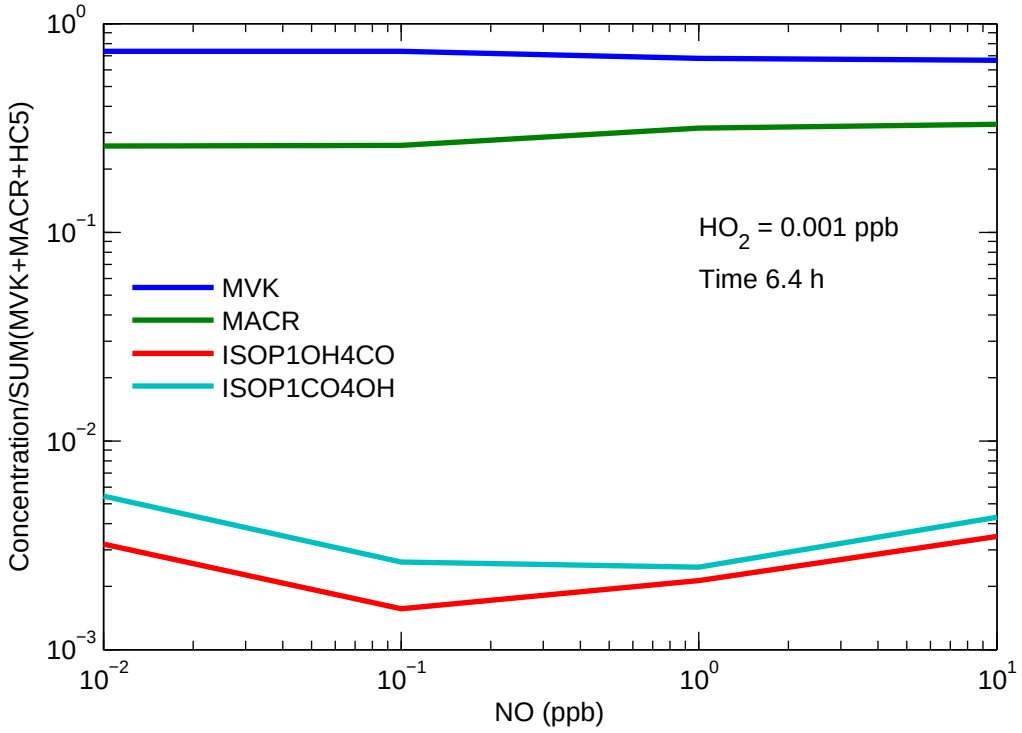

Figure G.5: The fractional amounts of MVK, MACR, and two 5-carbon hydroxyl carbonyl isomers as a function of fixed NO concentrations with a fixed HO_2 concentration of 0.001 ppb. Each concentration is shown as the fraction of the total MVK+MACR+HC5 concentration. Concentrations are shown at 6.4 h, when 90% of the initial isoprene has reacted. See text for initial conditions of the simulations.